*A Thesis Entitled*

# A Geochemical Study of Hydrothermal and Associated Sediments from Eastern Pacific Spreading Centres

by

**Russell Skirrow**

*A Thesis Submitted for the Degree of Doctor of Philosophy in the University of London*

Applied Geochemistry Research Group
Royal School of Mines
Imperial College
London May 1983

*"Besides, what we are pleased to call the riches of a mine are riches relative to a distinction which nature does not recognise. The spars and veinstones which are thrown out in the rubbish of our mines may be as precious in the eyes of nature, as conducive to the great object of her economy, and are certainly as characteristic of mineral veins, as the ores of silver or gold to which we attach so great a value."*

*PLAYFAIR, 1802*

*"The debouching solutions are evidently rich in iron, manganese, arsenic, chromium, lead and cadmium ..... Cobalt, nickel, copper, molybdenum, zinc and lead may also be indigenous to the mineralising emanations. The fact that these elements are less abundant in sediments in areas of high heat flow may be due to variations in residence time for these elements in seawater. The concentrations of the elements in the sediments do not necessarily reflect the absolute concentrations of the various elements in the mineralising emanations and their subsequent mixtures with seawater, but rather the relative rates with which the various constituents are precipitated. Some constituents may indeed have such short residence times that they precipitate just around or in the upper parts of the vents."*

*BOSTROM AND PETERSON, 1969*

## ABSTRACT

A variety of geochemical techniques which include bulk chemical (A.A. and I.C.P. spectrometry, and electron microprobe), stable isotopic and mineralogical (X.R.D., S.E.M. and reflected light microscopy) analysis, have been used to investigate hydrothermal and pelagic sediments on Eastern Pacific Spreading Centres. Special emphasis has been placed on determining the locus of hydrothermal activity, from which elements are dispersed into seawater and selectively fractionated from each other with increasing distance from the source.

Seven study areas on the Galapagos Rift and East Pacific Rise collectively display the full sequence of known hydrothermal precipitates, i.e. sulphides, nontronites, iron and manganese oxides. The association of these hydrothermal deposits is best seen at 86°W on the Galapagos Rift (the GRAFZI area), where inactive sulphide mounds, enriched in iron and copper with a pyrite/chalcopyrite mineralogy, are located along the faulted margins of the axial rift valley. Polymetallic sulphides are flanked by primary hydrothermal iron oxide hummocks, with subordinate manganese oxides. Dredged manganese oxide crusts, with adhering nontronite, complete the sequence of hydrothermal precipitates.

Isotopic studies of GRAFZI sulphides revealed a pyrite/chalcopyrite formation temperature of circa 390°C, with sulphur predominantly supplied by the reduction of seawater sulphate. Anomalous concentrations of manganese and zinc in sediments surrounding the polymetallic sulphides have been produced by dispersion from their hydrothermal source.

Serpentine-rich sediments from the Hess Deep have been investigated and are probably derived by slumping from the steep scarp slopes bounding this topographic low.

Sediments from the East Pacific Rise display an asymmetrical metal distribution about the axis due to westward dispersion of hydrothermal effluent from axial point sources, by mid-depth currents. In the 20°S region, three areas have been found which contain highly anomalous metal concentrations in sediments, including one, and possibly other, polymetallic sulphide deposits. Off-axial hydrothermal processes related to seamount genesis are considered to be important in this area.

ACKNOWLEDGEMENTS

I would like to begin my acknowledgements by thanking my good fortune in finding an applied research project which has provided me with an ideal opportunity of entering the minerals industry and pursuing a career as an explorationist. At one time, 3 years ago, this seemed unlikely, due to the cancellation of my original Indian Ocean manganese nodule program. Since this cancellation, with the loss of a substantial amount of time, a replacement project slowly began to form. The N.E.R.C., through Dr. Tom Huntingdon, have been very understanding throughout my research, and on every occasion have provided a great deal of sensitivity to my requests for financial assistance towards overseas travel and maintenance. I cannot overstate my gratitude to the N.E.R.C.

It is a difficult task to acknowledge everyone that has played a part, major or minor, in the eventual production of this thesis. However, although my parents have never heard of polymetallic sulphide deposits, their constant encouragement, moral support and plain common-sense deserves credit above all others, and it is to them that I wish to dedicate this work.

I have been fortunate enough to work with many professionals, and in this category I place my Supervisor, Dr. D.S. Cronan, who introduced me to marine geochemistry and whose exacting standards and critical nature have made me a better geologist, while teaching me how to organise my own research project.

Dr. Harald Backer (Preussag A.G., F.R.G.) and Dr. Alex Malahoff (National Ocean Survey, U.S.A.) have provided most of my samples and many excellent bathymetric maps, and I am particularly indebted to Dr. Backer for allowing my participation on the 1980 GEOMETEP cruise. A small number of samples were donated by the Institute of Oceanographic Sciences. My research has primarily been carried out in the Applied Geochemistry Research Group but also at Hawaii Institute of Geophysics, Institute of

Geological Sciences and Durham University. Dr. Hsueh-Wen Yeh (H.I.G.), Dr. Max Coleman (I.G.S.) and my old friends Mr. Roy Phillips, Dr. Mustafa Ozcelik and Dr. Rob Taylor (Durham), and Dr. Rob Ixer (Aston University), have been most helpful with regard to my stable isotope and reflected light microscope work.

The A.G.R.G. (and its members) have stimulated my thinking over the past 3½ years and due to it, I feel especially well prepared for new challenges. Outside of the A.G.R.G., I wish to thank Dr. Andy Rankin, Dr. Paul Suddaby, Dr. Harry Shaw and Mr. Ray Curtis for sharing their expertise. Finally, my typist, Dianne Howes, deserves special mention for her willingness to produce quality typescript at speed and to re-type pages where my own errors made this necessary.

TABLE OF CONTENTS


| | Page |
|---|---|
| Abstract | (i) |
| Acknowledgements | (ii) |
| Table of Contents | (iv) |
| List of Figures | (ix) |
| List of Tables | (xv) |
| List of Plates | (xvii) |
| GENERAL INTRODUCTION | 1 |
| PART 1 | |
| THE GALAPAGOS RIFT SPREADING CENTRE | 3 |
| INTRODUCTION | 4 |
| STUDY A CHAPTER 1 | |
| GEOLOGY, BATHYMETRY AND STRUCTURE OF THE GRAFZI AREA, 86°W. | 9 |
| CHAPTER 2 | |
| BULK GEOCHEMISTRY AND MINERALOGY OF SAMPLES FROM THE 86°W AREA. | 15 |
| 2.1 Sulphide Mound Facies. | 15 |
| 2.2 Ferromanganese Oxide Facies. | 24 |
| 2.3 R/V CONRAD Dredge Hauls. | 26 |
| 2.4 Short Sediment Cores. | 40 |
| 2.5 Statistical Analysis. | 46 |
| 2.6 Regional Sedimentation Pattern of the 86°W Area. | 58 |
| a) Sample Description. | 58 |
| b) Bulk Geochemistry. | 60 |
| c) Mineralogy. | 76 |
| d) Statistical Analysis - Additional Elements. | 79 |
| 2.7 Summary and Conclusions. | 88 |
| CHAPTER 3 | |
| REFLECTED LIGHT MICROSCOPE, ELECTRON MICROPROBE AND STABLE ISOTOPE STUDIES. | 90 |
| 3.1 Introduction. | 90 |
| 3.2 Reflected Light Microscopy. | 90 |
| 3.3 Electron Microprobe Investigations. | 109 |

Page

3.3.1 Introduction. 109
3.3.2 Chemistry of the Sulphides. 109
3.3.3 Chemistry of Dive 1001 Fe and Mn Oxides. 111
3.3.4 X-Ray Imaging. 116
3.4a) Quantitative Sulphide Mineralogy. 119
3.4b) Stable Isotopes: $^{34}S/^{32}S$ and $^{18}O/^{16}O$. 126

CHAPTER 4

HYDROTHERMAL PROCESSES AND THE EVOLUTION OF GALAPAGOS RIFT SULPHIDE MOUNDS. 136

4.1 Evolution of a Submarine Hydrothermal Massive Sulphide Deposit. 136
4.2 A Comparison of Modern and Ancient Submarine Sulphide Deposits. 143
4.3 Exploration Criteria for the Discovery of Polymetallic Sulphides. 148

STUDY B CHAPTER 5

THE DE STEIGUER DEEP AREA, 95°W. 150

5.1 Introduction. 150
5.2 Geology and Bathymetry of the 95°W Area. 150
5.3 Sample Description. 153
5.4 Bulk Geochemistry and Mineralogy. 153
5.4.1 Bulk Geochemistry. 153
5.4.2 Mineralogy. 165
5.4.3 Element Associations. 168
5.5 Future Exploration for Hydrothermal Deposits in the De Steiguer Deep Area. 169

STUDY C CHAPTER 6

THE HESS DEEP AREA OF THE GALAPAGOS RIFT AT 101°W, NEAR THE PACIFIC-COCOS-NAZCA PLATE TRIPLE JUNCTION. 171

6.1 Introduction. 171
6.2 Geology, Bathymetry and Structure. 173
6.2.1 The 101°W Area of the Galapagos Rift. 173
6.2.2 The Hess Deep, at 101°30'W. 176
6.3 Sample Description. 177
6.3.1 The 101°W Area of the Galapagos Rift. 177
6.3.2 The Hess Deep. 177

Page

6.4 Bulk Geochemistry. 181
6.4.1 Bulk Geochemistry of 101°W Area Sediments. 181
6.4.2 Bulk Geochemistry of Hess Deep Sediments. 188
6.5 Bulk Mineralogy of Hess Deep Sediments. 194
6.6 The < 0.5 μ Fraction of Hess Deep Sediments. 196
6.6.1 Geochemistry of the < 0.5 μ Fraction. 196
6.6.2 Mineralogy of the < 0.5 μ Fraction. 198
6.7 Scanning Electron Microscopy. 198
6.8 Element Associations.
6.8.1 Sediments from the 101°W Area of the Galapagos Rift. 204
6.8.2 Sediments from the Hess Deep. 204
6.9 Serpentinisation and the Origin of Serpentine-rich Sediments in the Hess Deep. 205
6.9.1 The Serpentinisation Process. 205
6.9.2 The Origin of Hess Deep Serpentine-rich Sediments. 206

PART 2

THE EAST PACIFIC RISE SPREADING CENTRE 210

INTRODUCTION 211

STUDY D CHAPTER 7

THE QUEBRADA FRACTURE ZONE SYSTEM AT 4°S ON THE E.P.R. 214
7.1 Introduction 214
7.2 Geology, Bathymetry and Structure of the 4°S Area. 214
7.3 Sample Description. 217
7.4 Bulk Geochemistry. 217
7.5 Conclusion. 218

STUDY E CHAPTER 8

THE 10°S AREA OF THE EAST PACIFIC RISE. 219
8.1 Introduction. 219
8.2 Geology, Bathymetry and Structure of the 10°S Area. 219
8.3 Sample Description. 221
8.4 Surface Sediment Geochemistry. 221

Page

8.5 Downcore Sediment Geochemistry. 228
8.6 Discussion. 229
8.7 Conclusions. 232

STUDY F CHAPTER 9

THE 13-15°S AREA OF THE EAST PACIFIC RISE. 234
9.1 Introduction. 234
9.2 Geology, Bathymetry and Structure of the 13-15°S Area. 234
9.3 Sample Description. 238
9.3.1 Sediments. 238
9.3.2 Ferromanganese Crusts. 238
9.3.3 Rocks. 241
9.4 Surface Sediment Geochemistry. 241
9.4.1 The Garret Fracture Zone. 241
9.4.2 The 13-15°S Area of the East Pacific Rise. 252
9.5 Geochemistry of Surface and Buried Sediments from the 13-15°S Area. 259
9.6 Discussion. 270
9.7 Conclusions. 272

STUDY G CHAPTER 10

THE 19-21°S AREA OF THE EAST PACIFIC RISE. 273
10.1 Introduction. 273
10.2 Geology, Bathymetry and Structure of the 19-21°S Area. 273
10.3 Sample Description. 279
10.3.1 Sediments. 279
10.3.2 Ferromanganese Oxide Crusts. 282
10.4 Surface Sediment Geochemistry. 282
10.5 Geochemistry of Surface and Buried Sediments from the 19-21°S Area. 300
10.6 Discussion of 19-21°S Area Hydrothermal Activity. 305
10.7 Conclusions. 307

PART 3

CHAPTER 11

SUMMARY AND CONCLUSIONS. 309
11.1 The Galapagos Rift. 310
11.2 The East Pacific Rise. 312

| | | Page |
|---|---|---|
| | APPENDICES | 315 |
| Appendix A : | Sample Collection. | 316 |
| Appendix B : | Analytical Techniques. | 318 |
| Appendix B.1: | General Element Determinations (Using the GEN HF Attack). | 318 |
| Appendix B.2: | The Determination of $SiO_2$ (Using the ROCK Attack). | 319 |
| Appendix B.3: | The Determination of As, Sb and Bi (by Volatile Hydride Generation). | 319 |
| Appendix B.4: | Clay Mineral Isolation. | 320 |
| Appendix B.5: | Mineralogical Determinations. | 322 |
| Appendix B.6: | Stable Isotope Determinations. | 322 |
| Appendix C : | Bulk Geochemical Data. | 323 |
| Appendix D : | Colour Coding Systems. | 323 |
| Appendix E : | Data Handling. | 324 |
| Appendix F : | Quality Control. | 328 |
| | REFERENCES | 331 |

# LIST OF FIGURES


| | | Page |
|---|---|---|
| 1. | Location of the Galapagos Rift. Study areas A, B, C shown. | 5 |
| 1.1 | Bathymetric map of the Galapagos Rift at 86°W, with ALVIN dives arrowed. Massive sulphides encountered during Dive 1001. | 8 |
| 1.2 | Medium resolution bathymetric map of the Galapagos Rift Valley, constructed from U.S. Navy S.A.S.S. data. | 10 |
| 1.3 | High resolution bathymetric map of the Galapagos Rift Area. | 11 |
| 1.4 | Schematic diagram of polymetallic sulphide stacks of the Galapagos Rift, 85°50'W. | 13 |
| 2.3.1 | X.R.D. chart of GRAFZI dredged manganese crusts with adhering clay mineral. | 32 |
| 2.4.1 | Core descriptions for Dive 1002 Stations 1 and 2. | 39 |
| 2.5.1 | Scatterplot: Cu vs Ag - sulphides. | 47 |
| 2.5.2 | Scatterplot: Fe vs Mn - Mn crusts. | 47 |
| 2.5.3 | Scatterplot: Mn vs Ni - Mn crusts. | 48 |
| 2.5.4 | Scatterplot: Ni vs Zn - Mn crusts. | 48 |
| 2.5.5 | Scatterplot: Ni vs Cu - Mn crusts. | 49 |
| 2.5.6 | Scatterplot: Cu vs Zn - Mn crusts. | 49 |
| 2.5.7 | Scatterplot: Al vs Co - carbonates. | 50 |
| 2.5.8 | Scatterplot: Al vs $Log_{10}$ Ni - carbonates. | 51 |
| 2.5.9 | Scatterplot: Al vs Cu - carbonates. | 52 |
| 2.5.10 | Scatterplot: Al vs Zn - carbonates. | 53 |
| 2.5.11 | Scatterplot: Al vs Ti - total batch. | 54 |
| 2.6.1 | Station locations for the Galapagos Rift 86°W area. | 56 |
| 2.6.2 | Core description of 131K. | 57 |
| 2.6.3 | Distribution of Fe, Mn, Cu, Zn in surface sediments from the Galapagos Rift at 86°W. | 59 |
| 2.6.4 | Element distribution/dispersion - perpendicular to the strike of the Galapagos Rift. | 61 |

| | | Page |
|---|---|---|
| 2.6.5 | Distribution of Mg, Al, Ti, V in surface sediments from the Galapagos Rift at 86°W. | 65 |
| 2.6.6 | Distribution of Co, Li in surface sediments from the Galapagos Rift at 86°W. | 66 |
| 2.6.7 | Distribution of Ni, Pb in surface sediments from the Galapagos Rift at 86°W. | 68 |
| 2.6.8 | Scatterplot to show $CaCO_3$ versus water depth. | 69 |
| 2.6.9.a) | Downcore element variations in 131K. | 71 |
| b) | Downcore element variations in 131K. | 72 |
| 2.6.10 | X.R.D. clay mineralogy of the <0.5μ fraction of sediments from the Galapagos Rift, 86°W. | 77 |
| 2.6.11a) | Scatterplot of $SiO_2$ vs Li and Al vs Li. | 82 |
| b) | Frequency distributions of Li, $SiO_2$ and Al. | 83 |
| 2.6.12a) | Scatterplot of $SiO_2$ vs V and Fe vs V. | 84 |
| b) | Frequency distributions of V and Fe | 85 |
| 3.2.1 | Hydrothermal mound paragenesis. | 105 |
| 3.4.1 | % Peak Height Ratio versus % chalcopyrite for the 8 samples subjected to calibrated X.R.D. | 117 |
| 3.4.2 | $\delta^{34}S$ vs % chalcopyrite/pyrite. | 129 |
| 4.1.1 | Idealised model for 86°W sulphide mound formation. | 140 |
| 4.1.2 | Sub-surface hydrothermal convection at 86°W. | 142 |
| 4.2.1 | Comparative sulphur isotopic data for some stratiform massive sulphide deposits associated with submarine volcanism. | 146 |
| 5.1.1 | Station locations in the De Steiguer Deep Area (95°W) on the Galapagos Rift. | 151 |
| 5.2.1 | Bathymetry of the De Steiguer Deep and surrounding area. | 152 |
| 5.4.1 | Mn distribution in surface sediments from the 95°W area. | 156 |
| 5.4.2. | Fe distribution in surface sediments from the 95°W area. | 157 |

| | | Page |
|---|---|---|
| 5.4.3 | Cu distribution in surface sediments from the 95°W area. | 158 |
| 5.4.4 | Zn distribution in surface sediments from the 95°W area. | 159 |
| 5.4.5 | Co distribution in surface sediments from the 95°W area. | 160 |
| 5.4.6 | Ni distribution in surface sediments from the 95°W area. | 161 |
| 5.4.7 | Pb distribution in surface sediments from the 95°W area. | 162 |
| 5.4.8 | Element variation with depth in core 147K. | 164 |
| 6.1.1 | Station locations in the 101°W area of the Galapagos Rift. | 172 |
| 6.2.1 | Bathymetry of the 101°W area of the Galapagos Rift. | 174 |
| 6.2.2 | Coring stations in the Hess Deep. | 175 |
| 6.3.1 | Core descriptions for stations taken in the Hess Deep. | 178 |
| 6.4.1 | Scatterplot of $CaCO_3$ versus water depth. | 182 |
| 6.4.2 | Fe/Mn ratios in surface sediments from the 101°W area. | 184 |
| 6.4.3 | Cu in surface sediments from the 101°W area. | 185 |
| 6.4.4 | Zn in surface sediments from the 101°W area. | 186 |
| 6.4.5 | Element variation with depth in core 188K. | 189 |
| 6.4.6 | Element variation with depth in core 10173. | 190 |
| 6.4.7 | Element variation with depth in core 10174. | 191 |
| 6.5.1 | X-ray diffraction on sediment from core 10178. | 193 |
| 6.9.1 | Cross section of Hess Deep showing the possible source of serpentine-rich sediments. | 208 |
| 2. | The seven study areas on the E.P.R. and Galapagos Rift (A - G). | 212 |
| 7.2.1 | Regional structure and plate tectonic setting of the E.P.R. between the Triple Junction and the Quebrada/ Gofar Transform Zone. | 215 |
| 7.2.2 | Bathymetry of the Quebrada Fracture Zone located in the 4°S area of the E.P.R. | 216 |
| 8.2.1 | Bathymetry and station locations in the 10°S area of the E.P.R. | 220 |
| 8.4.1 | Fe in surface sediments from the 10°S area. | 222 |
| 8.4.2 | Mn in surface sediments from the 10°S area. | 223 |
| 8.4.3 | Cu in surface sediments from the 10°S area. | 224 |
| 8.4.4 | Zn in surface sediments from the 10°S area. | 225 |

| | | Page |
|---|---|---|
| 9.1.1 | Station locations in the 13-15°S area of the E.P.R. | 235 |
| 9.2.1 | Bathymetry of the Garret Fracture Zone at 13°30'S, on the E.P.R. | 236 |
| 9.4.1 | The distribution of $CaCO_3$ in Garret Fracture Zone surface sediments. | 242 |
| 9.4.2 | The distribution of Fe in Garret Fracture Zone surface sediments. | 242 |
| 9.4.3 | The distribution of Mn in Garret Fracture Zone surface sediments. | 243 |
| 9.4.4 | The distribution of Cu in Garret Fracture Zone surface sediments. | 243 |
| 9.4.5 | The distribution of Zn in Garret Fracture Zone surface sediments. | 244 |
| 9.4.6 | The distribution of Ni in Garret Fracture Zone surface sediments. | 244 |
| 9.4.7 | The distribution of P in Garret Fracture Zone surface sediments. | 246 |
| 9.4.8. | The distribution of P/La in Garret Fracture Zone surface sediments. | 246 |
| 9.4.9. | Surface sediment locations in the 13-15°S area of the E.P.R. | 250 |
| 9.4.10 | Fe in 13-15°S area surface sediments. | 251 |
| 9.4.11 | Mn in 13-15°S area surface sediments. | 251 |
| 9.4.12 | Cu in 13-15°S area surface sediments. | 253 |
| 9.4.13 | Zn in 13-15°S area surface sediments. | 253 |
| 9.4.14 | Ni in 13-15°S area surface sediments. | 254 |
| 9.4.15 | Cu/Zn in 13-15°S area surface sediments. | 254 |
| 9.4.16 | P/La in 13-15°S area surface sediments. | 256 |
| 9.4.17 | Plot of $CaCO_3$ versus water depth in 13-15°S area surface sediments. | 256 |
| 9.4.18 | Elements and element ratios in surface sediments versus distance from the E.P.R. crest along latitude line 14°50'S. | 258 |

| | | Page |
|---|---|---|
| 9.5.1 | Fe vs Mn in 13-15°S area sediments. | 261 |
| 9.5.2 | Cu vs Fe in 13-15°S area sediments. | 261 |
| 9.5.3 | Zn vs Mn in 13-15°S area sediments. | 262 |
| 9.5.4 | Pb vs Mn in 13-15°S area sediments. | 262 |
| 9.5.5 | P vs La in 13-15°S area sediments. | 264 |
| 9.5.6 | Fe vs P/La in 13-15°S area sediments. | 264 |
| 9.5.7 | Mn vs P/La in 13-15°S area sediments. | 265 |
| 9.5.8 | Fe/Mn vs Al/Ti in 13-15°S area sediments. | 265 |
| 9.5.9 | Variations of Fe and Fe/Mn with depth in 5 cores from the 13-15°S area. | 267 |
| 10.1.1 | Station locations in the 19-21°S area of the E.P.R. | 274 |
| 10.2.1 | Bathymetry of the 19-21°S area of the E.P.R. | 275 |
| 10.2.2 | Detailed bathymetry of the 19-21°S area at longitude 114°W. | 276 |
| 10.2.3 | Hydrothermal vents and sulphide deposits mapped during the R/V MELVILLE cruise of 1981 in the area between 20°05'S and 20°10'S. | 277 |
| 10.4.1 | Surface sediment locations in the 19-21°S area of the E.P.R. | 281 |
| 10.4.2 | Fe in surface sediments from the 19-21°S area of the E.P.R. | 283 |
| 10.4.3 | Mn in surface sediments from the 19-21°S area of the E.P.R. | 283 |
| 10.4.4 | Cu in surface sediments from the 19-21°S area of the E.P.R. | 285 |
| 10.4.5 | Zn in surface sediments from the 19-21°S area of the E.P.R. | 285 |
| 10.4.6 | Cu/Zn in surface sediments from the 19-21°S area of the E.P.R. | 287 |
| 10.4.7 | P/La in surface sediments from the 19-21°S area of the E.P.R. | 287 |

| | | Page |
|---|---|---|
| 10.4.8 | Mo in surface sediments from the 19-21°S area of the E.P.R. | 288 |
| 10.4.9 | Ni in surface sediments from the 19-21°S area of the E.P.R. | 288 |
| 10.4.10 | Plot of $CaCO_3$ versus water depth in 19-21°S area surface sediments. | 290 |
| 10.4.11 | The distribution of As and the As/Fe ratio in crestal surface sediments from 19-21°S on the E.P.R. | 293 |
| 10.5.1 | Fe vs Mg in 19-21°S area sediments. | 301 |
| 10.5.2 | Mn vs Mg in 19-21°S area sediments. | 301 |
| 10.5.3 | Fe vs Mn in 19-21°S area sediments. | 302 |
| 10.5.4 | Cu vs Fe in 19-21°S area sediments. | 302 |
| 10.5.5 | Zn vs Mn in 19-21°S area sediments. | 303 |
| 10.5.6 | $SiO_2$ vs Mn in 19-21°S area sediments. | 303 |

## LIST OF TABLES


| | | Page |
|---|---|---|
| 2.1.1 | Inactive hydrothermal mounds: sulphide facies. | 20 |
| 2.2.1 | Inactive hydrothermal mounds: oxide facies. | 25 |
| 2.3.1 | Dredged manganese crusts and adhering sediments. | 27 |
| 2.3.2 | Mineralogical data for Dredge 2 smectites from the seamount located north of the Galapagos Rift at $0^{\circ}57'N$ and $85^{\circ}29'W$. | 33 |
| 2.3.3 | Comparative hydrothermal nontronite data. | 34 |
| 2.3.4 | Calculations to express nontronite composition on a ferro-manganese oxide free basis. | 35 |
| 2.3.5 | Comparative hydrothermal manganese crust data. | 37 |
| 2.4.1 | Short core carbonate sediments (carbonate-free data) | 41 |
| 2.5.1 | Short core carbonate sediments (raw data). | 45 |
| 2.6.1 | Geochemistry and mineralogy of the $<0.5\mu$ fraction of $86^{\circ}W$ area sediments | 75 |
| 2.6.2 | Correlation matrix for Galapagos Rift sediments, $86^{\circ}W$. | 80 |
| 2.7.1 | X-ray diffraction mineralogy. | 87 |
| 3.2.1 | Sulphide mineralogy of inactive hydrothermal vents, $86^{\circ}W$ - collected during Dive 1001. | 104 |
| 3.3.1 | Range and average element concentrations in chalcopyrite, pyrite, sphalerite, marcasite and Dive 1001 Fe-Mn oxides. | 108 |
| 3.4.1a) | Chemical analyses for the calibration standards. | 118 |
| b) | Quantitative chalcopyrite mineralogy of the 2 component mixtures. | 118 |
| 3.4.2 | Comparison of quantitative sulphide mineralogy from calibrated X.R.D. and chemistry. | 122 |
| 3.4.3 | Quantitative sulphide mineralogy and the theoretical yield of $SO_2$. | 123 |
| 3.4.4 | Sulphur isotope data. | 127 |
| 4.2.1 | Comparative geochemical data for mid-ocean ridge hydro-thermal massive sulphide deposits. | 144 |
| 5.4.1 | Geochemistry and mineralogy of the $<0.5\mu$ fraction of $95^{\circ}W$ area sediments. | 166 |

| | | Page |
|---|---|---|
| 5.4.2 | Correlation matrix for De Steiguer Deep area sediments, 95°W. | 167 |
| 6.5.1 | Bulk mineralogy of Hess Deep sediments. | 192 |
| 6.6.1 | Geochemistry and mineralogy of the <0.5μ fraction of Hess Deep sediments | 195 |
| 6.8.1 | Correlation matrix for Galapagos Rift sediments, 101°W. | 202 |
| 6.8.2 | Correlation matrix for Galapagos Rift sediments, from the Hess Deep. | 203 |
| 9.4.1 | Element concentrations and element ratios for stations 77D and 87D ferromanganese crusts. | 247 |
| 9.5.1 | Surface and downcore sediment correlation matrices. | 260 |
| 9.5.2 | Calculations dating the period of intense hydrothermal activity in cores 61, 70, 64, 69 and 60K. | 268 |
| 10.4.1 | As, Si, Bi data for surface sediments from the 20°S area. | 292 |
| 10.4.2 | Element concentrations and element ratios for Stations 14D and 26D ferromanganese crusts. | 296 |
| 10.5.1 | Surface and downcore sediment correlation matrices. | 299 |
| F.1 | Intra- and inter-batch element precision (A.A. Spectrophotometry). | 326 |
| F.2 | Quality control: precision and accuracy (I.C.P. Spectrometry). | 327 |
| F.3 | Precision and accuracy data for (I.C.P.) silica analysis. | 329 |

## LIST OF PLATES


| | | Page |
|---|---|---|
| 2.1.1 | Chalcopyrite-rich sample. | 16 |
| 2.1.2 | Pore-ridden gossan surface of massive sulphide. | 16 |
| 2.1.3 | Porous sulphide with oxidised rind and fibrous habit. | 17 |
| 2.1.4 | Locally abundant amorphous silica facies. | 17 |
| 2.1.5 | Sulphide with oxidised rind and fibrous habit. | 18 |
| 2.1.6 | Iron oxide-coated sulphide and an iron oxide coating on manganese oxide. | 18 |
| 2.1.7 | Chalcopyrite within a veinlet with a chilled margin and grading into gossan at the mound top. | 19 |
| 2.1.8 | Circular organic structure/? fossilised worm tube with an infill of mainly siliceous material. | 19 |
| 2.2.1 | Tubular iron oxides with inner linings of black manganese oxides. | 23 |
| 2.2.2 | Iron and manganese oxides. | 23 |
| 2.3.1 | Iron oxide overlain by manganese oxide and underlain by clay minerals. | 28 |
| 2.3.2 | Laminated manganese oxide overlain by iron oxide and underlain by clay minerals. | 28 |
| 2.3.3 | Manganese crust with adhering green material. | 29 |
| 2.3.4 | Irregular manganese crust and adhering green material. | 29 |
| 2.3.5 | Blocky, well-laminated, smooth manganese crust. | 30 |
| 2.3.6 | Iron oxide coating on manganese oxide. | 30 |
| 3.2.1 | Cavity infilled with amorphous silica and surrounded by primary sulphides. | 91 |
| 3.2.2 | Chalcopyrite grains with an unusual triangular, brecciated habit. | 91 |
| 3.2.3 | Rapid decrease in grain size of chalcopyrite towards the chilled margin of the veinlet. | 92 |
| 3.2.4 | Covellite forming from chalcopyrite. | 92 |
| 3.2.5 | Goethite replacing a large chalcopyrite grain. | 94 |
| 3.2.6 | Bladed marcasite grains enclosing chalcopyrite. | 94 |
| 3.2.7 | Cusp-like growths of amorphous silica enveloped by pyrite projecting upwards from a linear filament. | 97 |

| | | Page |
|---|---|---|
| 3.2.8 | Colloform association of pyrite and amorphous silica. | 97 |
| 3.2.9 | Euhedral pyrite above pyrite associated with curved filaments of a possible organic origin. | 100 |
| 3.2.10 | Corroded chalcopyrite grain etched with amorphous silica and surrounded by pyrite. | 100 |
| 3.2.11 | Caries texture shown by sphalerite in pyrite euhedra. | 102 |
| 3.2.12 | Outer growth zones of sphalerite within euhedral pyrite. | 102 |
| 3.3.1 | Backscattered electron map of colloform pyrite surrounded by amorphous silica. | 113 |
| 3.3.2 | X-ray image of sulphur. | 113 |
| 3.3.3 | X-ray image of silicon. | 113 |
| 3.3.4 | X-ray image of barium, present in baryte. | 114 |
| 3.3.5 | X-ray image of sulphur. Imaging of sulphur is strong for sulphide and less strong for sulphate. | 114 |
| 3.3.6 | X-ray image of iron, present in pyrite. | 114 |
| 3.3.7 | X-ray image of zinc, present in a grain of sphalerite enclosed by pyrite. | 115 |
| 3.3.8 | X-ray image of iron, present in pyrite. | 115 |
| 3.4.1 | Small pyrite euhedra enclosed within large chalcopyrite grains. | 125 |
| 3.4.2 | Intimate association of pyrite euhedra and anhedral chalcopyrite. | 125 |
| 6.3.1 | Core 10173 - the depth of the oxidised zone = 42 cms. | 179 |
| 6.3.2 | Core 10174 - the depth of the oxidised zone = 46 cms. | 179 |
| 6.7.1 | Coccolith with a wafer-thin coating, on a larger diatom. | 199 |
| 6.7.2 | Fibrous sheath of chrysotile in a matrix of siliceous microfossils. | 199 |
| 6.7.3 | Fibrous chrysotile and abundant siliceous microfossil fragments. | 199 |
| 6.7.4 | Large clast of a primary mineral, pseudomorphed by chrysotile, with a linear organic structure indicating dissolution by its etched nature. | 200 |
| 6.7.5 | Large clast at higher magnification and displaying a fibrous nature. | 200 |

| | | Page |
|---|---|---|
| 6.7.6 | Highly magnified view of the large clast, displaying individual fibres of chrysotile. | 201 |
| 6.7.7 | Rectangular platelets of talc with individual fibres of chrysotile. | 201 |
| 9.3.1 | Intimate association of botryoidal/fibrous ferromanganese crust. | 239 |
| 9.3.2 | Tubular basaltic structure with ferromanganese crust on surface. | 239 |
| 9.3.3 | Greenstone with white lath-like crystals. | 240 |
| 9.3.4 | Slickensided basaltic glass with an iron oxide coating. | 240 |
| 10.3.1 | The underside of the black manganese crust from Station 14D. | 280 |
| 10.3.2 | Carbonate sediment dusted on a ferromanganese crust. | 280 |

# GENERAL INTRODUCTION

It was not until the discovery of the Red Sea geothermal system in 1948 (Bruneau et al., 1953) that attention was focussed upon the phenomenon of hydrothermal sediments. A volume entitled "Hot Brines and Recent Heavy Metal Deposits in the Red Sea" (Degens and Ross, 1969) represented the first detailed study into the nature and genesis of high temperature, brine-derived, hydrothermal metalliferous sediments. This work still remains central to our understanding of submarine hydrothermal deposits.

It is beyond the scope of this thesis to describe the complexities of the Red Sea hydrothermal deposits and the reader is referred to the review of Cronan (1980). However, it is proposed to describe the model taken from the Atlantis II Deep of the Red Sea which forms a basis for marine geochemical exploration for hydrothermal deposits. This model explains the full fractionation sequence of hydrothermal precipitates into sulphides, silicates and oxides that form upon the progressive neutralising, cooling and oxidation of acidic hydrothermal solutions mixing with bottom sea-water.

The sediments found in the Atlantis II Deep were divided by Bischoff (1969) into "seven bedded and laterally correlative facies," which are:-

1. Detrital
2. Iron Montmorillonite
3. Goethite-amorphous
4. Sulphide
5. Manganosiderite
6. Anhydrite
7. Manganite

Refinement of this early work, by Backer and Richter (1973) and Bignell (1975), led to several facies sub-divisions. It was found that sulphides, silicates and oxides contained the greatest enrichments of metals. Further work by Bignell et al. (1976) related the different oxide facies

to the different mobilities of metals in seawater. The authors found dispersion haloes of Mn, i.e. Mn anomalies in sediments, up to 11 Kms from the Atlantis II Deep which they accounted for by the selective fractionation of Fe from Mn (Krauskopf, 1957) upon the increasing pH and Eh of the hydrothermal solutions on mixing with seawater. Mn was found to be dispersed further than Fe, and both of these elements increased in concentration towards the hydrothermal source.

It is known that nontronite (an Fe-silicate of the smectite group) synthesis occurs under reducing conditions at low temperatures (Harder, 1976) and can occur on the sea floor after sulphide deposition but before the oxidation of $Fe^{2+}$ to $Fe^{3+}$ and the formation of Fe oxides. Bischoff (1969) suggested that in the Red Sea the smectite (nontronite) facies forms at a lower level within the brine than the Fe oxide facies. Thus, in the area within and around the Atlantis II Deep, the fractional precipitation of sulphides, silicates, iron and manganese oxides has occurred in response to changes in physicochemical conditions.

The occurrences of hydrothermal mineral deposits from Eastern Pacific spreading centres reported in this thesis are discussed within the framework of the Red Sea model.

# PART 1

## THE GALAPAGOS RIFT SPREADING CENTRE


INTRODUCTION

STUDY A — THE GALAPAGOS RIFT AT 86°W

- Chapter 1 — Geology, Bathymetry and Structure of the GRAFZI Area, 86°W
- Chapter 2 — Bulk Geochemistry and Mineralogy of Sediments from the 86°W Area
- Chapter 3 — Reflected Light Microscope, Electron Microprobe and Stable Isotope Studies
- Chapter 4 — Hydrothermal Processes and the Evolution of Galapagos Rift Sulphide Mounds

STUDY B — THE GALAPAGOS RIFT AT 95°W

- Chapter 5 — The De Steiguer Deep Area, 95°W

STUDY C — THE GALAPAGOS RIFT AT 101°W

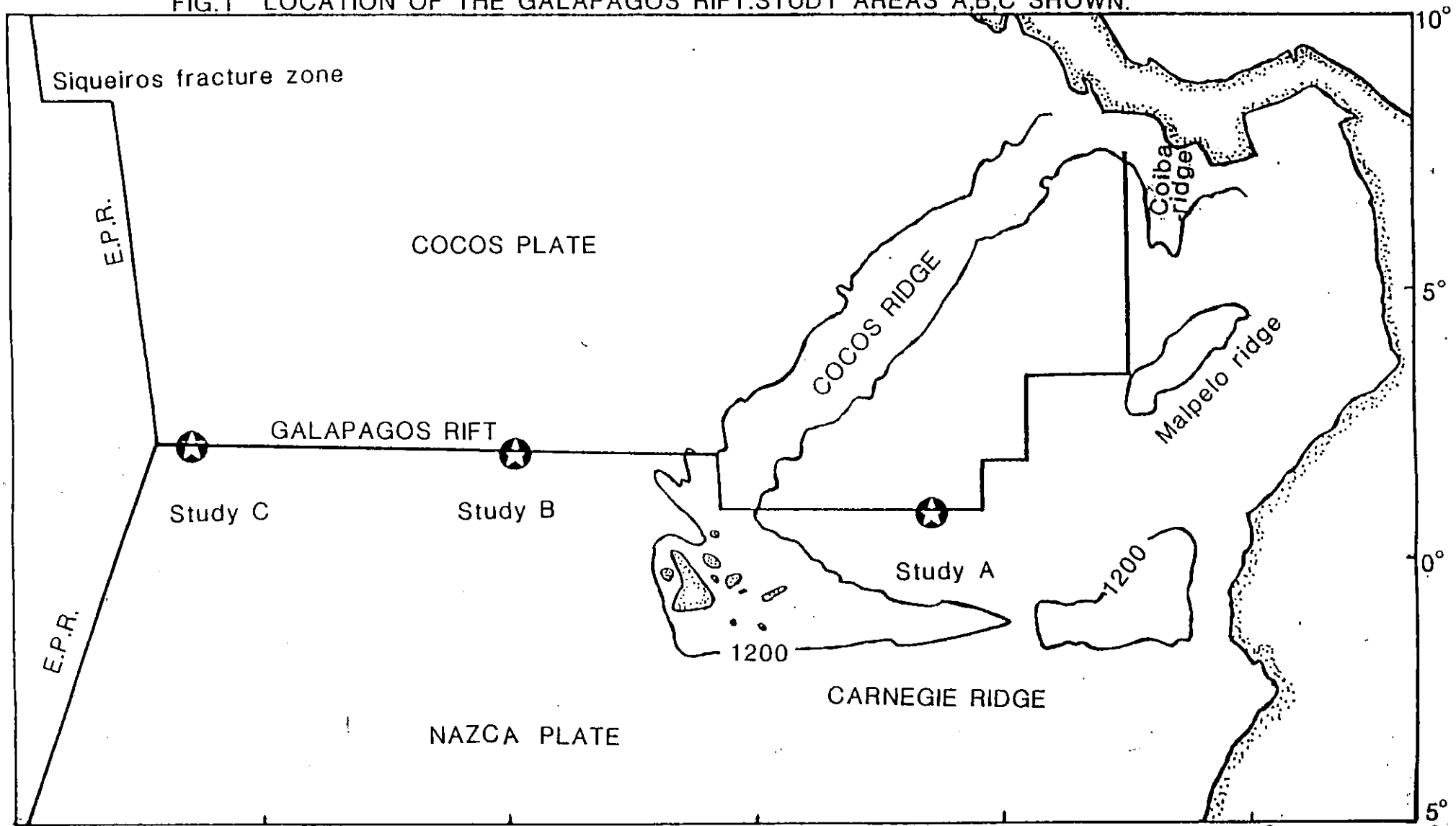
- Chapter 6 — The Hess Deep Area of the Galapagos Rift at 101°W, near the Pacific-Cocos-Nazca Plate Triple Junction

# INTRODUCTION

The Galapagos Rift (Figure 1) became a source of interest following geophysical exploration carried out in 1972 in the vicinity of 86°W. Heat flow, topographic and magnetic survey data (Sclater and Klitgord, 1973) suggested the presence of actively circulating convection cells of heated seawater, within the fractured, young oceanic crust. Subsequent deep-tow observations (Klitgord and Mudie, 1974; Lonsdale, 1977) ; measurements of heat flow variations (Williams et al., 1974) and bottom water temperature anomalies strongly substantiated this hypothesis. Williams et al., (1974) concluded that the heat flow variations were relatively uniform with a wavelength of 6 kms, approximately perpendicular to the spreading axis, and that hydrothermal convection may account for as much as 80% of the heat released near the ridge crest. This convective process may explain why observed heat flow values are anomalously low when compared with predicted values (Langseth and Von Herzen, 1971; Sleep, 1969; Sleep and Wolery, 1978).

Multibeam bathymetric charts gave the first evidence of the existence of fields of small sediment mounds associated with faulted, elevated areas of high heat flow between 18 and 25 kms south of the spreading axis (Williams et al., 1974). These hydrothermal mounds have been intensively studied chemically and mineralogically as a result of 2 legs of the Deep Sea Drilling Project, Legs 54 and 70 and comprise nontronite overlain by manganese oxides. This sequence represents part of the typical fractionation sequence of hydrothermal solutions on egress from oceanic crust, best exemplified by the Red Sea deposits (Cronan, 1980). The

FIG.1 LOCATION OF THE GALAPAGOS RIFT.STUDY AREAS A,B,C SHOWN.




adapted from Varnavas and Cronan(1981).

full fractionation sequence has been referred to previously but basically consists of sulphides, Fe silicates, Fe oxides and Mn oxides precipitating out of seawater in sequence, with increasing distance from the source.

Manned submersible operations on the Galapagos Rift at 86°W (Corliss and Ballard, 1977; Corliss et al., 1979) sampled hydrothermal solutions which were found to be exiting from basement at a maximum temperature of 10 - 17°C with a flow rate of 2 - 10 cms per second (Corliss et al., 1979) but were calculated to have interacted with basalt at temperatures of at least 300°C. On the E.P.R. at 21°N, solutions have been found with temperatures of approximately 350°C on exiting from the oceanic crust (Spiess et al., 1980).

Anomalously high levels of Mn, Fe, Cu, Zn and He in the water column (Gordeev and Demina, 1979; Klinkhammer et al., 1977; Lupton et al., 1977) have been found to be injected by hydrothermal plumes over the Galapagos Rift, and up to a distance of 2500 metres above the bottom in the Hess Deep (Gordeev and Demina, 1979). Furthermore, the presence of hydrothermal Mn crusts (Burnett and Piper, 1977; Moore and Vogt, 1976) indicate that the Galapagos Spreading Centre has the potential for other hydrothermal deposits to occur.

During early 1980, project GRAFZI (Galapagos Rift And Fracture Zone Intersection) was initiated to examine the tectonic and structural relations of the propagation of the Galapagos Rift and a fracture zone, in the vicinity of 86°W. The aims of this work were primarily geophysical. The use of the 'Seabeam'

survey (multi-beam soundings) for bathymetric mapping, later linked with 'Gloria' data (side-scan sonar imagery) produced high resolution maps of the sea-bed in this region. During this project, inactive sulphide mounds and sulphide talus cement were discovered by the submersible ALVIN, and study of these deposits forms the bulk of this section of the present thesis.

At the time, these sulphides represented only the second discovery of such high grade hydrothermal material to have been found on a mid-ocean ridge outside the Red Sea (Malahoff et al., 1983), the other locality being at 21°N on the E.P.R. (Hékinian et al., 1980). However, the chemistry and mineralogy of the GRAFZI deposits described in this study is substantially different to that of the E.P.R. sulphide deposit at 21°N (Hékinian et al., 1980).

Iron oxides, manganese oxide crusts with adhering clay minerals, and carbonate sediments were also recovered by submersible, or by dredging from the R/V CONRAD, in the GRAFZI area. Therefore, in this area the complete fractionation sequence described above was observed for the first time on a mid-ocean ridge.

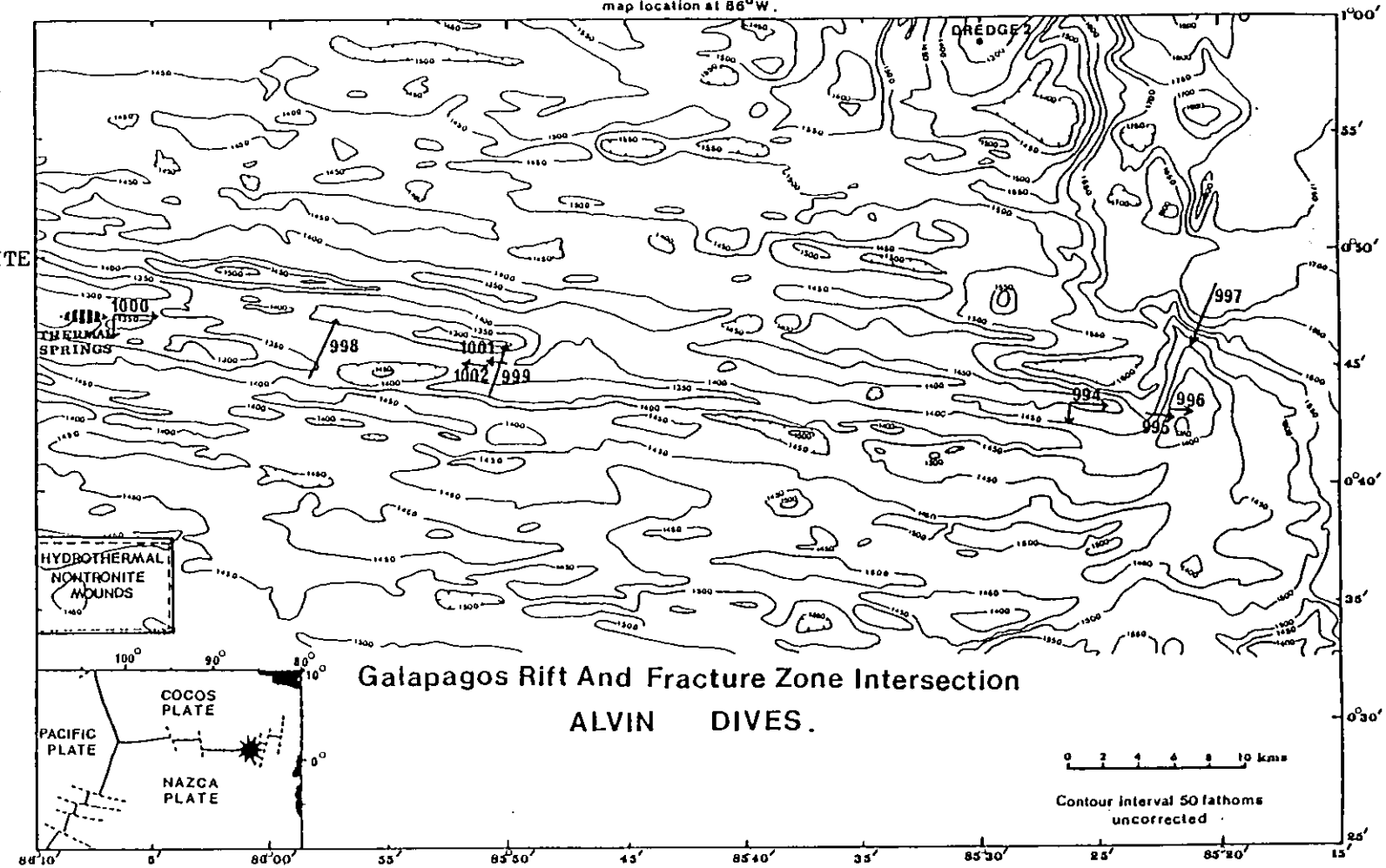
The following study attempts to describe the origin and formation of the inactive sulphide mounds whilst trying to establish the spatial relations between the vent material and the more widely dispersed Fe silicate, Fe oxide and Mn oxide products.

HYDROTHERMAL SITES.

THERMAL SPRINGS.
(Corliss et al.)
(1979).

HYDROTHERMAL NONTRONITE MOUNDS.
(Lonsdale, 1977).

Figure 1.1. Bathymetric map of the Galapagos Rift at 86°W, with ALVIN dives arrowed. Massive sulphides encountered on Dive 1001. Box indicates location of hydrothermal mounds. (Inset) Regional map of East Pacific accreting plate margins showing the map location at 86°W.



STUDY A

CHAPTER 1

# GEOLOGY, BATHYMETRY AND STRUCTURE OF THE GRAFZI AREA, 86°W

The geology, bathymetry and fine-scale structure of the GRAFZI area at 86°W, was mapped during 1980 using a multi-beam, narrow-beam ocean floor survey with the U.S. Navy S.A.S.S. (Sonar Array Sounding System) technique. This survey was conducted over the axial region of the Galapagos Rift crest between 85°10'W and 86°15'W. The structure of the area is dominated by topographic features striking parallel to the axial rift, in an east-west direction (Figure 1.1).

The Galapagos Rift is a medium rate spreading centre with a prominent rift valley, spreading at about 75 millimetres per year (Malahoff et al., 1983). The rift valley is about 40 metres deep, 1 - 5 kms wide and located between 0°42'N and 0°48'N, at this longitude. The locus of volcanic activity is to be found west of 86°W, and the rift valley is apparently continuous eastwards to 85°22'W where it is terminated against an active fracture zone (Figure 1.1). The structure of the rift valley at the locus of volcanic activity, west of 86°W has been thoroughly studied (Ballard et al., 1979) and fresh lava flows, lava lakes and collapse pits as well as active low temperature hydrothermal vents or thermal springs (Corliss et al., 1979) were found (Figure 1.1).

S.A.S.S. survey data over the ridge crest at 85°50'W and 0°45'N showed the presence of a double rift with axial rift elements striking in an east-west direction (Figure 1.2). ALVIN dives 1001 and 1002 were used to survey and sample this area of the two rift valleys, the principle rift valley located to the north and a "jumped" rift located to the south (Figure 1.2). The northern rift valley which is 1200 m wide is marked

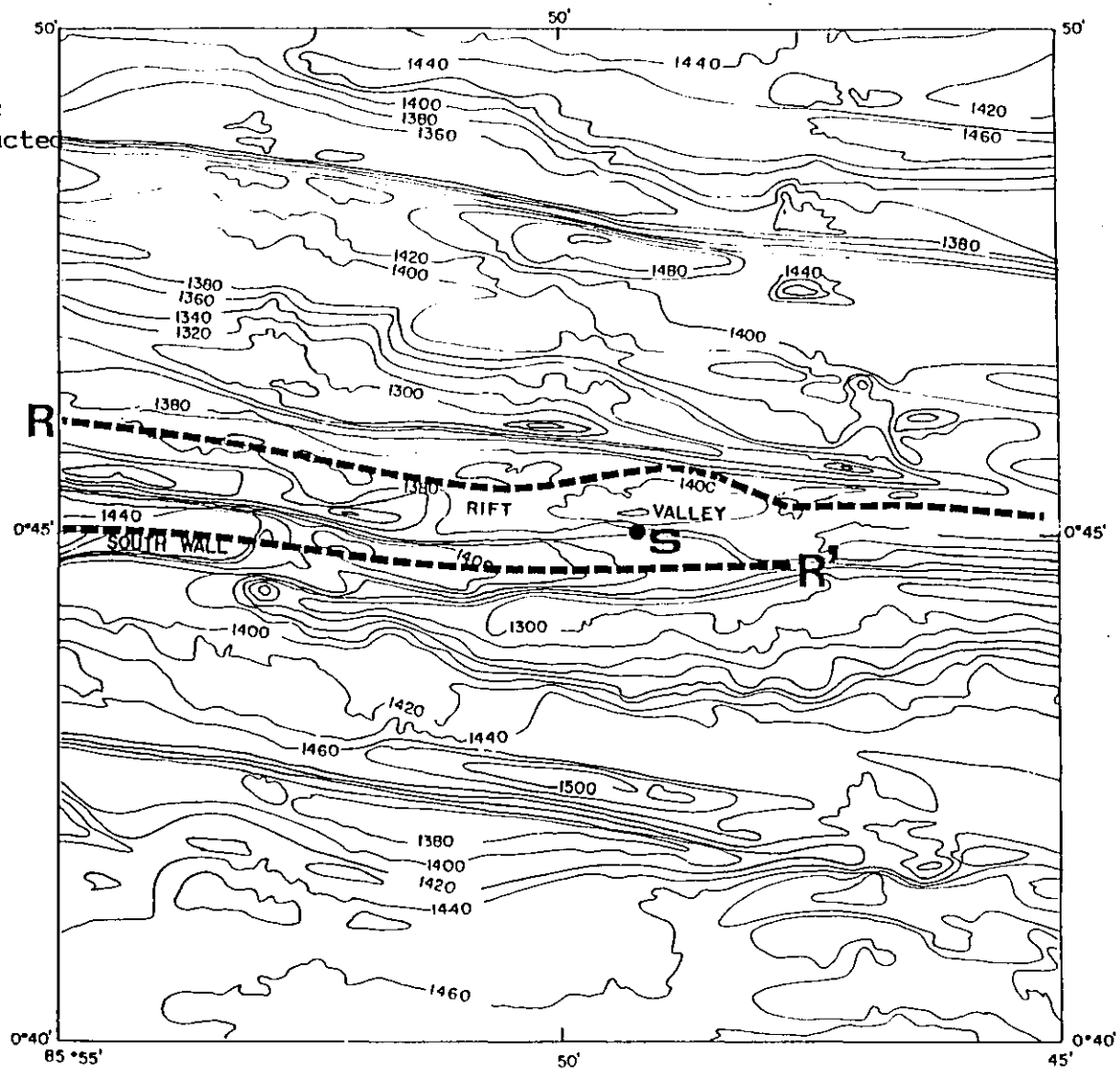
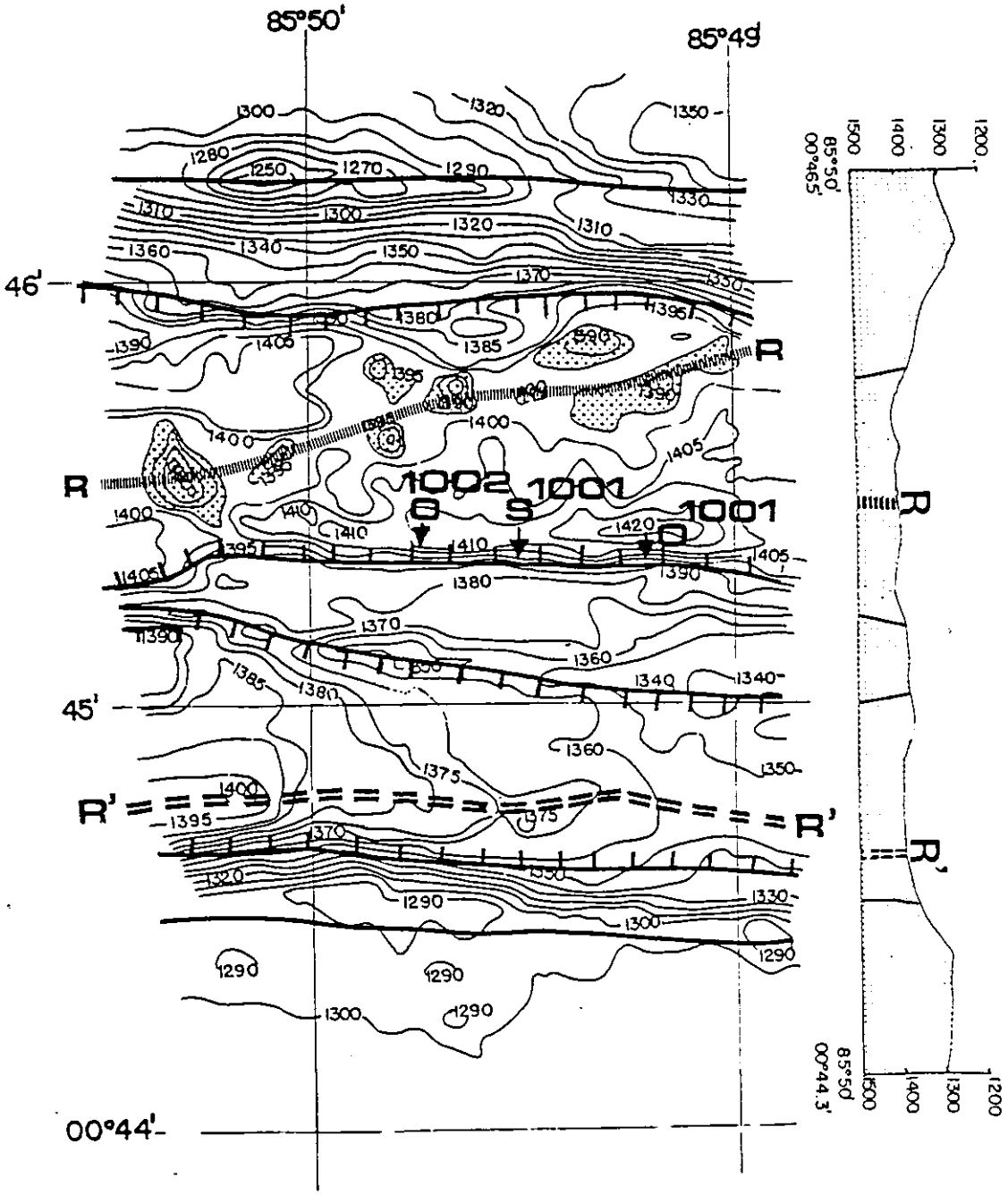



FIG. 1.2. Medium resolution bathymetric map of the Galapagos Rift valley, constructed from U.S. Navy S.A.S.S. data.
R-location of principal rift valley.
R'-location of "jumped" rift valley.
S-location of submarine polymetallic sulphide deposit.
(Depths in uncorrected fathoms).

FIG. 1.3.High resolution bathymetric map of the Galapagos Double Rift Area.R-principal rift axis;R'-"jumped"rift axis; Solid line delineates high crest on the tilted block;Dotted areas indicate axial volcanic piles;Hashures indicate down-thrown side of normal faults;O-location of hydrothermal iron oxides;S-location of hydrothermal sulphide deposit mapped on Dive 1001.

(Depths in uncorrected fathoms).



by a prominent 30 m high median ridge. The axis of the median ridge is crested by several 15 - 40 m high volcanic edifices (Figure 1.3). Dive 1001 showed the flanks of the ridge to consist of fresh pillows covered by a slight dusting of sediment. The sediment cover was found to increase towards a normal fault at the northern rift valley's southern margin where it merged into inactive hydrothermal iron oxide hummocks, 10 - 20 cms high, precipitated along a series of vents located at the base of the marginal fault scarp.

Dives 1001 and 1002 both encountered hydrothermal deposits at the base of the faulted rift margin (Figure 1.3). The principal sulphide deposits found on Dive 1001 appear to be flanked to the east and west by the inactive hydrothermal iron oxide deposits found on Dive 1001 and Dive 1002 (Figure 1.3). The sulphides were found at a depth of approximately 2850 m, in inactive denuded mound form and also as a talus cement in a breccia deposit located at the foot of a scarp slope. They have developed along the southern margin of the northern rift valley forming a line of coalesced chimneys between 100 and 750 m in length. The sulphide chimneys (also referred to as stacks or mounds) are generally 2 - 3 m in height with a maximum height of 7 m, and 1 - 2 metres in diameter (Figure 1.4). The area occupied by the chimneys is underlain by basaltic talus. The talus is indented by a 2 - 3 m deep depression along the base of the 36 m high fault scarp (Malahoff et al., 1983), and is cemented and occasionally overlain by a blanket of hydrothermal precipitates, up to 1 m in thickness.

In summary, the in situ sulphide mounds directly overlie basaltic basement, have an elevation of only a few metres and are in the process of oxidation as evinced by their being coated with, and surrounded by, an iron oxide gossan. Recently, (Malahoff, pers. comm., 1982) a much larger sulphide deposit, perhaps as large as

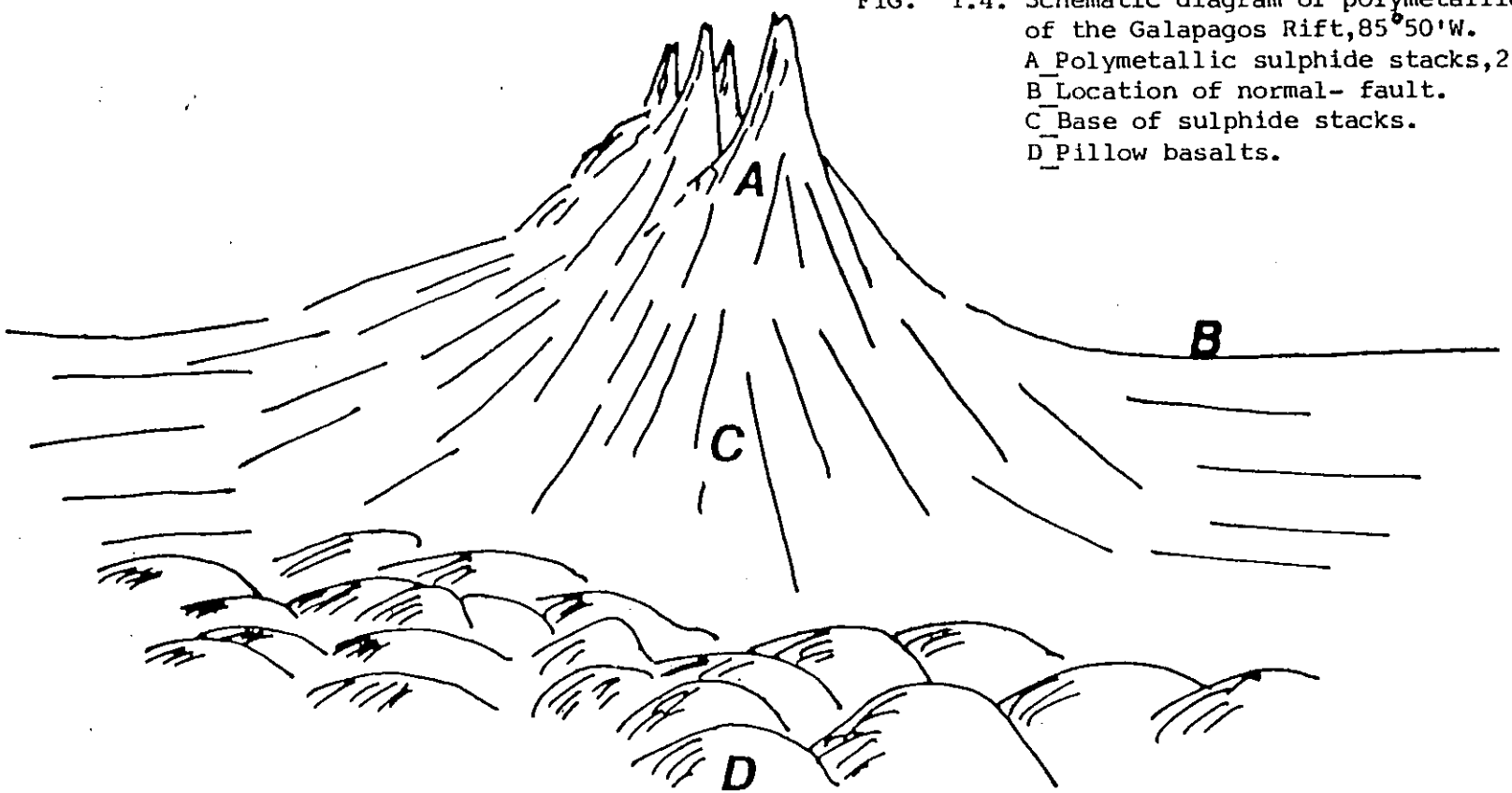



FIG. 1.4. Schematic diagram of polymetallic sulphide stacks of the Galapagos Rift, 85°50'W.
A Polymetallic sulphide stacks, 2 to 3 metres in height.
B Location of normal- fault.
C Base of sulphide stacks.
D Pillow basalts.

25 million tons, has been discovered associated with the marginal fault system, but on the southern scarp of the "perched" block, i.e. the northern wall of the southern rift valley (Figure 1.3).

A dredge haul in a water depth of 2500 m, located at about $0^{\circ}57'N$, $85^{\circ}29'W$ on a seamount, and about 28 kms north of the axis of the Galapagos Rift (Dredge 2; Figure 1.1), recovered laminated manganese crusts and adhering green clay minerals. Although these hydrothermal deposits are located near to the $85^{\circ}22'W$ fracture zone that separates the Galapagos from the Ecuador Rift, they apparently do not represent a fracture zone hydrothermal event (Malahoff et al., 1983). Subsequent dives with the ALVIN during September 1981, along the western flanks of the bathymetric high upon which Dredge 2 was located, showed a thick sediment cover, with no visible hydrothermal mounds akin to those at $86^{\circ}10'W$, $0^{\circ}35'N$ (Figure 1.1), described by Lonsdale (1977).

# CHAPTER 2

## BULK GEOCHEMISTRY AND MINERALOGY OF SAMPLES FROM THE 86°W AREA

A total of 69 samples were obtained from Dr. Alex Malahoff of the U.S. National Oceanic and Atmospheric Administration, collected during the GRAFZI Project of 1980. These samples can be divided into four types:-

1. Sulphide Mound Facies ..... 8 samples
2. Ferromanganese Oxide Facies ..... 14 samples
3. R/V CONRAD Dredge Hauls ..... 19 samples
4. Short Sediment Cores ..... 28 samples

The massive sulphides, ferromanganese oxides and short sediment cores were collected by the ALVIN. This material was supplemented by several dredged manganese crusts with adhering orange and green coatings, collected by the R/V CONRAD from a fracture zone and a seamount to the east of Dive 1001 (see Figure 1.1).

### 2.1 SULPHIDE MOUND FACIES

#### Sample Description

The 5 hand specimens collected can be seen in Plates 2.1.1 - 2.1.6. Generally, they consist of altered massive grey vuggy sulphides, with orange/red coatings on their surfaces, up to a few millimetres in thickness (Plates 2.1.1 - 2.1.3). The high porosity and common presence of conduits and passageways (Plate 2.1.2), suggests the passage of hydrothermal solutions through the samples. Some conduits are mineralised and have chilled margins while others show centimetre-scale circular structures which are associated with shell fragments and organic debris and are infilled with grey siliceous material. On the basis of the above observations, there appear to be two controls on the porosity of the sulphides, one being hydrothermal solutions, and the other, biogenic activity




PLATE 2.1.1. Chalcopyrite-rich sample.
x1.

PLATE 2.1.2. Pore-ridden gossan surface of massive sulphide.
x1.






PLATE 2.1.3. xl.

PLATE 2.1.4. Locally abundant amorphous silica facies.
xl.



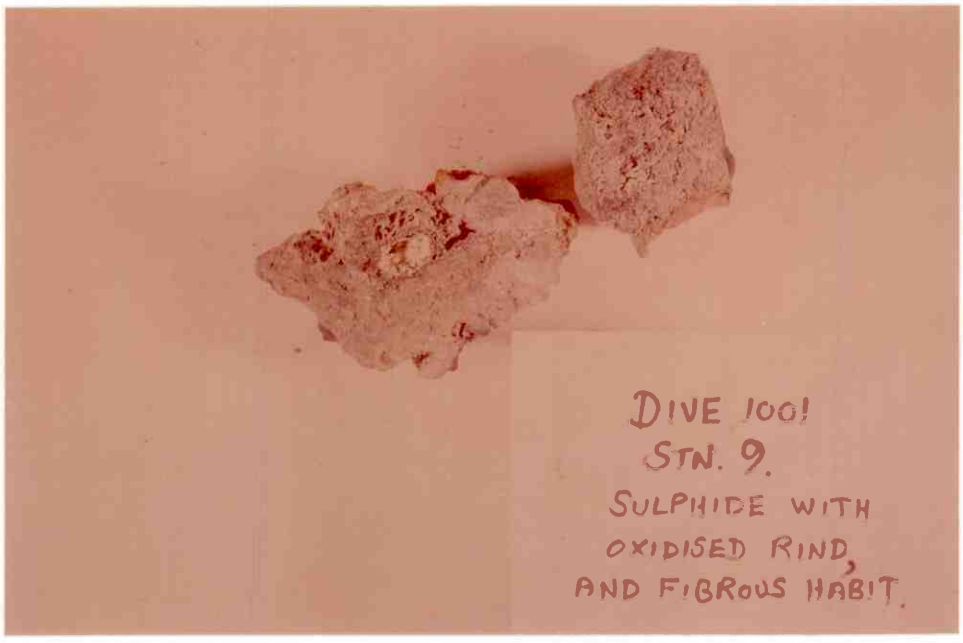
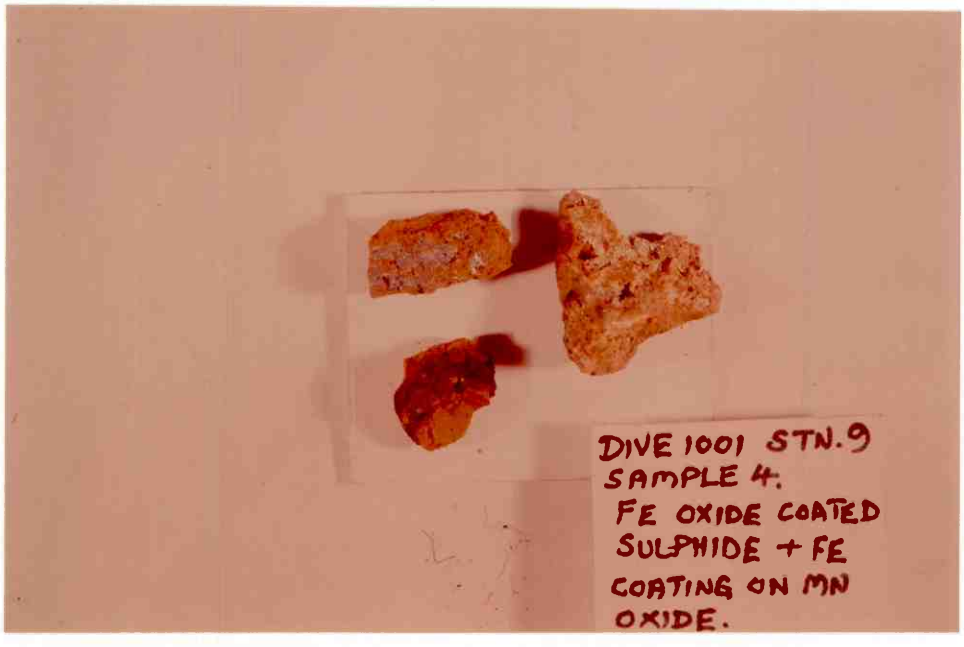



PLATE 2.1.5. x1.

PLATE 2.1.6. x1.



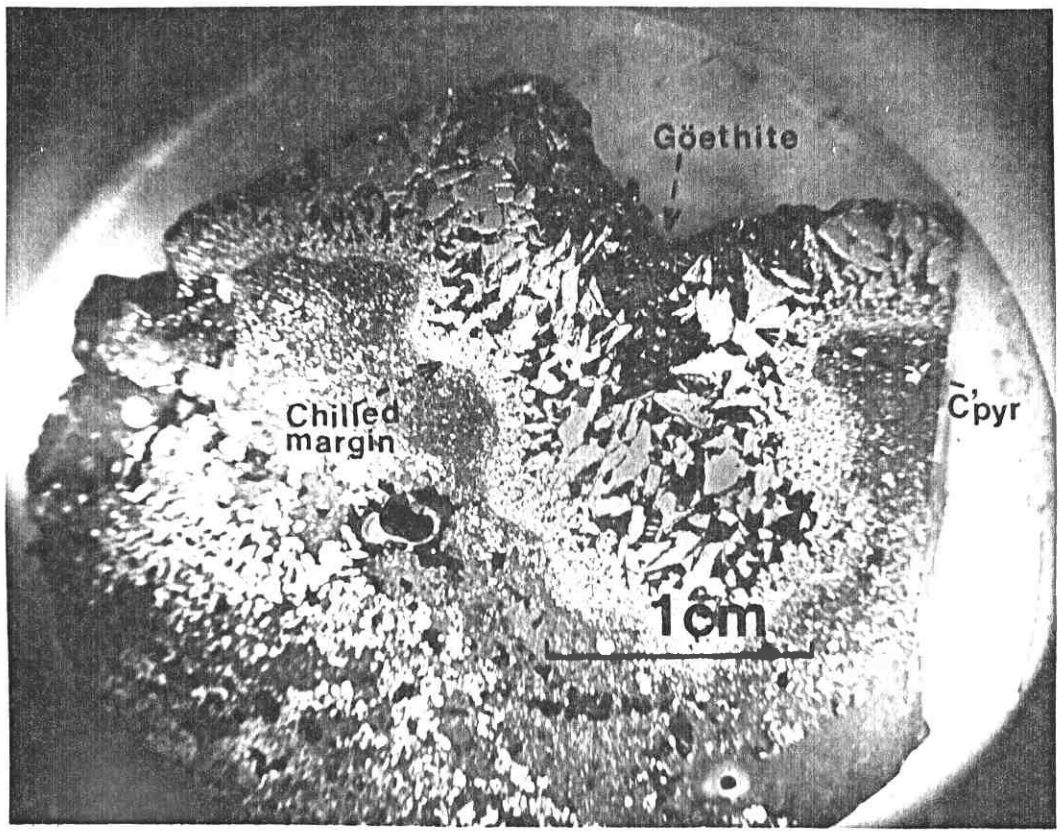



PLATE **2.1.7** Chalcopyrite occupying a veinlet with a chilled margin and grading into gossan at the mound top.

x3.5

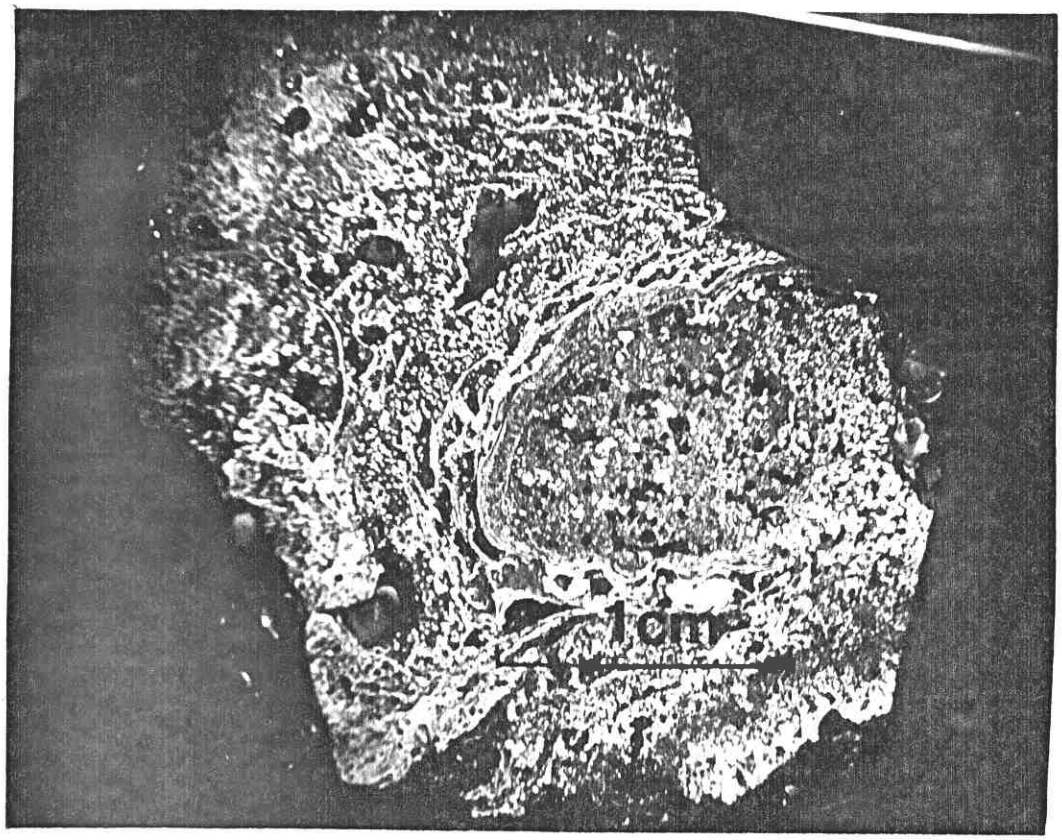



PLATE **2.1.8** Circular organic structure/?fossilised worm tube with an infill of mainly siliceous material.

x4

TABLE 2.1.1.

INACTIVE HYDROTHERMAL MOUNDS ; SULPHIDE FACIES

| SAMPLE DESCRIPTION | PERCENT FE | MN | CA | AL | ← PPM CO | NI | CU | ZN | PB | TI | AG | P/C $SiO_2$ |
|---|---|---|---|---|---|---|---|---|---|---|---|---|
| DIVE1001TOPNEEDLES | 27.68 | 0.01 | 0.03 | 0.34 | ND | ND | 267000 | 1900 | ND | ND | 55 | 8.70 |
| DIVE1001TOPMNDOXSURF | 25.36 | 0.01 | 0.04 | 0.36 | ND | ND | 136600 | 1800 | ND | ND | 28 | 23.64 |
| DIVE1001TOPMOUNDBULK | 18.72 | 0.08 | 0.03 | 0.58 | ND | ND | 172100 | 980 | ND | ND | 32 | 35.25 |
| DIVE1001MIDMNDOXSURF | 19.14 | 0.02 | 0.04 | 0.27 | 7 | ND | 36400 | 660 | 70 | ND | 40 | 47.75 |
| DIVE1001MIDMOUNDBULK | 31.24 | 0.01 | 0.04 | 0.61 | ND | ND | 79800 | 7000 | 38 | ND | 16 | 13.40 |
| DIVE1001SAMPLE4STN9 | 26.59 | 8.40 | 0.80 | 0.16 | 30 | 43 | 7195 | 8970 | 275 | ND | 3 | 16.83 |
| DIVE1001STN9SULPHIDE | 23.45 | 0.04 | 0.01 | 0.37 | ND | 55 | 61200 | 1865 | 23 | ND | 17 | 34.46 |
| DIVE1001=1STN9 | 2.10 | 0.01 | 0.01 | 0.10 | ND | 56 | 6283 | 14470 | 80 | ND | 26 | 86.58 |
| DETECTION LIMIT | | | | | .....6 | .....10 | | | .....10 | | .....60 | |

(ND=NOT DETECTED)

Mound Mineralogy.

| | MOUND TOP | MOUND MIDDLE |
|---|---|---|
| MAJOR | 1.CHALCOPYRITE | 1.PYRITE |
| | 2.PYRITE | 2.AMORPHOUS SILICA |
| | 3.AMORPHOUS SILICA | 3.CHALCOPYRITE |
| MINOR | 4.GOETHITE | 4.SPHALERITE |
| | 5.MARCASITE | 5.GOETHITE |
| | 6.COVELLITE | 6.MARCASITE |
| | 7.CHALCANTHITE | 7.COVELLITE |
| | | 8.CHALCANTHITE |

(In order of decreasing abundance.)

as seen on the E.P.R. at 21°N (Hékinian et al., 1980).

Often the grey sulphides are coated with orange iron oxide gossan (Plate 2.1.6) which attests to the fact that this assemblage was not in equilibrium with its environment on the sea-floor.

Bulk Geochemistry and Mineralogy

Bulk geochemical analysis was carried out by Atomic Absorption Spectrophotometry on the 8 representative sub-samples from the 5 hand specimens, for Fe, Mn, Ca, Al, Co, Ni, Cu, Zn, Pb, Ti and Ag (see Appendix B). $SiO_2$ was determined on the Inductively Coupled Plasma Spectrometer (see Appendix B). Table 2.1.1 shows the bulk geochemical data for representative samples and their location on the sulphide edifice.

Mineralogical identification was carried out on powder cavity mounts by X-Ray Diffractometry using CoK$\alpha$ radiation. More detailed mineralogy, determined by reflected light microscopy, is reported in Chapter 3. The mound mineralogy is shown in Table 2.1.1. Chalcopyrite ($CuFeS_2$) and pyrite ($FeS_2$) are the dominant mineral phases found in Dive 1001 sulphides, whilst sphalerite (ZnS) is much less common, and appears to be associated with amorphous silica ($SiO_2$). Important chemical and mineralogical differences exist between the mound top and mound middle which have been treated separately.

*Mound Top*

The maximum Cu value (26.7%) with associated high Fe (27.7%), occurs in a chalcopyrite-rich veinlet with individual grains up to 3 mm's in size, found at the top of the mound adjoining surficial iron oxide gossan (see Plate 2.1.1 and 2.1.7). This sample cannot be regarded as typical of the mound in general but merely represents a chalcopyrite enriched mineralised conduit. Generally, at the top of the mound Cu varies between 17.2% and 13.7%, the latter value occurring in the oxidised

surface sample. In the mound top samples, Cu and Fe average 15.5% and 22.1%, respectively. Mn, Ca, Al, Co, Ni, Pb and Ti are all low, but $SiO_2$ varies between 35.3% and 23.6%, with an average value of 29.5%. The chalcopyrite-rich veinlet (Plate 2.1.7) contains only 8.7% $SiO_2$, and this low value is probably due to the high chalcopyrite content. Zn is present in very low concentrations and shows a maximum of only 1900 ppm in the chalcopyrite needles sample and a minimum of 980 ppm in a bulk sample from the mound top.

Ag values as high as 55 ppm are found in the chalcopyrite needles, which is approximately the same level of concentration as that found in the Red Sea sulphide-rich metalliferous muds (Bischoff and Mannheim, 1969).

In summary, the mound top samples are rich in Fe, Cu, Ag and $SiO_2$. In addition, minor amounts of secondary minerals were found (see Table 2.1.1), e.g. chalcanthite ($CuSO_4.5H_2O$) with a major peak at 4.70 Å; marcasite ($FeS_2$) with major peaks at 2.71 Å and 1.76 Å; covellite (CuS) with a major peak at 2.81 Å. These minerals are described more fully in Chapter 3.

*Mound Middle*

Pyrite is the most common mineral in the mound interior, where Fe values reach 31.2%. As observed at the mound top, Cu is lower in concentration at the oxidised surface of the mound middle relative to the bulk fresh sulphide sample (Table 2.1.1). Cu ranges from 3.6% to 8.0% in the mound middle, with an average of 5.8%. Fe varies from 19.1% to 31.2%, varying inversely with $SiO_2$ content. Zn reaches a maximum of 1.45% in a sample containing 86.6% amorphous silica (Table 2.1.1) and this sample is shown in Plate 2.1.4. The association of Zn and $SiO_2$ seems to be variable but is best shown in samples from Dive 1001=1, Station 9. Apart from the oxidised surface sample, Zn is higher in the mound middle than at the top, and this can also be said of Pb, but on a much

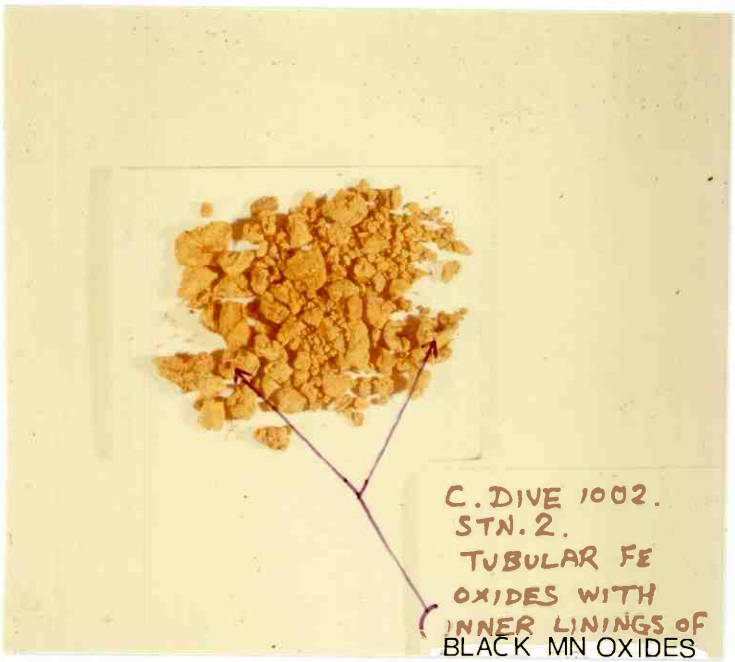



PLATE 2.2.1. x1.

PLATE 2.2.2. x1.



smaller scale. Mn, Ca, Al, Co, Ni, Pb and Ti are all low in concentration. Ag values are highest (26 ppm) along with Zn, Ni, Pb and $SiO_2$ in the Dive 1001=1 Station 9 sample, but Ag values are generally less than half those which occur in the Cu-rich mound top.

The mound middle samples are much less rich in Cu and Ag than those from the mound top, whereas Zn is enriched and seems to depend to some extent on the concentration of $SiO_2$ in the sample. Fe also seems to vary inversely with the concentration of amorphous $SiO_2$. The sulphide or oxide minerals may be diluted by large amounts of $SiO_2$. $SiO_2$ is sometimes associated with organic filaments, shell fragments and worm tubes (see Plate 2.1.8 and Chapter 3 on Reflected Light Microscopy) of biogenic origin.

Dive 1001 Sample 4, Station 9 is rich in Fe (26.6%) and Mn (8.4%) with some Co (30 ppm), Ni (43 ppm) and Pb (275 ppm). This sample consists of ferromanganese oxides with a small amount of admixed sulphide. Co, Ni, Pb and trace metals in general are typically low in hydrothermal ferromanganese oxides (Cronan, 1980) but Cu (0.72%) and Zn (0.90%) are high in this sample, suggesting the inclusion of sulphide fragments.

## 2.2 FERROMANGANESE OXIDE FACIES

### Sample Description

Dive 1002 encountered orange friable iron oxide material built into a series of small domes and hummocks, which in some cases showed concentric layering on a 0.5 cm scale. 11 samples were collected from these domes which were often encrusted with manganese oxides which could also be found lining small millimetre wide passageways in the orange friable iron oxide structures (Plate 2.2.1).

The samples were of low density due to their high porosity. Dive 1001 recovered one sample which comprised manganese oxide crust (3 mms thick) on an orange iron oxide substrate, shown in Plate 2.2.2. Three sub-samples were taken from this hand specimen which augmented the 11 taken on Dive 1002, making 14 samples in total.

TABLE 2.2.1.

INACTIVE HYDROTHERMAL MOUNDS ; OXIDE FACIES

| | PERCENT | ← PPM → | | | | | | | | P/C | |
|---|---|---|---|---|---|---|---|---|---|---|---|
| | FE | MN | CA | AL | CO | NI | CU | ZN | PB | TI | $SIO_2$ | Fe/Mn |
| DIVE1001STN62635FEOX | 33.75 | 5.04 | 0.97 | 0.04 | 15 | 30 | 220 | 4800 | ND | ND | 12.70 | 6.7 |
| DIVE1001STN62635MNCR | 3.83 | 42.50 | 1.62 | 0.17 | 122 | 110 | 1212 | 23000 | ND | 110 | | 0.1 |
| DIVE1001STN62635METR | 30.19 | 4.74 | 0.95 | 0.18 | 17 | 18 | 154 | 5685 | ND | ND | 15.30 | 6.4 |
| DIVE1002STN3SURFOCFL | 29.28 | 4.02 | 2.25 | 0.09 | 9 | 33 | 45 | 59 | ND | ND | | 7.3 |
| DIVE1002STN2STOPHUMM | 33.77 | 1.35 | 1.65 | 0.03 | 9 | 15 | 7 | 33 | ND | ND | | 25.0 |
| ADIVE1002STN2 | 29.92 | 3.36 | 1.60 | 0.03 | 12 | 45 | 10 | 62 | ND | ND | 14.26 | 8.9 |
| EDIVE1002STN2 | 28.53 | 4.90 | 1.90 | 0.07 | 10 | 43 | 9 | 65 | ND | ND | 13.49 | 5.8 |
| CDIVE1002STN2 | 29.94 | 0.81 | 1.35 | 0.05 | 9 | 10 | 5 | 36 | ND | ND | 21.44 | 37.0 |
| DDIVE1002STN2 | 29.69 | 3.13 | 1.48 | 0.03 | 8 | 53 | 10 | 69 | ND | ND | 13.77 | 9.5 |
| EDIVE1002STN2 | 31.38 | 1.18 | 1.35 | 0.05 | 9 | 15 | 19 | 27 | ND | ND | 17.81 | 26.6 |
| FDIVE1002STN3 | 28.28 | 2.71 | 2.75 | 0.13 | 11 | 40 | 17 | 82 | ND | ND | 15.50 | 10.4 |
| DIVE1002STN2VENTSAMP | 31.05 | 3.82 | 1.65 | 0.04 | 10 | 23 | 7 | 36 | ND | ND | | 8.1 |
| DIVE1002STN2SMALVENT | 28.90 | 6.53 | 2.35 | 0.06 | 11 | 38 | 20 | 55 | ND | ND | | 4.4 |
| DIVE1002STN2SMINHUMM | 32.42 | 2.36 | 1.65 | 0.02 | 9 | 30 | 8 | 52 | ND | ND | | 13.7 |
| DETECTION LIMIT..... | | | | | 7..... | | | | 10.....30 | | | |

(ND=NOT DETECTED)

Bulk Geochemistry and Mineralogy.

The mineralogy of the hydrothermal ferromanganese oxide facies consists of X-Ray amorphous Fe oxides, birnessite (major peak at 7.19 Å) and minor calcite and smectite (major peaks at 11.7 Å and 4.49 Å, for 001 and 110,020 diffractions, respectively). Typically the peaks obtained from X.R.D. of Fe and Mn oxides were either very diffuse or non-existent, due to poor crystallinity.

Three sub-samples from the Dive 1001 Station 6 sample had a different chemistry to the other samples taken during Dive 1002 (Table 2.2.1). In these sub-samples Fe has a maximum value of 33.8% with Fe/Mn of 6.7, whilst Mn has a maximum of 42.5% with Fe/Mn of 0.1. These sub-samples consisted of a Mn crust, an Fe oxide substrate, with the third sample a mixture of the two. The Mn crust contains more Co and Ni than the other two samples. Of particular interest are the high Cu and Zn values, 1212 ppm and 2.30% respectively in the Mn crust containing birnessite, and 220 ppm Cu and 0.48% Zn in the Fe oxide (Table 2.2.1). Such values are very high for hydrothermal Fe and Mn oxides, which are normally low in trace metals (Cronan, 1980) and a possible explanation is offered in the light of electron microprobe investigations, in Chapter 3. The $SiO_2$ values of 12.7% and 15.3% for the iron oxides with high Cu and Zn are similar to the $SiO_2$ content of the other ferromanganese oxide samples with lower trace metal contents.

The remaining ferromanganese oxides (excluding Dive 1001 sub-samples) consist of Fe, Mn and approximately 15% $SiO_2$ on average, with little else of consequence, attesting to their relatively pure hydrothermal nature. Fe values range from 33.8% to 28.3%, while Mn ranges from 6.5% to 0.81%. Fe/Mn ratios vary from 37 to 4 with a high value population of 3 and a lower value population of 11.

## 2.3 R/V CONRAD DREDGE HAULS

Sample Description

The R/V CONRAD dredges recovered a silicate-iron oxide-manganese oxide sequence, comprised of 2 Mn crusts from dredge 1 in the fracture zone

TABLE 2.3.1.

DREDGED MANGANESE CRUSTS AND ADHERING SEDIMENTS

| | PERCENT | | | ← PPM | | | | | | →P/C |
|---|---|---|---|---|---|---|---|---|---|---|
| | FE | MN | CA | AL | CO | NI | CU | ZN | PB | TI | $SIO_2$ |
| UNIDCRUSTFE0XSURFACE | 31.00 | 2.76 | 1.26 | 0.04 | 5 | 40 | 28 | 70 | ND | ND | |
| UNIDCRUSTBULK | 4.30 | 44.10 | 1.76 | 0.10 | 12 | 290 | 46 | 210 | ND | 60 | |
| UNIDCRUSTWHITEBASE | 2.40 | 16.00 | 19.70 | 1.14 | 24 | 190 | 72 | 180 | ND | 530 | |
| D2N01T0PMNCRUST | 8.16 | 35.90 | 1.37 | 0.08 | 7 | 50 | 11 | 30 | ND | 40 | |
| D2N01GREENMATERIAL | 18.88 | 13.20 | 0.48 | 0.03 | 9 | 40 | 10 | 30 | ND | ND | 32.37 |
| D2N01B0TT0MCRUST | 7.06 | 36.20 | 1.15 | 0.05 | ND | 140 | 25 | 100 | ND | ND | |
| D2N02KN0BBLYMNCRUST | 4.47 | 42.80 | 1.70 | 0.12 | 8 | 320 | 47 | 250 | ND | 70 | |
| D2N03FE0XIDEC0AT | 21.90 | 12.90 | 0.64 | 0.04 | 9 | 60 | 16 | 60 | ND | ND | 28.36 |
| D2N03BULKCRUST | 7.82 | 37.90 | 1.34 | 0.11 | 16 | 190 | 29 | 125 | ND | 85 | |
| D2N04FE0XIDEC0AT | 30.45 | 3.58 | 1.34 | 0.02 | ND | 50 | 35 | 50 | ND | ND | |
| D2N04T0P5MMMNCRUST | 11.15 | 27.90 | 1.15 | 0.10 | 4 | 250 | 35 | 190 | ND | 60 | |
| D2N04BULKCRUST | 12.10 | 25.40 | 0.83 | 0.01 | ND | 40 | 9 | 20 | 15 | ND | |
| D2N04B0TT0MGREENMAT | 21.20 | 8.43 | 0.41 | 0.02 | 7 | 40 | 17 | 40 | ND | ND | 36.36 |
| D2N05FE0XIDEC0AT | 27.20 | 2.94 | 1.40 | 0.03 | ND | 50 | 90 | 50 | ND | ND | |
| D2N05SURFMNLAYER | 5.46 | 40.80 | 1.93 | 0.02 | 8 | 30 | 14 | 20 | ND | ND | |
| D2N05MID1CMUNIT | 2.97 | 45.80 | 1.78 | 0.04 | ND | 90 | 23 | 50 | ND | ND | |
| D2N05BASALCRUST | 6.02 | 37.90 | 1.31 | 0.18 | 12 | 470 | 56 | 360 | ND | 100 | |
| GRAFZI80D10RANGEMNCR | 5.09 | 38.80 | 1.25 | 0.13 | 17 | 290 | 52 | 171 | ND | ND | |
| GRAFZI80D1FZMANCRUST | 5.00 | 38.90 | 1.28 | 0.06 | 15 | 133 | 29 | 65 | ND | ND | |
| DETECTION LIMIT | | | | | 3 | | | | 5 | 30 | |

(ND=N0T DETECTED)




PLATE 2.3.1. Iron oxide overlain by manganese oxide and underlain by clay minerals.
xl.

PLATE 2.3.2. Laminated manganese oxide overlain by iron oxide and underlain by clay minerals.
xl.






PLATE 2.3.3. x1.

PLATE 2.3.4. x1.






PLATE 2.3.5. x1.

PLATE 2.3.6. Iron oxide coating on manganese oxide.
x1.



at 85°22'W and 17 samples of silicates, Fe and Mn oxides from dredge 2 on the seamount at 0°57'N, 85°29'W.

Of the 19 samples collected, 7 of them represented coatings of green clay material or Fe oxide present as substrate or a surface coating on the Mn crusts. The green clay material was always found underlying the Mn crusts. Plates 2.3.1 and 2.3.2 show the association of silicate and oxide material, from the seamount. Plates 2.3.3 and 2.3.4 show green clay minerals adhering to the bases of Mn crusts, without Fe oxides, and these samples are also from the seamount. Fracture zone Mn crusts from 85°22'W show a blocky structure, with some laminated horizons up to 8 mms in thickness (Plate 2.3.5). A Mn crust from an unidentified location, coated with orange Fe oxide, is shown in Plate 2.3.6.

Bulk Geochemistry and Mineralogy

*Iron Oxides and Clay Minerals*

As stated, 7 samples were separated from the Mn crusts, either from their tops or their bases, and consist of green clay minerals and Fe oxides, with one exception. This sample was rich in Ca (19.7%) and was found to be pelagic foraminiferal calcite-rich sediment which had become mixed with the associated Mn crust on sampling. This explains the lower Fe and Mn content of this sample compared to the other Mn crusts. Trace metals are generally low, whilst Al (1.1%) and Ti (530 ppm) values indicate a small amount of contaminant basaltic detritus, and plagioclase was identified by X.R.D., subsequently in confirmation of this.

The Fe oxide coatings contained 31.0%, 21.9%, 30.5% and 27.2% Fe (see Table 2.3.1). The high Fe values of these samples, their low trace metal content and their similarity to deposits in the FAMOUS area of the Atlantic and in the N.E. Pacific (Hoffert et al., 1978; Grill et al., 1981) confirms their hydrothermal nature. Three of the four samples are low in Mn. When analysed by X.R.D. no identifiable peaks were observed, which is a feature typical of amorphous iron oxyhydroxides of a limonite character. The sample with 21.9% Fe and 12.9% Mn (see D2 No.3, Table 2.3.1) was found not to be a pure Fe-Mn oxide. The sample consisted of 28.4% $SiO_2$

FIG.**2.3.1.** X.R.D. Chart of GRAFZI Dredged Mn Crusts with Adhering Clay Mineral.

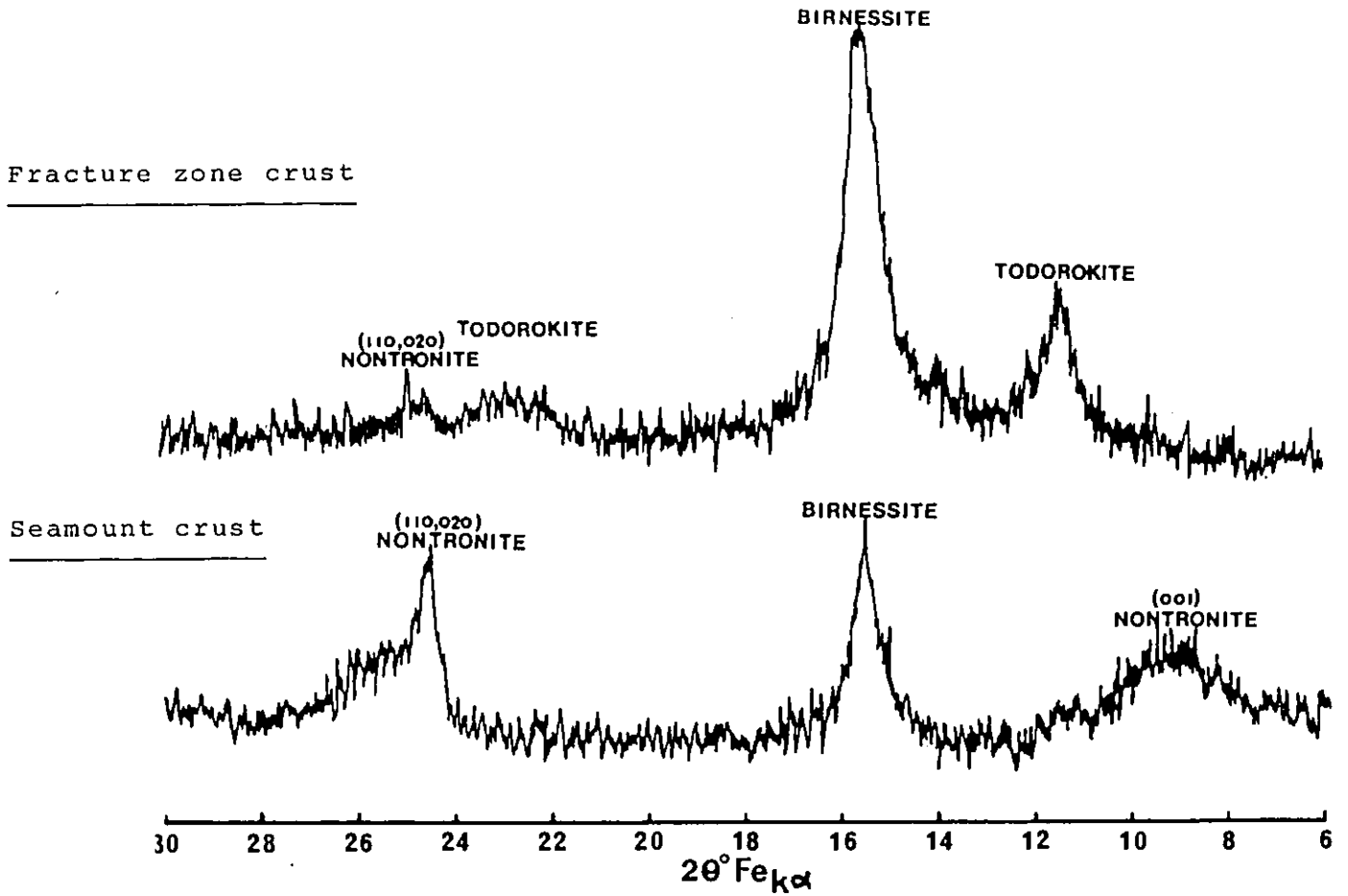


TABLE 2.3.2.

MINERALOGICAL DATA FOR DREDGE 2 SMECTITES FROM THE SEAMOUNT LOCATED NORTH OF THE GALAPAGOS RIFT AT $0^{\circ}57'N$ AND $85^{\circ}29'W$.

| | | | | |
|---|---|---|---|---|
| D2 No.1.....($SiO_2$ =32.4%) | | | | |
| Air dried hkl spacings (in Å) | (001) 12.1 | (110,020) 4.56 | (130,200) 2.58 | (330,060) 1.515 |
| Glycerated hkl spacings (in Å) | ↓ 18.5 | | | |
| D2 No.3.....($SiO_2$ =28.4%) | | | | |
| Air dried hkl spacings (in Å) | (001) 12.3-13.1 | (110,020) 4.54 | (130,200) 2.61 | (330,060) 1.522 |
| Glycerated hkl spacings (in Å) | ↓ 17.1 | | | |
| D2 No.4.....($SiO_2$ =36.4%) | | | | |
| Air dried hkl spacings (in Å) | (001) 12.3 | (110,020) 4.54 | (130,200) 2.59 | (330,060) 1.517 |
| Glycerated hkl spacings (in Å) | ↓ 18.5 | | | |

TABLE 1.3.3.

Comparative Hydrothermal Nontronite Data

| Wt% | GRAFZI, 86°W D2 No.1 | GRAFZI, 86°W D2 No.3 | GRAFZI, 86°W D2 No.4 | A FAMOUS AREA | B GALAPAGOS MOUNDS | C GALAPAGOS FIELD | D EXPLORER RIDGE | E GULF OF ADEN | F RED SEA |
|---|---|---|---|---|---|---|---|---|---|
| $SiO_2$ | 43.1 | 37.4 | 44.7 | 44.4 | 49.4 | 44.4 | 46.4 | 47.3 | 36.4 |
| $Al_2O_3$ | 0.08 | 0.10 | 0.05 | 0.20 | 0.52 | 0.53 | 1.59 | 0.62 | 2.10 |
| $Fe_2O_3$ | 31.0* | 36.2* | 30.2* | 35.6 | 30.4 | 28.9 | 29.3 | 32.5 | 31.5 |
| MgO | NR | NR | NR | 2.84 | 2.37 | 3.65 | 3.22 | 2.99 | 1.50 |
| CaO | 0.89 | 1.18 | 0.71 | 0.80 | 0.05 | 0.56 | 0.50 | 0.77 | 0.50 |
| $TiO_2$ | ND | ND | ND | 0.02 | 0.03 | 0.02 | 0.13 | 0.04 | NR |
| ppm | | | | | | | | | |
| Co | 9 | 9 | 7 | 2 | 3 | 3 | 2 | 12 | NR |
| Ni | 40 | 60 | 40 | 33 | 10 | 17 | 2 | 6 | NR |
| Cu | 10 | 16 | 17 | 49 | 30 | 21 | 9 | ND | 6,390 |
| Zn | 30 | 60 | 40 | 9 | 53 | 56 | 31 | 2 | 15,270 |
| Pb | <5 | <5 | <5 | NR | 55 | 16 | 4 | NR | NR |

(NR = not reported; ND = not determined)

(* = corrected for Fe in Ferromanganese Oxide phases)

Source of Data

A = Hoffert et al., 1978
B = Hékinian et al., 1978
C = Moorby and Cronan, in press
D = Grill et al., 1981
E = Cann et al., 1977
F = Bischoff, 1972.

TABLE 2.3.4.

CALCULATIONS TO EXPRESS NONTRONITE COMPOSITION ON A FERROMANGANESE OXIDE FREE BASIS (AS IN TABLE 2.3.3).

Equation 1..... $Fe^{*}_{(TOTAL)} - (Mn^{*}_{(TOTAL)} \times \frac{Fe}{Mn}_{(CRUST)}) = Fe_{(SMECTITE)}$

eg.D2No.1... 18.9% - ( 13.2% x $\frac{1}{5.13}$ ) = 16.3%.

D2No.3... 21.9% - ( 12.9% x $\frac{1}{4.85}$ ) = 19.2%.

D2No.4...21.2% - ( 8.4% x $\frac{1}{2.10}$ ) = 17.2%.

The ferromanganese oxide content of the samples, expressed as ($Fe_2O_3$+$MnO_2$) is calculated from:-

Equation 2..... $(Fe^{*}_{(TOTAL)} - Fe_{(SMECTITE)} \times \frac{Mol.Wt.Fe_2O_3}{2 \times At.Wt.Fe}) + (Mn^{*}_{(TOTAL)} \times \frac{Mol.Wt.MnO_2}{At.\ Wt.Mn})$ = Ferromanganese Oxide Content.

eg.D2No.1...( 18.9 - 16.3 X $\frac{160}{112}$ ) + ( 13.2 X $\frac{87}{55}$ ) = 24.6%

D2No.3...( 21.9 - 19.2 X $\frac{160}{112}$ ) + ( 12.9 X $\frac{87}{55}$ ) = 24.2%

D2No.4...( 21.2 - 17.2 X $\frac{160}{112}$ ) + ( 8.43 X $\frac{87}{55}$ ) = 19.0%

The major elements contained in the nontronite phase can then be expressed on a ferromanganese oxide free basis, as shown below and as reported in Table 2.3.3.

Equation 3..... $\frac{100\%}{(100-\text{Ferromanganese Oxide})\%}$ = Nontronite Major Element Correction Factor.

eg.D2No.1.....1.33

D2No.3.....1.32

D2No.4.....1.23

(* $Fe_{(TOTAL)}$ and $Mn_{(TOTAL)}$ are reported in Table 2.3.1.)

and X.R.D. peaks with (hkl) spacings are shown in Figure 2.3.1 and Table 2.3.2. Along with samples D2 No.1 and D2 No.4, the properties shown by D2 No. 3 are those which classically belong to smectites (Brindley and Brown, 1980). Expansion of the basal spacing (001) occurred upon glyceration, from 12.1 Å to 18.5 Å, for these smectites.

Nontronite, an Fe-rich member of the smectite group (Brindley and Brown, 1980), has been found commonly associated with hydrothermal systems (Bischoff, 1969; Corliss et al., 1978; Goulart, 1976; Grill et al., 1981; Hékinian et al., 1978; Hoffert et al., 1978; McMurtry et al., 1981) from a variety of locations on the World Mid-Ocean Ridge System. Harder (1976) found by experimental techniques that nontronite could precipitate from low temperature ferrous-ion rich solutions only under reducing conditions. Therefore, nontronite must form from solutions at a lower redox potential than Fe oxyhydroxides.

The nontronite samples (Table 2.3.3) were contaminated with adhering Mn crust material, so the Fe which is present in the ferromanganese oxide phase has been subtracted by using the Fe/Mn ratio of the ferromanganese oxide crust, in that particular sample. This should give a more accurate reflection of the bulk chemical composition of the clay mineral phase itself. The corrected Fe, present in smectite, is shown in Table 2.3.4, calculated from Equation 1. After correction for Fe contained in the ferromanganese oxide phase, the corrected Fe represents that within the nontronite phase but it is necessary to re-calculate the major elements from Table 2.3.1., on a ferromanganese oxide free basis, to understand the true chemical composition of GRAFZI nontronite reported in Table 2.3.3. Trace metals were left uncorrected as it is unknown what the relative contributions are from silicate and oxide phases. The ferromanganese oxide content and the calculated correction factor for the major elements is shown in Table 2.3.4, calculated from Equations 2 and 3, respectively.

TABLE 2.3.5.

Comparative Hydrothermal Mn Crust Data

| Wt% | GRAFZI, 86°W D2 No.1 | A TAG N.ATLANTIC 26°N | B FAMOUS N.ATLANTIC 37°N. | C GALAPAGOS RIFT 95°W | D E.P.R., 20°S (GEOMETEP) | E EXPLORER RIDGE, N.E.PACIFIC, 50°N | F S.W.PACIFIC 177°W, 27°S |
|---|---|---|---|---|---|---|---|
| Mn | 35.9 | 41.0 | 31.0 | 52.5 | 48.2 | 44.3 | 49.0 |
| Fe | 8.16 | 0.13 | 6.77 | 0.21 | 0.08 | 1.95 | 0.05 |
| Ca | 1.37 | NR | NR | NR | 1.10 | 1.14 | 2.20 |
| Al | 0.08 | 0.07 | 0.50 | 0.06 | ND | <0.05 | 0.03 |
| ppm | | | | | | | |
| Co | 7 | 6 | 83 | 10 | 15 | 2 | 8 |
| Ni | 50 | 440 | 163 | 67 | 554 | 6 | 93 |
| Cu | 11 | 104 | 143 | 88 | 170 | 6 | 24 |
| Zn | 30 | 195 | 102 | 495 | 94 | 13 | 110 |
| Pb | <5 | 4 | <1 | 7 | 17 | <1 | 9 |

(NR = not reported; ND = not determined)

Source of Data

A = Scott et al., 1974
B = Toth, 1980
C = Moore and Vogt, 1976
D = GEOMETEP (this work)
E = Grill et al., 1981
F = Cronan et al., in press

Table 2.3.3 attempts to synthesise previously published hydrothermal nontronite data which show similarities to GRAFZI nontronites. With the sole exception of the Red Sea smectite, all analyses show very low trace metal contents. The Red Sea smectite high trace metal content is probably due to the presence of admixed fine-grained chalcopyrite and sphalerite (Degens and Ross, 1969). The GRAFZI nontronite has between 37% and 45% $SiO_2$, with 30% to 36% $Fe_2O_3$ and only minor amounts of $Al_2O_3$ and CaO. MgO was not determined, but by analogy with the other reported nontronites, is presumably also low in concentration. The nontronite is thus a very pure, low trace metal, hydrothermal iron silicate.

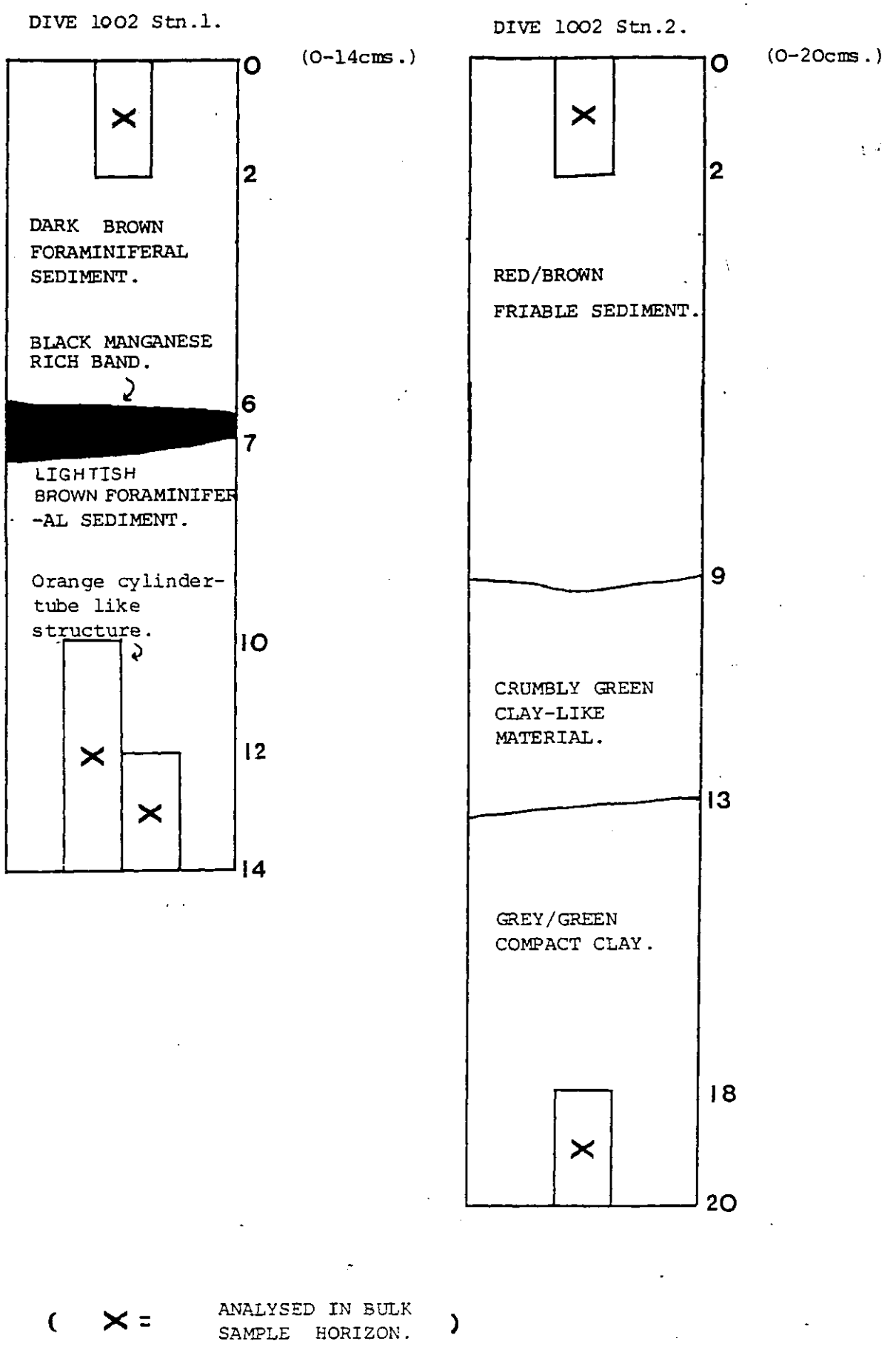
*Manganese Crusts*

The Mn crusts proper, show a range in Fe content from 3.0% to 12.1% and Mn from 25.4% to 45.8%. This variation is reflected in Mn/Fe ratios from 15.4 in sample D2 No.5, to 2.1 in sample D2 No.4. This latter ratio represents the hydrothermal ferromanganese oxide with the largest component of Fe, perhaps formed nearest to a hydrothermal vent. Peculiar to GRAFZI Mn crusts, is their high Fe content, and these may represent samples (as in Burnett and Piper, 1977) which truly represent hydrothermal precipitates transitional between the Fe and Mn end-members.

Well-crystalline birnessite was the most abundant Mn oxide mineral in the Mn crusts (see Figure 2.3.1) but todorokite was more abundant in 2 samples taken from the fracture zone at 85°22'W.

Trace metals are uniformly low in the Mn crusts compared with hydrogenous crusts, with a maximum of 17 ppm Co, 470 ppm Ni, 56 ppm Cu, 360 ppm Zn and 15 ppm Pb. Comparative data for other hydrothermal Mn oxides is given in Table 2.3.5. Sample D2 No.5 has the highest values for Ni, Cu and Zn. Co has been found to be markedly depleted in hydrothermal ferromanganese oxides (Cronan, 1975; Toth, 1980) which are thought to accumulate two or three orders of magnitude faster than hydrogenous Mn nodules (Scott et al., 1974; Moore and Vogt, 1976).

FIG.2.4.1. CORE DESCRIPTIONS.




( × = ANALYSED IN BULK SAMPLE HORIZON. )

Table 2.3.5 gives a comparison of the GRAFZI Mn crusts with other hydrothermal deposits on the World Mid-Ocean Ridge System. These hydrothermal Mn crusts show a variability in Fe and Mn content which can be explained by chemical fractionation. GRAFZI Mn crusts show a similarity to FAMOUS deposits, although compositional variability is marked in both areas (see Table 2.3.1 and Hoffert et al., 1978). However, TAG Mn crusts show an enrichment in Mn and very low Fe contents. Trace metal content is low throughout all the deposits compared to typical slowly accumulating Mn nodules (Cronan, 1980). Some of the hydrothermal Mn crusts shown in Table 2.3.5 contain relatively high Ni and Zn which may be due to additional metal supply from hydrogenous sources (Goldberg, 1954).

## 2.4 SHORT SEDIMENT CORES

### Sample Description

Of the 17 cores collected, 2 cores from Dive 1002 were highly ferruginous in nature, especially at their tops (Figure 2.4.1). Further down the cores the sediment becomes more grey/green in colour and of a clay-like consistency. The cores collected were all less than 37 cms in length and so have been termed ALVIN short cores. Samples were taken of horizons which appeared to be lithologically different from the adjacent sediment, whilst attempting to sample representatively over the whole core length.

Most of the cores show a gradational contact between dark yellow brown sediment in the upper core and grayish yellow sediment below. The amount of basaltic glass increased in the lower parts of the core where sand-sized fragments were common and occasionally fragments greater than 1 cm in diameter were found. The gradational contact between layers generally occurs around 15-20 cms below the core top, but core 995-3 shows a change in colour and constitution of the sediment 2 cms below the surface.

Short cores from ALVIN dives 995-1, 997-1, 998-1, 999-3 and 1001-1 show dark yellowish brown/chocolate brown sediment throughout their whole core lengths. This is, in part, due to the short nature of the cores, e.g. the core recovered on Dive 999-3 is only 15 cms long. However, the core from Dive 997-1 shows uniform brown coloration throughout 22 cms and this core was situated in the fracture

TABLE 2.4.1

SHORT CORE $CO_3$ SEDIMENTS

(Carbonate Free Data.)

| | %Fe | %Mn | %Ca | %Al | Co | Ni | Cu | Zn | Pb | Ti | %$CaCO_3$ | %$SiO_2$ |
|---|---|---|---|---|---|---|---|---|---|---|---|---|
| DIVE1002ST10-2CMS | 9.14 | 8.22 | 21.50 | 2.50 | 24 | 270 | 156 | 262 | ND | 2487 | 51.6 | 25.8 |
| DIVE1002STN110-14CYL | 30.62 | 0.23 | 5.60 | 0.27 | ND | 20 | 31 | 106 | ND | ND | 11.0 | 16.7 |
| DIVE1002STN112-14CMS | 13.47 | 2.12 | 20.50 | 2.52 | 29 | 116 | 168 | 274 | ND | 2938 | 49.1 | 24.5 |
| DIVE1002STN20-2CM | 30.23 | 1.31 | 2.05 | 0.05 | 7 | 15 | 8 | 34 | ND | ND | ND | 16.0 |
| DIVE1002STN218-20CM | 14.71 | 0.48 | 22.00 | 2.65 | 21 | 83 | 152 | 261 | ND | 2869 | 53.1 | 26.1 |
| ALVIN994=110-12CM | 4.41 | 1.80 | 27.50 | 4.29 | 45 | 180 | 327 | 225 | ND | 3675 | 67.1 | 39.8 |
| ALVIN994=125-27CM | 4.20 | 2.22 | 28.50 | 4.14 | 29 | 257 | 456 | 290 | ND | 3341 | 69.5 | 38.8 |
| ALVIN994=24-6CM | 4.02 | 2.97 | 26.00 | 4.66 | 35 | 284 | 225 | 233 | ND | 4355 | 63.2 | 42.9 |
| ALVIN994-218-21CM | 3.73 | 0.27 | 26.00 | 4.34 | 27 | 145 | 391 | 217 | ND | 3417 | 63.2 | 41.3 |
| ALVIN994=34-6CM | 3.73 | 2.50 | 23.00 | 3.60 | 31 | 285 | 170 | 232 | ND | 2319 | 55.4 | 39.6 |
| ALVIN994=319-23CM | 4.20 | 0.23 | 24.00 | 5.28 | 31 | 122 | 171 | 218 | ND | 4869 | 58.2 | 47.3 |
| ALVIN995=14-6CM | 3.37 | 2.28 | 24.50 | 4.24 | 39 | 225 | 208 | 274 | ND | 2906 | 59.3 | 39.3 |
| ALVIN995=24-6CM | 3.79 | 4.21 | 21.25 | 4.31 | 34 | 357 | 198 | 272 | ND | 3506 | 51.0 | 38.7 |
| ALVIN995=221-23CM | 5.61 | 0.71 | 22.00 | 4.38 | 31 | 198 | 146 | 248 | ND | 6260 | 53.1 | 41.4 |
| ALVIN995=310-12CM | 4.47 | 0.26 | 28.50 | 3.10 | 33 | 179 | 261 | 293 | ND | 3667 | 69.7 | 37.6 |
| ALVIN996=14-6CM | 3.07 | 1.85 | 30.50 | 3.82 | 39 | 225 | 162 | 181 | ND | 2759 | 74.6 | 40.4 |
| ALVIN997=15-7CM | 2.97 | 4.72 | 18.75 | 4.30 | 27 | 492 | 269 | 444 | ND | 2255 | 44.7 | 37.2 |
| ALVIN997=25-7CM | 3.48 | 4.13 | 22.00 | 4.97 | 38 | 384 | 317 | 394 | ND | 2556 | 53.1 | 38.8 |
| ALVIN997=227-29CM | 5.28 | 0.72 | 26.00 | 3.83 | 32 | 225 | 289 | 512 | ND | 2278 | 63.2 | 35.7 |
| ALVIN998=14-6CM | 3.28 | 2.97 | 27.75 | 3.95 | 40 | 318 | 199 | 223 | ND | 2831 | 67.6 | 38.7 |
| ALVIN998=24-6CM | 3.85 | 3.20 | 29.00 | 4.02 | 41 | 303 | 235 | 215 | ND | 3832 | 70.9 | 39.7 |
| ALVIN998=218-20CM | 4.09 | 0.24 | 29.00 | 3.88 | ND | 143 | 255 | 293 | ND | 2896 | 70.9 | 44.1 |
| ALVIN998=223-26CM | 4.00 | 0.17 | 28.85 | 3.26 | 20 | 158 | 218 | 323 | ND | 2773 | 70.4 | 41.1 |
| ALVIN999=13-5CM | 3.54 | 1.40 | 32.50 | 3.59 | 40 | 149 | 194 | 199 | ND | 3986 | 79.7 | 36.1 |
| ALVIN999=110-12CM | 4.09 | 0.77 | 33.25 | 3.87 | 44 | 100 | 210 | 160 | ND | 3871 | 81.7 | 37.7 |
| ALVIN999=37-9CM | 6.99 | 2.27 | 20.00 | 5.82 | 45 | 254 | 192 | 214 | ND | 8501 | 48.0 | 43.6 |
| ALVIN999=411-13CM | 6.65 | 1.03 | 21.75 | 5.82 | 45 | 123 | 165 | 181 | ND | 8439 | 52.3 | 43.3 |
| ALVIN1001=13-5CM | 5.67 | 3.59 | 25.25 | 3.61 | 51 | 313 | 659 | 394 | ND | 3435 | 61.2 | 38.5 |

p.p.m. unless stated.
N.D. = NOT DETECTED.

zone at 85°22'W, far removed from the proven site of hydrothermal activity at Dive 1001 (see Chapter 1, Figure 1.1).

Bulk Geochemistry and Mineralogy

Bulk chemical analyses for 28 sediment samples are shown in Table 2.4.1, and are expressed on a carbonate free basis using the method of Dymond et al (1976), described in Appendix D. The removal of the calcium carbonate component of pelagic sediment allows detailed study of the geochemical variation within the remaining sediment fractions.

The aim of this study of ALVIN short cores is to examine the distribution of elements and their dispersion away from known hydrothermal sources, e.g. Dive 1001, and to locate areas of anomalous metal concentrations possibly reflecting dispersion from other suspected hydrothermally active sites. This localised study will be supplemented by a regional study of sediment cores taken more widely over the 86°W area (see Section 2.6).

The sediments analysed fall into the foraminiferal marl and chalk ooze categories, according to the classification of Olausson (1960), with 30-60% $CaCO_3$ and greater than 60%, respectively. $CaCO_3$ varies between 44.7% and 81.7%, excluding cores taken during Dive 1002 in the hydrothermal ferromanganese oxide facies, where, in one sample, $CaCO_3$ is not present. Samples from Dive 1002 cores have a maximum of 30.6% Fe and 8.2% Mn with Fe/Mn ratios varying between 133 in the Fe rich sample (Dive 1002, Station 1, 10-14 cms; see Figure 2.4.1) and 1.1 in the uppermost layer from Dive 1002, Station 1, 0-2 cms. Trace metal content is variable with maxima of 29 ppm Co, 270 ppm Ni, 168 ppm Cu and 274 ppm Zn. The Dive 1002 Station 1 core has a relatively constant $SiO_2$ content throughout the core, from 25.8% at the top to 24.5% at the base. Similarly, $CaCO_3$ is constant at about 50%. The exception to this is the sample from 10-14 cms in a core taken from Dive 1002 Station 1, which is very rich in Fe and lower in $CaCO_3$ and $SiO_2$. Figure 2.4.1 shows a lithological description of this core, where Fe increases from 9.1% to 30.6% from top to bottom, whilst Mn decreases from 8.2% to 0.2%.

A Mn-rich band occurs at 6-7 cms depth. Episodic hydrothermal input, with Mn oxides as the last hydrothermal precipitates, have been noted in the varve-like Red Sea sediments (Backer and Richter, 1973). The Mn oxide layer may therefore represent the last product of hydrothermal activity, before processes were restarted.

The Dive 1002 Station 2 core also shows a decrease in Mn downcore from 1.3% to 0.5%, and in Fe from 30.2% to 14.7%, whilst the most enriched trace metal content occurs at the core bottom, but is still very low with 21 ppm Co, 83 ppm Ni, 152 ppm Cu and 261 ppm Zn. $CaCO_3$ varies from 53% to zero, from core bottom to top. Antipathetically to the variation of Fe and Mn, $SiO_2$ increases from 16% to 26% from top to bottom. This observation, coupled with a change in colour from red/brown to green in the sediment (Figure 2.4.1) suggests an increase in the clay mineral component downcore, identified as smectite by bulk X.R.D. From the above it is evident that cores from Dive 1002 Stations 1 and 2, show a smectite-iron oxide-manganese oxide fractionation throughout their lengths. Dives 1001 and 1002 together illustrate, for the first time outside the Red Sea, a sulphide-smectite-iron oxide-manganese oxide sequence.

The remaining cores were markedly less enriched in Fe and Mn oxides than Dive 1002 cores. A maximum Fe content of 7% occurs in sediment from Dive 999, and high Mn (3.6%) was found in a core taken during Dive 1001.

Examination of the bulk geochemical data from cores taken during Dives 994, 995, 996, 997 and 998 reveals more subtle enrichments of hydrothermal elements dispersed in seawater from their source. To appreciate anomalous metal concentrations it is necessary to adopt a geochemical background value, and the data of Moorby and Cronan (1983a) for 90 pelagic sediments from the Galapagos Hydrothermal Mounds Field have been used for this purpose as follows:-

| Mn | Fe | Ni | Co | Cu | Zn | Ti | |
|---|---|---|---|---|---|---|---|
| % | % | ppm | ppm | ppm | ppm | ppm | (Carbonate Free |
| 0.79 | 3.8 | 260 | 27 | 255 | 420 | 1730 | Data) |

The most markedly enriched samples, above this background value for Fe, are in cores from Dives 995 and 997. These cores also show very marked Mn enrichment above background values, of the magnitude reported by Bonatti et al (1971) and Moorby and Cronan (1982) for the surface oxidised layer of pelagic carbonate oozes in this area. This observation suggests two possible sources for Mn in the sediments, one from diagenetic remobilisation of Mn and its re-precipitation within the upper oxidised layer, as noted by Lynn and Bonatti (1965), and the other from hydrothermal dispersion of Mn from its source. Both of these mechanisms are likely to contribute Mn to GRAFZI pelagic sediments.

Of the trace metals, Co is very close to background , whilst Ni shows a maximum value of 492 ppm in a core from Dive 997. These two elements are not thought to be supplied by submarine hydrothermal solutions but by biogenous and hydrogenous processes (Goldberg, 1954; Sclater et al, 1976). Cu (659 ppm) is most abundant in sediment from the top of a core from Dive 1001, i.e. the known hydrothermal site, and is also high (456 ppm) in samples from Dive 994, compared to the background value of 255 ppm. A core from Dive 1001 contained 394 ppm Zn, which is below the assumed background of 420 ppm, while cores from Dive 997 contained up to 512 ppm Zn. It is interesting to note that the hydrothermal sulphide mounds were substantially richer in Cu than Zn, which was quantitatively depleted, and that the pelagic sediment cores tend to show a slight enrichment in Zn (with a maximum of 512 ppm) rather than Cu (with a maximum of 456 ppm). The Zn/Cu ratio for Dive 1001 sediment is 0.6 and this is similar to sediment from the E.P.R., $20^{\circ}S$, with a ratio of approximately 0.5 (see Part 2 of this work) whereas the normal pelagic sediment ratio for this area is 1.6.

The Cu enrichment seems to be restricted to the vicinity of the hydrothermal sulphide mounds (Dive 1001), whilst Zn, which is low in the sulphide mounds, seems to be more mobile and to have dispersed greater distances than Cu. Thus, Zn/Cu ratios may reflect the effects of hydrothermal dispersion in seawater although it must be borne in mind that both metals can be scavenged from a

**TABLE 2.5.1.**
(Raw Data.)

SHORT CORE CARBONATE SEDIMENTS

| | PERCENT | | | PPM | | | | | | P/C | P/C |
|---|---|---|---|---|---|---|---|---|---|---|---|
| | FE | MN | CA | AL | CO | NI | CU | ZN | PB | TI | CACO3 | $SIO_2$ |
| DIVE1002STN10-2CM | 4.50 | 4.05 | 21.50 | 1.23 | 12 | 133 | 77 | 129 | ND | 1225 | 51.6 | 12.49 |
| DIVE1002STN110-14CYL | 27.99 | 0.21 | 5.60 | 0.25 | ND | 18 | 28 | 97 | ND | ND | 11.0 | 14.87 |
| DIVE1002STN112-14CMS | 6.99 | 1.10 | 20.50 | 1.31 | 15 | 60 | 87 | 142 | ND | 1525 | 49.1 | 12.48 |
| DIVE1002STN20-2CM | 30.23 | 1.31 | 2.05 | 0.05 | 7 | 15 | 8 | 34 | ND | ND | ND | 15.95 |
| DIVE1002STN218-20CM | 7.05 | 0.23 | 22.00 | 1.27 | 10 | 40 | 73 | 125 | ND | 1375 | 53.1 | 12.26 |
| ALVIN994=110-12CM | 1.47 | 0.60 | 27.50 | 1.43 | 15 | 60 | 109 | 75 | ND | 1225 | 67.1 | 13.11 |
| ALVIN994=125-27CM | 1.29 | 0.68 | 28.50 | 1.27 | 9 | 79 | 140 | 89 | ND | 1025 | 69.5 | 11.82 |
| ALVIN994=24-6CM | 1.50 | 1.11 | 26.00 | 1.74 | 13 | 106 | 84 | 87 | ND | 1625 | 63.2 | 15.77 |
| ALVIN994=218-21CM | 1.39 | 0.10 | 26.00 | 1.62 | 10 | 54 | 146 | 81 | ND | 1275 | 63.2 | 15.19 |
| ALVIN994=34-6CM | 1.69 | 1.13 | 23.00 | 1.63 | 14 | 129 | 77 | 105 | ND | 1050 | 55.4 | 17.68 |
| ALVIN994=319-23CM | 1.79 | 0.10 | 24.00 | 2.25 | 13 | 52 | 73 | 93 | ND | 2075 | 58.2 | 19.76 |
| ALVIN995=14-6CM | 1.39 | 0.94 | 24.50 | 1.75 | 16 | 93 | 86 | 113 | ND | 1200 | 59.3 | 16.01 |
| ALVIN995=24-6CM | 1.89 | 2.10 | 21.25 | 2.15 | 17 | 178 | 99 | 136 | ND | 1750 | 51.0 | 18.98 |
| ALVIN995=221-23CM | 2.69 | 0.34 | 22.00 | 2.10 | 15 | 95 | 70 | 119 | ND | 3000 | 53.1 | 19.44 |
| ALVIN995=310-12CM | 1.37 | 0.08 | 28.50 | 0.95 | 10 | 55 | 80 | 90 | ND | 1125 | 69.7 | 11.39 |
| ALVIN996=14-6CM | 0.78 | 0.47 | 30.50 | 0.97 | 10 | 57 | 41 | 46 | ND | 700 | 74.6 | 10.27 |
| ALVIN997=15-7CM | 1.68 | 2.67 | 18.75 | 2.43 | 15 | 278 | 152 | 251 | ND | 1275 | 44.7 | 20.57 |
| ALVIN997=25-7CM | 1.67 | 1.98 | 22.00 | 2.38 | 18 | 184 | 152 | 189 | ND | 1225 | 53.1 | 18.20 |
| ALVIN997=227-29CM | 1 97 | 0.27 | 26.00 | 1.43 | 12 | 84 | 108 | 191 | ND | 850 | 63.2 | 13.14 |
| ALVIN998=14-6CM | 1.07 | 0.97 | 27.75 | 1.29 | 13 | 104 | 65 | 73 | ND | 925 | 67.6 | 12.55 |
| ALVIN998=24-6CM | 1.13 | 0.94 | 29.00 | 1.18 | 12 | 89 | 69 | 63 | ND | 1125 | 70.9 | 11.54 |
| ALVIN998=218-20CM | 1.20 | 0.07 | 29.00 | 1.14 | ND | 42 | 75 | 86 | ND | 850 | 70.9 | 12.83 |
| ALVIN998=223-26CM | 1.19 | 0.05 | 28.85 | 0.97 | 6 | 47 | 65 | 96 | ND | 825 | 70.4 | 12.17 |
| ALVIN999=13-5CM | 0.71 | 0.28 | 32.50 | 0.72 | 8 | 30 | 39 | 40 | ND | 800 | 79.7 | 7.32 |
| ALVIN999=110-12CM | 0.74 | 0.14 | 33.25 | 0.70 | 8 | 18 | 38 | 29 | ND | 700 | 81.7 | 6.89 |
| ALVIN999=37-9CM | 3.72 | 1.21 | 20.00 | 3.10 | 24 | 135 | 102 | 114 | ND | 4525 | 48.0 | 22.67 |
| ALVIN999=411-13CM | 3.23 | 0.50 | 21.75 | 2.83 | 22 | 60 | 80 | 88 | ND | 4100 | 52.3 | 20.65 |
| ALVIN1001=13-5CM | 2.23 | 1.41 | 25.25 | 1.42 | 20 | 123 | 259 | 155 | ND | 1350 | 61.2 | 14.93 |

DETECTION LIMIT.....3.....10

(ND=NOT DETECTED)

hydrogenous source also (Goldberg and Arrhenius, 1958). Zn and Cu enrichment are dealt with more thoroughly in the section on regional sedimentation (see Section 2.6).

X-Ray diffraction studies showed quartz and plagioclase to be ubiquitous, in small amounts, throughout these sediments, with occasional traces of pyroxene. In addition, Al contents of 3.1 to 5.8% and Ti values of 2260 to 8500 ppm imply that basaltic detritus and clay minerals (Al-silicates) occur in all the sediments sampled from the 86°W area. $SiO_2$ levels vary from 35.7% to 47.3%. Smear slide analysis showed that the sediments contained abundant siliceous microfossils, as might be expected since the GRAFZI area lies beneath the equatorial zone of high biological productivity.

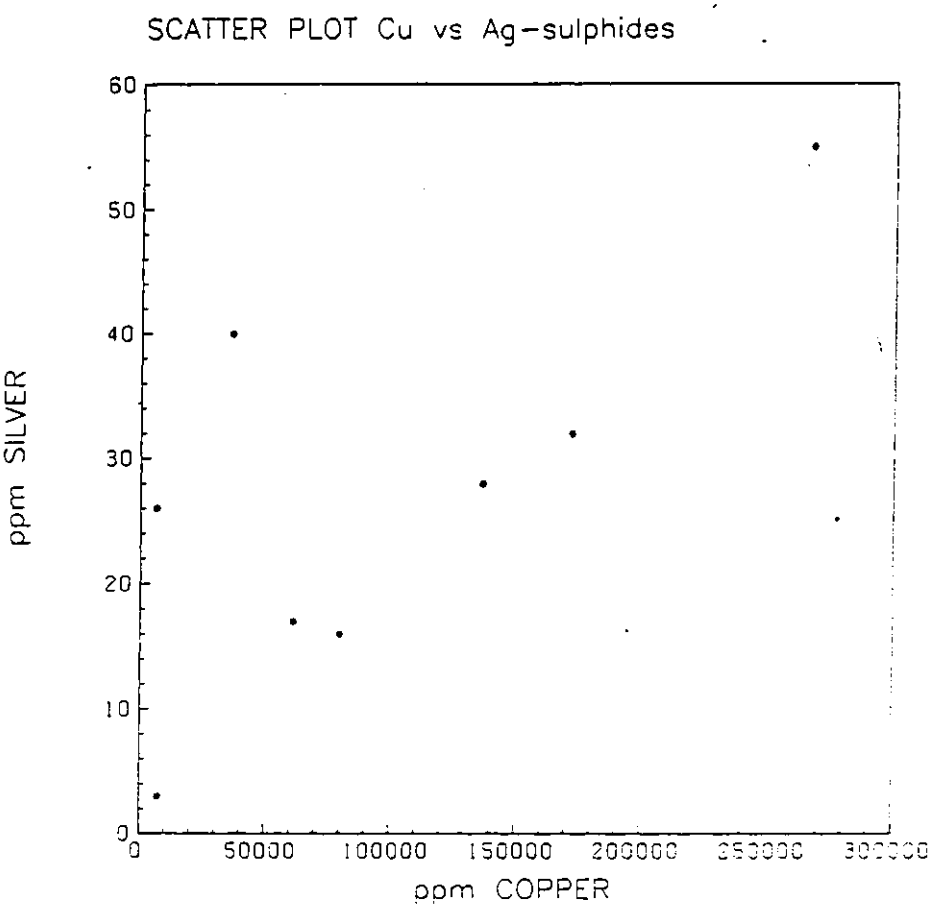
It would be premature at this stage to pinpoint hydrothermal sources other than the one found during Dive 1001. However, the enrichment of Mn and Zn in sediments from Dives 995 and 997 indicates that a second hydrothermal source may occur in this area around 85°22'W. In Section 2.6 a study of the regional sedimentation pattern is undertaken which examines this possibility in more detail.

## 2.5 STATISTICAL ANALYSIS

To understand inter-element relationships from multi-element geochemical analysis, it is useful to undertake statistical analysis of the raw data. Scatterplots and correlations as well as frequency distribution histograms have been used to statistically analyse the data (Table 2.5.1), at a 99% level of confidence. Log normal data were used to remove negatively skewed populations. The necessity for sub-division of the samples into the four groups described above was reinforced when it was found that certain groups demonstrated co-variance between certain elements whilst others did not.

In this section, the basic correlations for GRAFZI samples are reported, with critical values for r (correlation coefficient), determined from Neave (1981).

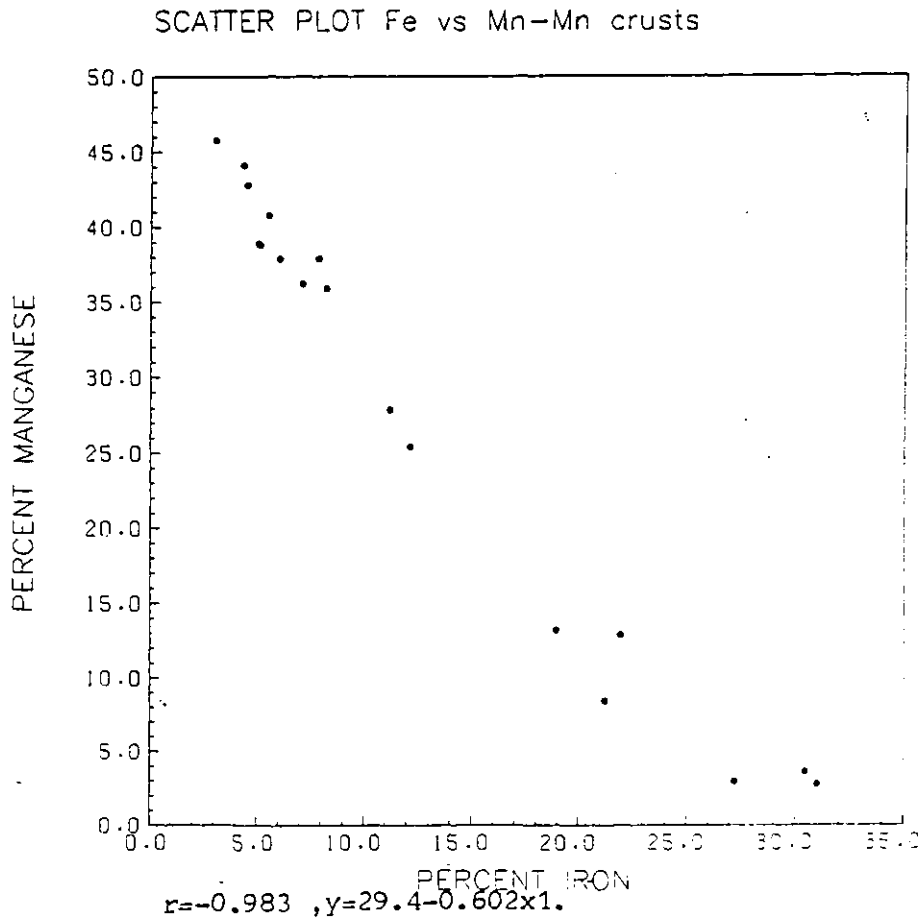
**FIG.2.5.1.**




r=0.710 ,y=-13811+4042x1.

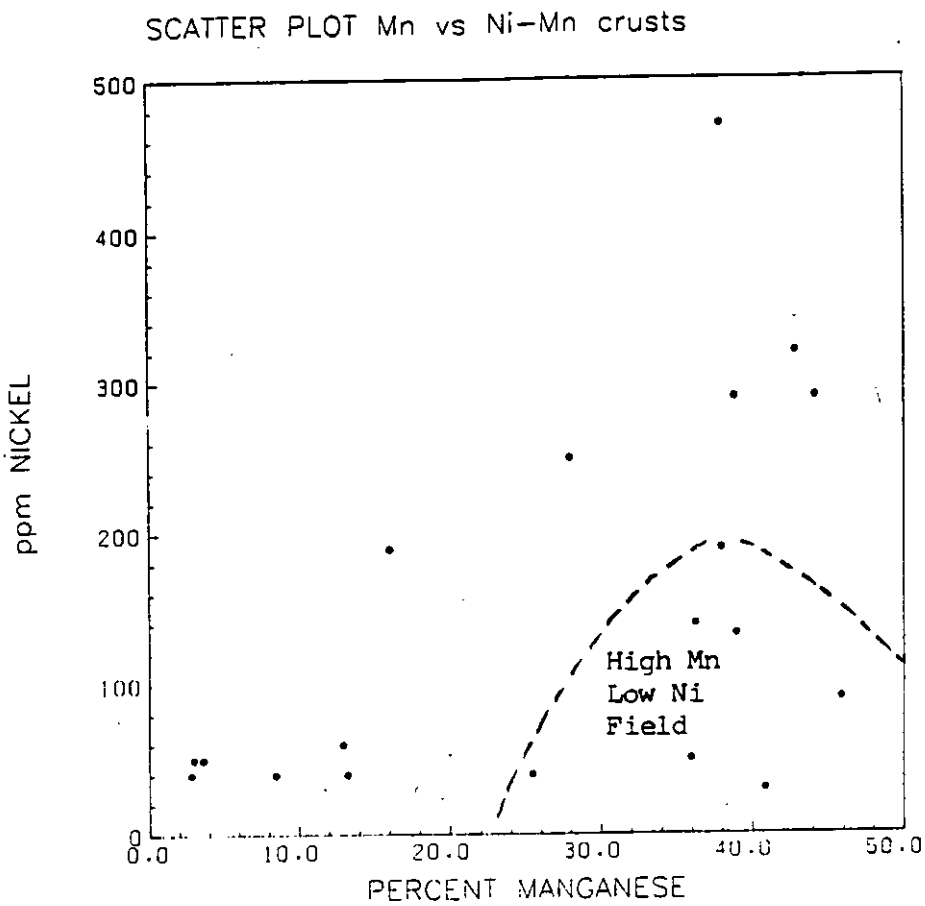
r=correlation coefficient.
y=regression equation.

**FIG.2.5.2.**




r=-0.983 ,y=29.4-0.602x1.

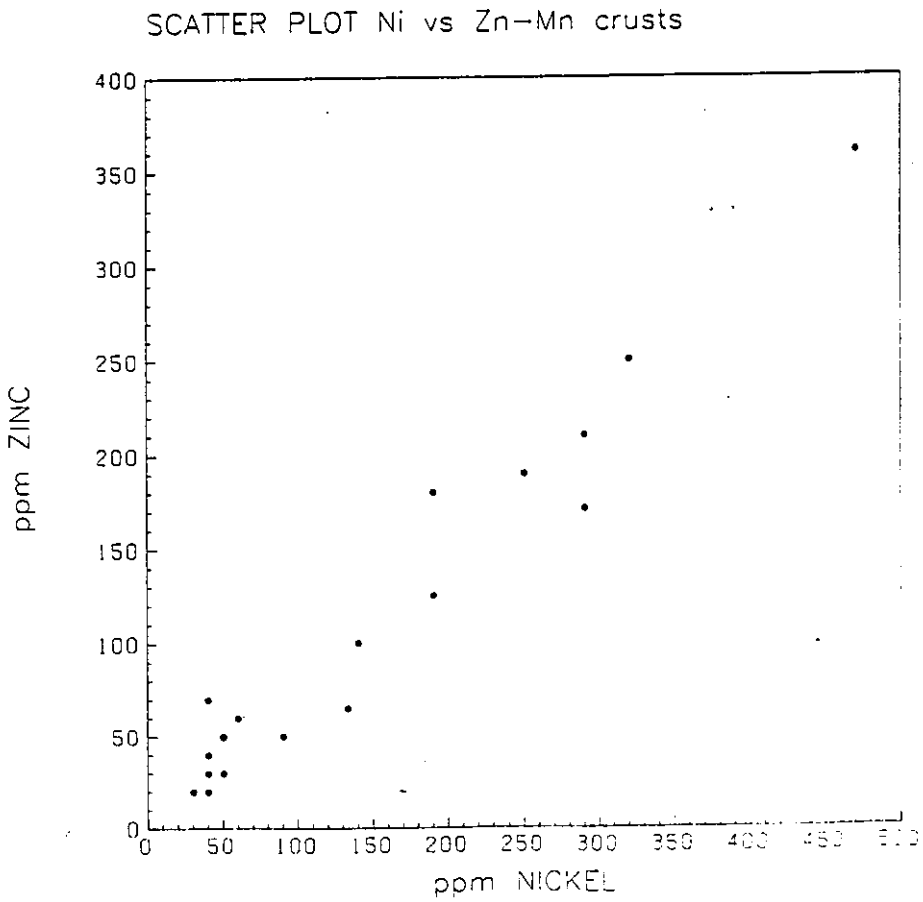
**FIG.2.5.3.**




r=0.616 ,y=-2.20+1.04x1.

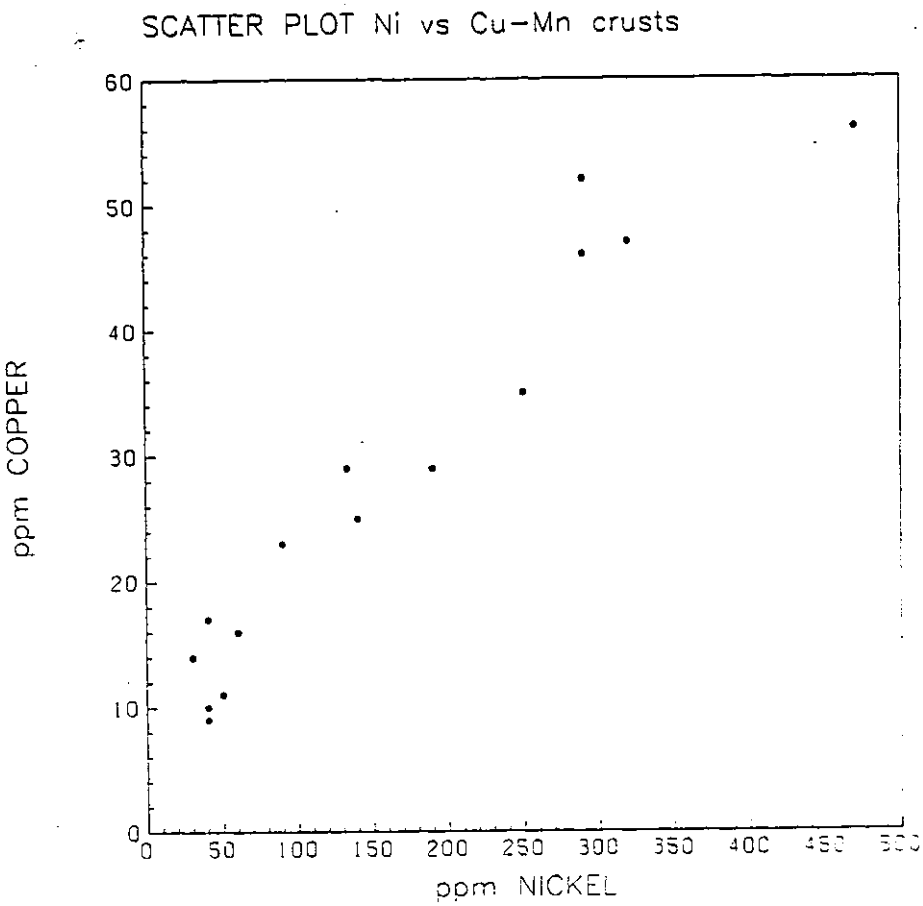
r=correlation coefficient.
y=regression equation.

**FIG.2.5.4.**



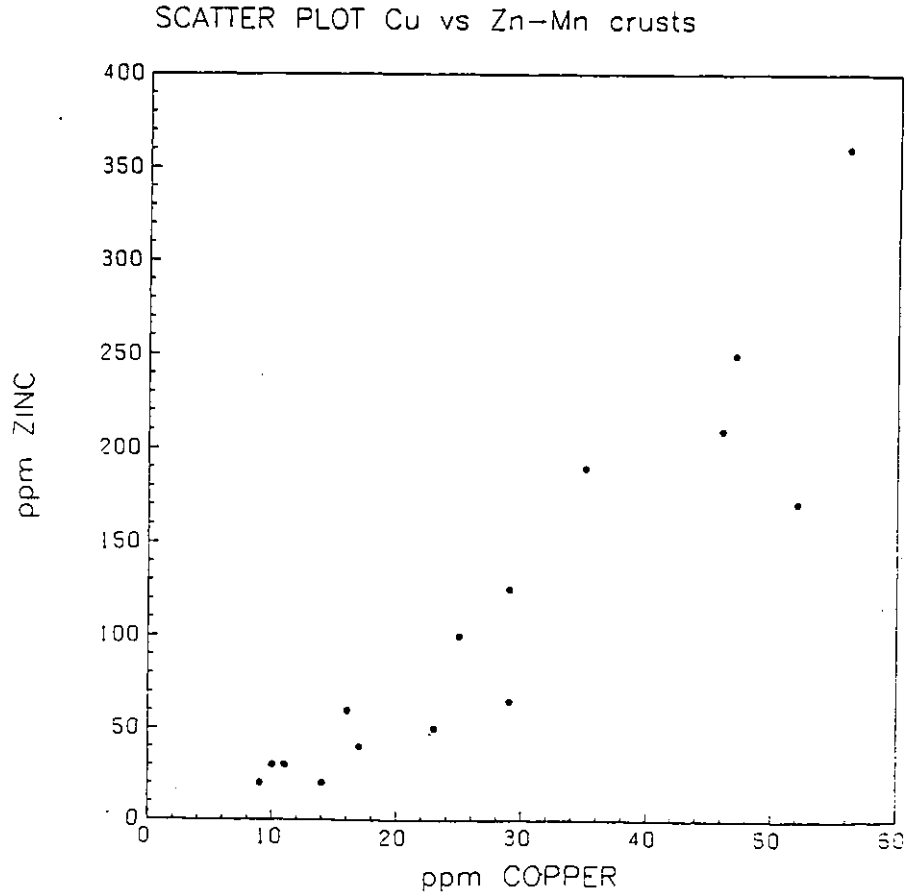

r=0.941 ,y=0.187+0.962x1.

**FIG.2.5.5.**



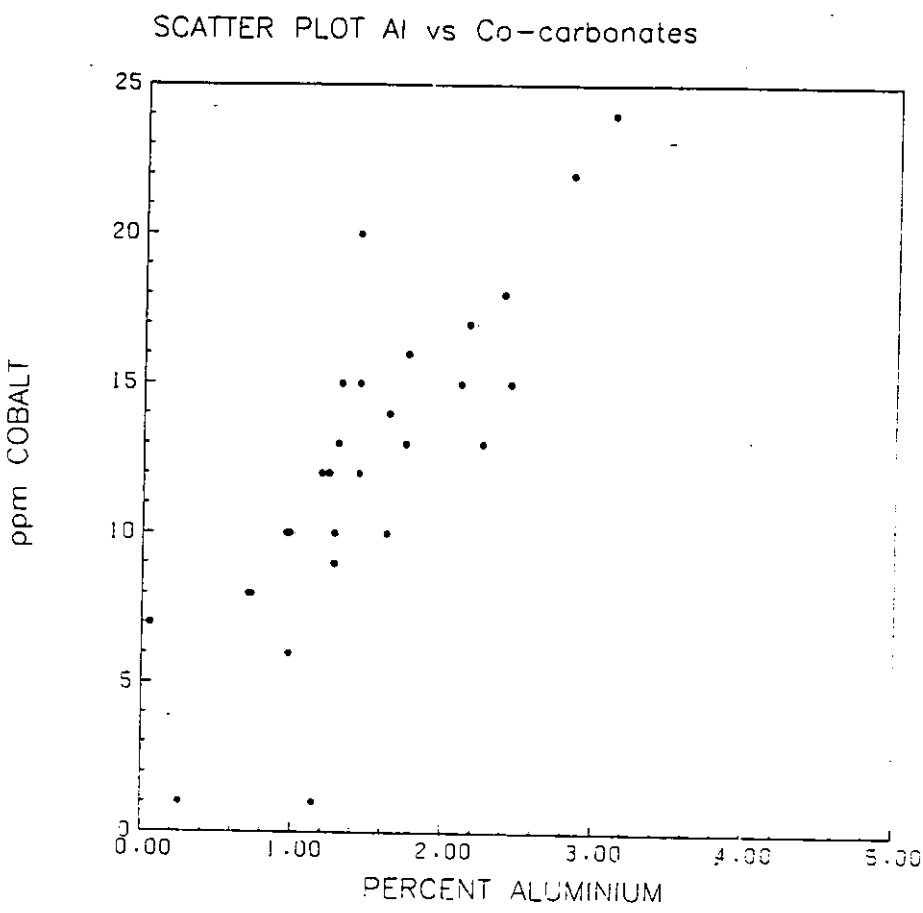

r=0.951 ,y=0.0899+1.43x1.

**FIG.2.5.6.**

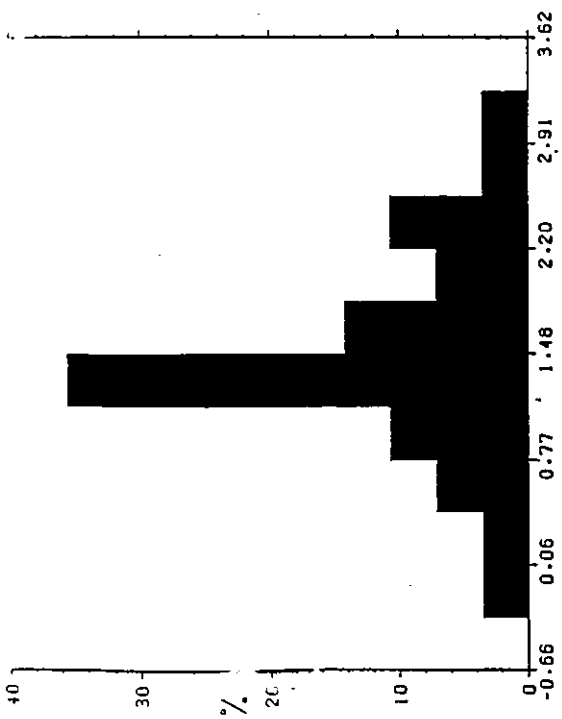



r=0.923 ,y=11.3+0.145x1.

FIG.2.5.7.




r=0.808 ,y=0.162+0.107x1.
r=correlation coefficient.
y=regression equation.



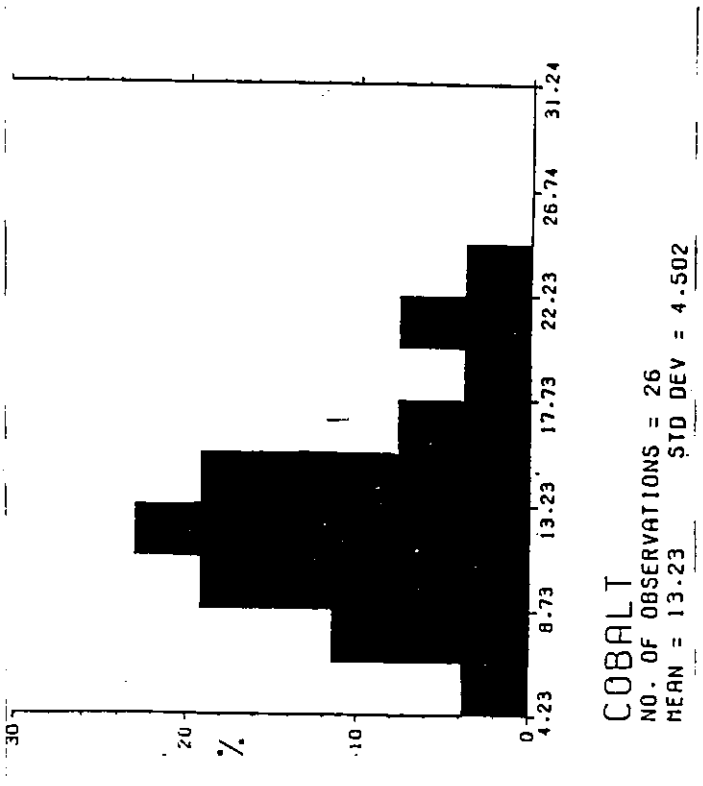
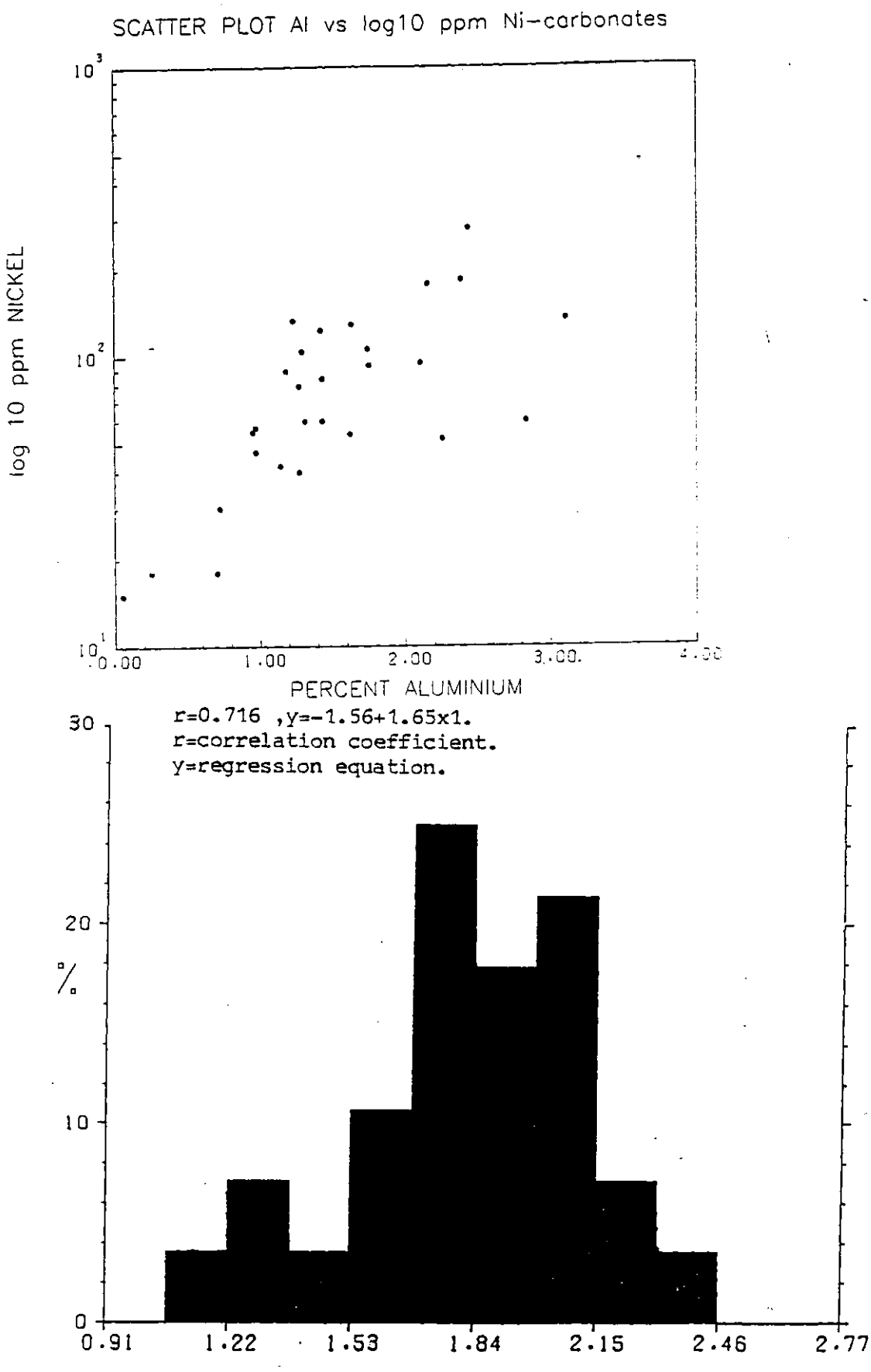



FIG. 2.5.8.



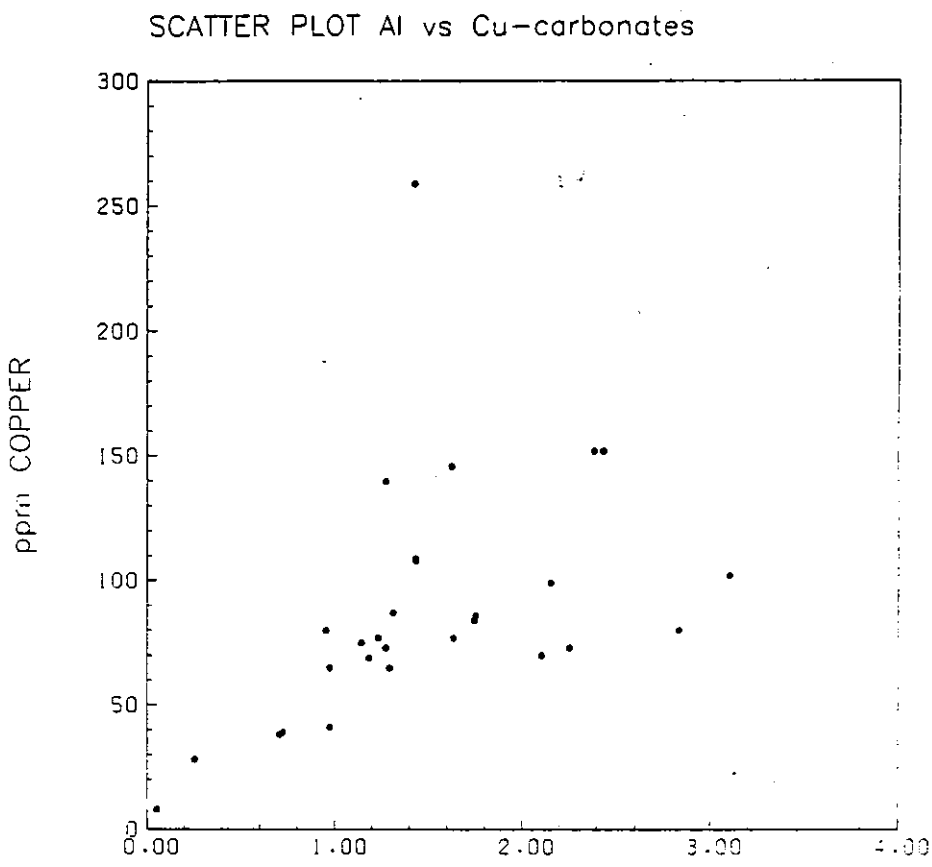

NICKEL

NO. OF OBSERVATIONS = 28

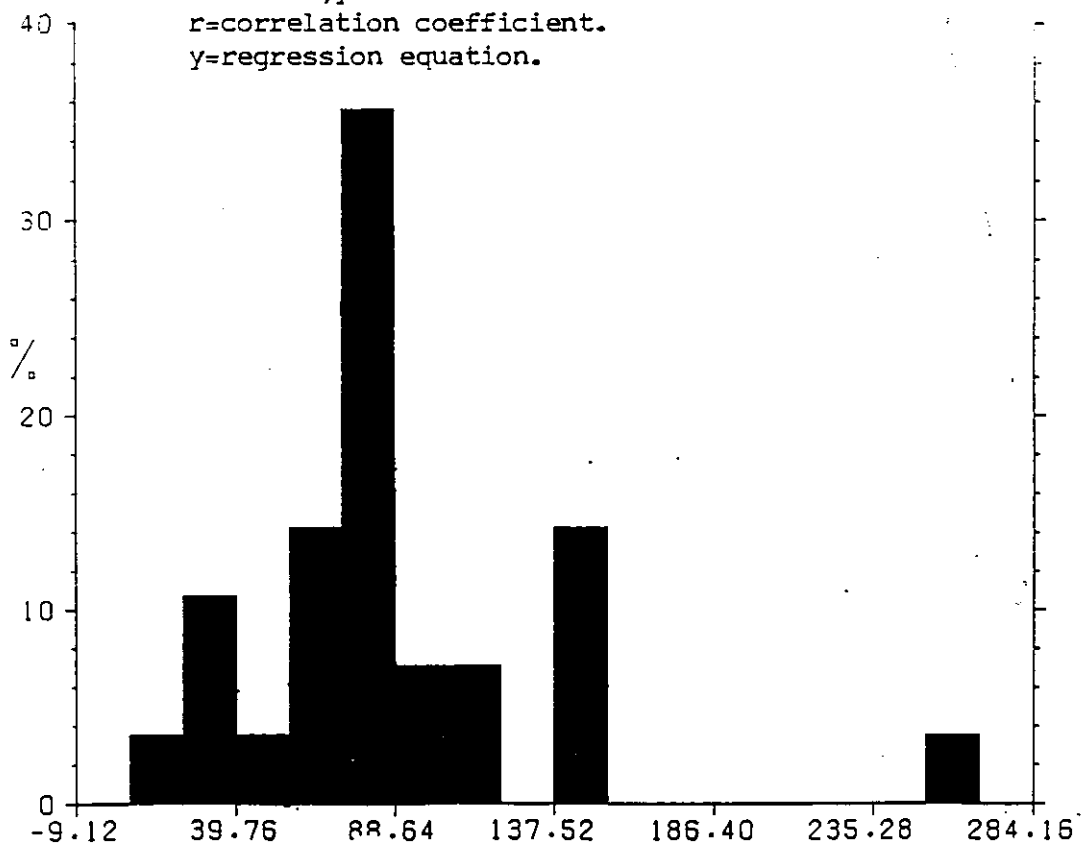
MEAN = 1.84 STD DEV = 0.309

NO. OF LOG10 TRANSFORMS = 1

**FIG.2.5.9.**

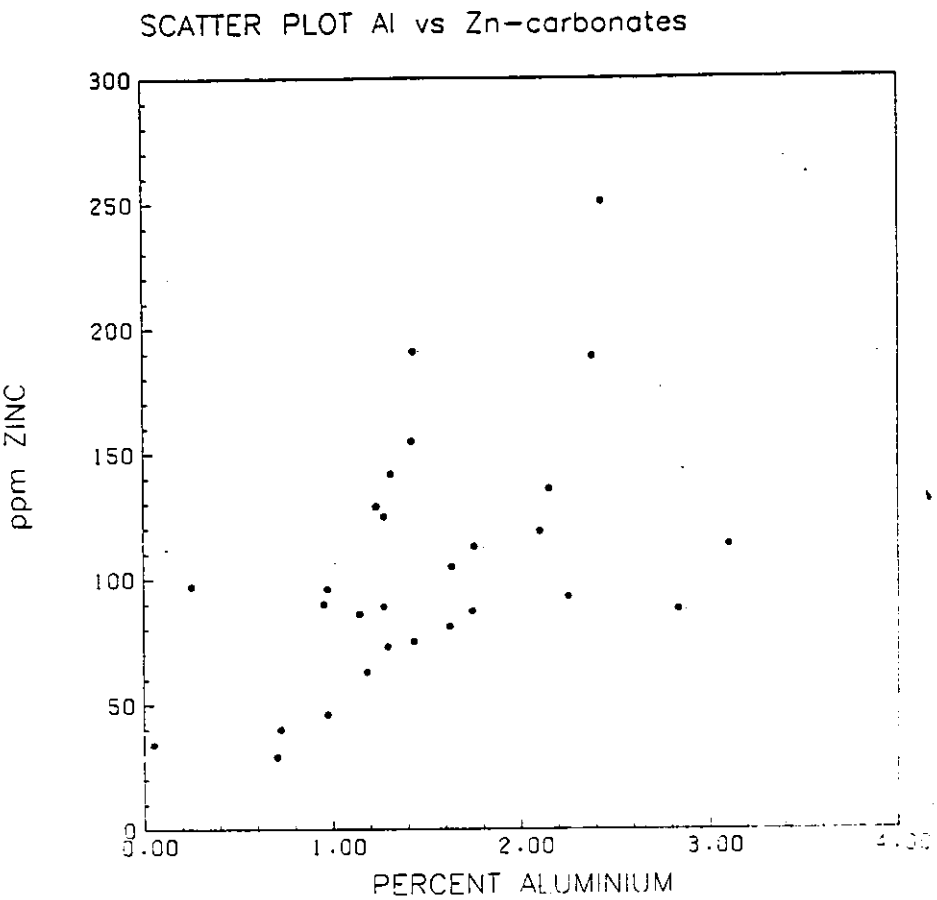



r=0.447 ,y=0.905+0.0065x1.
r=correlation coefficient.
y=regression equation.

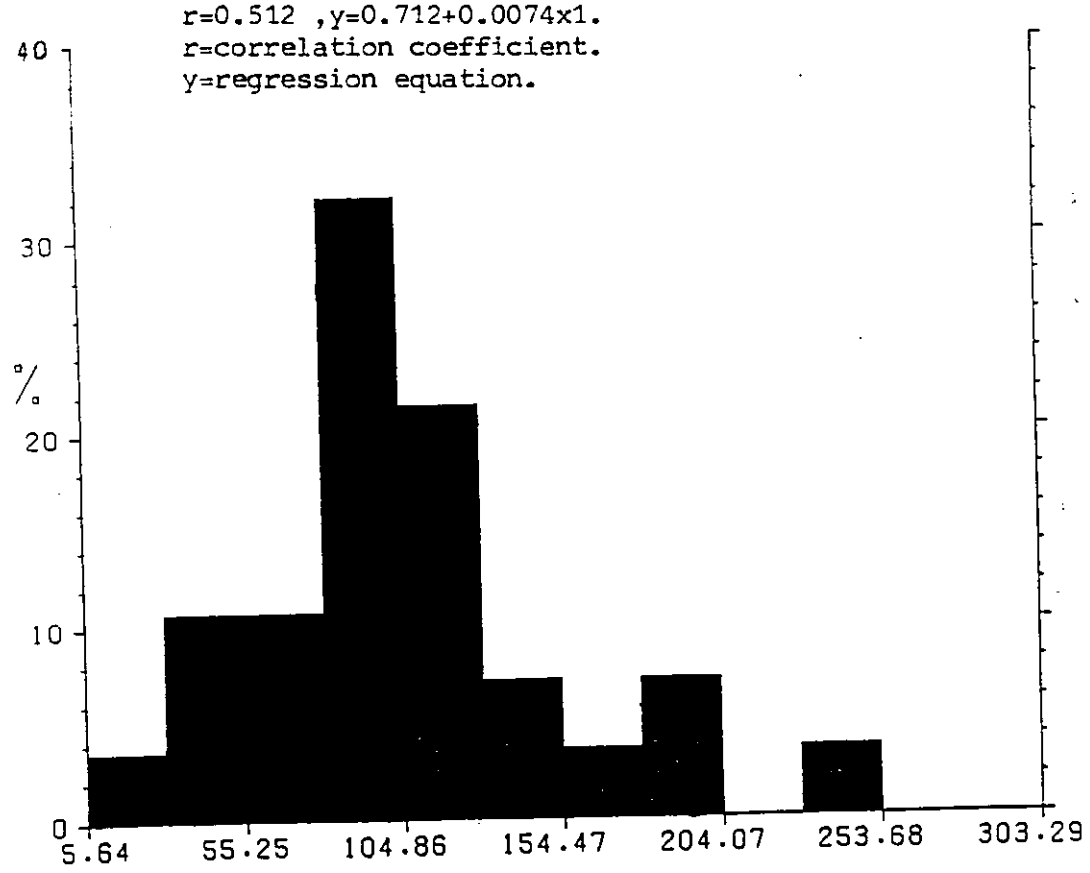



COPPER
NO. OF OBSERVATIONS = 28
MEAN = 88.64 STD DEV = 48.880

FIG.2.5.10.

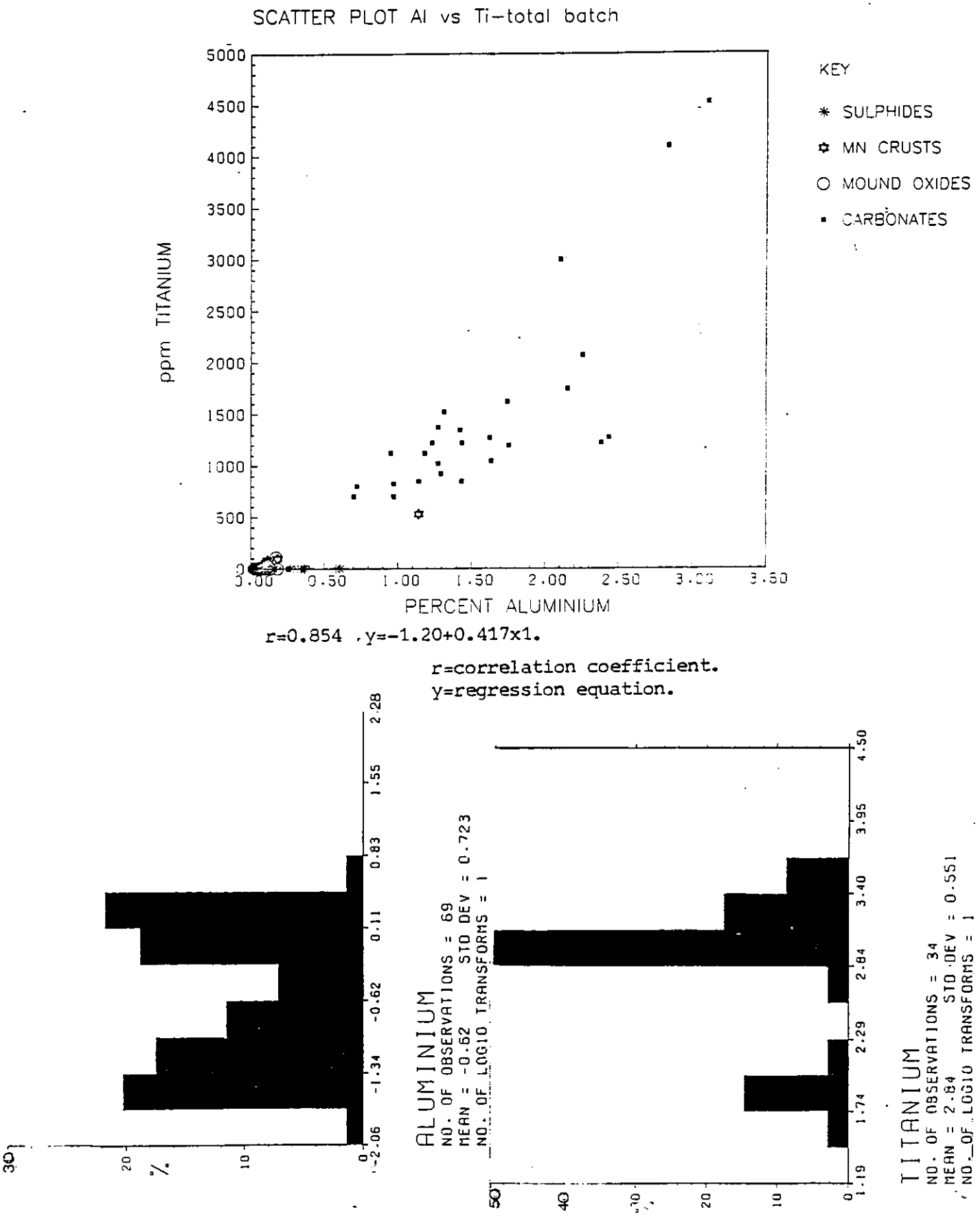



r=0.512 ,y=0.712+0.0074x1.
r=correlation coefficient.
y=regression equation.




ZINC
NO. OF OBSERVATIONS = 28
MEAN = 104.86 STD DEV = 49.608

**FIG.2.5.11.**




r=0.854 .y=-1.20+0.417x1.

r=correlation coefficient.
y=regression equation.

Hydrothermal Sulphides

The sulphide data should be treated with extreme caution as there are only 8 data points. However, it can be seen that Cu shows a significant positive correlation with Ag at the 97.5% confidence level (Figure 2.5.1). Hékinian et al. (1980) found the opposite trend, in microprobe analyses of several Ag-rich grains, from sulphides at 21°N on the E.P.R. Interpretation of this GRAFZI trend is discussed in the light of electron microprobe investigations in Chapter 3.

R/V CONRAD Dredge Hauls

Treatment of a limited data set (n = 19) showed a negative correlation of Fe and Mn (Figure 2.5.2). Positive correlations occur, of Mn with Ni and to a lesser extent of Mn with Cu and Zn, Zn with Ni, Cu with Ni and Cu with Zn (Figures 2.5.3-2.5.6). The scavenging properties of Mn oxides with respect to Ni, Cu, Zn and other cations noted by Goldberg and Arrhenius (1958) have already been mentioned.

Figure 2.5.3 is of particular interest because there is a large scatter of points and two separate clusters in the data set. One set show good linearity for Mn versus Ni which is presumably of hydrogenous origin, whilst the other set show a high Mn/low Ni field typical of low trace metal hydrothermal Mn oxides (Cronan, 1980) indicating a field of hydrothermal samples.

Short Sediment Cores

From a data set of 28 samples, several significant positive correlations at 99% confidence were detected, especially that of Al and the trace metals Co, Ni, Cu and Zn. The distribution of the data was normal except for Ni which was log normal (Figures 2.5.7-2.5.10). The maximum r value of 0.81 was observed for Al with Co. The association of Al with Ti has been ascribed to an inorganic detrital component of marine sediments (Böstrom, 1976). This inorganic detrital component may comprise detritus from terrigenous or submarine volcanogenic sources. Chester and Aston (1976) noted that Al is primarily held in aluminosilicates (both feldspars and clay minerals) while Ti can indicate a quantitative abundance of basaltic debris. The scatterplot of Al versus Ti (Figure 2.5.11) for the

FIG.2.6.1. Station locations for the Galapagos Rift 86°W area.
(S denotes sulphide locality of Dive 1001.)

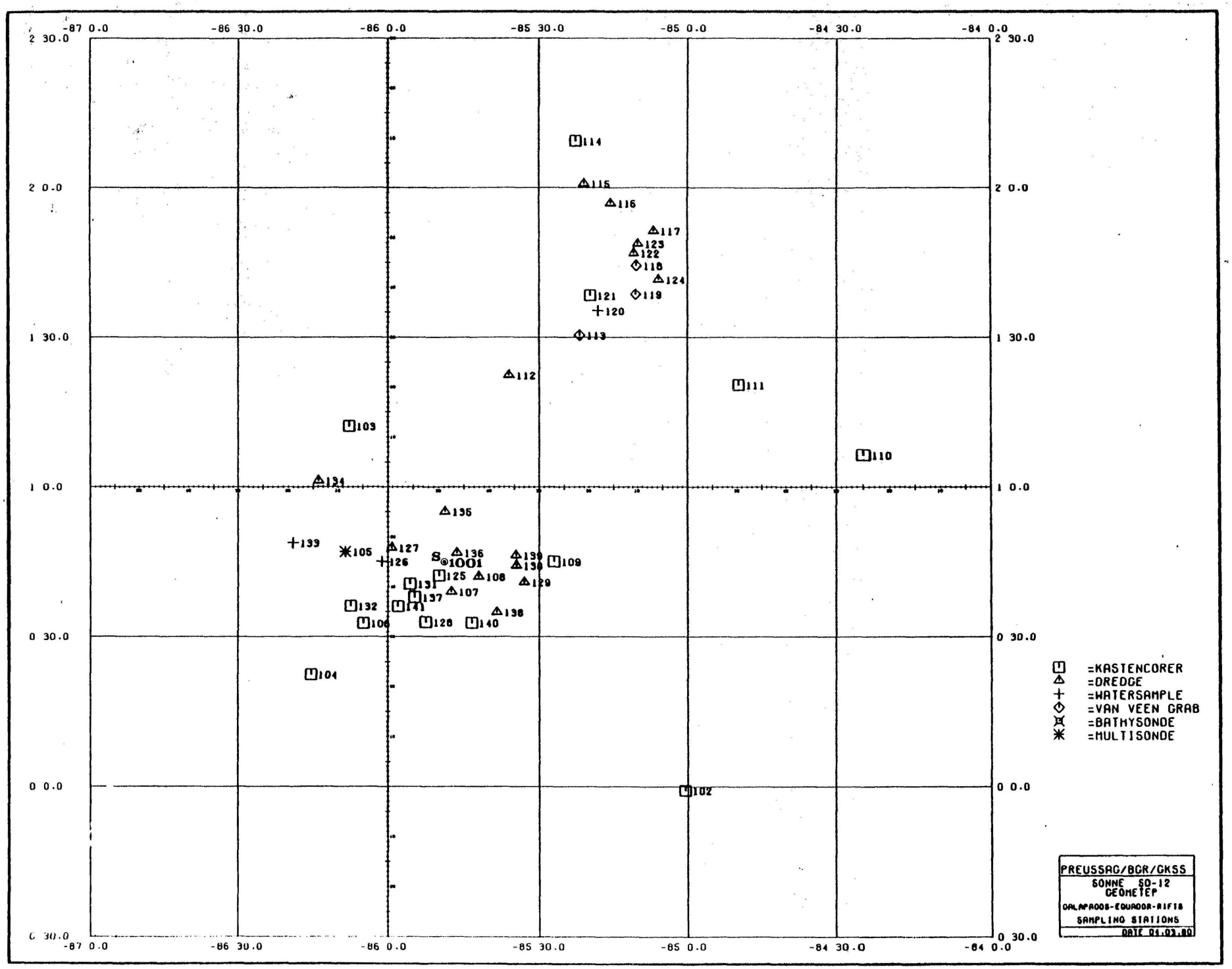
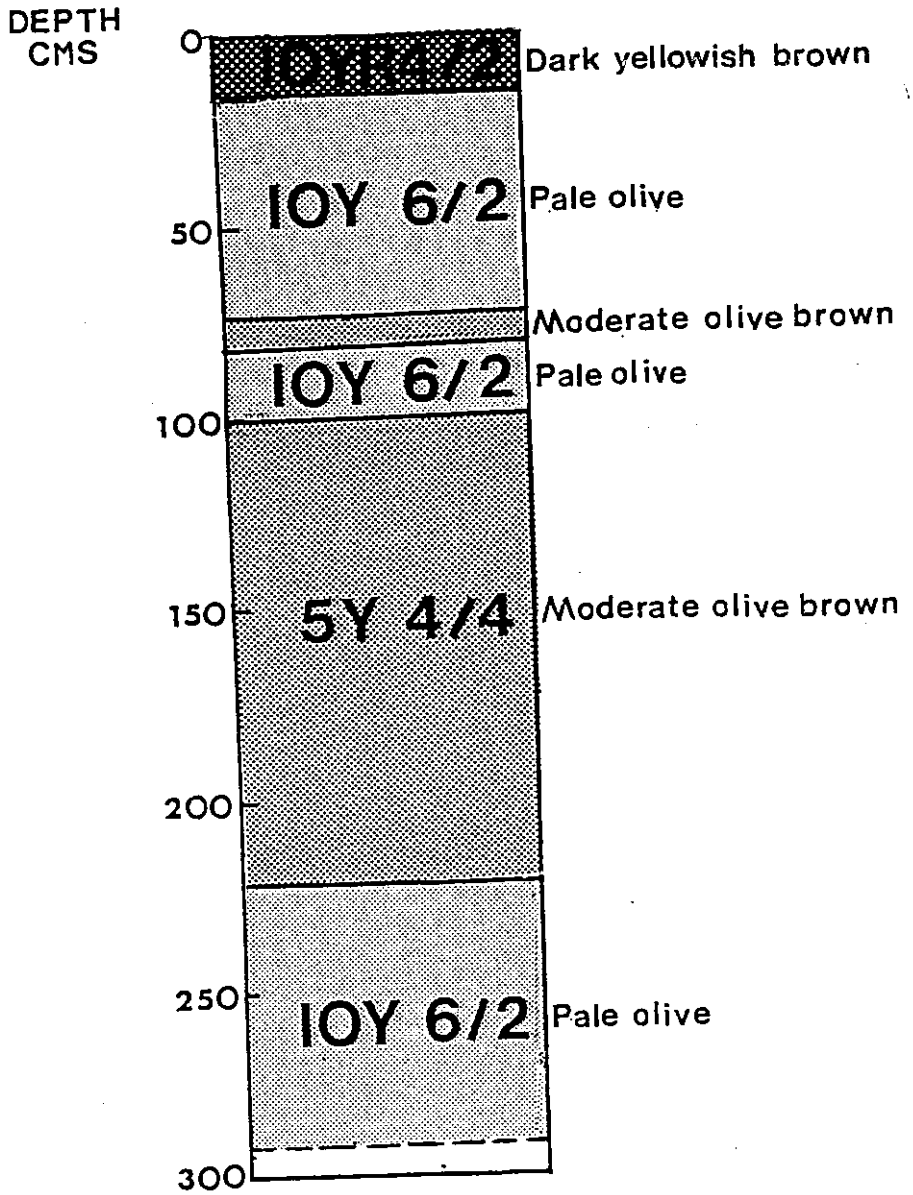


FIG.2.6.2. Core description of 131K.




U.S.G.S. Rock colour chart coding.

whole GRAFZI data set shows strong positive correlation of these elements (r = 0.85), but histograms indicate significant bimodal distributions for both Al and Ti which may represent these two different sources, i.e. volcanogenic and clay mineral. This being the case, it is not unreasonable to assume a basaltic and clay mineral origin for a signficant amount of Co, Ni, Cu and Zn found in GRAFZI pelagic sediments. The clay mineral content of the sediments will be discussed in Section 2.6 (b).

## 2.6 REGIONAL SEDIMENTATION PATTERN OF THE 86°W AREA

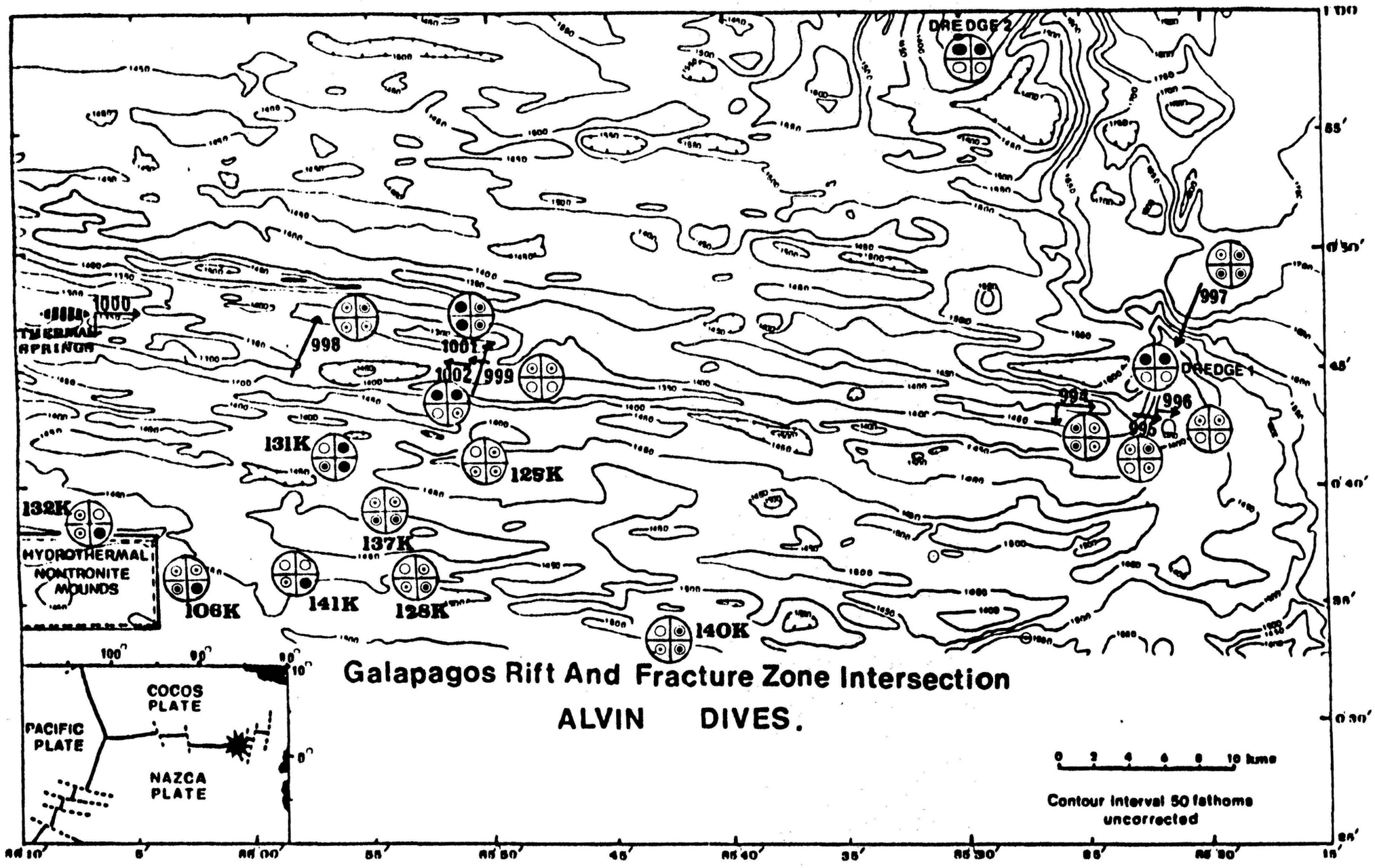
### 2.6(a) Sample Description

The R/V "Sonne", on Leg 3 of the GEOMETEP (Geothermal Metallogenesis Eastern Pacific) cruise, recovered 15 kasten or box cores from the 86°W area from depths of 2683-3347 metres, along with 17 dredge hauls. This study deals with a collection of 58 sediment samples taken from these 15 widely distributed cores, in order to determine regional geochemical variations in this area.

Figure 2.6.1 shows the co-ordinate positions of the GEOMETEP sediment cores and the sulphide locality of ALVIN Dive 1001 is also labelled. The cores were up to 3.95 metres in length and generally displayed a colour change from top to bottom, from dark yellowish brown through grayish green to pale olive, according to standard U.S.G.S. and Munsell colour coding systems (Figure 2.6.2). Volcanic glass fragments were common especially in the lower portions of the cores. Dredge haul 107, at 0°39.05'N and 85°50.47'W (see Figure 2.6.1), between 2633 and 2725 corrected metres water depth, produced hydrothermally altered basalts and greenstones of the greenschist facies (H. Bäcker, pers. comm.).

On board grain-size distribution of the sediments, carried out by sieving, showed as much as 86.5% present in the $< 63\ \mu$ fraction. At the tops of the cores however, the $< 63\ \mu$ (clay/silt) fraction was much less and in some cases was absent altogether, where granular carbonate was dominant. Generally, the grain size of the sediments decreased downcore, as the green colouration became more pronounced.

FIG.2.6.3. Distribution of Fe,Mn,Cu,Zn in surface sediments from the Galapagos Rift at 86°W.




| | % Fe | % Mn | P.P.M. Cu & Zn |
|---|---|---|---|
| ● | >5 | >5 | > 400 |
| ◉ | 4-5 | 3-5 | 3 - 400 |
| ⊙ | 3-4 | 1-3 | 2 - 300 |
| ○ | <3 | <1 | < 200 |

Fe Mn
Cu Zn

CARBONATE FREE DATA.

## 2.6(b) Bulk Geochemistry

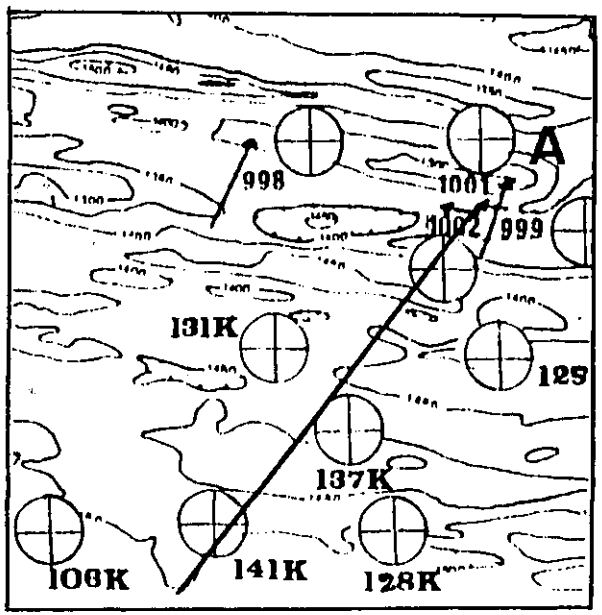
The 58 sediment samples ranged in $CaCO_3$ content from 39% to 81% and so fit into the foraminiferal marl (30-60% $CaCO_3$) and chalk (> 60% $CaCO_3$) ooze categories of the classification of Olausson (1960), as was the case for the ALVIN short cores collected from this area. The other major component of pelagic sediments, $SiO_2$, varied from 34 to 53%, on a carbonate free basis. The mineralogy of the $SiO_2$-bearing phases is discussed in Section 2.6(c), but most $SiO_2$ is present either in siliceous organisms or clay minerals.

On a carbonate free basis (Appendix C), Na and K constituted up to 8% and 1.4% of the sediment respectively, but on average, levels of 4-6% Na and 0.6-0.8%K were more common. Na and K are generally acknowledged as cations present partly as seawater salts in marine sediments (GRAFZI sediments contained about 6•5% salt content) but Na and K are also incorporated in authigenic minerals such as phillipsite (Glaccum et al., 1976) and basaltic detritus (Taylor, 1964). Chester and Aston (1976) noted that the bulk of Na and K in pelagic sediments is associated with clay minerals.

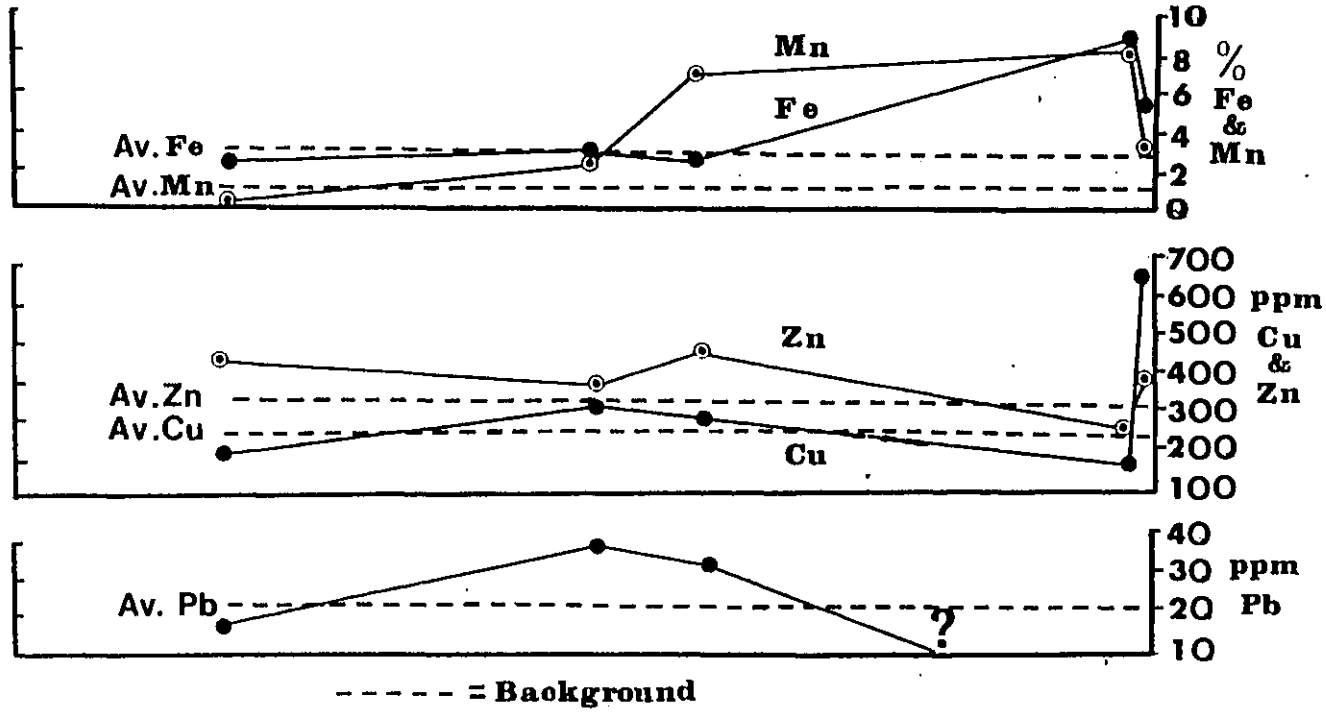
Figure 2.6.3 shows the distribution of Fe, Mn, Cu and Zn in surface sediments or sediments taken from the upper oxidised layer when it was not possible to sample surface sediment, in the 86°W area. Figure 2.6.3 combines previously described ALVIN dive data with new GEOMETEP core data (identified by a K after the core number). Fe, Mn, Cu and Zn have been treated together as all 4 elements are known to have a hydrothermal origin, though they can be supplied from other sources.

As is shown in Figure 2.6.3, Mn shows a wider dispersion than Fe, from known hydrothermal sites and this was also noted by Klinkhammer et al.,(1977). Dredges 1 and 2 have been included on Figure 2.6.3 to show comparative hydrothermal Mn crust data. Mn values greater than 3% can still be found 14 kms from the ridge axis (e.g. 140K, Figure 2.6.3) and Mn reaches a maximum of 7.1% at the top of core 131K,located at 0°41'N and 85°56'W.

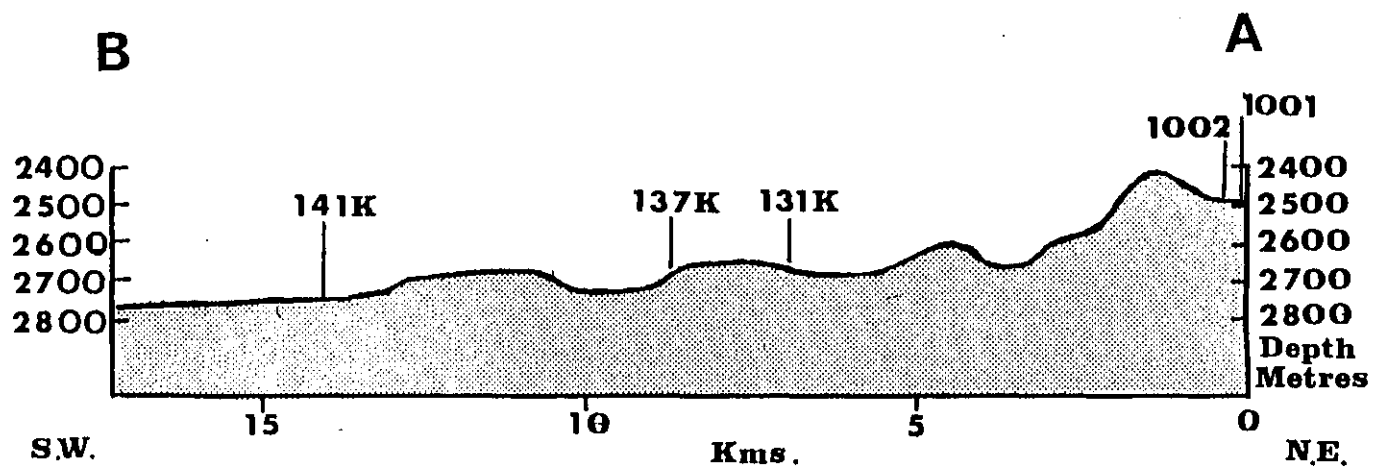
FIG.2.6.4. Element distribution/dispersion — perpendicular to the strike of the Galapagos Rift.




Line of section.




Vertical Exaggeration x6



Cu is most abundant in sediment at Dive site 1001; the hydrothermal sulphide locality which is dominated by chalcopyrite; where it reaches 659 ppm. Cu falls off to 200-300 ppm away from the ridge axis, although Dive site 997 in the fracture zone and cores 106K, 131K and 137K show values greater than 300 ppm. Zn tends to show as wide a dispersion as Mn, perpendicular to ridge crest strike, with values greater than 400 ppm from cores 106K, 131K, 132K and 141K, at distances of up to 14 kms from hydrothermal site 1001 (see Figure 2.6.4). The highest Zn concentration (763 ppm) occurs at 25-50 cms depth in core 140K. Figure 2.6.4 shows that Mn and Zn are concentrated above background values at distances further removed from their hydrothermal source, than are Fe and Cu. The Zn/Cu and Mn/Fe ratios away from the ridge crest neovolcanic zone, termed zone 1 (Francheteau et al., 1981), will be discussed in the context of hydrothermal element dispersion and the seawater chemistry of these elements.

— — —

*Element Dispersion*

The recognition of dispersion haloes around hydrothermal vents (Smith and Cronan, 1975; Bignell et al., 1976) has important implications for marine mineral exploration and the location of hydrothermal vents themselves where sulphides may be concentrated. Figure 2.6.4 shows a profile (A-B) approximately perpendicular to the strike of the ridge crest and the associated Fe, Mn, Cu, Zn and Pb concentrations from 5 localities up to 14 Kms from hydrothermal Dive site 1001. Cu and Fe concentrations fall off markedly over short distances from Dive 1001, relative to Zn and Mn. Background values represent approximate averages of all surface sediments taken from the 86$^{o}$W area. Pb is very low in concentration but does show a maximum in the sediment at about 8 kms from Dive 1001. Mn is anomalous to a distance of about 12 kms from its presumed source, although concentration decreases rapidly from about 7 to 9 kms. Zn is still anomalous at 14 kms from Dive 1001, although the trend is variable. Whether Pb is added to the sediment by hydrogenous processes or from a source at hydrothermal Dive site 1001 is not clear from the data but Chapter 3 indicates the presence of Pb, albeit in trace amounts of galena, deposited from hydrothermal solutions at Dive site 1001.

The overall level of Zn in the sediments is greater than Cu, at 86°W, while the opposite trend is found on the E.P.R. at 20°S (this work; Part 2) where Zn/Cu ratios equal about 0.5. An examination of the Zn/Cu ratio may give a valuable indication of the relative dispersion of these two hydrothermally supplied elements. At the source, Dive 1001, Zn/Cu = 0.6,whereas Zn/Cu = 2.1 at a distance of 14 kms,(core 141K at 0°36'N and 85°58'W.) This increase in Zn/Cu with distance from the source is also shown by the Mn/Fe ratio. From the mineralogy of the sulphide mounds it was shown that the assemblage is dominated by chalcopyrite ($CuFeS_2$) and depleted in sphalerite (ZnS). It seems therefore that most of the Cu supplied by hydrothermal solutions is precipitated close to the source but that the same is not true for Zn and that by contrast more Zn may be dispersed significant distances from the hydrothermal source.

To invoke hydrothermal dispersion of Zn and more tenuously Pb, from Dive site 1001, it becomes necessary to investigate the form and stability of these two metals in seawater. On egress from the oceanic crust, effluent hydrothermal solutions precipitate insoluable Fe, Cu, Zn and Pb sulphides (see Chapter 4) whilst excess metals, or metals not incorporated into sulphide phases, are dispersed into seawater. Of these metals, Zn is thermodynamically stable in solution in the following chemical species, $ZnOH^+$, $Zn^{2+}$, $ZnCO_3^o$ (Murray and Brewer, 1977) with a residence time of $2 \times 10^4$ years (Goldberg et al., 1971), provided the solubility product of its least soluble phase, $ZnCO_3$, is not exceeded. Normally, Zn is present in seawater at 1 to $10 \times 10^{-6}$ g/litre whereas the solubility product of $ZnCO_3$ is $28.8 \times 10^{-6}$ g/litre (Murray and Brewer, 1977). Goldschmidt (1937) noted that metals in seawater were concentrated at lower levels than the solubility product, due to adsorption on particulate matter. Similarly, Pb can exist in seawater as $PbCO_3$, $Pb(CO_3)_2^{2-}$, with a shorter residence time than Zn, of $4 \times 10^2$ years (Goldberg et al., 1971).

It is unlikely that hydrothermal solutions would raise the concentration of Zn and Pb in seawater to such a level that their least soluble compounds would precipitate. This being the case, adsorption

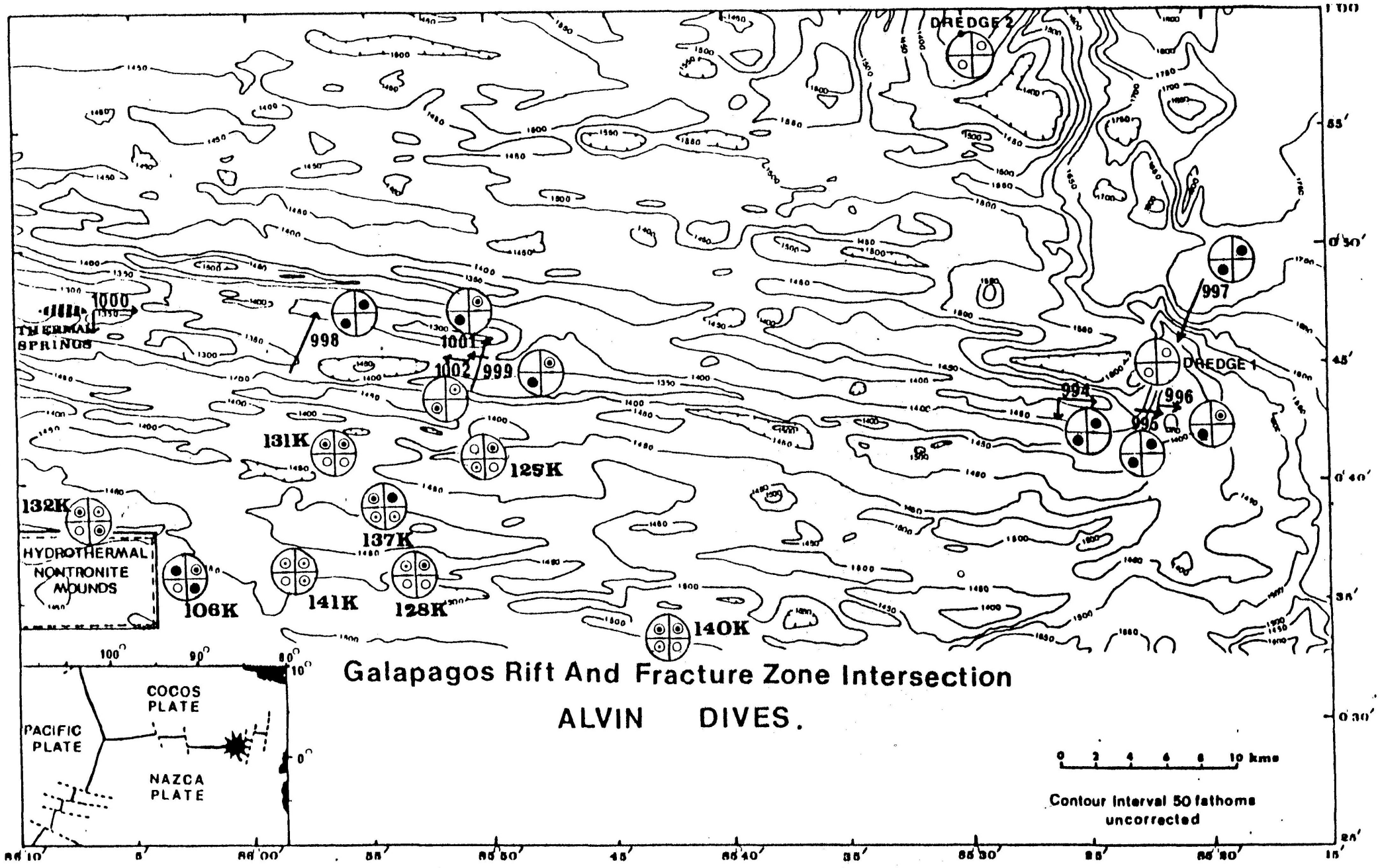
represents a mechanism by which these elements can leave solution and be incorporated in pelagic sediments. Hem (1977) noted that Cu in an experimental system is lowered in concentration by mild chemical reduction involving ferric hydroxide-ferrous ion redox processes. In the GRAFZI area, both Cu and Fe are restricted to the vicinity of the hydrothermal mounds and the rapid oxidation of Fe may account for the limited dispersion of Cu which is adsorbed onto ferric hydroxides. Furthermore, the deposition of Mn oxides such as $Mn_3O_4$ in oxygenated water is catalysed by coupling to ferrous-ferric redox reactions (Hem, 1977). Once formed, these may disproportionate giving $Mn^{4+}$ oxides. This catalytical oxidation of Mn on ferric hydroxide particles continues upon dispersion and becomes autocatalytic while ferric hydroxides and Mn oxides immobilise dissolved species of Zn and Pb (Goldschmidt, 1937; Goldberg, 1954; Riley and Sinhaseni, 1958; Kinniburgh, 1973).

The above discussion represents a mechanism by which hydrothermally derived Cu, Zn and Pb may be removed from solution by scavenging and adsorption onto ferric hydroxides and more importantly for Zn and Pb, Mn oxides. This is a thermodynamically stable sequence of events and is more likely than the reworking of sphalerite and galena from Dive 1001 and incorporation in pelagic sediments by bottom current activity.

The dispersion of Zn is perhaps more substantial than of Pb which is present in very low concentration. To some extent, Zn reflects the profile of Mn (Figure 2.6.4), with a decrease between 7 and 9 kms. However, another possible explanation for the higher Zn/Cu at distance from the vents at Dive site 1001, is that although hydrothermal solutions may supply Cu to the sediment locally, Zn is regionally added to the sediment by organisms such as diatoms (Martin and Knauer, 1973). The importance of Zn related to biochemical cycling was noted by Bruland et al., 1978 and Bruland, 1980. Biogenic addition of Zn to GRAFZI sediments in the equatorial zone of productivity may also explain why the Zn/Cu ratio is higher than that found at the E.P.R., $20^{\circ}S$ where biological supply of this element decreases.

— — —

FIG.2.6.5. Distribution of Mg,Al,Ti,V in surface sediments from the Galapagos Rift at 86°W.




Mg Al Ti V

| | % Mg | % Al | P.P.M. Ti | P.P.M. V |
|---|---|---|---|---|
| ● | >2·00 | > 4 | >2500 | > 200 |
| ◉ | 1·75–200 | 3–4 | 2–2500 | 175–200 |
| ⊙ | 1·50–1·75 | 2–3 | 15·2000 | 150–175 |
| ○ | < 1·50 | < 2 | <1500 | < 150 |

CARBONATE FREE DATA

◿ = No Data

FIG.2.6.6. Distribution of Co,Li in surface sediments from the Galapagos Rift at 86°W.

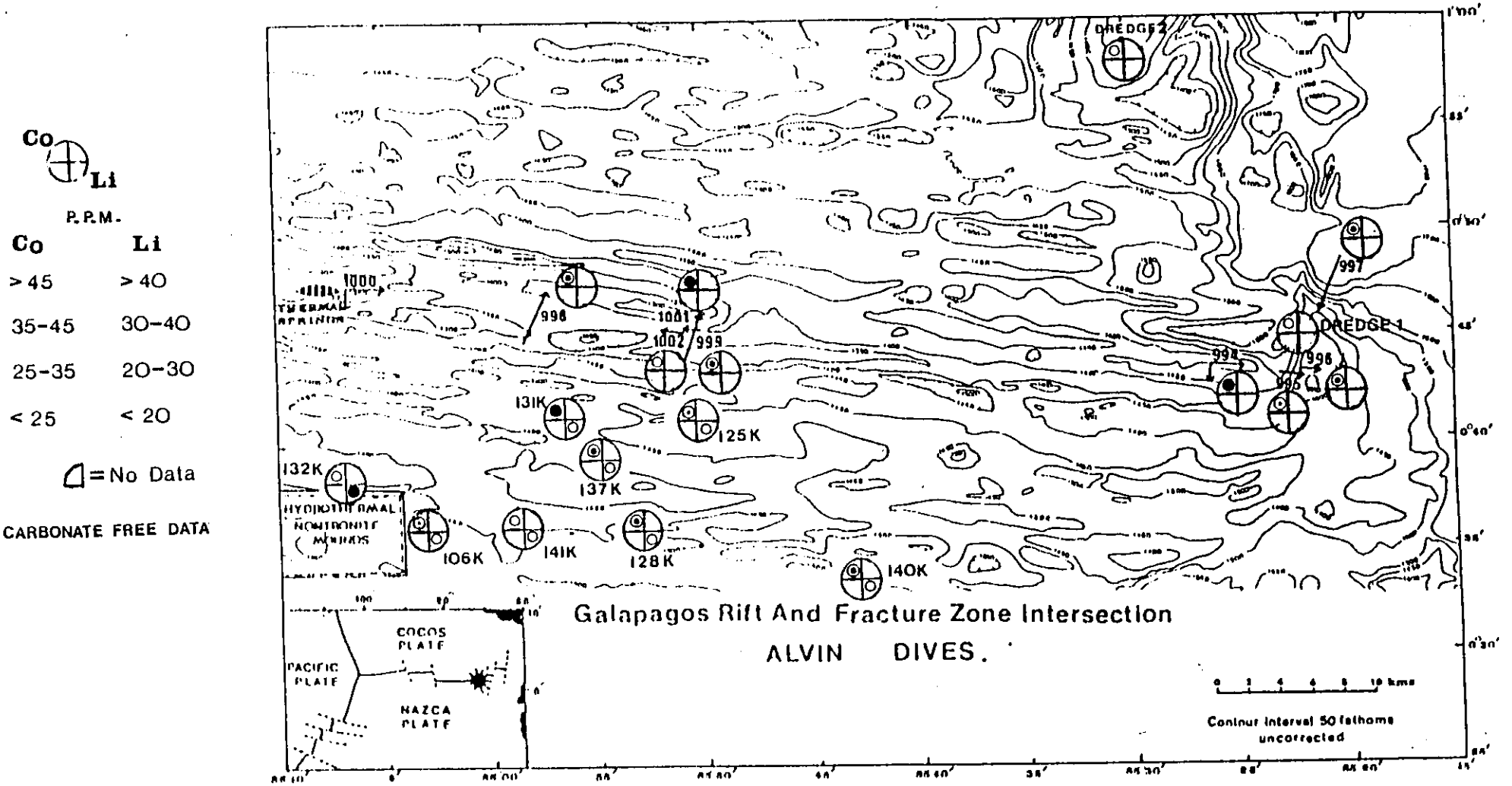


Figure 2.6.5 shows the distribution of Mg, Al, Ti and V in surface sediments. These elements are usually associated with lithogenous material or volcanogenic basaltic detritus (Hékinian et al., 1978) although clay minerals are also an important source (see Clay Mineralogy; this section). Al and Ti co-vary, with maximum abundances in areas of youngest oceanic crust, both from the ridge crest and the fracture zone at 85°22'W. In these areas, Al exceeds 4%, while Ti exceeds 2500 ppm (Figure 2.6.5). Visual and X-Ray diffraction studies suggest that these abundances might be due to shards of volcanic glass of varying size, which are very common in areas of thin sediment cover near the volcanic extrusion zone, zone 1.

Mg is most abundant (greater than 2%) in areas away from zone 1, and especially around 86°05'W where hydrothermal nontronite has been found (Corliss et al., 1978). However, although Mg is most abundant here, 2% is still low when compared to values in Hess Deep sediments (see Chapter 6). V is highest (256 ppm) in core 106K surface sediment, but values up to 469 ppm can be found at depth in core 114K from the Ecuador Rift (Figure 2.6.1), and up to 424 ppm at depth in core 125K. Previous workers have ascribed V in pelagic sediments to a lithogenous source (Bŏstrom, 1976; Burton, 1966; Chester et al., 1970) while Goldberg and Arrhenius (1958) noted volcanogenic, clay mineral and Fe oxide sites for this element. Clay minerals and volcanogenic debris are likely to provide most of the V, in the GRAFZI area.

Figure 2.6.6 shows the limited data available for Co and Li from surface sediments at 86°W. Both of these elements are low in concentration. Horder (1979) showed a volcanogenic origin for Li in Indian Ocean sediments, present in clay mineral and basaltic components, while Moorby and Cronan (1982) showed a hydrothermal supply in the Galapagos Mounds Field. Data here show a maximum surface concentration of 44 ppm for Li in core 132K, while it reaches 69 ppm at depth in core 121K, from the Ecuador Rift. Co is high in core 131K (45 ppm) and in sediment at Dive site 1001 (51 ppm), but is significantly higher in core 114K (81 ppm) from the Ecuador Rift (see Figure 2.6.1), suggesting a hydrogenous origin for Co (Goldberg and Arrhenius, 1958).

FIG.2.8.7. Distribution of Ni,Pb in surface sediments from the Galapagos Rift at 86°W.

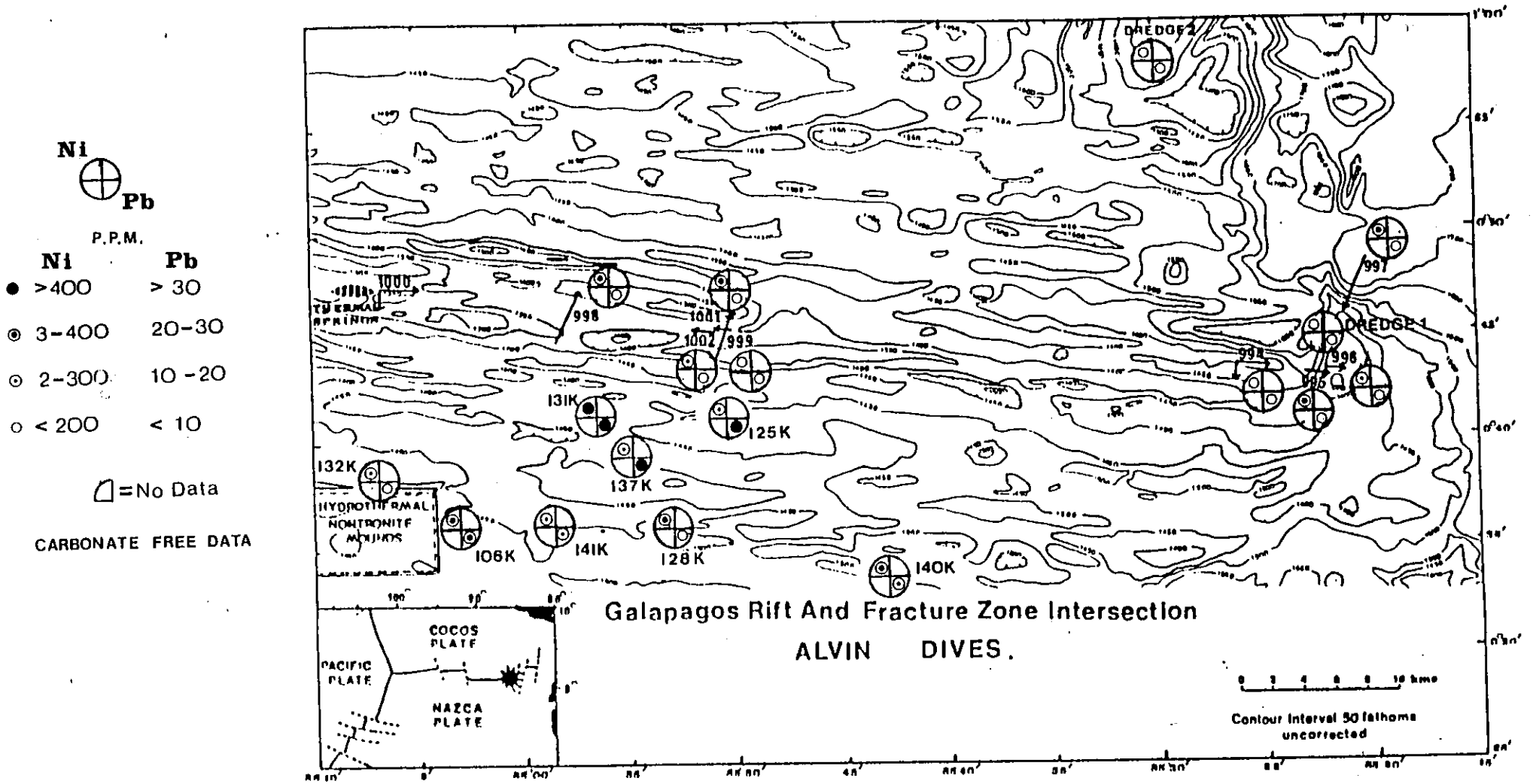
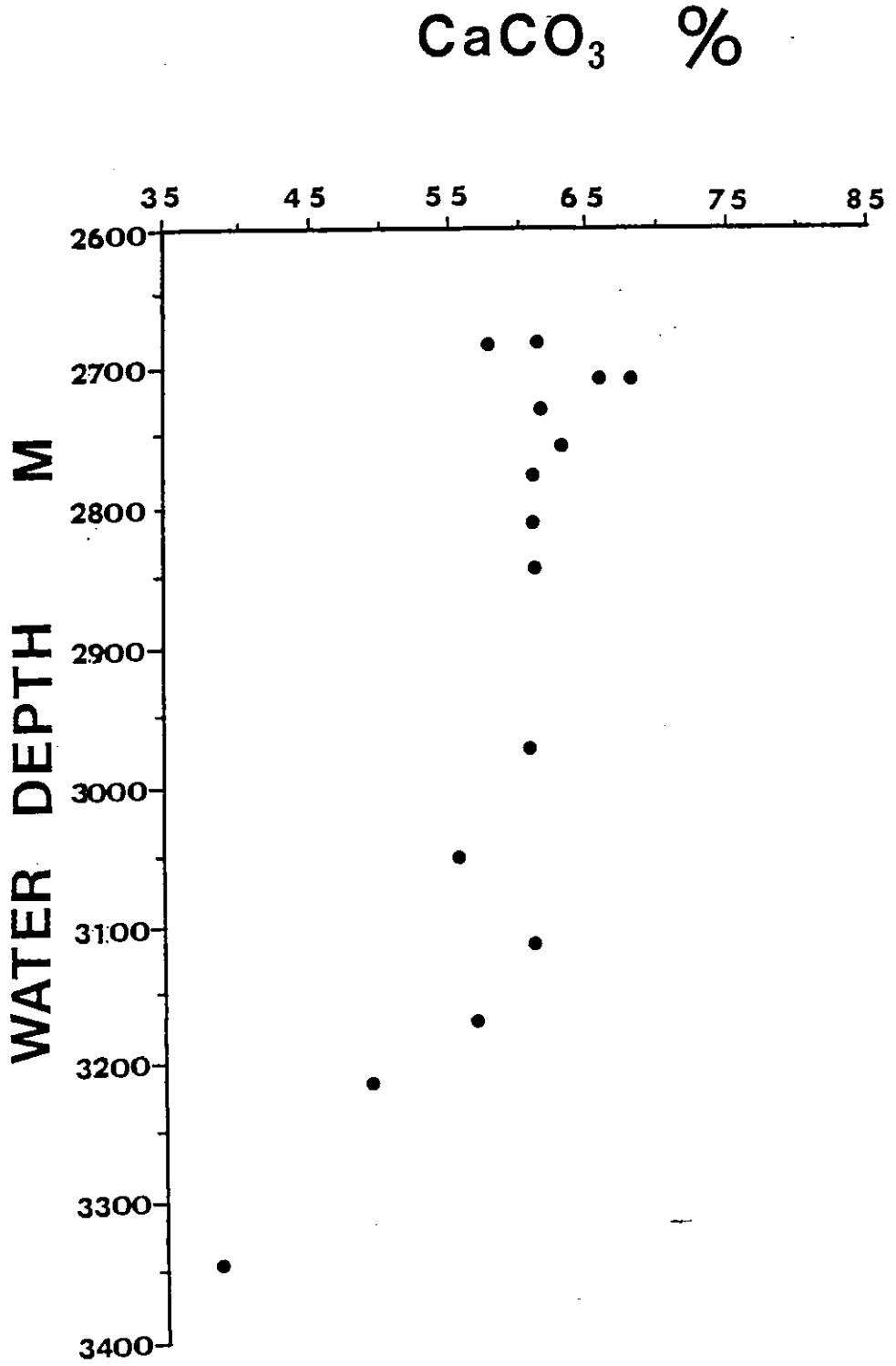


FIG.2.6.8. Scatter plot to show $CaCO_3$ versus Water Depth.

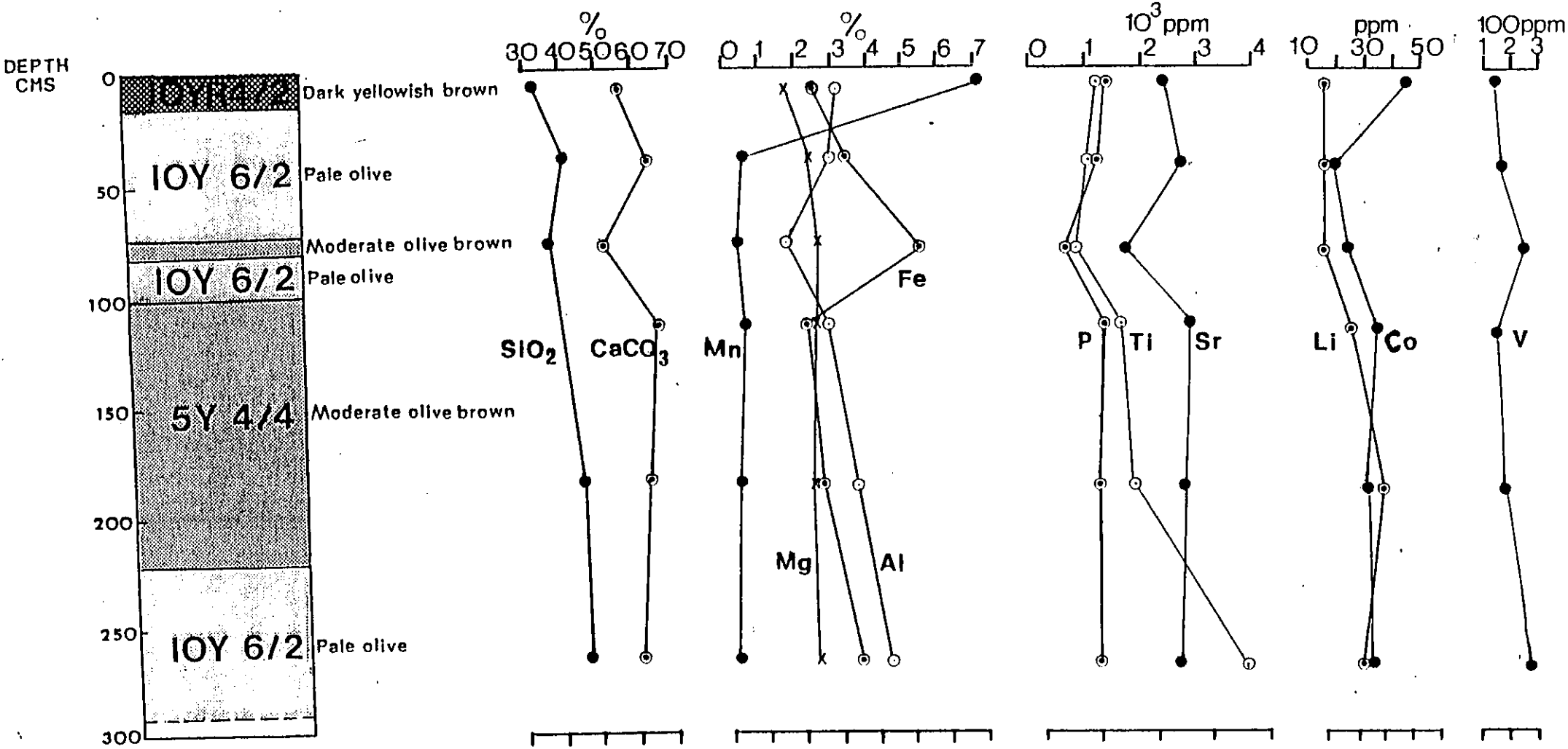


Ni and Pb distributions in surface sediments are shown in Figure 2.6.7. Maximum surface concentrations of Ni are 671 ppm and of Pb are 40 ppm. Pb reaches a maximum value of 56 ppm at depth in core 128K. These elements are also associated with hydrogenous processes, as noted by Dymond (1981) for Ni in Nazca Plate sediments. Pb may be supplied hydrothermally, in small amounts, to GRAFZI sediments, as discussed above, as well as from a hydrogenous source. Ni shows a maximum of 759 ppm in core 114K from the Ecuador Rift, which is far removed from any known hydrothermal site and it is likely that hydrogenous processes dominate the sediment composition in this area.

The close association of Sr with $CaCO_3$ is well known for foraminiferal material (Emiliani, 1955) where Sr isomorphically substitutes for Ca in skeletal material and Sr is therefore reported as raw data in Appendix C, as a carbonate correction would not be valid. P is known to occur in biogenous apatite and in phosphatic fish debris ( Arrhenius et al., 1957; El Wakeel and Riley, 1961).

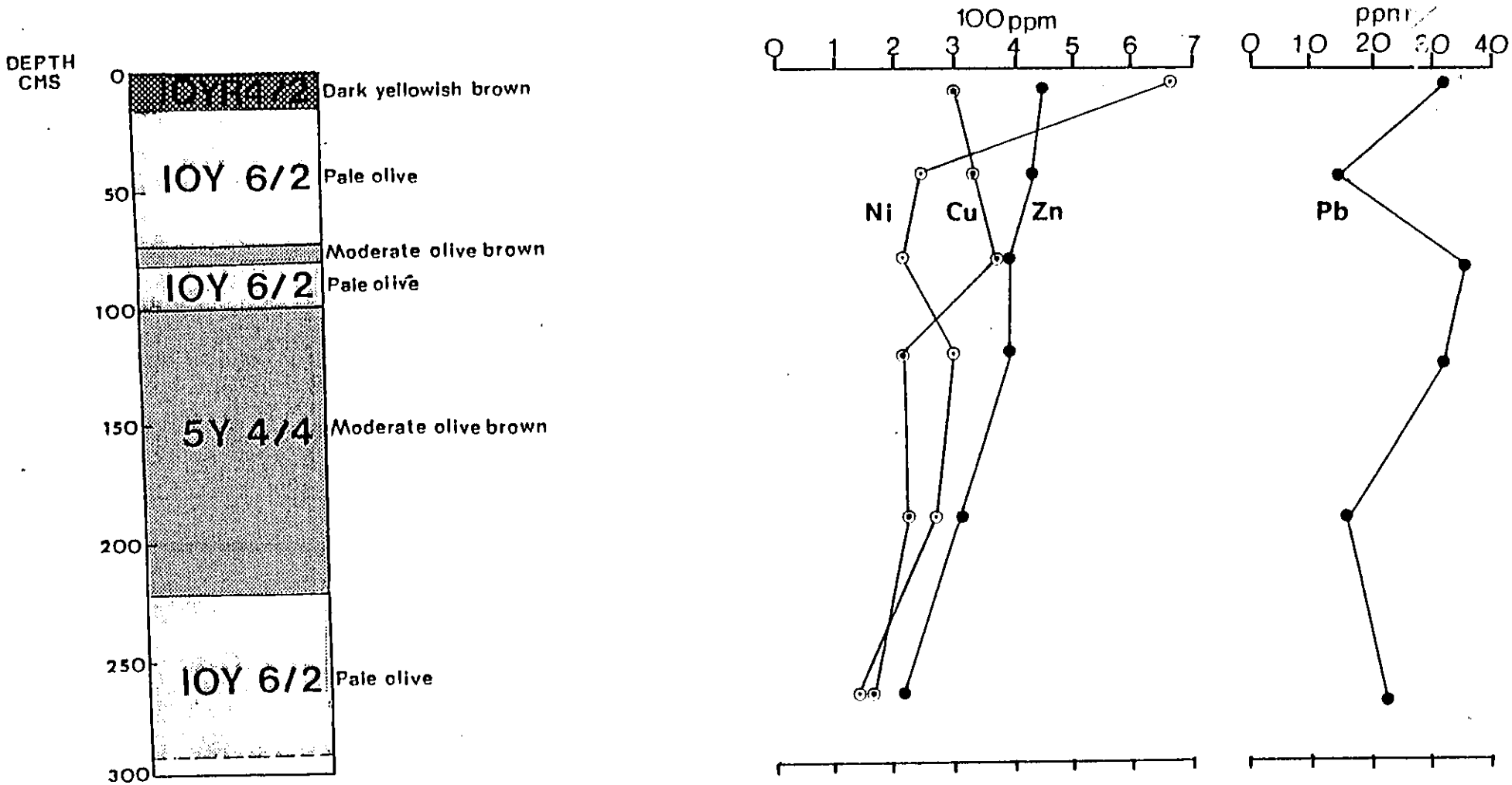
Cronan and Varnavas (1981) have shown that sediment $CaCO_3$ contents can be controlled by slumping and dissolution which can be related to water depths and bottom topography. These processes may be important in the GRAFZI area and the depth of the lysocline is discussed later. Sr at 1060 ppm (raw data) and P at 1700 ppm (carbonate free data), represent maximum abundances in 86°W area sediments, from cores 137K and 140K, respectively. Core 114K contains the highest amount of $CaCO_3$ (81%) in sediments from the region, with an associated high value of 1030 ppm for Sr. This core also contains 2010 ppm P, and this may indicate a small apatite contribution to the sediment. La shows no great variation in sediments from the 86°W area, and has a level of 30-50 ppm.

Previous work has shown a clear relationship between $CaCO_3$ abundance in surface sediment and water depth (Berger et al., 1976). Below 3100 m a noticeable decrease occurs in $CaCO_3$ content of the sediments (see Figure 2.6.8 ). This observation is taken to represent the pressure induced, increased dissolution of $CaCO_3$ at the depth of the lysocline. Berger et al. (1976), suggested that the calcite




U.S.G.S. Rock colour chart coding.

FIG.2.6.9 (a) Downcore element variations in 131K.




U.S.G.S. Rock colour chart coding.

FIG.2.6.9 (b) Downcore element variations in 131K.

compensation depth (C.C.D) occurs at 3600 metres in this area which would agree well with the data given in Figure 2.6.8 if extrapolated to zero $CaCO_3$ values. The lysocline depth is important in that trace metals are liberated from foraminifera for possible incorporation in sediments below this depth (Martin, 1970; Riley and Chester, 1971).

*Geochemical Variations with Depth*

A single core, 131K, was studied in detail from 6 samples taken down the 3 m core length. The aims were to identify differences between the upper oxidised and lower reduced zones in terms of element concentrations and their chemical speciation, and also to identify inter-relations between the elements and to identify the phases that contain them. Figures 2.6.9 (a) and (b) show the downcore variations in core 131K on a carbonate free basis. The sources of certain elements are well understood and it is hoped to relate to these, the elements whose geochemistry is less well known.

The upper 16 cms of dark yellowish brown foraminiferal marl ooze represents the upper oxidised zone of the sediment. Bonatti et al. (1971) showed that this zone is generally between 8-15 cms thick in the 86°W area. The profiles of the major components of the pelagic sediment, i.e. $SiO_2$ and $CaCO_3$, are fairly constant down the core, but $SiO_2$ increases gradually with depth perhaps due to diagenetic reactions. There is a pronounced low for $CaCO_3$ at a moderate olive brown horizon (5Y 4/4) between 72-80 cms, where Fe in particular is abundant. It has been shown that the gradual lowering of redox potential with increasing depth in sediment is probably due to the oxidation of organic matter as shown by decrease in nitrogen with depth (Bonatti et al., 1971). In response to the lowering of Eh due to the oxidation of organic matter in the sediment, Mn concentrations are drastically lower below the uppermost 16 cms of sediment, where $Mn^{4+}$ is reduced to soluble $Mn^{2+}$. In the upper oxidised layer Mn values reach a maximum of 7.1%. This high level of Mn is thought to be supplied by hydrothermal processes at 86°W (Malahoff et al., 1983) although diagenetic recycling may have played a part in Mn enrichment at the core top (Lynn and Bonatti, 1965). At depth, Mn rarely exceeds 0.6% and the profiles of Co and Ni to some degree reflect that of Mn, suggesting a

close association of these elements.

Fe shows a slight increase with depth although a pronounced peak at 72-80 cms, where abundance is greater than 5%, may reflect the fixing of $Fe^{3+}$ in the oxide phase. V and especially Cu show similar profiles to that of Fe.

P and Sr have a close resemblance to the profile of $CaCO_3$. It has already been suggested that Sr isomorphically substitutes for Ca in $CaCO_3$ and that Ca and P could occur in these sediments in apatite, although none was detected by X.R.D. Since P values are less than 1000 ppm it is unlikely that apatite would be present in other than trace amounts. Al and Ti both increase downcore, due to a greater component of basaltic detritus in the lowermost sediment. Li tends to follow the trends of Al and Ti and also shows a slight increase with depth. Mg is remarkably constant down the core and suggests fixation of this element in phases which vary little with depth. This is substantiated by relatively constant $SiO_2$ values as these two elements are commonly associated with clay minerals (see later). Pb may be related to the profiles of Mn and Fe.

In summary, Sr and P vary with $CaCO_3$ and represent biogenic and authigenic mineral (apatite) components in the sediment. $Mn^{4+}$ is reduced to $Mn^{2+}$ below the upper oxidised 16 cms of sediment and the thermodynamically stable cations of the $Mn^{4+}$ oxide structure such as $Co^{3+}$, $Ni^{2+}$, $Zn^{2+}$ and $Pb^{4+}$ (Burns and Burns, 1977) must accordingly enter solution in a reducing environment. This post-depositional mobility of metals is therefore largely controlled by redox reactions within the core, namely the reduction of $Mn^{4+}$ to $Mn^{2+}$ and the dissolution of the Mn oxide phase at depths of greater than 16 cms.

Fe and V have been found to be associated with the lithogenous component of marine sediments (Chester and Messiha-Hanna, 1970) and like Al and Ti, these elements decrease downcore. However, Fe may have hydrothermal, hydrogenous and halmyrolytic sources also. Li, Al and Ti all occur in mid-ocean ridge tholeiitic basalts

Table 2.6.1. Geochemistry and Mineralogy of <0.5μ Fraction of 86°W Area Sediments

| Core | Depth (cms) | Major Elements as Oxides in % | | | | | | | | | | Minor Elements in ppm | | | | |
|---|---|---|---|---|---|---|---|---|---|---|---|---|---|---|---|---|
| | | $SiO_2$ | $Al_2O_3$ | $Fe_2O_3$ | MgO | CaO | $Na_2O$ | $K_2O$ | $TiO_2$ | $P_2O_5$ | $MnO_2$ | Li | Sr | Ba | V | Cr |
| 125K | 0-20 | 47.5 | 9.80 | 7.15 | 1.90 | 3.88 | 1.04 | 0.54 | 0.44 | 0.80 | 0.30 | 26 | 720 | 680 | 73 | 29 |
| 125K | 100-125 | 47.5 | 8.91 | 6.93 | 2.33 | 4.80 | 0.98 | 0.67 | 0.47 | 0.29 | 0.13 | 34 | 390 | 600 | 300 | 35 |
| 128K | 0-6 | 58.8 | 8.64 | 4.67 | 1.51 | 0.86 | 1.44 | 0.55 | 0.28 | 0.25 | 0.19 | 31 | 158 | 1030 | 97 | 42 |
| 128K | 50-70 | 47.3 | 6.69 | 8.59 | 2.41 | 2.30 | 1.01 | 0.54 | 0.25 | 0.36 | 0.28 | 33 | 420 | 810 | 220 | 42 |
| 131K | 0-16 | 50.4 | 9.26 | 6.29 | 1.82 | 2.10 | 1.66 | 0.56 | 0.34 | 0.55 | 0.76 | 24 | 430 | 850 | 73 | 34 |
| 131K | 72-80 | 48.3 | 2.88 | 16.7 | 3.48 | 0.51 | 1.81 | 0.34 | 0.08 | 0.09 | 0.22 | 29 | 200 | 176 | 185 | 49 |
| 131K | 175-200 | 36.4 | 5.66 | 6.55 | 2.57 | 3.39 | 2.17 | 0.37 | 0.20 | 0.28 | 0.41 | 32 | 540 | 1150 | 168 | 31 |
| 137K | 80-100 | 44.1 | 7.29 | 5.40 | 2.29 | 4.77 | 1.07 | 0.59 | 0.25 | 0.26 | 0.23 | 29 | 740 | 800 | 91 | 30 |
| 137K | 150-175 | 48.0 | 8.13 | 7.07 | 2.80 | 3.62 | 1.30 | 0.70 | 0.31 | 0.26 | 0.30 | 34 | 650 | 1000 | 193 | 33 |
| 141K | 50-75 | 48.8 | 4.23 | 11.5 | 2.63 | 2.61 | 2.18 | 0.42 | 0.14 | 0.29 | 0.31 | 25 | 380 | 167 | 147 | 43 |

| Core | Depth (cms) | Minor Elements in ppm | | | | | | | *Mineralogy | d(001) Air dried Å | d(001) Glycerated Å | d(001) 550°C Å |
|---|---|---|---|---|---|---|---|---|---|---|---|---|
| | | Mo | Co | Ni | Cu | Ag | Zn | Pb | | | | |
| 125K | 0-20 | <1.0 | 11 | 93 | 320 | <1.0 | 380 | 37 | S + C | 12.7 | 18.0 | 10.2 |
| 125K | 100-125 | 2.7 | 28 | 170 | 160 | 3.3 | 620 | 54 | S + C | 12.4-13.5 | 17.4 | 10.1 |
| 128K | 0-6 | 2.6 | 17 | 183 | 290 | 1.1 | 640 | 21 | S + C | 13.2 | 17.7 | 9.9 |
| 128K | 50-70 | 1.6 | 30 | 270 | 370 | 10.3 | 700 | 20 | S + C | 14.5 | 18.3 | 10.2 |
| 131K | 0-16 | 2.7 | 13 | 120 | 191 | <1.0 | 570 | 82 | S + C | 13.5 | 17.1 | 10.1 |
| 131K | 72-80 | 3.9 | 23 | 170 | 360 | 6.5 | 650 | 45 | S | 11.8 | 19.0 | 10.0 |
| 131K | 175-200 | 2.8 | 34 | 240 | 230 | 3.3 | 600 | 20 | S + C | 13.9 | 18.0 | 9.9 |
| 137K | 80-100 | 2.5 | 24 | 210 | 210 | 4.7 | 530 | 17 | S + C | 13.5 | 17.7 | 9.9 |
| 137K | 150-175 | 2.6 | 36 | 200 | 163 | 3.2 | 630 | 19 | S + C | 14.3 | 17.7 | 9.9 |
| 141K | 50-75 | 4.4 | 19 | 178 | 370 | 5.4 | 590 | 58 | ?S | 13.9 | - | - |

Analyses expressed to 3 significant figures except for majors <1% and minor elements <100 ppm

* S = smectite C = chlorite (in order of abundance)

(Taylor, 1964) and volcanic debris is likely to be a source for these elements. Al, Fe, Mg and $SiO_2$ are present in varying amounts in clay minerals (see later). X-Ray diffraction studies did not reveal sulphides in the reduced layer of the core although $Fe^{2+}$ and $Cu^{2+}$ may be fixed in the sulphide phase in reduced sediments, due to their relatively immobile nature (Bonatti et al., 1971).

2.6(c). Mineralogy.

The chemical and physical techniques used to isolate the clay fraction of the sediment are given in Appendix B. X-Ray diffraction mineralogical studies were carried out on the bulk and $<0.5\,\mu$ splits and these were both analysed for major and minor elements (see Appendix B). The bulk chemical analyses have already been described. The chemical composition and mineralogy of the $<0.5\,\mu$* clay fraction of the sediment is shown in Table 2.6.1.

*Bulk Mineralogy*

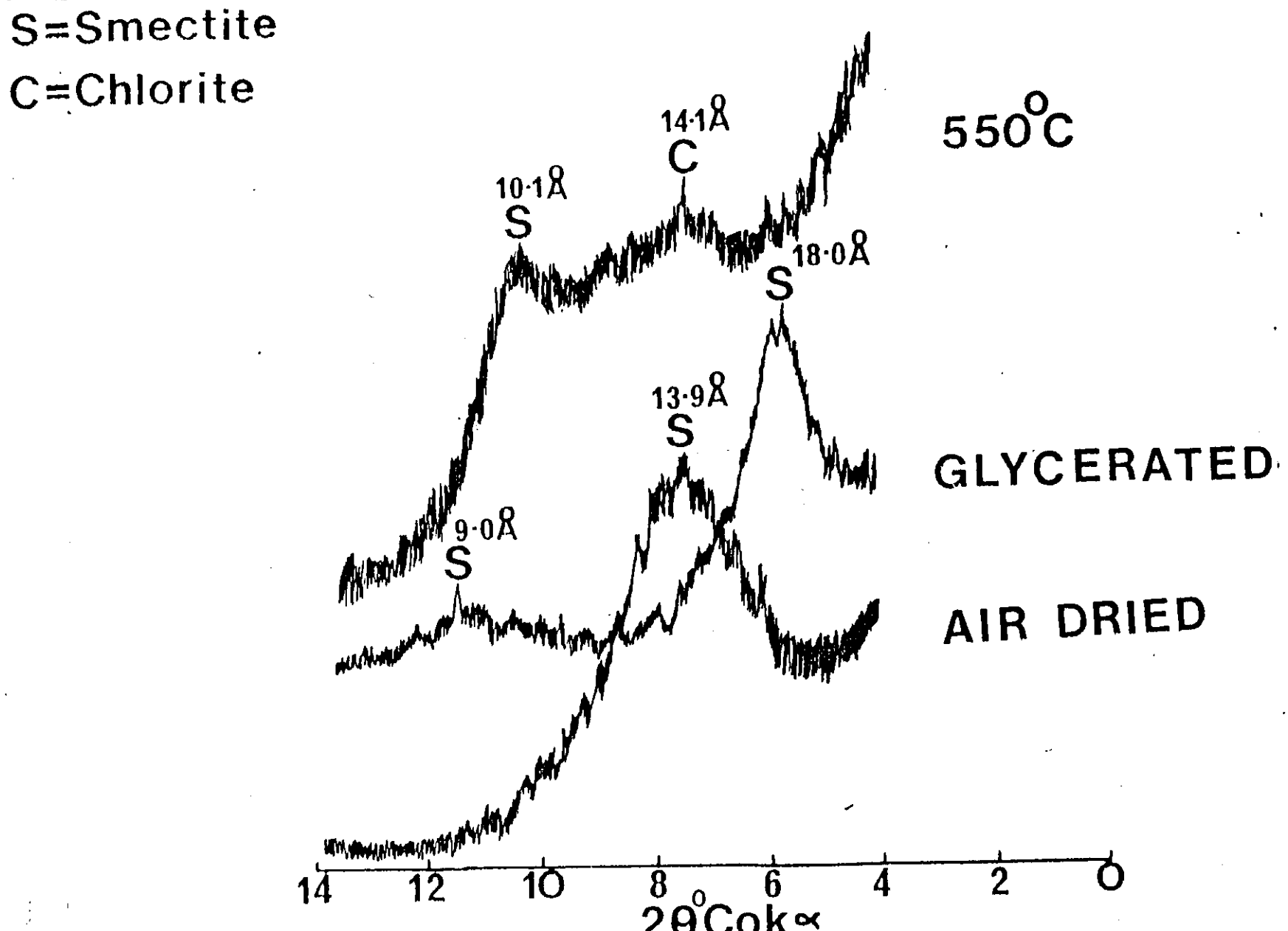
Twelve samples from 10 cores throughout the 86°W area were studied by X-Ray diffractometry using Co and Fe k$\alpha$ radiation. The abundance of calcite and halite in the bulk samples completely masks the clay minerals. Calcite, halite and quartz are ubiquitous in all the cores, as is plagioclase. These imply biogenic, sea-salt (hydrogenous) and lithogenic/volcanogenic contributions to the sediment, respectively.

*<0.5 u clay fraction chemistry and mineralogy*

The mineralogy of the $<0.5\,\mu$ fraction, separated as a suspension after centrifugation, is dominated by smectite with subordinate chlorite (Fig. 2.6.10). The basal spacing, d (001), of the smectite mineral ranges from 11.8 - 14.3 Å, and tends to be broad and diffuse. The only other peak which always appears is the non-basal spacing with hk indices of (02,11) and this varies between 4.39 -4.47 Å. This peak normally shows a steeper limb on the low 2θ side. Tests carried out which diagnostically identified the mineral as belonging to the smectite group included basal expansion with glycerol and heat treatment up to 550° (Table 2.6.1). Glyceration expanded the d (001) peak to between 17.4 - 19.0 Å. This is in accordance with classical smectite behaviour under these conditions (Brindley and Brown, 1980), as was the observed collapse of d (001) to 9.9 - 10.2 Å, upon heating.

* This grain size was chosen because it contained abundant smectite.

FIG.2.6.10. X.R.D. Clay Mineralogy of the <0.5μ fraction of Sediments from the Galapagos Rift, 86°W.



Chlorite is much less abundant than smectite and was only unequivocally identified in some glycerated and all heat treated specimens, where small peaks could be seen (Figure 2.6.10). Air dried discs of the sample had chlorite peaks swamped by the much more abundant smectite. It was observed that after heat treatment the d (001) spacing for some chlorites was shifted slightly from 14.2 Å to 13.7 Å, although this varied from one sample to another. Typical chlorite behaviour was shown as the 14.2 Å - 13.7 Å peak intensity increased at 550°C while the air-dried definitive 7.1 Å peak disappeared. Identification of an Fe or Mg chlorite is not possible on the basis of the data accumulated but it is generally observed that the (001) peak (Intensity = 20%) for an Fe-rich chlorite is more enhanced than the equivalent (001) peak (Intensity = 70%) for an Mg chlorite, after heat treatment. This is most easily explained by consideration of an (001)/(002) ratio for an Fe chlorite which is increased considerably more than in an Mg chlorite, on heating to 550°C. Chemical analyses do not resolve this problem as chlorite is present in only small amounts and the bulk chemistry largely reflects smectite composition (Table 2.6.1).

To understand the chemistry and nature of the smectite mineral present in the sediments it is necessary to state a few basic points. Montmorillonite is a dioctahedral Al, Mg smectite with layer charge arising from Mg for Al substitution in octahedral positions and has the formula:-

$$(M^{+}_{y}\ nH_2O)(Al_{2-y}Mg_y)Si_4O_{10}(OH)_2$$

(Brindley and Brown, 1980)

Nontronite is also a dioctahedral smectite with layer charge principally derived from Al for Si substitution in tetrahedral sheets, with the formula:-

$$(M^{+}_{x}\ nH_2O)Fe_2^{3+}(Si_{4-x}Al_x)O_{10}(OH)_2$$

(Brindley and Brown, 1980)

Substitutions of $Si^{4+}$ by $Al^{3+}$ in the tetrahedral position, and $Al^{3+}$ or $Fe^{3+}$ by $Mg^{2+}$ or $Fe^{2+}$ in the octahedral position, yield a net negative charge which is balanced by inter-layer cations such as $Na^{+}$, $Ca^{2+}$ or $Mg^{2+}$.

Often it is difficult to distinguish nontronite from montmorillonite by X-Ray Diffraction studies, but the nontronites described earlier (Table 2.3.3, Section 2.3) show important chemical differences to those clay minerals shown in Table 2.6.1. The nontronites have considerably more $Fe_2O_3$ (up to 36%) and much less $Al_2O_3$ (up to 1.6%) than the $<0.5$ μ fraction smectite. MgO and $SiO_2$ levels are approximately the same but CaO and $TiO_2$ are both higher in the $<0.5$ μ fraction smectites. Considering the above differences it is reasonable to assume that the 10 samples in Table 1.5.1 are not pure nontronites. Comparison of these samples with smectite from the DOMES area, which is an Fe-rich montmorillonite (Hein et al., 1979), containing 45.6% $SiO_2$, 14.1% $Al_2O_3$, 9.2% $Fe_2O_3$ and 3.1% MgO, shows that they are similar chemically. Therefore, it is reasonable to term the $<0.5$ μ fraction of Galapagos Rift, 86°W sediments as predominantly an Fe-rich montmorillonite.

Table 2.6.1 shows chemical analyses for 22 elements determined on the above samples. 131K (72-80 cms) shows relatively higher $Fe_2O_3$ (16.7%) and lower $Al_2O_3$ (2.9%) compared to the other Fe-rich montmorillonites, and sample 141K (50-75 cms) also shows this but to a lesser extent. These samples may be of more nontonitic character. Of the trace elements, Ba, Sr, Zn and Cu are the most abundant. Li, Cr, Mo, Co, Ag and Pb do not exceed 100 ppm and are often present at much lower concentrations. Of particular interest is the maximum Ag value of 10 ppm in GRAFZI montmorillonites, which seems high when compared with the nontronites of the Galapagos Mounds Field (1 ppm Ag or less - Moorby, pers. comm.) possibly due to scavenging and adsorption from seawater (Krauskopf, 1956) to a greater extent, by the GRAFZI montmorillonites. The trace metals are probably present as interlayer cations balancing the layer charges induced by substitutions such as $Al^{3+}$ for $Si^{4+}$.

2.6(d) Statistical Analysis - Additional Elements

Statistical analysis of the major elements has already been carried out in Section 2.5. Section 2.6(b) dealt with downcore profile associations for some additional trace elements. This section reports statistical evidence for trends on hitherto little studied elements.

TABLE 2.6.2. Correlation Matrix for Galapagos Rift sediments, 86°W.

| | NA | K | MG | AL | MN | FE | CA | CACARB |
|---|---|---|---|---|---|---|---|---|
| K | .550 | | | | | | | |
| MG | .754 | .592 | | | | | | |
| AL | | .781 | | | | | | |
| MN | | | | | | | | |
| FE | .716 | .525 | .718 | | | | | |
| CA | -.752 | -.741 | -.802 | -.566 | | -.618 | | |
| CACARB | -.752 | -.741 | -.802 | -.565 | | -.618 | 1.000 | |
| SILICA | .476 | .876 | .733 | .819 | | .474 | -.878 | -.878 |
| LI | | .540 | | .600 | | | -.467 | -.468 |
| SR | -.451 | -.426 | -.732 | -.443 | | -.472 | .765 | .765 |
| LA | | | | | | | | |
| TI | | | | .716 | | | | |
| V | | .479 | .604 | .484 | | .557 | | |
| CO | | | | .426 | .604 | | | |
| NI | | | | | .673 | | | |
| CU | .770 | .621 | .590 | | | .759 | -.671 | -.671 |
| ZN | .676 | .634 | .683 | | | .485 | -.633 | -.633 |
| PB | .441 | .525 | .577 | .425 | | .484 | -.593 | -.593 |
| P | | .449 | | .502 | .523 | | | |

| | SILICA | LI | SR | LA | TI | V | CO | NI |
|---|---|---|---|---|---|---|---|---|
| LI | .525 | | | | | | | |
| SR | -.810 | -.461 | | | | | | |
| LA | | | | | | | | |
| TI | | | | .580 | | | | |
| V | .642 | .447 | -.476 | | .503 | | | |
| CO | | | | | | | | |
| NI | | | | | | | .595 | |
| CU | .443 | | | | | | | .413 |
| ZN | .668 | | -.452 | | | | | .506 |
| PB | .658 | | -.598 | | | .438 | | .433 |
| P | | | | .413 | | | .556 | |

| | CU | ZN |
|---|---|---|
| ZN | .708 | |
| PB | .495 | .562 |
| P | | |

The cut-off for the correlation coefficient at 99.9% confidence=0.41.

At the 99.9% confidence limit, the correlation coefficient (r) is significant at values greater than 0.41 (Neave, 1981). Table 2.6.2 shows a correlation matrix significant at the 99.9% confidence limit.

Na correlates positively with K, Mg, Fe, $SiO_2$, Cu, Zn and Pb and K with Mg, Al, Fe, $SiO_2$, Li, V, Cu, Zn, Pb and P. The association of these two elements with sea-salts is well known, but correlations of K with $SiO_2$, Li and V also tend to suggest a significant silicate source of this element, either in the lithogenous/volcanogenic fraction or with authigenic/diagenetic clay minerals (Section 2.6(c)). Mg shows positive correlation with Fe, $SiO_2$, V, Cu, Zn and Pb and has been found by chemical analysis along with these elements in the Galapagos Rift montmorillonites (this Section).

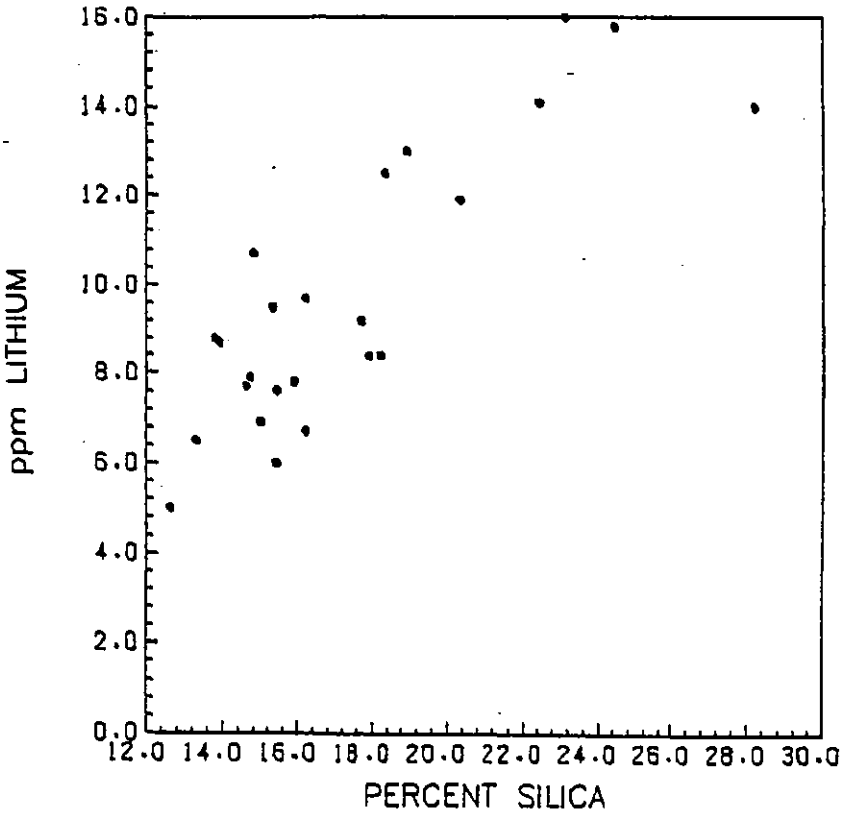
Al correlates significantly with $SiO_2$, Li, Ti, V, Co, Pb and P. Ti correlates positively only with Al, La and V and is a sensitive indicator of a volcanogenic component of the sediment. Mn correlates with Co, Ni and P and is presumably in the hydrogenous fraction of the sediment while Fe correlates with $SiO_2$, V, Cu, Zn and Pb and seems to be present in clay mineral and volcanogenic components. The lack of correlation between Fe and Ti may suggest that Fe and its associated elements are largely contributed from the clay minerals rather than basaltic detritus.

The normal procedure of reporting sediments on a carbonate free basis is given further support by the lack of correlation of elements other than Sr with $CaCO_3$,which is thus shown to be a relatively pure diluent phase of the sediment. La correlates positively with Ti and P and along with the other rare earths, has been shown to have a seawater origin (Elderfield and Greaves, 1982).

Relatively little is known concerning the marine geochemistry of Li and V, but they seem intimately bound up with silicate phases according to the correlation matrix (Table 2.6.2). Li is associated with K, Al, $SiO_2$, V,while V is associated with K, Mg, Al, Fe, $SiO_2$, Li,

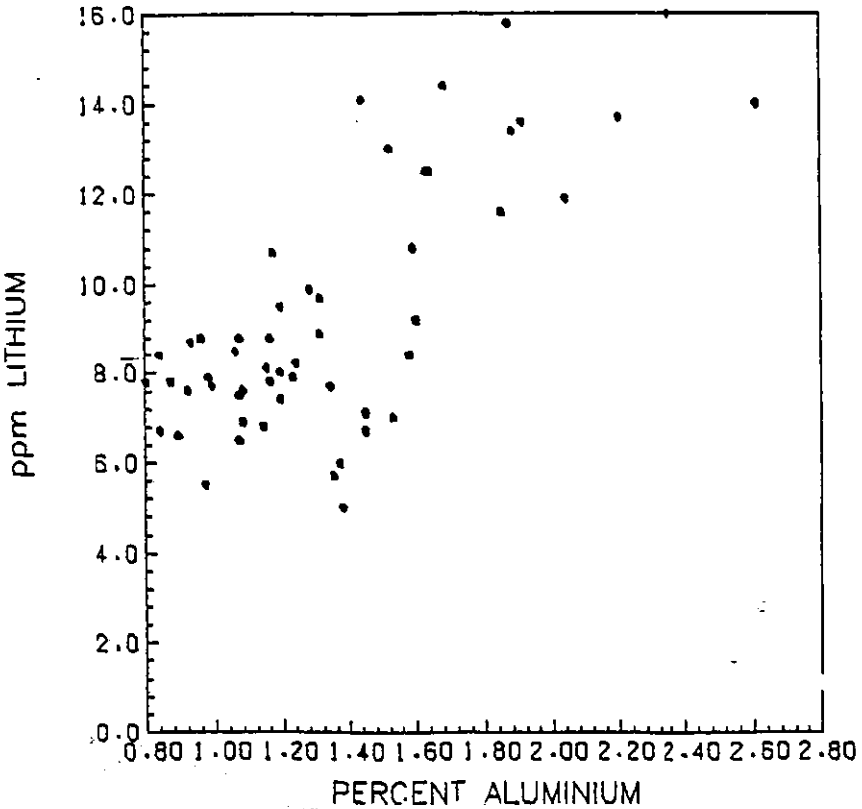
FIG.2.6.11(a)

SCATTER PLOT – SiO2 vs Li

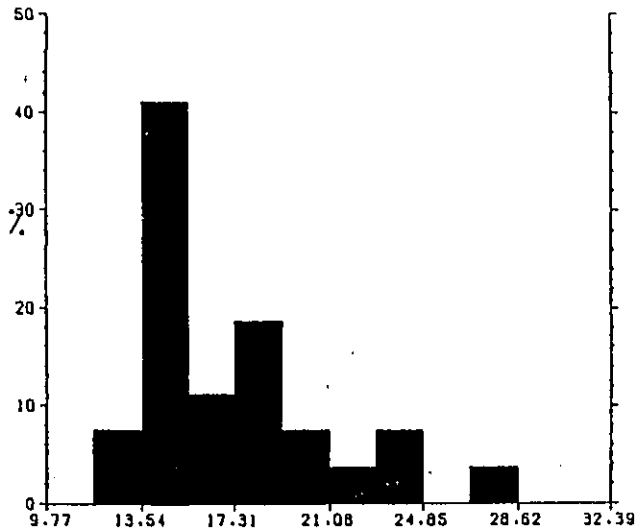



r=0.525 ,y=0.624+0.581x1.
r=correlation coefficient.
y=rgeression equation.

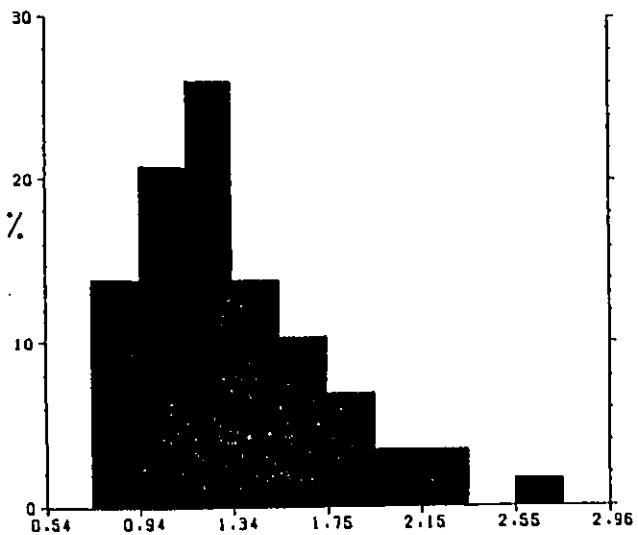
SCATTER PLOT – Al vs Li




r=0.600 ,y=2.80+5.14x1.




SILICA
NO. OF OBSERVATIONS = 27
MEAN = 17.31 STD DEV = 3.769




ALUMINIUM
NO. OF OBSERVATIONS = 58
MEAN = 1.34 STD DEV = 0.403

LITHIUM
NO. OF OBSERVATIONS = 58
MEAN = 9.70 STD DEV = 3.456

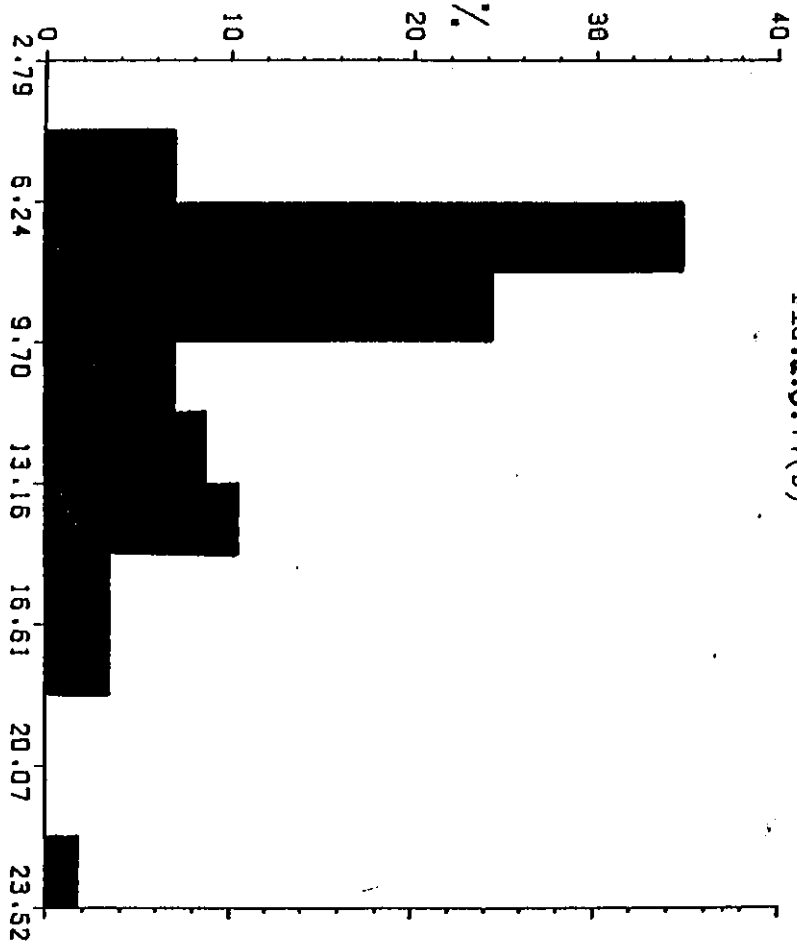
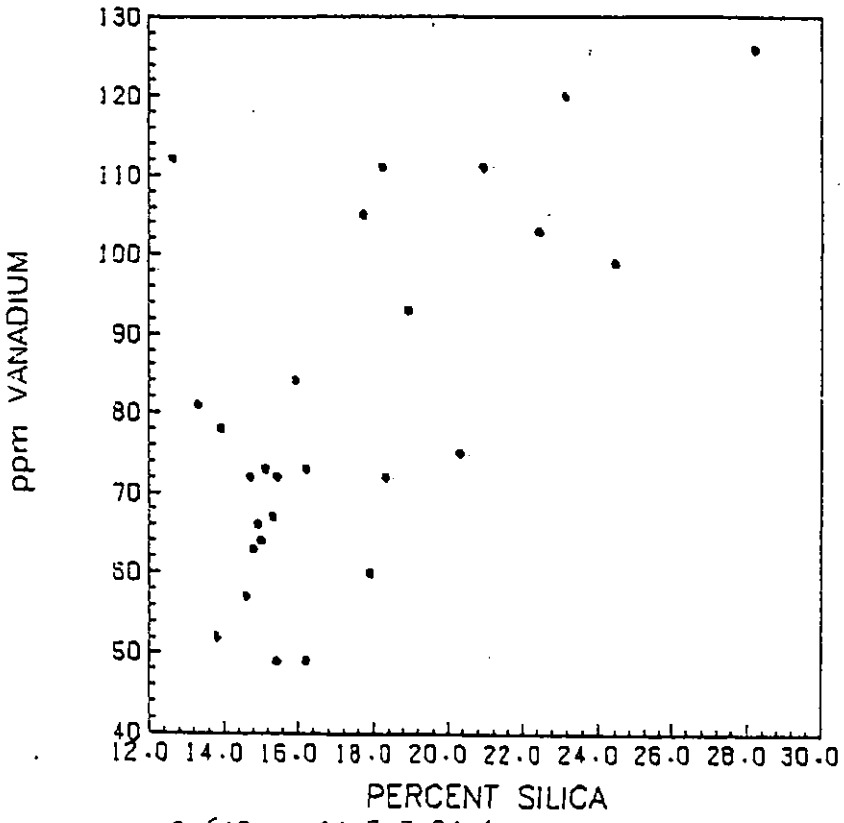



FIG.4.6.11(b)

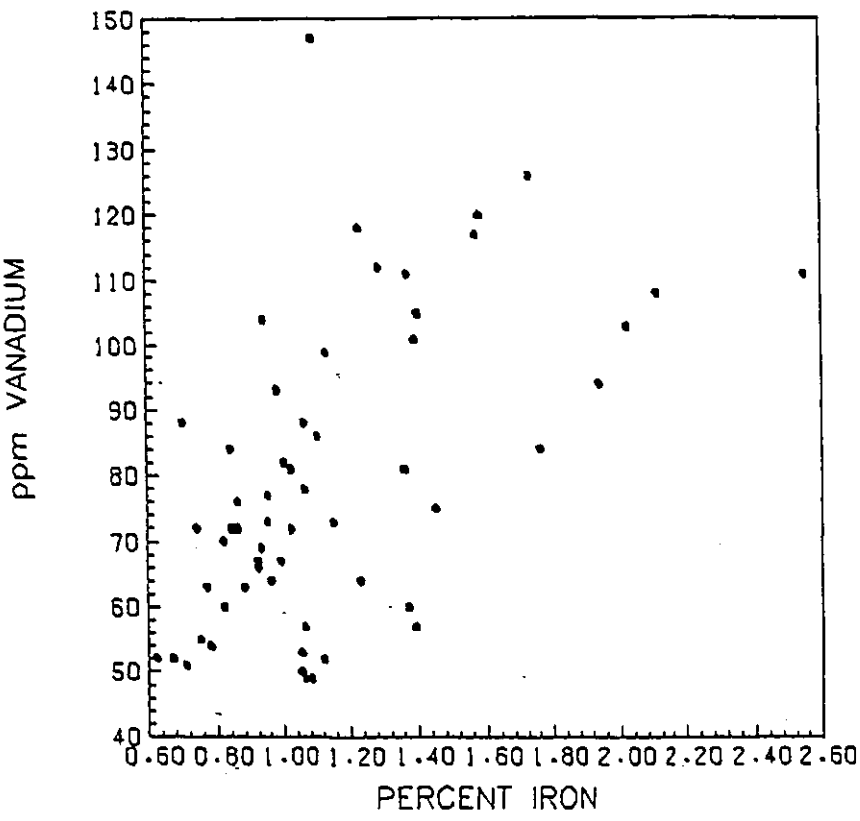
FIG.1.6.12(a)

SCATTER PLOT – SiO2 vs V



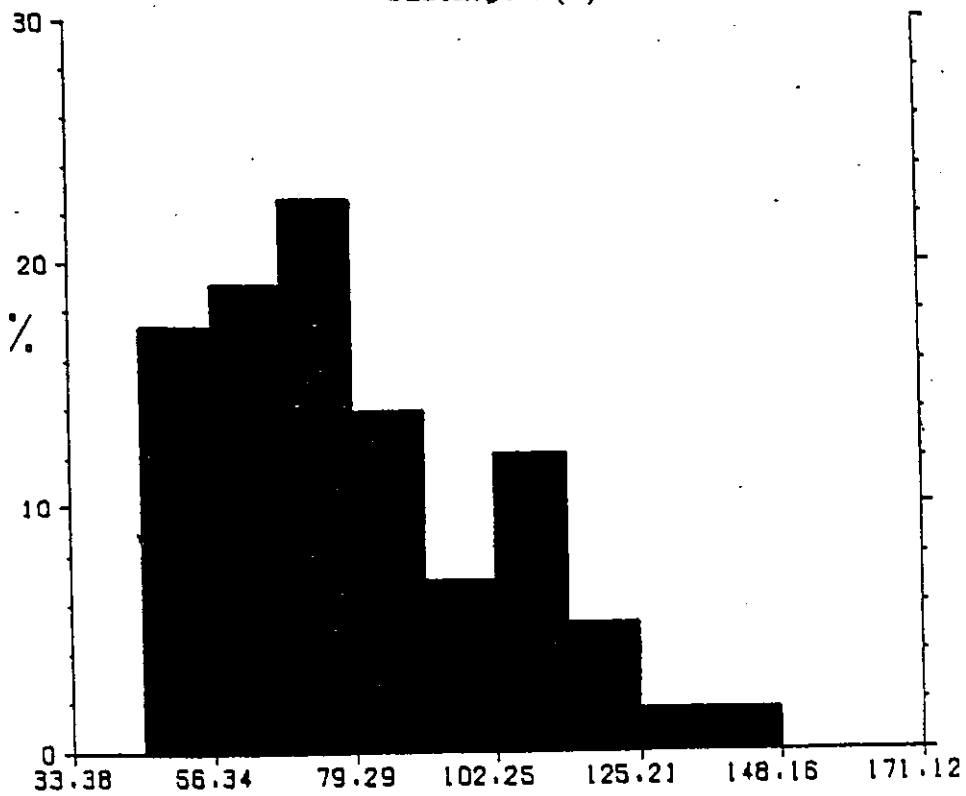

r=0.642 ,y=14.5+3.84x1.
r=correlation coefficient.
y=regression equation.

SCATTER PLOT – Fe vs V

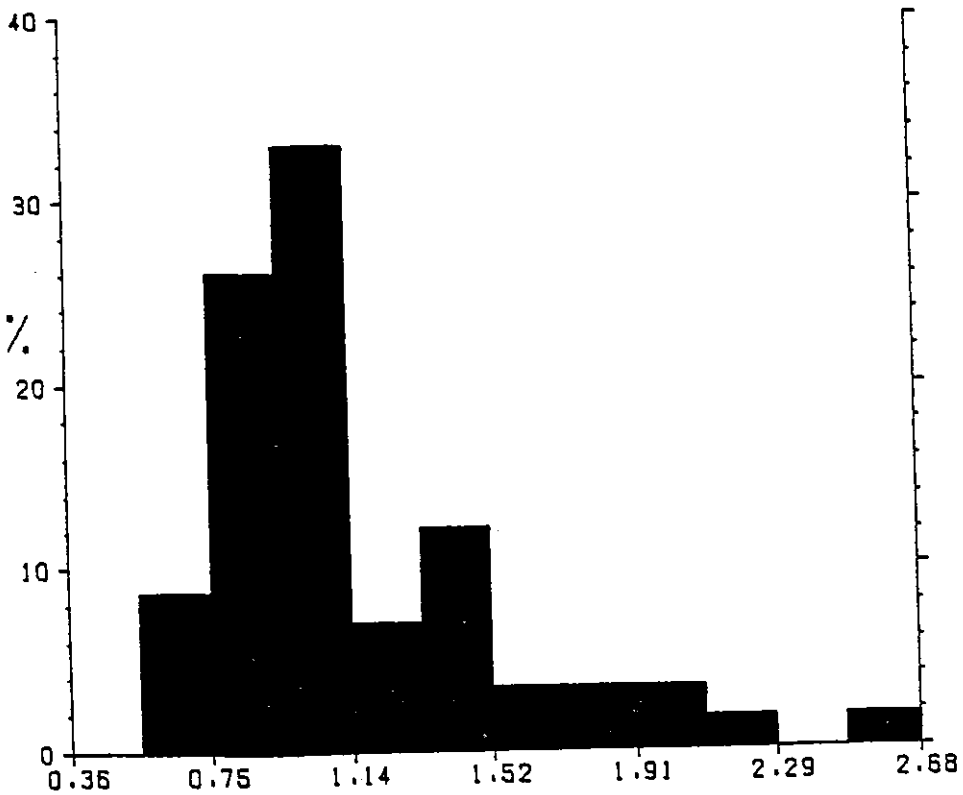



r=0.557 ,y=41.7+33.1x1.

FIG.1.6.12(b)




VANADIUM
NO. OF OBSERVATIONS = 58
MEAN = 79.29 STD DEV = 22.956




IRON
NO. OF OBSERVATIONS = 58
MEAN = 1.14 STD DEV = 0.386

Ti and Pb. The $<0.5$ μ clay fraction chemical analyses (Table 2.6.1) show Li and V abundance in the montmorillonite. The levels found are compatible with the suggestion that these elements may have been derived from weathering of volcanic debris, although Li was enriched by a factor of 3 in the clay fraction compared to oceanic basalts in which Li averages 10 ppm (Taylor, 1964).

Multiple regression on V using 8 variables or predictors, i.e. 8 elements which are positively correlated with V, as above, yielded a value of $r^2$ (coefficient of determination) of 82%. The correlation coefficient, r, of 0.91, shows that V is almost totally governed by the chemistry of K, Mg, Al, Fe, $SiO_2$, Li, Ti and Pb. This suggests that the major site for V is in lithogenous material, as noted by Chester and Aston (1976), with the major amount in clay minerals and lesser amounts in basaltic detritus.

Figure 2.6.11(a) shows the strong association of Li with both Al and $SiO_2$ while Figure 2.6.11(b) shows the distribution of the data for Li, Al and $SiO_2$. Li shows a bimodal shape to some extent and Al and $SiO_2$, slightly positive skews. For statistical purposes these were assumed to represent normal distributions and logging the data made little difference to the values of r or the shape of the scatterplots. V is intimately associated with Fe and $SiO_2$ (Figure 2.6.12(a)) although there is some scatter and the distribution of data in Figure 2.6.12(b) is again fairly normal.

In summary, the element correlations and inter-relations seen in sediments from the Galapagos Rift area at 86°W show that the elements studied are present in the following phases:

1. BIOGENOUS PHASE
   $CaCO_3$, $SiO_2$, Sr, P
2. HYDROTHERMAL PHASE
   Fe, Mn, Cu, Zn, ?Pb
3. HYDROGENOUS PHASE
   Na, K, ?Mg, Mn, La, Co, Ni, ?Pb

TABLE 2.7.1.

X-RAY DIFFRACTION MINERALOGY

| Sample Batch | Dominant Minerals | Subsidiary Minerals |
|---|---|---|
| SULPHIDES | PYRITE, CHALCOPYRITE, (SILICA - cf microscope work) | SPHALERITE, COVELLITE, CHALCANTHITE, GOETHITE, MARCASITE |
| MOUND OXIDE FACIES | GOETHITE (GOSSAN) | ? ILLITE/MONTMORILLONITE, CALCITE, BIRNESSITE |
| DREDGED MANGANESE CRUSTS | TODOROKITE, BIRNESSITE and ubiquitous NONTRONITIC SMECTITE (strong peak at 4.54 - 4.56Å) | CALCITE, QUARTZ |
| SHORT CORE CARBONATES | CALCITE | HALITE, QUARTZ, PLAGIOCLASE, AMPHIBOLE Amorphous IRON OXIDE SMECTITE. |

Samples irradiated with Cobalt Kα radiation, and Iron Kα radiation when samples were high in manganese - this eliminated fluorescence effects.

4. VOLCANOGENOUS PHASE

K, Mg, Al, Fe, $SiO_2$, Li, Ti, V, Co, Ni, Cu, Zn

5. CLAY MINERAL PHASE

Na, K, Mg, Al, Mn, Fe, $SiO_2$, Li, V, P, Cr, Ba, Co, Cu, Zn, Ag

Where an element is present in more than one phase, the major source of the element is underlined.

## 2.7 SUMMARY AND CONCLUSIONS

The data presented from the study of hydrothermal and associated sediments in the GRAFZI, Galapagos Rift, 86°W area can be summarised as follows:-

1. A hydrothermal sulphide deposit, enriched in Fe and Cu and considerably depleted in Zn, compared to similar deposits on the E.P.R., 21°N (Hékinian et al., 1980), was found associated with faulting at the rift valley margin, in a water depth of around 2850 metres, located at approximately 0°45'N, 85°50'W.

2. The double rift system at 85°50'W, with an associated intermediate topographic high, is mineralised along the southern margin of the northern rift valley. This margin is faulted with a throw of 40 metres and has a line of coalesced sulphide chimneys, 2 to 3 metres in height, along its base, which are flanked by hydrothermal iron oxide deposits.

3. Mineralogically, the sulphides are simple in nature and consist of primary chalcopyrite, pyrite and subsidiary sphalerite and their alteration products, eventually leading to the formation of iron oxide (goethite) gossan.

4. The GRAFZI area at 86°W, produced a suite of hydrothermal products and pelagic sediments (summarised in Table 2.7.1) which, for the first time since the discovery of the Red Sea deposits, displayed in one area the full sequence of minerals produced by fractionation of hydrothermal solutions. However, the spatial and temporal relations of these minerals are not as clear as those found in the Red Sea.

5. A dredge haul in a water depth of 2500 metres at $0^{o}57'N$, $85^{o}29'W$ on a seamount yielded manganese crusts and adhering nontronite of hydrothermal origin. These samples recovered 28 kms north of the Galapagos Rift spreading axis were similar to those described by Corliss et al. (1978) which were found in hydrothermal mounds at about $0^{o}35'N$, $86^{o}10'W$, and about 20 kms south of the spreading axis. The manganese crusts showed a rather high Fe content for hydrothermal Mn oxides. This represents a further discovery, subsequent to that of Burnett and Piper (1977), of ferromanganese oxides intermediate between hydrothermal Fe and Mn end-members and indicates the incomplete fractionation of Mn from Fe.

6. Analysis of geographical variations in uppermost oxidised layer sediments from the $86^{o}W$ area showed anomalous concentrations of Fe, Mn, Cu, Zn and to a lesser extent Pb. Mn and Zn in particular were found dispersed up to 14 kms from a source at Dive site 1001, which has important implications for marine and land-based mineral exploration. Zn/Cu ratios may be useful in locating hydrothermal sulphide orebodies. These ratios increase away from the source.

7. Foraminiferal marl and chalk oozes predominate in the Galapagos Rift, $86^{o}W$ area. Clay minerals provide the major amounts of K, Mg, Al, Fe, $SiO_2$, Li, V, Co, Cu and Ag to the bulk sediment composition.

8. The volcanogenic fraction of GRAFZI pelagic sediments decreased away from the neovolcanic zone, zone 1, where little sediment cover was found and hence, admixed basaltic basement material was abundant.

9. Data presented possibly indicate that a second hydrothermal site may exist at the fracture zone/Galapagos Rift intersection, at $85^{o}22'W$. This was inferred from the presence of Zn and Cu enrichment in sediments and from the presence of hydrothermal Mn oxide crusts.

# CHAPTER 3

## REFLECTED LIGHT MICROSCOPE, ELECTRON MICROPROBE AND STABLE ISOTOPE STUDIES

### 3.1 INTRODUCTION

In order to elucidate the origin and mechanism of formation of the GRAFZI hydrothermal sulphide mounds at 86°W, detailed mineralogy, fine scale electron microprobe chemistry and stable isotope studies were carried out on samples collected. Of special interest was the mineral paragenesis and the low abundance of Zn in the GRAFZI deposits compared to those at 21°N on the East Pacific Rise, which was discussed in Chapter 2. Stable isotope studies were carried out to compare GRAFZI and 21°N sulphide deposits, and also to find the temperature of formation of sulphide minerals which make up the presently inactive hydrothermal mounds.

Data presented here lead to the synthesis of a model for the formation of a polymetallic sulphide deposit at a modern mid-oceanic spreading centre (Chapter 4).

### 3.2 REFLECTED LIGHT MICROSCOPY

Mineral identification was achieved by reflected light microscopy on polished thin sections and polished mounts, carried out at the University of Durham in 1981.

#### Textural Relationships

The hydrothermal sulphide mounds consist of primary chalcopyrite ($CuFeS_2$), pyrite ($FeS_2$), sphalerite (ZnS) and amorphous silica ($SiO_2$) with secondary covellite (CuS), chalcanthite ($CuSO_4.5H_2O$), marcasite ($FeS_2$) and goethite ($\alpha$FeO.OH), see Chapter 2. The polished sections are prone to blue discoloration over a very short period of time and this suggests that the mineral assemblage is unstable in its present environment, undergoing rapid alteration to chalcanthite.

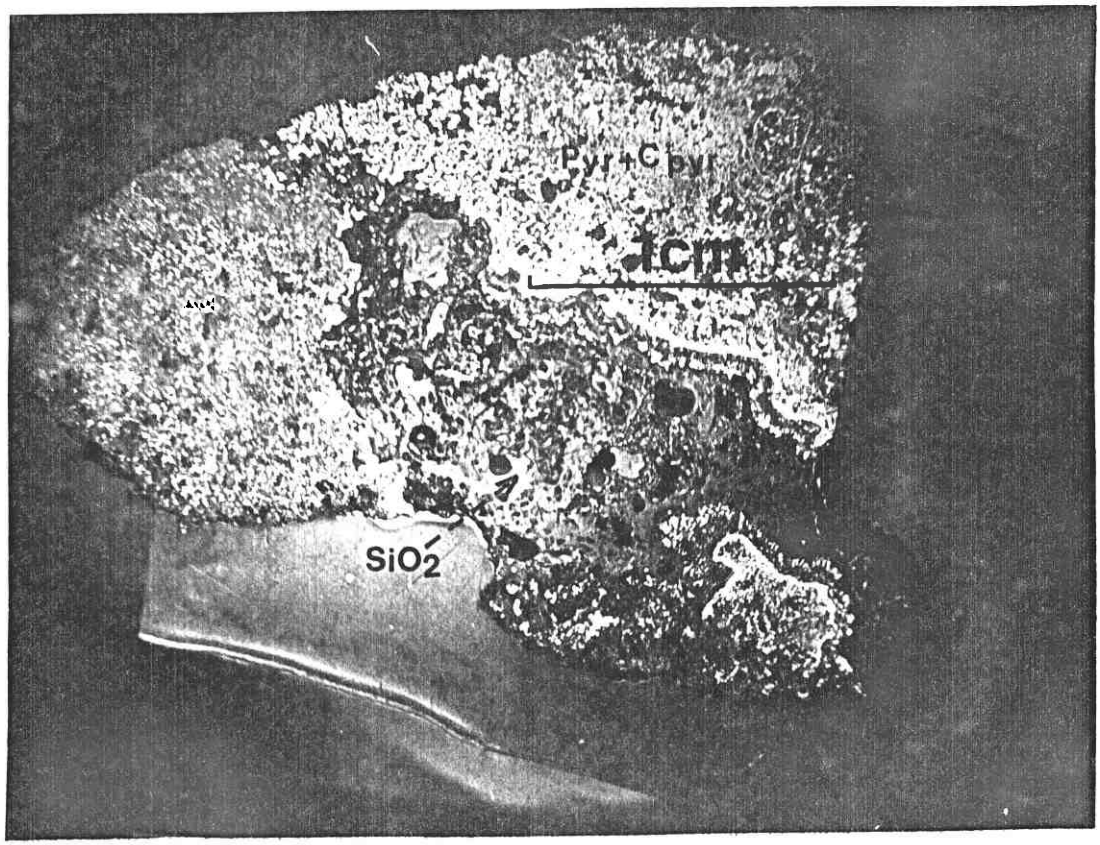
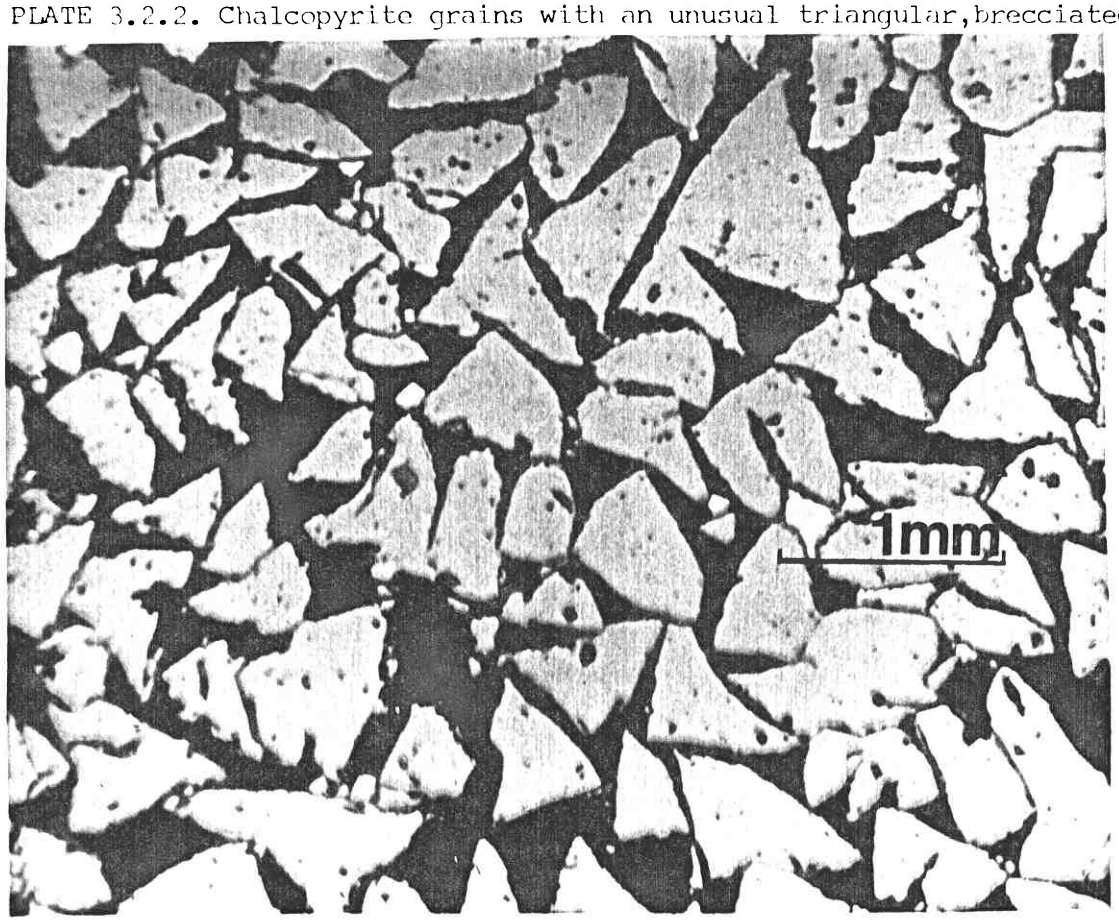



PLATE 3.2.1. Cavity infilled with amorphous silica and surrounded by primary sulphides.

PLATE 3.2.2. Chalcopyrite grains with an unusual triangular,brecciated habit.



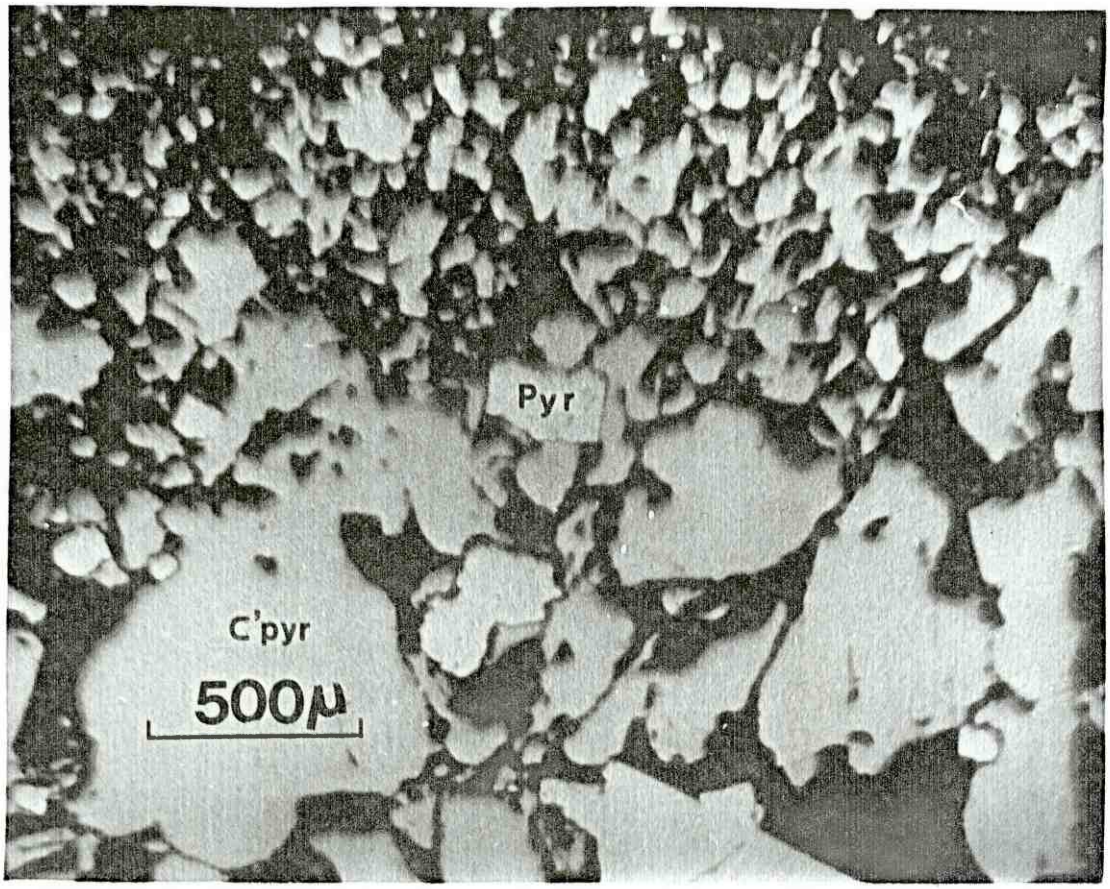
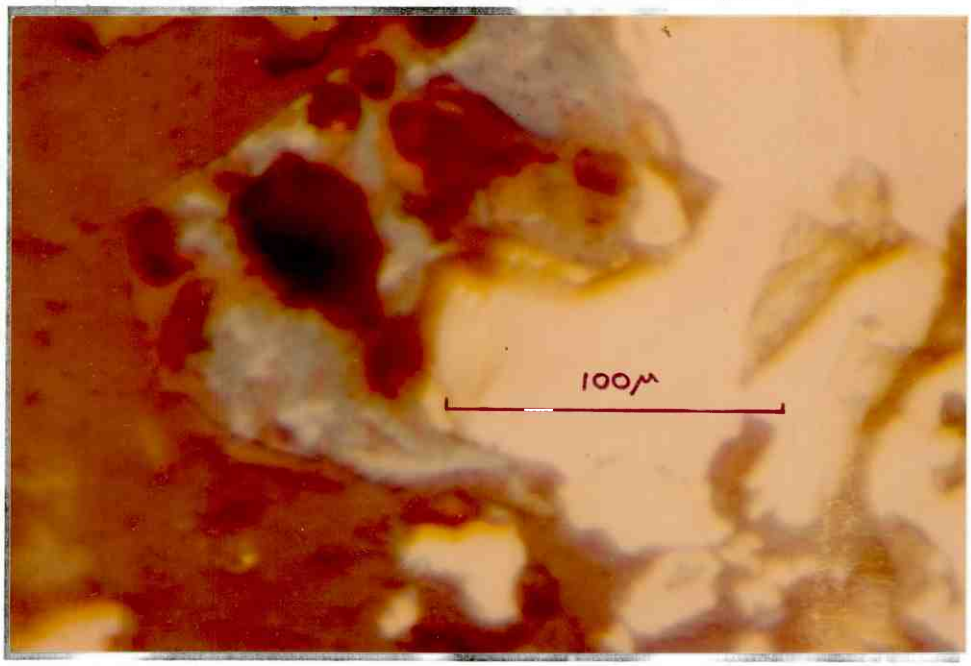



PLATE 3.2.3. Rapid decrease in grain size of chalcopyrite towards the chilled margin of the veinlet.

PLATE 3.2.4. Covellite (blue) forming from chalcopyrite(yellow).



The aim of the reflected light microscope work is to understand the sequence of precipitation or paragenesis that produced the hydrothermal sulphide mounds and to find a genetically linked mineral pair to carry out sulphur isotope geothermometry. Due to mineralogical differences, the mound top and mound middle samples are dealt with separately.

*Mound Top.*

A typical sulphide and amorphous silica relationship within different areas of the same mound top sample is shown in Plate 3.2.1. Pores are common and a chalcopyrite rim to the siliceous area may represent ingrowth of this mineral from the walls of a cavity, later filled with amorphous silica.

Generally, the top of the mound produced samples richest in chalcopyrite, as stated in Chapter 2. Chalcopyrite grains could be found up to 3 mm in size associated with smaller pyrite euhedra, as will be discussed in Section 3.4(b). A veinlet area especially rich in large chalcopyrite grains was chosen for more detailed study. Plates 3.2.2 and 3.2.3 show parts of this area in which chalcopyrite displays an unusual triangular "brecciated" habit, with some pyrite euhedra to be found interstitially. Most chalcopyrite outside the veinlet occurs within the gangue as anhedral masses up to 0.5 mm across, although the more common size is 250$\mu$. Chalcopyrite, which is extensively altered to covellite, is occasionally intergrown with sphalerite and enclosed within this mineral. However, sphalerite was not found enclosed in chalcopyrite, as also found in E.P.R. 21$^{\circ}$N sulphides (Oudin, 1981). Minor inclusions of chalcopyrite (2 - 10$\mu$) occur within pyrite, indicating the close paragenetic link of these two minerals. The reverse case of pyrite euhedra within chalcopyrite is also found.

Chalcopyrite tarnishes easily to a more brassy yellow colour and is found in triangular shaped grains within the veinlet, whereas it is normally found in ore deposits as roughly equidimensional grains or in the presence of other ore minerals, as a filling of wedge-shaped spaces due to its allotriomorphic nature (Ramdohr, 1980). This unusual

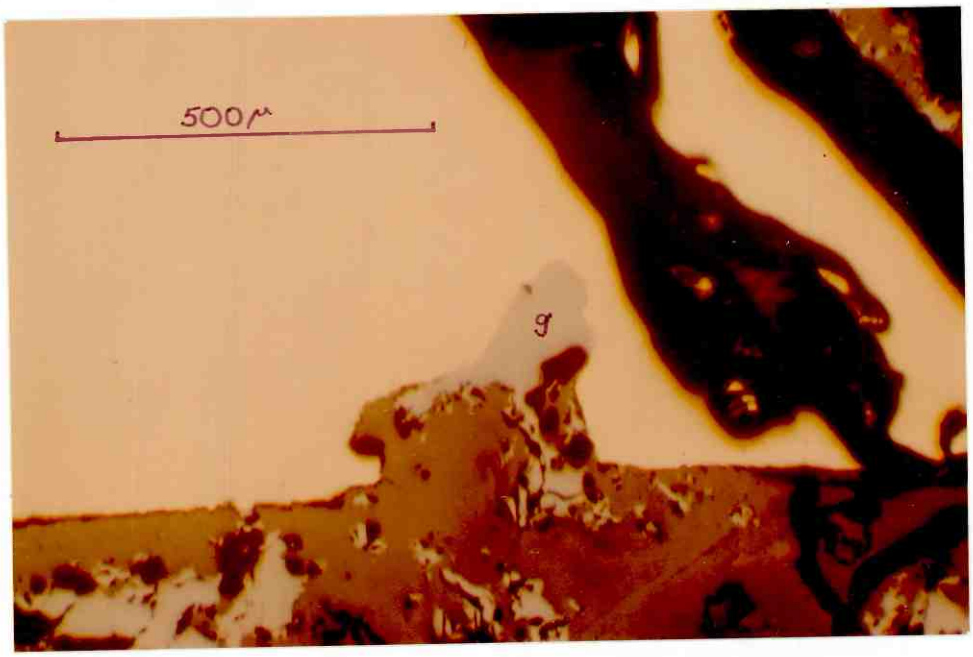
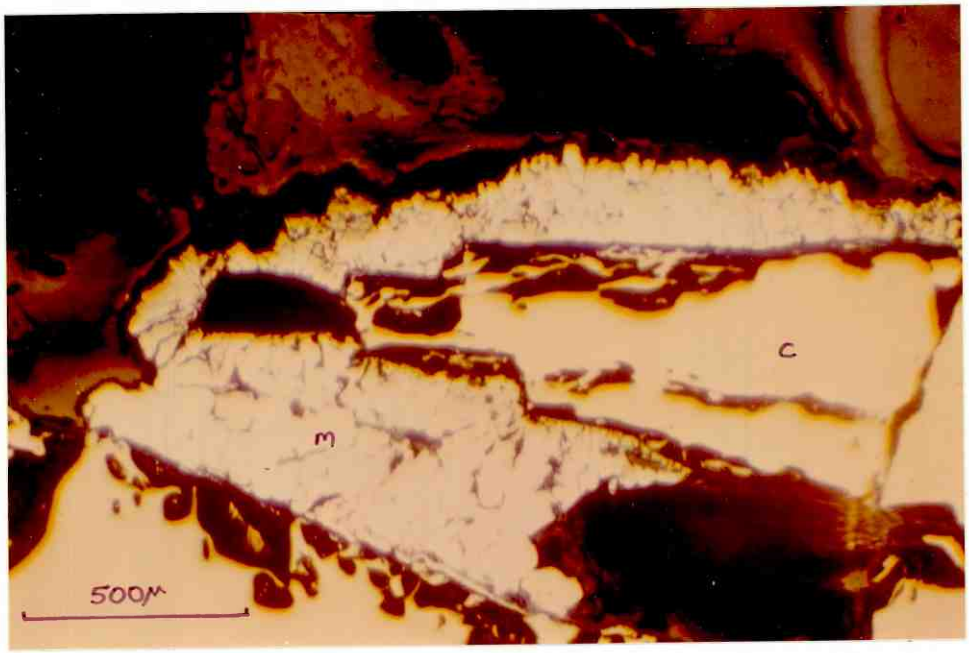



PLATE 3.2.5. Goethite (g) replacing a large chalcopyrite grain.

PLATE 3.2.6. Bladed marcasite (m) grains enclosing chalcopyrite (c).



phenomena of "brecciated" grain habit may be explained by mechanical deformation of chalcopyrite grains which grew inwards from the walls of the veinlet. High velocity hydro-thermal solutions which were chilled against the conduit margins and precipitated chalcopyrite, with a rapid decrease in grain size towards the chilled margin (see Plate 3.2.3), could dislodge and exploit weaknesses within the crystal structure of chalcopyrite. This may have been responsible for producing the observed grain habit. Zoning and internal structures are not found within chalcopyrite grains. High temperature $CuFeS_2$ normally takes ZnS into solid solution, which is later exsolved at lower temperatures (Ramdohr, 1980). The lack of exsolution observed here may indicate the presence of Zn in solid solution with Cu in chalcopyrite, as at 21°N (Oudin, 1983). A detailed knowledge of the paragenesis and temperatures of sulphide precipitation may aid in this regard (see Section 3.4(b)).

Study of the alteration products of chalcopyrite has yielded many commercial benefits to the modern exploration geochemist. The mobilisation of Cu and the relative loss of Fe, yields a sequence of secondary sulphide and sulphate minerals richer in Cu than the protore or hypogene minerals, and often concentrated in a zone of supergene enrichment found below the water table, on land. In GRAFZI sulphides, the supergene zone can be recognised by the presence of covellite (CuS) and chalcanthite ($CuSO_4.5H_2O$). Plate 3.2.4 shows the formation of covellite at the expense of a chalcopyrite subhedral grain, under high magnification. In the E.P.R., 21°N sulphide deposits, similar processes were observed (Hékinian et al., 1980) and the presence of goethite (Plate 3.2.5) etching chalcopyrite in the GRAFZI deposits, shows the relative instability of the latter mineral, as was also noted in mineralised metabasalts from the Mid Atlantic Ridge (Bonatti et al., 1976). A goethite (limonite) oxidised zone of a few millimetres in thickness is commonly found sheathing fresh primary sulphide material, and this represents the gossan or barren zone.

Marcasite is texturally less closely linked to chalcopyrite than covellite, chalcanthite and goethite and always fills the interstices

between pyrite and chalcopyrite primary sulphides. Marcasite is certainly a late stage mineral which may be secondary in origin.

Chalcopyrite found in the amorphous silica matrix is extensively altered to covellite with small chalcopyrite crystals (up to 20$\mu$) totally pseudomorphed by covellite, and larger chalcopyrite grains having covellite rims up to 10$\mu$ wide. Very fine grained covellite of less than 1$\mu$ is scattered throughout the silica matrix. Covellite and rare blaubleibender covellite replaces chalcopyrite and sphalerite along cleavage and grain edges producing pseudomorphs up to 100$\mu$ after chalcopyrite and 20 x 1$\mu$ laths after sphalerite. Goethite is often found in spherulitic form, especially at the exposed surfaces of the sulphide samples, in gossan areas, but replacement of colloform pyrite within the samples also occurs.

Tentative identification of one grain (4$\mu$ in size) of tetrahedrite, one patch of haematite present in the gangue mass (200$\mu$ in diameter) and trace amounts of galena (up to 15$\mu$ in diameter) were made. Some Pb was found in the sulphides by chemical analysis (Section 2.1), supporting the presence of galena.

Marcasite (Plate 3.2.6) displays a whiter colour than its polymorph pyrite, and shows strong anisotropy. Twinned bladed marcasite 10 - 50$\mu$ wide but up to 100$\mu$ in length is intergrown with both colloidal and euhedral pyrite or it is found interbanded with them, as 100 x 20$\mu$ banded radiating marcasite rosettes. Characteristically, this mineral encloses and overgrows euhedral pyrite and may replace it. Larger aggregates of marcasite, 100 - 200$\mu$ in diameter, occur within the gangue host rock, away from the main pyrite. Bands of marcasite rhythmically interlayered with pyrite and silica may be due to pyrite or ?pyrrhotite replacement (Uytenbogaardt and Burke, 1971). Rarely, it can be found as small 5 - 10$\mu$ anhedral crystals in pyrite. Of particular interest are the radiating marcasite aggregate features of overgrowth and pressure twinning that cross-cut original grain boundaries. Marcasite is extensively altered along crystallographic planes and

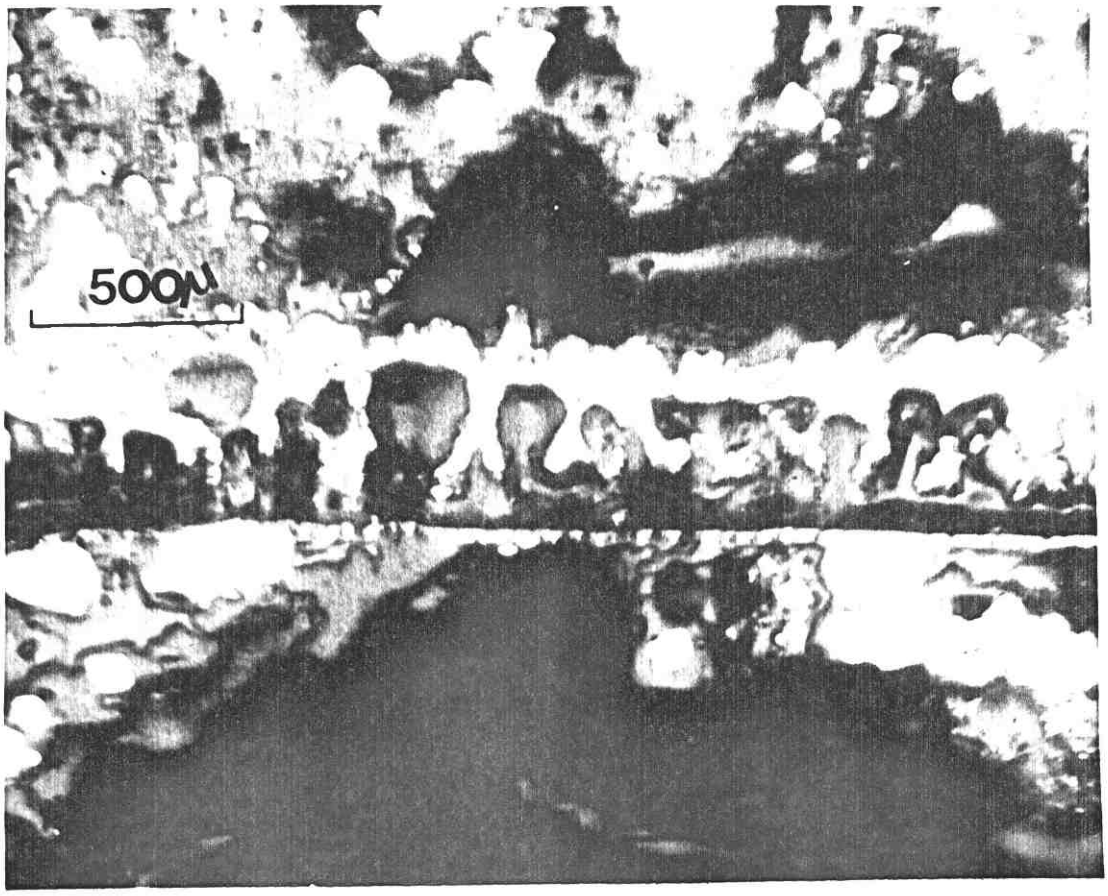
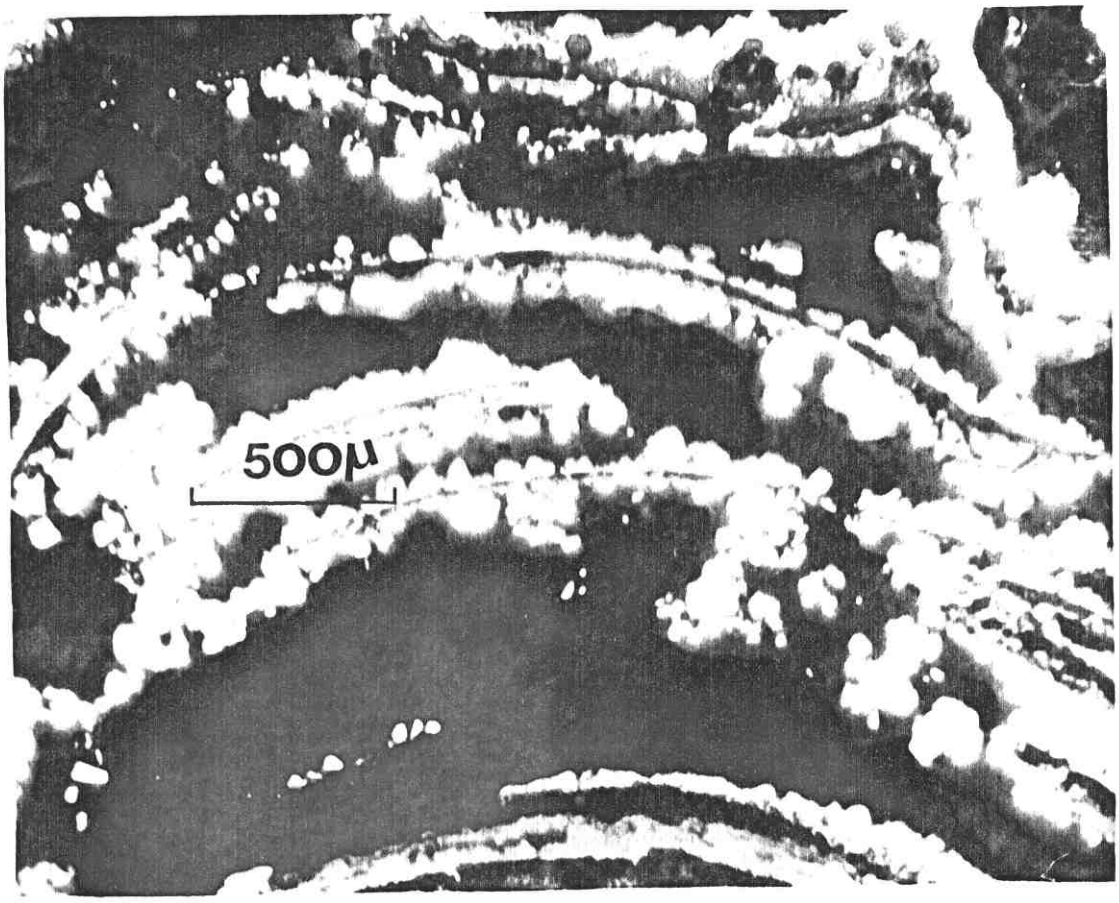



PLATE 3.2.7. Cusp-like growths of amorphous silica enveloped by pyrite projecting upwards from a linear filament.

PLATE 3.2.8. Colloform association of pyrite and amorphous silica.



importantly, no sphalerite or chalcopyrite inclusions were seen in this mineral, although it may itself be replaced by silica, adding support to its late stage formation.

Nowhere in the samples studied was pyrrhotite found, although it is well known that marcasite is commonly found as a replacement mineral of pyrrhotite (Uytenbogaardt and Burke, 1971). This suggests that pyrrhotite, so common in the 21°N "black smokers" (Spiess et al., 1980), was either totally replaced by marcasite or was not formed. Oudin (1983) has shown that unstable phases are either dissolved or transformed, supporting pyrrhotite replacement.

*Mound Middle.*

The minerals so far not described, i.e. pyrite, sphalerite and silica, are most abundant in the mound middle rather than the mound top, where chalcopyrite and its associated secondary minerals are most common. Pyrite is found intimately associated with sphalerite and amorphous silica, but in a different habit with each of these two minerals. Pyrite commonly exhibits an idiomorphic nature in euhedral grains, with many inclusions of sphalerite. However, the association of pyrite with silica is shown by remarkably well-formed colloform banding with rhythmically precipitated pyrite and silica. This indicates that conditions in the hydrothermal solution were close to the conditions for precipitation of these two minerals, perhaps triggered off by slight changes in pressure or temperature. Plate 3.2.7 shows cusp-like growths of silica enveloped by pyrite, both emanating from a linear filament.

Colloidal pyrite encompasses a number of different pyrite types ranging from a brown, poorly polished pyrite to a yellow rhythmically precipitated pyrite. A number of fabrics are common, including:-

1. a half-moon texture (50 - 150$\mu$m in diameter) composed of small 2 - 4$\mu$m individuals;
2. irregular cauliflower-like or stromatoporoid-like masses of rhythmical pyrite and fine-grained quartz/amorphous silica (40 - 400$\mu$m in diameter);

3. irregular anhedral masses of poorly polished pyrite (up to 100μ).

Colloidal pyrite often acts as a nucleus to a radiating sequence of alternating bands of euhedral pyrite, marcasite and fine silica, which are about 10 - 20μ thick and 30 - 100μ long. Colloidal pyrite sometimes has 5 - 30μ size euhedral pyrite growing out from the colloidal pyrite surface, or small concentric or framboidal pyrite (5 - 20μ) acts as a core to the euhedral pyrite. Colloform pyrite and silica represent the bulk of the samples from the mound middle (Plates 3.2.8 and 3.2.9). This texture often appears to have grown out from the walls of long tubes/spines, growing into hollow centres. Colloform textures often appear as open-space fillings. The straight or slightly curved filaments are thought to be of an organic origin, and organic debris was common throughout the sulphides of the GRAFZI area, as relict infilled worm burrows and shell fragments, as was noted at 21°N on the E.P.R. (Hékinian et al., 1980).

In the geological record, many examples can be found of sulphide nucleation at organic sites. In the GRAFZI deposits, sulphide grains appear to have stuck to organic material and shell fragments which acted as a nucleus for precipitation alternately of pyrite and silica, due to changing solution chemistry, in a fine grained colloidal gel. Later solidification and diagenesis of the mounds is evident as pores were filled and worm burrows were sealed by amorphous silica and secondary minerals. The position of the colloform pyrite/silica banding in the paragenesis is difficult to ascertain but it may represent a "quench" texture as the hot hydrothermal solutions were rapidly chilled on egress from oceanic crust. Solidification of the colloidal gel produced by this "quenching" may have yielded the textures seen. Further growth into cavities both late in the sequence and diagenetically, have produced a tightly bound internal structure to the sulphide mounds, which may have made oxidation very difficult below the top few millimetres of gossanised surface.

The sulphide mounds may be more resistant to oxidation than previously realised. Ophiolite sulphide deposits such as those of the Troodos Comple.. (Adamides, 1979) were either resistant to total gossanisation

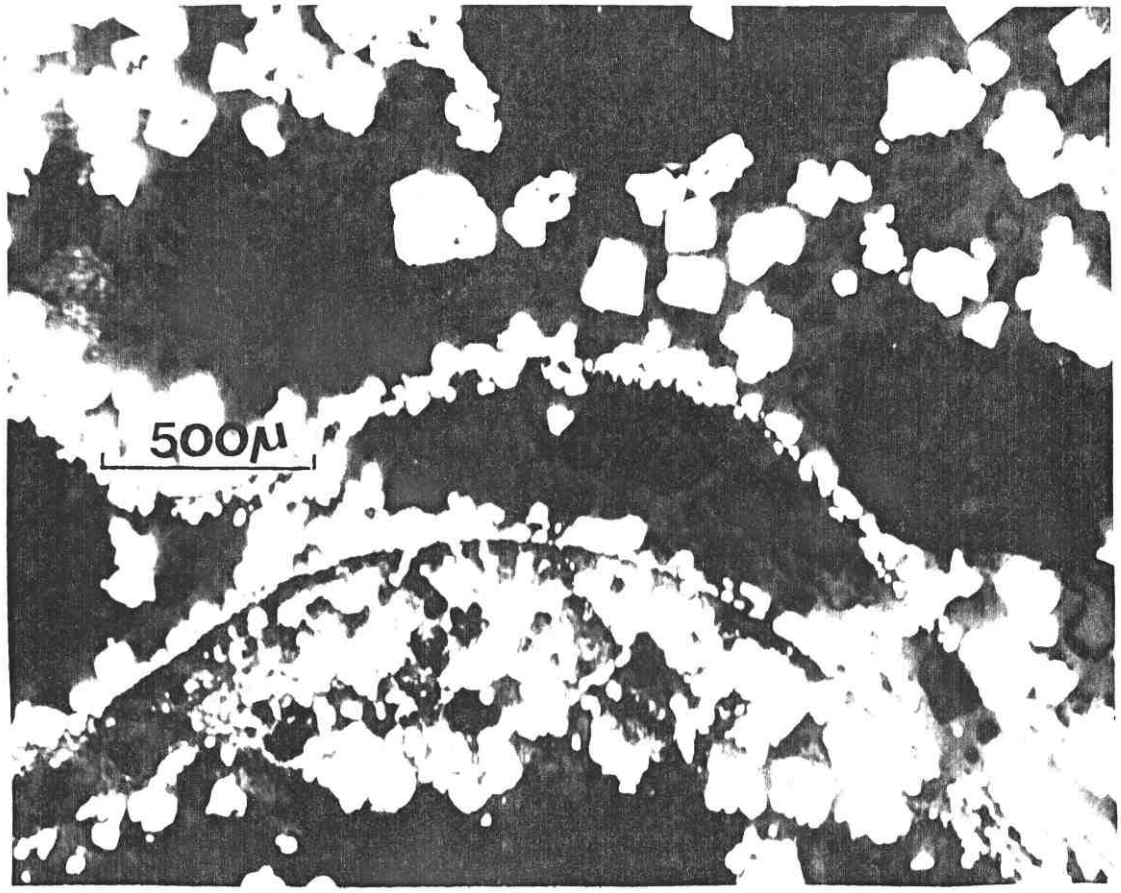
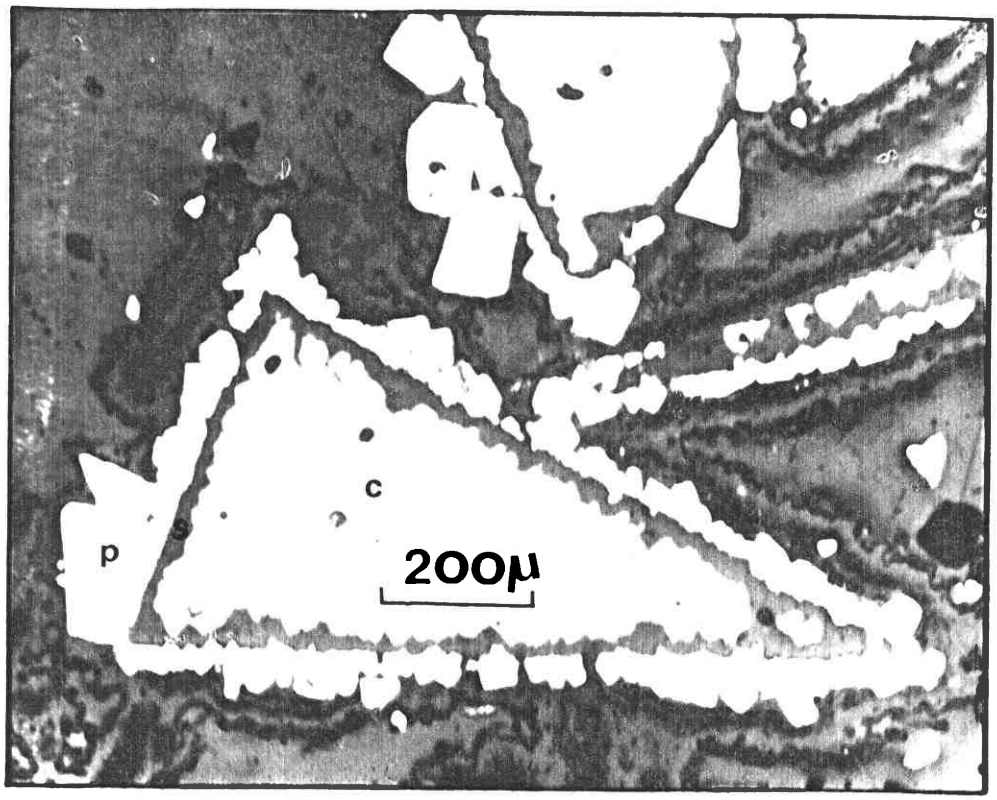



PLATE 3.2.9. Euhedral pyrite above pyrite associated with curved filaments of a possible organic origin.

PLATE 3.2.10.Corroded chalcopyrite grain (c) etched with amorphous silica (s) and surrounded by pyrite (p).



or were buried soon after formation, by extrusive volcanism. In the light of evidence produced by sectioning, after which the GRAFZI sulphides alter to secondary minerals within days, it is thought that although burial by lava flows may be rapid in geological terms, sulphide preservation is ultimately dependant on compaction and the internal sealing of conduits by diagenesis, thereby decreasing mound permeability.

Plate 3.2.9 shows the above colloform banding but areas of idiomorphic pyrite euhedra can be seen scattered throughout the colloidal gel matrix. These pyrite euhedra are thought to be high temperature precipitates and may represent "fall-out" from the "black-smokers". No pyritefor pyrrhotite replacement textures were seen (see above), and isotopic evidence (Section 3.4(b)) confirms the primary high temperature formation of this pyrite, as distinct from colloform pyrite/silica banding formed later in the paragenesis, e.g. Plate 3.2.10 shows silica and pyrite etching an earlier "brecciated" chalcopyrite grain.

High magnification of pyrite euhedra show the presence of sphalerite which, although indicated by the chemical analysis, could not be confirmed by X-ray diffraction techniques. The dominant habit of this generation of pyrite is pentagonal dodecahedral and crystal size ranges from 10 - 50$\mu$ with a 10$\mu$ wide enclosing silica skin (cockade texture). This pyrite often overgrows colloidal pyrite and is intergrown with or enclosed within tabular twinned marcasite. Some reflectance zoning (or zones lying parallel to crystal edges) can be seen by trails of small gangue or sphalerite inclusions (1 - 5$\mu$ in size) lying within the outer pyrite zones. These sphalerite euhedra seem to have precipitated at the same time as the outer zone of the pyrite grains, after a change in temperature and chemistry of the solutions since the pyrite nucleus was formed. However, 5 - 10$\mu$ rounded irregular sphalerite inclusions and 2 - 10$\mu$ chalcopyrite anhedral grains could also be found, the former mineral being observed in an emulsoid or 'Caries texture' typical of replacement by dissolution in later pyritiferous fluids. Dissolution of sulphide phases has also been shown in the 21$^{o}$N deposit (Oudin, 1981; Oudin, 1983).

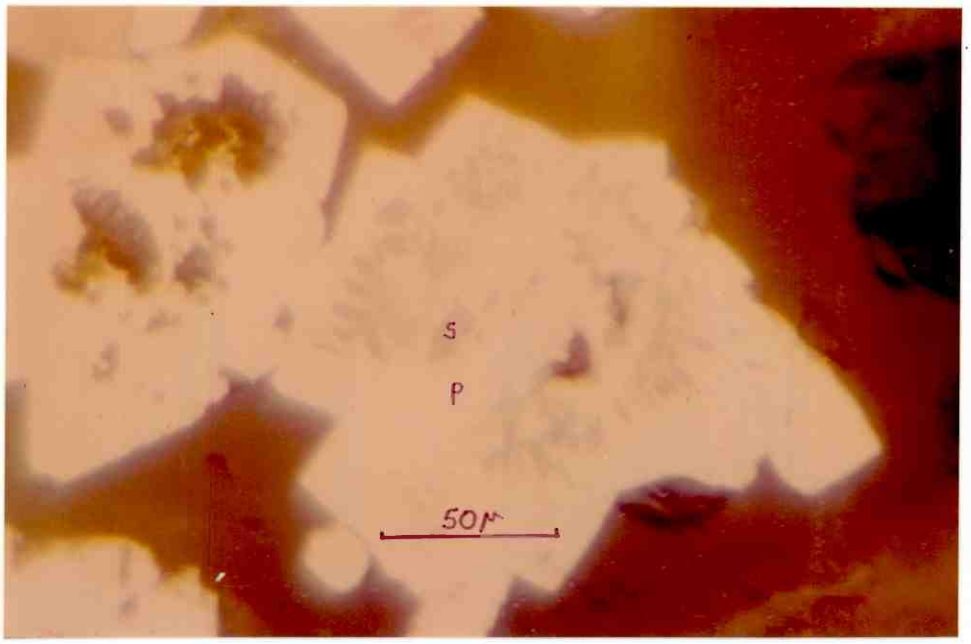
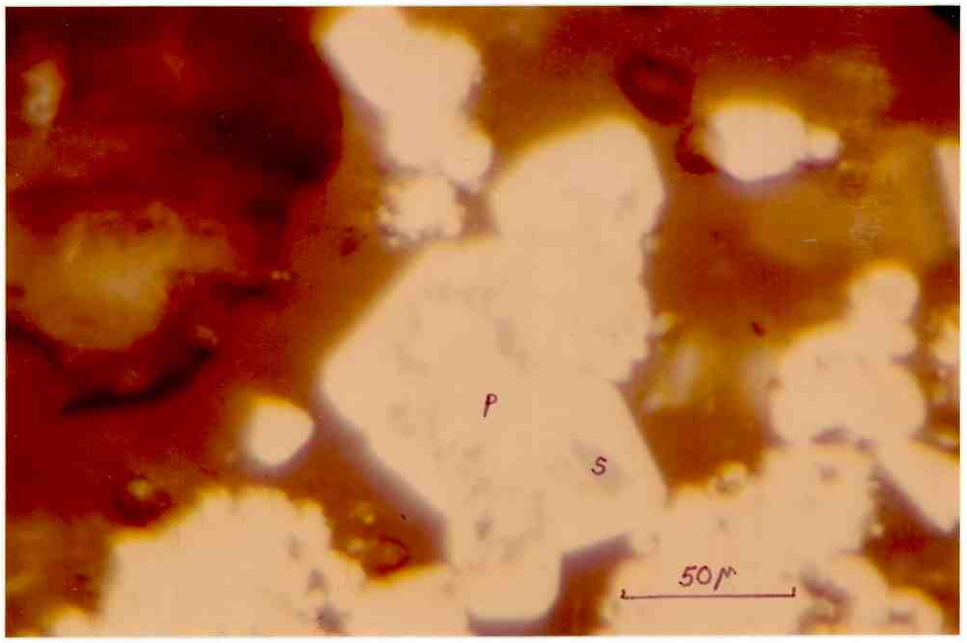



PLATE 3.2.11. Caries texture shown by sphalerite (s) in pyrite euhedra (p).

PLATE 3.2.12. Outer growth zones of sphalerite (s) within euhedral pyrite (p).



These two situations represent a paradox, i.e. contemporary-outer grain pyrite/sphalerite precipitation and also sphalerite dissolution due to instability in the presence of later and hotter pyritiferous solutions. It is necessary to appreciate the possibilities that exist in order to arrive at a plausible mechanism which could account for this phenomena. Sphalerite, from 2 - 25$\mu$ in size, can be seen in two situations; the first, as euhedra growing coevally with pyrite in its outer growth zones; secondly, as anhedral rounded grains that radiate from the pyrite centres in an emulsoid-like 'Caries texture' (see Plates 3.2.11 and 3.2.12), being essentially a dissolution feature. An explanation which can be ruled out, is that exsolution of ZnS (as sphalerite) which was miscible at high temperatures with pyrite, became a discrete phase on cooling. Ramdohr (1980) noted that exsolution of other phases in pyrite is practically unknown.

The most plausible explanation for the pyrite/sphalerite textures relies on temperature as the most important controlling factor. On the E.P.R., at 21$^{o}$N, the hottest smokers, with temperatures exceeding 350$^{o}$C have been seen depositing Fe-Cu sulphides whilst fluid inclusion studies have shown that Zn-rich sulphides formed at about 300$^{o}$C (Le Bel and Oudin, 1982). At lower temperatures still, pyrite and silica are intimately associated in the "white smokers" (Haymon and Kastner, 1981). Therefore, firstly chalcopyrite/pyrite and then pyrite/sphalerite may precipitate on the natural cooling of a hydrothermal solution. However, if there was an increase in the temperature of the solutions, this could result in a change in chemistry and mineralogy produced in the sulphide deposits. Earlier, lower temperature, sphalerite[1] would be unstable and susceptible to dissolution replacement by pyrite which would be stable in these new hotter conditions.

---

[1] Footnote: Oudin (1983) has shown that wurtzite is unstable and transforms to sphalerite which may account for the lack of wurtzite in GRAFZI sulphides.

TABLE 3.2.1.

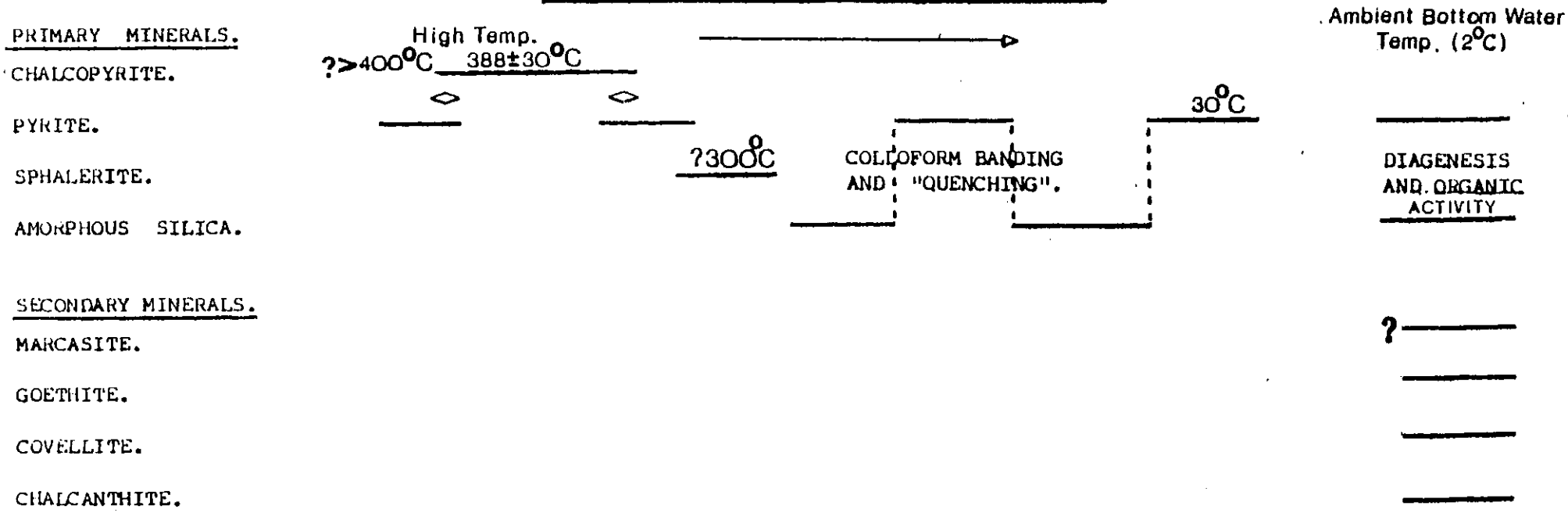
Sulphide Mineralogy of Inactive Hydrothermal Vents, 86°W - collected during DIVE 1001

| Mineral Name | Chemical Formula | Quantitative Abundance | Position found (when significant) | Miscellaneous |
|---|---|---|---|---|
| Chalcopyrite | $CuFeS_2$ | Major | Common throughout but most abundant at top of mound and in hydrothermal veinlet | The most common mineral found, and often in "shark's tooth" triangular grains particularly within veinlets. Often the chalcopyrite euhedra have etched and unstable rims coated with both silica and pyrite. Apparently of high temperature formation |
| Pyrite * | $FeS_2$ | Major | Most common from the middle of the mound | Pyrite occurs as 1) euhedra inmixed with chalcopyrite, and as 2)scattered euhedra and also colloform anhedral texture with silica in a colloidal gel, commonly associated and nucleating around organic remains. At least two generations of pyrite precipitation. |
| Sphalerite | ZnS | Minor | Only seen optically in the mound middle | Only found within the middle of the mound, displaying corroded 'Caries' texture within pyrite euhedra |
| Covellite † | CuS | Minor | Associated with chalcopyrite | A secondary mineral with characteristic blue colouration in reflected light, and present in the oxidised rind areas, with formation due to Chalcopyrite degradation |
| Marcasite * | $FeS_2$ | Minor | Rims around pyrite and chalcopyrite | Possibly a late stage formation in the mound after hydrothermal activity cessation. Diagenesis and compaction of the pore-ridden mound probably resulted in marcasite precipitation as coatings on other grains |
| Chalcanthite † | $CuSO_4.5H_2O$ | Minor | Associated with chalcopyrite and oxidised rind | Likecovellite, this mineral is also a secondary product of chalcopyrite oxidation, and it can be seen to grow on the surfaces of week old polished sections,with a characteristic blue colour |

* Polymorphs of $FeS_2$ formula

† Sulphide alteration product

FIG 3.2.1. HYDROTHERMAL MOUND PARAGENESIS.




(Temperature data from this study; ARNOLD & SHEPPARD, 1981; STYRT et al., 1981. - E.P.R, 21°N.)

Isotopic evidence for the high temperature formation of a chalcopyrite/pyrite mineral pair is discussed in Section 3.4(b). It is interesting to note that intimately associated chalcopyrite/pyrite from the West Shasta Cu-Zn District of California was formed at 340-365°C (Casey and Taylor, 1982), where significantly, pyrite was found to pre- and post-date chalcopyrite in the paragenesis, as seen in GRAFZI sulphides.

Whilst chalcopyrite seems to occupy a restricted position in the paragenesis, pyrite seems to occupy much of the paragenetic sequence and is found:-

1. closely associated with chalcopyrite;
2. with silica in a colloform texture;
3. as isolated pyrite euhedra from black smoker "fall-out";
4. with marcasite, as minerals of a late stage and possible diagenetic origin.

Paragenesis

Table 3.2.1 shows some of the more important observations from the reflected light microscopy and reports where in the mound the samples were taken. However, the microscope study should not be viewed in isolation and it should be remembered that chemically, the mound top was richer in Fe-Cu sulphides than the middle, which was richer in Zn and $SiO_2$. Coupled with this, is the observation that a nearby hydrothermal Mn crust was found to have more than 2% Zn and that Zn was widely dispersed into pelagic sediments of the GRAFZI area, compared to Cu and Fe. This evidence provides a strong case that hydrothermal solutions in the GRAFZI sulphide mounds either re-dissolved previously precipitated Zn or simply dispersed it onto the ocean-floor, while Fe and Cu sulphides formed at high prevailing temperatures, at the source.

Just as the microscope work should not be viewed without the chemistry of the deposits, neither should the paragenesis (Figure 3.2.1) be considered without the stable isotope constraints on temperature (Section 3.4(b)). Possible reasons for the instability of ZnS and its pyritisation due to the changing state of the hydrothermal solutions, are discussed in Chapter 4.

The main paragenetic sequence of events observed in GRAFZI sulphides (Figure 3.2.1) is shown below:-

1. Original sulphide mineral precipitation produced an assemblage of pyrite-sphalerite-amorphous silica, around the hydrothermal vent and on basaltic crust, as interpreted from the mound middle samples. Based on temperature data from analagous deposits on the E.P.R., at 21°N, this occurred at around 300°C.

2. This was then followed by a phase of hydrothermal activity at higher temperatures, producing an assemblage dominated by pyrite and chalcopyrite, which capped the first-formed sulphides.

3. The onset of the higher temperature sulphide precipitation was represented by the formation of euhedral pyrite inclusions enclosed within chalcopyrite grains.

4. A period of extensive chalcopyrite precipitation then followed, forming the upper parts of the mound, which occurred over a restricted temperature range at about 390°C (see Section 3.4(b)).

5. Pyrite precipitation filled in the interstices between chalcopyrite grains, with pyrite euhedra also distributed around the vent as scattered "smoker fall-out". It is thought that the above pyrite and chalcopyrite precipitation, i.e. events 3, 4 and 5, may have formed within the upper crust or lower mound due to the large, 3 mm chalcopyrite grain size and the lack of any quench textures.

6. The effect of these higher temperature fluids on the mound-middle (lower temperature) mineralogy, was to subject sphalerite to re-solution, as shown by "Caries" texture. Therefore, irregular, corroded sphalerite grains, which formed originally at lower temperatures (possible as wurtzite), were enveloped by higher temperature pyrite grains, with the net loss of Zn from the mounds. This 'flushing out' of Zn produced regional enrichment of this element in sediments throughout the GRAFZI area, due to extensive dispersion

TABLE 3.3.1 Range and average element concentrations in chalcopyrite, pyrite, sphalerite, marcasite and Dive 1001 Fe-Mn Oxides

| | CHALCOPYRITE(n=10) | | PYRITE(n=12) | | | | SPHALERITE(n=3) | | MARCASITE(n=5) | | MIXED GRAINS(n=3) | | | | FE OXIDE(n=4) | | MN OXIDE(n=4) | |
|---|---|---|---|---|---|---|---|---|---|---|---|---|---|---|---|---|---|---|
| | | | Colloform(n=4) | | Euhedral(n=8) | | | | | | a. | b. | c. | | | | | |
| t% | Range | Average | Range | Average | Range | Average | Range | Average | Range | Average | | | | Wt% | Range | Average | Range | Average |
| Ag | 0.00- 0.32 | 0.32 | NR | NR | NR | NR | NR | NR | NR | NR | ND | ND | ND | $Na_2O$ | 4.27- 9.95 | 7.73 | 2.95- 5.53 | 4.25 |
| Al | 0.00- 0.28 | ND | NR | NR | NR | NR | NR | NR | NR | NR | 0.26 | ND | 0.36 | MgO | 0.50- 1.06 | 0.72 | 1.05- 1.89 | 1.58 |
| Fe | 0.00- 0.15 | 0.09 | 0.11- 2.13 | 0.63 | 0.05- 0.17 | 0.10 | 0.05- 0.12 | 0.09 | 0.00- 0.30 | 0.18 | 0.18 | ND | 14.9 | $Al_2O_3$ | ND | ND | 0.00- 0.19 | 0.07 |
| S | 33.3 -35.7 | 34.6 | 49.6 -55.3 | 53.0 | 51.9 -53.8 | 52.9 | 32.7 -33.2 | 33.0 | 52.8 -54.1 | 53.3 | 48.9 | 49.1 | 26.9 | $SiO_2$ | 16.1 -19.5 | 17.6 | 0.18- 2.48 | ND |
| Sb | 0.00- 0.10 | ND | NR | NR | NR | NR | NR | NR | NR | NR | 0.06 | ND | ND | $K_2O$ | 0.32- 0.43 | 0.38 | 1.03- 1.15 | 1.08 |
| Fe | 29.5 -31.1 | 30.3 | 43.4 -47.5 | 45.8 | 44.4 -45.7 | 45.2 | 3.89- 4.72 | 4.33 | 45.1 -47.3 | 46.1 | 36.1 | 35.7 | 22.2 | CaO | 0.91- 1.25 | 1.05 | 1.20- 2.38 | 1.80 |
| Co | ND | ND | 0.00- 0.12 | ND | 0.00- 0.11 | ND | 0.00- 0.20 | ND | ND | ND | NR | ND | ND | $TiO_2$ | ND | ND | 0.00- 0.10 | ND |
| Ni | 0.00- 0.16 | ND | ND | ND | 0.00- 0.12 | ND | ND | ND | ND | ND | ND | ND | ND | $MnO_2$ | 0.00- 0.30 | 0.14 | 61.2 -72.5 | 66.7 |
| Cu | 32.9 -36.6 | 35.3 | 0.00- 0.27 | 0.17 | 0.00- 0.65 | 0.21 | 0.18- 0.32 | 0.23 | 0.00- 0.84 | 0.39 | 0.28 | 0.18 | ND | $Fe_2O_3$ | 41.5 -52.2 | 45.7 | 0.47- 7.43 | 2.68 |
| Zn | 0.00- 0.24 | ND | 0.00- 0.30 | ND | 0.00- 0.38 | ND | 62.9 -64.1 | 63.5 | 0.00- 0.29 | ND | 14.1 | 15.0 | 0.38 | P | 0.45- 0.97 | 0.71 | 0.00- 0.15 | ND |
| As | 0.12- 0.79 | 0.57 | ND | ND | 0.10- 0.15 | 0.13 | ND | ND | 0.00- 0.11 | ND | NR | NR | NR | S | 0.15- 0.28 | 0.21 | 0.22- 0.24 | 0.23 |
| Se | 0.00- 0.19 | 0.11 | 0.00- 0.28 | 0.10 | ND | ND | ND | ND | 0.00- 0.14 | ND | NR | NR | NR | Cu | 0.00- 0.27 | 0.15 | 0.00- 0.20 | ND |
| Ag | 0.00- 0.15 | ND | ND | ND | 0.00- 0.15 | ND | 0.00- 0.29 | 0.12 | ND | ND | ND | ND | ND | Zn | 0.00- 0.34 | 0.14 | 0.50- 3.00 | 1.57 |
| Cd | ND | ND | ND | ND | 0.00- 0.23 | ND | 0.00- 0.15 | ND | ND | ND | NR | NR | NR | As | ND | ND | ND | ND |
| Ba | ND | ND | NR | NR | NR | NR | NR | NR | NR | NR | 0.15 | ND | ND | Se | ND | ND | ND | ND |
| Pb | 0.00- 0.35 | ND | ND | ND | ND | ND | ND | ND | ND | ND | ND | ND | ND | | | | | |
| Total | 97.1-103.5 | 101.1 | *95.7-103.3 | 100.0 | 97.1 -99.8 | 98.7 | 101.1-102.1 | 101.7 | 98.3-101.7 | 100.4 | 100.0 | 100.1 | *64.9 | | *69.8 -79.6 | 74.5 | *73.5 -85.5 | 81.0 |

* Low totals probably due to oxygen (not analysed) contained in amorphous $SiO_2$ phase, or in hydrated oxides of Fe and Mn

a. = Pyrite + Sphalerite

b. = Pyrite + Sphalerite

c. = Pyrite + Silica

ND = Not Detected

NR = Not Determined

7. Upon the waning of hydrothermal activity, or in the outer envelope of the hydrothermal plume, a colloidal gel of pyrite and silica formed. This is manifested by colloform banding and the alternating rhythmic precipitation of pyrite and silica which seems to indicate the closeness of these two minerals in the paragenetic sequence.

8. The lithification of the mound and the filling in of pore spaces, which were produced by organisms and hydrothermal conduits, occurred during diagenesis, after extinction of hydrothermal activity. A surficial limonitic, iron oxide gossan was formed rapidly along with alteration products of the primary sulphides, such as covellite, chalcanthite, marcasite and goethite.

## 3.3 ELECTRON MICROPROBE INVESTIGATIONS

### 3.3.1 Introduction

The electron microprobe (see Appendix B) was used to examine the fine-scale chemistry of the GRAFZI sulphides and also to examine the ferro-manganese oxide with high Zn and Cu contents from Dive 1001 (see Chapter 2).

### 3.3.2 Chemistry of the Sulphides

The range and average element concentrations in the sulphide phases is reported in Table 3.3.1. Values reported exceed $2\sigma$ (see Counting Statistics, Appendix B) for each element analysed and $2\sigma$ was chosen as the detection limit.

*Chalcopyrite.*

Ten spot analyses of large chalcopyrite grains from the mound top reveal that this mineral is very poor in Al, Si, Ca, Co, Ni, Zn, Ag, Cd, Ba and Pb. Bulk analyses of chalcopyrite grains (see Chapter 2) indicate a maximum Ag concentration of 55 ppm, while the electron microprobe indicates a maximum value of 0.15% for one grain, shown in Table 3.3.1. The positive correlation of Cu and Ag, described in Section 2.5, which is at variance with the E.P.R., 21°N microprobe data of Hékinian et al., (1980) is thought merely to reflect the abundances of Ag-bearing chalcopyrite in the GRAFZI deposits, while at 21°N, the Ag is linked with a

different mineral phase. The maximum microprobe value for Zn is 0.24% and Zn may be present in limited solid solution with Cu or as extremely fine inclusions or exsolutions of sphalerite in chalcopyrite (Uytenbogaardt and Burke, 1971; Ramdohr, 1980), although none were seen microscopically (see Section 3.2).

The chalcopyrite contains an average of 35.3% Cu, 30.3% Fe and 34.6% S, totalling 100.2%, and is therefore a relatively pure mineral with the formula $Cu_{1.02}Fe_{1.00}S_{1.98}$. This is close to the stoichiometric formula of $CuFeS_2$, with 34.6% Cu, 30.4% Fe and 35.0% S. The slight depletion in S for the chalcopyrite analysed may be due to replacement of S by As and Se which average 0.57% and 0.11%,respectively.

Comparison of GRAFZI chalcopyrite with the E.P.R. 21°N chalcopyrite (Hékinian et al., 1980) shows that the two are very similar in composition, with regard to Cu, Fe, S and the low concentrations of Zn, Ni and Ag. However, a chalcopyrite from 21°N described in Oudin (1983) showed a higher Zn concentration, present in solid solution with Cu.

*Colloform and Euhedral Pyrite.*

The chemistry of colloform and euhedral pyrite is broadly similar, with the following differences. Colloform pyrite is more enriched in Si and, to a much lesser extent, in Fe. This is undoubtedly linked to the paragenetic sequence, where colloform banding of pyrite and silica shows the close association of these two phases. Euhedral pyrite is slightly richer than colloform pyrite in Ni, Cu, Zn, As, Ag and Cd. This also seems to be due to the paragenetic sequence, where the earlier formed (higher temperature) euhedral pyrite has taken into its structure trace metals not available, or available in lesser amounts, when colloform pyrite formed, at a later stage (lower temperature).

The S/Se ratio can also be used as a geochemical tool in ore genesis studies (Fleischer, 1955; Stanton, 1972) where a ratio of less than

22,000 for pyrite indicates a hydrothermal exhalative origin, while a ratio of around 100,000 indicates sedimentary pyrite. Although Se was below the detection limit of around 0.07% for euhedral pyrite, the S/Se ratio in colloform pyrite is about 530 which lends further support to the hydrothermal origin of deposition.

*Sphalerite.*

Sphalerite euhedra within pyrite (see Section 3.2) contain, on average, 63.5% Zn, 33.0% S and 4.3% Fe, with minor amounts of Si, Co, Cu, Ag and Cd. Some of the Fe and all of the Cu may be contained in minute inclusions of chalcopyrite within the sphalerite. Ag values average 1200 ppm and of all the sulphides analysed, sphalerite appears to contain the highest Ag values. Platy Ag-bearing minerals occur in sphalerite from the E.P.R., 21°N sulphide deposit (Hékinian et al., 1980). Cd often substitutes for Zn (Ramdohr, 1980) and this would account for the Cd found in sphalerite (up to 0.15%).

*Marcasite.*

On average, marcasite consists of 46.1% Fe and 53.3% S, with minor Si, Cu, Zn, As and Se. The composition of marcasite is similar to both colloform and euhedral pyrite, although there is more Si in colloform pyrite. Marcasite may have replaced original pyrrhotite or pyrite, as has been shown by Uytenbogaardt and Burke (1971).

*Mixed Grains.*

Three grains were analysed using 'scan' analysis rather than 'spot' analysis and the results are shown in Table 3.3.1. The grains consisted of mixed amounts of sphalerite, pyrite and silica. Therefore, the analyses do not represent any one mineral.

### 3.3.3 Chemistry of Dive 1001 Fe and Mn Oxides

The aim of analysing Fe and Mn oxides from Dive 1001 is to determine the origin of the Fe oxides; whether originally a sulphide which was gossanised, or a primary hydrothermal Fe oxide; and to examine the high trace metal (Zn and Cu) content of the oxides.

The Fe oxide shown in Table 3.3.1 contains 45.7% $Fe_2O_3$ and relatively high abundances of Cu (1500 ppm) and Zn (1400 ppm) as was also reported for the bulk analyses, in Section 2.2. The range of $SiO_2$ in the Fe oxides, is from 16.1% to 19.6%, averaging 17.6%. This level of $SiO_2$ is similar to the levels found for samples from the hydrothermal ferromanganese oxide facies (see Table 2.2.1) which are primary Fe oxides and not degraded sulphides. The levels of $SiO_2$ found associated with sulphide samples is generally higher but varies considerably and reaches up to 86.6% (see Table 2.1.1).

The Dive 1001 Fe oxide values for Ca and Al are also similar to the values of the hydrothermal Fe oxides, while the sulphides show lower Ca and higher Al. Some Mn (up to 0.3% $MnO_2$) is contained in Dive 1001 Fe oxides. Mn would not be expected to be found in an Fe oxide formed from an original sulphide (Hékinian et al., 1980), due to the low abundances of Mn in these sulphides which is due to the dispersion of $Mn^{2+}$ in seawater, to more distal parts of the hydrothermal system.

Using the microscope on the electron microprobe, it was possible to examine the structure of these Fe oxides and no sulphide minerals or secondary alteration products were observed. Similarly, low abundances of S (see Table 3.3.1) give further evidence that this Fe oxide, despite the high Zn and Cu contents, is not a gossan. Furthermore, the Mn oxide which caps the Fe oxide is not likely to precipitate on a reducing sulphide substrate due to the high redox potential needed to oxidise $Mn^{2+}$ to $Mn^{4+}$ (Krauskopf, 1957). This Mn oxide contains 66.7% $MnO_2$ and up to 0.2% and 3.0% of Cu and Zn respectively. The association of Zn with the Mn oxide phase, upon dispersion from a hydrothermal vent, has already been mentioned (see Section 2.6).

In summary, the following lines of evidence confirm that Dive 1001 Fe oxides are primary hydrothermal precipitates and not degraded sulphides (gossan).

(i) $SiO_2$, Ca, Al and Mn concentrations are analagous to those found for the hydrothermal Fe oxide facies and different to those found for hydrothermal sulphides.

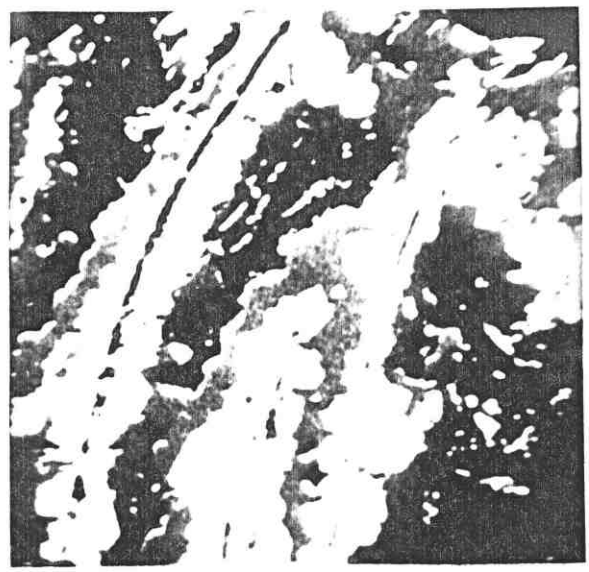


PLATE 3.3.1. Backscattered electron map of colloform pyrite (light areas) surrounded by amorphous silica (grey areas).
Magnification = x200 Field of view = 400μ

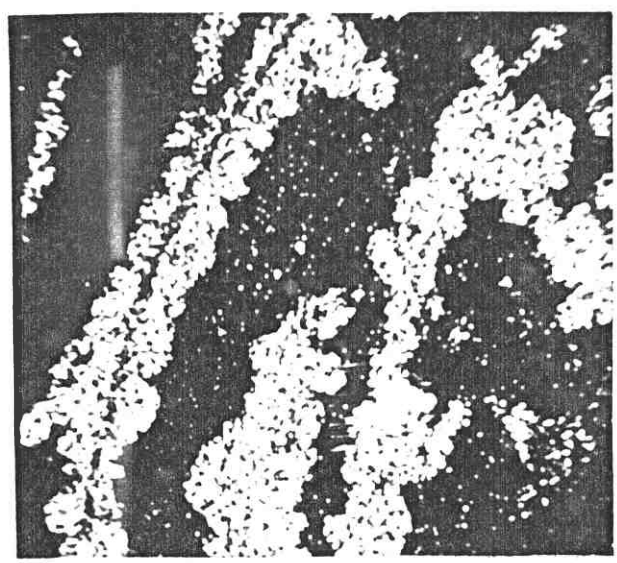


PLATE 3.3.2. X-ray image of sulphur.
Magnification = x200 Field of view = 400μ



PLATE 3.3.3. X-ray image of silicon.
Magnification = x200 Field of view = 400μ

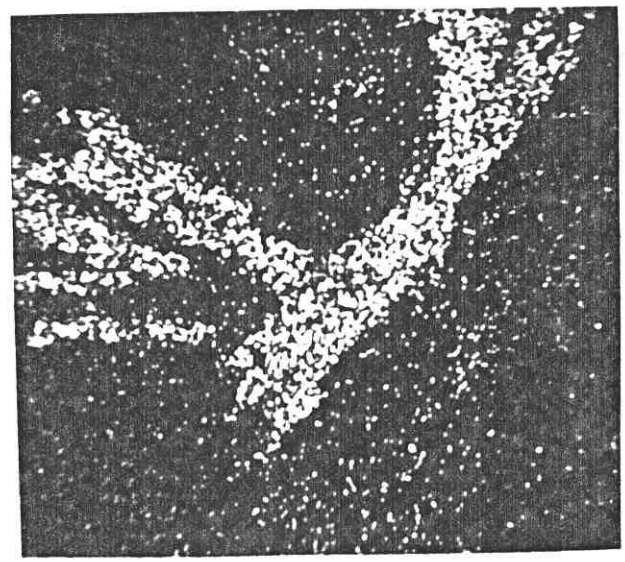


PLATE 3.3.4. X-ray image of barium, present in baryte.
Magnification = x150 Field of view = 530μ

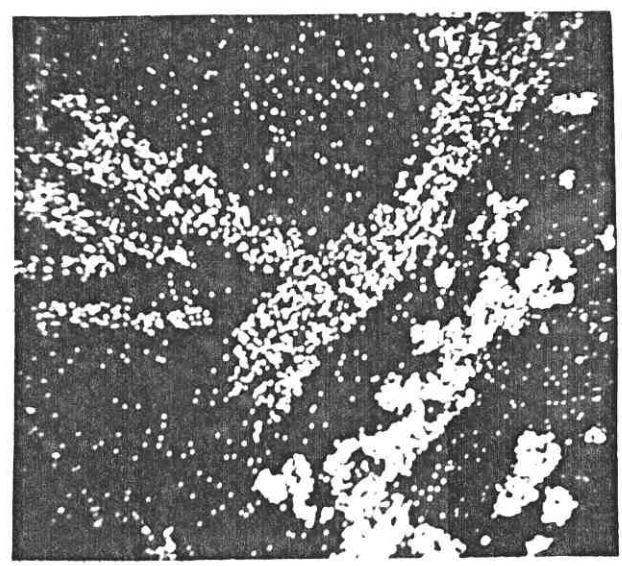


PLATE 3.3.5. X-ray image of sulphur. Imaging of sulphur is strong for sulphide and less strong for sulphate.
Magnification = x150 Field of view 530μ

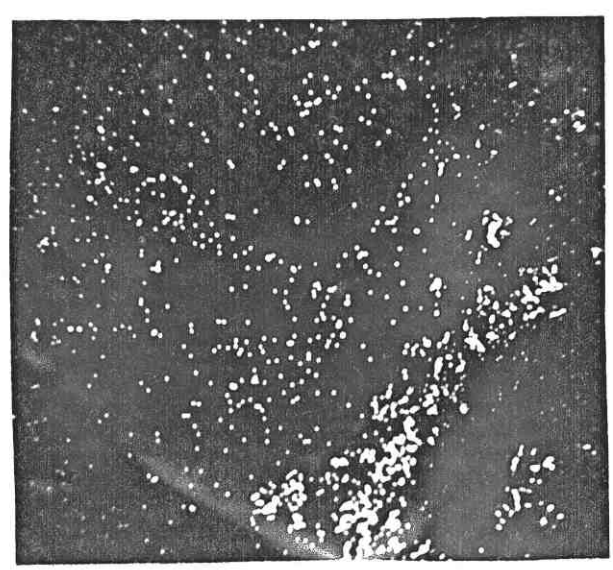


PLATE 3.3.6. X-ray image of iron, present in pyrite (lower right of frame).
Magnification = x150 Field of view = 530μ

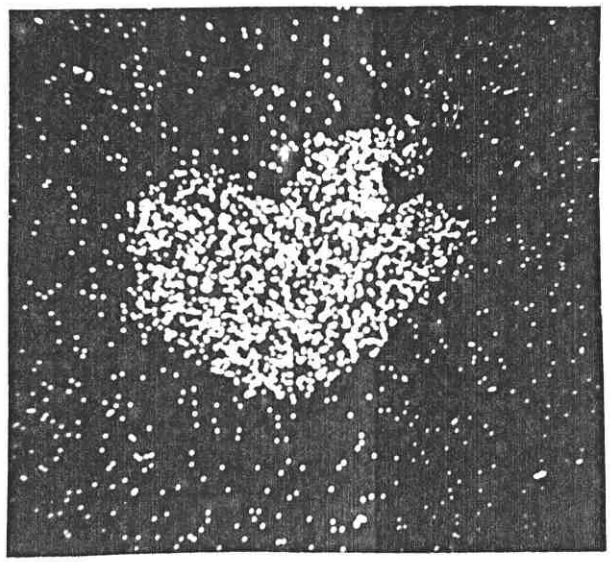
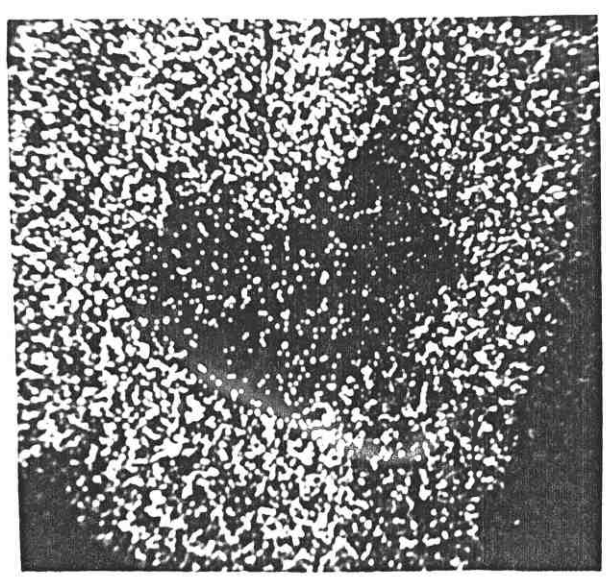


PLATE 3.3.7. X-ray image of zinc, present in a grain of sphalerite enclosed by pyrite.
Magnification = x1200 Field of view = 67$\mu$

PLATE 3.3.8. X-ray image of iron, present in pyrite.
Magnification = x1200 Field of view = 67$\mu$



(ii) Mn could not precipitate on a reducing substrate, such as sulphide material, due to the low redox potential of this environment.

(iii) No relict sulphide textures or secondary minerals are contained in Dive 1001 Fe oxides.

The inference from the above evidence is that primary Fe and Mn oxides of a hydrothermal origin may contain high concentrations of Cu and especially Zn, if the rate of supply of these elements is substantial. Zn is known to be flushed out of the hydrothermal mounds during the latter stages of their growth (see Section 3.2).

3.3.4 X-Ray Imaging

To examine the distribution of elements between the different mineral phases, the technique of X-ray imaging was used (see Appendix B). The backscattered electron map shown in Plate 3.3.1 clearly delineates areas of pyrite and amorphous silica, due to the different amounts of backscattering related to element atomic numbers (see Appendix B), within an area of colloform banding. The X-ray imaging of S (Plate 3.3.2) and of Si (Plate 3.3.3) highlights the two different mineral phases and also shows that the organic filament which forms the nucleus of pyrite precipitation is not of a siliceous nature. The original material forming this filament may have been replaced and is now represented by a void space or it may consist of an element which was not investigated by X-ray imaging.

Plates 3.3.4 to 3.3.6 show a fibrous Ba-rich mineral, identified as baryte ($BaSO_4$) on the basis of the lower amounts of S associated with the sulphate phase (where S is diluted with O) than with the sulphide phase, as shown in Plate 3.3.5, where S imaging is less dense in the baryte. The sulphide mineral is rich in Fe (see Plate 3.3.6) and this, coupled with the crystal habit, confirms the presence of pyrite.

It has already been noted that small sub-rounded sphalerite grains (see Section 3.2) can be found enclosed by pyrite. Direct evidence of this is shown in Plates 3.3.7 and 3.3.8, where a 30$\mu$ sub-rounded sphalerite grain is enclosed within pyrite.

FIG. 3.4.1. % Peak Height Ratio versus % Chalcopyrite for the 8 samples subjected to Calibrated X.R.D.

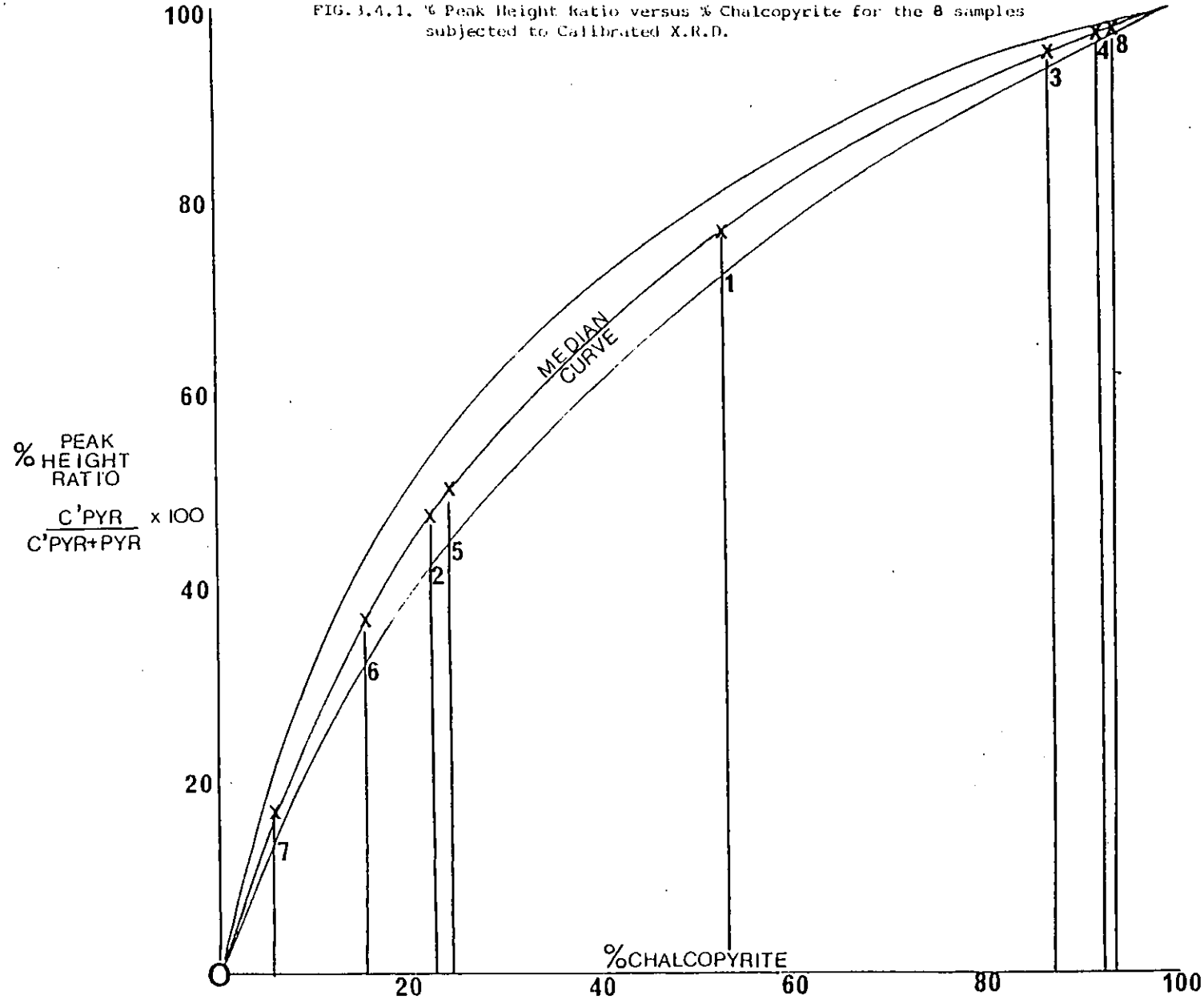


TABLE 3.4.1.

(a) Chemical Analyses for the calibration standards

| | % Fe | Mn | Al | Co | Ni | Cu | Zn | Pb |
|---|---|---|---|---|---|---|---|---|
| Pyrite (Peru) | 48.6 | 61 | 210 | 49 | ND | 39 | 29 | 20 |
| Chalcopyrite (Zambia) | 23.2 | 35 | 30 | 81 | ND | 32.4 % | 810 | ND |

(ppm. unless stated)(ND=Not Determined).

(b) Quantitative chalcopyrite mineralogy of the 2 component (pyrite+, chalcopyrite) mixtures.

| Sample Identification | P.H.R. x 100(%) | % Chalcopyrite | Maximum % Error* |
|---|---|---|---|
| 1. Mound Top Oxidised Surface | 76.6 | 53.0 ± 5.5 | ± 10.4 |
| 2. Mound Middle Bulk | 47.2 | 22.6 ± 4.0 | ± 17.7 |
| 3. Mound Top Bulk | 95.2 | 87.0 ± 3.0 | ± 3.4 |
| 4. Mound Top Needles. | 97.3 | 92.2 ± 2.0 | ± 2.2 |
| 5. Station 9 Sulphide. | 50.3 | 24.5 ± 4.5 | ± 18.4 |
| 6. Mound Middle Oxidised Surface | 36.3 | 15.8 ± 3.0 | ± 19.0 |
| 7. Mid Mound Bulk | 16.9 | 6.0 ± 1.0 | ± 16.7 |
| 8. Mound Top Needles | 97.9 | 94.6 ± 1.5 | ± 1.6 |

* Determined from the medium curve (see Figure 3.4.1)

+ Pyrite mineralogy = (100 % - Chalcopyrite)

3.4(a) QUANTITATIVE SULPHIDE MINERALOGY

Quantitative sulphide mineralogy was carried out by the use of calibrated X-ray diffraction. This procedure was necessary to determine the purity of the sulphide samples taken for isotopic analysis and to find the amount of pyrite and chalcopyrite present in the mixture, which is needed to calculate the yield of $SO_2$ evolved from the samples (see Section 3.4(b)). Pyrite and chalcopyrite are intimately associated in the paragenesis and for this reason it was not possible to isolate the two pure minerals by direct sampling methods. Rather, a series of 8 samples representing a range from pyrite-rich to chalcopyrite samples were checked for their pyrite/chalcopyrite content (Figure 3.4.1).

Figure 3.4.1 shows the calibration envelope obtained by repeated X-ray diffraction analysis of different mixtures of two calibration standards; one pure chalcopyrite (from Mufulira, Zambia) and one pure pyrite (from Peru). The chemical analyses for these standards are reported in Table 3.4.1(a). These high purity pyrite and chalcopyrite samples were mixed in the following proportions:-

Calibration Standard Mixtures

| | | | | | |
|---|---|---|---|---|---|
| 1) | 5% | Pyrite | + | 95% | Chalcopyrite |
| 2) | 10% | " | + | 90% | " |
| 3) | 20% | " | + | 80% | " |
| 4) | 40% | " | + | 60% | " |
| 5) | 60% | " | + | 40% | " |
| 6) | 80% | " | + | 20% | " |

The calibration envelope in Figure 3.4.1 represents the spread of results from the above mixtures, which were run at least three times each.

The Peak Height Ratio

The Peak Height Ratio (P.H.R) of chalcopyrite/(chalcopyrite + pyrite) x 100%, was determined on the 3.03Å chalcopyrite and 2.70Å pyrite peaks. This is convenient as they occur close together and require short periods of time when scanning with Co K$\alpha$ radiation (see Appendix B), at $1^{\circ}$ ($2\theta$) per minute. Peaks which are separated by high values of $2\theta$, are not useful for accurate calibrated X.R.D., as a reduction in peak

intensity occurs at high 2θ's.

Limits of Accuracy and Quality Control

Eight sulphide-rich samples of chalcopyrite and pyrite were selected for quantitative mineralogical (and sulphur isotope) studies and on sampling it was hoped to separate them into dominantly mono-minerallic mixtures. The results of replicate X.R.D. analyses for these 8 samples are shown in Figure 3.4.1 and Table 3.4.1(b).

The concentration of one mineral in the sample (expressed by the P.H.R.) influences the accuracy of the reading from the calibration envelope. This is an inherent limitation of this technique and will be discussed later. The worst accuracies occur from 40 - 80% P.H.R. (the widest part of the envelope) and fortuitously the samples of most interest, the ones richest in pyrite or chalcopyrite, lie outside this area, where accuracy is better. For example, a sample with P.H.R. of 50% would have approximately 25% chalcopyrite, taken from the median curve of the envelope, but with an uncertainty of $\pm$ 4.5%. In % error terms, this represents $\pm$ 18% error in the chalcopyrite value which is high. This figure represents a maximum possible error and these are reported for the eight samples in Table 3.4.1(b) at the appropriate % chalcopyrite concentrations.

Examination of Table 3.4.1(b) reveals that low percentages of chalcopyrite give large errors while high % chalcopyrite values, which are of prime importance in the isotope study (see Section 3.4(b)), give low % errors.

The inherent limitation of the above calibration envelope with regard to accuracy has been dealt with but it is also important to appreciate the precision or reproducibility of any one value, both as a function of (1) machine variation and (2) as a function of the limitations of smear slide preparation. This was examined by; (1) running the same sample three times and (2) repeatedly running different smears of the same sample. Results indicated that:

1. Machine variation over three runs of the same sample gave a precision of approximately $\pm$ 0.5% for any one value.
2. Four different smears of the same samples gave P.H.R. values of 78.9, 78.8, 73.2 and 75.2% with a mean of 76.6% and a precision of $\pm$ 4.4%.

From quantitative calibrated X.R.D., a total precision of approximately $\pm$ 5% was found, indicating that the greatest source of error was the calibration envelope for the two component, pyrite-chalcopyrite mixtures.

Inherent Limitations of the Technique

1. Smear slide preparation by evaporation of ethanol may allow different orientations and inhomogeneities to occur. Cavity mounts would be more suitable in eliminating these deficiences, as noted by Tatlock (1966), but this was not possible to implement for this study, due to lack of material. Replicate sample analysis was carried out to attain reproducible results.

2. Generally, the samples themselves gave more reproducible results than the calibration standard mixtures and this may be due to different grain sizes obtained in grinding the pure pyrite and pure chalcopyrite standards. Amorphous sulphide dust coats the grains if grinding is too fine, reducing peak heights, whilst orientation effects occur if the grain size is too coarse (Tatlock, 1966).

Comparison of Mineralogy Deduced from Chemistry and X.R.D.

From the above it is apparent that the determination of the sulphide mineralogy has an approximate error of $\pm$ 10% for the eight samples, although it is better for those at high chalcopyrite or pyrite concentration, which are the most important with regard to isotope work. To obtain the most reasonable results for the sulphide mineralogy, the quantitative calibrated X.R.D. mineralogy was compared with that deduced from the chemistry. The assumptions that were made for calculating the mineralogy from the chemistry, are as follows:

TABLE 3.4.2.

COMPARISON OF QUANTITATIVE SULPHIDE MINERALOGY FROM CALIBRATED X.R.D. AND CHEMISTRY

| Sample Identification | *BULK CHEMISTRY | | | CHEMICAL | | +(%) SUM OF | °CALIBRATED X.R.D. | | (%) SUM OF |
|---|---|---|---|---|---|---|---|---|---|
| | % Cu | % Fe | % $SiO_2$ | % $CuFeS_2$ | % $FeS_2$ | 3 COMPONENTS | % $CuFeS_2$ | % $FeS_2$ | 3 COMPONENTS |
| 1. Mound Top Oxidised Surface | 13.7 | 25.4 | 23.6 | 39.3 | 28.8 | 92 | 40.5 | 35.9 | 100 |
| 2. Mound Middle Bulk | 7.98 | 31.2 | 13.4 | 23.0 | 51.9 | 88 | 19.6 | 67.0 | 100 |
| 3. Mound Top Bulk | 17.2 | 18.7 | 35.3 | 49.5 | 8.0 | 93 | 56.3 | 8.4 | 100 |
| 4. Mound Top Needles | 26.7 | 27.7 | 8.70 | 76.8 | 9.2 | 95 | 84.2 | 7.1 | 100 |
| 5. Station 9 Sulphide | 6.12 | 23.5 | 34.5 | 17.6 | 38.7 | 91 | 16.1 | 49.5 | 100 |
| 6. Mound Middle Oxidised Surface | 3.64 | 19.1 | 47.8 | 10.5 | 34.3 | 93 | 8.3 | 44.0 | 100 |
| 7. Mid Mound Bulk | 1.39 | 34.8 | 11.0 | 4.0 | 72.0 | 87 | 5.3 | 83.7 | 100 |
| 8. Mound Top Needles | 26.0 | 25.8 | 6.70 | 74.8 | 6.4 | 88 | 88.3 | 5.0 | 100 |

* See Section 2.1

+ 3 components of the samples are Cu Fe $S_2$, $FeS_2$ and $SiO_2$

° These values have been recalculated from Table 3.4.1. to include the third component of the samples, amorphous silica.

TABLE 3.4.3.

QUANTITATIVE SULPHIDE MINERALOGY AND THE THEORETICAL YIELD OF $SO_2$

At S.T.P. (Standard Temperature and Pressure);

10 mg of chalcopyrite produces 3.478 mg S or 6.956 mg $SO_2$.

BUT, 1 mole of $SO_2$ (64g) occupies 22,400 $cms^3$.

$\therefore$ 10 mg of chalcopyrite produces 2.435 $cms^3$ of $SO_2$

SIMILARLY, 10 mg of pyrite produces 3.733 $cms^3$ of $SO_2$

By combining the pyrite and chalcopyrite contributions of $SO_2$ at the calculated percentages of these two minerals, for a given weight of sample the theoretical yield may be calculated, and is shown below for the 8 samples:-

| Sample Identification | Sulphide Mineralogy % $CuFeS_2$ | % $FeS_2$ | Weight of Sample (mg) | Yield of $SO_2$ ($Cms^3$) |
|---|---|---|---|---|
| 1. Mound Top Oxidised Surface | 39 | 32 | 15 | 3.216 |
| 2. Mound Middle Bulk | 20 | 59 | 12 | 3.227 |
| 3. Mound Top Bulk | 50 | 8 | 20 | 3.034 |
| 4. Mound Top Needles | 77 | 7 | 15 | 3.204 |
| 5. Station 9 Sulphide | 16 | 44 | 15 | 3.048 |
| 6. Mound Middle Oxidised Surface | 8 | 39 | 18 | 2.972 |
| 7. Mid Mound Bulk (I.G.S.) | 4 | 78 | 10 | 3.009 |
| 8. Mound Top Needles (I.G.S.) | 75 | 5 | 15 | 3.019 |

1. The samples generally consist of three components, chalcopyrite, pyrite and silica. Secondary minerals and sphalerite were disregarded due to their low abundance.
2. The values of Cu determined from bulk analysis (Section 2.1) are totally held within the chalcopyrite phase and the remaining Fe from bulk analysis, after subtraction from that within chalcopyrite, is in the pyrite phase.

Table 3.4.2 reports the maximum % of chalcopyrite and pyrite possible, deduced from the chemistry, and compares those values with the calibrated X.R.D. results which have been re-calculated from Table 3.4.1 to include the third component of the samples, amorphous silica.

Chalcopyrite values from chemical and calibrated X.R.D. techniques show close agreement, confirming that virtually all of the Cu is contained in the chalcopyrite phase and only traces in such minerals as covellite. However, the pyrite abundances based on mineralogy are somewhat higher than those found from the chemistry and this is due to the fact that X.R.D. determinations of chalcopyrite and pyrite were for a 2 component system, totalling 100%. These values were then recalculated to include the amount of $SiO_2$, and this 3 component system also totalled 100%. Chemical results however, as shown in Table 3.4.2, for chalcopyrite, pyrite and silica, generally totalled around 90%, indicating the presence of trace amounts of other phases and/or analytical error. Trace amounts of goethite, covellite and chalcanthite have been found (see Section 2.1) and these probably contribute in small amounts to the remaining 10% of sample not accounted for. For this reason, the calibrated X.R.D. results may be slightly too high when compared to the chemical results.

The mineralogical values used for the isotope study are shown in Table 3.4.2 and expanded in Table 3.4.3 to show the amount of $SO_2$ evolved from such a sulphide mixture, which was then used to calculate the yield. The % chalcopyrite and % pyrite values represent averages of the two techniques, mineralogical and chemical, or if one value was considered too high, the lower value was taken which was thought to reflect more nearly, the true composition of the sample.

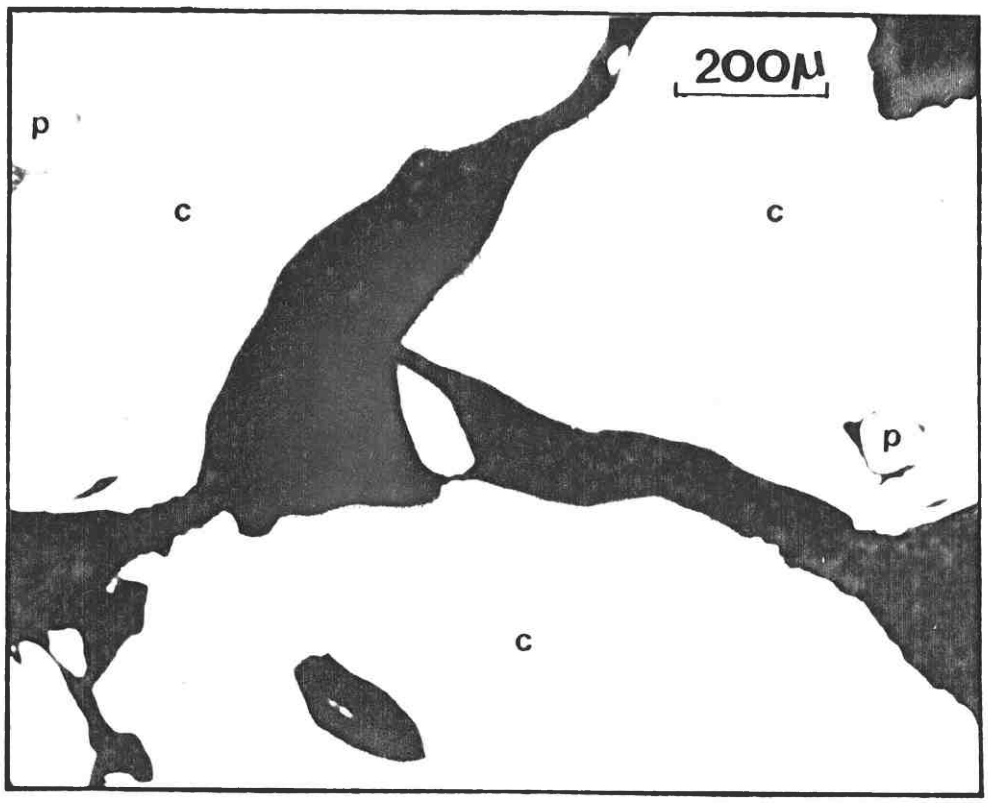
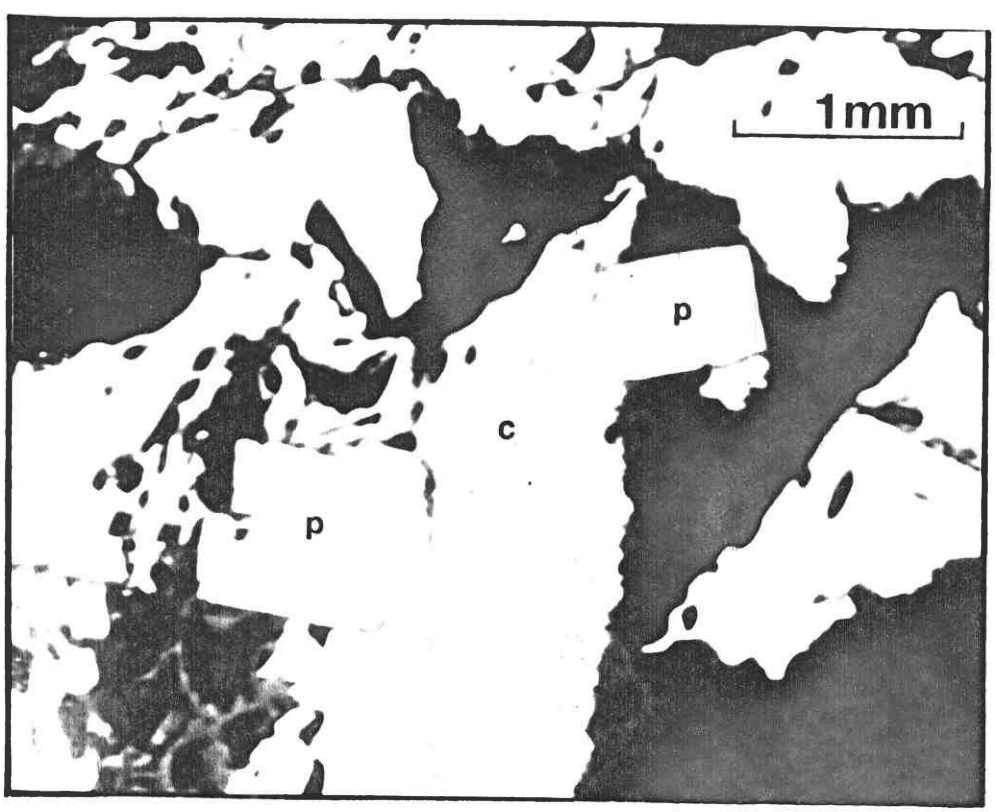



PLATE 3.4.1. Small pyrite euhedra (p) enclosed within large chalcopyrite grains (c).

PLATE 3.4.2. Intimate association of pyrite euhedra (p) and anhedral chalcopyrite (c).



Great emphasis has been placed on the quality control and the errors contained in the above determinations. This is necessary in order to interpret low or high yields of $SO_2$ for isotopic analysis and ultimately to interpret isotopic results.

3.4(b) STABLE ISOTOPES: $^{34}S/^{32}S$ and $^{18}O/^{16}O$

Reflected light microscopy (see Section 3.2) was used to select samples in which the finely intergrown pyrite and chalcopyrite appeared to have precipitated cogenetically. Plates 3.4.1 and 3.4.2 show the close association of pyrite and chalcopyrite which are the first formed minerals in the paragenesis. The 8 samples selected were subjected to quantitative X-Ray diffraction, as detailed above, and then sulphur isotopic analysis.

In addition to the above 8 samples, 2 samples of amorphous silica were isolated for oxygen isotope analysis. Prior to their analysis, the samples were purified by the removal of secondary iron oxides, by a citrate/dithionite buffered leach (see Appendix B) and then heavy mineral separation, to remove intermixed sulphides.

The 8 sulphide samples were analysed for their $^{34}S/^{32}S$ ratios and the 2 samples of amorphous silica for their $^{18}O/^{16}O$ ratios. The techniques used to liberate $SO_2$ and $CO_2$ for sulphur and oxygen isotope determinations by mass spectrometer are detailed in Appendix B, from Robinson and Kusakabe (1975) and Clayton and Mayeda (1963).

The isotopic data presented in this study are expressed as parts per thousand (i.e. per mil or ‰) variation from the relevant international standard, either Canon Diablo Meteorite, Troilite phase (C.D.T.) for sulphur, or Standard Mean Ocean Water (S.M.O.W.) for oxygen.

$$\text{e.g. } \delta^{34}S = \frac{(^{34}S/^{32}S)_{sample} - (^{34}S/^{32}S)_{standard}}{(^{34}S/^{32}S)_{standard}} \times 1000‰$$

## Table 3.4.4 SULPHUR ISOTOPE DATA.

| Nº | Sample | % Chalcopyrite | % Pyrite | Nº of runs * | $\delta^{34}S_{CDT}$ (‰) | Precision (‰) |
|---|---|---|---|---|---|---|
| **MOUND TOP** | | | | | | |
| 1 | Mound Top Ox Surf | 55 | 45 | 2 | +5.42 | ±0.04 |
| 3 | Mound Top Bulk. | 86 | 14 | 3 | +5.97 | ±0.04 |
| 4 | Top Needles. | 92 | 8 | 2 | +5.45 | ±0.05 |
| 8 | Top Needles (IGS) | 94 | 6 | 6 | +5.44 | ±0.04 |
| **MOUND MIDDLE** | | | | | | |
| 2 | Middle Mound Bulk | 25 | 75 | 3 | +5.58 | ±0.04 |
| 5 | Dive 1001 Stn.9 | 27 | 73 | 4 | +5.96 | ±0.05 |
| 6 | Mid Mound Ox Surf | 17 | 83 | 2 | +6.28 | ±0.05 |
| 7 | Mid Mound Bulk (IGS) | 5 | 95 | 6 | +6.34 | ±0.03 |

* Sample continually analysed until precision for 2 or more samples is ±0.05‰ or better.

Aims of Stable Isotope Studies

The aim of this study is to use isotopic evidence, for both sulphur and oxygen, to investigate the evolution and geothermometry of GRAFZI inactive hydrothermal sulphide mounds in the following ways:-

1. To determine the $\delta^{34}S$ composition of the 8 sulphides and to compare them with the only other similar data available, from the E.P.R. at 21°N (e.g. Arnold and Sheppard, 1981; Styrt et al., 1981). The isotopic evidence may clarify the relative amounts of sulphur contributed to the hydrothermal solutions from seawater and basaltic/magmatic sources.

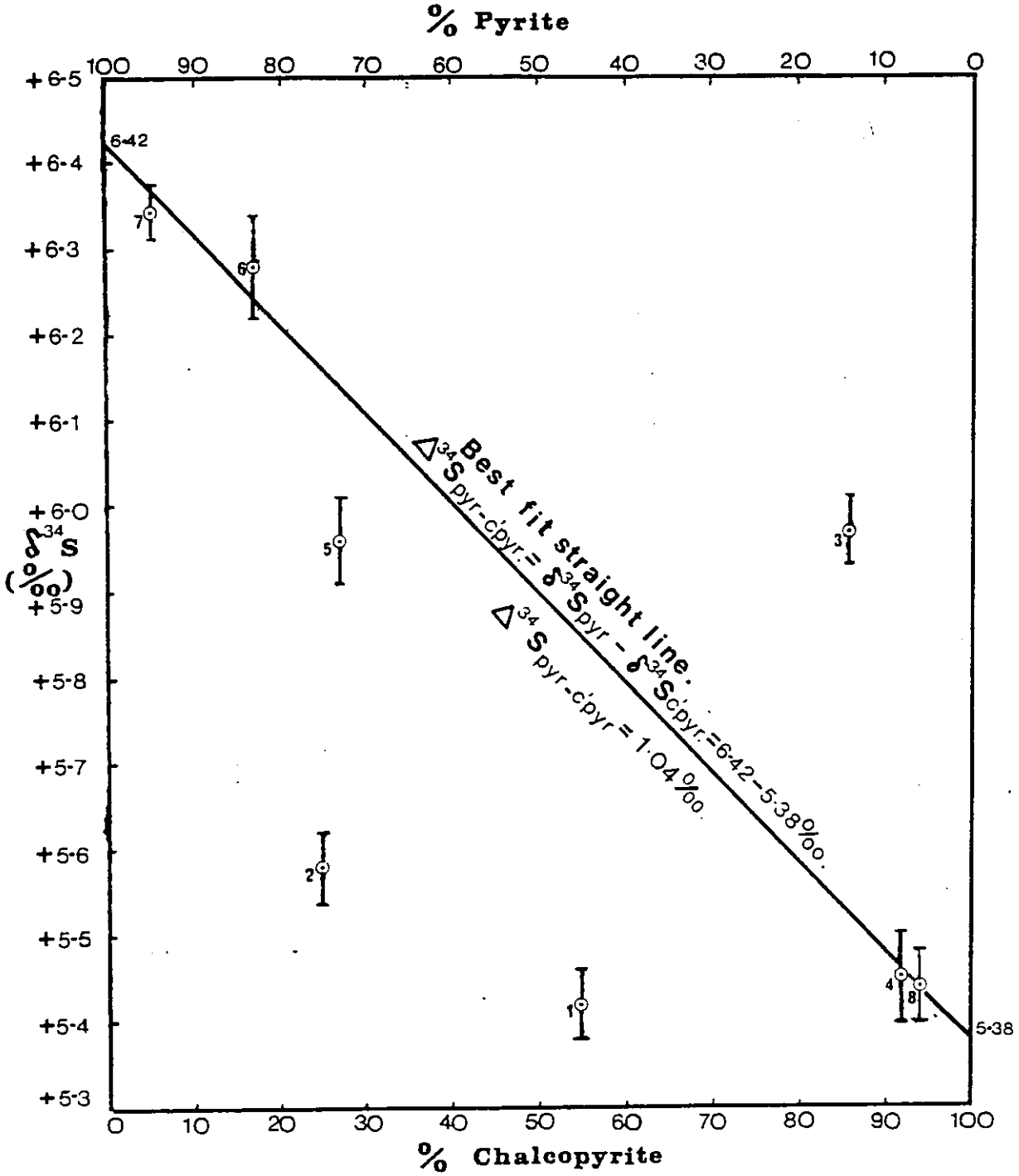
2. To evaluate the $\delta^{34}S$ results in terms of the seawater/basalt ratios which produced the hydrothermal solutions in the study area and hence the permeability of the young oceanic crust.

3. To use a pyrite-chalcopyrite mineral pair, formed in isotopic equilibrium, as a geothermometer to find the temperature of formation of the sulphide assemblage. Oxygen isotope analysis on the two silica-rich samples could add further detail to knowledge of the paragenetic sequence (Figure 3.2.1) by providing the temperature of formation of the amorphous silica which formed later than the sulphide assemblage.

Results

Table 3.4.4 shows the $\delta^{34}S$ data and the location of the samples, with the % of the two sulphur dioxide producing minerals present. Results with a precision worse than $\pm$ 0.05‰ during replicate sample analysis were rejected. Invariably, the values rejected were linked to low yields of $SO_2$ due to loss of gas somewhere along the isotope line. The yields obtained for all samples were never lower than 90% or greater than 110%, with respect to theoretical yields, supporting the calibrated X-ray diffraction mineralogical accuracy of better than $\pm$ 10%. Isotopic results were only accepted when reproducibility was good from 2 or more values.

**FIG. 3.4.2**
**$\delta^{34}S$ vs % Chalcopyrite\Pyrite.**




Samples 1,3,4,8 from chalcopyrite-rich mound top.
Samples 2,5,6,7 from pyrite-rich mound middle.

*Mound Top.*

The mineralogical composition of the samples (expressed as 2 component mixtures of $FeS_2$ and $CuFeS_2$) and the $\delta^{34}S$ values are shown in Figure 3.4.2, with precision indicated by error bars. Generally, the chalcopyrite-rich samples from the mound top cluster around +5.42 to +5.45 $\pm$ 0.05‰ . The two samples of highest chalcopyrite purity (Nos. 4 and 8) give $\delta^{34}S$ of +5.45 and +5.44‰ for 92% and 94% $CuFeS_2$, respectively. The other samples are less rich in chalcopyrite and one sample (No. 3) with 86% $CuFeS_2$/14%$FeS_2$, shows an isotopically heavier value of +5.97 $\pm$ 0.04‰ , which will be discussed later.

*Mound Middle.*

The two samples of highest pyrite content (Nos. 6 and 7) give $\delta^{34}S$ of +6.28 and +6.34 $\pm$ 0.05‰ for 83% and 95% $FeS_2$, respectively. Ore microscope work indicates that these two samples are most likely to consist of pyrite which formed and co-precipitated with chalcopyrite. Values somewhat isotopically lighter at +5.58 and +5.96 $\pm$ 0.05‰, are found for samples with 75% and 73% $FeS_2$, respectively; the reasons for this will be discussed later.

Sulphur Isotope Geothermometry

Figure 3.4.2 shows a large scatter for the 8 samples and it is difficult to extrapolate values back to pure end-member pyrite and chalcopyrite and thus to examine the temperature dependant fractionation factor, $\alpha$ (Rye and Ohmoto, 1974), between these two minerals formed in equilibrium. However, there is a linear relationship for the most monominerallic mixtures (Nos. 4, 6, 7 and 8). The isotopic difference between pure pyrite and chalcopyrite ($\delta^{34}S_{pyr} - \delta^{34}S_{c'pyr}$) would be (+6.42‰) - (+5.38‰) which equals 1.04‰ and can be represented by $\Delta^{34}S_{pyr - c'pyr}$ (Rye and Ohmoto, 1974). $\Delta^{34}S$ is, to an approximation, equal to 1000 $\ln\alpha$, where $\alpha$ is the isotopic fractionation factor for pyrite and chalcopyrite species. $\alpha$ can be calculated without approximation from the following relationship;

Equation (1)

$$\alpha^{pyr}_{c'pyr} = \frac{1000 + \delta^{34}S_{pyr}}{1000 + \delta^{34}S_{c'pyr}} \quad \text{(Rye and Ohmoto, 1974)}$$

$$= \frac{1006.42}{1005.38}$$

Therefore, $1000 \ln \alpha^{pyr}_{c'pyr} = \underline{1.03}$ (cf. $\Delta^{34}S_{pyr - c'pyr} = 1.04‰$)

Using the calibration of Kajiwara and Krouse (1971), $\alpha$ can be used to calculate the temperature of pyrite-chalcopyrite isotopic fractionation;

Equation (2)

$$1000 \ln \alpha^{pyr}_{c'pyr} = 4.5 \ (10^5 \ T^{-2})$$

Therefore, $T^2 = 43.7 \times 10^4$ K

$T = 661$ K or $\underline{\underline{388^oC}}$

By using the values of analytical precision (Table 3.4.4), the range of uncertainty in the temperature of formation of GRAFZI pyrite and chalcopyrite can be calculated using the above calibration and this equals $\pm$ 20°C.

Oxygen Isotope Geothermometry

Analysis of the 2 silica-rich samples produced the following results;

| Sample 9 | Sample 10 |
|---|---|
| $\delta^{18}O = +25.2 \pm 0.8‰$ | $\delta^{18}O = +17.0 \pm 0.4‰$ |

The large errors in the data are probably due to the presence of water in hydrated silica which may be retained to varying extents during analysis. Nevertheless, the two samples are isotopically very different. This implies formation at different temperatures or mixtures containing differing proportions of a high and low temperature stage of amorphous silica. Consequently, neither can be assumed to represent a specific temperature by calculation between it and the assumed water value.

However, it is interesting to note the range of temperatures indicated by calculations. The isotopic composition of the water may vary between that of pure sea-water, to a heavier one, which would represent exchange with hot magmatic material. Craig et al. (1980) measured a value of +1.64‰ for a 21°N vent (E.P.R.), but values of +2‰ have been recorded subsequently. Therefore, for comparison, temperatures for both 0‰ and +2‰ waters, have been calculated. The full range of values is between 60°C and 172°C, taking into account all the variability of isotopic fractionation and calibrations (Bottinga and Javoy, 1973; Matsuhisa et al., 1979).

These temperatures suggest either considerable low temperature diagenetic additions of $SiO_2$ or the result of a much lower temperature phase of emissions than that which produced the sulphides. For comparison, fluid inclusion studies on quartz from a volcanogenic exhalative sulphide deposit indicated a crystallisation temperature of 174°C (Southwood, 1982) which is very similar to the highest temperature of 172°C for GRAFZI amorphous silica.

Discussion

To satisfy the original aims of the stable isotope study; i.e. to compare GRAFZI and E.P.R., 21°N sulphide deposits; it is necessary to state the following facts. The hottest hydrothermal vents on the E.P.R. at 21°N, are actively debouching fluids at 380 ± 30°C (Spiess et al., 1980) and these solutions are depositing Cu-rich sulphides, whilst chimneys with exit temperatures of less than 300°C are depositing Zn-rich sulphides (Styrt et al., 1981). The temperatures indicated for the GRAFZI sulphides are in close agreement (390° ± 20°C) with the E.P.R., 21°N hottest Cu-depositing fluids. However, the overall geochemistry of the sulphide mounds is very different, with Zn enrichment up to 50% at 21°N (Hékinian et al., 1980) and with only up to 1.5% Cu. GRAFZI sulphides, by contrast, comprise up to 27% Cu and only 1.5% Zn.

$\delta^{34}S$ (CYAMEX) values for 21°N sulphides, taken from Février (1981), are as follows:-

| PYRITE | > | SPHALERITE | > | CHALCOPYRITE |
|---|---|---|---|---|
| + 3.45‰ | | +2.80‰ | | +2.10‰ |

Geothermometric calculations on mineral pairs from statistical averages and for global-pooled results, for 21°N sulphides, indicate that the pyrite-chalcopyrite mineral pair formed at 590°C - 400°C and the pyrite-sphalerite mineral pair formed at 400° - 275°C (Février, 1981).

Styrt et al. (1981) published values of $\delta^{34}S$ from +1.3 to +4.1‰, while Arnold and Sheppard (1981) gave a range from +1.4 to +3.0‰ for E.P.R., 21°N sulphides. R.M. Haymon (pers. comm., 1981) showed a slightly lower range of +0.4 to +2.0‰. These authors generally accept that the values are consistent with sulphur derivation from both reduced seawater sulphate and basaltic/magmatic sources, with approximate compositions of + 20‰ and +0.5 to 1.0‰ (Sakai et al., 1978), respectively.

Arnold and Sheppard (1981) concluded that their $\delta^{34}S$ values for E.P.R., 21°N sulphides, indicate a seawater sulphate contribution of 10%, to the total hydrothermal sulphur. Styrt et al. (1981) agreed with this and proposed a 10 - 20% marine sulphate sulphur contribution with the remaining 90 - 80% of sulphur obtained from basaltic leaching. However, Styrt et al. (1981) mentioned that in dynamic convectively circulated seawater systems, sulphur, totally from reduced seawater sulphate, may give $\delta^{34}S$ values as low as +5‰.

GRAFZI sulphide $\delta^{34}S$ values show a range of +5.4 to +6.3‰, which is considerably isotopically heavier than E.P.R., 21°N sulphides, by +2 to +3‰. These GRAFZI values support experimental evidence (Ohmoto et al., 1976) which shows that values greater than +5‰ may occur in sulphides when seawater is interacted with basalt at temperatures above 250°C. The absence of micro-inclusions of anhydrite ($CaSO_4$) in GRAFZI samples rules out the possibility of isotopically heavy sulphides resulting from contaminant sulphate inclusions ($\delta^{34}S$ of + 20‰), as was noted by Arnold and Sheppard at 21°N.

As mentioned, GRAFZI sulphides have a substantially heavier isotopic composition than their E.P.R. analogues. This may well indicate a greater contribution from reduced seawater sulphate, to the total hydrothermal sulphur content. It is not proposed to specify the quantity of sulphur from seawater sulphate added to the hydrothermal sulphide deposits, but it is evidently a major contribution. This evidence indicates that the convective cells of hydrothermal solutions have high seawater /rock ratios (or rapid flow rates) in the oceanic crust, and that the permeability and domination of this system by seawater is apparently greater than at 21°N on the E.P.R.

Stockwork Hydrothermal Solution Transport

In a dynamic system of convectively circulated seawater, in which seawater interacts continuously with igneous rocks at different temperatures and a variety of water/rock ratios, and where $H_2S$ and $SO_4^{2-}$ are lost from solution by precipitation of sulphide and sulphate minerals, the $^{34}S/^{32}S$ ratios in the hydrothermal solutions must constantly be changing. In this case the values in Figure 3.4.2 can be rationally interpreted due to the constantly changing sulphur budget. The values which fall below the best-fit straight line are generally rich in pyrite and are isotopically lighter in $^{34}S$ than co-genetic pyrite/chalcopyrite samples would be. This anomaly can be explained in two ways due to the fact that pyrite in these samples formed at a different time than high temperature chalcopyrite (cf. colloform and late stage pyrite, see Section 3.2). The first mechanism for producing isotopically light pyrite would involve biological and diagenetic activity which could reset and lower $\delta^{34}S$ values. The presence of organic debris was commonplace in both GRAFZI (Malahoff et al., 1983) and E.P.R., 21°N sulphides (Hékinian et al., 1980). The second mechanism which could lower $\delta^{34}S$ pyrite values would involve augmenting the hydrothermal fluids with an increased basaltic sulphur component, of lower $^{34}S$ content than seawater sulphate, as the fluids became progressively depleted in their seawater sulphate content due to precipitation of sulphate and sulphide minerals within the upper crust.

The $\delta^{34}S$ value which lies above the best fit straight line (Sample 3, Figure 3.4.2) is somewhat problematical. This sample, with 86%

chalcopyrite, could represent a precipitate from a hydrothermal solution which became isotopically heavier with time, possibly due to addition of more seawater sulphate. Alternatively, although perhaps less likely, assuming a simple closed reservoir model, where residual hydrothermal solutions became enriched in the heavier $^{34}S$ isotope as $^{32}S$ preferentially left the solutions upon sulphide mineral precipitation, then these fluids could deposit sulphides enriched in $^{34}S$.

Conclusions

1. GRAFZI sulphides consist dominantly of a chalcopyrite/pyrite assemblage and these two minerals were found by geothermometry to have formed from hydrothermal solutions at a temperature of $388^{\circ} \pm 20^{\circ}C$, which is very similar to the hottest 'black smokers' from the E.P.R., $21^{\circ}N$.

2. GRAFZI sulphides with $\delta^{34}S$ of +5.4 to +6.3‰, are isotopically heavier than sulphides from the E.P.R., $21^{\circ}N$ (+1.3 to +4.1‰; Styrt et al., 1981). This indicates a greater component of reduced seawater sulphate sulphur contributed to the total hydrothermal sulphur content of the GRAFZI hydrothermal fluids than on the E.P.R. at $21^{\circ}N$. This suggests convection within oceanic crust which may be more permeable and/or hydrothermal solution flow rates may be more rapid, than on the E.P.R., at $21^{\circ}N$, and that the system in the GRAFZI area is seawater dominated.

# CHAPTER 4

# HYDROTHERMAL PROCESSES AND THE EVOLUTION OF GALAPAGOS RIFT SULPHIDE MOUNDS

## 4.1 EVOLUTION OF A SUBMARINE HYDROTHERMAL MASSIVE SULPHIDE DEPOSIT

Synthesis of data from geological, chemical, mineralogical and stable isotope studies has led to the construction of a model which describes the evolution and extinction of a hydrothermal sulphide-depositing vent. It is necessary first to appreciate some of the more important aspects of sub-surface hydrothermally convected seawater interacting with basalt. This process is responsible for producing metalliferous solutions which deposit the sulphides observed on the sea-floor.

### Seawater/Basalt Interaction

Great controversy exists over the interpretation of seawater/basalt ratios. However, the importance of interaction of downwelled, cold seawater with basaltic crust, in deriving metalliferous solutions, is not in dispute. Experimental work has provided the basic knowledge for an understanding of the mechanisms of seawater/basalt interaction, augmented by studies on mineralogy, chemistry and oxygen isotope composition of greenstones dredged from mid-ocean ridges (Muehlenbachs and Clayton, 1972; Humphris and Thompson, 1978).

Hajash (1975) and Mottl and Holland (1978) investigated seawater/basalt interaction at temperatures from 200 - 500$^{o}$C and 500 - 1000 bars pressure, at water/rock ratios of 5 or less. Further experimental work led to Seyfried and Bischoff (1981) reporting results from a system where water/rock ratios of 10, temperatures of 300$^{o}$C and pressures of 500 bars were used. This was thought to simulate the end-member hydrothermal solutions reacting with basalt, at depth under the Galapagos Rift, proposed by Edmond et al. (1979). Results indicated that seawater gained Ca, $H_2S$, $CO_2$, K, Fe, Mn, Ba, Al and $H^+$, whilst losing Mg and $SO_4$. Basaltic glass and dolerite were replaced by minerals such as smectite, chlorite and anhydrite.

Mottl and Seyfried (1980) and Mottl et al. (1979) found that under similar experimental conditions Cu and Zn were also leached from basalt and that basalt-derived ferrous iron was responsible for seawater sulphate reduction. Mottl and Seyfried (1980) concluded that a water/rock ratio of 50 $\pm$ 5 may represent the cut-off between a rock dominated system (at lower ratios) and a seawater dominated system (at higher ratios). Above this ratio of 50, the authors noted that cations can be stripped easily from basalt, whereas at lower ratios than 50, much higher temperatures are needed to achieve this, as also noted by Seyfried and Bischoff (1981).

All the above workers agree that the loss of magnesium hydroxy sulphate from seawater produces acidic hydrothermal solutions. Only under high seawater/rock ratios, i.e. greater than 50, can this acidity be maintained due to the $Mg^{2+}$ ion buffering the low pH of the solutions. At lower ratios, where Mg is almost completely removed from seawater, silicate hydrolysis reactions consume the earlier formed $H^{+}$ and acidity, coupled with high metal concentrations, cannot be maintained in solution.

The application of these facts to the GRAFZI deposits, along with stable isotope results (Skirrow and Coleman, 1982, 1982a), indicate that high seawater/rock ratios were responsible for producing GRAFZI sulphides. These high seawater/rock ratios were produced by either rapid hydrothermal solution flow rates or a permeable oceanic crust with many conduits open to the passage of these solutions, or a combination of both of these two factors.

Sulphide Precipitation

Mineral paragenesis studies (Chapter 3, Section 2) indicate that chalcopyrite and pyrite represent the onset of the higher temperature, later phase of sulphide precipitation within the uppermost basaltic crust, or within the hydrothermal mound, on egress of the hydrothermal solutions onto the sea-bed. However, data presented above show a compositional difference between the middle and upper parts of the sulphide mound. Cu is considerably more enriched at the top than the middle of the mound, where Fe, Zn and $SiO_2$ are most abundant.

Sphalerite is only observed as small grains enclosed within pyrite euhedra and these are found in 'Caries Texture'. Sphalerite was unstable in the presence of solutions which precipitated the mound-top chalcopyrite/pyrite assemblage formed at 390 $\pm$ 20°C, as found by mineral-pair sulphur isotope geothermometry (see Section 3.4(b)). The sphalerite dominated sulphide assemblage found at 21°N on the E.P.R. was formed at temperatures below 350°C (Haymon and Kastner, 1981). By analogy with the E.P.R. deposits, the present mound middle would have formed at temperatures of $\leq$350°C with an assemblage consisting of pyrite, amorphous silica, sphalerite and minor chalcopyrite. The changing temperature and chemistry of the hydrothermal solutions with time was responsible for redissolving previously precipitated sphalerite which was unstable at temperatures of around 390°C. The net effect over the whole mound was that Zn was lost into the Galapagos Rift bottom waters, either by re-solution from the mound middle or simply by non-precipitation due to temperatures which were too high for sphalerite deposition.

The associated occurrence described in Chapter 2, of primary Fe and Mn oxides of hydrothermal origin with high Zn (and to a lesser extent Cu) contents simply reflects an abundant supply of Zn in bottom waters, available for scavenging and adsorption. The possibility that the Fe oxide is a gossan from a pyrite-sphalerite precursor has been ruled out in Section 3.3.

Pyrite formation in the "black smoker ", upon settling, led to the scattering of pyrite euhedra within the mound mass of colloform pyrite/amorphous silica gel. This colloform texture may represent a "quenching" of the hydrothermal solution after the main period of sulphide precipitation and it probably occurred at the periphery of the hydrothermal plume where mixing with ambient bottom waters occurred. Amorphous silica $^{18}O$ isotope results indicate a maximum temperature of formation of 172°C, which compares favourably with the association of pyrite and amorphous silica in E.P.R., 21°N "white smokers" (Haymon and Kastner, 1981). Organic debris acted as a nucleus for sulphide (pyrite) precipitation and is often associated with colloform banding

textures. Amorphous silica $^{18}O$ isotope results also indicate that this mineral could have formed at 60°C, or as a precipitate from a cooler phase of emissions. Alternatively, this temperature may represent a mixture of high temperature (172°C) amorphous silica and diagenetically reworked amorphous silica. Worm burrows were found to be infilled with amorphous silica and secondary minerals from degraded sulphides, which may suggest mixing of high temperature and diagenetically formed amorphous silica.

The cessation of hydrothermal activity was followed by rapid surficial oxidation of primary sulphide material that was not in equilibrium with the oxidising conditions prevailing on the sea-bed. The mobilisation of Cu and S, as noted by Hékinian et al. (1980) at 21°N, from chalcopyrite, was responsible for the formation of secondary minerals such as covellite and chalcanthite and ultimately a gossan of spherules of amorphous iron oxyhydroxides of a limonite character. Marcasite may have formed from pyrrhotite. Diagenesis was responsible both for sealing conduits with reworked amorphous silica and filling pores, resulting in a general compaction of the mounds. A gossan surface of a few millimetres in thickness caps the mounds and this seems to have protected the massive sulphides from further oxidation and destruction. The denudation of the chimneys which once emitted "black smokers" was responsible for building talus around the mound.

It is not known how long the sulphide mounds have survived since cessation of hydrothermal activity. Ultimately their survival may be dependant upon diagenetic compaction and the presence of a relatively impermeable gossan cap on their surface.

The Mechanism of Mound Extinction

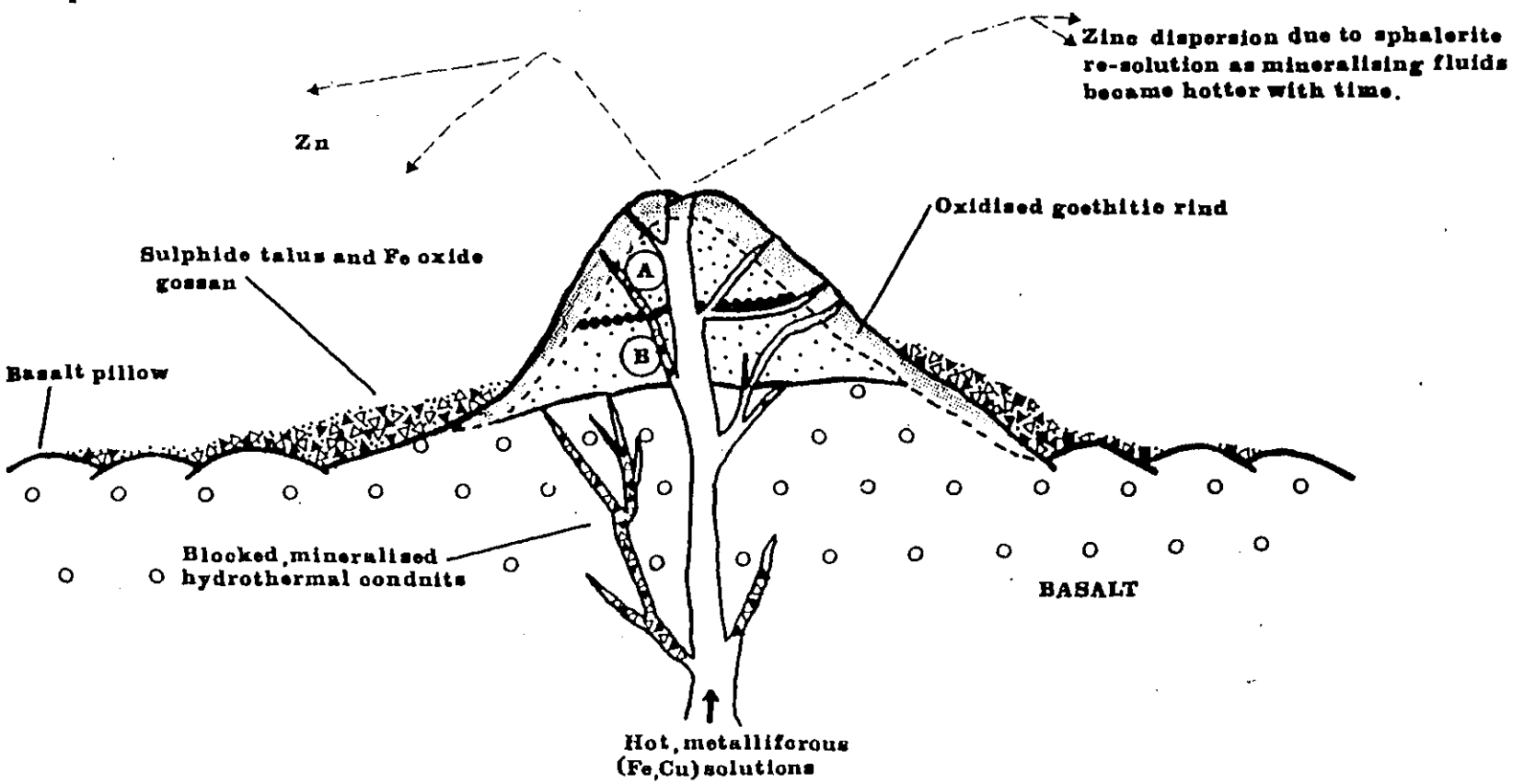
The reasons for mound extinction have been neglected in this study until now but seem to be intimately bound up with sub-surface sulphide precipitation. Valuable evidence can be gleaned from the increase in the temperature of formation or an increase in Cu content of the hydrothermal sulphide deposits with time, although the exact position of the samples in the mound structure was not well detailed and this sets

FIGURE 4.1.1.

# IDEALISED MODEL FOR 86°W SULPHIDE MOUND FORMATION.

(A) **MOUND TOP** – up to 27% Cu, with a dominant chalcopyrite assemblage. Change in hydrothermal solution chemistry/temperature.

(B) **MOUND MIDDLE** – up to 1·4% Zn. Original hydrothermal fluids deposited sphalerite before re-solution.



limitations on any interpretation. The difficulty in geological interpretation of processes operating in the stockwork zone of the hydrothermal system is largely due to the fact that evidence of these processes cannot be seen. However, sulphide precipitation within the stockwork undoubtedly occurred and chalcopyrite and pyrite formation in this zone has already been described above.

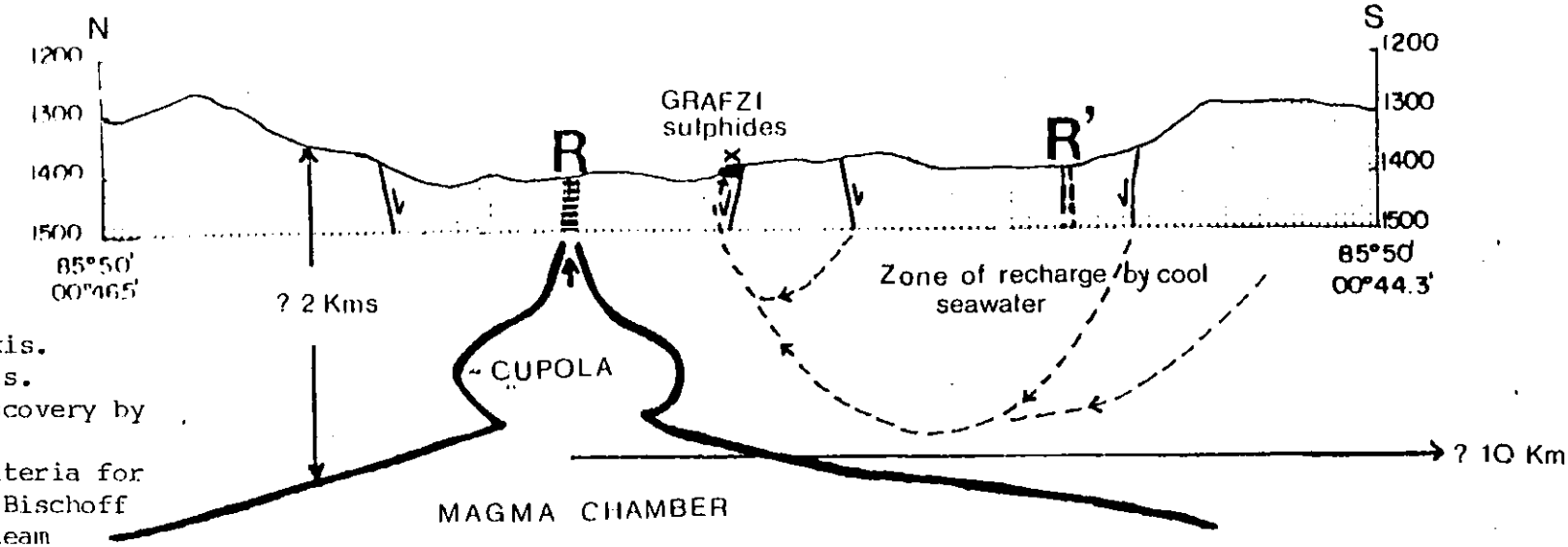
Figure 4.1.1 shows an idealised cross-section and a possible model for the formation of a hydrothermal polymetallic sulphide mound at 86°W, based on synthesis of all the previous data. Sub-surface sulphide precipitation within the stockwork zone of the basement is thought to have caused the change in chemistry and temperature of the hydrothermal solutions with time, manifested by Cu enrichment at the mound top and Zn depletion throughout mound areas A and B (see Figure 4.1.1). The mineralisation and blockage of conduits would have led the solutions to find new passageways and perhaps exit from the sea-bed at a different locality. Alternatively, the decrease in permeability of the stockwork zone due to sulphide precipitation, ultimately causing a blockage in the plumbing system, would lead to the increased use of the conduits still unblocked. The release of pressure and heat from the crust could only be maintained by increasing the flow velocity of the solution and its temperature, in the main or central conduit. Relatively diffuse penetration of hydrothermal fluids would be focussed into a narrow area, as shown in Figure 4.1.1, the location of which is dictated by the blocked sub-surface conduits.

Ultimately, the central conduit would itself be blocked by sulphide precipitation and a new vent would form elsewhere. This is presently occurring on the E.P.R. at 21°N where central zones and upper portions of sulphide chimneys are dominated by chalcopyrite whereas previously, lower temperature Zn rich sulphides (wurtzite and sphalerite) were dominant (Haymon and Kastner, 1981).

The ability of hot, high velocity hydrothermal solutions to propagate cracking fronts in the basaltic crust (Lister, oral comm., 1982) would lead to new passageways and new vents being formed, as old ones became

FIGURE.4.1.2. SUB-SURFACE HYDROTHERMAL CONVECTION AT 86$^{0}$W.

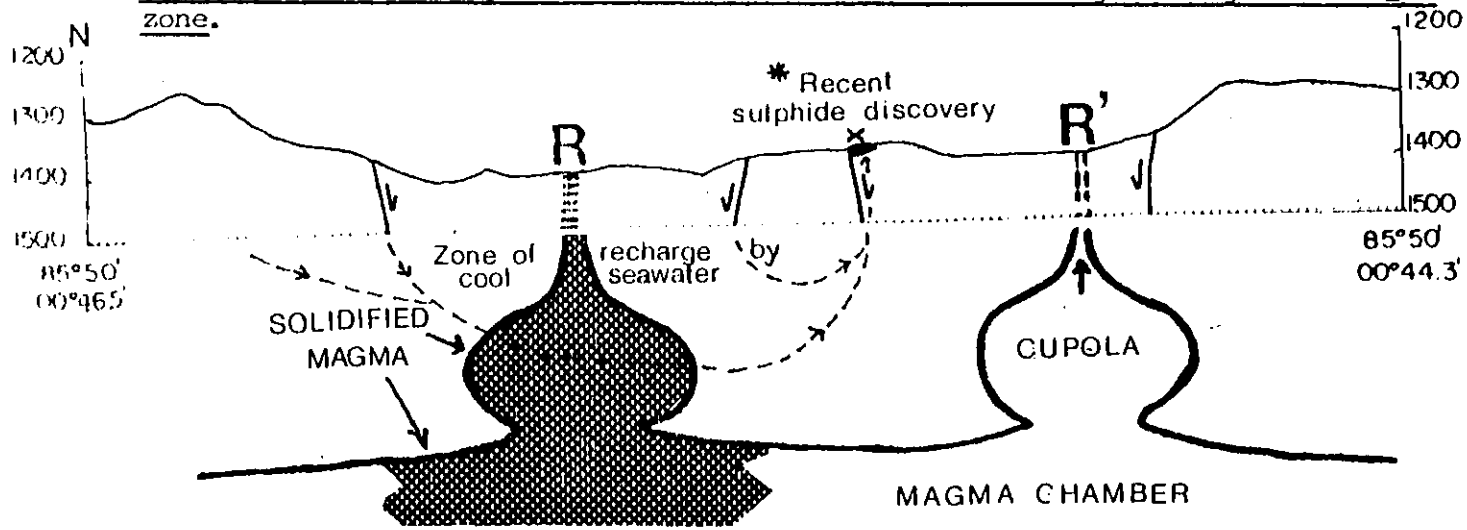
a). Hydrothermal convection cell responsible for GRAFZI sulphide formation.




KEY.

R=Principal Rift Axis.
R'="Jumped" Rift Axis.
* Recent sulphide discovery by Malahoff (1982).
Depth and width criteria for magma chamber from Bischoff (1980) and CYAMEX team (1981).

b). Recent sulphide discovery related to the "jumped" spreading centre and the formation of a new cupola after solidification of the original magma extrusion zone.



blocked. Theoretical work (Cann and Strens, 1982) indicates that a cluster of three "black smokers", active for 800 years, would produce a 3 million ton sulphide ore deposit and this would require the latent heat of solidification of 20 $Kms^3$ of basaltic magma. The total sulphide assemblage in the GRAFZI area is thought to be in the order of 25 million tons (Malahoff, pers. comm., 1982), although this is based on extremely limited data. This would involve the solidification of approximately 175 $Kms^3$ of basaltic magma, on the basis of 7 $Kms^3$ 'frozen' magma per 1 million tons of sulphide (Cann and Strens, 1982).

The Failure of Seafloor Spreading

The solidification of magma described above is extensive and may well have produced a failure in seafloor spreading due to the shutdown of the driving force, the magma chamber. This is speculation but is enlightening when it is considered that the 86°W area of the Galapagos Rift contains a "jumped" rift (see Chapter 1), as seafloor spreading shifted from one site to another. A possible reason for this jump may be due to the extensive solidification of the magma chamber due to hydrothermal heat loss.

A N-S geological cross section taken across the double rift and perched block structure at longitude 85°50'W is shown in Figure 4.1.2, with the location of GRAFZI sulphides and the later discovery of a more massive deposit, found on the northern margin of the southern rift (Malahoff, pers. comm., 1982). The speculative sub-surface geology has been included to show hydrothermal convection cells and the cupola on the magma chamber which may have migrated to a more southerly location, due to hydrothermal heat loss, initiating seafloor-spreading there and setting up new hydrothermal convection cells responsible for depositing the sulphide deposit , as shown in Figure 4.1.2.

## 4.2 A COMPARISON OF MODERN AND ANCIENT SUBMARINE SULPHIDE DEPOSITS

The more detailed information that becomes available from studies of the genesis of modern submarine hydrothermal sulphide deposits

TABLE 4.2.1. Comparative Geochemical Data for Mid-Ocean Ridge Hydrothermal Massive Sulphide Deposits

| | * GRAFZI | | | + GALAPAGOS RIFT, 86°W | + E.P.R., 21°N | + JUAN DE FUCA RIDGE |
|---|---|---|---|---|---|---|
| SOURCE OF DATA | This study MAX. | MEAN | MIN. | Malahoff (1982) | CYAMEX Hékinian (1980) | Delaney et al '82) |
| Fe (%) | 31.2 | 21.1 | 2.1 | 10.0 | 8.9 | 8.0 |
| Cu (%) | 26.7 | 10.8 | 0.6 | 10.0 | 0.3 | 0.3 |
| Zn (%) | 1.4 | 0.4 | <0.1 | 0.1 | 49.7 | 54.0 |
| Ag (ppm) | 55 | 31 | 16 | 300 | 380 | 290 |
| Pb (ppm) | 80 | <34 | <10 | 1000 | 640 | 2500 |
| Cd (ppm) | NOT REPORTED | | | 100 | 300 | 490 |

* GRAFZI values taken from Table 2.1.1., which were averaged after the exclusion of Sample 4 Station 9, which was contaminated with ferro-manganese oxides.

+ Representative analyses from published literature.

increasingly strengthens the case for comparisons to be drawn with ancient deposits of ophiolitic and greenstone belt affinity. To put these comparisons into their proper context it is important to review the composition of the modern massive sulphide deposits found to date, all of which are from the Eastern Pacific.

Modern Submarine Sulphide Deposits

Chemical analyses reported in Table 4.2.1 show a combination of values which highlight chemical differences between the sulphides. The values reported are representative of the particular sulphide deposit concerned and for comparison the maximum, minimum and mean values are reported for GRAFZI sulphides.

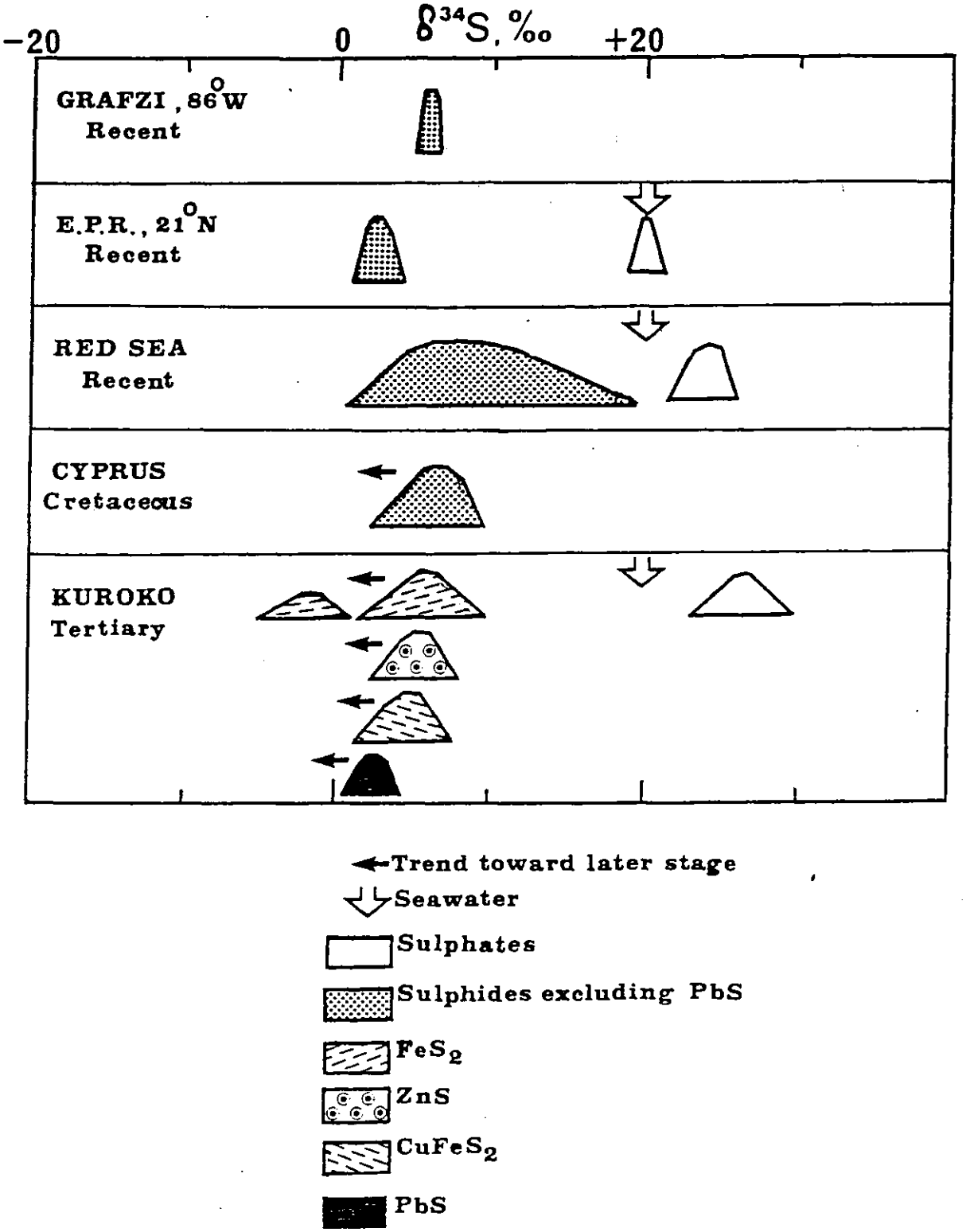
The data indicates that the GRAFZI deposits, from this study and from Malahoff (1982), are much more Cu-rich and less Zn- and Ag-rich than their counterparts, from 21°N on the E.P.R. They are also different from those on the Juan de Fuca Ridge, where Zn reaches 54%, and Ag reaches 290 ppm.

It has been shown that temperature is a very important factor in determining whether a sulphide assemblage is Zn- or Cu-rich, and this may be related to the depth of the heat source below the sea-bed. Bischoff (1980) noted that 21°N sulphides represent the very top of the hydrothermal system and may not be representative of the whole. The limited evidence available (Bischoff, 1980) suggests that pyrite or pyrrhotite may be found within the basement, representing earlier higher temperature precipitates.

Ancient Submarine Sulphide Deposits

In recent years much literature has been produced comparing land-based economic ore deposits with Red Sea-type submarine hydrothermal deposits. Some comparisons have been tenuous whilst others have gained much support, especially those on sulphide bodies associated with ophiolite sequences, e.g. the Semail Nappe, Oman (Pearce et al., 1979) and the Troodos Complex, Cyprus (Spooner, 1976). The tectonic setting of modern mid-ocean ridges and ophiolite complexes are similar but there

FIGURE.4.2.1. Comparative sulphur isotopic data for some stratiform massive sulphide deposits associated with submarine volcanism,adapted from Ohmoto and Rye(1979).




The sources of data on Cyprus and Kuroko are summarised in Rye and Ohmoto (1974).The data on the Red Sea is from Kaplan et al.(1969),and Shanks and Bischoff (1975).East Pacific Rise,21°N,data is from Arnold et al.(1969), and Styrt et al.(1981).

is also a great deal of similarity between the hydrothermal processes operating in island-arc and mid-ocean ridge tectonic regimes.

The West Shasta Cu-Zn District of California is a prime example of a hydrothermal system which evolved in a Devonian island-arc setting (Casey and Taylor, 1982). The similarities between the hydrothermal processes producing the sulphide deposit and those which produced the GRAFZI deposit are noteworthy. The West Shasta deposit is enclosed by dacite and underlain by the Copley Greenstone (basaltic andesite) which has been hydrothermally altered by seawater. $^{18}O$ compositions of the rocks indicate similarities to Mid-Atlantic Ridge meta-basalt (Stakes, 1978) and altered oceanic rocks of the Troodos Complex (Heaton and Sheppard, 1976), with interaction occurring at about $200^{\circ}$ - $300^{\circ}C$. The sulphide deposit consists of pyrite, chalcopyrite and sphalerite. Geothermometry of a pyrite/chalcopyrite pair from the West Shasta deposit indicated a temperature of formation of $340^{\circ}$ - $365^{\circ}C$ for these two minerals whilst GRAFZI sulphides formed at $390^{\circ} \pm 20^{\circ}C$. Further isotopic comparison can be drawn as $\delta^{34}S$ values vary between +4.1 to +5.3‰ for the West Shasta sulphides, which are similar, if slightly lower, than those for GRAFZI sulphides (up to +6.4‰). Casey and Taylor (1982) concluded that on the basis of isotopic evidence from O, H and S, the hydrothermal fluid was dominantly an evolved seawater, as suggested for GRAFZI sulphides.

The above comparison indicates that although the igneous assemblages differ in island-arc and mid-oceanic terrains the hydrothermal processes do not, as was also shown by Ozcelik (1982) for sulphides from the Anatolian Ophiolite Belt of Turkey. Valid comparisons can be made between a Devonian metamorphosed intermediate rock-hosted volcanogenic massive sulphide and a present-day basalt-hosted equivalent. To emphasise this point, Figure 4.2.1. shows that modern and ancient sulphide deposits have very similar $\delta^{34}S$ values, regardless of their tectonic setting. The common factor is that all of these have been derived from an evolved seawater mineralising fluid. Red Sea $\delta^{34}S$ values show a large spread and may reflect biological activity, while sulphate $\delta^{34}S$ values reflect precipitation from heated-ambient seawater, rather than the hydrothermal solutions. The slight

differences in $\delta^{34}S$ suggests the relative amounts of sulphur from reduced seawater sulphate and from basaltic sources, contributed to the hot mineralising fluids, as outlined in Section 3.4(b).

The analogy between GRAFZI and Cyprus-type sulphide ores is not just related to their similar location at faulted-rift valley margins (Malahoff et al., 1983). Stockwork hydrothermal fluid temperatures for the Troodos sulphides range between 250° - 350°C (Heaton and Sheppard, 1976; Spooner, 1976). Heaton and Sheppard (1976) postulated a seawater/rock ratio of between 1 and 5, responsible for producing disseminated stockwork cupriferous pyrites ( $\delta^{34}S$ = + 5.1‰), whilst massive pyrite gave a $\delta^{34}S$ value of +4.3‰. These values are similar to GRAFZI $\delta^{34}S$ values and Spooner (1976) suggested a major component of sulphur contributed to the sulphides from reduced seawater sulphate at Troodos, up to a possible maximum of 100%.

The above comparisons are of considerable value in commercial massive sulphide exploration. Scheibner and Pearce (1978) found that Paleozoic metabasalts from New South Wales which erupted during the opening phase of a major ocean, chemically resemble metabasalts from the Troodos Massif of Cyprus and thus were of great exploration potential, for Cu-rich massive sulphides.

## 4.3 EXPLORATION CRITERIA FOR THE DISCOVERY OF POLYMETALLIC SULPHIDES

Guidelines for exploration for hydrothermal sulphides of potential ore grade are as follows:-

1. High resolution bathymetric mapping of the rift valley, using the SEABEAM or Sonar-Array Sounding System (S.A.S.S.) technique coupled with the acoustic SEAMARK system. Exploration should focus at both axial and faulted margin locations.

2. Geophysical investigations to include determination of the spreading rate, heat flow variations, gravity, magnetic and seismic refraction surveys to obtain high resolution crustal properties along the spreading centre and gain knowledge of the source of new oceanic crust, the nature of the axial magma chamber and the depth of hydro-

thermal circulation. Electromagnetic techniques to locate sulphides could be used once the above procedures have selected a target area.

3. Regional geochemical reconnaissance study of the area, focussed in the vicinity of axial fractures or faulted margins of the rift valley, with an end to locating Mn anomalies in the sediments. Detailed sampling of an area with Mn enrichment would produce a trend of increasing Mn and decreasing Zn/Cu ratios towards the hydrothermal source. The source may or may not host sulphides, depending on the temperature of the effluent hydrothermal solutions, dictated by the extent to which sub-surface mixing with ambient bottom waters has occurred.

STUDY B CHAPTER 5

# THE DE STEIGUER DEEP AREA, 95°W

## 5.1 INTRODUCTION

The work of Moore and Vogt (1976) focussed attention on the De Steiguer Deep Area of the Galapagos Rift at 95°W, where two separate dredge hauls recovered hydrothermal manganese crusts. Station D6, on basement which was located on the north wall of the axial valley of the active spreading centre, was dredged at a water depth of about 2930 metres and on oceanic crust dated magnetically at 0.3 million years age. Station D9 was located on a basement ridge 25 Kms northeast of D6, at a water depth of about 2560 metres and on oceanic crust of 2.4 million years age.

Figure 5.1.1 shows D6 and D9 and their location relative to the Galapagos Spreading Axis. The R/V SONNE revisited the De Steiguer Deep Area in 1980 (see Figure 5.1.1) and the stations sampled are described in Section 5.3.

## 5.2 GEOLOGY AND BATHYMETRY OF THE 95°W AREA

The original aim of the 1972 cruise to the 95°W Area (Moore and Vogt, 1976) was to investigate a zone of high magnetic anomaly amplitudes (Vogt and Johnson, 1973) centred on the Galapagos archipelago which is thought to be a mantle intra-plate hot spot (Morgan, 1972). The magnetic anomalies were thought to occur due to the nature of the basaltic crust which is enriched in Fe and Ti (Vogt and Johnson, 1973) and hence termed FeTi basalt.

At 95°27'W, the Galapagos Spreading Axis (G.S.A.) is offset by a sinistral strike slip fault or fracture zone. The easterly part of the G.S.A., terminated by the fracture zone, is enclosed by the basin termed the De Steiguer Deep which is shaded below the 3000 m contour in Figure 5.2.1. The basin is elongated east-west, along the direction

FIG.5.1.1. Station locations in the De Steiguer Deep Area (95°W) on the Galapagos Rift. D6 and D9 represent the sites where hydrothermal Mn crusts were found by Moore and Vogt (1976).

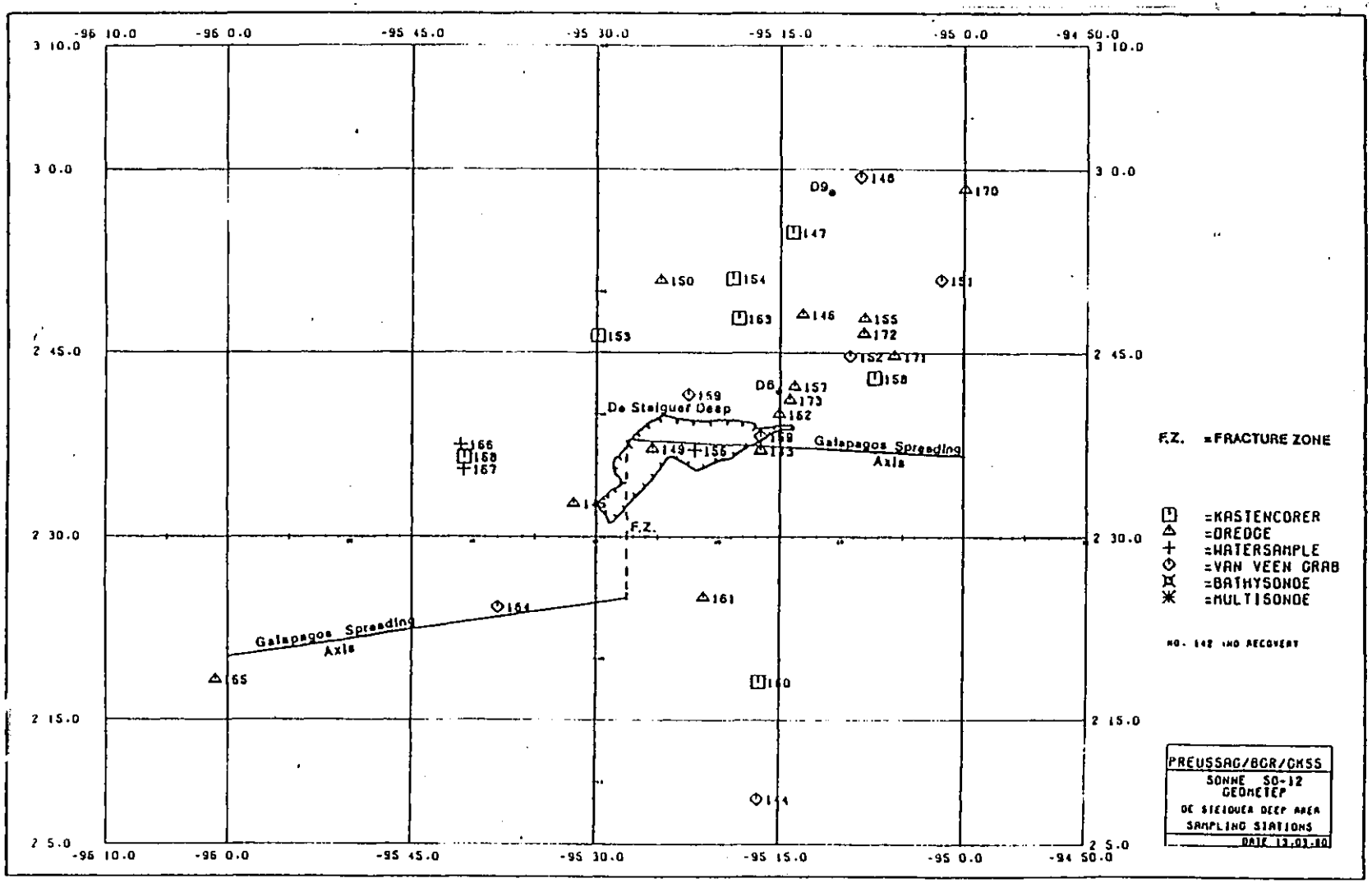
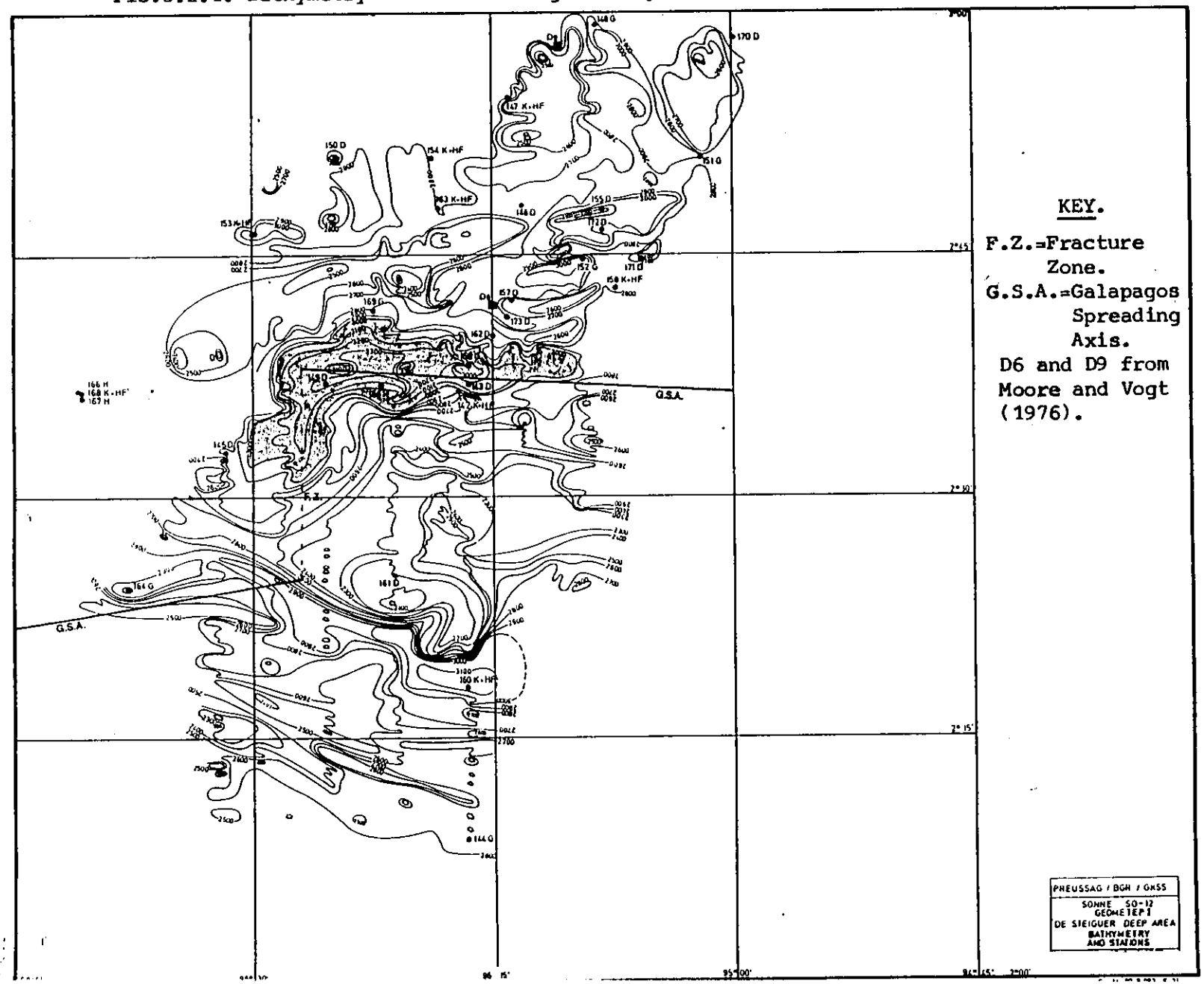


FIG.5.2.1. Bathymetry of the De Steiguer Deep (shaded) and surrounding area.



of the G.S.A. and has a maximum depth of more than 3300 m. The southernmost extension of the De Steiguer Deep encloses part of the fracture zone where a cross section of the mid-ocean ridge occurs in the easterly wall.

The majority of the samples collected were taken from the north flank of the G.S.A. where the bathymetric data (Figure 5.2.1) indicate an east-west strike for the topography which consists of small basins and ridges and isolated seamounts shoaling to 2500 metres. South of the G.S.A. there is a sharp increase in depth from 2200 m to 3100 m at $2^{o}20'N$ and $95^{o}17'W$, where core 160K was recovered. One of the abyssal hills, at $2^{o}48'N$ and $95^{o}13'W$, was dredged at a water depth of about 2750 m (Station 146D) and pillow lava basalts (without a glassy margin) were recovered. The surface of the basalt was partly altered, with yellow and red Fe-hydroxides, coated by botryoidal Fe/Mn crusts up to 7 mm in thickness. This dredge was located between Stations D6 and D9 of Moore and Vogt (1976), (see Figure 5.2.1).

## 5.3 SAMPLE DESCRIPTION

Seven cores, 14 dredge hauls and 7 Van Veen grab stations were sampled, while water samples were collected from 3 other stations (see Figure 5.1.1). Thirty-four samples were analysed (see Appendix B), taken from 7 cores, 2 dredge hauls and 1 Van Veen grab (see Appendix C). From top to bottom of the cores, the sediment grades from dark to moderate yellowish brown (10YR 4/2, 10YR 5/4) through grayish yellow/orange (5Y 8/4, 10YR 7/4) to pale greenish yellow (10Y 8/2). Shipboard grain size determinations for the cores showed that there is no silt/clay fraction (i.e. $< 63\mu$) in the surface sediment which comprises foraminiferal ooze but that this fraction increases up to a maximum of 64%, at 2 metres core depth.

## 5.4 BULK GEOCHEMISTRY AND MINERALOGY

### 5.4.1 Bulk Geochemistry

Data for 18 elements, $CaCO_3$ and $SiO_2$ is reported for the 34 samples on a carbonate free basis, in Appendix C. According to the classification of Olausson (1960), the sediments can be termed foraminiferal chalk oozes and $CaCO_3$ varies from 61.9% to 92.9%. $SiO_2$ was only analysed in 3 samples and varies from 45.9% to 56.7%, on a carbonate free basis, averaging about 50% of the non-carbonate fraction of the sediments.

The results obtained from the data handling on a carbonate free basis have been used to examine geochemical variation within the non-carbonate fraction. However, in these high carbonate sediments where $CaCO_3$ values as high as 92.9% are found, the remaining sediment fraction is very small and as shown above, $SiO_2$, where analysed, averages about 50% of this fraction. Salt (NaCl) is also a significant component of the non-carbonate sediment fraction and selection of a few Galapagos Rift sediments showed that about 6.5% weight loss occurred after washing the samples with de-ionised water.

As weight loss determinations were not carried out on every sample, the non-carbonate fraction of the sediment has not been salt-corrected.

Na values of up to 15.8% (see Appendix C) can largely be ascribed to sea-salt in the samples, although Welby (1958) showed that Na and K in deep-sea sediments are associated with the clay minerals. Chester and Aston (1976) found that sodic feldspars occur in minor amounts in pelagic sediments. Mineralogical evidence (Section 5.4.2) indicates that feldspars are of minor abundance, suggesting that sea-salt and to a lesser extent, clay minerals contribute most of the Na to De Steiguer Deep Area sediments.

Berger et al., (1976) showed that the C.C.D. in the 95°W area is located at about 3600 m water depth, with a "transition zone" of 100 m thickness above it, where high carbonate values decrease to low ones with increasing depth towards the C.C.D. All the samples analysed from this area are from stations in water depths shallower than 3176 m and are therefore well above the C.C.D.

Sr and P are known to be associated with $CaCO_3$-rich pelagic sediments (El Wakeeland Riley, 1961; Emiliani, 1955). Sr substitutes for Ca in the $CaCO_3$ lattice and P is present in skeletal apatite, which is also an efficient adsorber of lathanides (Arrhenius et al., 1957). These associations explain the fact that the sample highest in $CaCO_3$, surface sediment from 160K, also contains the most Sr, P and La (see Appendix C).

High concentrations of Mg, Al, Ti and V tend to occur together in the same samples, suggesting the close association of these elements. Mg, Al and V have been ascribed to clay mineral and basaltic detritus sources in GRAFZI area sediments (see Chapter 2), with a major contribution from the clay minerals. Hékinian et al. (1978) reported 1.14% Ti for Galapagos Rift FeTi basalts. To determine the contribution of Mg, Al and V from basaltic and clay mineral components in the sediment, the Mg/Ti, Al/Ti and V/Ti ratios compared to those in Galapagos Rift FeTi basalts were examined.

FeTi basalts (Hékinian et al., 1978) have a Mg/Ti ratio of 2.9, Al/Ti of 6.0, V/Ti of 0.04, while 95°W sediments give much higher ratios in all cases, e.g. Mg/Ti of 11.5 to 22.8, Al/Ti of 16.4 to 22.7, V/Ti of 0.07 to 0.31. These higher ratios show that Mg, Al and V are present in the sediments at greater levels than would be expected from a FeTi basalt component. Therefore, this indicates that a major site of Mg, Al and V in 95°W sediments is in clay minerals (see Section 5.4.2).

The fact that Li is highest in sediments which, on the basis of their Ti content, have a low content of basaltic debris suggests that clay minerals may be the major site for this element, as is the case in GRAFZI area sediments (Chaper 2).

*Regional Element Distribution in 95°W Area Surface Sediments.*

The elements Fe, Mn, Co, Ni, Cu, Zn and Pb are commonly associated with marine ferromanganese oxide deposits (Cronan, 1980) and as shown previously, Fe, Mn, Cu, Zn and possibly Pb can be dispersed from a hydrothermal source and incorporated in these ferromanganese oxides (see Chapter 2).

Figures 5.4.1 - 5.4.7 show the distribution of Mn, Fe, Cu, Zn, Co, Ni and Pb in surface sediments from the 95°W area. The upper oxidised layer was found to penetrate to at least 25 cms below the sediment/water interface. The limited data available suggest that sediment from core 153K and dredge 146D are most enriched in Mn (>4%, on a carbonate free basis, see Figure 5.4.1) and sediment from core 160K is most enriched in Fe (>8%, see Figure 5.4.2). The existence of

FIG.5.4.1. Mn distribution in surface sediments from the 95°W Area.

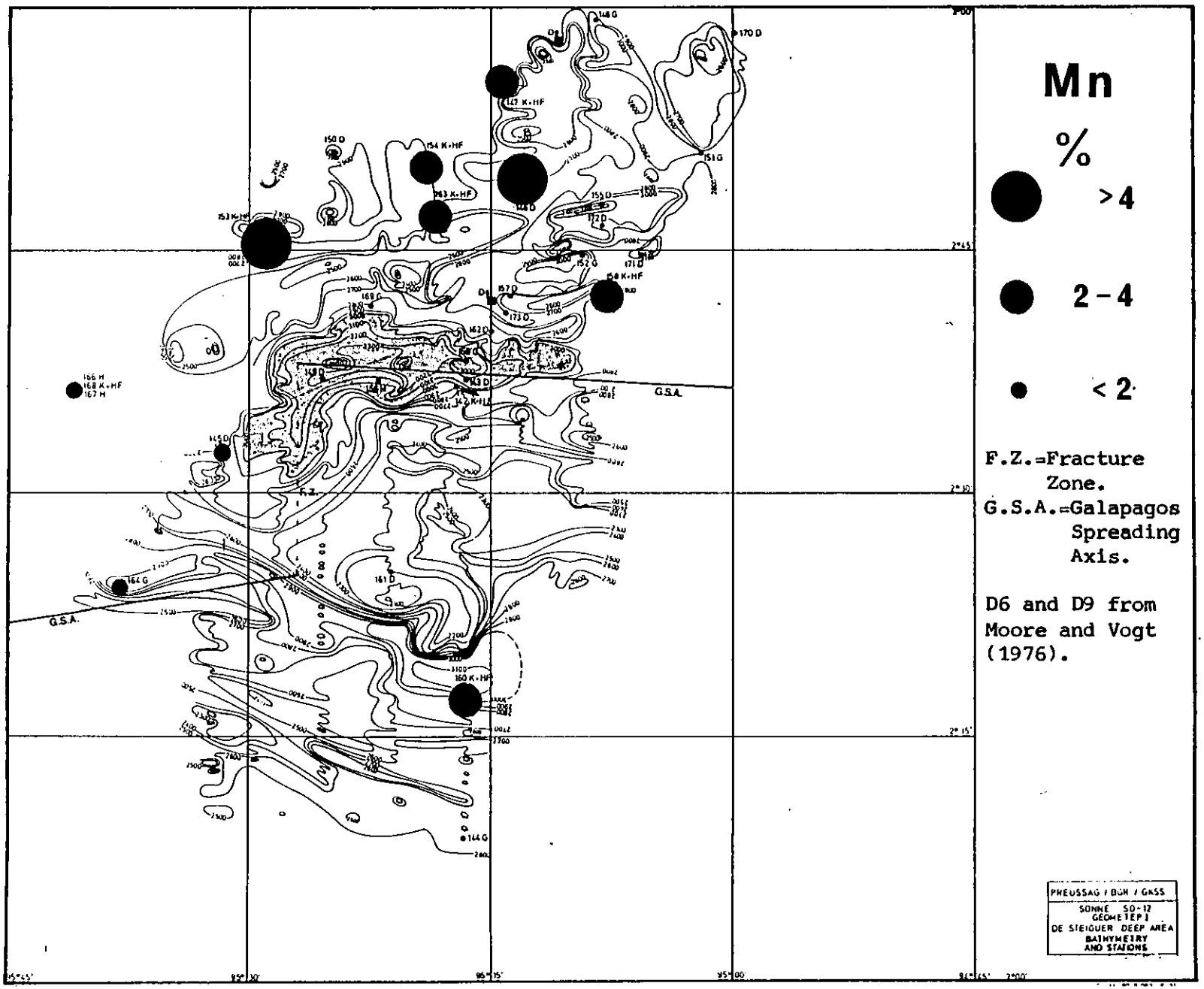


FIG.5.4.2. Fe distribution in surface sediments from the 95°W Area.

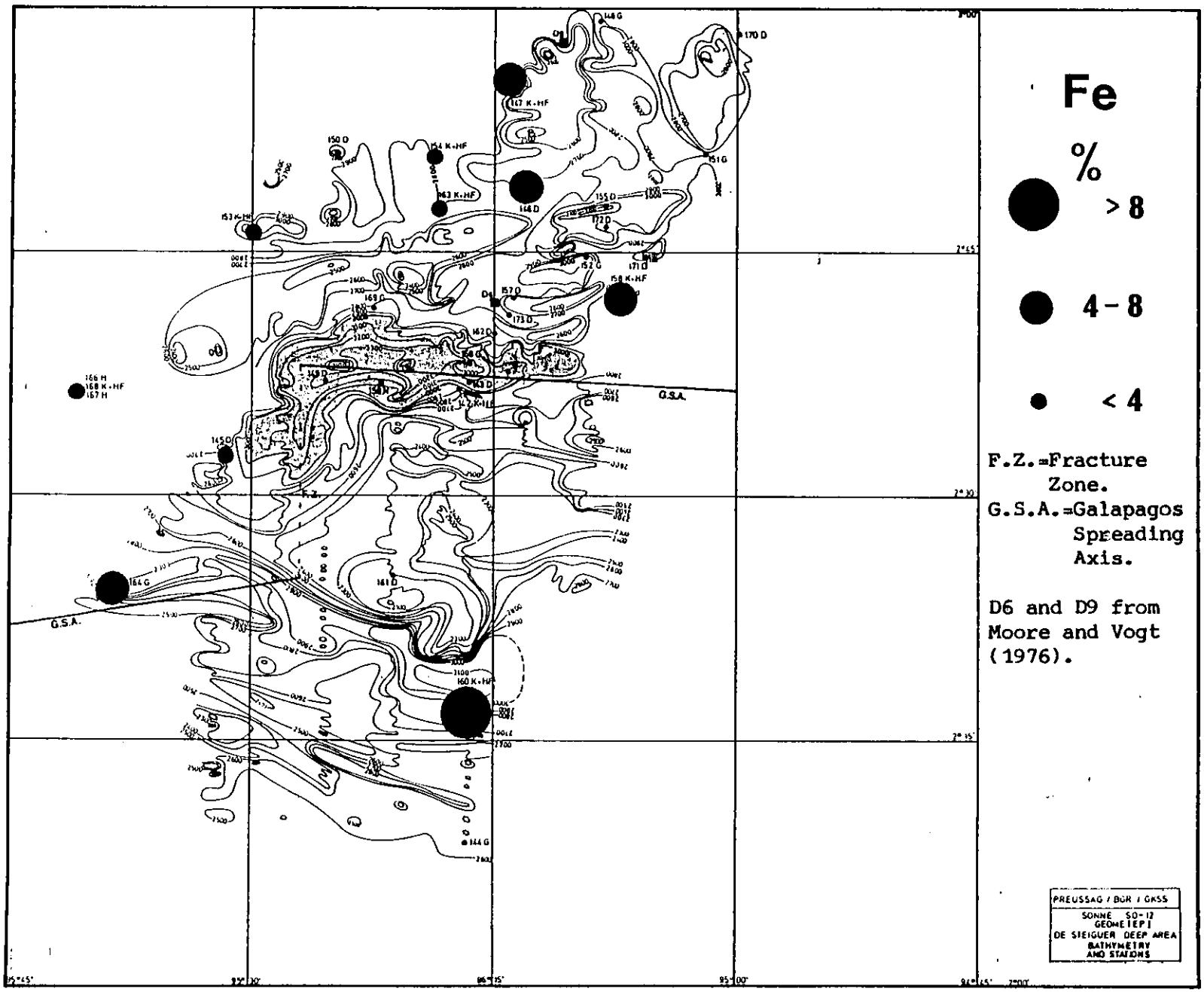


FIG.5.4.3. Cu distribution in surface sediments from the 95°W Area.

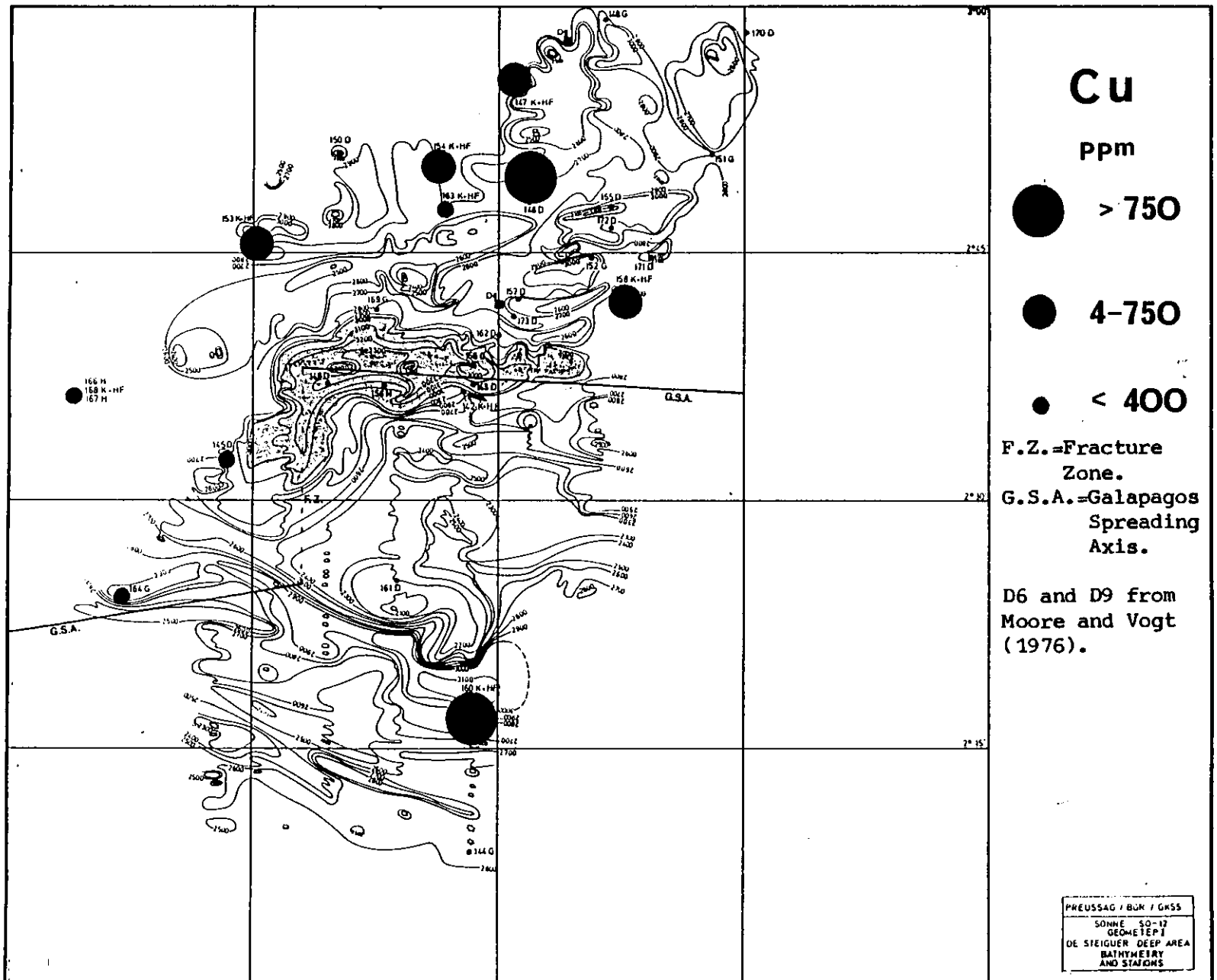


FIG.5.4.4. Zn distribution in surface sediments from the 95°W Area.

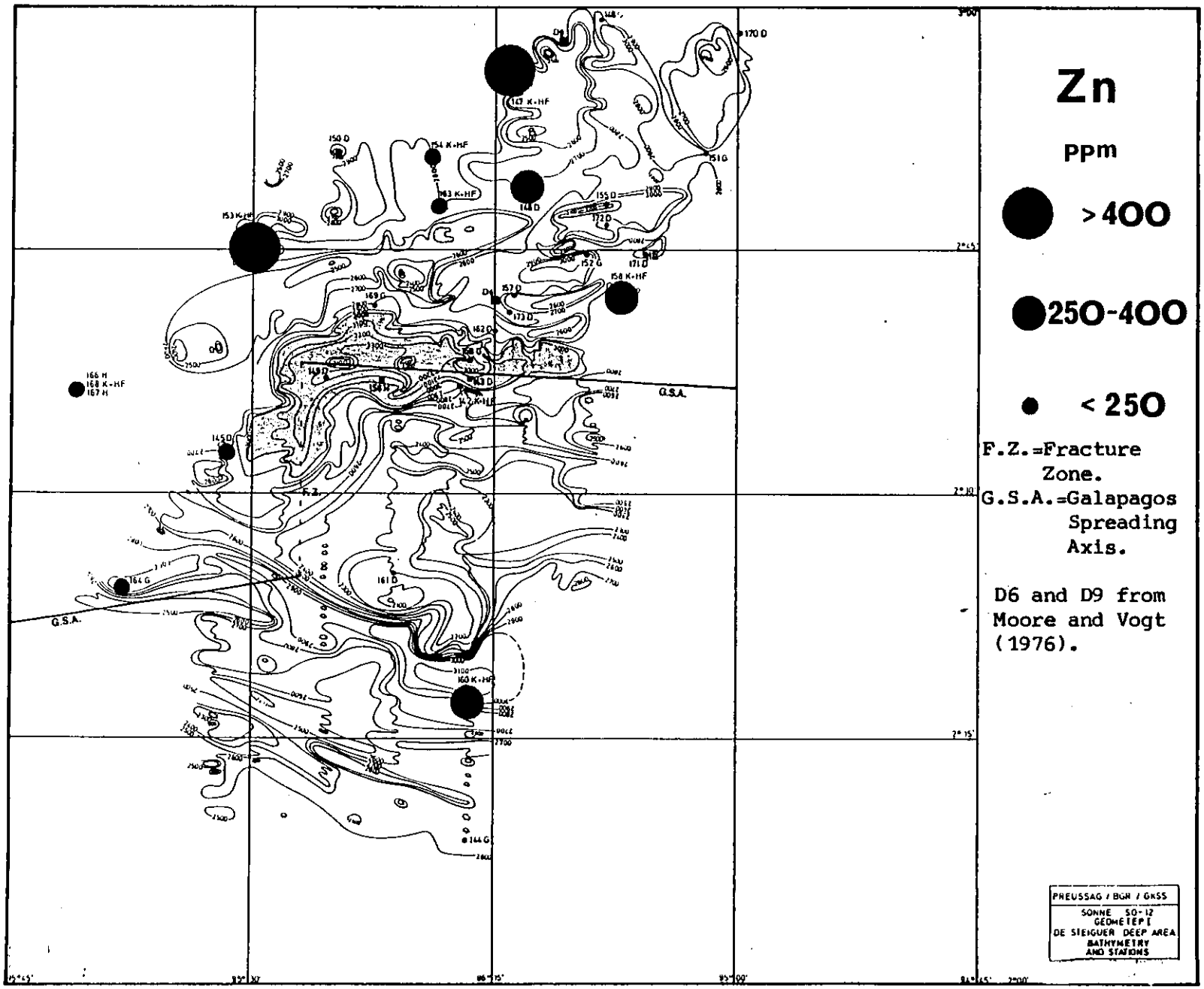


FIG.5.4.5. Co distribution in surface sediments from the 95°W Area.

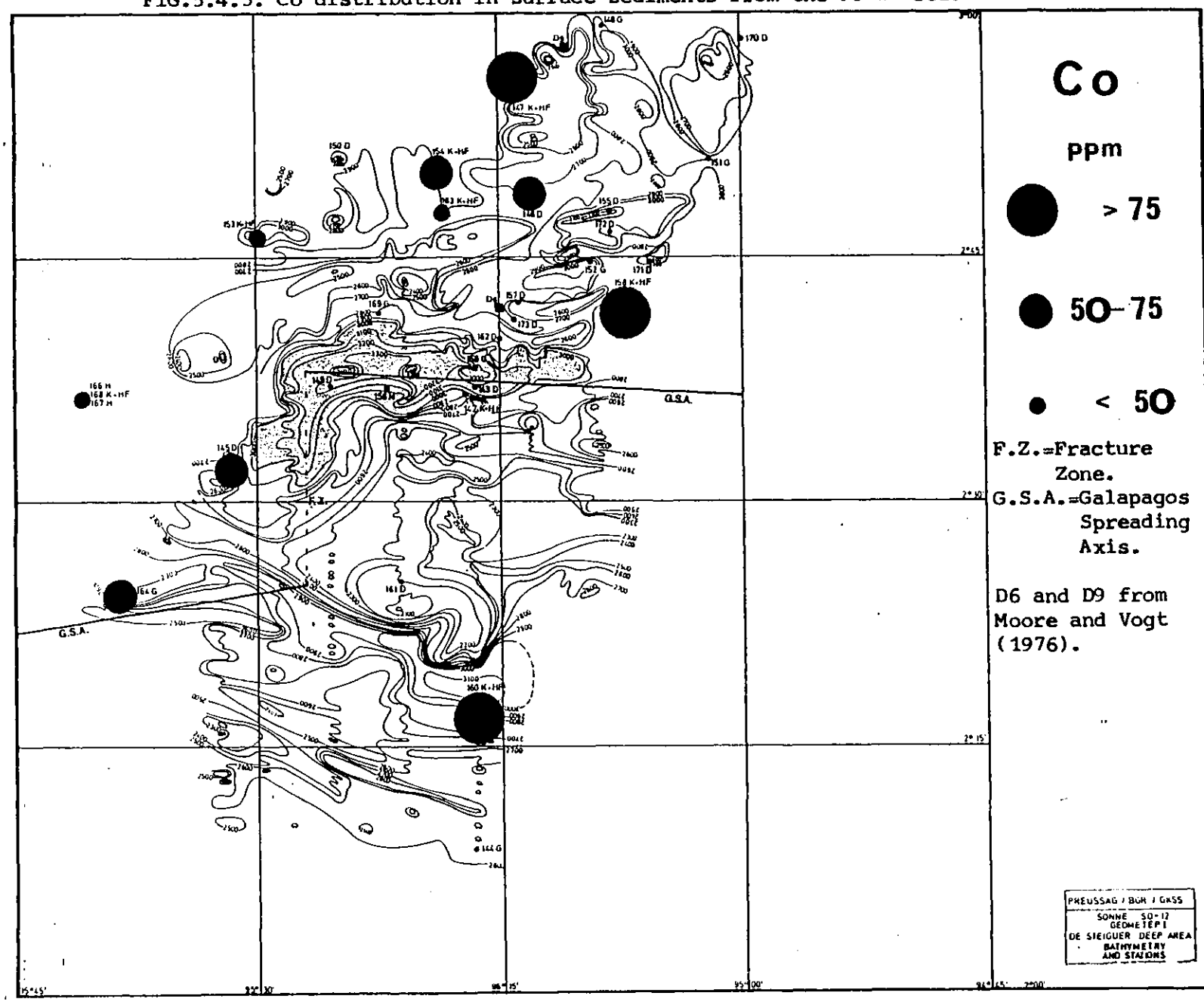


FIG.5.4.6. Ni distribution in surface sediments from the 95°W Area.

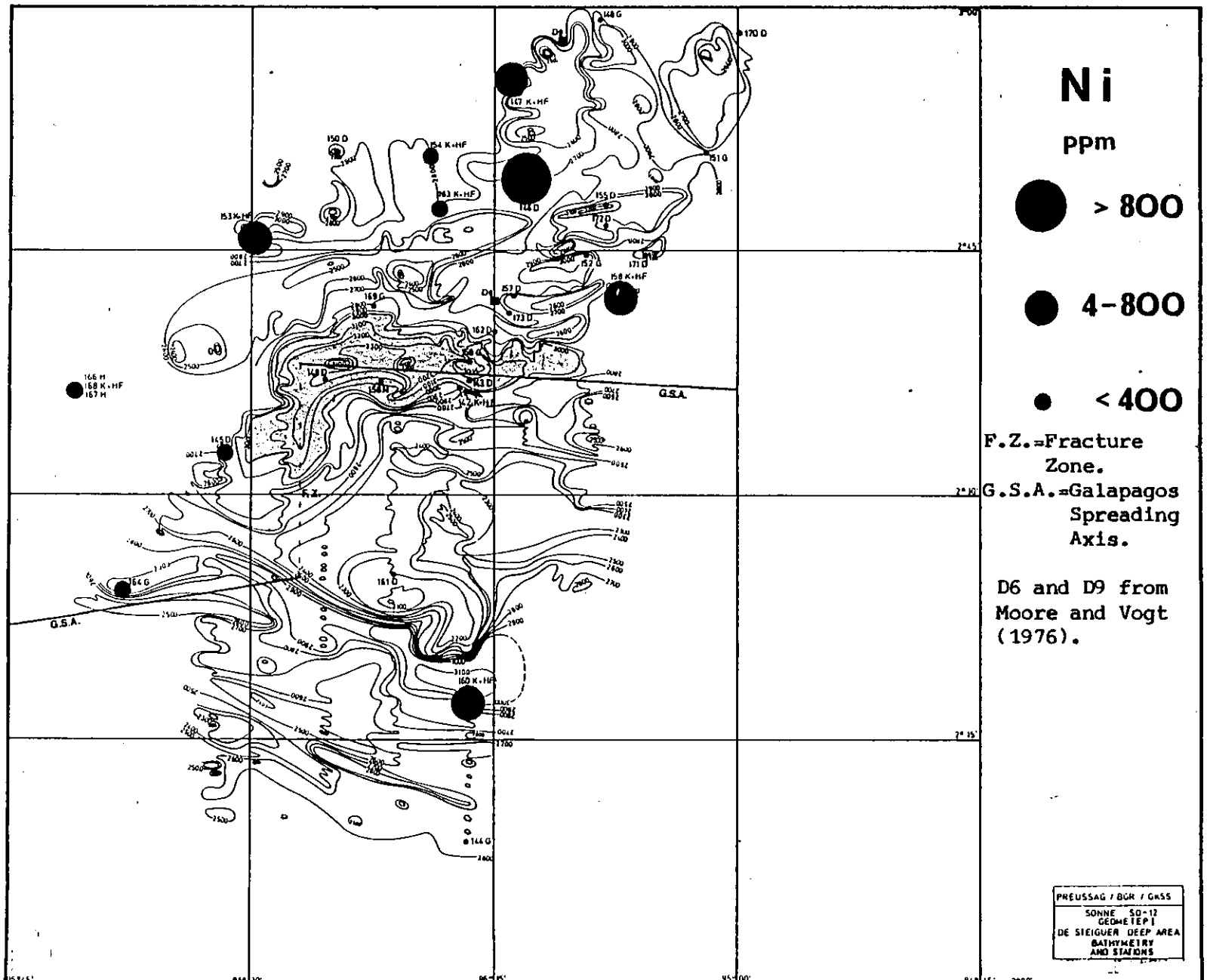
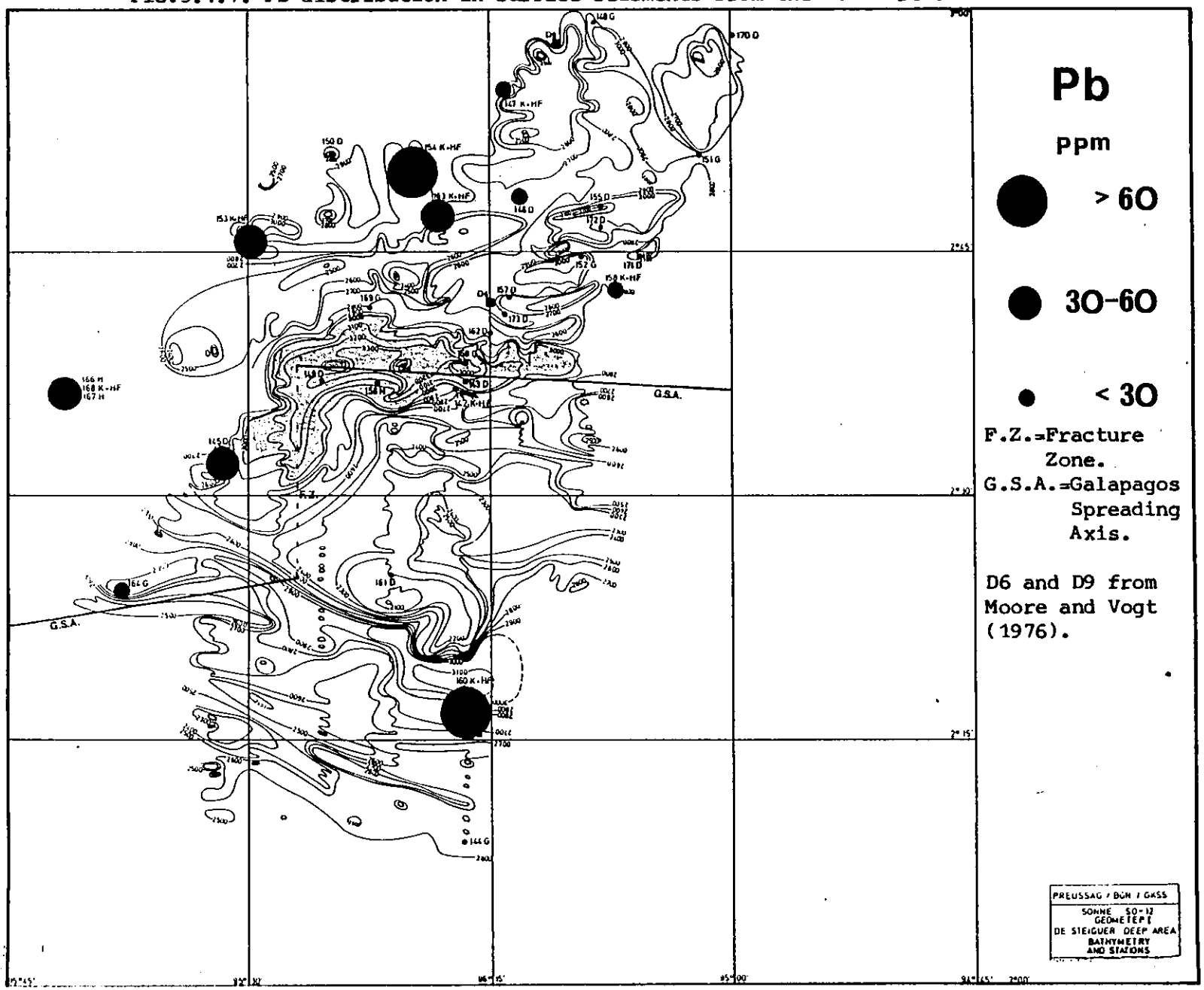


FIG.5.4.7. Pb distribution in surface sediments from the 95°W Area.



FeTi basalt with more than 10% total Fe (Hékinian et al., 1978) in this area may explain the level of Fe in 95°W area sediments, although Fe/Ti ratios which are much higher for 95°W sediments (from 16.2 to 35.3) than for FeTi basalts (about 7.3) suggest that clay minerals and Fe oxide sites for Fe are more important. Mn is known to be concentrated in the top oxidised sediment layer by diagenetic remobilisation (Lynn and Bonatti, 1965) although its ultimate source may be hydrothermal. The Mn enrichment in 146D is notable because this station is situated between two known hydrothermal Mn crusts, D6 and D9, found by Moore and Vogt (1976).

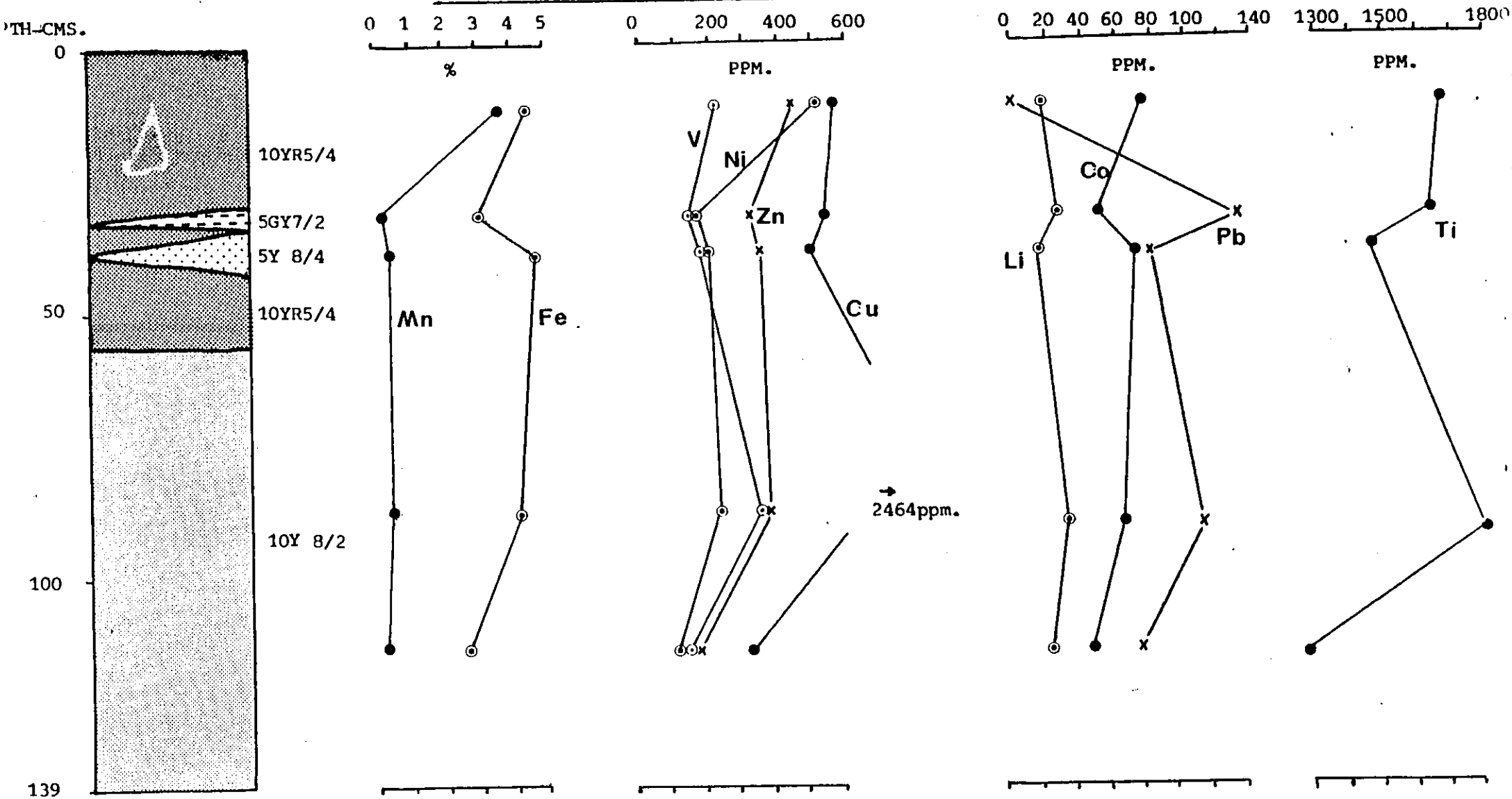
Cu reaches a maximum abundance in sediments from core 160K and dredge 146D (see Figure 5.4.3) which can be associated with the maximum abundances of Fe and Mn, respectively. Zn, Co, Ni and Pb (Figures 5.4.4 - 5.4.7) all show relatively high levels in core 160K and variable enrichment in cores 147K, 153K, 154K and 158K and dredge 146D. The relative lack of Pb and to a lesser extent Co, in 146D, may indicate a hydrothermal ferromanganese oxide component in the sediment as these metals are normally low in hydrothermal deposits and high in hydrogenous deposits (Cronan, 1980). However, a high Ni content also suggests some hydrogenous characteristics in 146D sediment. Cu and Zn are more enriched in 146D than Co, and the former elements may be transported with particulate hydrothermal Mn oxides (see Chapter 2). Core 160K is more enriched in Co and Pb, indicating that its ferromanganese oxide component may be of a more hydrogenous nature.

*Geochemical Variations with Depth.*

One of the seven cores from the 95°W area, 147K, was subsampled along its length to examine element trends with depth (see Figure 5.4.8).

The elements reported in Figure 5.4.8 generally show, to varying degrees, an association with Fe or Mn. The decrease in Mn content below about 30 cms can be ascribed to reducing conditions in the lower sections of the core, caused by the oxidation of organic matter (Bonatti et al., 1971). Changes in redox conditions from top to bottom of the core are responsible for enrichment of Mn, Ni and Co in the upper layer of

FIG.5.4.8. Element variation with depth in core 147k.



sediment. The mechanism responsible for postdepositional mobility of the elements is by diffusion through interstitial pore solutions (Lynn and Bonatti, 1965).

The profiles for core 147K indicate some similarity between the variations in concentration of Mn, Ni, Co and Zn. V and Cu increase to their highest levels in the depth interval, 75 - 100 cms. The V content can be explained by a slight increase in the abundance of clay minerals with depth downcore. The very high Cu content of 2460 ppm may be due to the fixing of Cu in a sulphide phase within the reduced zone of the core, as shown by Bonatti et al. (1971).

Li, Pb and Ti profiles all exhibit the same shape, although Pb enrichment is more marked between 30 and 34 cms, than that for Li and Ti. These element associations can be explained by their incorporation in clay minerals and to a lesser extent, in basaltic detritus.

5.4.2 Mineralogy

As stated previously, the 95°W area sediments are dominated by calcium carbonate and identification of clay minerals is only possible after removal of sea salt, calcium carbonate, iron oxyhydroxides and size separation of the coarse fraction (see Appendix B). By X-ray diffraction analyses, the coarse fraction was found to consist mainly of plagioclase, hornblende and minor quartz.

The clay mineralogy of the <0.5$\mu$ fraction is dominated by smectite with only minor chlorite. The air-dried smectite with a basal spacing (001) of 14.3Å, expanded to 17.9Å upon glyceration and collapsed to less than 9.9Å, upon heating to 550°C (see Table 5.4.1). Chlorite gave only minor peaks when the air dried and glycerated traces were studied. However, chlorite was unequivocally identified in the heat treated samples and gave its most prominent peak at 13.9Å which is slightly shifted from the normal 14.2Å, for the (001) diffraction.

Table 5.4.1 shows the chemistry of the 3 smectite-rich clay fractions analysed and the chemistry of DOMES area smectite for comparison,

TABLE 5.4.1. Geochemistry and Mineralogy of <0.5μ Fraction of 95°W Area Sediments.

| Core | Depth (cms) | Major Elements as Oxides in % | | | | | | | | | | Minor Elements in ppm. | | | | |
|---|---|---|---|---|---|---|---|---|---|---|---|---|---|---|---|---|
| | | $SiO_2$ | $Al_2O_3$ | $Fe_2O_3$ | MgO | CaO | $Na_2O$ | $K_2O$ | $TiO_2$ | $P_2O_5$ | $MnO_2$ | Li | Sr | Ba | V | Cr |
| 160K | 100-125 | 39.9 | 3.72 | 7.32 | 1.68 | 9.68 | 1.05 | 0.29 | 0.23 | 0.60 | 0.09 | 17 | 520 | 995 | 116 | 35 |
| 160K | 200-225 | 46.9 | 6.31 | 7.57 | 3.36 | 3.67 | 2.69 | 0.34 | 0.31 | 0.30 | 0.14 | 37 | 190 | 1660 | 210 | 49 |
| 164G | GRAB | 44.2 | 11.7 | 8.24 | 8.70 | 4.13 | 2.03 | 0.21 | 0.67 | 0.23 | 0.16 | 17 | 200 | 400 | 139 | 82 |
| DOMES smectite (Hein et al. 1979) | | 45.7 | 14.1 | 9.24 | 5.46 | 0.88 | 3.49 | 2.24 | 0.65 | ND | 0.52 | ND | ND | 500 | ND | ND |

| | | Minor Elements in ppm. | | | | | |
|---|---|---|---|---|---|---|---|
| | | Mo | Co | Ni | Cu | Zn | Pb |
| 160K | 100-125 | 4.2 | 26 | 132 | 263 | 385 | 59 |
| 160K | 200-225 | 5.6 | 47 | 320 | 280 | 492 | 40 |
| 164G | GRAB | 6.2 | 26 | 81 | 134 | 231 | 21 |
| DOMES smectite (Hein et al. 1979) | | ND | 200 | 500 | 1100 | 1300 | ND |

| *Mineralogy | d(001) Air Dried Å | d(001) Glycerated Å | d(001) 550°C Å |
|---|---|---|---|
| S+C | 14.3 | 17.9 | 9.8 |
| S+C | 14.3 | 17.7 | 9.5 |
| S+C | 14.3 | 17.9 | 9.9 |
| S | — | — | — |

Analyses expressed to 3 significant figures except for majors <1% and minor elements <100ppm
* S = Smectite C = Chlorite (in order of abundance).

ND = NOT DETERMINED.

TABLE.5.4.2. Correlation Matrix for De Steiguer Deep Area sediments, 95°W.

| | NA | K | MG | AL | MN | FE | CA | CACO3 |
|---|---|---|---|---|---|---|---|---|
| K | .882 | | | | | | | |
| MG | .550 | | | | | | | |
| AL | | | .964 | | | | | |
| MN | | | | | | | | |
| FE | | | .959 | .962 | | | | |
| CA | -.759 | -.738 | -.790 | -.747 | | -.761 | | |
| CACO3 | -.759 | -.737 | -.790 | -.747 | | -.762 | 1.000 | |
| SIO2 | | | .858 | .899 | | .820 | .602 | -.602 |
| LI | | | | | | | | |
| SR | | | -.632 | -.543 | | -.575 | .706 | -.706 |
| LA | .688 | .781 | | | | | .544 | -.544 |
| TI | | | .976 | .991 | | .964 | .709 | -.709 |
| V | .786 | .749 | .808 | .721 | | .802 | .891 | -.891 |
| CO | .779 | .754 | .654 | .587 | | .703 | .716 | -.716 |
| NI | .849 | .827 | | | | | .623 | -.622 |
| CU | | | | | | | | |
| ZN | .745 | .808 | | | | | .717 | -.717 |
| PB | | | | | | | | |
| P | | | | | | | | |

| | SIO2 | LI | SR | LA | TI | V | CO | NI |
|---|---|---|---|---|---|---|---|---|
| LI | | | | | | | | |
| SR | | | | | | | | |
| LA | | | | | | | | |
| TI | .893 | | -.553 | | | | | |
| V | | | -.603 | .635 | .717 | | | |
| CO | | | | .640 | .578 | .781 | | |
| NI | | | | .710 | | .607 | .783 | |
| CU | | | | | | | | |
| ZN | | | | .656 | | .739 | .748 | .816 |
| PB | | | | | | | | |
| P | | | | .662 | | | | |

The cut-off value for r (correlation coefficient) at 99.9% confidence is ± 0.54.

taken from Hein et al. (1979). It should be noted that the high level of Sr and Ca in 160K (100 - 125 cms) suggests the incomplete removal of $CaCO_3$. Generally, the level of $SiO_2$, Fe, Mg, Na and Ti are broadly similar, although variations do exist. DOMES smectite is higher than 95°W smectites in Al, K and Mn (see Table 5.4.1), whereas Ca is appreciably higher in 95°W smectites. Fe/Al ratios range from 0.9 to 2.6 in 95°W area smectites while DOMES smectite has an Fe/Al of 0.9. Of the trace metals, Co, Ni, Cu and Zn are more enriched in DOMES smectites which are located in the equatorial North Pacific trace metal-enriched Mn nodule belt (Hein et al., 1979). Although Ba is more enriched in 95°W smectites, the DOMES authigenic smectites exhibit greater concentrations of trace metals. In spite of the differences outlined above, 95°W smectite composition, although variable, is broadly similar to DOMES smectite and is typical of an Fe-rich montmorillonite, as was found for the clay fraction of GRAFZI area sediments.

### 5.4.3 Element Associations

Significant correlations at the 99.9% confidence level for the 34 samples from the De Steiguer Deep Area are reported in Table 5.4.2. The analysis of element correlations is used to confirm the associations between certain elements in the downcore profiles (Section 5.4.1) and to identify further element associations. Na and K correlate positively with Mg, La, V, Co, Ni and Zn, and it has already been noted that Na and K are dominantly associated with clay minerals in deep-sea sediments (Welby, 1958). Therefore, it is likely that these elements occupy smectite sites in 95°W area sediments, as found in the GRAFZI area. Mg and Al show strong positive correlation with Fe, $SiO_2$, Ti, V and Co. In summary, element associations confirm the previously stated hypothesis that, in order of importance, clay minerals and FeTi basalt detritus are the major element suppliers in the non-carbonate fraction of 95°W area sediments.

The purity of the $CaCO_3$ phase is confirmed by the fact that $CaCO_3$ only correlates with Sr. The correlation of La with P appears to confirm the possibility that lanthanide phosphates, namely skeletal

apatite, occurs in 95°W area sediments. No correlations of trace metals with Mn occur, suggesting the quantitative unimportance of Mn oxides as element suppliers to 95°W area sediments, although association of Mn with trace metals was found previously in 146D and 160K sediments.

## 5.5 FUTURE EXPLORATION FOR HYDROTHERMAL DEPOSITS IN THE DE STEIGUER DEEP AREA

The maximum Mn content of 4.7% in De Steiguer Deep Area surface sediments is found in dredge 146D, compared to a maximum in GRAFZI sediments of 8.2% Mn. Moore and Vogt (1976) reported the finding of hydrothermal Mn oxides at Stations D6 and D9 (see Figure 5.1.1). Station 146D is positioned between these two hydrothermal Mn oxide localities, and on crust less than 2 million years old. Sampling at Station 146D also recovered Fe hydroxide-stained basalts, providing further evidence of hydrothermal activity.

Localities D6, 146D and D9 all lie on a linear traverse perpendicular to the G.S.A. Moore and Vogt (1976) commented that sample D9 had a 3 mm-thick hydrogenous Mn crust overlying the hydrothermal Mn oxide and that about 1 million years had elapsed since hydrothermal activity ceased. This would date the termination of hydrothermal activity at Site D9 which was at that time located on crust of 1.4 million years of age, i.e. in the vicinity where 146D surface sediment is currently being deposited. The implication of this is that the hydrothermalism occurred on oceanic crust younger than 1.4 million years of age. This is supported by a hydrothermal Mn crust from D6 (0.3 million years crustal age) and surface sediment from 146D, which can be tenuously ascribed a hydrothermal origin.

Hydrogenous precipitation of ferromanganese oxides occurred as Site D9 was transported to its present position by seafloor spreading. It is not known exactly where the hydrothermally active area is located but future exploration should be focussed on the traverse between 146D and the G.S.A., on oceanic crust younger than about 1.4 million years old.

Two other potential exploration targets for hydrothermal deposits exist in this area;

1. Basins where ponded metalliferous sediments may accumulate. These structures have been well detailed as possible sites for hydrothermal deposits (Cronan, 1980).
2. The fracture zone at 95°27'W, where structures within the oceanic crust below the mid-ocean ridge are exposed.

The first exploration target was to some extent sampled by core 160K, which recovered ferromanganese oxides but of a hydrogenous nature. The second exploration target is potentially more interesting, as the deep stockwork of a possible hydrothermal system might be exposed (see Chapter 6), where sulphides may be deposited.

STUDY C CHAPTER 6

# THE HESS DEEP AREA OF THE GALAPAGOS RIFT AT 101°W, NEAR THE PACIFIC-COCOS-NAZCA PLATE TRIPLE JUNCTION

## 6.1 INTRODUCTION

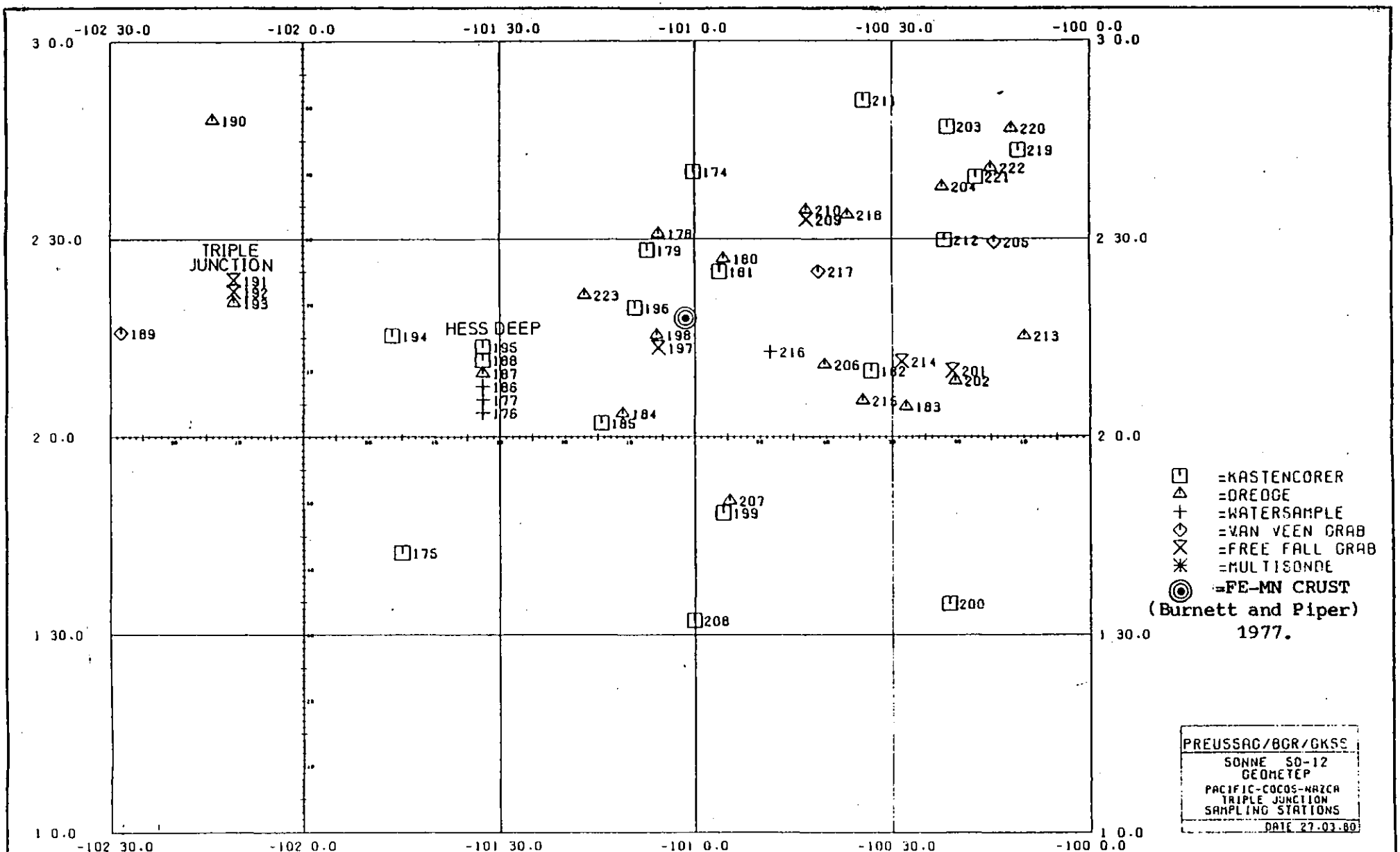
Burnett and Piper (1977) provided the first evidence showing that hydrothermal deposits were to be found at 101°W on the Galapagos Rift. These authors reported a 16 mm-thick ferromanganese oxide crust which formed at a rate of about 1 mm/$10^3$ years.

More recent investigations of this area were carried out by the R/V 'SONNE' in 1980, during the GEOMETEP cruise. Bathymetric data from this cruise indicate that the Fe-Mn crust reported by Burnett and Piper (1977), at a depth of 3150 m, is located considerably further east than the deepest part of the Hess Deep (See Figure 6.1.1).

Gordeev and Demina (1979) observed that Hess Deep near-bottom waters contain unusually high contents of Fe, Mn, Cu and Zn in suspension and high concentrations of these metals in solution, in the vicinity of supposed hydrothermal vents. The authors interpreted the high suspended concentrations of Fe, Mn, Cu and Zn as due to the adsorption of metals by amorphous hydroxides of Fe and Mn, as proposed here for the GRAFZI area (see Chapter 2). Anomalous metal concentrations in suspension could be detected in seawater at a distance of up to 2500 m from the bottom of the Hess Deep (Gordeev and Demina, 1979).

Further evidence of hydrothermal processes operating in the Hess Deep was given by the discovery of hydrothermal talc (Murdmaa and Rozanova, 1976) and serpentine (Schmitz et al., 1982). Both of these minerals have been found to have a hydrothermal origin in the Red Sea (Backer, 1976; Schneider and Schumann, 1979). Hydrothermal talc and serpentine have also been reported in the Gulf of California (Lonsdale et al., 1980) and at the 21°N site on the E.P.R. (Oudin, 1983), respectively.

FIG.6.1.1. Station locations in the $101^{0}$W area of the Galapagos Rift.



The present study utilises 45 sediment samples (from 12 cores, 4 dredge barrels, 1 grab - see Figure 6.1.1) recovered from the 101°W area of the Galapagos Rift, during the GEOMETEP cruise of 1980. Besides this regional approach, a more localised study of the Hess Deep is included and is based upon 21 samples from the R/V 'DISCOVERY' cruise of 1980. These samples comprise 2 cores, 1 mud pellet and 1 ferromanganese oxide-coated pebble. Sediments from the Hess Deep and from the Galapagos Rift, in the 101°W area, are different in composition and are treated separately in the following sections.

## 6.2 GEOLOGY, BATHYMETRY AND STRUCTURE

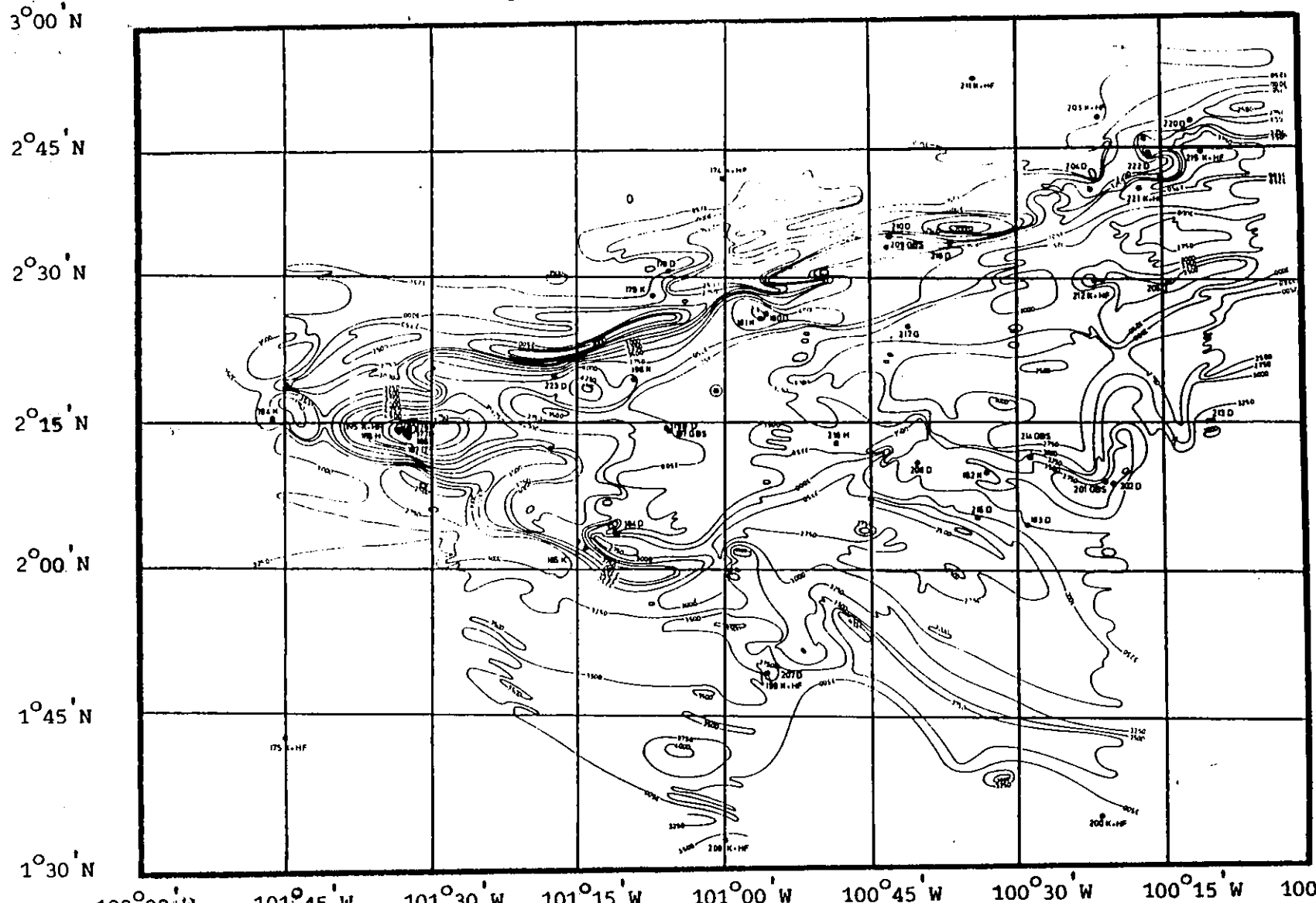
### 6.2.1 The 101°W Area of the Galapagos Rift

Hey (1977) and Lonsdale (1977a) considered that the Cocos and Nazca Plates formed approximately 25 million years ago, due to the break-up of the ancient Farallon Plate. This break-up is thought to have occurred in the vicinity of the Marquesas Fracture Zone. Since then, the Triple Junction (i.e. the Pacific-Cocos-Nazca Plate Triple Junction) has shifted from about 5°S to its present position, at 2°11'N and 102°10'W (Hey et al., 1972).

Hey et al. (1972) observed that seafloor spreading from the 3 spreading axes caused a wedge of crust accreted from the Galapagos Spreading Axis (G.S.A.). This wedge is flanked by marginal highs and is much rougher topographically than crustal material formed from the faster accreting E.P.R. The wedge-shaped crust, which widens to 90 Kms at its eastward extremity, is also about 400 m shallower than the E.P.R. flanks. However, topographic variation is pronounced, varying from 2190 m on the G.S.A. flanks to over 5000 m in the Hess Deep. This Deep is located some 50 Kms from the Triple Junction and from this point the Galapagos Rift widens eastwards, with the oldest crust dated at 30 million years of age (Hey et al., 1972).

Lonsdale (1977a) stressed that morphological differences between the Galapagos Rift; with a deep axial valley flanked by topographically irregular crust; and the E.P.R.; typically with an axial 100 to 400 m high ridge of about 10 to 30 Kms width; could be explained by spreading rate differences. Hey et al. (1977) found differences in spreading

FIG.6.2.1. Bathymetry of the 101°W area of the Galapagos Rift.



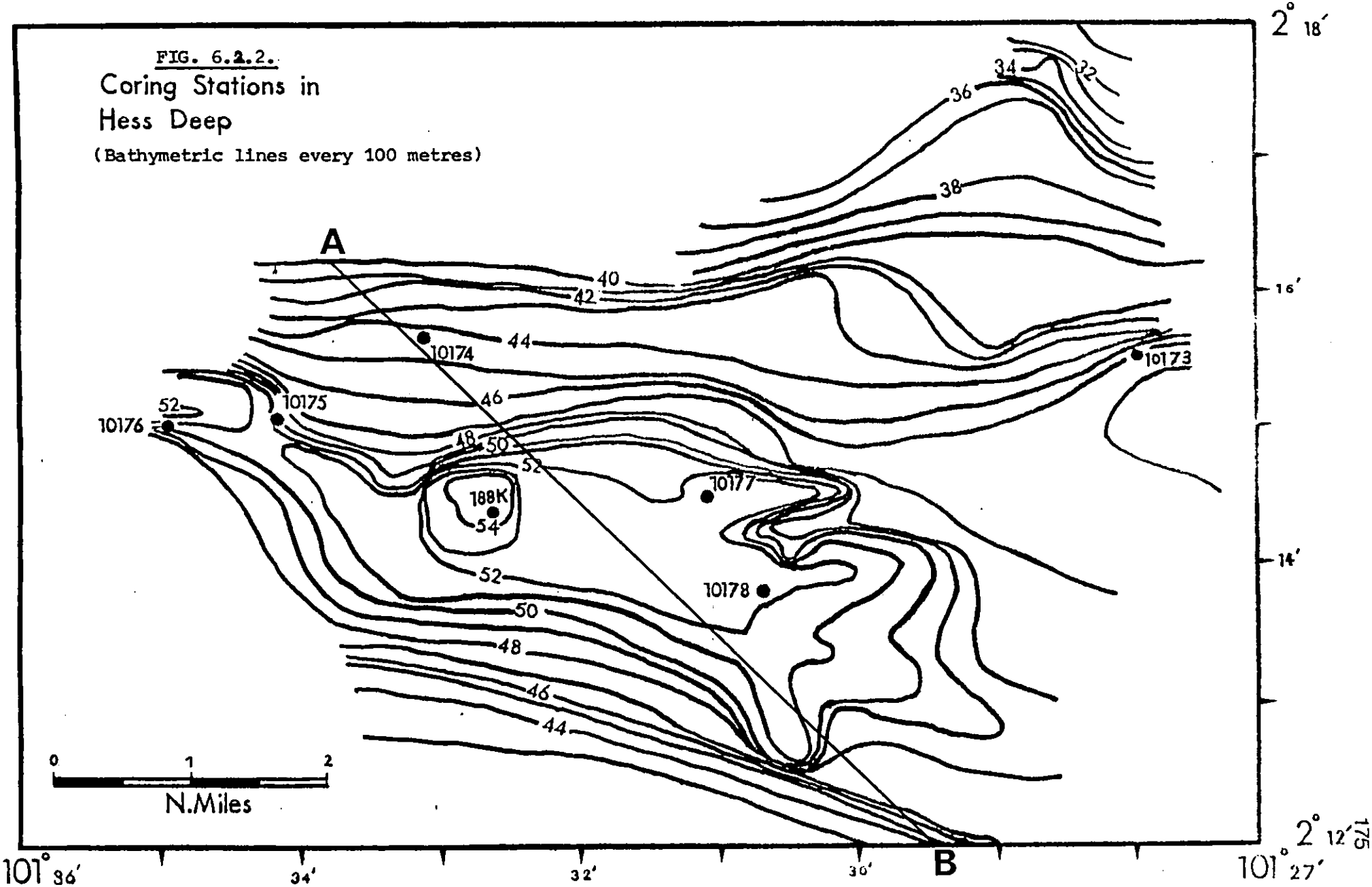

KEY

⊙ FE-MN CRUST
(Burnett & Piper, 1977)

FIG. 6.2.2.

Coring Stations in Hess Deep

(Bathymetric lines every 100 metres)



rates for the Panama Fracture Zone area of the G.S.A. (72 mm/year) and the Triple Junction area of the G.S.A. (42 mm/year). These are responsible for maintaining the wedge-shaped structure of crust accreted from the G.S.A. The same authors also observed asymmetric accretion on the Galapagos Rift and the magnetic record suggests that this is due to small, discrete jumps of the G.S.A. in a southerly direction, both forming and destroying transform faults.

The wedge-shaped topographically irregular crust, in the 101°W area, which is flanked by marginal highs was mapped during the R/V 'SONNE' cruise of 1980 and is shown, along with station locations, in Figure 6.2.1.

### 6.2.2 The Hess Deep, at 101°30'W

The Hess Deep was described by Hey et al. (1972) and bathymetric data from this work show that the maximum water depth is about 5440 m. The R/V 'DISCOVERY' bathymetric chart is shown in Figure 6.2.2., along with station locations (the Section A-B is referred to later).

The Deep occupies a unique position, at the apex of the wedge-shaped crust formed at the G.S.A. Zonenshain et al. (1980) included the Hess Deep within this wedge, while Lonsdale (1977a) stated that the Hess Deep is an extensional split in relatively old oceanic crust that has been invaded by the lengthening magma chamber beneath the G.S.A. He also suggested that the Hess Deep walls are tilted and uplifted parts of the east flank of the E.P.R.

The differences of opinion concerning the Hess Deep, i.e. whether it is located on E.P.R. crust or on crust accreted from the G.S.A., in part, stem from the poorly-defined limits of the structure itself. From the bathymetric data now available, the writer has taken the Hess Deep to be that area lying deeper than the 4000 m contour, in the 101°30'W area, as such depths are unusual for typical Eastern Pacific spreading centres.

## 6.3 SAMPLE DESCRIPTION

The 45 sediments that were taken from the GEOMETEP cruise have been sub-divided. Six of them (from core 188K) were located within the Hess Deep and are discussed later. The remaining 39 samples came from the 101°W area, outside of the Hess Deep.

### 6.3.1 The 101°W Area of the Galapagos Rift

The grain size of all top sediment samples from the cores studied is dominated by the >63μ fraction, due to the presence of abundant foraminifera. However, the silt and clay fraction, i.e. less than 63μ, increases up to more than 50% at depth in some cores. The cores generally display changes in colour with increasing depth, typically from dark to light yellowish brown (10 YR 4/2, 10 YR 6/4 - see Appendix D) to grayish yellow green (5 GY 7/2) and pale olive (10 Y 6/2). Occasionally, thin volcanic ash bands can be found in the lower portions of the cores, with fragments up to 8 mm in size.

Dredges in the 101°W area recovered ferromanganese oxide - stained basalts and also sediment samples with the carbonate fraction in various states of dissolution. A smear slide study of these sediments, from various water depths, indicates that foraminifera are badly corroded between 3450 and 3882 m and this is related to the C.C.D. (see Section 6.4).

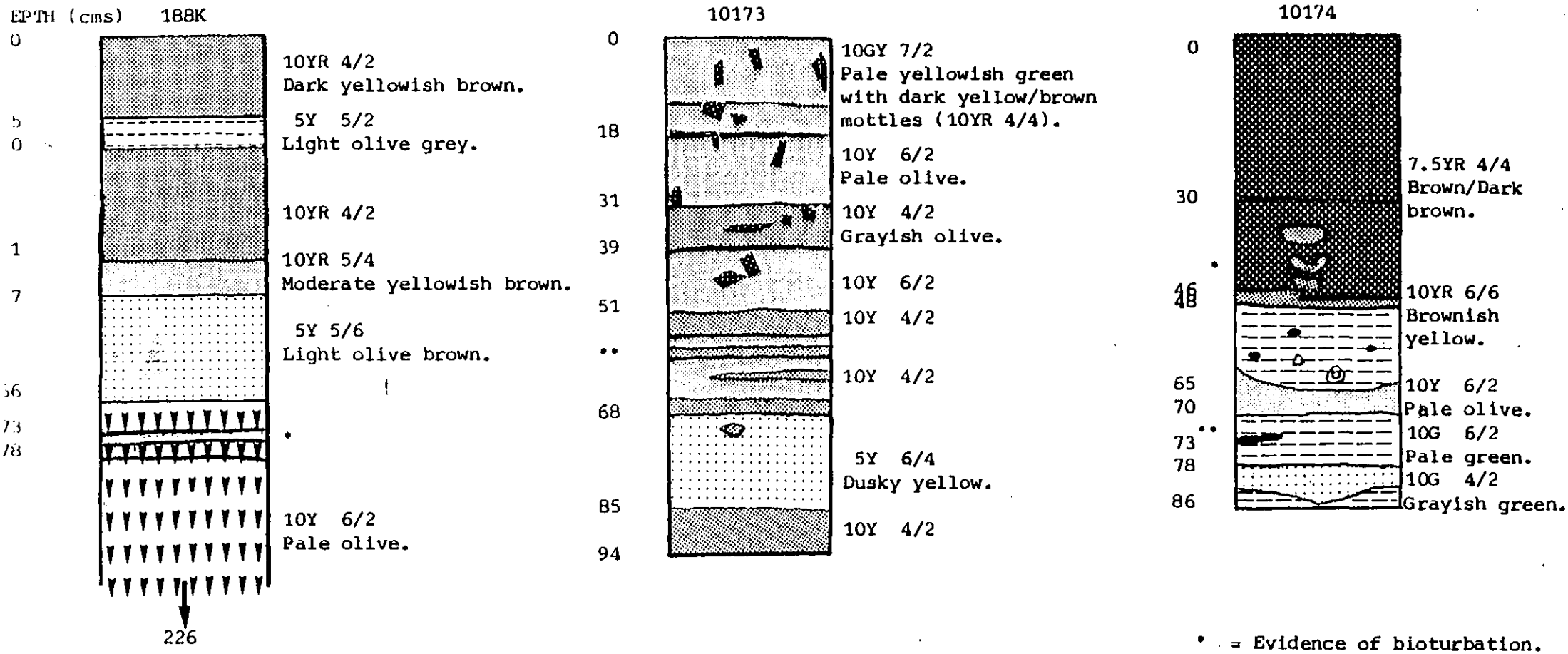
### 6.3.2 The Hess Deep

Twenty seven samples from the Hess Deep were recovered during the two cruises mentioned above and the sedimentology of some of these samples is described below.

*Station 10176 (Depth = 5122 m)*

The core only retrieved one ferromanganese oxide-coated pebble of 7 cms diameter. A 1 cm-thick ferromanganese oxide crust was taken from the side of the pebble interpreted as the top, while a 2 mm-thick ferromanganese oxide coating was sampled from the bottom, where a shark's tooth was found.

FIG. 6.3.1. Core descriptions for stations taken in the Hess Deep.




• = Volcanic ash-rich laminations.

•• = Volcanic ash-rich bands intercalated with pale olive clay from 51-68 cms.

• = Evidence of bioturbation.

•• = Lens of ash-rich material

COLOUR CODING ACCORDING TO STANDARD U.S.G.S. AND MUNSELL ROCK AND SOIL COLOUR CHARTS.

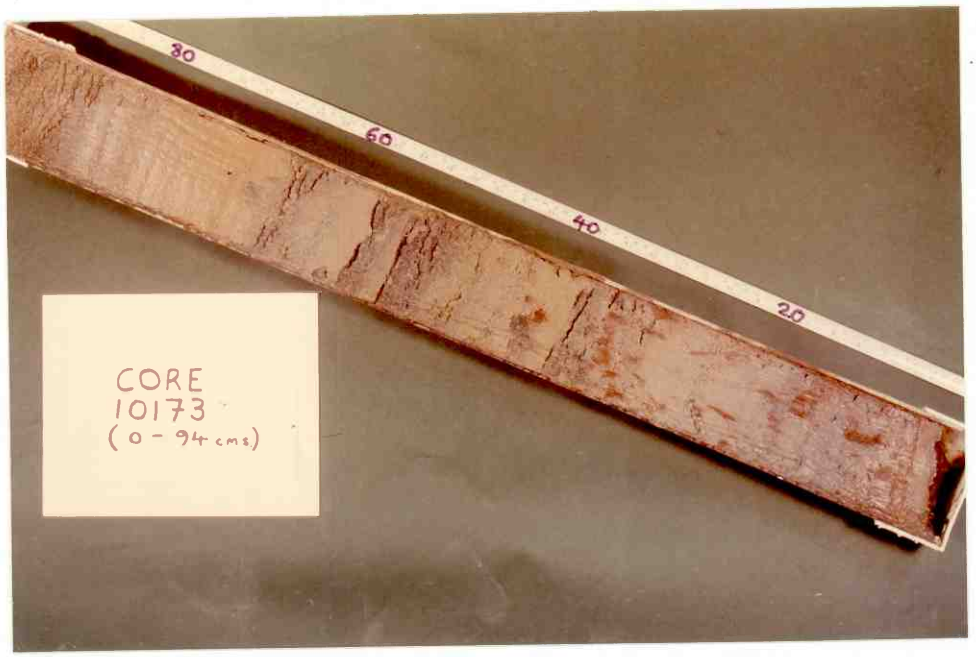



PLATE 6.3.1. Core 10173- the depth of the oxidised zone = 42 cms.

PLATE 6.3.2. Core 10174- the depth of the oxidised zone = 46 cms.



*Station 10178 (Depth = 5198 m)*

One pellet of firm, red-brown mud (Hue 2.5 YR 4/4), with patches of grayish yellow (Hue 5 GY 7/2), was recovered. Some sponge spicules and brown semi-opaque grains are present, as is chalcedonic silica. However, the smear slide of this sediment is dominated by reddish-tinged green clay minerals and basaltic glass.

*Station 188K (Depth = 5440 m)*

This core has been documented in detail in Schmitz et al. (1982) and consists of an upper oxidised zone of about 46 cms thickness which is ferruginous and with little $CaCO_3$. Below this depth, the reduced layer extends to the core base at 226 cms depth, with some fine volcanic ash laminations (see Figure 6.3.1). The sand-size fraction of the core (>63$\mu$) consists of basaltic debris and from 52 - 58 cms also contains a small amount of $CaCO_3$. The <63$\mu$ fraction of the core increases to a maximum of 90%, between 74 and 200 cms. Smear slide analysis identified abundant biogenic silica and clay minerals in this fraction. A description of core 188K is shown in Figure 6.3.1.

*Station 10173 (Depth = 4716 m)*

Core 10173 is 94 cms long, with an upper oxidised layer of about 42 cms thickness, characterised by dark yellow, brown mottles (Hue 10 YR 4/4) within a pale olive matrix (Hue 10 Y 6/2). Five smear slides were taken from core 10173 (see Figure 6.3.1 and Plate 6.3.1) and the sediments are described below.

The smear slides from the upper oxidised zone of the core contain orange, semi-opaque, subhedral ferric hydroxides and broken fragments of mosaic structures of spherical and spiral-shaped radiolaria. Calcite grains (with a corroded appearance), quartz, chalcedonic silica and sponge spicules can also be identified, along with abundant green clay minerals occurring in aggregates and often enclosing black, opaque fragments. With increasing depth downcore, the abundance of jagged volcanic fragments increases and these are often rimmed with clay minerals which become lighter in colour with depth.

*Station 10174 (Depth = 4567 m)*

Core 10174 is 86 cms in length and has a much more pronounced upper oxidised layer than core 10173. This layer extends to 46 cms depth (see Figure 6.3.1 and Plate 6.3.2). The upper sediment layer (Hue 7.5 YR 4/4, dark brown) is less indurated and less friable than the lower sediment layer (Hue 10 G 6/2, pale green), which shows some disturbance due to bioturbation. The lower core is mottled with darker grayish green patches (Hue 10 G 4/2) and with occasional ash-rich horizons and burrow-like structures.

Smear slide analysis of core 10174 shows that it contains abundant siliceous microfossils with brown clay minerals at their margins, along with semi-opaque ferric hydroxides and rare calcite rhombs. As in core 10173, the amount of volcanic ash fragments increases with depth, as the clay minerals take on a green hue below the upper oxidised sediment layer.

## 6.4 BULK GEOCHEMISTRY

As with the previous section, sediments from the 101°W area of the Galapagos Rift and from the Hess Deep are treated separately in the following sections due to important geochemical and mineralogical differences between them.

### 6.4.1 Bulk Geochemistry of 101°W Area Sediments

According to the classification of Olausson (1960), the 39 sediments from the 101°W area of the Galapagos Rift, outside of the Hess Deep, are foraminiferal marl (6 samples) and chalk (33 samples) oozes. The $CaCO_3$ content ranges from 40% to 92% between water depths of 4377 m and 3060 m.

The depth of the C.C.D. in this area was placed at about 3600 m, by Berger et al. (1976), with a transition zone of 100 m thickness above it, where $CaCO_3$ contents decreased towards the C.C.D. Previous smear slide descriptions (Section 6.3) showed the increasing effects of calcium carbonate dissolution between 3450 m and 3882 m water depth, which agrees with the data of the above authors.

FIG.6.4.1.Scatter plot of $CaCO_3$ versus Water Depth.

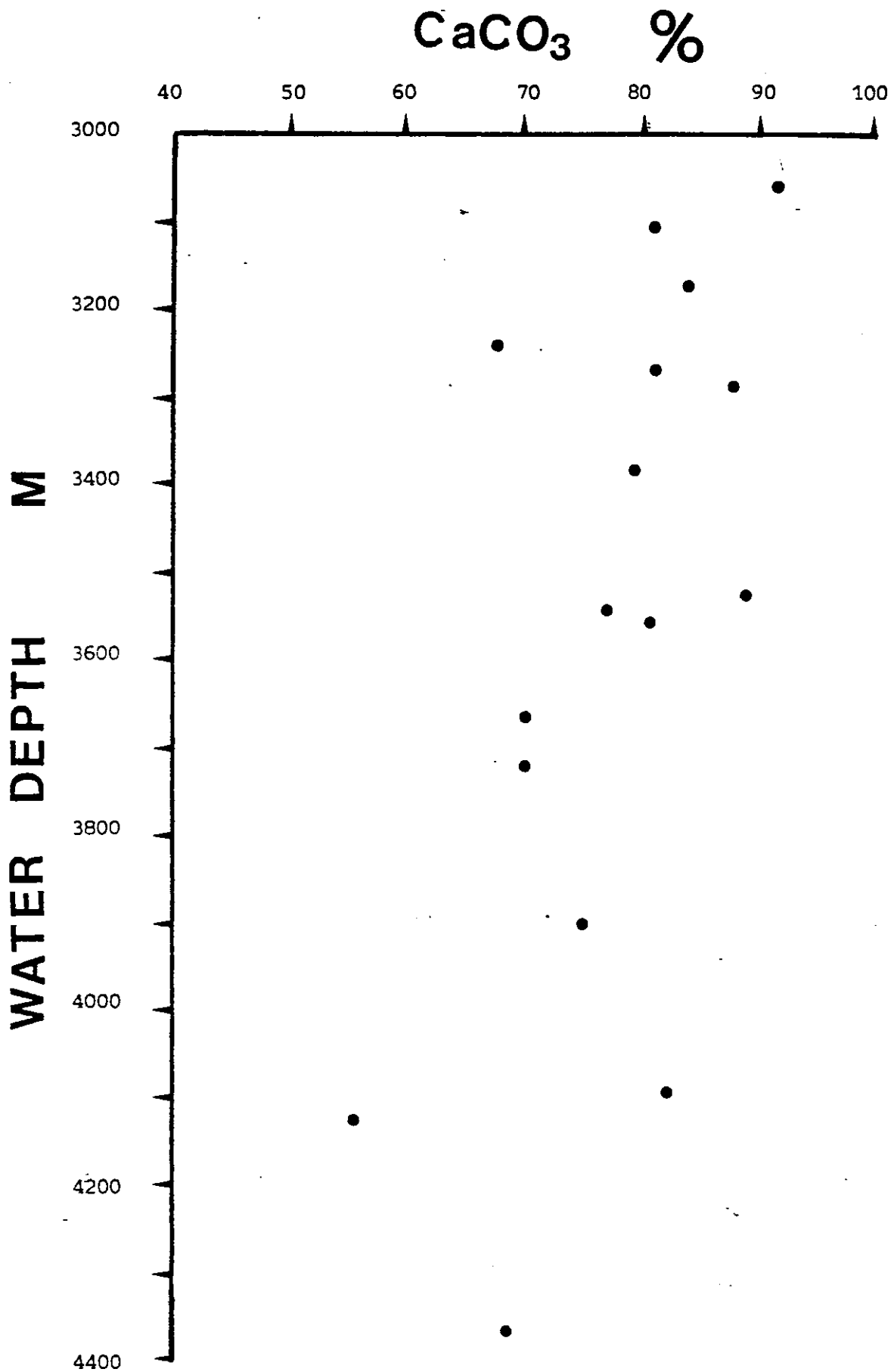


Figure 6.4.1 shows the content of $CaCO_3$ in 101°W area surface sediments, expressed as a function of water depth. The scatter plot shows that $CaCO_3$ occurs below the level of the C.C.D. which is probably related to extensive slumping of material from topographically higher locations, as noted by Cronan and Varnavas (1981) at 9°S, on the E.P.R.

Samples from core 181K, which were located at a depth of 4377 m, contain the least amounts of $CaCO_3$ (40%). A maximum value of 46% $SiO_2$ for this core can be accounted for by the presence of abundant biogenic debris and clay minerals. Basaltic debris and clay minerals may both supply Mg and Al to sediments in the 101°W area. However, Na, K, Mg and Al all show high concentrations in the same samples (reported in Appendix C, on a carbonate free basis) and the quantitative lack of basaltic debris, compared to clay minerals, suggests that the latter is the dominant site for the elements.

Sr (maximum of 1250 ppm), La (maximum of 173 ppm) and P (maximum of 5210 ppm) are known to be associated with deep-sea carbonate sediments and biogenic material (Arrhenius et al., 1957; El Wakeel and Riley, 1961; Emiliani, 1955). Sr-substituted foraminiferal tests and lanthanide-rich skeletal apatite have been shown to contribute these elements in the GRAFZI and De Steiguer Deep areas and the same is thought to occur in 101°W area sediments.

Ti shows a maximum abundance of 2770 ppm in a sample containing 4% Al and the association of these two elements in basaltic detritus is common. Goldberg and Arrhenius (1958) noted basaltic, clay mineral and Fe oxide sites for V while Horder (1979) showed a volcanogenic origin for Li, which was present in both clay mineral and basaltic components of the sediment. Although the maximum abundances of Li (82 ppm) and V (371 ppm) do not occur in the sample richest in Ti, basaltic debris, and more importantly, clay minerals, are thought to contribute these elements, as found elsewhere on the Galapagos Rift (this study). Statistical analysis confirms the close association of Ti, V and Li (see Section 6.8).

FIG.6.4.2. Fe/Mn ratios in surface sediments from the 101°W area.

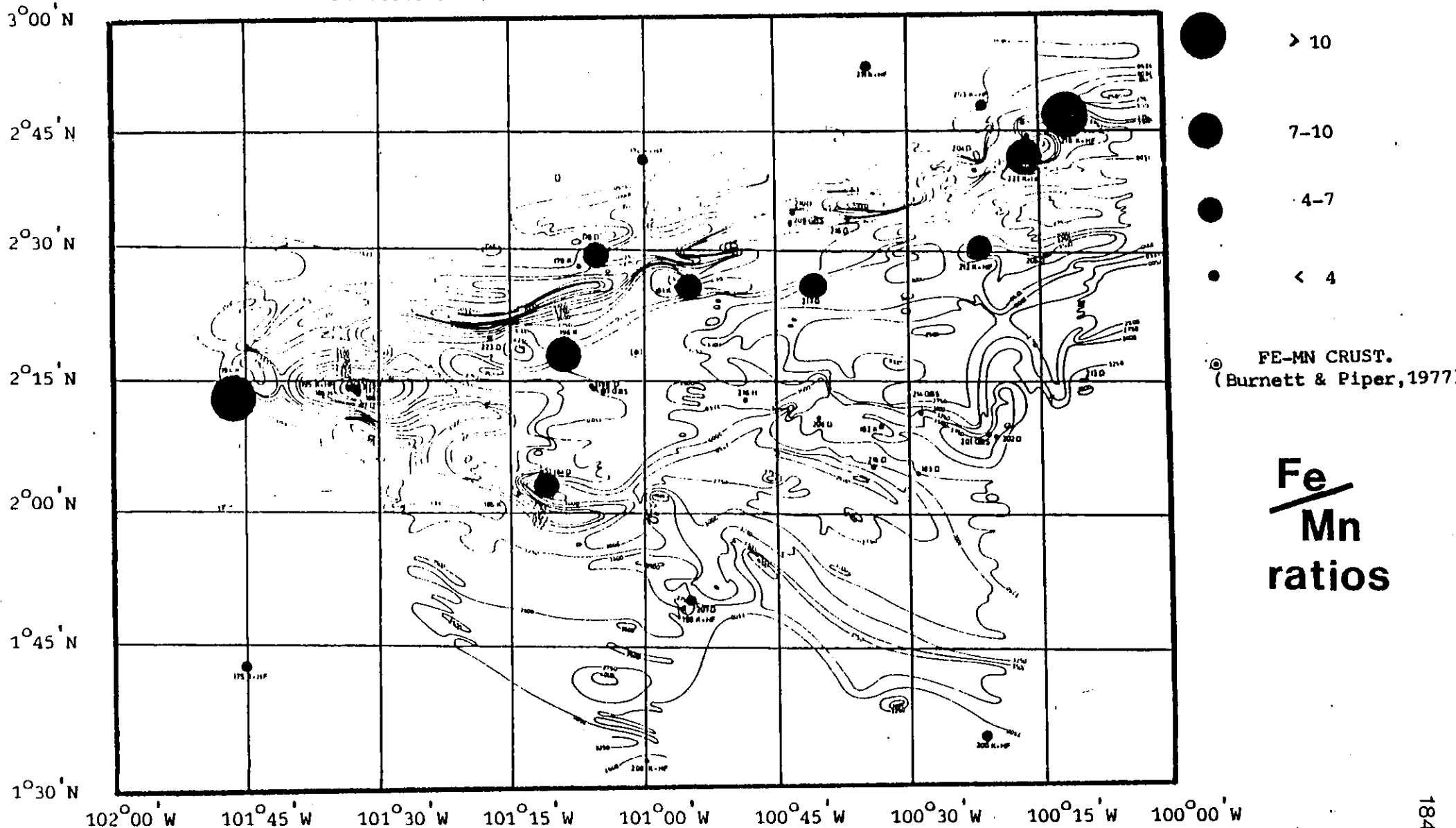


FIG.6.4.3. Cu in surface sediments from the 101°W area.

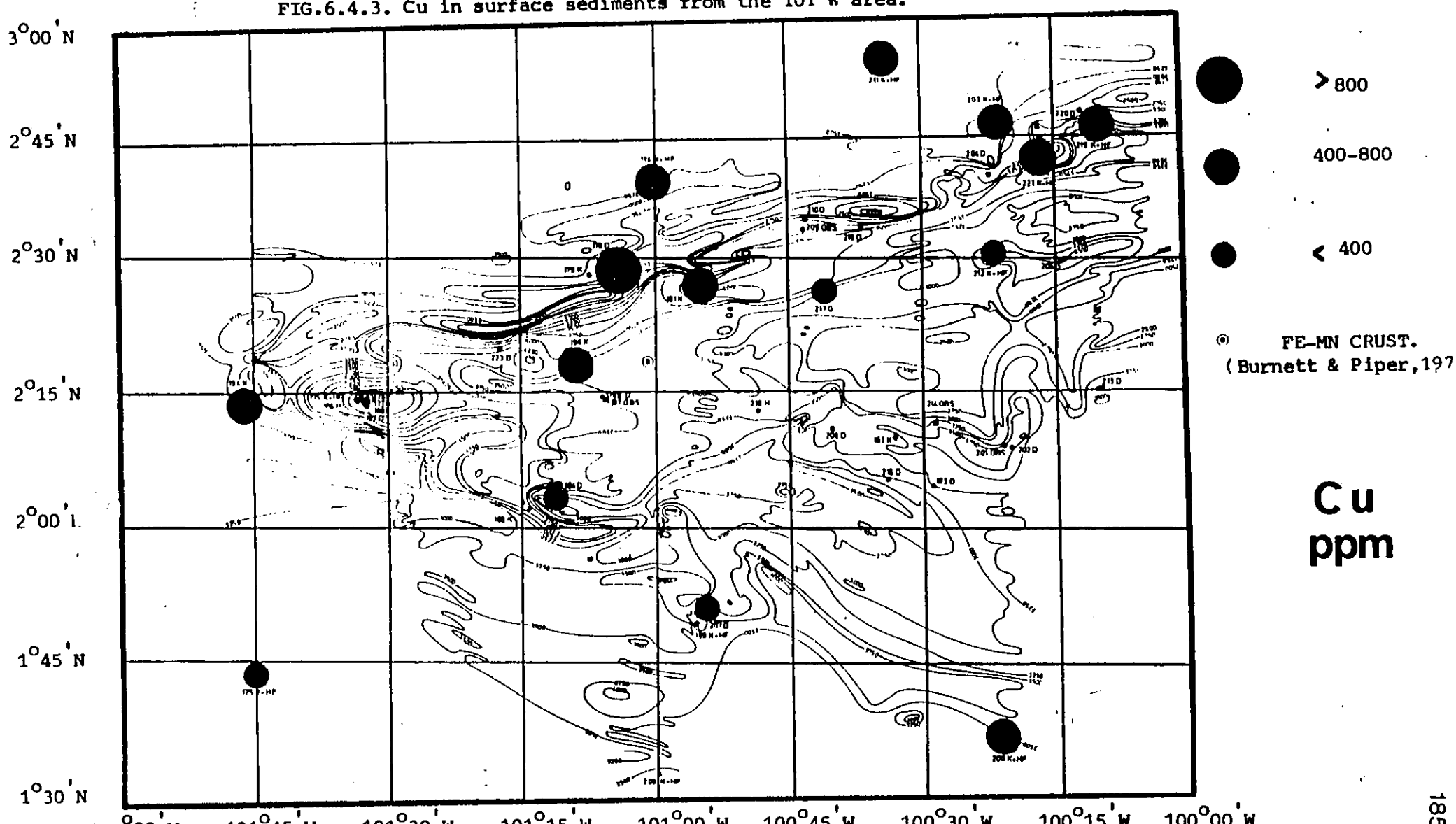
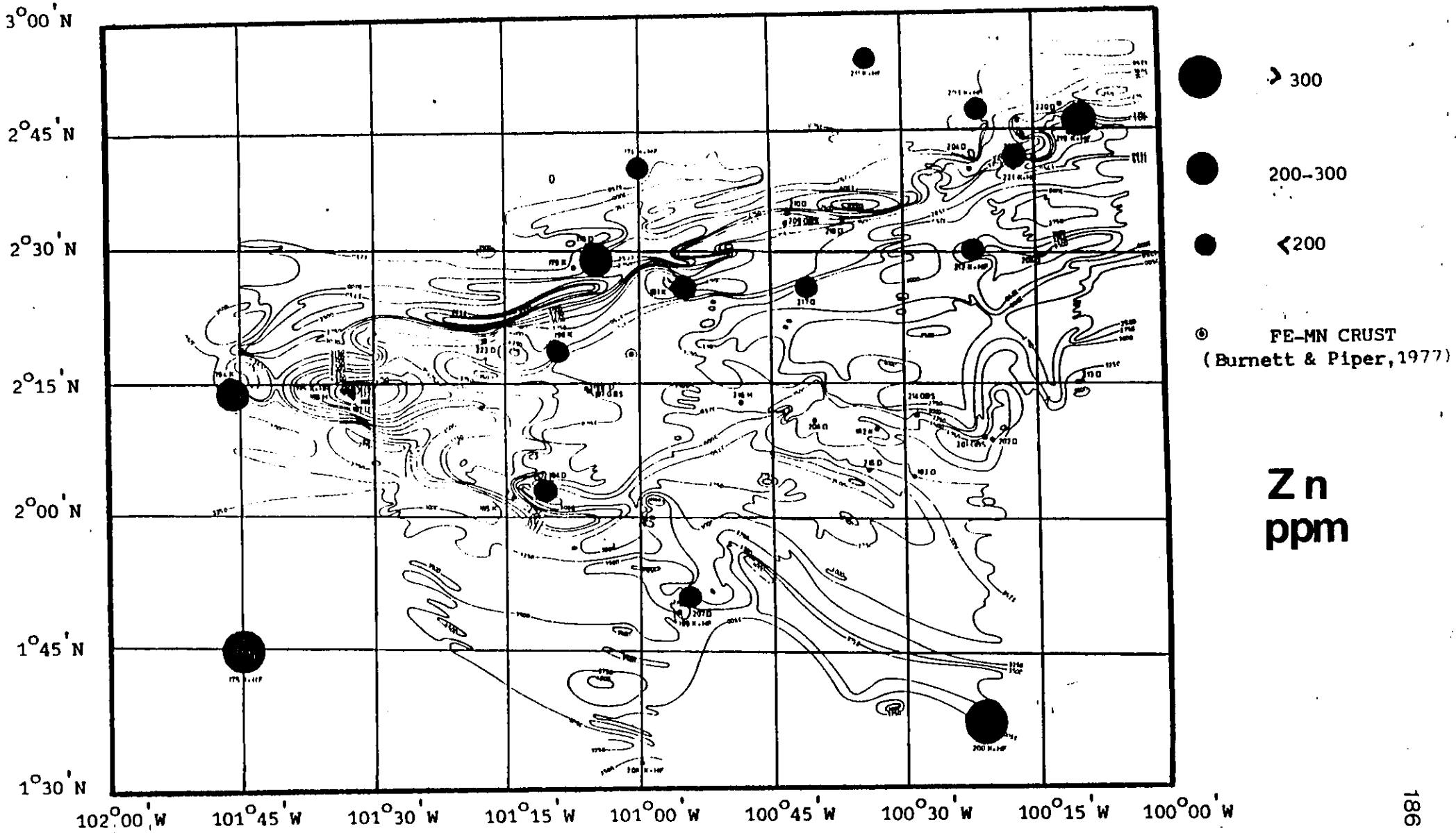


FIG.6.4.4.Zn in surface sediments from the 101°W area.



Co, Ni and Pb show maxima of 142 ppm, 443 ppm and 86 ppm respectively, in the same sample, which can be ascribed to the adsorption of these elements onto the oxides of Fe and Mn. To investigate the possibility of a hydrothermal supply of elements in the 101°W area, the concentrations of Fe, Mn, Cu and Zn in surface sediments is now examined.

The spatial relationship between Fe/Mn, Cu and Zn concentrations in surface sediments in the 101°W area is shown in Figures 6.4.2 - 6.4.4. In the sediments, the clay mineral content is low (see Section 6.3.1) and they largely consist of $CaCO_3$. Similarly, basaltic debris is not common at the core tops and smear slides have shown that the dominant source of Fe and Mn is from amorphous oxyhydroxides. The Fe/Mn ratio may reflect to what degree these two elements have fractionated from a possible original hydrothermal source.

Burnett and Piper(1977) found an Fe-Mn oxide crust without severe fractionation of Fe from Mn in this area. Figure 6.4.2 shows that core 194K, at the apex of the crust accreted from the G.S.A. (Section 6.2), and core 219K, in the marginal high area of G.S.A. accreted crust, both show high Fe/Mn ratios and may be located near hydrothermal vents, where $Mn^{2+}$ has been dispersed in seawater (see Chapter 2) and $Fe^{3+}$ precipitated as oxides. The maximum abundance of Fe (9.7%) in surface sediment is found in dredge 178D, which is situated in the marginal highs area. However, the Mn content of 2.1% lowers the Fe/Mn ratio in this sample. The maximum abundance of Mn (3.0%) in surface sediment is found in core 200K, which is located much further south than the other stations (see Figure 6.4.2).

Cu/Zn ratios are fairly constant and range from 0.9 to 3.3. The latter value is found in dredge 178D sediment as shown above, containing 9.7% Fe. In the GRAFZI area, high Fe values and high Cu/Zn ratios are found in the vicinity of hydrothermal sulphide mounds. Cu (Figure 6.4.3) and Zn (Figure 6.4.4) show maximum abundances in surface sediments from stations 178D and 200K, respectively, which also show

high concentrations of Fe and Mn. Of interest is the observation that maxima of Mn and Zn and of Fe and Cu in the same sample, may show the preference of each trace element to adsorb onto Mn or Fe oxides. This was especially important in the GRAFZI area (see Chapter 2) where it was found that Zn, adsorbed onto Mn oxides, was dispersed considerably further distances than Cu, generally associated with Fe oxides.

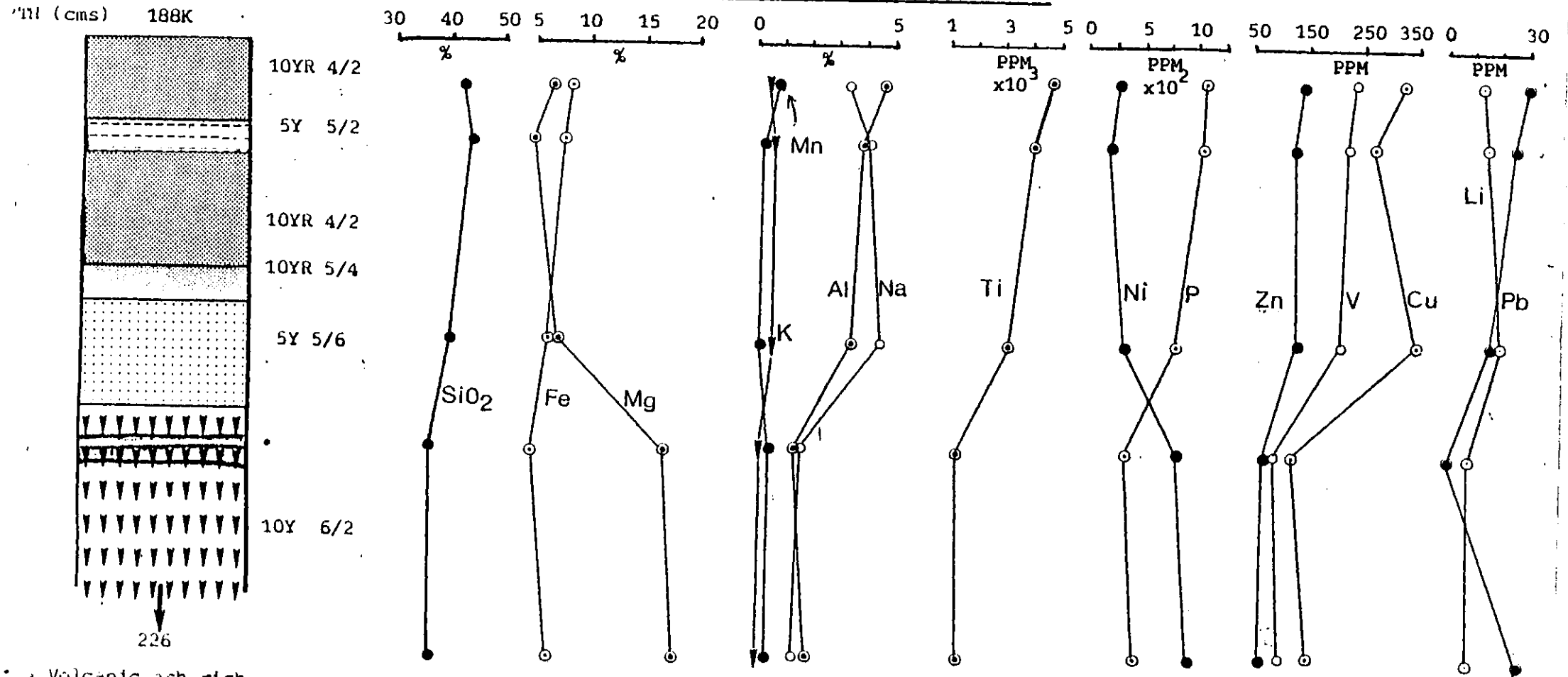
6.4.2 Bulk Geochemistry of Hess Deep Sediments

The Hess Deep sediments studied are dominantly diatom and radiolarian oozes. $CaCO_3$ values range from zero to 38.9%, while $SiO_2$ varies from 34.6% to 44.4%. Some sedimentological work on these sediments has been described in Section 6.3.2, and is typical of largely-carbonate free sediments from below the C.C.D.

In addition to the 25 Hess Deep sediments, 2 Fe-Mn oxide encrustations from a 7 cm diameter pebble were analysed. They are of similar composition, with Fe/Mn ratios of 3.0 to 3.3, and with maximum Fe and Mn contents of 23.3% and 7.7%, respectively. Trace metal values are very similar to those reported for the rapidly-deposited Fe-Mn oxide crust of Burnett and Piper (1977) with the exception of Ni, which at 870 ppm, is less than half the value reported by these authors, of 1950 ppm. The Fe/Mn ratio of 3.0 is greater than the 1.3 reported by Burnett and Piper (1977), although both of these Fe-Mn oxides exhibit a lack of severe fractionation of Fe from Mn.

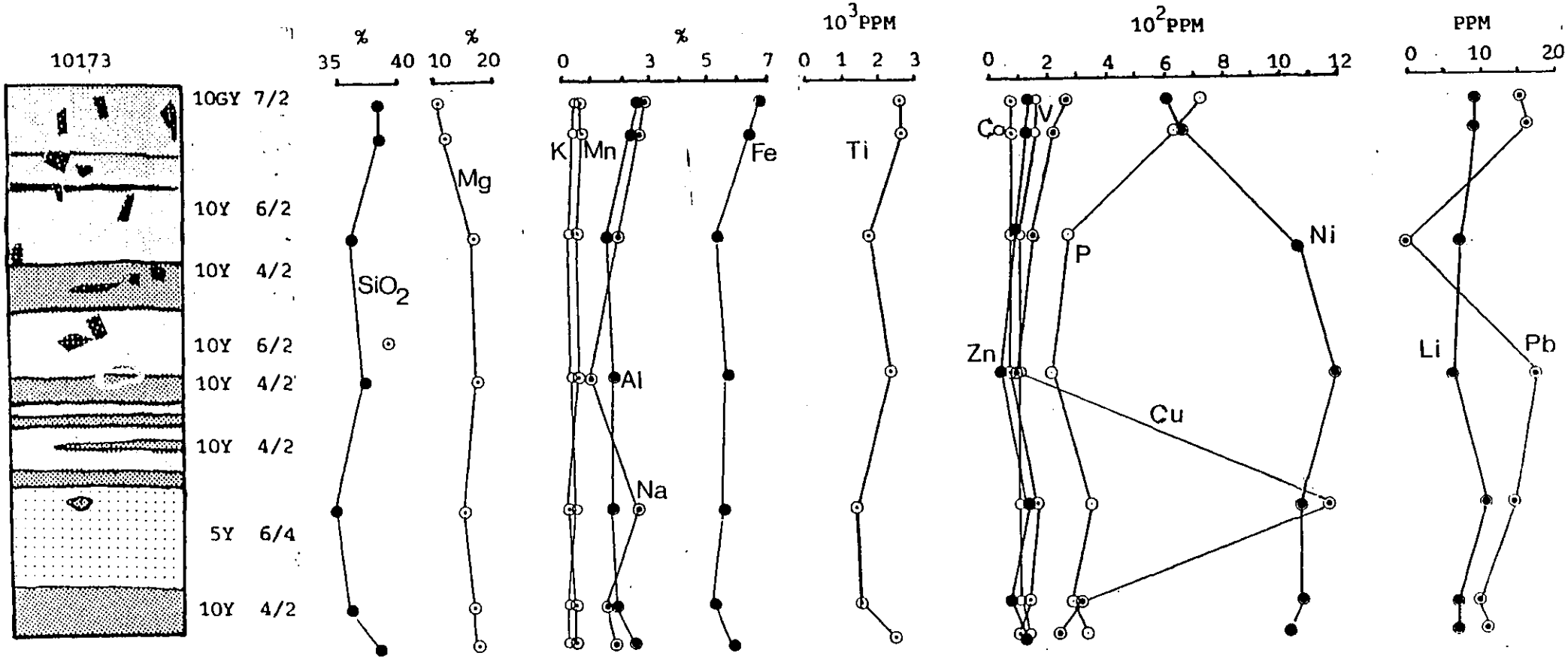
Mn is low in abundance in sediments from the Hess Deep, with a maximum of only 1.95% and concentrations of generally about 0.3%. Anomalous concentrations of Mg and Ni occur in Hess Deep sediments, the former reaching more than 16% in cores 188K, 10173, and 10178, while Ni commonly exceeds 1000 ppm in core 10173. In core 10173, below 27 cms, the Mg and Ni content increases sharply, while this phenomena occurs below 73 cms in core 188K. Therefore, it seems that at depth, in cores 10173 and 188K, there is an increase in a mineral phase enriched in Mg and Ni, and this enrichment was also noted in a mud pellet from station 10178.

FIG.6.4.5. Element variation with depth in core 188K.



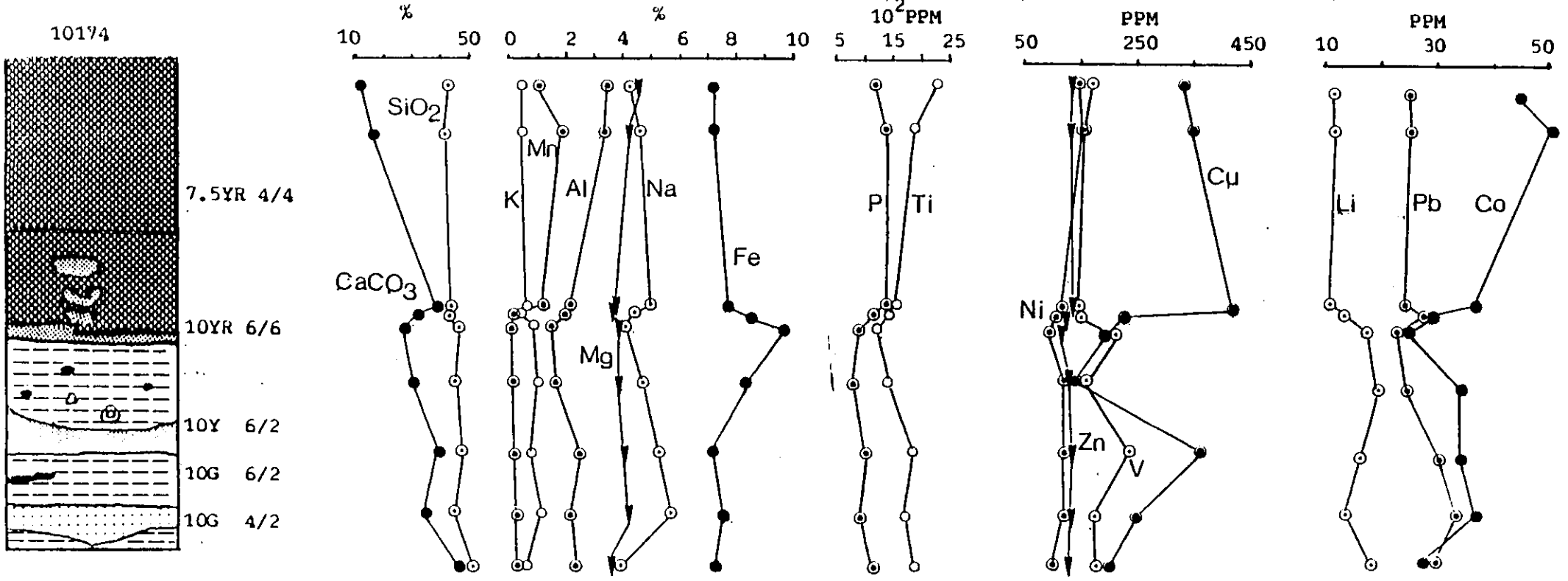

• = Volcanic ash-rich laminations.

FIG.6.4.6. Element variation with depth in core 10173.




= Volcanic ash-rich bands intercalated with pale olive clay from 51-68 cms.

FIG.6.4.7. Element variation with depth in core 10174.




= Evidence of bioturbation.

• = Lens of ash-rich material

TABLE 6.5.1. Bulk Mineralogy of Hess Deep sediments.

| CORE 10173 | MINERALS IN ORDER OF ABUNDANCE |
|---|---|
| Depth interval...3-5 (cms) * | 1.Chrysotile 2.Calcite 3.Smectite 4.Chlorite 5.Plagioclase 6.Quartz |
| ...9-11 * | 1.Chrysotile 2.Calcite 3.Smectite 4.Chlorite 5.Plagioclase |
| ...27-29 * | 1.Chrysotile 2.Smectite 3.Chlorite 4.Calcite 5.Plagioclase 6.Hornblende 7.?Kaolinite 8.?Phillipsite |
| ...51-53 * | 1.Chrysotile 2.Smectite 3,Chlorite 4.Plagioclase 5.Calcite |
| ...73-75 * | 1.Chrysotile 2.Calcite 3.Smectite 4.Chlorite 5.Plagioclase |
| ...90-92 * | 1.Chrysotile 2.Calcite 3.Chlorite 4.Plagioclase 5.Hornblende 6.?Kaolinite 7.?Phillipsite |
| CORE CATCHER * | 1.Chrysotile 2.Calcite 3.Smectite 4.Chlorite 5.Plagioclase |

| CORE 188K | MINERALS IN ORDER OF ABUNDANCE(data from Schmitz et al.(1982) & this work.) |
|---|---|
| ...0-46 | 1.Chlorite 2.Smectite 3.Plagioclase 4.Chrysotile 5.Calcite 6.Hornblende 7.Diopside 8.Quartz 9.Kaolinite |
| ...46-66 | 1.Smectite 2.Chrysotile 3.Calcite 4.Chlorite 5.Plag. 6.Diopside 7.Qtz. |
| ...70-200 * | 1.Chrysotile 2.Smectite 3.Chlorite 4.Hydrotalcite 5.Plag. 6.Diopside |

| CORE 10174 | MINERALS IN ORDER OF ABUNDANCE |
|---|---|
| Depth interval..4-6 (cms) | 1.Calcite 2.Smectite 3.Chlorite 4.Plagioclase 5.Hornblende 6.Quartz |
| ..13-15 | " " " |
| ..44-46 | " " " |
| ..46-48 | " " " |
| ..48-50 | " " " |
| ..56-58 | " " " |
| ..68-70 | " " " |
| ..79-81 | " " " |
| CORE CATCHER | 1.Calcite 2.Smectite 3.Chlorite 4.Plagioclase 5.Hornblende 6.Quartz 7.Diopside 8.Pyrophyllite |

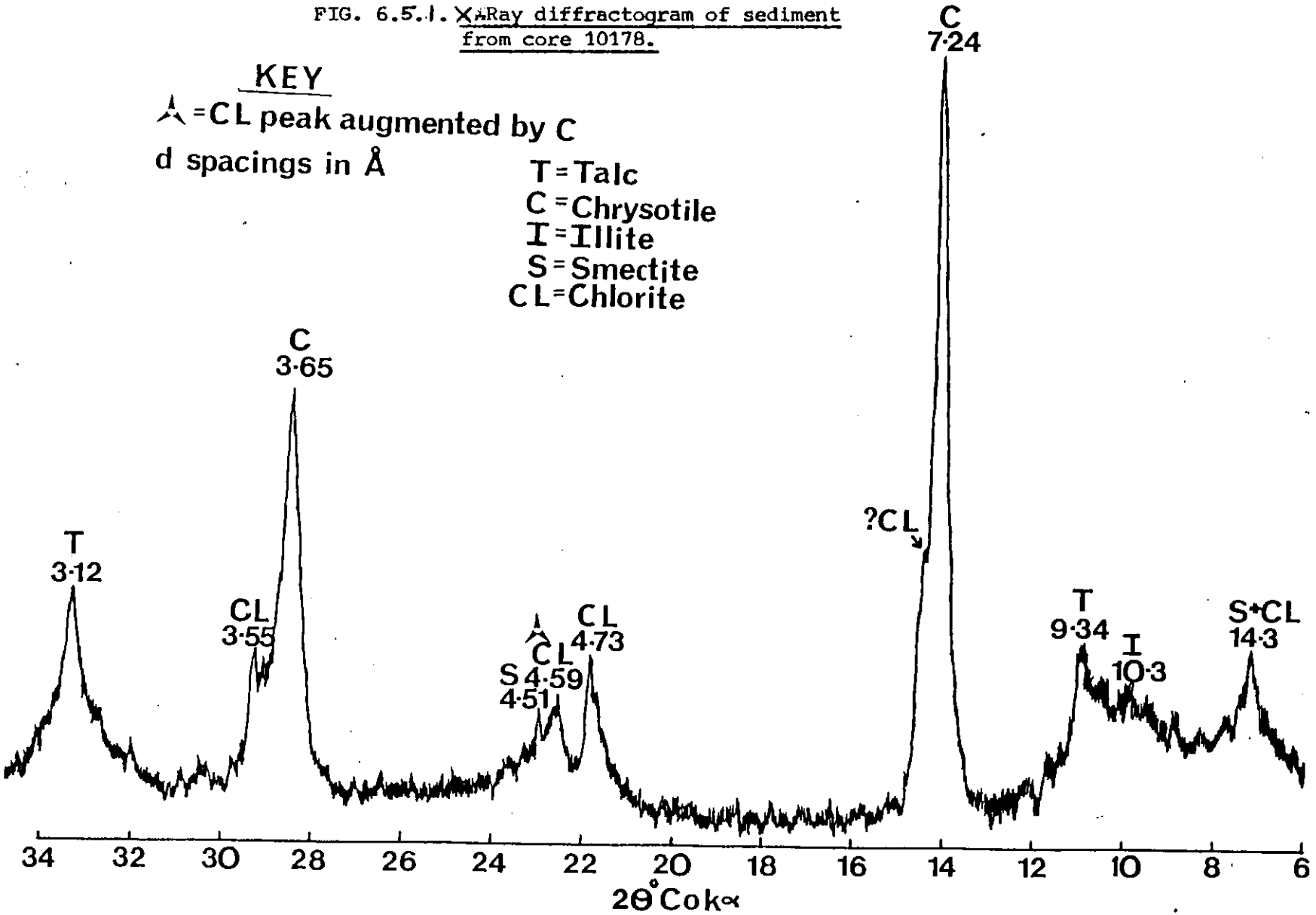
CORE 10178-MUD PELLET

| MINERALS IN ORDER OF ABUNDANCE | MAJOR PEAKS IDENTIFIED |
|---|---|
| 1.Chrysotile | 7.24Å,3.65Å |
| 2.Talc | 9.34Å,3.12Å,1.69Å |
| 3.Illite | 10.3Å,2.69Å,2.53-2.49Å |
| 4.Chlorite | 14.3Å,4.73Å,3.55Å |
| 5.Smectite | 14.3Å,4.51Å,1.53Å |

KEY:- * = CHRYSOTILE ABUNDANT

CHRYSOTILE = $Mg_3Si_2O_5(OH)_4$ ; TALC = $Mg_3Si_4O_{10}(OH)_2$ ; PYROPHYLLITE = $Al_2Si_4O_{10}(OH)_2$

FIG. 6.5.1. X-Ray diffractogram of sediment from core 10178.



Within the depth interval 73-75 cms, in core 10173, the Cu content reaches the highest level in all of the sediments analysed, 1140 ppm. Bonatti et al. (1971) noted that immobilisation of Cu in the sulphide phase may occur in the reduced layer of deep-sea sediments. Rozanova (1976) found troilite and pyrrhotite in Hess Deep sediments, although no Cu-rich sulphides were found. This work did not identify Cu sulphides by X.R.D. but they may be present in minor amounts.

*Element Variations with Depth*

Element variations with depth in cores 188K, 10173 and 10174 are shown in Figures 6.4.5 - 6.4.7. The Mn content of the cores is low but decreases sharply below 46 cms in core 10174, which is the depth to which the oxidised zone extends. The profiles of Co, and to a lesser extent Cu, are similar to that of Mn, decreasing below 46 cms in core 10174. However, Cu rises sharply in the reduced zone of cores 10173 and 10174 (see above). Fe and $SiO_2$ tend to show a fairly constant composition down the cores, but Fe increases between 48 and 58 cms in core 10174, while $CaCO_3$ decreases within this depth interval.

The concentrations of Mg and Ni in the cores appear to be linked and this can be seen in cores 188K, 10173 and 10174 (see Figures 6.4.5 - 6.4.7). The inference from this observation is that there is a mineralogical control on the abundances of Mg and Ni, which varies with core depth.

## 6.5 BULK MINERALOGY OF HESS DEEP SEDIMENTS

The results from X-ray diffraction analysis (see Appendix B) of bulk samples of Hess Deep sediments are shown in Table 6.5.1. Chrysotile, a serpentine mineral with the formula $Mg_3Si_2O_5(OH)_4$, dominates the mineralogical assemblage in core 10173, core 10178 and in the lower sections of core 188K. Major peaks for this mineral occur at 7.24 - 7.29 Å and 3.65 Å. Talc, $Mg_3Si_4O_{10}(OH)_2$, is abundant in core 10178, with major peaks at 9.34Å and 3.12 Å, and a mineral identified as hydrotalcite by Schmitz et al. (1982), was found in the chrysotile-rich

Table 6.6.1. Geochemistry and Mineralogy of the <0.5μ Fraction of Hess Deep Sediments

| Core | Depth (cms) | Major Elements as Oxides in % | | | | | | | | | | % Oxides | Minor Elements in ppm | | | | |
|---|---|---|---|---|---|---|---|---|---|---|---|---|---|---|---|---|---|
| | | $SiO_2$ | $Al_2O_3$ | $Fe_2O_3$ | MgO | CaO | $Na_2O$ | $K_2O$ | $TiO_2$ | $P_2O_5$ | $MnO_2$ | | Li | Sr | Ba | V | Cr |
| 188K | 15-20 | 48.6 | 5.57 | 10.1 | 6.53 | 0.94 | 3.12 | 0.49 | 0.26 | 0.28 | 0.11 | 76 | 23 | 38 | 630 | 73 | 52 |
| 188K | 52-58 | 50.6 | 4.96 | 10.6 | 8.84 | 1.05 | 1.50 | 0.38 | 0.24 | 0.22 | 0.10 | 79 | 19 | 55 | 1550 | 64 | 69 |
| 10173 | 3-5 | 41.0 | 2.01 | 7.55 | 24.3 | 0.66 | 1.98 | 0.19 | 0.11 | 0.42 | 0.13 | 78 | 9 | 27 | 178 | 43 | 92 |
| 10173 | 73-75 | 36.4 | 1.34 | 7.16 | 28.6 | 1.19 | 1.33 | 0.14 | 0.06 | 0.12 | 0.17 | 77 | 10 | 97 | 69 | 37 | 112 |
| 10173 | C.C. | 35.8 | 1.55 | 6.50 | 30.9 | 0.66 | 2.23 | 0.08 | 0.13 | 0.28 | 0.11 | 78 | 7 | 44 | 24 | 41 | 97 |
| 10174 | 4-6 | 29.1 | 2.16 | 7.22 | 3.56 | 0.90 | 8.88 | 0.19 | 0.08 | 0.37 | 0.09 | 53 | 12 | 52 | 920 | 29 | 29 |
| 10174 | 48-50 | 34.7 | 1.59 | 10.1 | 2.19 | 2.23 | 10.8 | 0.52 | 0.04 | 0.46 | 0.10 | 63 | 9 | 71 | 400 | 77 | 27 |
| 10174 | 68-70 | 31.2 | 1.37 | 7.98 | 2.09 | 1.72 | 8.34 | 0.28 | 0.03 | 0.42 | 0.08 | 54 | 8 | 63 | 500 | 230 | 47 |
| 10174 | C.C. | 45.9 | 1.92 | 13.5 | 3.44 | 2.22 | 3.09 | 0.31 | 0.05 | 0.46 | 0.15 | 71 | 14 | 90 | 810 | 79 | 39 |

| | | Minor Elements in ppm | | | | | | | | d(001) Air dried Å | d(001) Glycerated Å | d(001) 550°C Å |
|---|---|---|---|---|---|---|---|---|---|---|---|---|
| | | Mo | Co | Ni | Cu | Ag | Zn | Pb | *Mineralogy | | | |
| 188K | 15-20 | 10 | 52 | 181 | 460 | 2.1 | 450 | 48 | S + C + CL | 13.2 | 17.9 | 10.1 |
| 188K | 52-58 | 7 | 75 | 280 | 490 | <1.0 | 230 | 13 | S + C + CL | 12.4 | 18.2 | 10.1 |
| 10173 | 3-5 | 12 | 59 | 710 | 330 | 2.6 | 190 | 16 | C + S + CL | 14.9 | 17.9 | 9.7 |
| 10173 | 73-75 | 10 | 173 | 1360 | 1570 | 1.3 | 210 | 23 | C + S + CL | 14.7 | 17.9 | 10.0 |
| 10173 | C.C. | 11 | 82 | 1190 | 290 | 1.8 | 141 | <5 | C + S + CL | 14.7 | 17.9 | 10.0 |
| 10174 | 4-6 | 8 | 13 | 89 | 330 | 1.8 | 200 | 22 | S + CL + C | 12.2 | 16.6 | 9.8 |
| 10174 | 48-50 | 6 | 17 | 67 | 200 | 6.2 | 95 | 25 | S + CL | 13.9 | 17.9 | 10.0 |
| 10174 | 68-70 | 7 | 25 | 85 | 460 | 5.4 | 111 | 17 | S | 12.5 | 17.3 | 9.5 |
| 10174 | C.C. | 8 | 30 | 104 | 370 | 4.4 | 280 | 20 | S + CL | 13.2 | 16.1 | 9.5 |

Analyses expressed to 3 significant figures except for majors <1% and minor elements <100 ppm.
* C= Chrysotile, S = Smectite, CL = Chlorite C.C. = core catcher

lower sections of 188K. Minor occurrences of pyrophyllite (see Table 6.5.1), $Al_2Si_4O_{10}(OH)_2$, occur in the core catcher sample from core 10174. The minerals chrysotile and to a lesser extent talc, (see Figure 6.5.1) account for the high concentrations of Mg (see Section 6.4.2) in Hess Deep sediments. A common analogue of chrysotile, which displays Ni-substitution for Mg in octahedral sites (Springer, 1974), is garnierite (Brindley and Brown, 1980), $(Mg,Ni)_3Si_2O_5(OH)_4$, and this may explain the anomalous Ni concentrations found in Hess Deep sediments, produced by Ni-substitution in the chrysotile structure.

Clay minerals are discussed in more detail in Section 6.6 and it is sufficient to note that chlorite and smectite are common in Hess Deep sediments and minor amounts of kaolinite and the zeolite, phillipsite are also present. Some differences were found in this work to the clay mineral identification of Schmitz et al. (1982).

Minerals normally associated with detrital ultramafic igneous rocks include plagioclase (ubiquitous to all Hess Deep sediments), hornblende, and diopside which are all common in minor amounts in the sediments studied. The association of minerals normally regarded as metamorphic in origin (i.e. chrysotile, talc and pyrophyllite), with detrital phases from ultramafic igneous rocks is detailed in Section 6.9 and is commonly ascribed to the hydration and serpentinisation of peridotites (Christensen, 1972).

## 6.6 THE <0.5μ FRACTION OF HESS DEEP SEDIMENTS

### 6.6.1 Geochemistry of the <0.5μ Fraction

The <0.5μ fraction of 9 Hess Deep sediments was studied after the removal of sea-salts, calcium carbonate, and Fe-Mn oxides (see Appendix B). The geochemistry of these samples is shown in Table 6.6.1, with a brief description of the mineralogy (see Section 6.6.2) which consists of a mixed chrysotile, smectite and chlorite assemblage. The geochemistry is not representative of any one mineral but a mixture of minerals, with the exception of sediment from core 10174 (68 - 70 cms), where only smectite was identified.

The composition of the clay minerals is variable and on the assumption that, 100% - % oxides (calculated from chemical analyses) ≃ % water, then 6 samples contain between approximately 21% and 29% water, which compares with an ignition loss of 18% for the DOMES smectite of Hein et al. (1979). However, 3 samples contain low % oxide contents of 53%, 54% and 63% (Table 6.6.1), coupled with a high Na content. This is likely to be due to the dilution of the clay fraction with excess sodium dithionite reagent (see Appendix B) which was not removed during washing. This dilution effect is supported by the relatively low $SiO_2$ contents of these 3 samples.

The Mg content of the samples reflects the chrysotile abundance (see Section 6.5), particularly in core 10173 where Mg reaches a maximum of 18.6 % (MgO = 30.9%). Core 188K displays lower levels of Mg enrichment while core 10174 contains a maximum of only 2.2% Mg (3.6% MgO, see Table 6.6.1) and this can be explained by the lack of chrysotile, only identified in trace amounts in the top sediment of this core. The Fe content increases as chrysotile abundance decreases and this reflects the increasing smectite contribution to the clay fraction. The true chemical composition of the smectite cannot be accurately detailed as the only sample which appears to contain only smectite, yields a very low % oxide content (Table 6.6.1) and therefore is presumed to be contaminated with sodium dithionite.

Enrichment of Cr (112 ppm), Co (173 ppm), Ni (1360 ppm) and Cu (1570 ppm) is shown by the chrysotile-rich samples. These trace metal enrichments, with the exception of Cu, were also found for Mid-Atlantic Ridge serpentinites (Bonatti et al., 1973). The high level of Cu found between 73 and 75 cms in core 10173 has also been described in downcore element profiles (see Section 6.4.2) and ascribed to the possible presence of fine sulphide particles. The trace element geochemistry of upper sediment layers from core 188K and sediment from core 10174 is different to that of sediment from core 10173. Ba, V and to a lesser extent, Li, Ag, Zn and Pb, are enriched in chrysotile-depleted sediments of a smectite-chlorite mineralogy.

### 6.6.2 Mineralogy of the <0.5μ Fraction

Two important differences emerged from the present work and that of Schmitz et al. (1982), in regard to the clay mineralogy of Hess Deep sediments.

1. A "high-charge" smectite was identified by Schmitz et al. (1982) on the basis of no observed expansion of the lattice, after treatment with glycerol. The present work on the same sediment layer, produced an expansion of 12.4 Å to 18.2 Å, upon glyceration, with a subsequent collapse of the smectite structure to 10.1 Å, upon heating to 550°C (see Table 6.6.1).

2. Chlorite was not identified by Schmitz et al. (1982) but they observed a mineral with a peak at 14.25 Å. However, these authors did identify kaolinite in core 188K. Chlorite was identified unequivocally (this work) by thermal analysis at 550°C, whereupon the (001) reflection was found to be enhanced relative to the (002) reflection. Also, the (001) peak was slightly shifted from 14.1 Å to 13.9 Å, as is normal for chlorites (Brindley and Brown, 1980).

This work suggests that the 14.25 Å mineral of Schmitz et al. (1982) may be chlorite. Kaolinite peaks disappear upon heating to 550°C and although the (002) chlorite and (001) kaolinite have similar d-spacings at about 7.1 Å, the presence of peaks at 550°C favours chlorite. The only kaolinite found in this work was identified by high angle (2θ) peaks and this mineral was present in only small amounts.

## 6.7 SCANNING ELECTRON MICROSCOPY

Scanning Electron Microscopy, S.E.M. (see Appendix B), was used to examine the morphology and to positively identify minerals and structures present in Hess Deep sediments. Biogenic debris, in the form of diatoms, radiolaria and coccoliths are found in abundance throughout the sediments (Plates 6.7.1 - 6.7.3). Bundles of fibrous chrysotile, 9 - 16μ by 18 - 27μ, are common (Plates 6.7.2 and 6.7.3) and appear to be concentrated in localised areas which is contrary to the findings of Schmitz et al. (1982) who reported that 2M-clinochrysotile was only rarely bundled into sheaths.

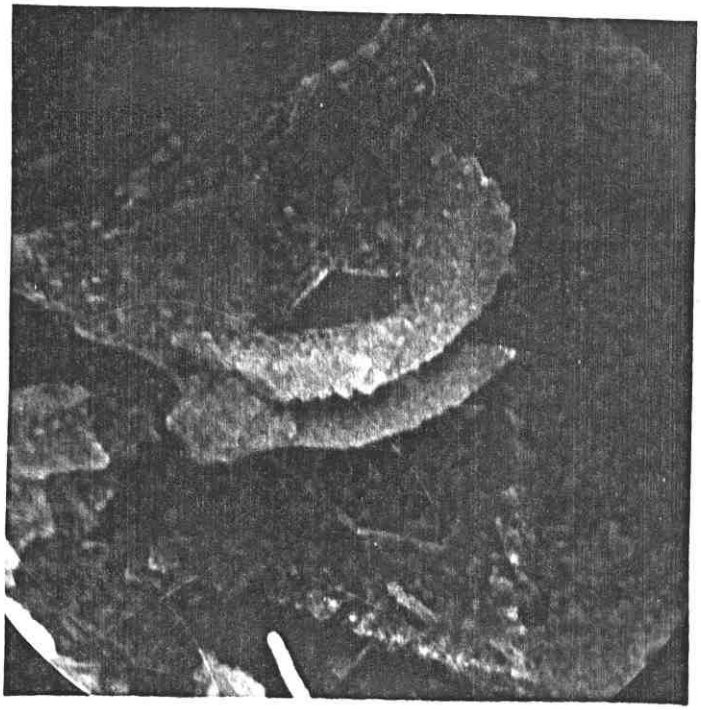


PLATE 6.7.1.
Coccolith with wafer-thin coating, on larger diatom.

FIELD OF VIEW = 6 $\mu$m IN BOTH DIMENSIONS.



PLATE 6.7.2.
Fibrous sheath of chrysotile (lower middle of frame) in a matrix of siliceous microfossils.

FIELD OF VIEW = 38 $\mu$m IN BOTH DIMENSIONS.



PLATE 6.7.3.
Fibrous chrysotile and abundant siliceous microfossil fragments.

FIELD OF VIEW = 45 $\mu$m IN BOTH DIMENSIONS.

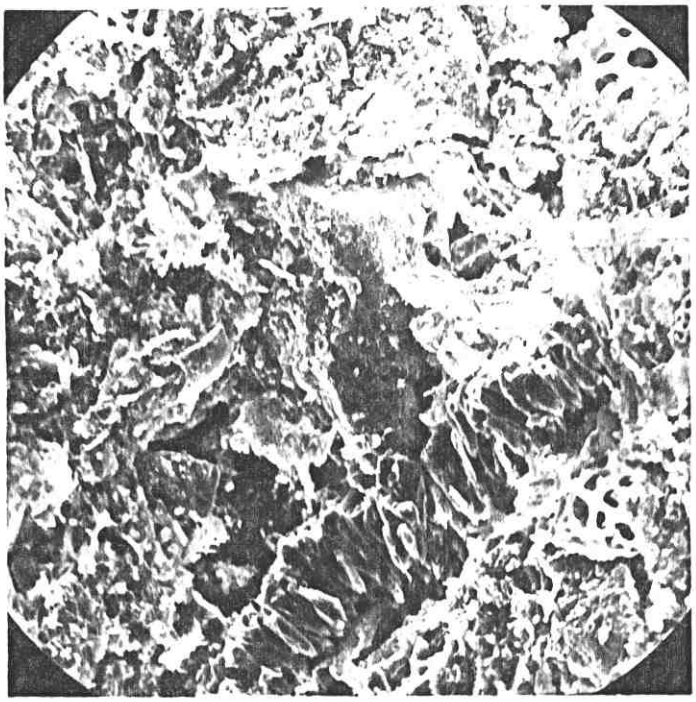
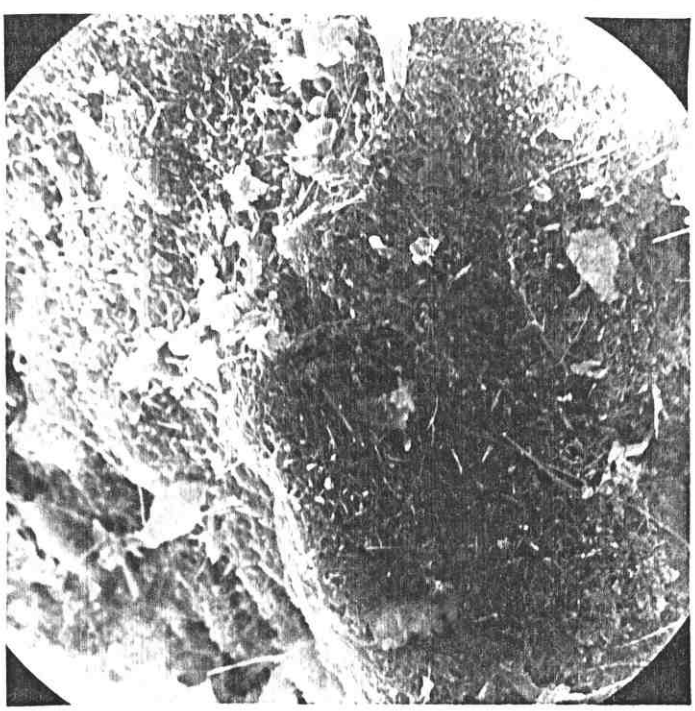


PLATE 6.7.4.
Large clast of primary mineral, pseudomorphed by chrysotile (centre of frame), with linear organic structure indicating dissolution by its etched nature.
FIELD OF VIEW = 225$\mu$ IN BOTH DIMENSIONS.

PLATE 6.7.5.
Large clast shown in PLATE 6.5.4. at higher magnification and displaying a fibrous nature.
FIELD OF VIEW = 45$\mu$ IN BOTH DIMENSIONS.



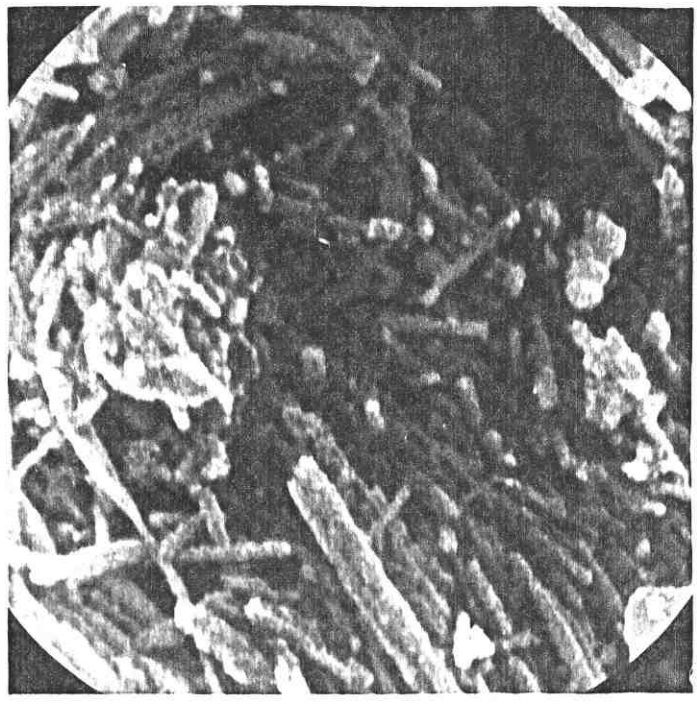


PLATE 6.7.6.
Highly magnified view of the large clast, displaying individual fibres of chrysotile.
FIELD OF VIEW = 4.5$\mu$ IN BOTH DIMENSIONS.

PLATE 6.7.7.
Rectangular platelets of talc with individual fibres of chrysotile.
FIELD OF VIEW = 15$\mu$ IN BOTH DIMENSIONS.

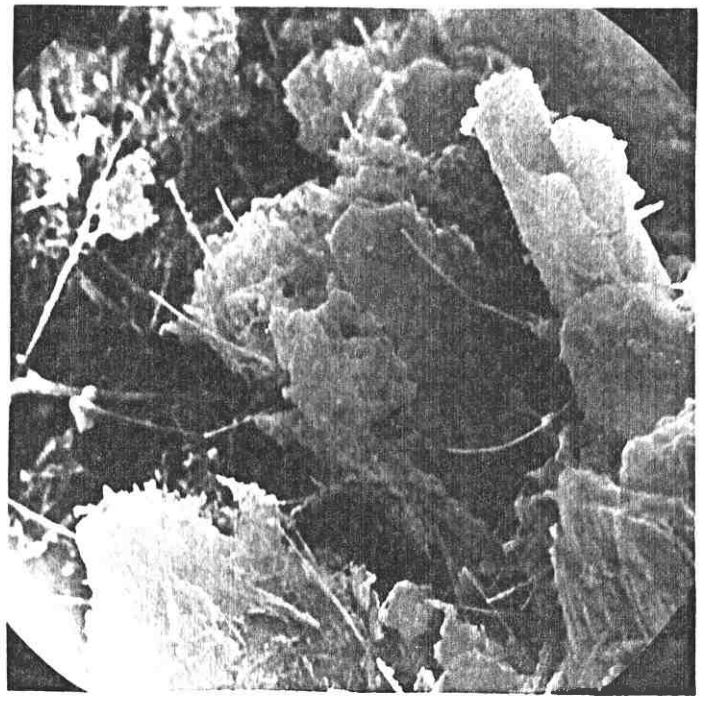


TABLE 6.8.1. Correlation Matrix for Galapagos Rift sediments, 101°W.

| | NA | K | MG | AL | MN | FE | CA | CACO3 |
|---|---|---|---|---|---|---|---|---|
| K | .944 | | | | | | | |
| MG | ↓ | ↓ | | | | | | |
| AL | .595 | .645 | .552 | | | | | |
| MN | ↓ | ↓ | ↓ | ↓ | | | | |
| FE | .647 | .701 | .660 | .882 | | | | |
| CA | -.596 | -.575 | -.819 | -.834 | | -.935 | | |
| CACO3 | -.903 | -.921 | -.789 | -.828 | | -.900 | 1.000 | |
| SIO2 | ↓ | ↓ | .479 | .878 | | .828 | -.933 | -.954 |
| LI | .564 | .622 | ↓ | .721 | | .713 | -.672 | -.624 |
| SR | -.867 | -.860 | -.681 | -.919 | | -.928 | .941 | .926 |
| LA | .585 | .606 | ↓ | ↓ | | ↓ | ↓ | -.490 |
| TI | .554 | .598 | .566 | .997 | | .866 | -.821 | -.762 |
| V | .749 | .827 | ↓ | .936 | | .889 | -.812 | -.856 |
| CO | ↓ | ↓ | .939 | .734 | | .788 | -.878 | -.729 |
| NI | ↓ | ↓ | .982 | ↓ | | .586 | -.753 | -.713 |
| CU | .646 | .741 | ↓ | .560 | | .648 | -.591 | -.654 |
| ZN | .684 | .780 | ↓ | .772 | | .840 | -.740 | -.758 |
| PB | .479 | .489 | .550 | .578 | ↓ | .732 | -.709 | ↓ |
| P | .742 | .803 | ↓ | .604 | .472 | .666 | -.518 | -.746 |

| | SIO2 | LI | SR | LA | TI | V | CO | NI |
|---|---|---|---|---|---|---|---|---|
| LI | .677 | | | | | | | |
| SR | -.919 | -.714 | | | | | | |
| LA | ↓ | ↓ | ↓ | | | | | |
| TI | .900 | .711 | -.913 | | | | | |
| V | .685 | .742 | -.882 | | .917 | | | |
| CO | .678 | .518 | -.785 | | .744 | .628 | | |
| NI | ↓ | ↓ | -.588 | | .474 | ↓ | .926 | |
| CU | ↓ | .488 | -.575 | | .527 | .743 | ↓ | ↓ |
| ZN | .616 | .619 | -.755 | | .754 | .854 | .532 | |
| PB | .677 | ↓ | -.599 | ↓ | .565 | .588 | .634 | .512 |
| P | ↓ | .495 | -.558 | .552 | .554 | .692 | ↓ | ↓ |

| | CU | ZN | PB |
|---|---|---|---|
| ZN | .682 | | |
| PB | .534 | .647 | |
| P | .626 | .704 | .555 |

The cut-off value for the correlation coefficient at 99.9% confidence = 0.47

TABLE 6.8.2. Correlation Matrix for Galapagos Rift sediments, from the Hess Deep.

| | NA | K | MG | AL | MN | FE | CA | CACO3 |
|---|---|---|---|---|---|---|---|---|
| K | | | | | | | | |
| MG | | -.867 | | | | | | |
| AL | | | | | | | | |
| MN | | | | | | | | |
| FE | | | | | .978 | | | |
| CA | | | -.757 | | | | | |
| CACO3 | | | -.763 | | | | 1.000 | |
| SIO2 | | | | | | | -.913 | -.899 |
| LI | | | -.799 | | | | | |
| SR | | | | | | | | |
| LA | | | -.706 | | | | | |
| TI | | | | | .861 | .868 | | -.842 |
| V | | | | .740 | | .769 | | |
| CO | | -.736 | .793 | | .941 | .943 | | -.728 |
| NI | | -.891 | .979 | | | | -.714 | -.706 |
| CU | | | | | .671 | | | |
| ZN | .822 | | | | .956 | .927 | | |
| PB | .948 | | | | .947 | .925 | | |
| P | | | | | .829 | | | |

| | SIO2 | LI | SR | LA | TI | V | CO | NI |
|---|---|---|---|---|---|---|---|---|
| LI | | | | | | | | |
| SR | -.717 | | | | | | | |
| LA | | | | | | | | |
| TI | .670 | | | | | | | |
| V | | | | | | | | |
| CO | | | | | .882 | | | |
| NI | | -.774 | | -.668 | | | | |
| CU | | | | | | | .746 | |
| ZN | | | | | .809 | | .912 | |
| PB | | | | | .753 | | .902 | |
| P | | | | | | | | -.673 |

| | CU | ZN |
|---|---|---|
| ZN | .677 | |
| PB | | .984 |

The cut-off value for the correlation coefficient at 99.9% confidence = 0.66

Evidence is shown in Plates 6.7.4 - 6.7.6 of serpentine fibres that formed from the degradation of a precursor mineral, assumed to be either pyroxene or olivine (see Section 6.9). The sequence of Plates 6.7.4 - 6.7.6 show the pseudomorphing of a primary mafic mineral (50$\mu$ by 110$\mu$) by chrysotile fibres, at progressively higher magnifications.

Talc was identified previously by X.R.D. and is shown intimately associated with fibrous chrysotile in Plate 6.7.7. The small platelets of talc have the dimensions of 3$\mu$ by 8$\mu$. The association of serpentine and talc is important in terms of the genesis of the assemblage, as Seyfried and Dibble (1978) have shown that interaction of mantle-derived peridotite with sea-water at elevated temperatures and pressures results in the replacement of enstatite (pyroxene) by talc. In this system, talc then reacts with seawater $Mg^{2+}$ to generate serpentine.

## 6.8 ELEMENT ASSOCIATIONS

### 6.8.1 Sediments from the 101°W Area of the Galapagos Rift

Correlations significant at the 99.9% confidence level for 101°W area sediments are shown in Table 6.8.1. Na and K correlate positively with Al, Fe, Li, La, Ti, V, Cu, Zn, Pb and P, but not with $SiO_2$. Mg correlates positively with Al, Fe, $SiO_2$, Ti, Co, Ni and Pb. Al displays a similar pattern to the correlations of Na, K and Mg. These element associations have been described elsewhere on the Galapagos Rift and support geochemical data (Section 6.4.1), in confirmation of element sites in clay minerals, basaltic detritus and sea-salts.

Mn does not correlate with any elements except P, which attests to the relative unimportance of Mn oxides as suppliers of trace metals to 101°W area sediments. Of the remaining correlations, only Sr with $CaCO_3$ and La with P suggest input of an element from one source only, namely calcareous microfossil remains and skeletal apatite, respectively, which indicates the polygenetic nature of the sediments.

### 6.8.2 Sediments from the Hess Deep

Correlations reported in Table 6.8.2 are significant at the 99.9% level of confidence. The more interesting correlations include the lack of

association of K with Mg, Co and Ni and of Mg with $CaCO_3$, Li and La. This indicates that Mg is not associated with the phases common in Galapagos Rift pelagic sediments (i.e. smectites, sea-salts, carbonates) but is quantitatively associated with chrysotile, as are Ni and to a lesser extent, Co. The positive correlation of Fe and Mn and trace metals (see Table 6.8.2) is thought to reflect minor abundances of ferromanganese oxides.

## 6.9 SERPENTINISATION AND THE ORIGIN OF SERPENTINE-RICH SEDIMENTS IN THE HESS DEEP

### 6.9.1 The Serpentinisation Process

An understanding of the process of serpentinisation and the minerals formed is essential in order to interpret the data accumulated on Hess Deep sediments. An outline of the major points of interest follows and is largely taken from the review of Moody (1976).

Ultramafic complexes commonly feature lizardite, chrysotile, magnetite $\pm$ brucite $\pm$ antigorite among their alteration products. Lizardite - chrysotile assemblages are more common than antigorite which is formed in a higher pressure/temperature regime. The ultramafic complexes largely comprise dunite, harzburgite and lherzolite rock types (Wyllie, 1976; Coleman, 1971; Moores, 1973) with olivine, orthopyroxene, clinopyroxene and chromite as the major minerals.

A feature of the serpentinisation of an olivine-rich peridotite (Moody, 1976) is a locally-reducing environment, indicated by the presence of native Fe and low-sulphur sulphides. One of the major reactions in the serpentinisation process can be summarised as follows:-

$$6Mg_2SiO_4 + Mg_3Si_4O_{10}(OH)_2 + 9H_2O = 5Mg_3Si_2O_5(OH)_2$$

(Forsterite) (Talc) (Chrysotile)

.... after Chernosky (1973)

This reaction and the chrysotile - talc - forsterite assemblage was found to occur at temperatures of about 420°C and pressures up to 7

kilobars. Lizardite and chrysotile span the zeolite - prehnite/ pumpellyite - lower greenschist facies of metamorphism.

The Hess Deep serpentine assemblage is exclusively chrysotile. Wicks (1969) observed that lizardite grows with ease on an olivine substrate whereas chrysotile does not. The inference for Hess Deep sediments is that original lizardite may have been replaced by chrysotile and this commonly occurs in the late stages of serpentinisation. O'Neil (pers. comm. in Moody, 1976) has stated that it is likely that the lizardite - chrysotile assemblage does not form at temperatures in excess of 200°C.

The features of the serpentinisation process described above and the mineralogy produced are related below to Hess Deep serpentine-rich sediments.

6.9.2 The Origin of Hess Deep Serpentine-rich Sediments

There is some evidence that hydrothermal solutions are supplying Fe, Mn, Cu and Zn to Hess Deep bottom waters (Gordeev and Demina, 1979). However, the report of discoveries of authigenic troilite, pyrrhotite and cerolite (a mixture of a talc-like silicate, a non-ordered inter-stratification, and serpentine) by Rozanova (1976) and the identification of clinochrysotile by Schmitz et al. (1982), both ascribed an hydrothermal origin, may have to be revised in the light of the present work. Rozanova (1976) states that "the reaction between thermal solutions and calcitic foraminiferal tests has caused replacement of calcite by magnesian silicates and has enriched the solutions in $Ca^{2+}$ and $CO_3^{2-}$" and that this occurred at around 450°C. Schmitz et al. (1982) also cite an origin of precipitation from a hydrothermal solution for clinochrysotile, inferred largely from the lack of any ultramafic primary precursor minerals.

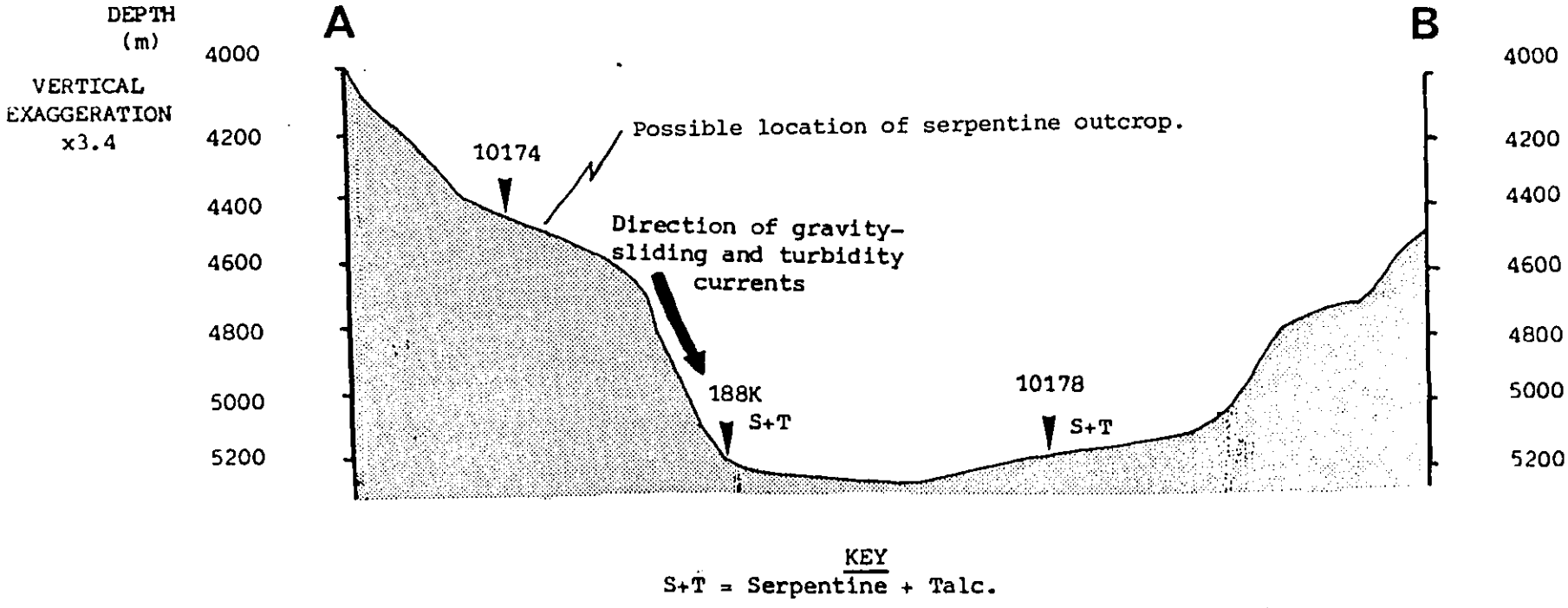
The present work has shown direct evidence for the growth of chrysotile from a precursor mineral which has been pseudomorphed (see Section 6.7). It is suggested therefore that the interpretations of Rozanova (1976)

and Schmitz et al. (1982) need modification because of this visual evidence and a number of other arguments, as follows. First, significant amounts of unaltered primary minerals would not be expected if serpentinisation is extensive. Second, chemical evidence from experimental work (e.g. Seyfried and Mottl, 1977) shows that Mg is quantitively depleted in hydrothermal solutions and this is difficult to reconcile with the precipitation of a Mg-rich silicate from such a solution. Third, the presence of pyrrhotite and troilite in Hess Deep sediments cannot be used to prove a hydrothermal origin for the serpentine mineral as low-sulphur sulphides are commonly associated with serpentinised ultramafic material.

In support of the above argument are the data accumulated from other occurrences of talc and serpentine minerals in the World Ocean. The discovery of hydrothermal talc from the Gulf of California (Lonsdale et al., 1980) confirms experimental evidence regarding Mg-depletion in hydrothermal solutions as this talc is Fe-rich, in contrast to the Mg-rich talc of the Hess Deep which suggests a different origin for the latter. Chrysotile has been reported from the 37$^{o}$N area of the Mid-Atlantic Ridge (Hoffert et al., 1978). The authors noted that olivine was replaced by chrysotile and no support was given for the "Schmitz et al."-type of hydrothermal chrysotile precipitation.

Of the many occurrences of oceanic serpentinites, the sedimentary serpentinites (i.e. reworked and sedimented serpentinised rocks) from the Romanche Fracture Zone of the Mid-Atlantic Ridge (Bonatti et al., 1973) are most similar to those of the Hess Deep. The lizardite - clinochrysotile assemblage found in indurated sediments was formed by "gravity-sliding, slumping and turbidity current transport of serpentinite masses originating from the upper levels of ultramafic transverse ridges in the Romanche Fracture Zone", (Bonatti et al, 1973). Classic turbidite sequences with layering and graded bedding were reported by these authors. Turbidite sediments were reported to be

FIG.6.9.1. Cross section of Hess Deep showing the possible source of serpentine-rich sediments.




THE STATION LOCATIONS HAVE BEEN PROJECTED ONTO THE LINE OF SECTION A-B (see FIG.6.2.2.)

common in the Hess Deep (Schmitz et al., 1982) where steep scarp slopes occur in water depths up to 5440 metres and where serpentinised peridotites might be expected (Christensen, 1972).

Although no signs of graded bedding were found in Hess Deep sediments, the persistence of $CaCO_3$ well below the C.C.D. and the presence of volcanic ash-rich layers suggest pelagic turbidity current action, under gravity, from the steep scarp slopes of the Deep.

It is considered on the basis of the work described above that Hess Deep serpentines originated from serpentinised peridotite material which has been incorporated in sediments by turbidity current activity, slumping and gravity slides, rather than by hydrothermal precipitation in situ. The presence of smectite can be ascribed to alteration in the marine environment of a serpentine mineral, as found by Boillot et al. (1980).

The conclusions reached in the previous paragraph do not allow for the in situ hydrothermal precipitation of chrysotile and low-sulphur sulphides. However, a hydrothermal supply of trace metals in Hess Deep bottom waters (Gordeev and Demina, 1979) provides some evidence of the existence of hydrothermal activity in the Deep.

Figure 6.9.1 shows a cross-section (A-B, see Figure 6.2.2) of the Hess Deep, with the locations of the serpentine-rich sediments. The station locations do not lie on section line A-B but they have been projected onto Figure 6.9.1, as they lie in the immediate vicinity.

# PART 2

## THE EAST PACIFIC RISE SPREADING CENTRE

### INTRODUCTION

STUDY D

Chapter 7 — The Quebrada Fracture Zone at 4°S on the East Pacific Rise.

STUDY E

Chapter 8 — The 10°S Area of the East Pacific Rise

STUDY F

Chapter 9 — The 13 - 15°S Area of the East Pacific Rise

STUDY G

Chapter 10 — The 19 - 21°S Area of the East Pacific Rise

# INTRODUCTION

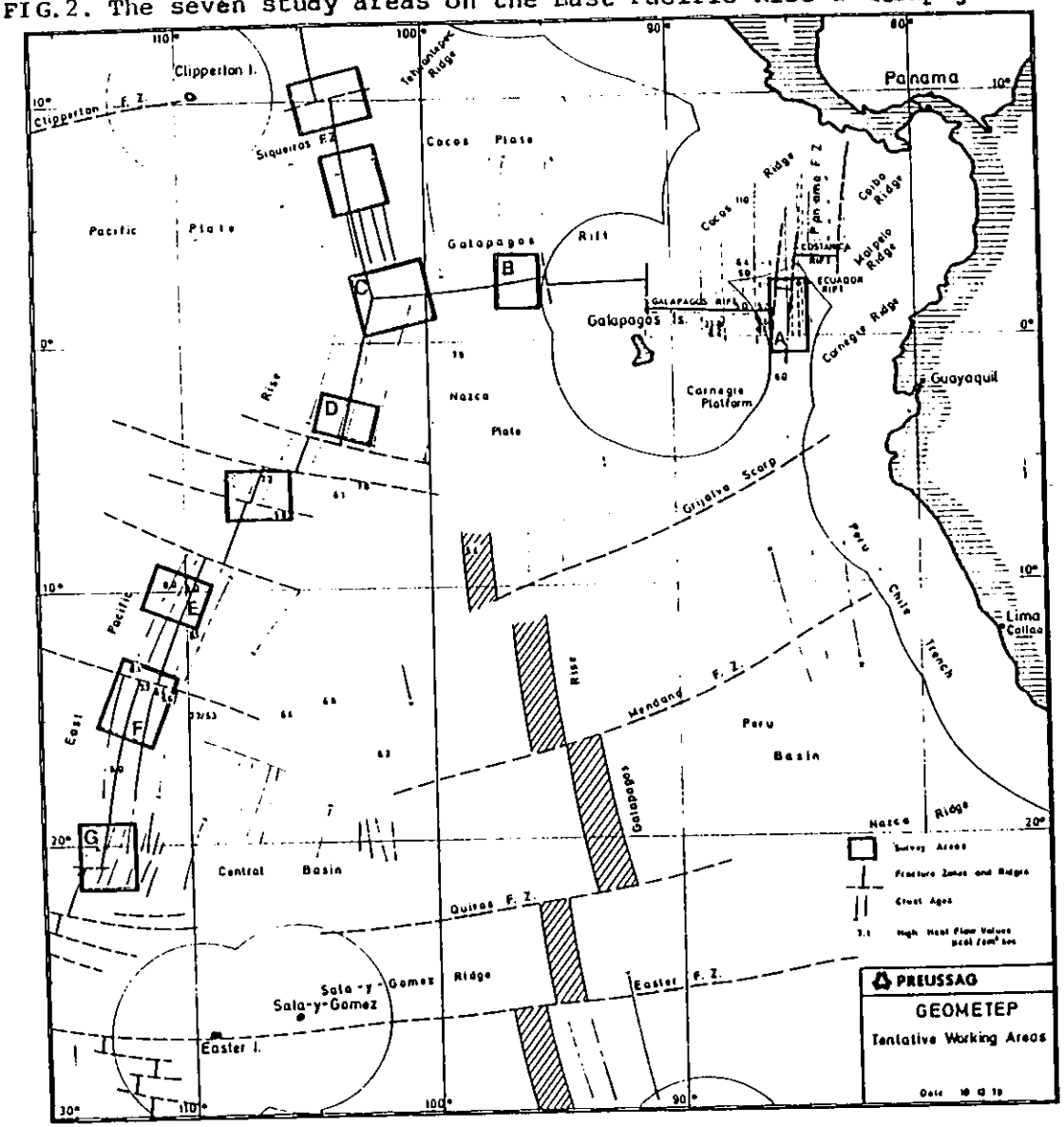
The seven study areas investigated in this thesis and their locations on the East Pacific Rise and Galapagos Rift are shown in Figure 2. Study areas D, E, F and G on the E.P.R. form Part 2 of this thesis and were sampled during the GEOMETEP (Geothermal Metallogenesis Eastern Pacific) cruise of 1980. In order to explain the aims of this cruise it is necessary to describe the background of metalliferous sediment investigations on the E.P.R., south of the equator.

Revelle (1944) and El Wakeel and Riley (1961) reported the presence of metal-enriched pelagic sediments on the E.P.R., but the credit for the discovery of what are now regarded as metalliferous sediments belongs to Bostrom and Peterson (1966). These authors found enhanced concentrations of Fe, Mn, Cu, Cr, Ni and Pb in the sediments. At about the same time, Bonatti and Joensuu (1966) reported a hydrothermal Fe and Mn oxide deposit, located on the summit of the AMPH D2 seamount at $10^{\circ}$S on the E.P.R., which showed extreme fractionation of Fe from Mn.

The anomalously metal-enriched E.P.R. sediments are characterised by high values of Fe and Mn extending to a depth of at least 6 m below the sediment/water interface (Bostrom and Peterson, 1969). The Fe, Mn-rich (and Al, Ti-poor) nature of the sediments led Bostrom and co-workers to adopt element ratios in an attempt to characterise metalliferous sediments. However, the validity of using the metal/Al ratio, e.g. (Fe + Mn)/Al (Bostrom, 1973), has been called into question (McArthur and Elderfield, 1977) and recently, Dymond (1981) has postulated a possible hydrothermal source for Al.

Heath and Dymond (1977) suggested a polygenetic origin for metalliferous sediments on the Nazca Plate portion of the E.P.R. whose geochemistry could be accounted for by varying proportions of four factors:-

FIG.2. The seven study areas on the East Pacific Rise & Galapagos Rift. (A-G)



1. Hydrothermal
2. Detrital
3. Hydrogenous
4. Biogenic

For example, at the E.P.R. crest, the hydrothermal component can account for 80% or more of the sediment (Dymond, 1981). Recent work by Heath and Dymond (1981) has added a fifth component to the above model termed the 'solution residue' factor, formed upon the dissolution of biogenic debris.

Dymond et al. (1973) found that the colloidal hydrothermal ferro-manganese oxide precipitates typical of metalliferous sediments showed little evidence of bulk chemical changes with time or diagenetic alteration. This has been confirmed by Marchig and Gundlach (1982).

In recent years, discoveries have been made of low temperature, hydrothermal Fe montmorillonite from the E.P.R. at 10°S (McMurtry and Yeh, 1981) and more recently, polymetallic sulphides at 20°S (Francheteau and Ballard, in press). Thus, the full fractionation sequence of sulphides, silicates, iron and manganese oxides of the Red Sea model has now been found on the E.P.R., south of the equator, but not all in the same place,indicating that at each location found, we are only seeing part of the fractionation sequence.

The work outlined above was used in the selection of certain sites on the E.P.R. for sampling during the GEOMETEP cruise. The following study is on deposits obtained on that cruise and orientated towards using the results produced to aid in the development of geochemical exploration methods for submarine hydrothermal deposits based on multi-element techniques. Based on this work, a number of exploration targets have been identified.

STUDY D CHAPTER 7

# THE QUEBRADA FRACTURE ZONE SYSTEM AT 4°S ON THE E.P.R.

## 7.1 INTRODUCTION

A detailed study of sedimentation processes in the 4°S area is hampered by the extremely limited number of samples (13) obtained from the GEOMETEP cruise of 1980. These 13 sediments were taken from 2 cores and 3 dredges in the Quebrada Fracture Zone (Q.F.Z.) area, shown in Figure 7.2.1.

## 7.2 GEOLOGY, BATHYMETRY AND STRUCTURE OF THE 4°S AREA

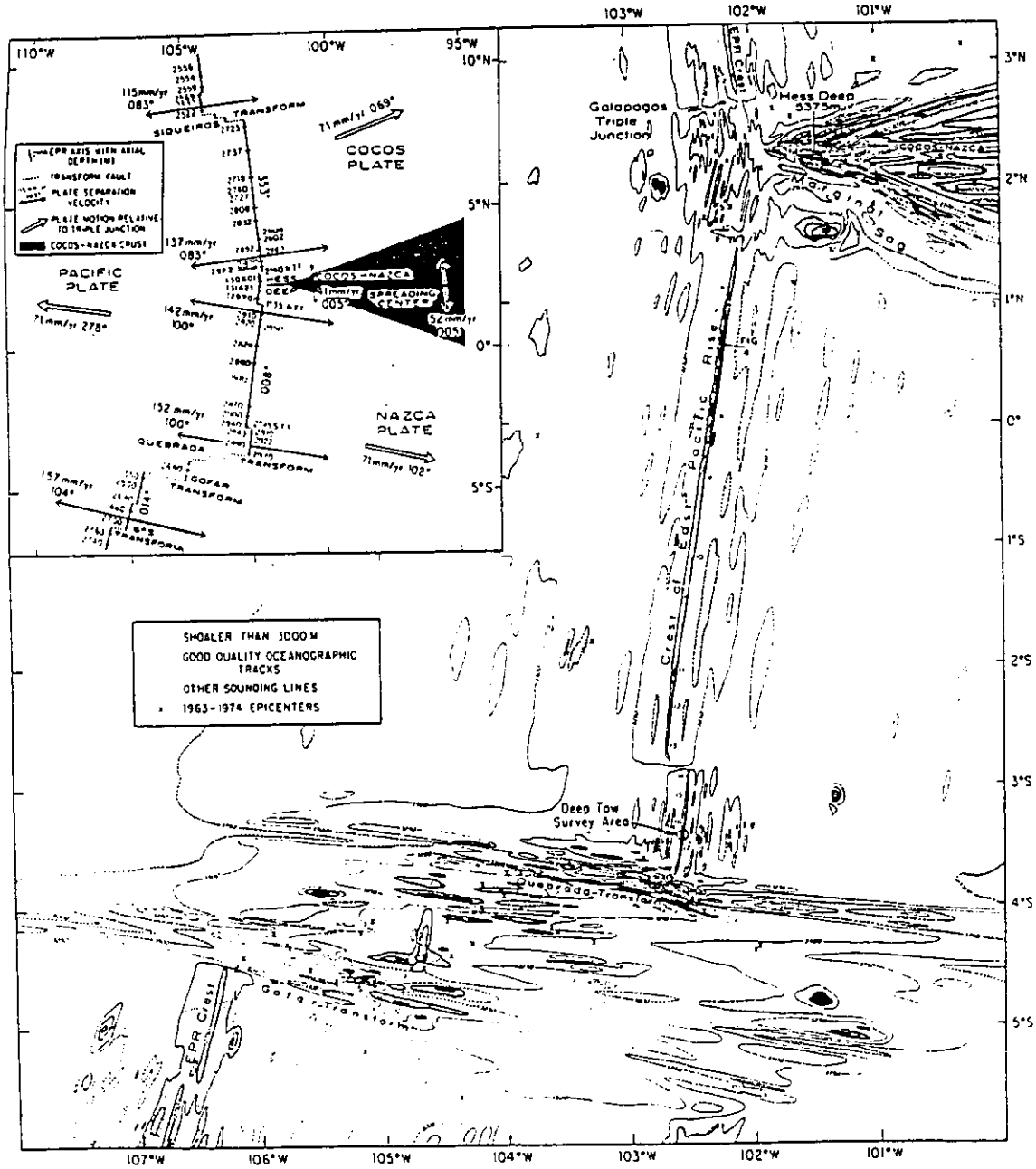
Surface-ship reconnaissance during Expedition PLEIADES 1, 1976 (Lonsdale, 1977a) showed that the E.P.R., between the equator and the Q.F.Z., is characterised by a long spreading axis orthogonal to infrequent transform faults (see Figure 7.2.1). The Q.F.Z. system represents the first major offset of the E.P.R., south of the Triple Junction,for 600 Kms (Lonsdale, 1977a).

Between 3°50'S and 4°30'S, the E.P.R. crest is offset right-laterally by a complex and imperfectly surveyed system of faults. This 400 Km offset was mapped as a pair of transform zones (the Q.F.Z. and the Gofar Fracture Zone, G.F.Z., of Lonsdale, 1977a), with an intervening 50 Km long spreading axis at 104°40'W (see Figures 7.2.1 and 7.2.2.). Each transform zone is approximately 50 Kms wide, with several *en echelon* faults. Pelagic sedimentation rates were measured at 2.2 cms per 1000 years in this area (Lonsdale, 1977b). This area of the E.P.R. was initiated as an active spreading centre 5.4 million years ago (Rea, 1975), as activity shifted from the fossil Galapagos Rise to the E.P.R.

According to analysis of earthquake epicentres (Anderson and Sclater, 1972), the Q.F.Z. strikes at 105° and a maximum depth of 4700 m was encountered at dredge station 225D. However, Mammerickx et al. (1975)

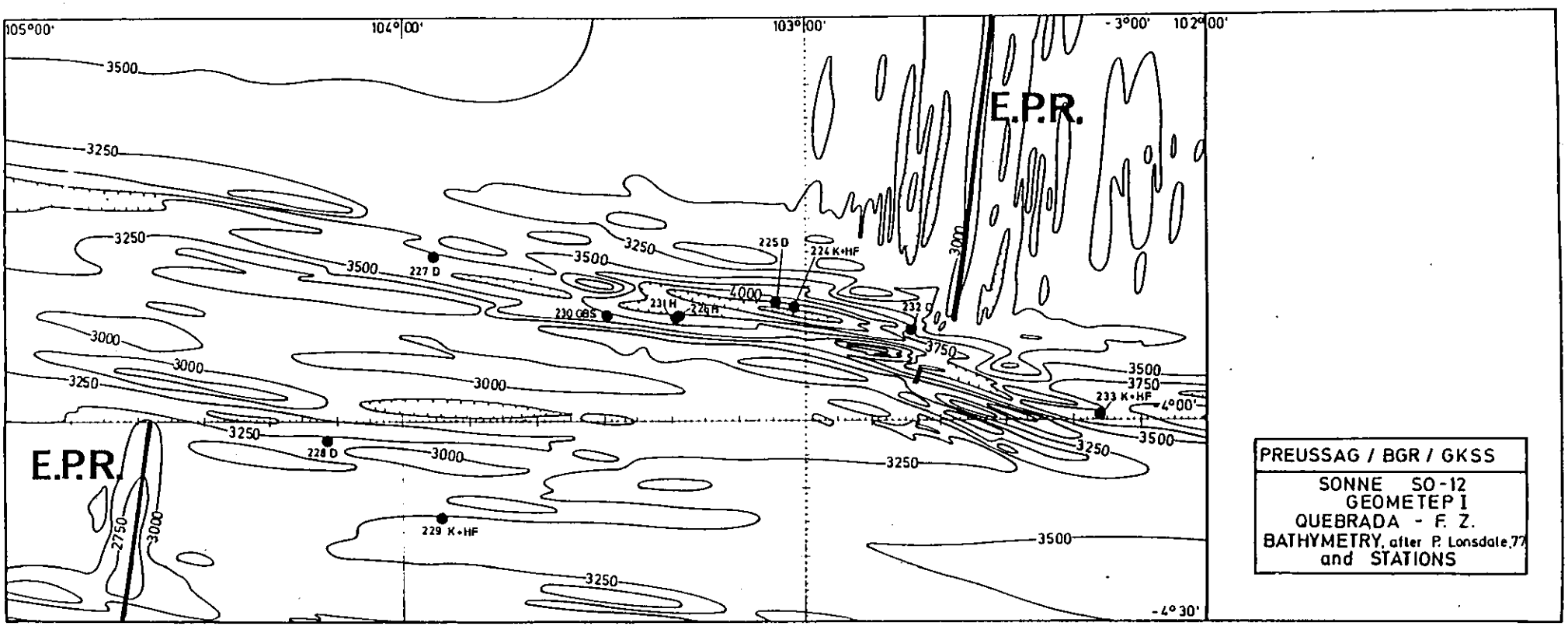
FIG.7.2.1. Regional structure and plate tectonic setting of the East Pacific Rise between the Triple Junction and the Quebrada /Gofar TransformZone.

(from Lonsdale,1977a).




Bathymetric map of the equatorial East Pacific Rise, contours in meters corrected using Matthew's tables, Area 41. Inset shows relative plate motions, after Hey *et al.*, 1977, and depth of the spreading axis; except near the Galapagos triple junction (depths in brackets) the axis is taken as the shallowest point on each crossing.

FIG.7.2.2. Bathymetry of the Quebrada Fracture Zone located in the 4°S area of the East Pacific Rise.



located a "hole" at $4^{o}35'S$ and $105^{o}05'W$, with a maximum depth of 4905 m, which is approaching depths found in the Hess Deep (see Chapter 6).

## 7.3 SAMPLE DESCRIPTION

The 2 cores sampled display a change in colour down their lengths, from light yellowish brown (10 YR 6/4) to pale greenish yellow (10 Y 8/2), coupled with an increase in the silt and clay fraction ($< 63\mu$) of the sediment. Sediments and basalts were recovered from water depths between 4453 m and 4697 m during dredge 225D and the sediment consists of silty and sandy-grade material with some calcareous and biogenic debris. Fragments of volcanic glass are also included in this sediment.

The dredged basalts from this area show some palagonitisation, and some have a thin veneer of Fe-Mn oxides. The pillow lavas are plagioclase and olivine-phyric. Smear slides show badly preserved foraminifera from depths between 3721 m and 3933 m and these depths appear to coincide with the supposed depth of the C.C.D. in this area, estimated at around 3600 m to 4000 m, by Berger et al. (1976).

## 7.4 BULK GEOCHEMISTRY (SEE APPENDIX C)

Although data is very limited, a brief description of certain interesting element concentrations is justified. $CaCO_3$ content varies from 15% to 97% and the sediments are dominantly foraminiferal chalk oozes. Data expressed on a carbonate-free basis (see Appendix C) at high values of $CaCO_3$ should be treated with caution, as a small error in $CaCO_3$ determination will drastically alter the correction factor applied to the other elements. This appears to be the case for the high metal values in sediment from dredge 227D (see Appendix C).

High values of Al, Ti and V in sediments from dredges 225D and 232D, illustrate the abundance of volcanogenic components in sediments from the sparsely-sedimented scarp slopes of the north wall of the Q.F.Z. In the Q.F.Z., contrary to the findings in the GRAFZI area, the Cu content of sediments exceeds the Zn content. High Cu (467 ppm) and

Pb (135 ppm) values occur in the same sample but neither Fe or Mn values are high, which makes it difficult to explain the concentration of Cu and Pb, in terms of adsorption onto Fe and Mn oxides.

## 7.5 CONCLUSION

The extremely limited data and the nature of the samples preclude the assignation of a hydrothermal or a hydrogenous origin to the thin Fe - Mn oxide films found on dredged rocks from this area. It is not possible to rule out hydrothermal activity in the Q.F.Z. but insufficient evidence exists to verify its presence.

STUDY E CHAPTER 8

# THE 10°S AREA OF THE EAST PACIFIC RISE

## 8.1 INTRODUCTION

A total of 18 samples were collected from the 10°S area of the E.P.R. during the GEOMETEP cruise of 1980. They consist of sediments from 3 dredges, 3 Van Veen grabs and 1 kasten or box-core. Data from these samples supplement data from previous detailed studies in the 10°S area (e.g. Dasch, 1981; Dymond, 1981; Heath and Dymond, 1981; McMurtry et al., 1981; McMurtry and Yeh, 1981; Veeh, 1981; Veeh and Bostrom, 1971). The locations of 12 cores described in these other works are shown later.

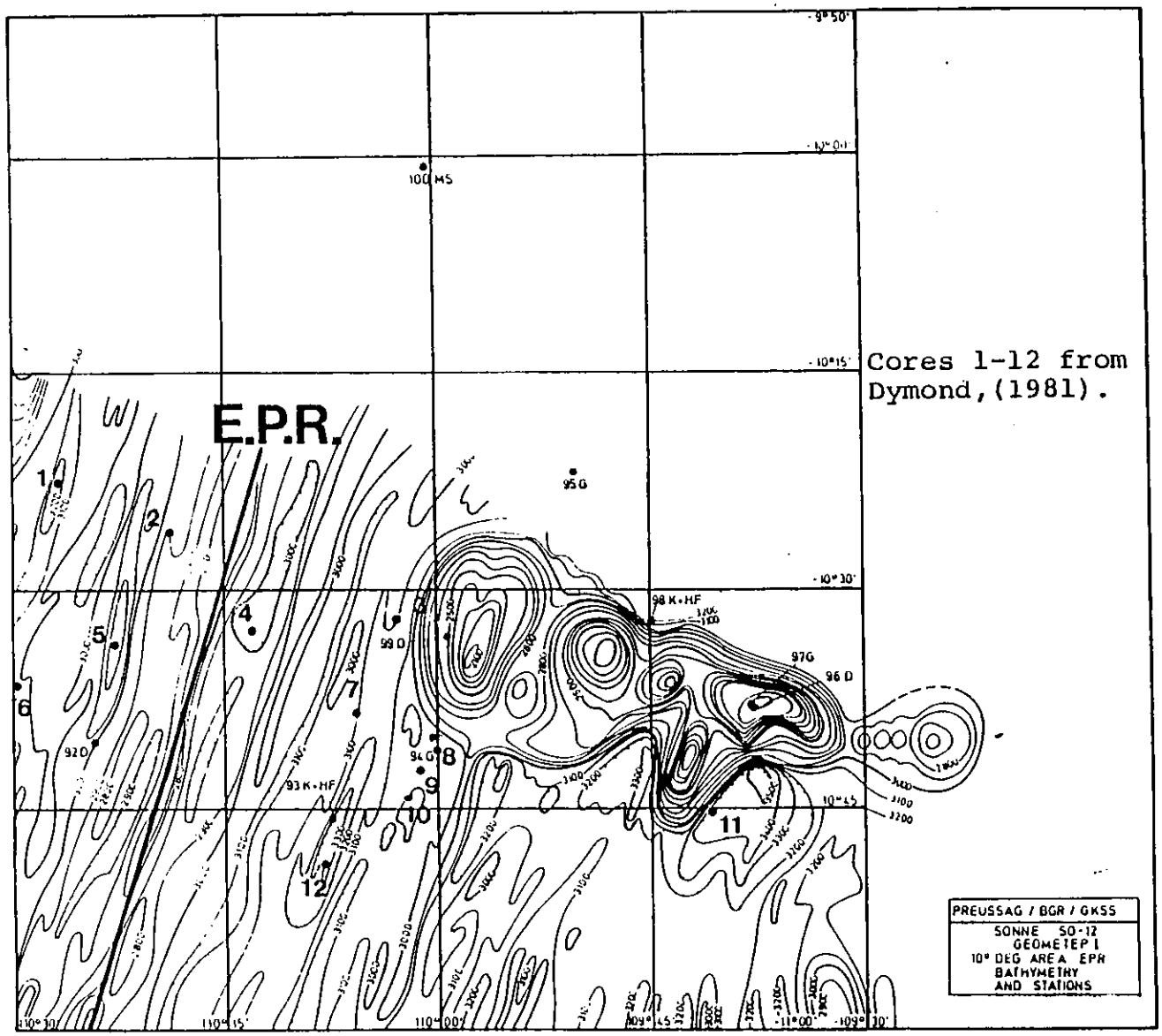
## 8.2 GEOLOGY, BATHYMETRY AND STRUCTURE OF THE 10°S AREA

The geology, bathymetry and structure of the 10°S area of the E.P.R. has been studied in detail by Rea (1975 and 1976). The axis of the E.P.R. is represented by a topographic block, 15 Kms wide and 300 to 350 m high, flanked by 100 to 200 m high abyssal hills which are 3 to 5 Kms wide.

Rea (1976) observed an axial block offset of about 10 Kms, in a left lateral direction, at 10°S, while a similar offset, in a right lateral direction, occurs at 11°30'S. Magnetic anomaly data indicates that these left and right lateral transform faults formed between 1.7 to 0.9 million years ago and 0.7 million years ago to present day, respectively (Rea, 1976). The author interpreted the small axial offsets as a result of either brief episodes of asymmetric seafloor spreading or discrete "jumps" of the site of spreading activity, with both axial shifts to the west.

Seafloor spreading was initiated on the E.P.R. between 9°S and 13°30'S in the late Miocene, about 8.2 million years ago (Rea, 1976). The

FIG.8.2.1. Bathymetry (after Rea,1976) & station locations in the 10°S area of the E.P.R.



seafloor spreading rates, during the last 1.7 million years, have equalled 8 cms per year westwards and 7.7 cms per year eastwards, totalling a separation rate of 15.7 cms per year. Van Andel et al. (1976) observed a broad 'shoal' zone to the west of the E.P.R. and south of 10°S, which may be related to the slightly asymmetric spreading rate.

The 10°S area of the E.P.R. is shown in Figure 8.2.1, where the E.P.R. axis trends approximately along 018° and is defined by depths shallower than 3000 m (Rea, 1976), with minimum depths of 2700 m. Station locations from the GEOMETEP cruise and other works are also shown in Figure 8.2.1. The unusual topographic high, located east of the E.P.R. axis, and with horizontal dimensions of 60 Kms by 20 Kms, represents the multi-summited, AMPH D2 seamount of Bonatti and Joensuu (1966), which is elongated perpendicular to the E.P.R. axis. The seamount spans a depth range from 1800 to 3200 m.

## 8.3 SAMPLE DESCRIPTION

Sediments from the 10°S area vary in grain size and colour, from chocolate brown sediment from dredge 92D, to light beige, coarse globigerina sands of grab 97G. The remaining sediments are generally light beige foraminiferal carbonates but with subtle variations in colour between the two extremes mentioned above. Thin Fe-Mn crusts were found coating basalts from dredge 96D.

## 8.4 SURFACE SEDIMENT GEOCHEMISTRY

A synthesis of all data, both from this study and from previous works, allows a detailed analysis of the geochemistry of surface sediments from the 10°S area. The GEOMETEP sediments can be classified as foraminiferal chalk oozes (see Appendix C) and results are reported on a carbonate free basis, with the exception of grab 97G sediment which consists almost entirely of $CaCO_3$.

Van Andel et al. (1976) placed the lysocline at about 3700 m in this area while Berger et al. (1976) placed the C.C.D. at between 4000 and 4500 m water depth. Therefore, carbonate dissolution is not a process

FIG.8.4.1. Fe in surface sediments from the 10°S area.

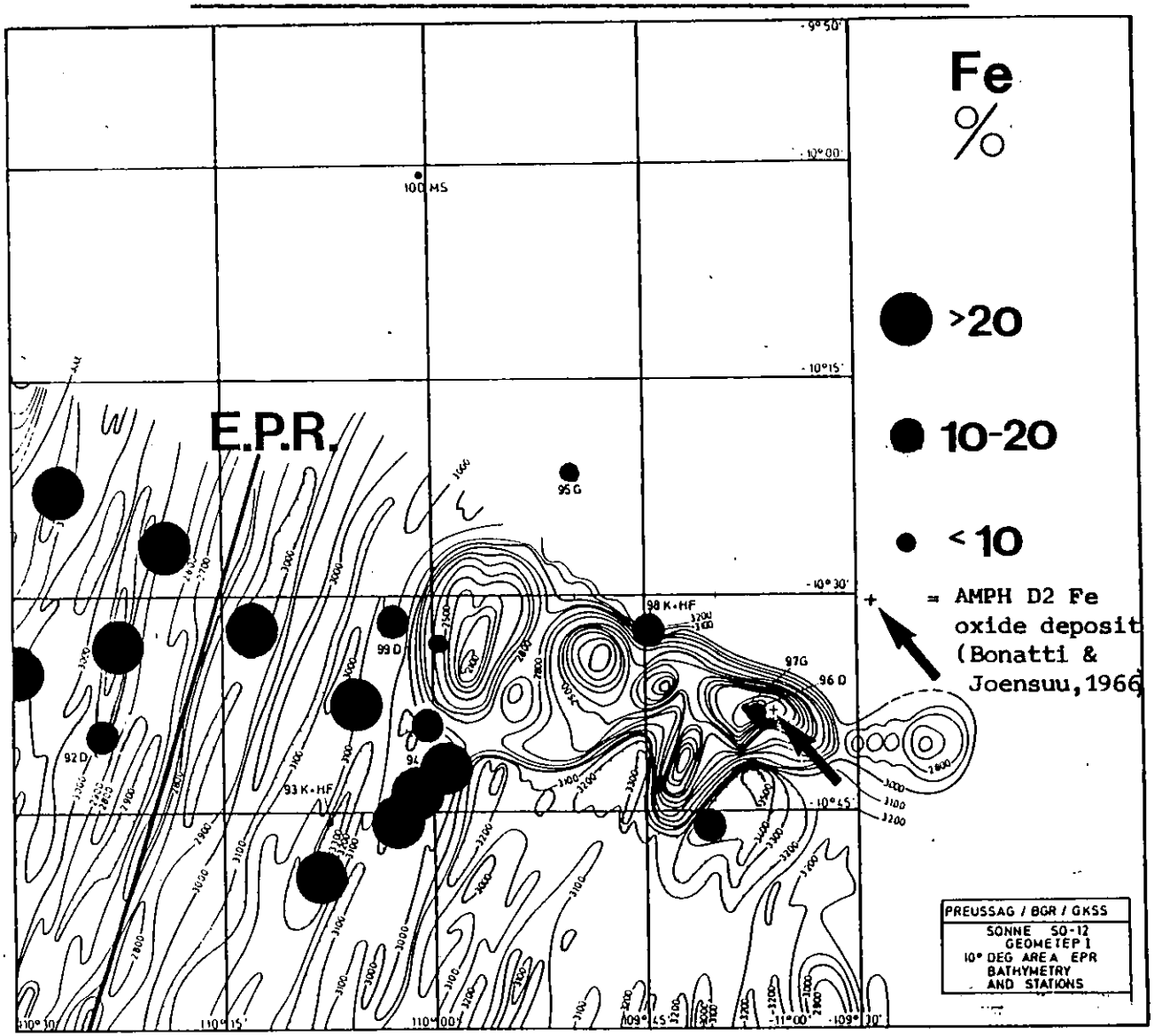


FIG.8.4.2. Mn in surface sediments from the 10°S area.

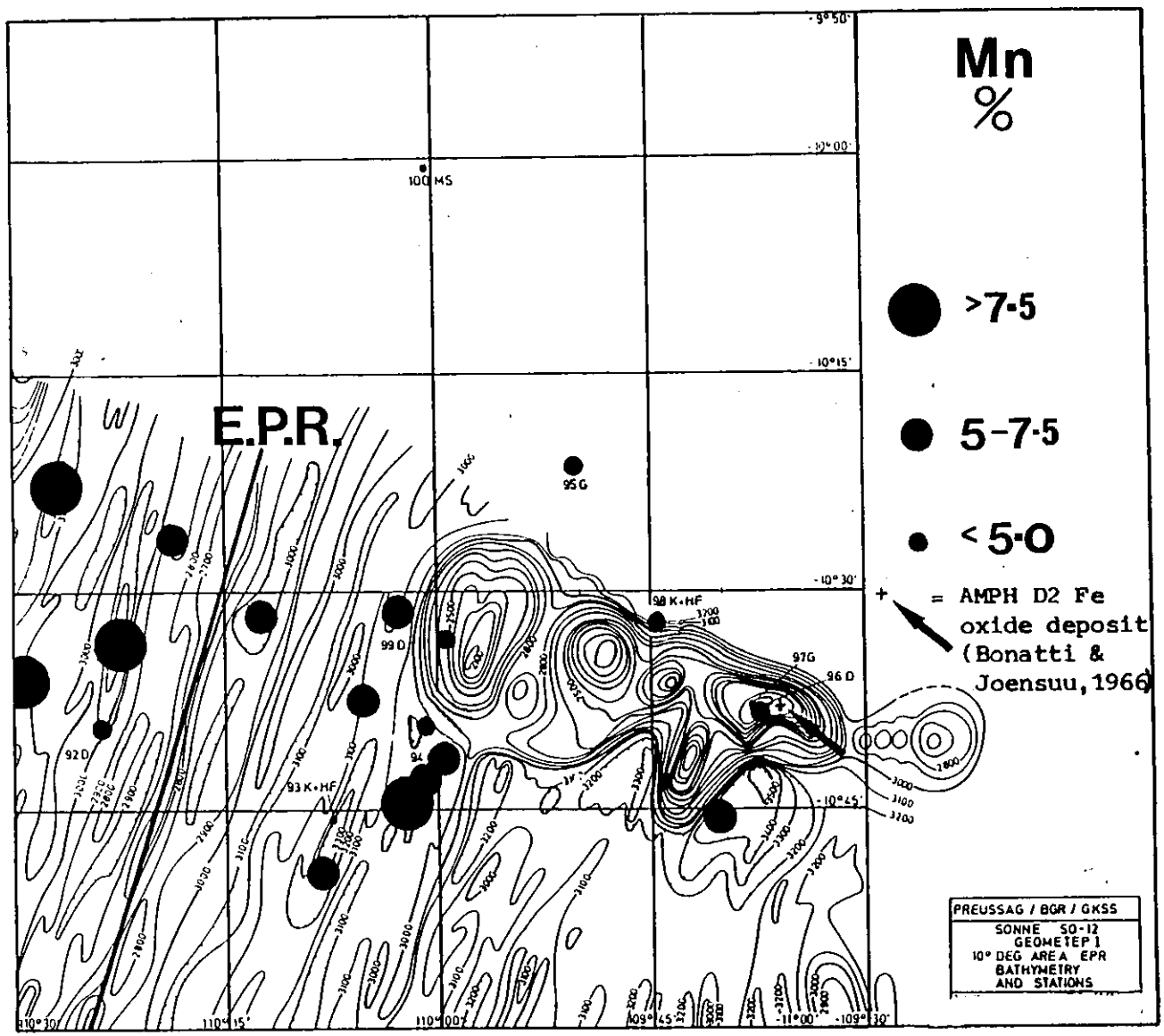


FIG.8.4.3. Cu in surface sediments from the 10°S area.

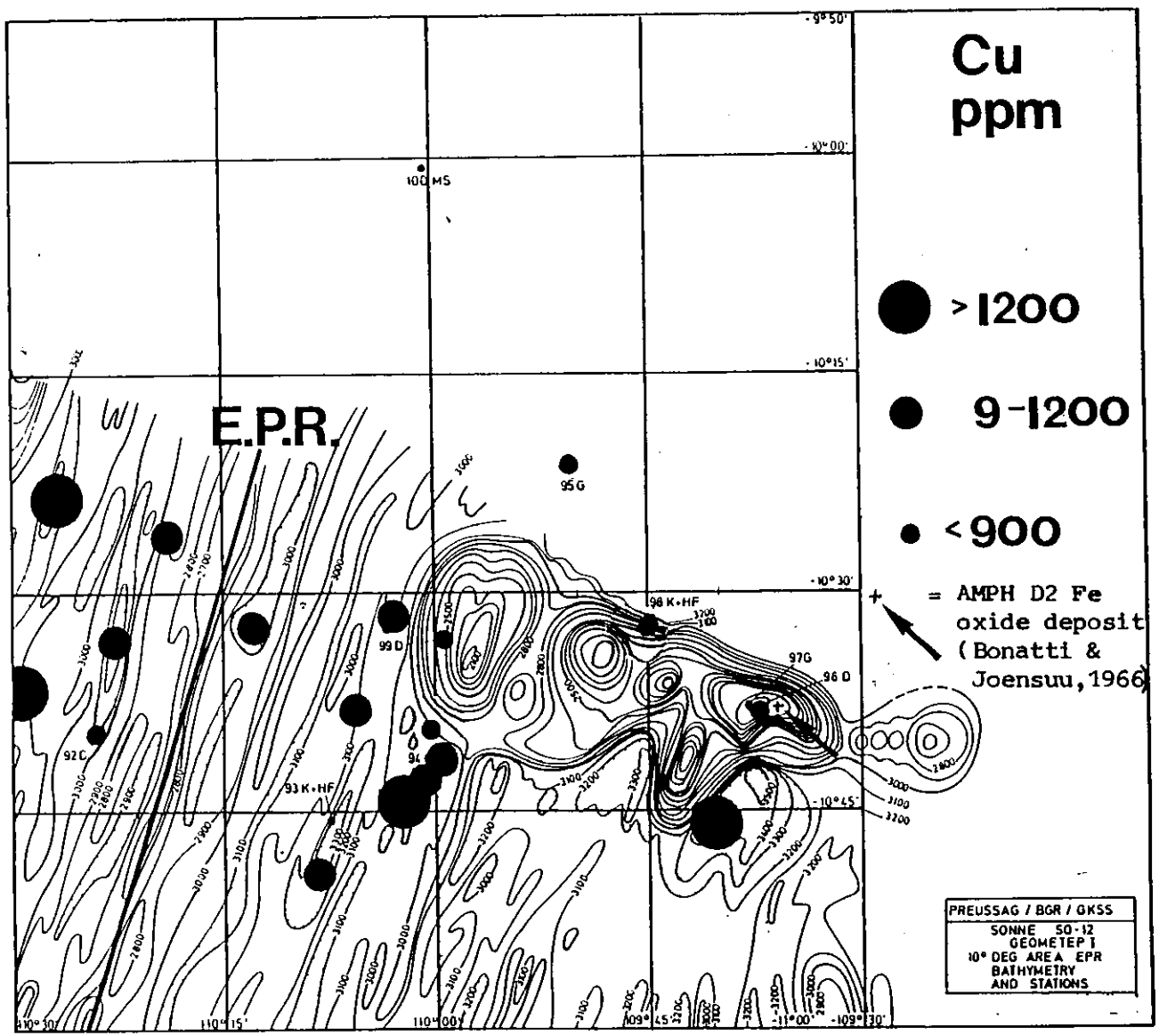
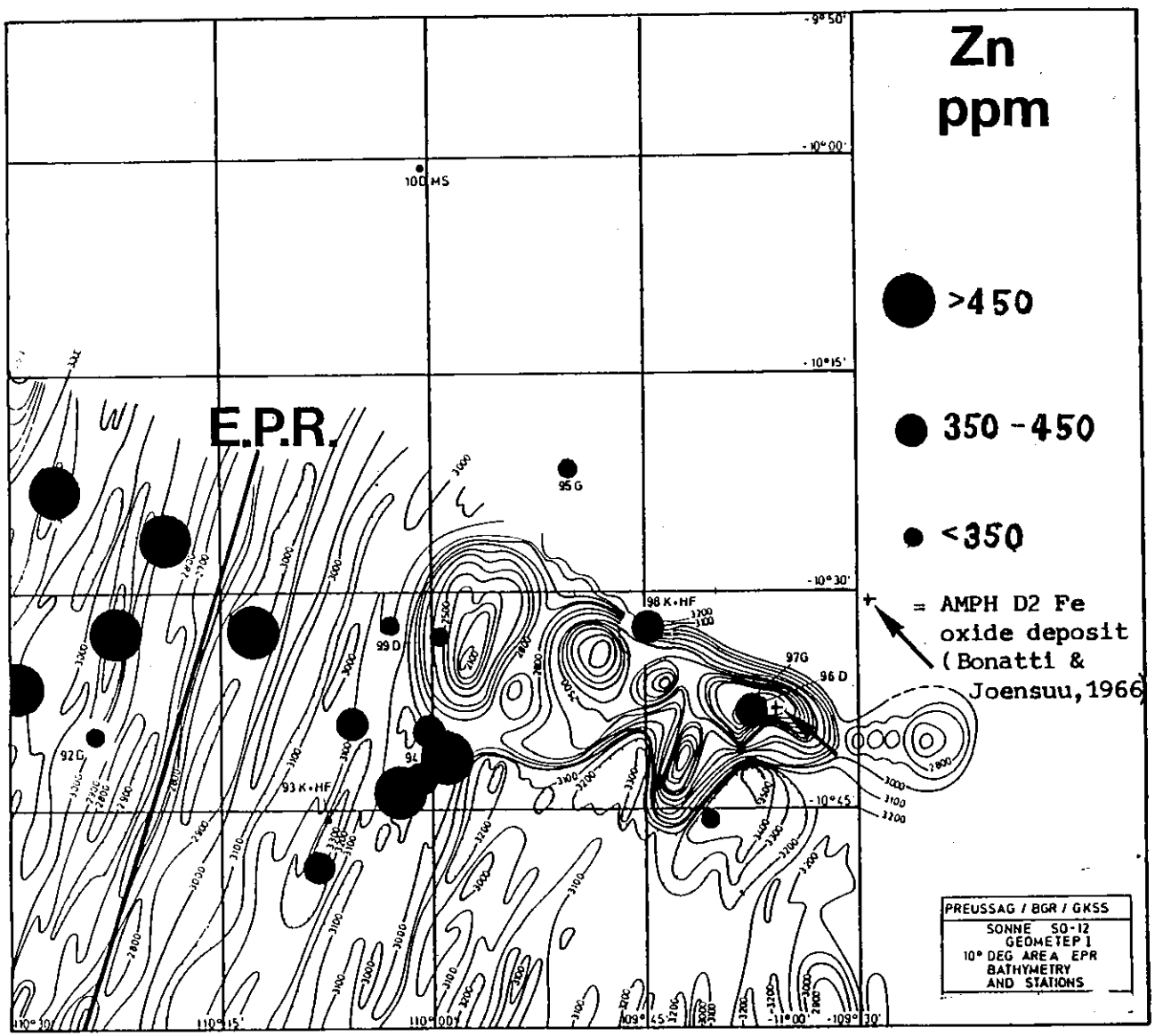


FIG.8.4.4. Zn in surface sediments from the 10°S area.



which is likely to affect the geochemical composition of the sediments studied, all of which are from depths shallower than the lysocline.

The majority of surface sediments shown in Figures 8.4.1 to 8.4.4 are located within a 50 Km diameter zone about the E.P.R. axis and the concentrations of Fe, Mn, Cu and Zn should therefore reflect hydrothermal contributions to the sediment. Dymond (1981) noted that the hydrothermal component of sediments was generally greater than 80%, within 100 Kms of the E.P.R. axis.

*Fe*

Within the immediate vicinity of the E.P.R. axis, Fe values in surface sediment exceed 20% (Figure 8.4.1), reaching a maximum of 27.8% in core 6 (see core location in Figure 8.2.1). Fe contents reported for GEOMETEP sediments are lower than those reported by Dymond (1981) and this is probably largely due to the closer proximity to the E.P.R. axis of the samples of the latter author.

The bulk of the GEOMETEP surface sediments which are, in the most part, concentrated around the AMPH D2 seamount to the east of the E.P.R. axis, contain lower amounts of Fe than those immediately adjacent to the spreading axis. In the case of sediment from stations 96D and 97G, only 2.3% Fe (carbonate free data) and 0.1% Fe (raw data) were detected. The latter sample consists almost entirely of $CaCO_3$. These low Fe contents demonstrate the sharp fractionation of Fe that can occur in the vicinity of a hydrothermal centre, i.e. the AMPH D2 Fe oxide deposit of Bonatti and Joensuu (1966).

*Mn*

The Mn distribution in $10^{\circ}S$ area surface sediments (Figure 8.4.2) shows that while Mn is generally greater than 7.5% on the west flank of the E.P.R., only one sediment sample (from core 10) contains this amount of Mn on the east flank. In sediments adjacent to the E.P.R. axis, but on the east side, Mn concentrations vary between 5.0 and 7.5%. GEOMETEP surface sediments from around the AMPH D2 seamount often contain less than 5% Mn, with a minimum of 0.4% Mn at station 96D.

The AMPH D2 deposit (Bonatti and Joensuu, 1966) contains Mn oxide crusts with up to 39% Mn. However, no great enrichment in Mn can be detected in surface sediments from the vicinity which further suggests a highly fractionated, spatially-restricted hydrothermal system there (see later).

*Cu*

Cu is most enriched in sediments located about 20 to 30 Kms from the E.P.R. axis (Figure 8.4.3) and also in core 11, from the base of the southerly slope of the AMPH D2 seamount. In these sediments, Cu concentrations exceed 1200 ppm, with a maximum of 1370 ppm in core 6 (see core location in Figure 8.2.1), from the E.P.R. west flank. The high Cu content found in core 11 coincides with a high Fe/Mn ratio in the sediment.

*Zn*

The highest concentrations of Zn found in the 10°S area (Figure 8.4.4) are contained in sediments from the crestal area of the E.P.R. A maximum of 550 ppm Zn can be found in core 6, which also contains the highest concentrations of Fe, Mn and Cu. The distribution of Zn about the crestal area of the E.P.R. appears to be more uniform than that of Cu.

*Cu/Zn*

Crestal E.P.R. surface sediments yield Cu/Zn ratios which occupy a narrow range from 2.35 to 2.95. However, the maximum value for the Cu/Zn ratio, 3.51, is found in core 11. The uniformity of the Cu/Zn ratio in crestal sediments has also been observed in the 13° - 15°S area of the E.P.R. (see Chapter 9).

A closer inspection of GEOMETEP surface sediments shows that the Cu/Zn ratio of 0.25, observed for surface sediment from station 96D, is the lowest found in the 10°S area. This sample also had the highest Fe/Mn

ratio, 6.43, and therefore, would appear to contain more Fe, relative to Mn, and more Zn, relative to Cu, than any other sediment from this area. The association of Fe with Cu along with high Cu/Zn ratios in proximal hydrothermal deposits, has been noted in the GRAFZI area (see Chapter 2). The abundance of Zn, 350 ppm, in the station 96D sample is compatible with the observation that this sample is highly fractionated, with respect to the Fe/Mn ratio, compared to the original deposit described by Bonatti and Joensuu (1966). Thus, the 96D surface sediment metal concentrations can be considered as distal to the hydrothermal source, compared to the AMPH D2 Fe oxide deposit.

Similarly, a low Cu/Zn ratio of 0.84 is found in surface sediment from Station 99D. Following the above argument that high Cu/Zn ratios occur in the immediate vicinity of hydrothermal vents, then station 99D can also be considered as distal to a hydrothermal source (see later).

## 8.5 DOWNCORE SEDIMENT GEOCHEMISTRY

The previous section has described the surface distribution of hydrothermally derived elements in the 10°S area. In order to investigate possible diagenetic changes within older sediments and temporal variations in hydrothermal activity, it is necessary to study downcore sediments. The 300 cm-long core 98K represents the only core collected from the 10°S area during the GEOMETEP cruise of 1980. However, data is also available from the Y71-7-44P core (core 9, see Figure 8.2.1) of Heath and Dymond (1981), which is 464 cms long.

Heath and Dymond (1981) noted that "even mildly reducing conditions in the sediments lead to depletion of Mn downcore" in the 10°S area. Core 9 contains 6.6% Mn at 7 cms depth and 1.5% Mn at 67 cms depth. A similar decrease in Mn content from 3.5% to 1.7% occurs below 50 cms in core 98K. The cause of this is the diagenetic remobilisation of Mn under reducing conditions (Lynn and Bonatti, 1965). Fe, Mg to a lesser extent, and the trace metals, Li, La, V, Co, Ni, Cu, Zn, Pb and P, are also reduced in concentration below about 50 cms depth. However, between 200 and 225 cms depth in core 98K, increased concentrations of

Fe (10%), Mn (2.6%), and certain trace elements (e.g. Li, La, Ti, V, Co, Ni, Cu, Zn and P), indicate a past period of hydrothermal activity. Furthermore, the increases observed in Al and Ti contents within this depth interval suggest the presence of more abundant volcanogenic debris, confirmed by smear slide analysis. Similarly, core 9 (Heath and Dymond, 1981) also show increased metal concentrations, at 212 and 228 cms depth.

It is possible to date the hydrothermal episode at between 194,000 and 221,000 years ago for the depth interval 200 to 228 cms, using the mean sedimentation rate data for the 10°S area, from Heath and Dymond (1981), of 0.97 cms/1000 years. Dymond and Veeh (1975) independently measured the sedimentation rate of a core from this area and arrived at the value of 0.93 cms/1000 years, which agrees with the work of Heath and Dymond (1981). Core 9 which is now located 31 Kms to the east of the E.P.R. axis, would have been located 16 Kms from the axis at the end of this hydrothermal episode, assuming a half-spreading rate of 7.7 cms/year (Rea, 1976). Similarly, core 98K which is now located 55 Kms to the east of the E.P.R. axis, would have been located about 40 Kms from the axis.

## 8.6 DISCUSSION

It has been shown that lesser contributions of the hydrothermal component of 10°S area sediments, from the east flank of the E.P.R., have been deposited since 194,000 years ago. It has also been shown that concentrations of metals increased in the upper layers of the two cores studied. Increased concentrations of Fe, Cu and Zn in west flank surface sediments (Heath and Dymond, 1981) and the discovery of hydrothermal Fe-montmorillonites in 10°S area surface sediments from both flanks of the E.P.R. (McMurtry and Yeh, 1981), strongly support a recent increased supply of the hydrothermal component of sediments. Heath and Dymond (1981) estimated that this component comprised 62% of east flank surface sediments and 78% of west flank surface sediments.

In terms of absolute metal contents (Heath and Dymond, 1981) and U/Th ratios (Veeh, 1981), there is a marked asymmetry in 10°S sediments from the west and east flanks of the E.P.R. The former authors postulated a recent change in near-bottom current circulation that now is responsible for sweeping hydrothermal debris westwards. There is some support for this hypothesis, from work in the 13° - 15°S area (see Chapter 9), where the same asymmetry in metal contents of surface sediments is observed. Reid (1981) found a west to south west direction for the flow of mid-depth currents in this general area. McMurtry et al. (1981) showed that lower accumulation rates observed for Fe and Mn, in the 10°S area, were due to loss of the metalliferous component of sediment due to bottom current activity, but these authors suggested movement to the north.

Although downcore sediment data is limited, it is possible to conclude that upon transport of sediment outside the zone of most intense hydrothermal activity, by seafloor spreading, the E.P.R. east flank cores have received reduced contributions of hydrothermal precipitates. This is possibly due to the inception of the westward flow of bottom currents which have been dated at a similar time, between 169,000 to 236,000 years ago, in the 13° - 15°S area of the E.P.R. (this work). In addition, the decrease in metal concentrations observed in sediments deposited between 194,000 years and until recently, may simply reflect increased distance from source areas along the axial region of the E.P.R. However, renewed hydrothermal activity has recently supplied both west and east flank surface sediments in the axial region of the E.P.R. with increased metal contents, (e.g. Fe, Cu and Zn) along with low temperature, colloidally-transported, hydrothermal Fe montmorillonites (McMurtry and Yeh, 1981).

Besides the regional supply of metals from hydrothermal activity associated with the crestal region of the E.P.R., there is also a smaller hydrothermal system centred on the AMPH D2 Fe oxide deposit of Bonatti and Joensuu (1966). The deposit fits into the 'goethite-

amorphous ferric hydroxide' facies of the Red Sea deposits (Bischoff, 1969). Metallogenesis associated with seamounts is known in the following locations - the GRAFZI area (see Chapter 2); Loihi submarine volcano, Hawaii (Malahoff et al., 1982); Larson's Seamounts, E.P.R., 21°N (Lonsdale et al,, 1982). The latter hydrothermal deposit is particularly interesting due to similarities with the AMPH D2 deposit, both in the type of deposit and its location, i.e. off-axis, but adjacent to the E.P.R. The style of hydrothermal process is distinctly different from that observed regionally over the E.P.R. axis. Hydrothermal activity is much more localised and the extreme fractionation of Fe from Mn and Cu from Zn is attested to by the presence of both Fe oxide rocks and Mn oxide rocks in the same dredge haul and also the low Cu/Zn ratio observed in adjacent station 96D surface sediment.

It is not known whether polymetallic sulphides exist near the AMPH D2 Fe oxide deposit, either at the surface, or at depth. However, polymetallic sulphides dominated by Cu, have been found associated with Fe oxide deposits in the Larson's Seamounts (Lonsdale et al., 1982). To carry the analogy further, the eastern summit of the AMPH D2 seamount is most distant from the E.P.R. axis and it is here that the Fe oxides were found, as in Larson's Seamounts. The nearest, most eastern, volcano to the E.P.R. axis in Larson's Seamounts contains polymetallic sulphides while the nearest, most western, volcano of the AMPH D2 seamount has been largely unexplored. However, station 99D sediment contains low Fe/Mn and Cu/Zn ratios which may be indicative of a distal hydrothermal facies. On this basis, the western summit of the AMPH D2 seamount should be a future exploration target.

Dating of the AMPH D2 Fe oxide deposit by U series isotopes indicates that it was formed less than 8,000 years ago (Veeh and Bostrom, 1971). This evidence proves that the deposit formed close to its present distance from the E.P.R. axis. As the western summit of the seamount-structure is located nearer to the source of seafloor spreading, it is

interesting to speculate whether the increased proximity to the heat source may allow the formation of a higher temperature sulphide deposit on the sea-bed there.

Finally, the high Cu content and high Fe/Mn and Cu/Zn ratios observed for surface sediment from core 11, located at the base of the southerly slope of the eastern summit of the AMPH D2 seamount, may suggest an adjacent hydrothermal vent. However, equally feasible, is an origin of this sediment from slumping of material from the summit of the seamount, where the AMPH D2 Fe oxide deposit is located. Bostrom et al. (1974) have noted the importance of winnowing of fine-grained hydrothermal precipitates on topographic highs located near the E.P.R., and redeposition at greater depths. Cronan and Varnavas (1981) also noted ponding of hydrothermal precipitates in basins on the floor of the Wilkes Fracture Zone at 9°S, on the E.P.R.

## 8.7 CONCLUSIONS

The following conclusions may be drawn from the above data:-

1. Two types of hydrothermal activity have produced the high Fe, Mn, Cu and Zn contents in 10°S area sediments. They are:-
   (i) Regional hydrothermal activity associated with the axial zone of the E.P.R.
   (ii) Localised seamount hydrothermal activity.

2. The most extensive hydrothermal activity, type (i), has affected the whole axial zone of the E.P.R. at 10°S. Relatively constant Cu/Zn ratios and abundances of these elements typify crestal sediments.

3. Westward flowing bottom currents have produced an asymmetry in metal concentrations in sediments from the west and east flanks of the E.P.R. West flank surface sediments are more enriched in the hydrothermal component than are east flank sediments (Heath and Dymond, 1981).

4. Since 194,000 years ago, until recently, east flank sediments have received lesser amounts of hydrothermally derived metals which may, in part, be due to seafloor spreading away from the axial source of supply. In addition, the initiation of westward-flowing bottom currents at around 194,000 years ago, as found in the 13 - 15°S area (see Chapter 9), may be partly responsible for the differences observed.

5. A recent hydrothermal episode has enriched 10°S area surface sediments in Fe, Mn, Cu and Zn, present in ferromanganese oxides. McMurtry and Yeh (1981) have also shown the presence of low temperature, hydrothermal,colloidally-transported Fe-montmorillonites in these sediments.

6. The second type of hydrothermal activity is more localised and is centred at the AMPH D2 Fe oxide deposit (Bonatti and Joensuu, 1966). This system is highly fractionated with regard to Fe/Mn and Cu/Zn ratios observed in sediments.

7. By analogy with Larson's Seamounts (Lonsdale et al., 1982), the westernmost summit of the AMPH D2 seamount has considerable potential for polymetallic sulphide occurrence.

STUDY F CHAPTER 9

# THE 13 - 15°S AREA OF THE EAST PACIFIC RISE

## 9.1 INTRODUCTION

The GEOMETEP cruise of 1980 investigated the E.P.R. between latitudes 13 - 15°S and recovered 130 samples comprising 126 sediments and 4 ferromanganese oxide crusts from the stations shown in Figure 9.1.1. Twenty-three of these samples represent surface sediments.

A bathymetric survey was conducted in the Garret Fracture Zone at 13°30'S (see Figure 9.2.1) and this is the only part of the 13 - 15°S area where bathymetric data is available.

## 9.2 GEOLOGY, BATHYMETRY AND STRUCTURE OF THE 13 - 15°S AREA

The history of the E.P.R., south of the Pacific-Cocos-Nazca Plate Triple Junction, has been mentioned elsewhere (see Chapters 7 and 8). In summary, re-orientation of plates in the Central and Eastern Pacific in Miocene time, produced a 900 Km westward shift in seafloor spreading activity, from the Galapagos Rise to the E.P.R. This shift or "jump" has been extensively studied (e.g. Anderson and Sclater, 1972; Anderson et al., 1974 and 1978; Handschumacher, 1976; Herron, 1972; Mammerickx et al., 1975; Rea et al., 1973; Rea, 1975 and 1976; Sclater et al., 1971). Plate tectonic reconstructions of this event rely upon magnetic anomaly data, bathymetric data, seafloor age-depth relationships and earthquake fault-plane solutions. Generally, the above authors agree that seafloor spreading migrated from the Galapagos Rise to the E.P.R. between 20 and 6 million years ago. Seafloor spreading activity on the E.P.R. was initiated about 20 million years ago between 35 - 15°S (Herron, 1972; Handschumacher, 1976). North of 15°S, up to the Galapagos Rift - E.P.R. Triple Junction, the initiation of seafloor spreading activity has been variably dated at 6.5 million years (Anderson and Sclater, 1972), 8.2 million years (Rea, 1976) and 10 million years (Herron, 1972; Handschumacher, 1976).

FIG.9.1.1. Station locations in the 13-15°S area of the East Pacific Rise.

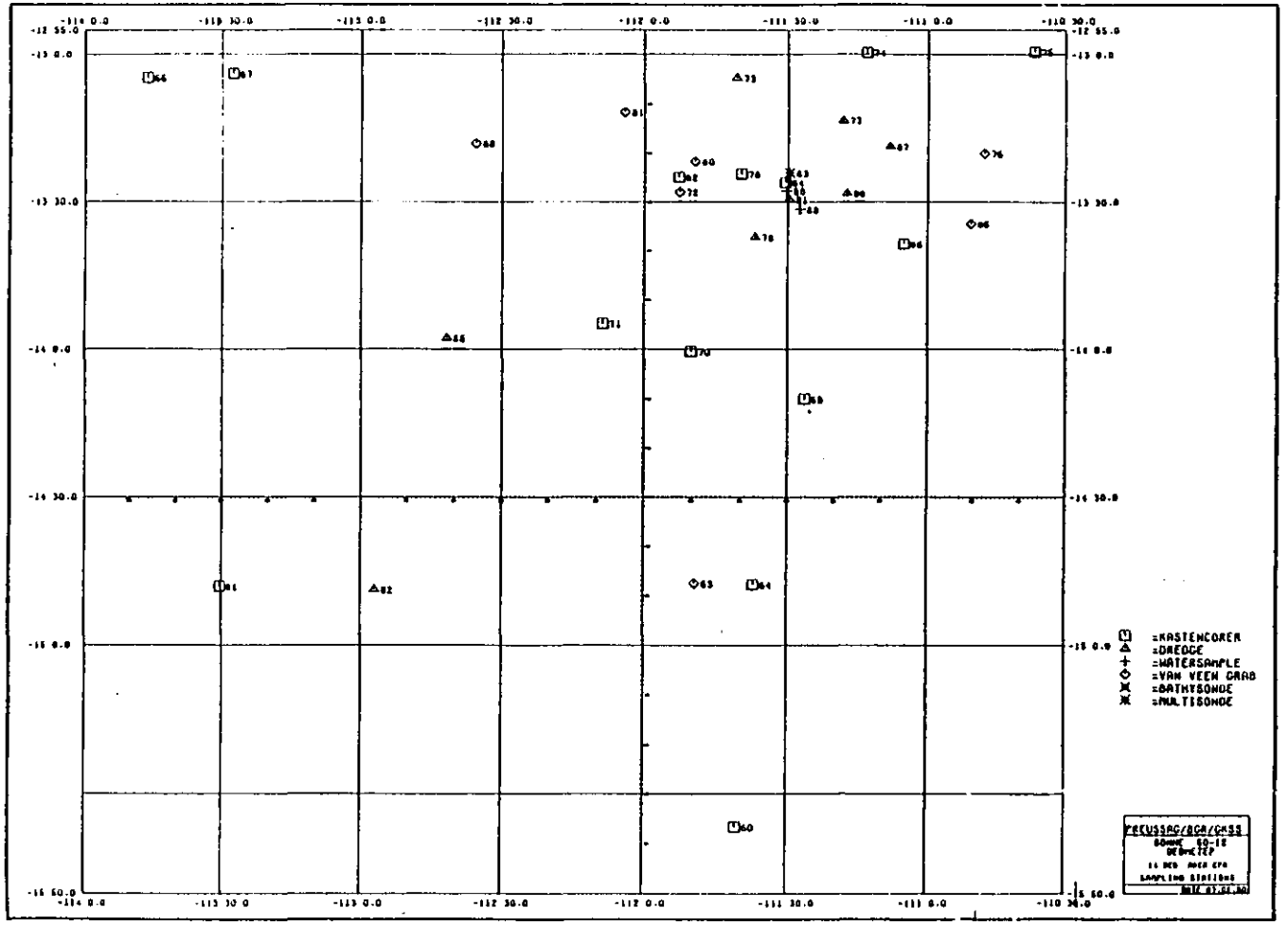
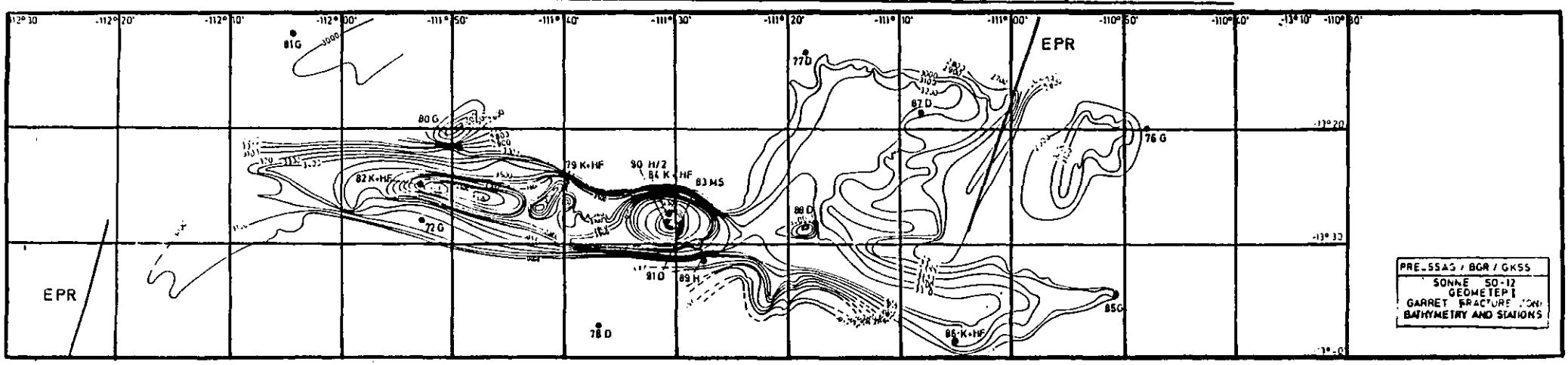


FIG.9.2.1.Bathymetry of the Garret Fracture Zone at 13°30'S,on the E.P.R.



The above evidence suggests that the Garret Fracture Zone, at 13°30'S, separates segments of the E.P.R. which started seafloor spreading processes at different times. The segment of the E.P.R. south of the Garret Fracture Zone started accreting lithospheric material about 10 million years before the northern segment (Mammerickx et al., 1975). These authors have attempted to correlate the Garret Fracture Zone with the Tuamotu Fracture Zone to the west and the Mendana Fracture Zone to the east. As a corollary of this, the Garret Fracture Zone may represent part of the ancestral fracture zone system which originally sinistrally offset the Galapagos Rise.

Early evidence for the existence of the Garret Fracture Zone was reported during the Scripps Institution expeditions CAPRICORN (in 1952), DOWNWIND (in 1957) and RISEPAC (in 1961). A dextral offset of the E.P.R. was found, of about 110 Kms, with an azimuth of 110°, but with a change in orientation to 102°, west of 113°W (see Fracture Zone VII of Mammerickx et al., 1975). Different offsets and orientations have been found by Handschumacher (1976), who reported an offset of 184 Kms, with an azimuth of 095°, on the basis of magnetic data, and by Anderson et al. (1978) who found an offset of 130 Kms, with an azimuth of 115°. The differences reported may be due to the fact that the geomagnetic equator is located near the 14°S area of the E.P.R. and this results in seafloor magnetic anomalies being of very low amplitude, < 50 nT, (Anderson et al., 1978). Bathymetric data from the GEOMETEP cruise show a dextral offset of the E.P.R. of about 138 Kms in the Garret Fracture Zone, with an azimuth of 110°. The above orientations agree with the general trend of the E.P.R. fracture zones (Anderson et al., 1974).

Localised large magnetic anomalies, with amplitudes up to 1250 nT, were reported from stations in the Garret Fracture Zone by Anderson et al., (1978), who considered this as being due to high Fe and Ti content in dredged basalts. Seventeen heat flow stations in the fracture zone region, taken during expedition SOUTHTOW Leg 8, showed that E.P.R. crestal heat flow values were low, and this was interpreted as due to thin sediment cover (Anderson et al., 1978). Low heat flow values obtained from the base of the central horst of the E.P.R. crest were interpreted as being due to seawater circulation along the fracture zone scarp.

In the absence of other data, the half spreading rate of 88 mm/year, found by Rea et al. (1973) for the 11°S area, can be assumed to represent the approximate half spreading rate in the 14°S area. Fracture zone topography consists of a complicated zone of about 60 Kms width (Anderson et al., 1978), with shoal regions at the intersections of the E.P.R. crest with the fracture zone, interpreted by these authors as representing volcanic piles.

Figure 9.2.1 shows the Garret Fracture Zone with a central depression reaching depths of 4900 m. Dredge station 91D recovered greenstones from this central depression from a depth range of 4616 to 4820 m. The sediments, rocks and ferromanganese crusts recovered from this area are described below.

## 9.3 SAMPLE DESCRIPTION

### 9.3.1 Sediments

The 126 sediments from 23 core, grab and dredge stations in the 13 - 15°S area of the E.P.R. consist of a suite of samples which range from variably metal-enriched sediments through to normal pelagic foraminiferal carbonates (see Section 9.4). The brown/dark brown colour of the most metal-enriched samples corresponds to Hue 7.5 YR 4/4 of the colour coding system shown in Appendix D. Smear-slide analysis of a limited number of these sediments reveals that they comprise principally two phases; firstly, well-preserved and often rust-coloured foraminifera and secondly, semi-opaque ferromanganese oxide grains, termed R.S.O's (red-brown semi-opaque oxides) by Yeats and Hart et al. (1976). Rarely, fish scales and small basaltic fragments can be found, the latter displaying characteristic concave, jagged margins.

### 9.3.2 Ferromanganese Crusts

Ferromanganese oxide crusts were recovered from dredge stations 77D and 87D, and are shown in Plates 9.3.1 and 9.3.2. The station 77D crust was sub-sampled in order to investigate the geochemical variation between surface, bulk and fibrous material (see Appendix C). The part-botryoidal and part-fibrous nature of the black, 1 cm-thick ferromanganese crust is




PLATE 9.3.1.

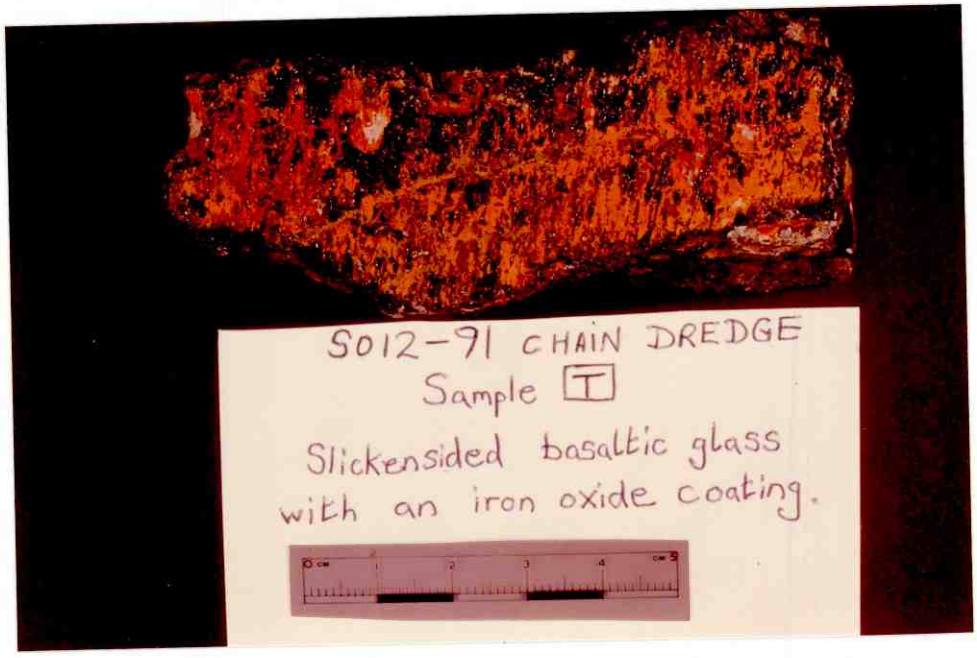
PLATE 9.3.2.






PLATE 9.3.3.

PLATE 9.3.4.



displayed in Plate 9.3.1. The tubular basaltic structure shown in Plate 9.3.2 is encrusted with orange ferromanganese oxide material which was sampled and analysed (see Appendix B). This crust is different in habit to that from dredge 77D and the geochemical differences are discussed later.

### 9.3.3 Rocks

Dredge haul 91D located in the Garret Fracture Zone recovered a great variety of rock types from depths between 4616 and 4820 m. Two rock samples are shown in Plates 9.3.3 and 9.3.4. The greenstone with secondary recrystallised laths (Plate 9.3.3) is typical of the dredge station 91D rocks described by Bideau et al. (1982). These authors identified metagabbros and metaperidotites with stain-induced recrystallisation, along with metamorphic assemblages which spanned the greenschist and amphibolite facies.

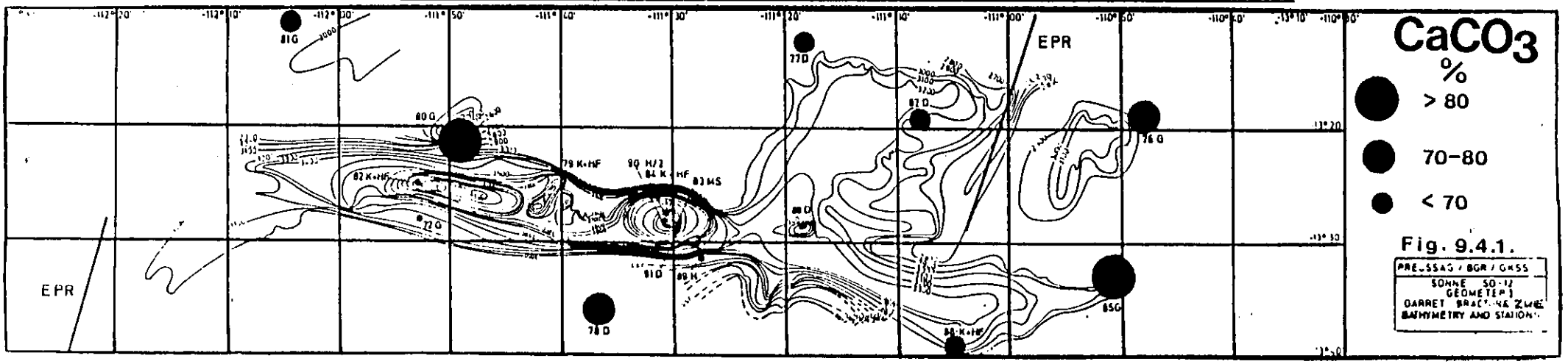
According to Bideau et al. (1982), the ultramafic rocks of station 91D consist of tectonites (e.g. harzburgites) and cumulates (e.g. plagioclase dunites and olivine gabbros). These rocks have undergone plastic deformation and cataclasis with the formation of a retrogressive (hydrothermal) metamorphism-induced secondary mineralogy. The authors considered that the above phenomena could be explained by lateral transfer, off the ridge axis, of plutonic lower crust/upper mantle rocks and subsequent emplacement on the bottom of the Garret Fracture Zone. The close relationship between tectonic and hydrothermal activity is further supported by the fresh basalt (Plate 9.3.4) which has a slickensided surface covered by a coating of orange iron oxide.

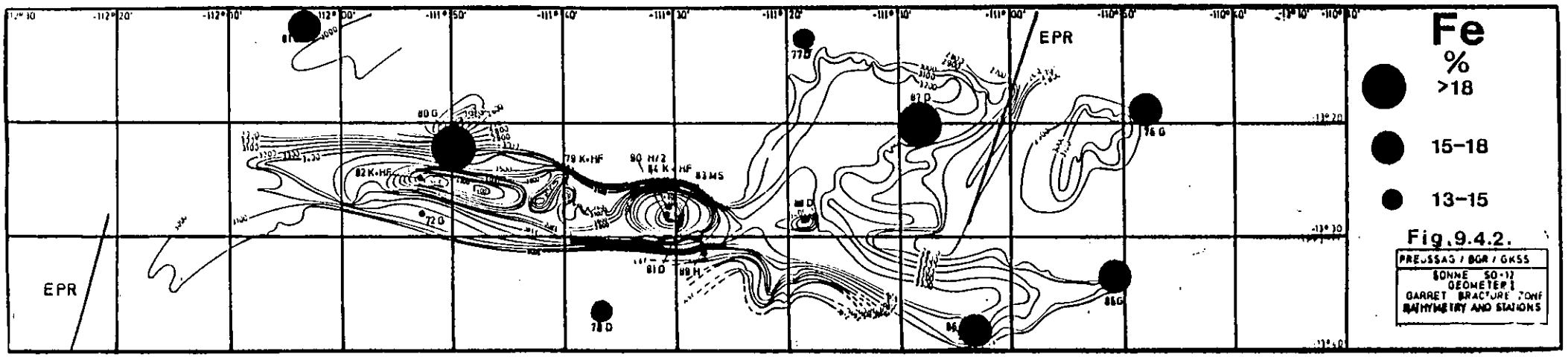
## 9.4 SURFACE SEDIMENT GEOCHEMISTRY

### 9.4.1 The Garret Fracture Zone

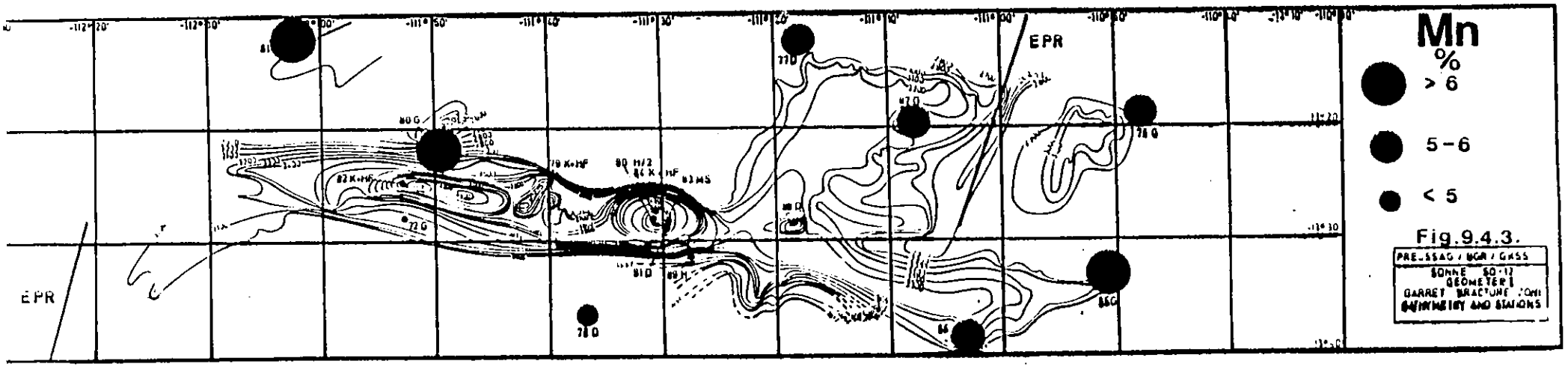
Due to the acquisition of detailed bathymetric data from the Garret Fracture Zone, it is possible to examine the distribution of elements and element ratios, in surface sediments and to relate these to the topography of the area. Such an examination allows a study of presently or recently

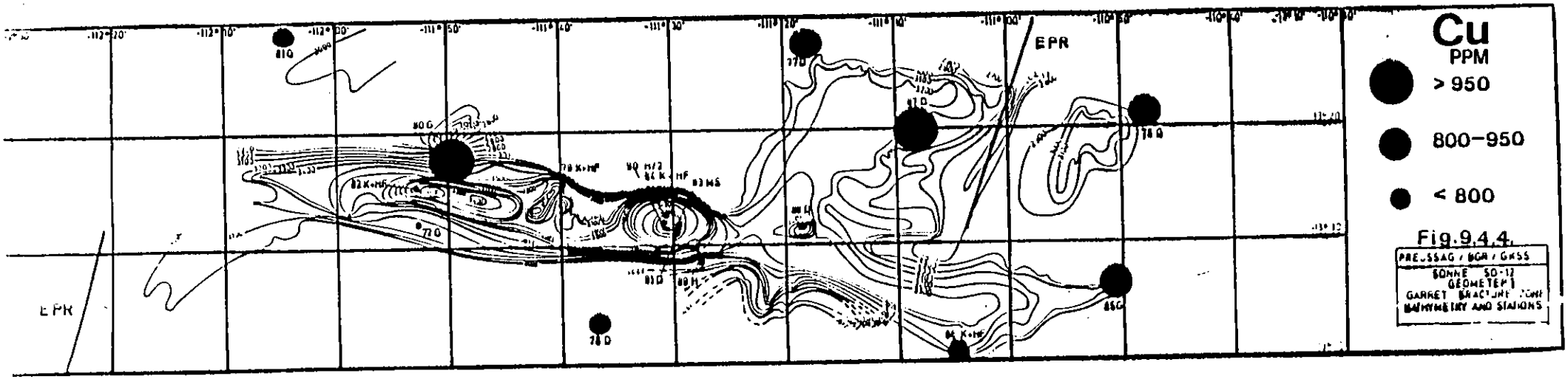
FIGS.9.4.1.& 9.4.2. The distribution of $CaCO_3$ and Fe in Garret Fracture Zone surface sediments.



FIGS.9.4.3.& 9.4.4. The distribution of Mn and Cu in Garret Fracture Zone surface sediments.



FIGS.9.4.5.& 9.4.6. The distribution of Zn and Ni in Garret Fracture Zone surface sediments.

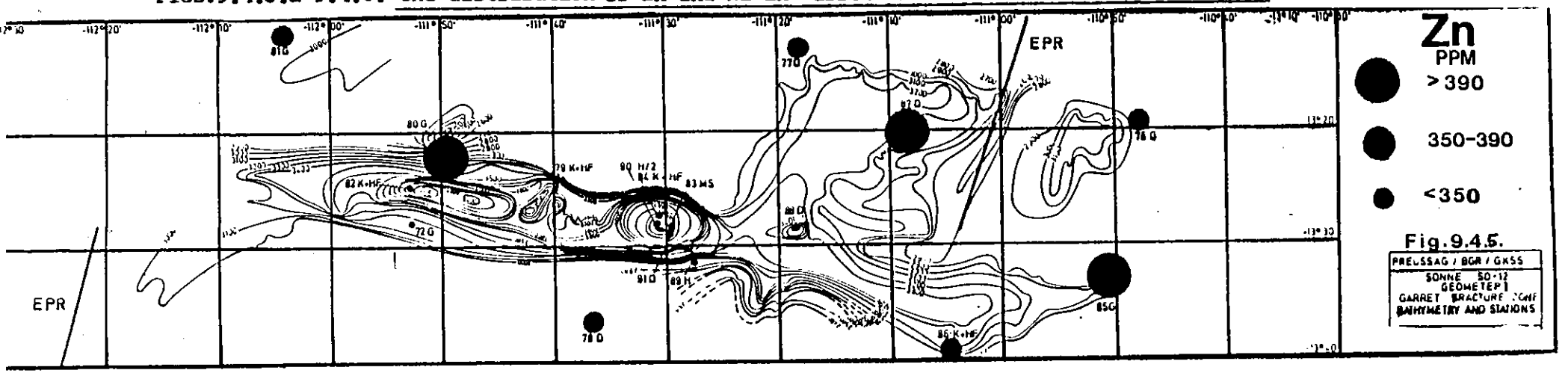



Fig.9.4.5.

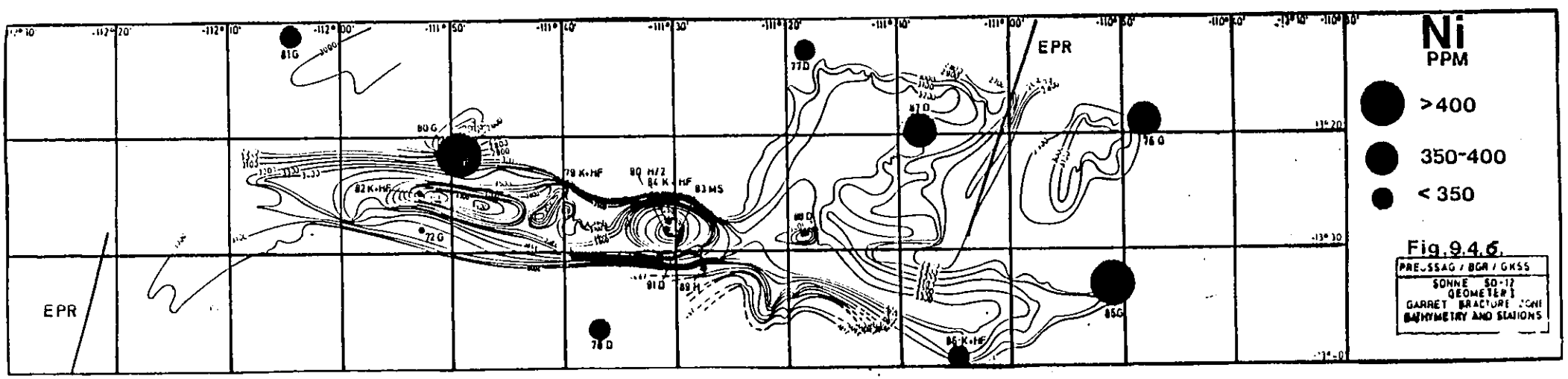



Fig.9.4.6.

active hydrothermal processes in the vicinity of the E.P.R. crest and the Garret Fracture Zone. All data are reported on a carbonate free basis, and are contained in Appendix C.

*$CaCO_3$*

The $CaCO_3$ content of all the surface sediments is greater than 60% and so they may be termed foraminiferal chalk oozes (after Olausson, 1960). Figure 9.4.1 shows the distribution of $CaCO_3$ throughout the survey area and it is found that the samples containing most $CaCO_3$ (>80%) are located on topographic highs.

*Fe*

Sediments from stations 80G and 87D contain more than 18% Fe (see Figure 9.4.2) and thus may be adjacent to hydrothermal vents. Sediment from station 87D also contains the highest Fe/Mn ratio, 3.18, found in the area. Station 80G is located on the northern fault scarp of the Garret Fracture Zone, while station 87D is located to the west of the E.P.R. axis.

*Mn*

The distribution of Mn in surface sediments (Figure 9.4.3) indicates that Mn is less enriched relative to Fe at station 87D compared to other surface sediments and that Mn is more enriched (>6% Mn) at sites 81G and 85G, which are distal to suspected hydrothermal vents. The maximum Mn abundance of 6.4% occurs in surface sediment from station 80G.

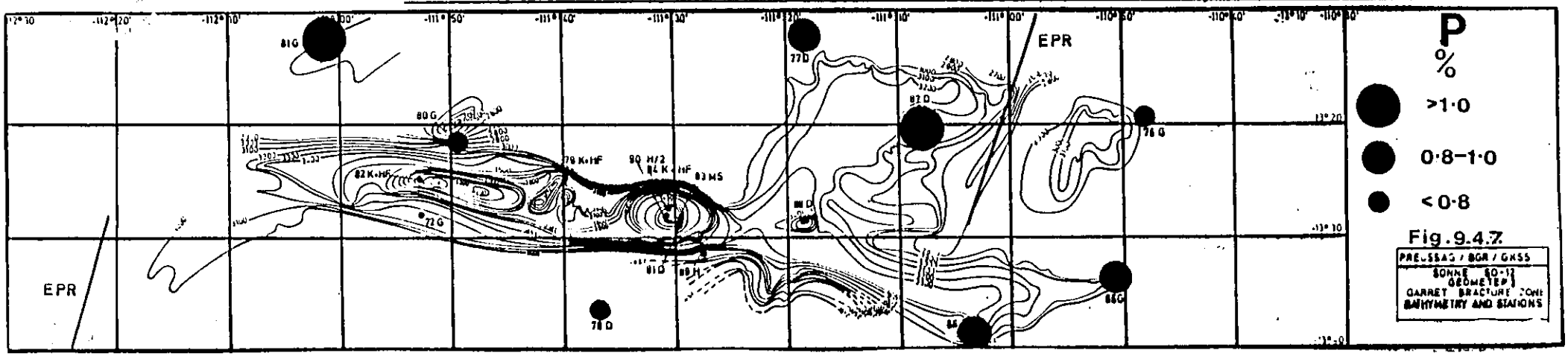
*Cu and Zn*

The distributions of Cu and Zn in surface sediments from the survey area are shown in Figures 9.4.4 and 9.4.5. Maximum values for Cu (1020 ppm) and Zn (430 ppm) are contained in sediments from stations 87D and 80G, respectively. The Cu/Zn ratio of station 77D surface sediment , 2.7, is the highest value found, but there is a general excess of Cu over Zn in all of the surface sediments.

*Ni*

The Ni distribution (Figure 9.4.6) follows that of Mn, with a maximum abundance of 415 ppm in 85G surface sediment. A similar Ni value, of

FIGS.9.4.7.& 9.4.8. The distribution of P and the P/La ratio in Garret Fracture Zone surface sediments.



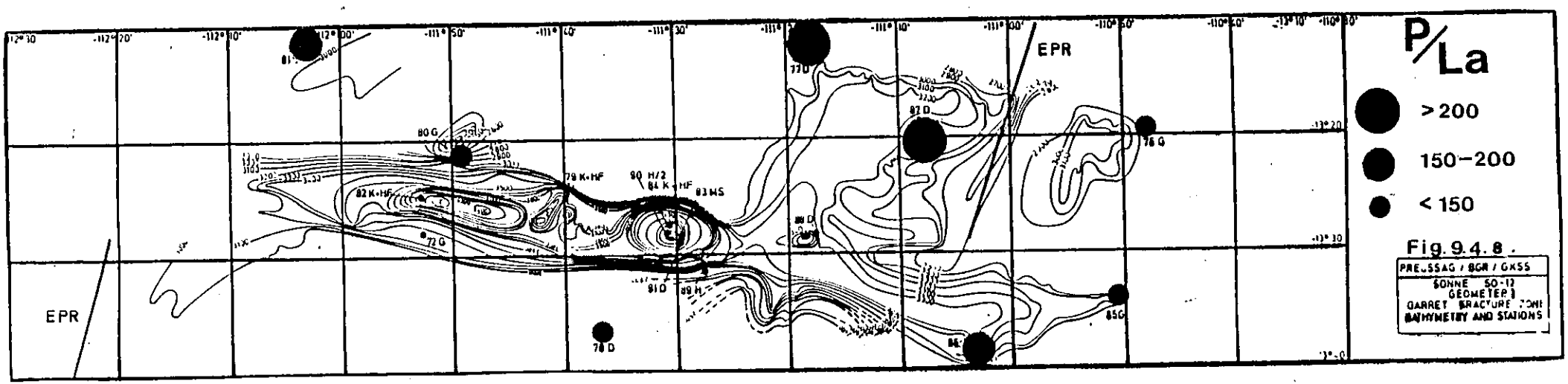



TABLE 9.4.1 Element concentrations and element ratios for station 77D and 87D Ferromanganese Crusts

| Station No. | Sample Type | % Fe | % Mn | *Co | *Ni | *Cu | *Zn | Mn/Fe | Mn/Co | Mn/Ni | Mn/Cu | Mn/Zn | Fe/Cu |
|---|---|---|---|---|---|---|---|---|---|---|---|---|---|
| 77D | Surface Crust | 0.34 | 46.3 | 29 | 2,330 | 820 | 3,030 | 136 | 15,970 | 199 | 565 | 153 | 4 |
| 77D | Bulk Crust | 0.49 | 45.5 | 21 | 268 | 88 | 233 | 93 | 21,670 | 1,698 | 5,170 | 1,953 | 56 |
| 77D | Fibrous Crust | 0.16 | 46.9 | 137 | 161 | 44 | 42 | 293 | 3,423 | 2,913 | 10,660 | 11,170 | 36 |
| 87D | Coating on Basalt | 24.3 | 8.59 | 327 | 778 | 665 | 558 | 0.35 | 263 | 110 | 129 | 154 | 365 |
| LINE ISLANDS CRUSTS (n = 59) (taken from Aplin, 1983) | | 17.0 | 20.4 | 5,450 | 3,860 | 1,540 | 590 | 1.2 | 37 | 53 | 132 | 346 | 110 |

* Trace elements in ppm.

400 ppm, contained in station 80G surface sediment is also high in this sample of high Fe and Mn contents (see above).

*P*

The capacity of volcanogenic Fe oxyhydroxides to remove the phosphate ion from seawater by adsorption is well known (Berner, 1973; Bloch, 1978; Froelich et al., 1977). The latter authors observed that P was deposited 20 times faster on the E.P.R. crest than on its flanks. Froelich et al. (1977) suggested that P was supplied dominantly by seawater but that hydrothermal contributions could not be ruled out.

P concentrations exceeding 1% occur in surface sediments from stations 81G and 87D (Figure 9.4.7). Station 87D is located near the E.P.R. crest which may support a hydrothermal contribution for P.

*P/La*

The rationale for the use of the P/La ratio (Marchig et al., 1982) is that P can be derived from hydrothermal and hydrogenous/biogenic apatite sources (Arrhenius et al., 1957; El Wakeel and Riley, 1961), while La is primarily derived from the latter sources (Elderfield and Greaves, 1982). The P/La ratio should increase as the hydrothermal contribution of P increases and therefore, this ratio can be used as a tool in geochemical exploration (Marchig et al., 1982). In the present work the highest P/La ratios are found in surface sediments from stations 77D and 87D (see Figure 9.4.8) which have previously been shown to have a hydrothermal affinity.

*Ferromanganese Crusts*

A preliminary study of the chemical analyses reported in Table 9.4.1 (taken from data in Appendix C) reveals that station 77D crusts are much richer in Mn than is the 87D crust. An increased Fe content and lower Mn/Fe ratio in 87D surface sediment compared to surface sediment from 77D, was noted earlier.

The station 87D crust has a Mn/Fe ratio of 0.35, similar to hydrothermal ferromanganese oxide crusts from the 19 - 21°S area of the E.P.R. (see

Chapter 10). By contrast, the extremely manganiferous crust from station 77D with about 46% Mn and low trace metal content (see Table 9.4.1) has a Mn/Fe ratio of 93-293 and resembles the hydrothermal Mn oxide deposit reported by Moore and Vogt (1976) from the Galapagos Rift. Then, the two ferromanganese crusts each resemble known hydrothermal deposits.

Although the Fe and Mn content of all of the 4 crusts resembles that found in hydrothermal deposits, the Co, Ni, Cu and Zn content in the uppermost layer of 77D crust is an order of magnitude higher than in the 3 other crusts. This high trace metal content suggests more hydrogenous characteristics for this particular sample, even though the Mn/Fe ratio of 136 is much higher than that generally observed for hydrogenous ferromanganese crusts. This represents a paradoxical situation, with the Mn/Fe ratio suggesting a hydrothermal origin for the 77D crust whilst high trace metal contents suggests hydrogenous growth. However, absolute concentrations of trace metals cannot unequivocally designate a particular origin for the samples, but a consideration of their element ratios, normalised to Fe or Mn, may aid in this regard. Line Islands crusts (Aplin, 1983), shown in Table 9.4.1, represent samples which reflect the hydrogenous end-member of ferromanganese oxide deposits and as such provide a base for comparison.

The station 87D crust element ratios show that Fe and Zn have been supplied in excess (relative to Mn), with respect to hydrogenous Line Island crusts, whilst Co, Ni and Cu have not. The Co, Ni and Cu content in crust 87D is lower than in the Line Island crusts, although the Mn/Cu ratio is similar.

A study of Co, Ni, Cu and Zn in the 77D crusts, normalised to Mn, indicates little significant incorporation of Co, Ni and Cu. However, although Zn is low in the bulk and fibrous crusts (see Table 9.4.1), a low Mn/Zn ratio found in surficial 77D crust could be indicative of a hydrothermal supply of Zn in excess of that supplied hydrogenously, by analogy with hydrothermal GRAFZI crusts which are Zn enriched. The Cu

FIG.9.4.9 .Surface sediment locations in the $13^{o}$-$15^{o}$S area of the E.P.R.

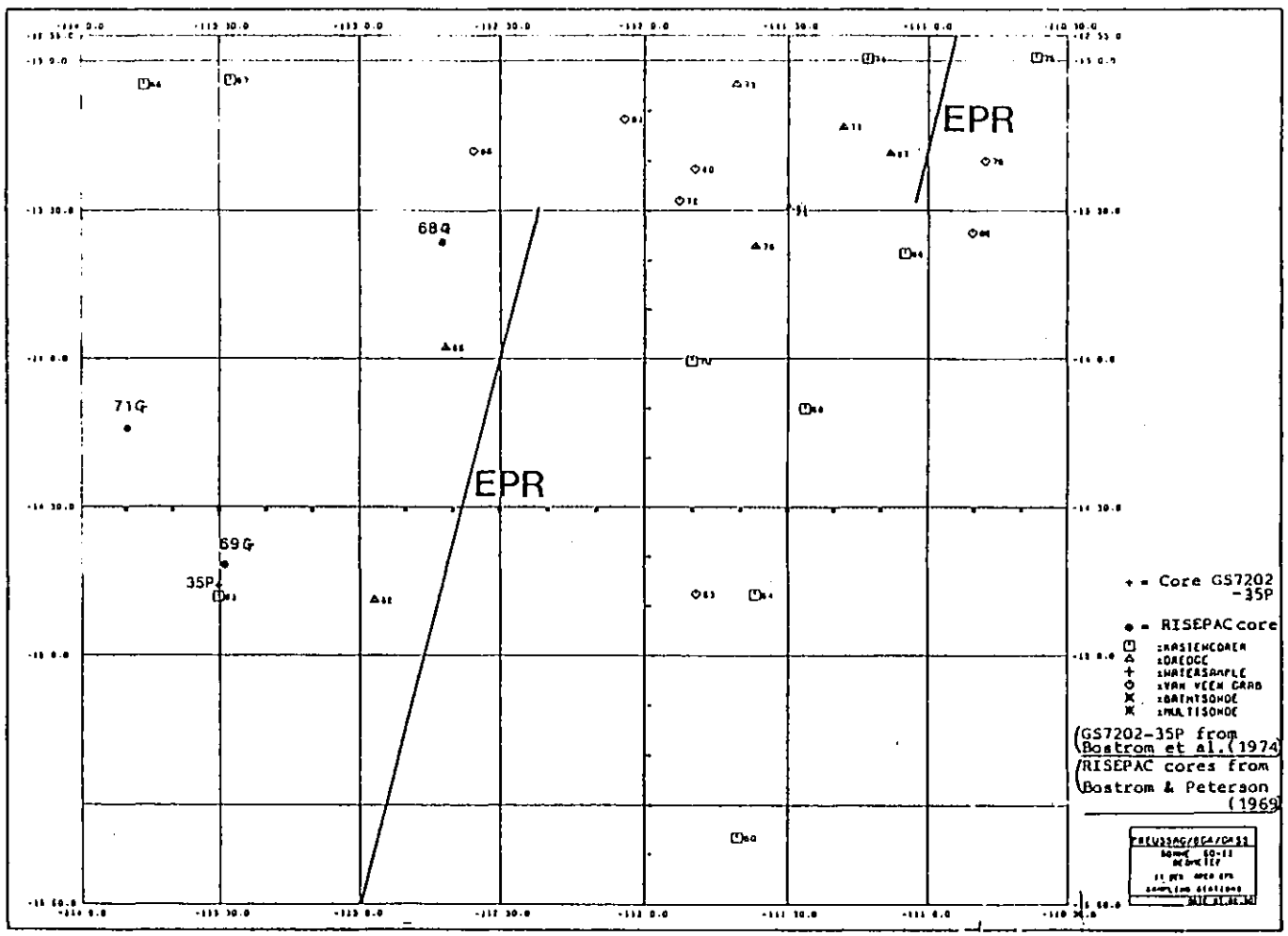


FIG.9.4.10. Fe in 13°-15°S area surface sediments.

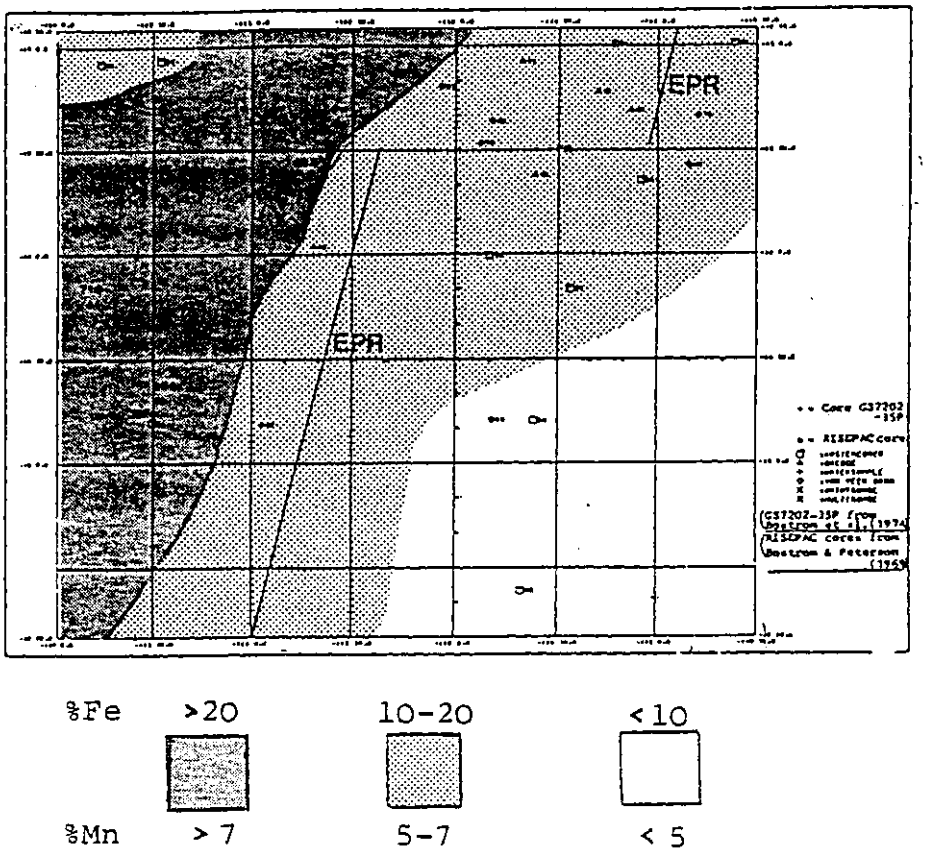
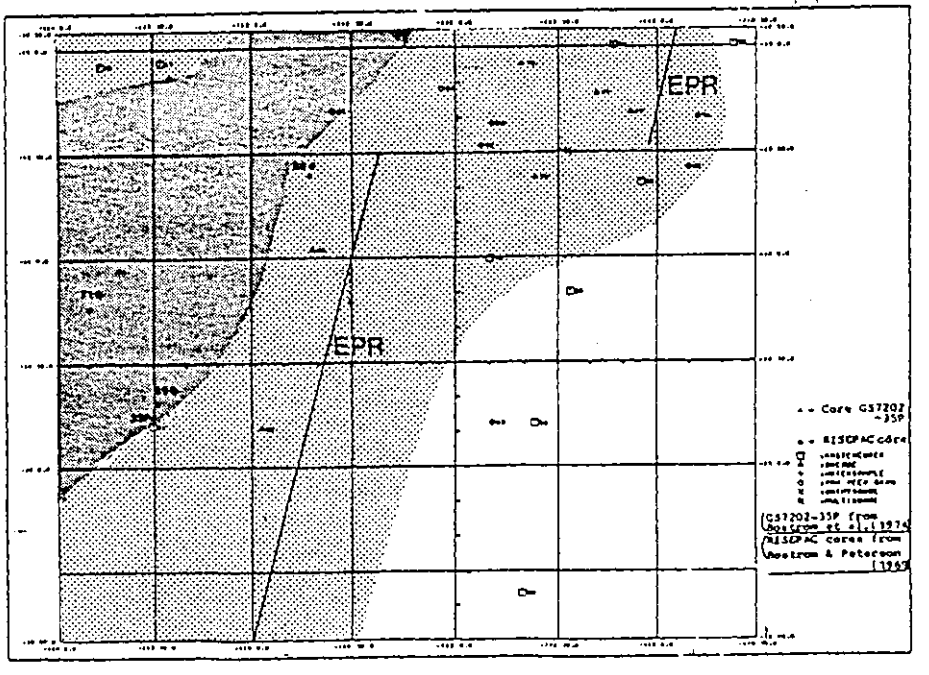



FIG.9.4.11. Mn in 13°-15°S area surface sediments.



content of 820 ppm in surficial 77D crust is higher than in the bulk and fibrous sub-samples and a high Cu/Zn ratio was previously observed for station 77D surface sediment.

A case can thus be made for an excess supply of Zn to crusts from stations 77D and 87D, over and above the hydrogenous supply of this element. The high trace metal contents of surficial 77D crust suggest a different rate of supply of elements or a different growth rate for this sample, which will be discussed later.

9.4.2 The 13 - 15°S Area of the East Pacific Rise

GEOMETEP surface sediment locations in the 13 - 15°S area, along with additional samples reported by Bostrom and Peterson (1969) and Bostrom et al. (1974), are shown in Figure 9.4.9. Distribution patterns of element concentrations and element ratios in this area are described below.

*Fe*

The distribution of Fe in 13 - 15°S area surface sediments can be described by three zones which trend sub-parallel to the E.P.R. axis (Figure 9.4.10). The zone on the east flank of the E.P.R. (not shaded - Figure 9.4.10) is characterised by Fe values of less than 10%. The central or crestal zone encloses about 75 Kms of crust at either side of the E.P.R. axis, on the southern segment of the E.P.R., and this zone contains Fe values which range from 12 to 19%. Further west than 75 Kms from the axis, Fe values reach their highest, e.g. 22% (this work), although Bostrom et al. (1974) reported 31% Fe in surface sediment from core GS7202-35P, at 14°48'S and 113°30'W.

*Mn*

The Mn contents of 13 - 15°S area surface sediments are shown in Figure 9.4.11. The 3 zones described above for Fe, also apply for Mn. The western, central and eastern zones are characterised by Mn content of 8%, 6% and 2%, respectively.

FIG.9.4.12. Cu in 13°-15°S area surface sediments.

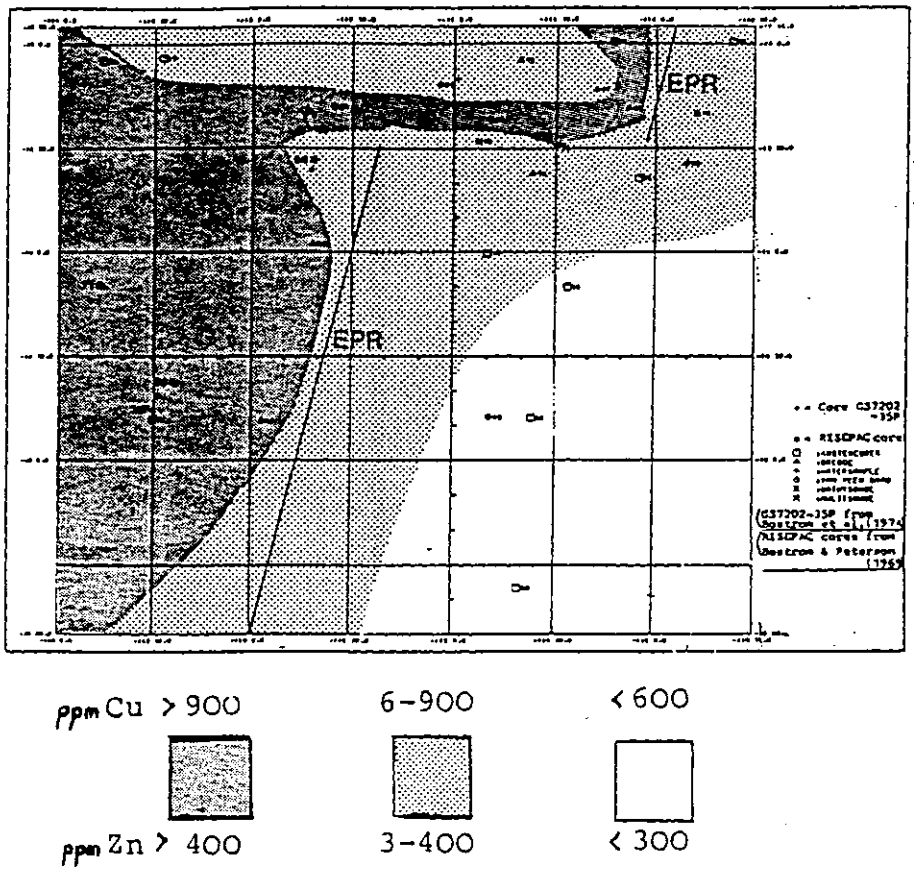



FIG.9.4.13. Zn in 13°-15°S area surface sediments.

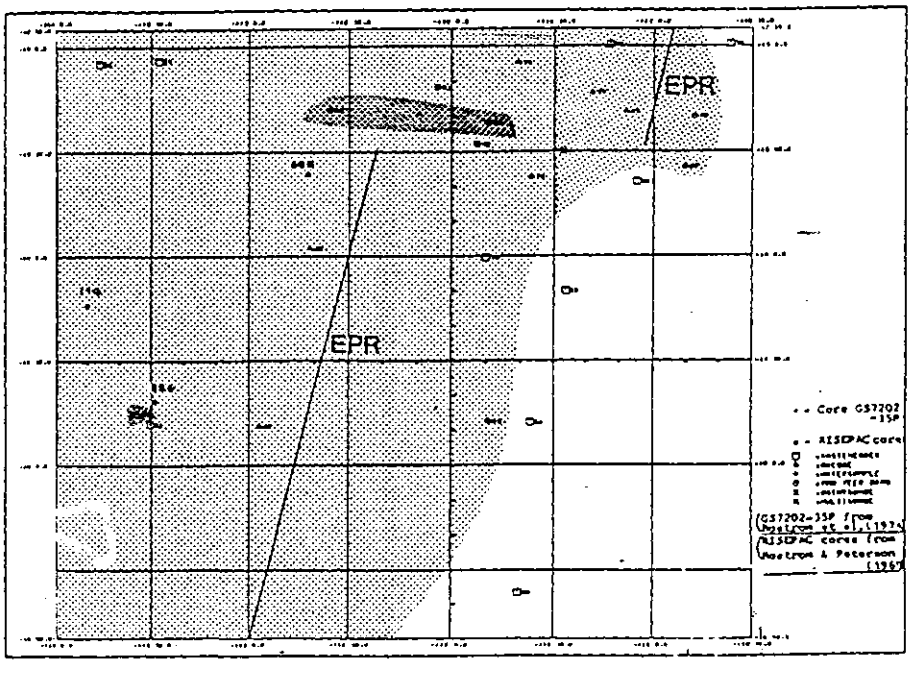


FIG.9.4.14. Ni in 13°-15°S area surface sediments.

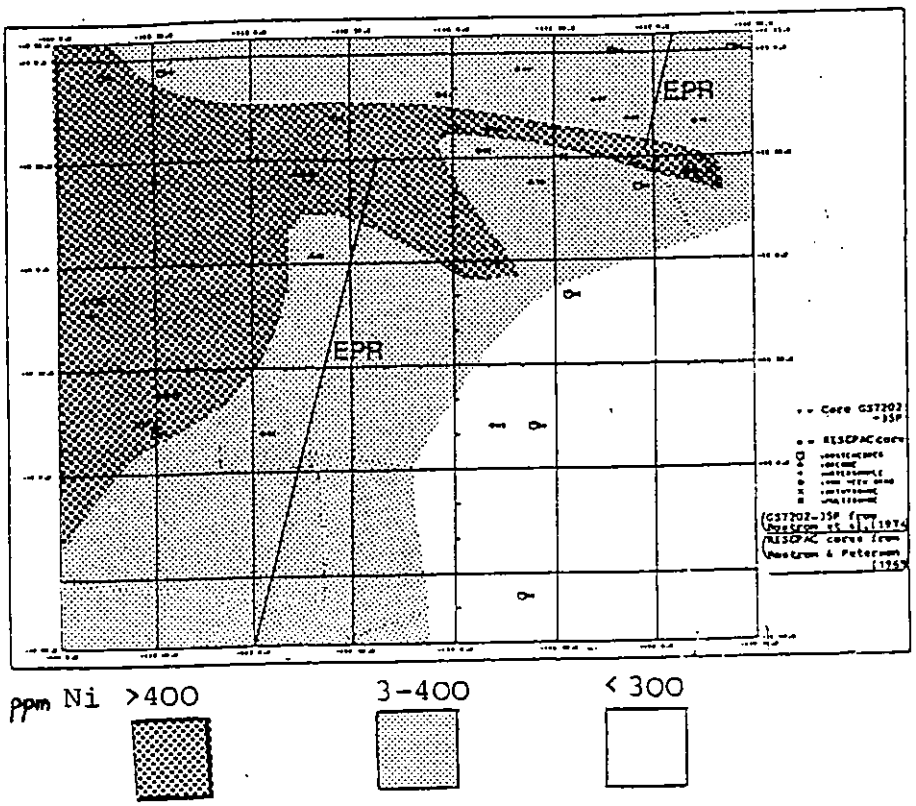
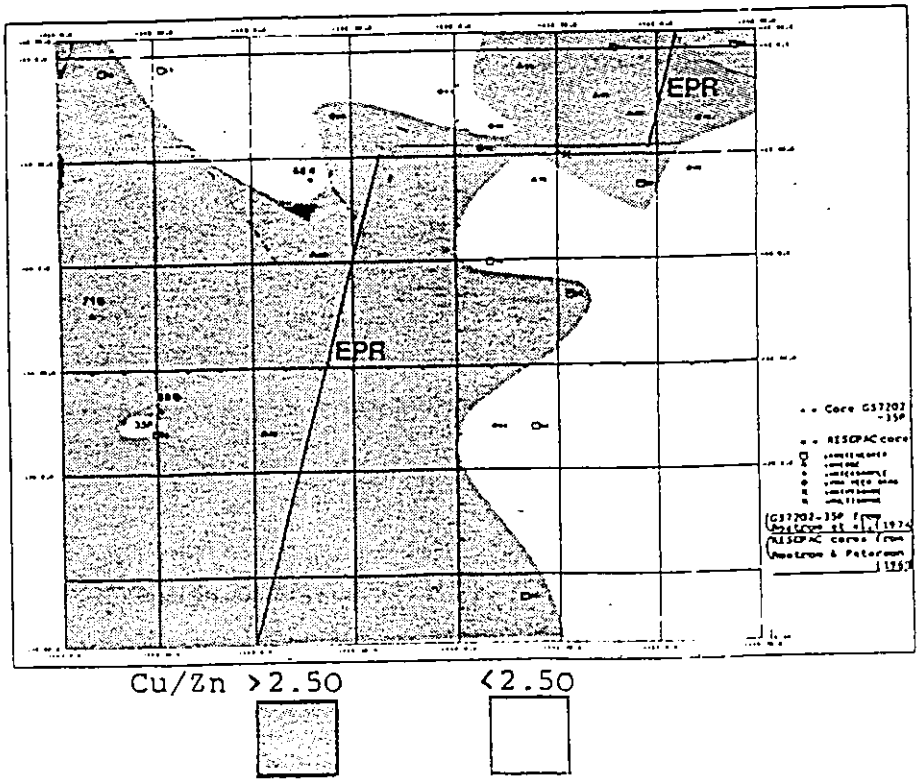



FIG.9.4.15. Cu/Zn in 13°-15°S surface sediments.



*Cu*

The Cu distribution in surface sediments from the 13 - 15°S area of the E.P.R. (Figure 9.4.12) reflects the three zones previously described for Fe and Mn. However, the pattern that Cu displays is different to that of Fe and Mn. High Cu contents in surface sediments occur in 3 general areas; the area immediately west of the northern segment of the E.P.R., the Garret Fracture Zone, and the broad area to the west of the southern E.P.R. segment. The highest Cu content in surface sediment is 1020 ppm, from station 87D (see Section 9.4.1). High Cu values tend to follow the E.P.R. axis, on its western flank, and also the Garret Fracture Zone.

*Zn*

The Zn contents of 13 - 15°S area surface sediments (Figure 9.4.13) are more uniform and lower than the copper contents. The previously described western and crestal zones of the E.P.R. are fused together to form an area with 300 to 400 ppm Zn, with localised high concentrations. Bostrom et al. (1974) reported 630 ppm Zn for surface sediment from core GS7202-35P (see Figure 9.4.13) and 450 ppm Zn in surface sediment occurs (this work) at the intersection of the Garret Fracture Zone and the southern E.P.R. segment. The east flank of the Rise contains a maximum of 260 ppm Zn found in surface sediment from core 75K which is located about 35 Kms east of the Rise axis.

*Ni*

The Ni distribution in 13 - 15°S area surface sediments deviates from the above distributions (Figure 9.4.14). High Ni values (greater than 400 ppm) extend from the west flank of the E.P.R., along the Garret Fracture Zone and also in a lobate-shaped area, east of the Rise axis. Ni values of 300 to 400 ppm are representative of crestal zone surface sediments. A possible reason for the Ni distribution is discussed later.

*Cu/Zn*

A Cu/Zn ratio of 2.5 separates crestal and west flank surface sediments, from east flank surface sediments, south of the Garret Fracture Zone. Throughout the shaded region (Figure 9.4.15), the Cu/Zn ratio is

FIG.9.4.16. P/La in 13°-15°S area surface sediments.

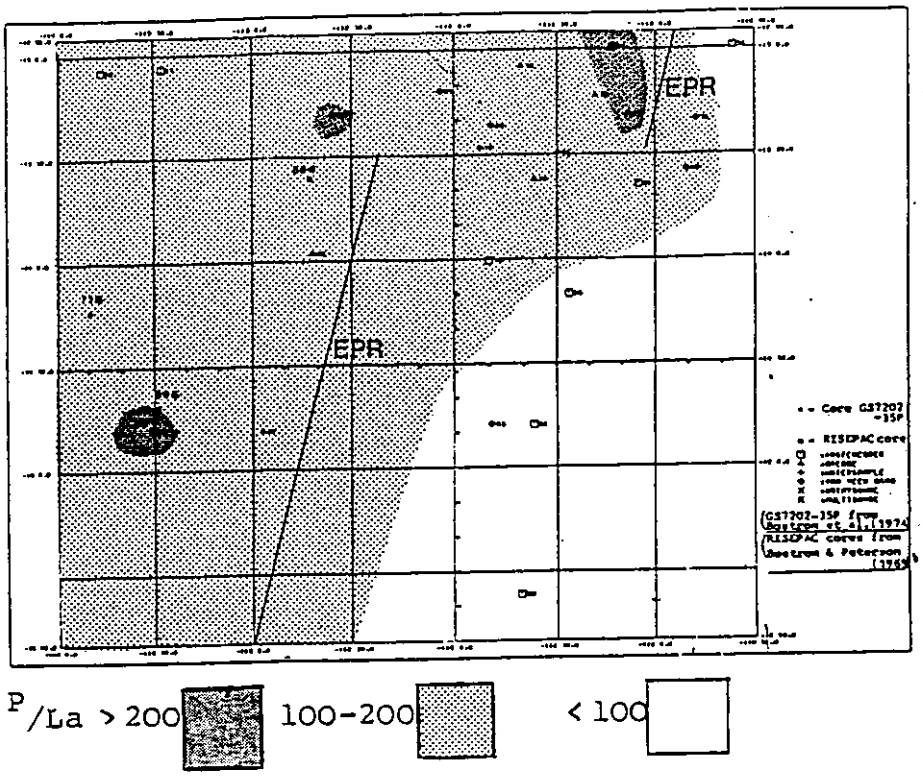
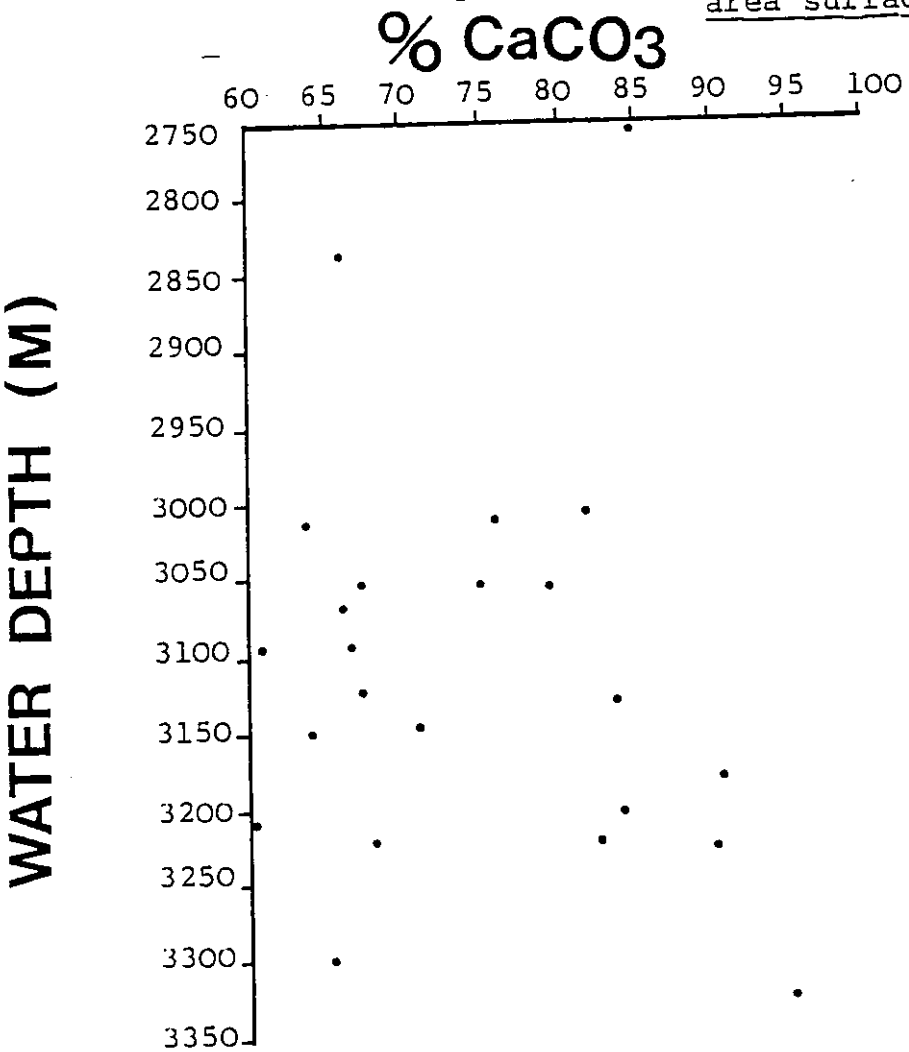



FIG.9.4.17. Plot of $CaCO_3$ versus Water Depth in 13°-15°S area surface sediments.



relatively uniform, ranging from 2.5 to 3.0.

*P/La*

Three areas can be found with P/La ratios of greater than 200 (see Figure 9.4.16);

1. The west flank of the E.P.R. adjacent to the northern segment of the spreading centre.

2. An area at about $13^{\circ}20'S$, $112^{\circ}35'W$ where the southern segment of the E.P.R. intersects the Garret Fracture Zone.

3. The area at about $14^{\circ}50'S$, $113^{\circ}30'W$ where Bostrom et al. (1974) reported highly metalliferous sediment from a topographic high.

All three of these areas have been identified as sites adjacent to active hydrothermal vents, on the basis of the above data and it would appear that the P/La ratio is equally effective in identifying hydrothermally enriched sediments.

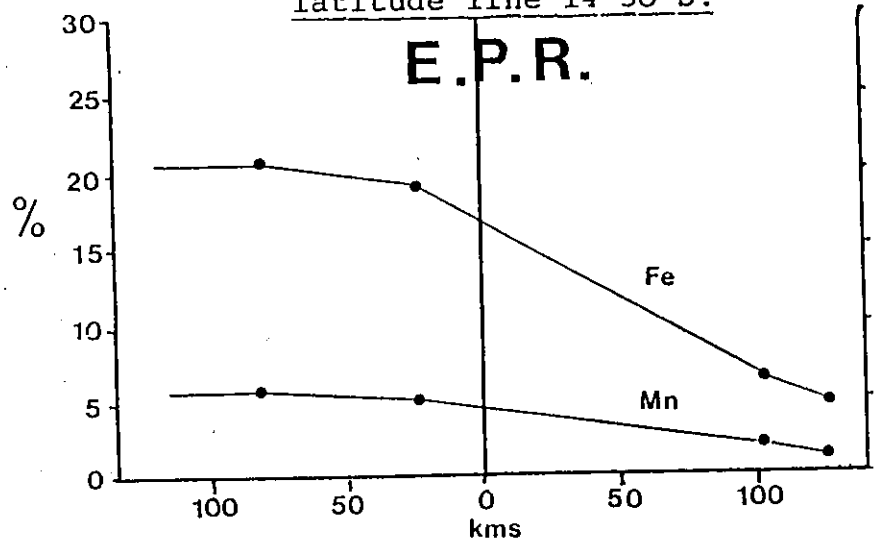
*$CaCO_3$*

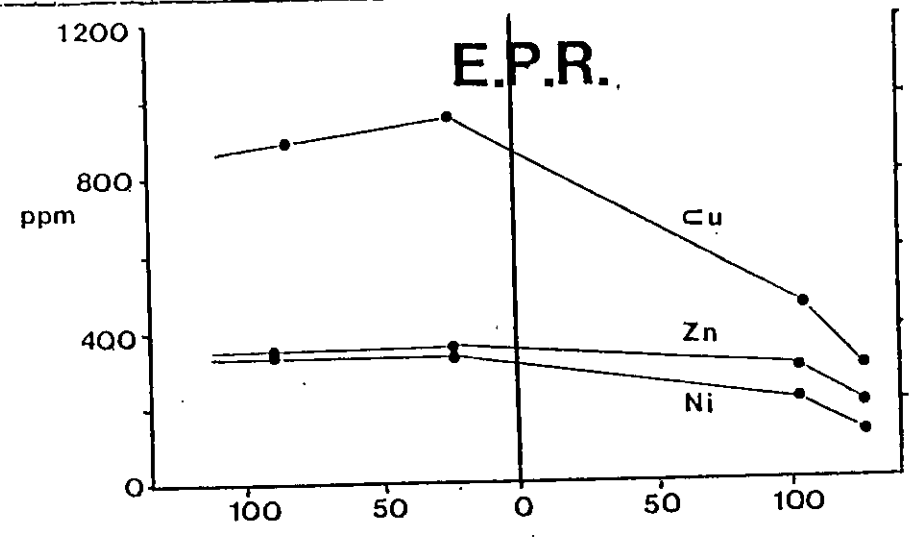
A plot of $CaCO_3$ versus water depth for surface sediments from the 13 - $15^{\circ}S$ area is shown in Figure 9.4.17. The scatter of the data, even for samples located at similar water depths, reflects the observations of Cronan and Varnavas (1981), namely, that slumping and dilution of the $CaCO_3$ content of sediments by input of hydrothermal ferromanganese oxides, are widespread phenomena in the vicinity of the E.P.R. Bostrom et al. (1974) showed that sediments from topographic highs suffer loss of fine-grained hydrothermal precipitates by winnowing and that these may be ponded in topographic lows. Therefore, the $CaCO_3$ content of 13 - $15^{\circ}S$ area surface sediments depends largely upon bottom topography.

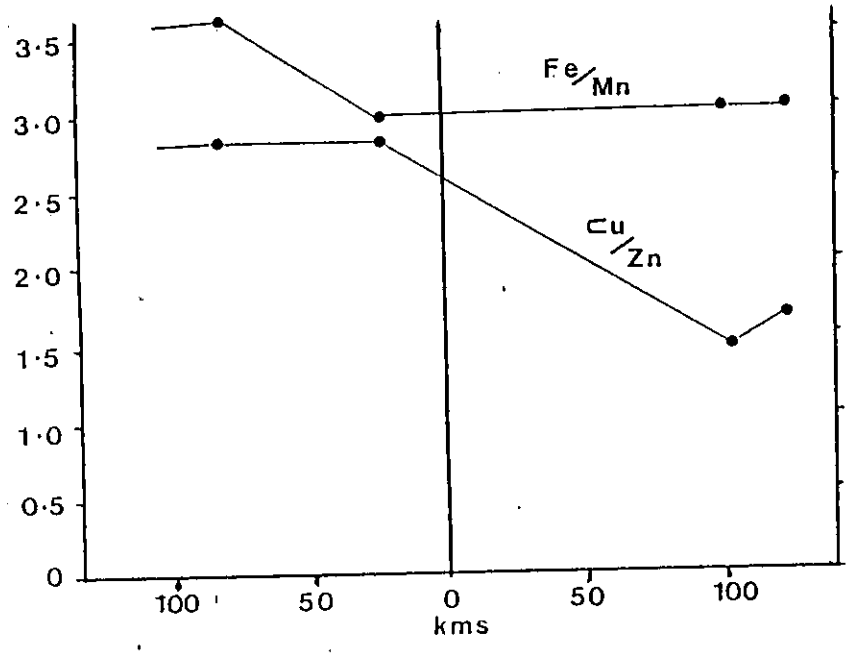
*Variations of Elements/Element Ratios in a Ridge Normal Traverse*

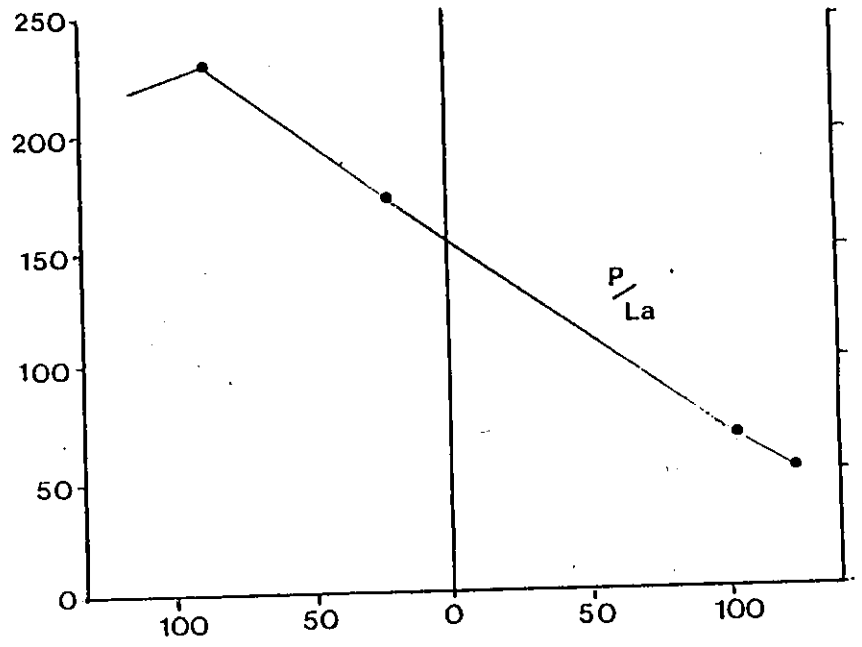
The contour maps of element concentrations and element ratios shown above can be best appreciated by plotting them against distance from the crest

FIG.9.4.18. Elements and element ratios in surface sediments versus distance from the E.P.R. crest along latitude line 14°50'S.



of the E.P.R. (see Figure 9.4.18). The profiles of Fe, Mn, Cu, Zn, Ni, Fe/Mn, Cu/Zn and P/La all show to varying degrees that the west flank of the E.P.R. is considerably more enriched in metals than the east flank. The relative uniformity of the Fe/Mn and Cu/Zn ratios, throughout the area, are noteworthy and whilst subtle variations can be observed, the differences are small compared to those found in highly fractionated hydrothermal deposits observed at some mid-ocean ridge locations (e.g. see Chapter 2 and the FAMOUS Area, Hoffert et al., 1978).

The constant enrichment of Fe over Mn and Cu over Zn illustrate the large area affected by a hydrothermal element supply.

## 9.5 GEOCHEMISTRY OF SURFACE AND BURIED SEDIMENTS FROM THE 13 - 15°S AREA

Section 9.4 describes metal enrichments in surface sediments and identifies presently or recently active hydrothermal processes. To investigate temporal variations in hydrothermal activity it is necessary to study samples from greater depths in cores from the 13 - 15°S area. Imprinted upon these temporal hydrothermal variations may be changes in sediment geochemistry caused by diagenesis.

Heath and Dymond (1977) developed a model whereby the polygenetic origin of Nazca Plate sediments could be accounted for in terms of hydrothermal, detrital, hydrogenous and biogenic components. More recent work (Dymond, 1981) has led to the addition of a fifth component, termed 'solution residue', formed by the dissolution of biogenic debris. The same author showed that, on a carbonate and salt free basis, surface sediments within 100 Kms of the E.P.R. crest comprise greater than 80% of the hydrothermal component. The following work compares surface and down-core sediments from the 13 - 15°S area, in an attempt to illustrate variations in the hydrothermal component, which is quantitatively the most influential component, with regard to sediment geochemistry, and also to examine the relative importance of diagenetic processes.

Table 9.5.1 shows correlation matrices for raw surface sediment and down-core sediment data. Values reported are significant at the 99.9% level

# TABLE 9.5.1.

## SURFACE SEDIMENT CORRELATION MATRIX.

| | NA | K | MG | AL | MN | FE | CA |
|---|---|---|---|---|---|---|---|
| K | .90[illegible] | | | | | | |
| MG | .92[illegible] | .80[illegible] | | | | | |
| AL | | | .833 | | | | |
| MN | .929 | .900 | .77[illegible] | | | | |
| FE | .95[illegible] | .922 | .790 | | .99[illegible] | | |
| CA | -.888 | -.920 | -.81[illegible] | | -.966 | -.970 | |
| LI | | | | | | | |
| SR | | | | | | | |
| LA | .789 | .804 | .743 | | .936 | .925 | -.917 |
| TI | .668 | | .887 | .979 | | | |
| V | .934 | .903 | .775 | | .993 | .994 | -.960 |
| CO | .847 | .895 | .834 | | .973 | .971 | -.949 |
| NI | .853 | .874 | .795 | | .990 | .977 | -.961 |
| CU | .852 | .892 | .795 | | .980 | .977 | -.944 |
| ZN | .947 | .905 | .782 | | .983 | .981 | -.953 |
| PB | | | | | | | |
| P | .802 | .829 | .684 | | .938 | .958 | -.923 |

| | LA | V | CO | NI | CU | ZN |
|---|---|---|---|---|---|---|
| LA | | | | | | |
| TI | | | | | | |
| V | .917 | | | | | |
| CO | .930 | .967 | | | | |
| NI | .953 | .975 | .977 | | | |
| CU | .886 | .986 | .962 | .970 | | |
| ZN | .904 | .983 | .972 | .976 | .985 | |
| PB | | | | | | |
| P | .842 | .951 | .918 | .909 | .928 | .951 |

Correlation coefficient (r) = 0.62 at 99.9% confidence.
(n = 23)

## DOWNCORE SEDIMENT CORRELATION MATRIX.

| | NA | K | MG | AL | MN | FE | CA | LI |
|---|---|---|---|---|---|---|---|---|
| K | .999 | | | | | | | |
| MG | 1.000 | .999 | | | | | | |
| AL | .427 | .322 | .427 | | | | | |
| MN | .951 | .797 | .951 | | | | | |
| FE | .899 | .872 | .899 | | .973 | | | |
| CA | -.874 | -.859 | -.874 | | -.904 | -.933 | | |
| LI | .412 | .414 | .412 | | | | | |
| SR | -.353 | | -.353 | | | | .379 | |
| LA | .710 | .699 | .710 | | .949 | .939 | -.794 | |
| TI | .559 | .482 | .559 | .949 | .373 | .436 | -.450 | .349 |
| V | .871 | .834 | .871 | | .995 | .992 | -.922 | |
| CO | .797 | .717 | .797 | .319 | .932 | .921 | -.937 | |
| NI | .799 | .729 | .799 | | .975 | .942 | -.870 | |
| CU | .852 | .797 | .852 | | .954 | .959 | -.900 | |
| ZN | .957 | .793 | .957 | | .970 | .956 | -.904 | |
| PB | .522 | .453 | .522 | | .590 | .510 | -.521 | |
| P | .952 | .915 | .952 | | .903 | .942 | -.875 | |

| | LA | TI | V | CO | NI | CU | ZN |
|---|---|---|---|---|---|---|---|
| LA | | | | | | | |
| TI | .379 | | | | | | |
| V | .840 | .409 | | | | | |
| CO | .795 | .407 | .932 | | | | |
| NI | .873 | .377 | .953 | .905 | | | |
| CU | .907 | .420 | .979 | .944 | .939 | | |
| ZN | .915 | .415 | .979 | .949 | .941 | .976 | |
| PB | .519 | | .922 | .927 | .894 | .909 | .895 |
| P | .793 | .320 | .934 | .951 | .952 | .995 | .911 |

| | PB |
|---|---|
| P | .935 |

Correlation coefficient (r) = 0.30 at 99.9% confidence.
(n = 126)

FIG.9.5.1.

Fe vs Mn in 13–15°S Area sediments

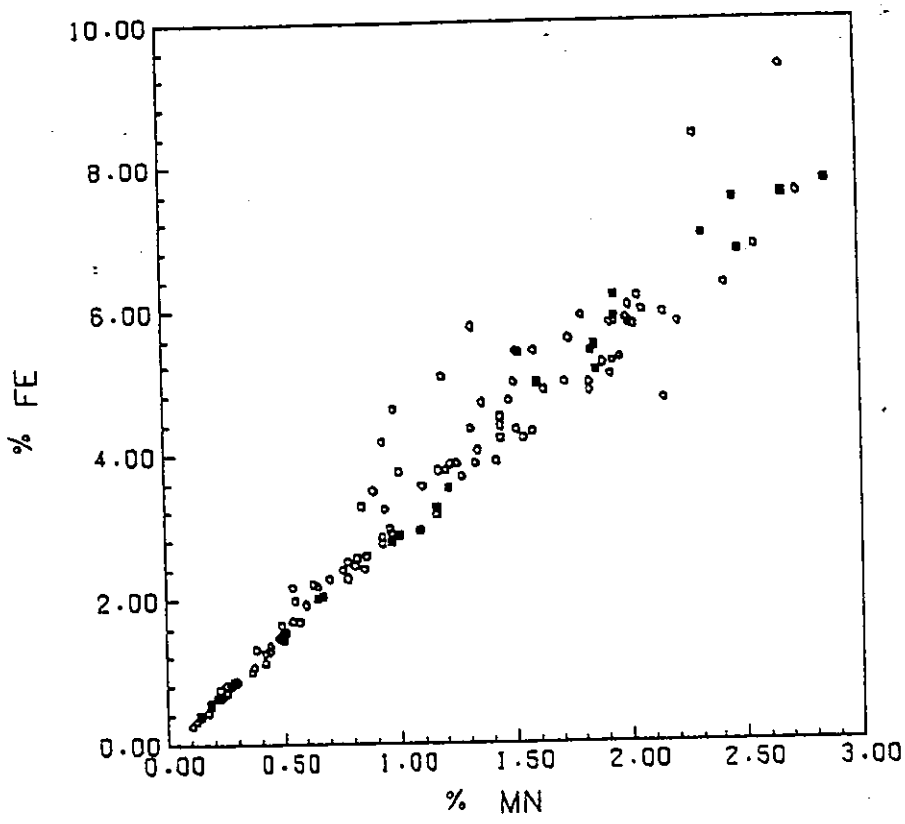



FIG.9.5.2.

Cu vs Fe in 13–15°S Area sediments.

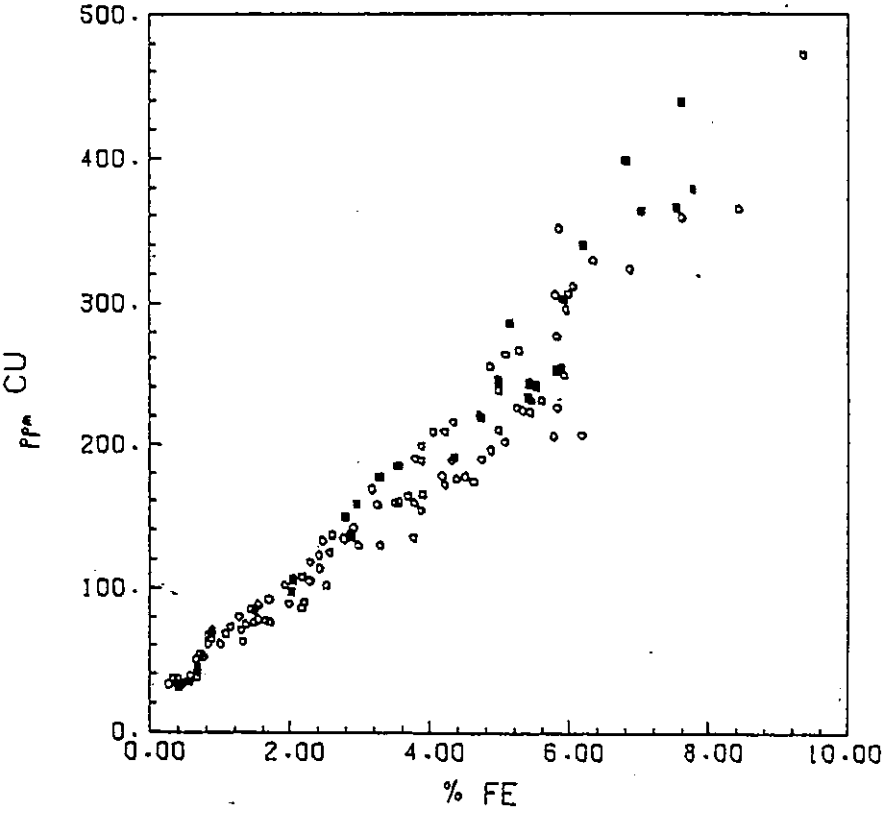


FIG.9.5.3.

Zn vs Mn in 13–15S Area sediments.

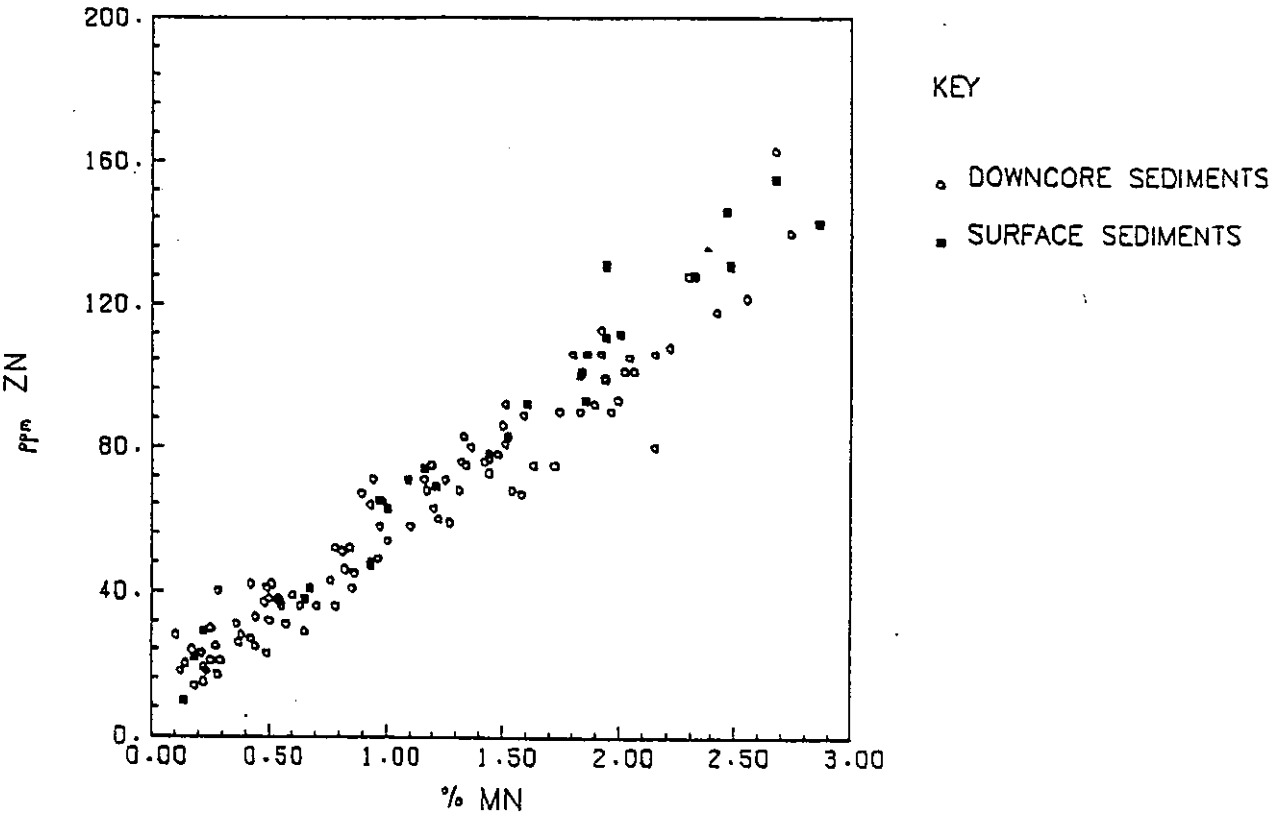
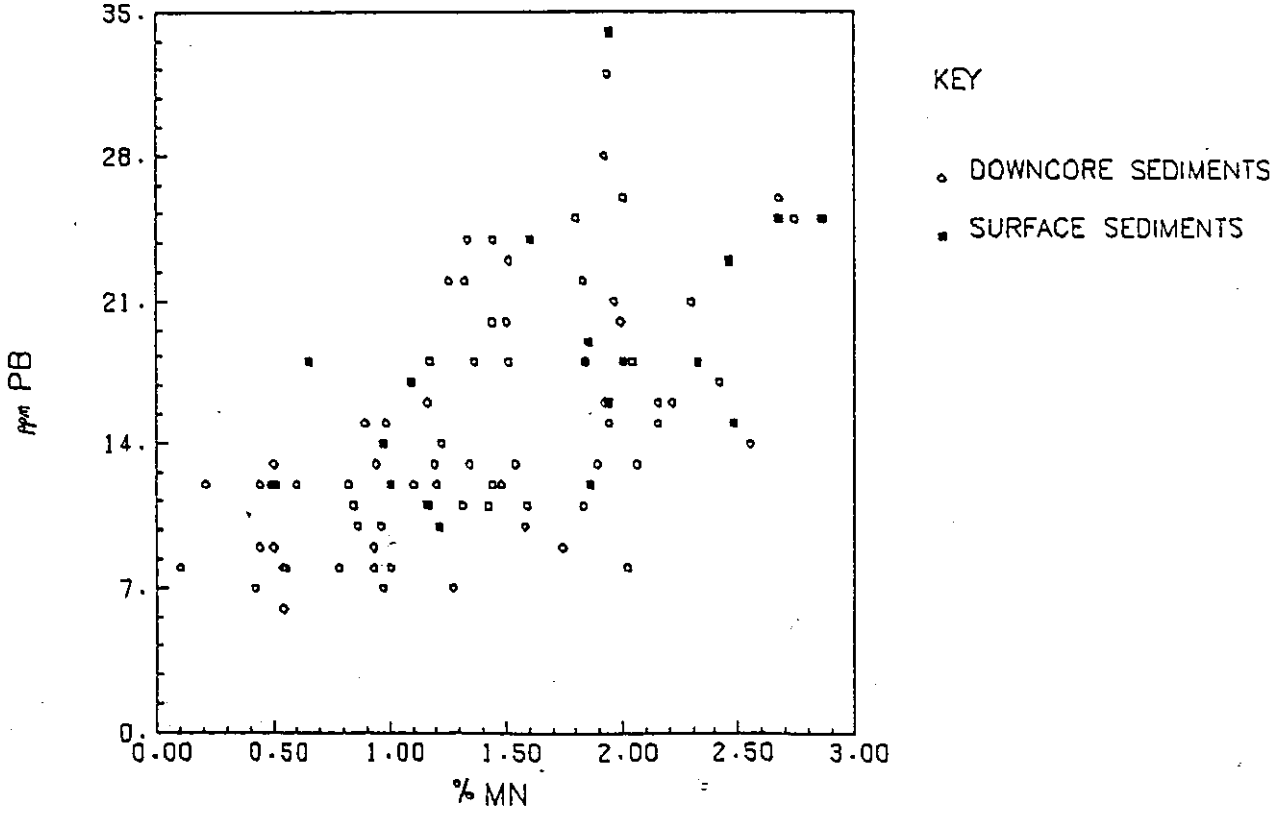



FIG.9.5.4.

Pb vs Mn in 13–15S Area sediments.



of confidence. The geochemistry of Na, K, Mg and Ca is largely accounted for by sea-salt, clay mineral, basaltic debris and calcium carbonate contributions to the sediment (Chester and Aston, 1976). Glaccum (1976) showed that zeolites may contain important amounts of alkali metals but these minerals are not normally concentrated in areas of rapid sedimentation, such as the E.P.R. Attention is focussed upon correlations between the major elements, Fe, Mn and Al, and the trace elements, Li, La, Ti, V, Co, Ni, Cu, Zn, Pb and P.

Correlation matrices for both sets of data are very similar, with the notable exceptions of Al with Co, and Ti with Li, La, V, Co, Ni, Cu, Zn and P, which can only be found in downcore sediments (Table 9.5.1). These correlations suggest that basaltic fragments are more abundant in downcore sediments, than in surface sediments.

Scatterplots have been used to compare surface and downcore sediments from the 13 - 15°S area. A strong positive correlation exists for Fe with Mn (Figure 9.5.1). Both surface and downcore sediments show a range of Fe and Mn values reflecting different amounts of hydrothermal input of these metals, or different $CaCO_3$ contents at separate locations. The variability observed in downcore sediment data, from depths up to 3 m in the core, can be explained by the same processes that lead to variability in surface sediments. The strong positive correlation of Fe with Mn shows the very limited amount of fractionation that has taken place between these two metals, which is unexpected when compared to other hydrothermal systems where Fe is strongly fractionated from Mn.

Cu with Fe, and Zn with Mn, respectively, are strongly correlated (see Figures 9.5.2 and 9.5.3). Cu with Mn, and Zn with Fe, show very similar trends, as do La, V, Co and Ni with both Fe and Mn. The scatterplot of Pb with Mn (Figure 9.5.4) shows a less strong correlation. Dasch et al., (1971) showed by isotopic analysis that Pb in E.P.R. metalliferous sediments was derived from mid-ocean ridge basalts and Pb present in volcanic debris may account for the observed scatter of the data, in the plot of Pb versus Mn. P correlates strongly with Fe (see Table 9.5.1)

FIG.9.5.5.

P vs La in 13-15S Area sediments.

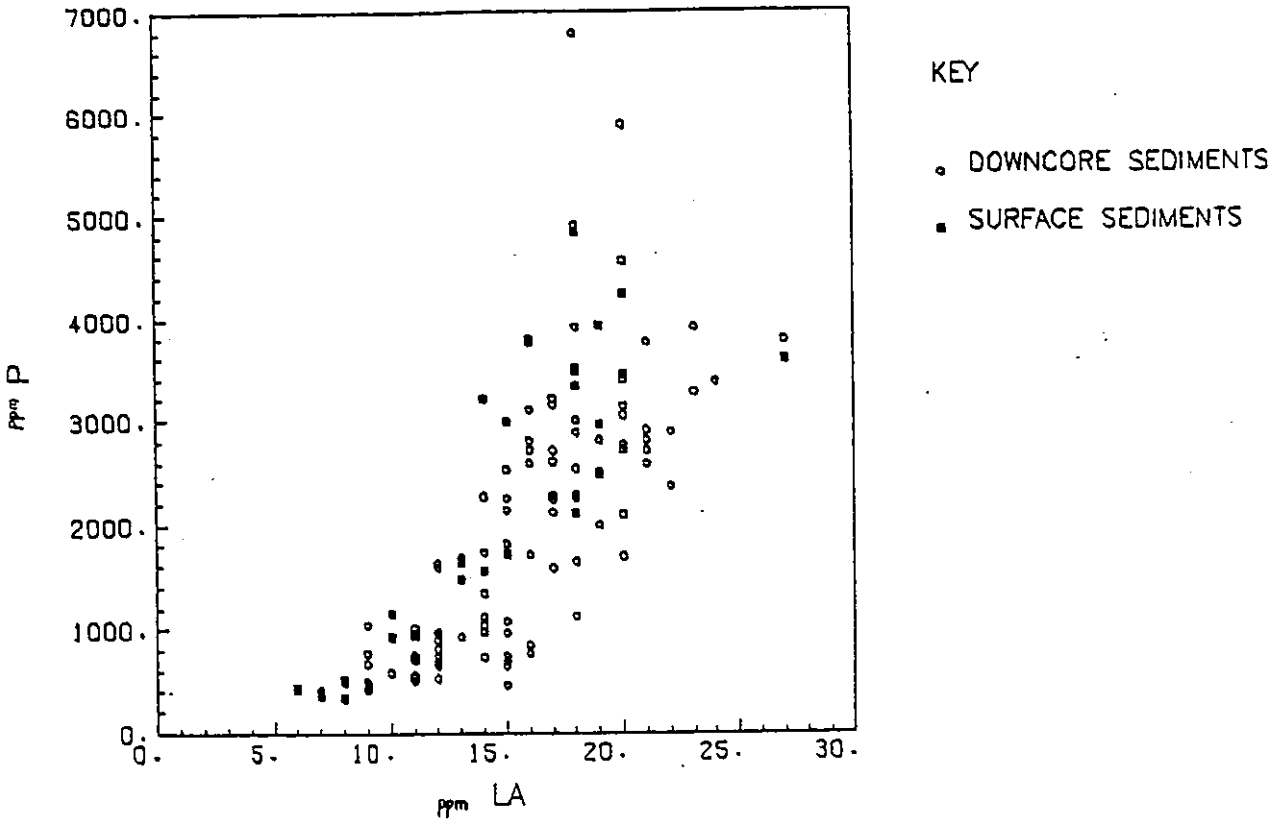



FIG.9.5.6.

Fe vs P/La in 13-15S Area sediments.

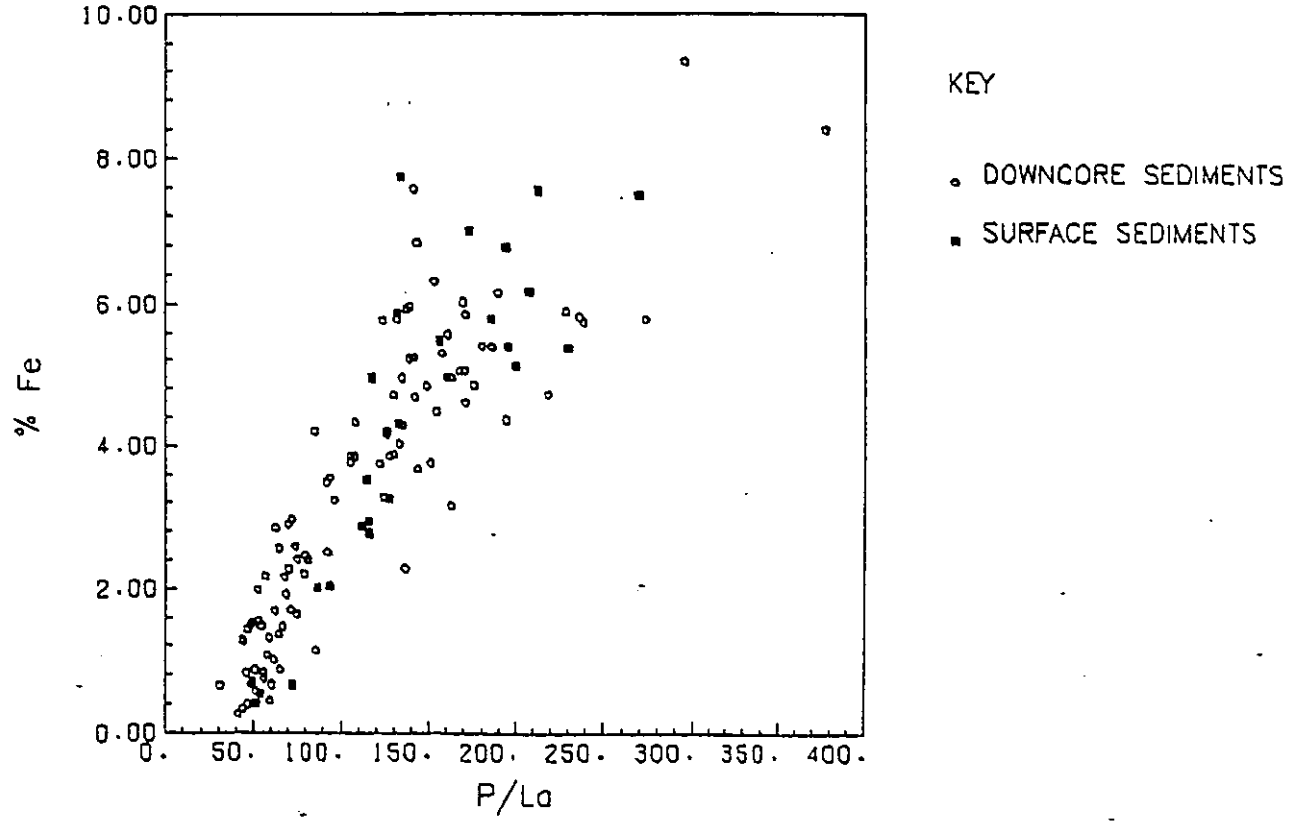
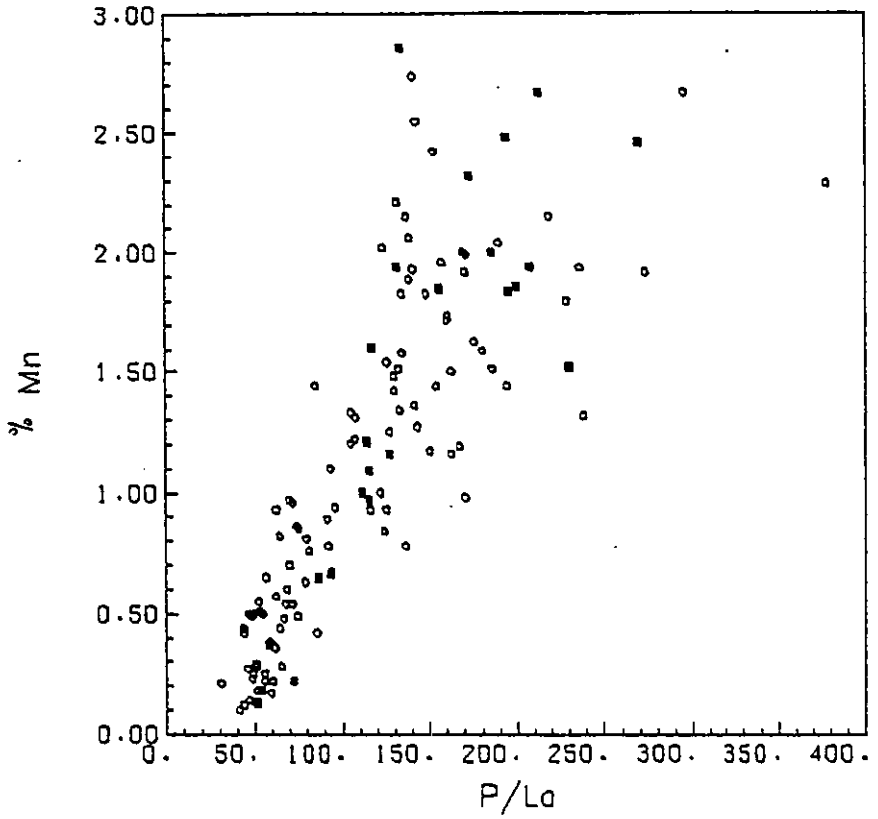


FIG.9.5.7.

Mn vs P/La in 13–15S Area sediments.



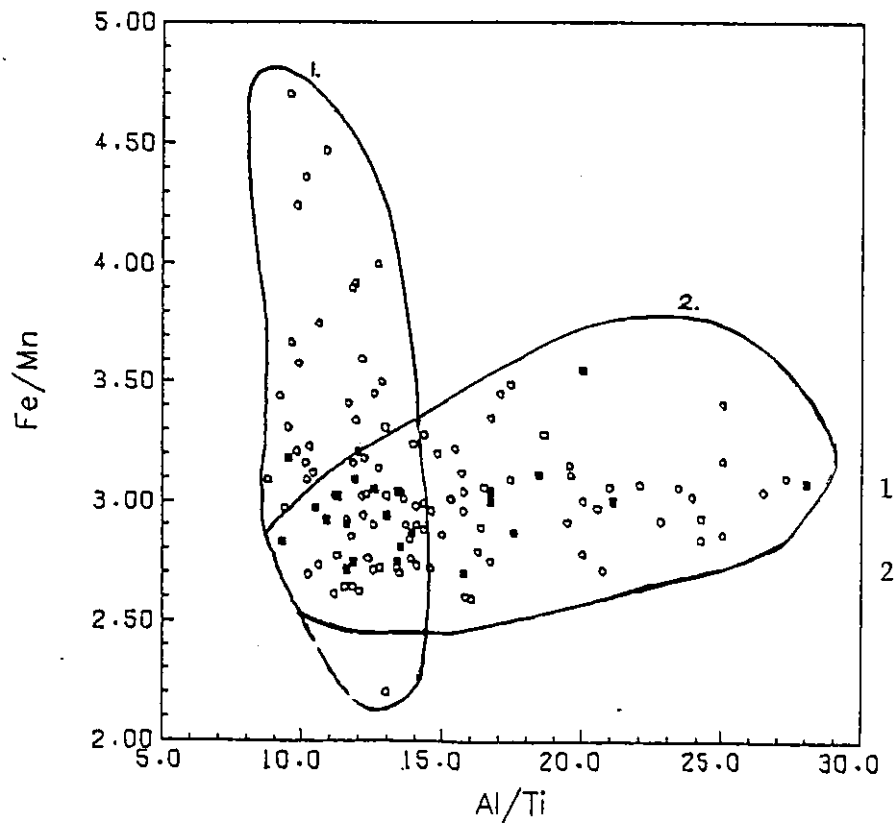

KEY

∘ DOWNCORE SEDIMENTS

▪ SURFACE SEDIMENTS

FIG.9.5.8.

Fe/Mn vs Al/Ti in 13–15S Area sediments.




KEY

∘ DOWNCORE SEDIMENTS

▪ SURFACE SEDIMENTS

1. Constant Al/Ti, variable Fe/Mn field.
2. Constant Fe/Mn, variable Al/Ti field.

as found by Berner (1973); Bloch (1978); Froelich et al. (1977), due to adsorption of the phosphate ion onto volcanogenic ferric hydroxides. The scatterplot of P with La shows a strong correlation between the two elements (Figure 9.5.5). The Fe content of 13 - 15°S area sediments correlates strongly with the P/La ratio (Figure 9.5.6) and the plot of Mn versus the P/La ratio (Figure 9.5.7) shows a similar trend. The highest values of Fe and the P/La ratio occur in downcore sediments. The P/La ratio varies from less than 50, to greater than 350, and varies in the same way as absolute Fe and Mn abundances in 13 - 15°S sediments.

The scatterplot of Fe/Mn with Al/Ti shows two distinct fields (Figure 9.5.8). Field 1 can be described as a highly variable Fe/Mn ratio field (2.2 to 4.7), at relatively constant Al/Ti ratios (9 to 14). Field 2 encloses data with a highly variable Al/Ti ratio (9 to 28), at relatively constant Fe/Mn ratios (2.6 to 3.5). The most Fe-rich, Al-poor sediments in Field 1 are downcore sediments. This may suggest that the most metalliferous sediments from the 13 - 15°S area reflect previous hydrothermal events, with a high Fe/Mn ratio indicative of a proximal hydrothermal source (see later). Field 2 represents sediments with relative uniformity in the Fe/Mn ratio but with varying Al/Ti ratios, caused by fluctuations in the clay mineral and basaltic detritus contents of the sediments.

The above scatterplots and correlations indicate that although there is a great range of metal values throughout both data sets, there are no significant differences between surface and downcore sediments. Evid - ently , the geochemistry of the whole 3 m cores is governed by the same processes that are presently forming surface sediments. This observation agrees with the work of Bostrom and Peterson (1969) and Heath and Dymond (1981).

Dymond et al. (1973) observed that metalliferous sediments display little tendency to recrystallise with time, although both Dymond et al. (1977) and Marchig and Gundlach (1982) showed that amorphous ferric hydroxides were diagenetically transformed into goethite. The above observations

FIG.9.5.9. Variations of Fe & Fe/Mn with depth in 5 cores from the 13-15°S Area.

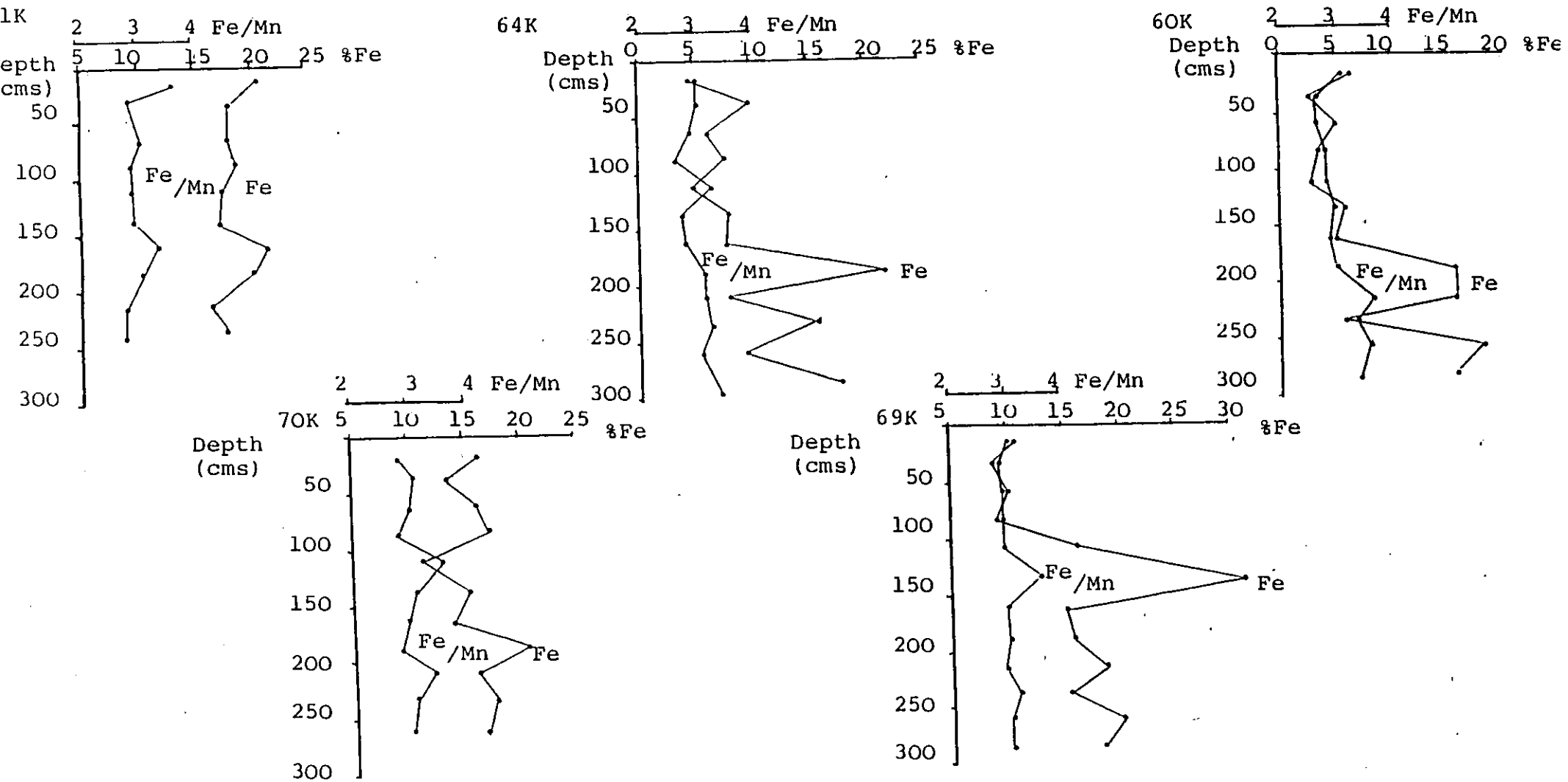


TABLE 9.5.2 Calculations dating the period of intense hydrothermal activity in cores 61, 70, 64, 69 and 60K

(See Figure 9.5.9)

| CORE NO. | DISTANCE FROM E.P.R. AXIS | 1. AGE OF CRUST ($\times 10^6$ years) | 2. DATE OF INTENSE HYDROTHERMAL ACTIVITY ($\times 10^3$ Years) | 3. PROJECTED DISTANCE FROM E.P.R. AXIS |
|---|---|---|---|---|
| 61K | 88 Kms to west | 1.0 | 203 - 236 | 70 Kms to west |
| 70K | 75 Kms to east | 0.85 | 236 - 270 | 54 Kms to east |
| 64K | 123 Kms to east | 1.40 | 236 - 270 | 102 Kms to east |
| 69K | 125 Kms to east | 1.42 | 169 - 203 | 105 Kms to east |
| 60K | 142 Kms to east | 1.61 | 236 - 304 | 121 Kms to east |

1. Calculated assuming a half spreading rate of 88 mm/year (Rea et al., 1973)

2. Calculated assuming a sediment accumulation rate of 0.74 cm/1000 years (Rydell et al., 1974)

3. This distance represents the position of the core relative to the E.P.R. axis, when intense hydrothermal activity ceased.

and the compositional homogeneity that exists between surface and downcore sediments, suggest that diagenesis is not responsible for substantially modifying the geochemistry of downcore sediments studied here and that Mn remobilisation is not likely to enhance the Mn content of 13 - 15°S area surface sediments.

On the basis of the above conclusions, the metal contents throughout the core may reflect primary temporal variations in hydrothermal activity. An area was chosen to investigate temporal variations in hydrothermal activity on the E.P.R., which was not associated with Garret Fracture Zone metallogenesis. The area chosen was the segment of the E.P.R., south of the Garret Fracture Zone, where some sediment accumulation rate data are known (Rydell et al., 1974). However, it should be noted that sediment accumulation rates may be variable and that the value used may not be representative of the 5 cores studied. Variations in Fe content (on a carbonate free basis) and in the Fe/Mn ratio with depth are shown for cores 61K, 70K, 64K, 69K and 60K in Figure 9.5.9. The locations of these cores have been shown previously, but their respective distances from the E.P.R. axis can be seen in Table 9.5.2. The depth interval between 175 and 200 cms generally contains the highest Fe and Fe/Mn values, but core 61K shows a maximum Fe value of 22.5%, between 150 and 175 cms, while core 69K shows a maximum Fe value of 30.9%, between 125 and 150 cms.

The Fe/Mn ratio generally peaks along with the Fe content although occasionally the two show an inverse relationship (see core 70K between 100 and 125 cms in Figure 9.5.9). Below the most Fe enriched horizon, the Fe contents, although variable, are higher than those from shallower depth intervals in the 4 cores from the E.P.R. east flank. The E.P.R. west flank core (i.e. 61K) shows a fairly uniform profile in Fe and Fe/Mn values, both above and below the peak observed between 150 and 175 cms depth.

Sediment accumulation rate data; from Rydell et al., (1974) for core GS7202-35P, in the immediate vicinity of core 61K (see previous maps); allow approximate dating of the cessation of the period of most intense hydrothermal activity. The results of dating calculations are shown in Table 9.5.2. From the 0.74 cms/1000 yrs accumulation rate, the end of the intense hydrothermal event occurred from approximately 169,000 to 236,000 years ago, for the 5 cores studied. If the sediment accumulation rate was too low - a possibility noted by Rydell et al. (1974) due to sediment winnowing-then cessation of this intense hydrothermal event may have occurred at a younger age.

In summary, cores 61, 70, 64, 69 and 70K all received high Fe contents between approximately 169,000 and 304,000 years ago and upon cessation of this period of intense hydrothermal activity, these cores were located within a 190 Km zone extending from 70 Kms west of the E.P.R. axis, through to 121 Kms east of the E.P.R. axis (see Table 9.5.2).

## 9.6 DISCUSSION

Metallogenesis associated with the Garret Fracture Zone has produced hydrothermal deposits such as Fe oxide staining on basalt (see Figure 9.3.4). Indications of hydrothermal activity, related to the north fault scarp of the Garret Fracture Zone, were seen in extensively hydrothermally metamorphosed greenstones. Although surface sediment from station 80G contains high concentrations of Fe, Mn, Cu, Zn and Ni, it is not known if this phenomenon has been caused by proximal fracture zone metallogenesis, or by distal E.P.R. metallogenesis and subsequent transport westward of particulate Fe and Mn oxides with adsorbed trace metals. The low P/La ratio observed in this sediment may indicate the latter process.

Surface sediment from station 87D contains high Fe, Fe/Mn, Cu, Zn, P and P/La values and is thought to be proximal to a hydrothermal vent. Ferromanganese crusts from stations 87D and 77D are highly fractionated with respect to Fe and Mn, the former with a much higher Fe content than the

latter. Surface sediment from 87D with 18.5% Fe contains 1020 ppm Cu.

While station 87D deposits may be considered as proximal hydrothermal deposits, with characteristic high Fe and Cu contents, the crust from station 77D shows distal affinity. The 77D ferromanganese crusts contain about 46% Mn. The surficial crust shows evidence of an excess supply of Zn (3030 ppm) to that which, on the basis of previous discussion (Section 9.4.1), can be supplied hydrogenously. This particular sub-sample shows an increased metal supply compared to the other sub-samples and may indicate a recent pulse of hydrothermal activity from a low temperature vent, causing high Mn and Zn contents.

From a synthesis of the data presented above, two possibilities exist which may explain the high west flank metal concentrations in the 13 - 15°S area of the E.P.R. The first possibility involves a heat source underneath the west flank of the E.P.R., as found at 20°S by Rea (1978). If this were the case then it would be reasonable to expect isolated vent areas there, although none have been found. The second possibility would involve westward transport of hydrothermally derived particulate ferromanganese oxides, from a source near the E.P.R. axis, to a west flank depositional site. Heath and Dymond (1981) came to this conclusion in regard to sediments from the 10°S area of the E.P.R. The physical homogenisation of hydrothermal precipitates would produce a relatively uniform hydrothermal component with constant Fe/Mn ratios, as is observed in the present samples.

The second of the above possibilities can best explain the present data. Metals injected into seawater near the E.P.R. axis are swept westward by prevailing bottom currents and incorporated into west flank sediments as particulate Fe-Mn oxides with adsorbed trace metals. Dymond (1981) suggested that currents flow predominantly through large fracture zones, although they may flow over the E.P.R. axis. Convincing evidence of the westward flow of mid-depth ocean currents, over the 15°S area of the E.P.R. has been given by Reid (1981).

## 9.7 CONCLUSIONS

A synthesis of all the geochemical data available from the 13 - 15°S area of the E.P.R. indicates the following major conclusions:-

1. There is ongoing metallogenesis associated with both the Garret Fracture Zone and the E.P.R. crestal region.

2. Sediment geochemistry reveals that Fe and Cu are more enriched than Mn and Zn, and that Fe/Mn and Cu/Zn ratios are reasonably constant throughout the area.

3. The P/La ratio appears sensitive to a hydrothermal supply of metals and can be used to locate areas containing vents.

4. The geochemistry of surface and buried sediments is similar, suggesting little diagenesis has occurred.

5. An investigation of temporal variations in hydrothermal activity indicates that while metal enrichment processes on the west flank of the E.P.R. remained fairly constant with time, this is not the case for the east flank.

6. Upon transport of the core locations outside the zone of most intense hydrothermal activity, west flank cores have been augmented in hydrothermal precipitates by westerly flowing mid-depth currents.

7. East flank core locations have been starved of hydrothermal precipitates as a result of the westward hydrothermal effluent dispersal. This produces an asymmetrical metal distribution over the axial region of the E.P.R., in the 13 - 15°S area.

STUDY G

# CHAPTER 10

## THE 19 - 21°S AREA OF THE EAST PACIFIC RISE

### 10.1 INTRODUCTION

The 1980 GEOMETEP cruise recovered 142 samples from the 17 - 21°S area of the E.P.R. With the exception of 12 samples taken from core 59K, recovered near 17°S, all the remaining samples are located in the map area shown in Figure 10.1.1. The 142 samples comprise 138 sediments (36 surface sediments) and 4 ferromanganese oxide crusts. In the following sections a multi-element geochemical approach is adopted in an attempt to locate hydrothermal sources in the study area and to study element ratios for the development of submarine mineral exploration techniques following on from work in the 13 - 15°S area (see Chapter 9).

### 10.2 GEOLOGY, BATHYMETRY AND STRUCTURE OF THE 19 - 21°S AREA

The bathymetry of the area is shown in Figure 10.2.1. The dextral offset of the E.P.R. at 20°40'S corresponds to Fracture Zone VIII of Mammerickx et al. (1975). This offset was first located during expedition DOWNWIND of the Scripps Institution of Oceanography. Deep troughs of 3374 m and 3582 m were reported for this feature, with an azimuth of 107° (Mammerickx et al., 1975). Rea and Blakely (1975) found that the E.P.R. in the 20°S area is spreading at a rate of 162 mm/year in the direction of 103° and that a small positive magnetic anomaly of 50 - 100 nT is associated with the axial ridge crest. The anomaly is thought to be caused by magnetised extrusive basalt.

Rea (1978) showed that during the last 2.4 million years, crustal accretion has occurred asymmetrically in the 20°S region, with half spreading rates of 70 mm/year and 92 mm/year for west and east flanks, respectively. The topographic profiles across the E.P.R. crest also show marked asymmetry, where the east flank is 100 to 150 m deeper than the west flank (Rea, 1978). The same author found that heat flow values

FIG.10.1.1. Station locations in the 19-21°S area of the East Pacific Rise.

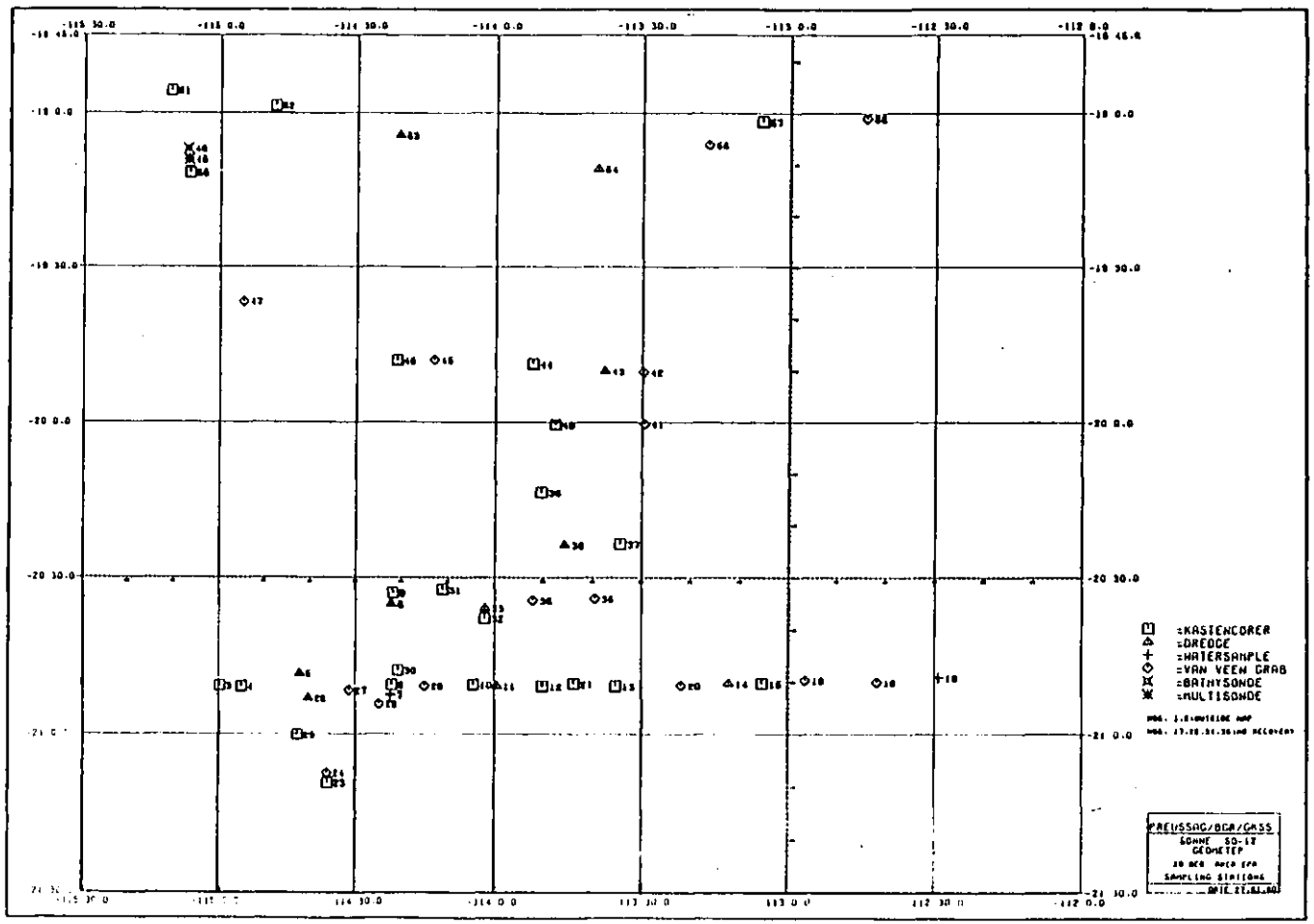


FIG. 10.2.1. Bathymetry of the 19-21°S area of the East Pacific Rise. S denotes sulphide locality of Francheteau & Ballard (in press).

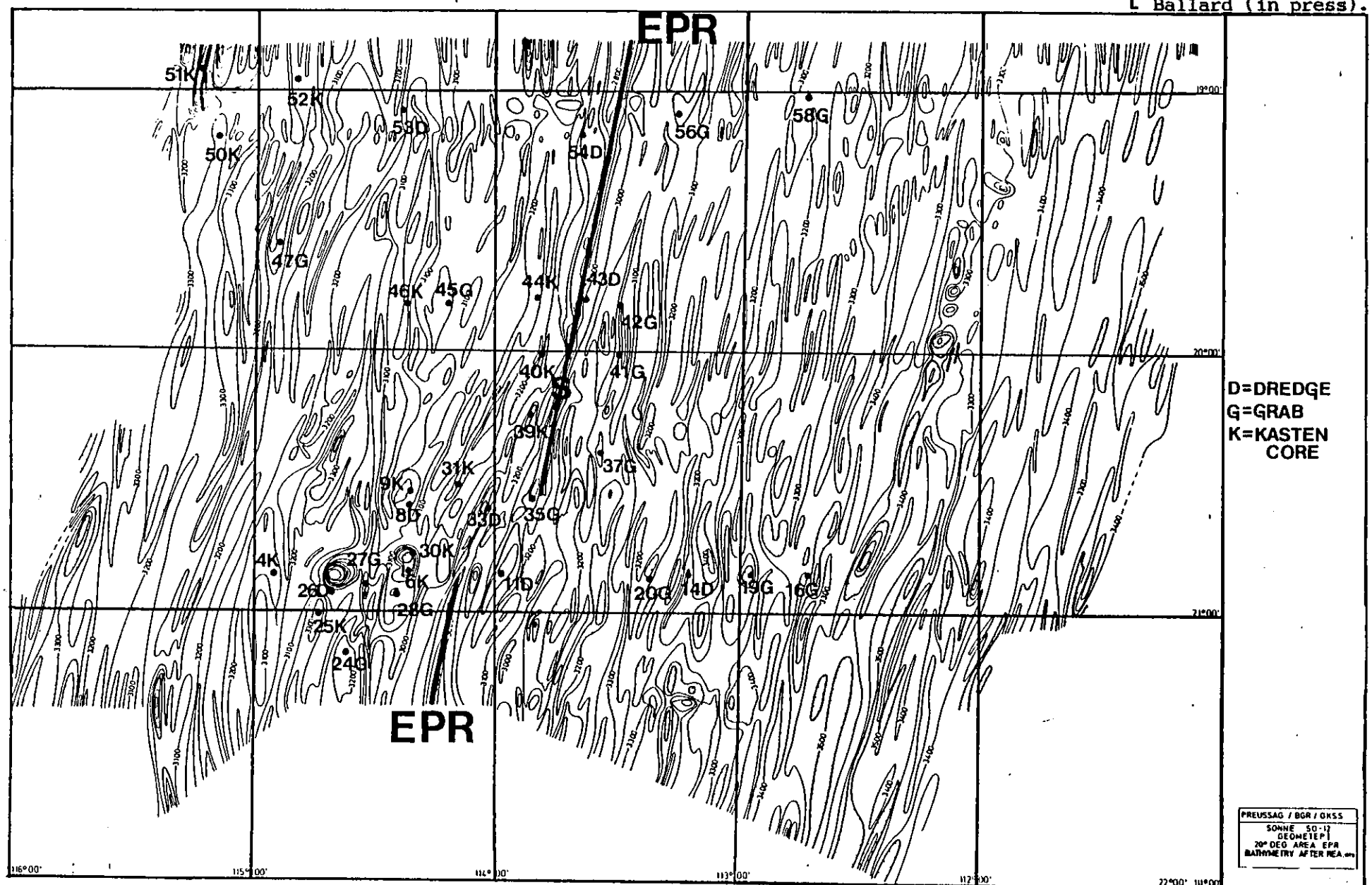
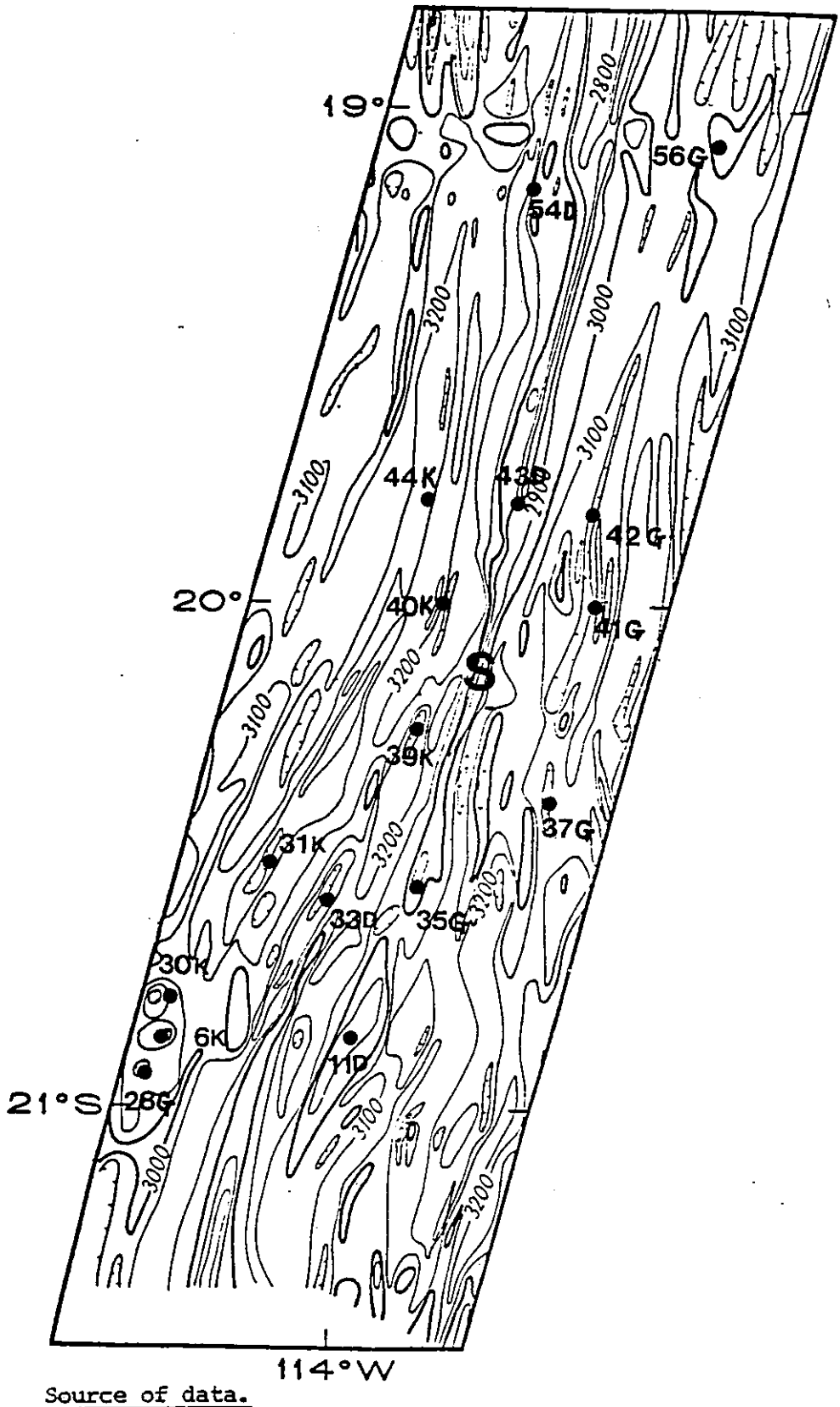


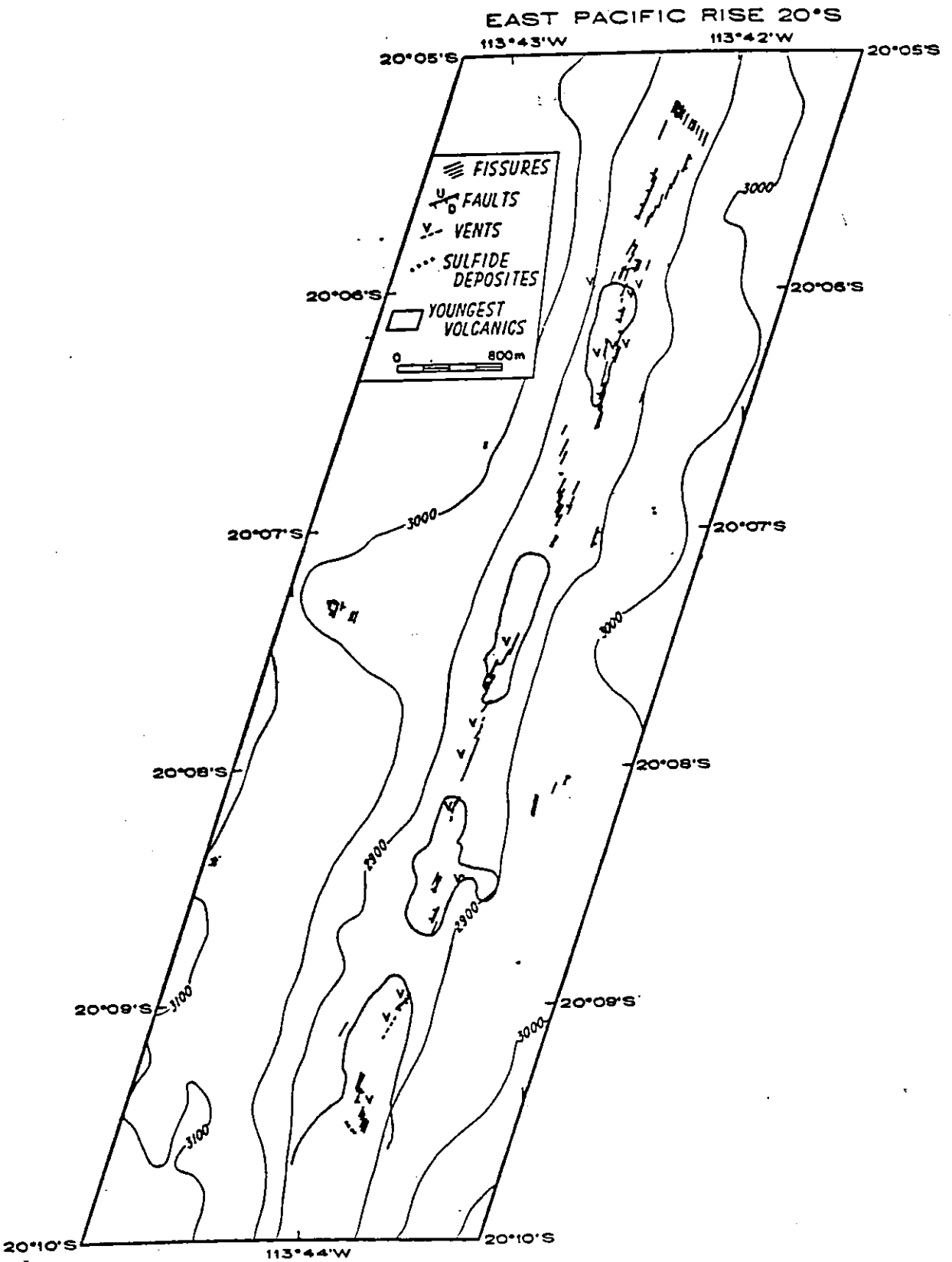
FIG.10.2.2. Detailed bathymetry of the 19-21°S area at longitude 114°W.




Source of data.

The station locations shown were sampled during the GEOMETEP cruise of 1980. The sulphide locality (S) is reported in Francheteau & Ballard (in press) which is also the source of the map, originally described by Rea(1978).

FIG.10.2.3. Hydrothermal vents and sulphide deposits mapped during the R/V MELVILLE cruise of 1981 in the area between 20°05' & 20°10' S. The map was taken from Francheteau & Ballard (in press).



were higher on the western flank. The dextral offset of the E.P.R. at 20°40'S, which has a strike-slip displacement of 15 Kms, was interpreted by Rea (1978), on the basis of magnetic anomaly data, as being a 30 - 40 Km wide zone of shearing and not a simple transform fault. This fracture zone, with a maximum depth of about 3500 m (see Figure 10.2.1), is thought to have resulted from a small jump of the site of the E.P.R. spreading axis, around 2 million years ago.

The E.P.R. axis consists of a low ridge which is 15 Kms wide and 300 to 400 m high, with a depth ranging from 2800 to 3000 m. The surrounding abyssal hills are 100 to 200 m high and orientated subparallel to the E.P.R. axis. A small seamount is located near 20°50'S and 114°40'W (see Figure 10.2.1).

In summary, the 20°S area of the E.P.R. shows asymmetry in depth, heat flow and spreading rates across its flanks which Rea (1978) interpreted as being due to a heat source under the west flank, which retards lithospheric cooling on that flank and so produces faster accretion on the east flank.

During the expedition SEARISE II, the R/V JEAN CHARCOT mapped the 20° to 21°30'S area of the E.P.R. following up the earlier work of Rea (1978), shown in Figure 10.2.2. Mapping was carried out by the SEABEAM multi-narrow beam bathymetric surveying system, with locations fixed by an acoustic transponder navigation network. Francheteau and Ballard (in press) reported an axial swell of 7 Kms width and 500 m height, shoaling at 2850 m, between 20°05' and 20°10'S (see Figure 10.2.3). In this area, the RAIE deep-towed system recorded photographic evidence of on-going hydrothermal activity.

More recently, in 1981, the R/V MELVILLE returned to this area during expedition VULCAN Leg 8, with the ANGUS deep-towed system. Lava lakes and fluid lava flows were found on the axial-ridge summit while pillow lavas occupied the slopes (Francheteau and Ballard, in press). These authors reported a series of active hydrothermal vents, of both the

Galapagos low-temperature type (Corliss et al., 1979) and of the E.P.R., 21°N high-temperature type (Spiess and MacDonald, 1980). The high temperature vent fields are located in the centre of lava lakes in the southern part of the map, taken from Francheteau and Ballard (in press) and shown in Figure 10.2.3. "White smokers" with high methane concentrations in the effluent fluids were also reported, in addition to high temperature sulphide vents. This is the first evidence of sulphide metallogenesis occurring in the 20°S area of the E.P.R., although the area has long been known to contain highly anomalous metal-enrichments in sediments (see later).

## 10.3 SAMPLE DESCRIPTION

### 10.3.1. Sediments.

The 138 sediments recovered from the 19 - 21°S area of the E.P.R. consist of a suite of samples ranging from highly metalliferous sediments to pelagic foraminiferal carbonates. These sediments are generally more enriched in metals than those from the 13 - 15°S area described in Chapter 9. However, the hues of the most metal-enriched samples from both areas correspond to 7.5 YR 4/4 (see Appendix D).

The sediments in this study have been subjected to sedimentological analysis by other workers and some of this data has been described in Marchig and Gundlach (1982). These authors showed that the >63μ fraction of the sediments is totally dominated by $CaCO_3$, as white or rust-coloured foraminiferal tests. The <63μ fraction consists of $CaCO_3$ and fine-grained red/brown semi-opaque oxides, termed R.S.O's by Yeats and Hart et al. (1976). Work carried out by the writer during the summer of 1980, at the Hawaii Institute of Geophysics, revealed that after removal of sea-salts, $CaCO_3$, Fe and Mn oxides, followed by size-separation of the finer fraction (see Appendix B), clay minerals could not be isolated from these sediments. Thus, two phases dominate the sediments, $CaCO_3$ and R.S.O's.

The data that follows represent geochemical analyses reported on a carbonate free basis and so largely reflect the R.S.O. composition of the sediments, i.e. the hydrothermal component.

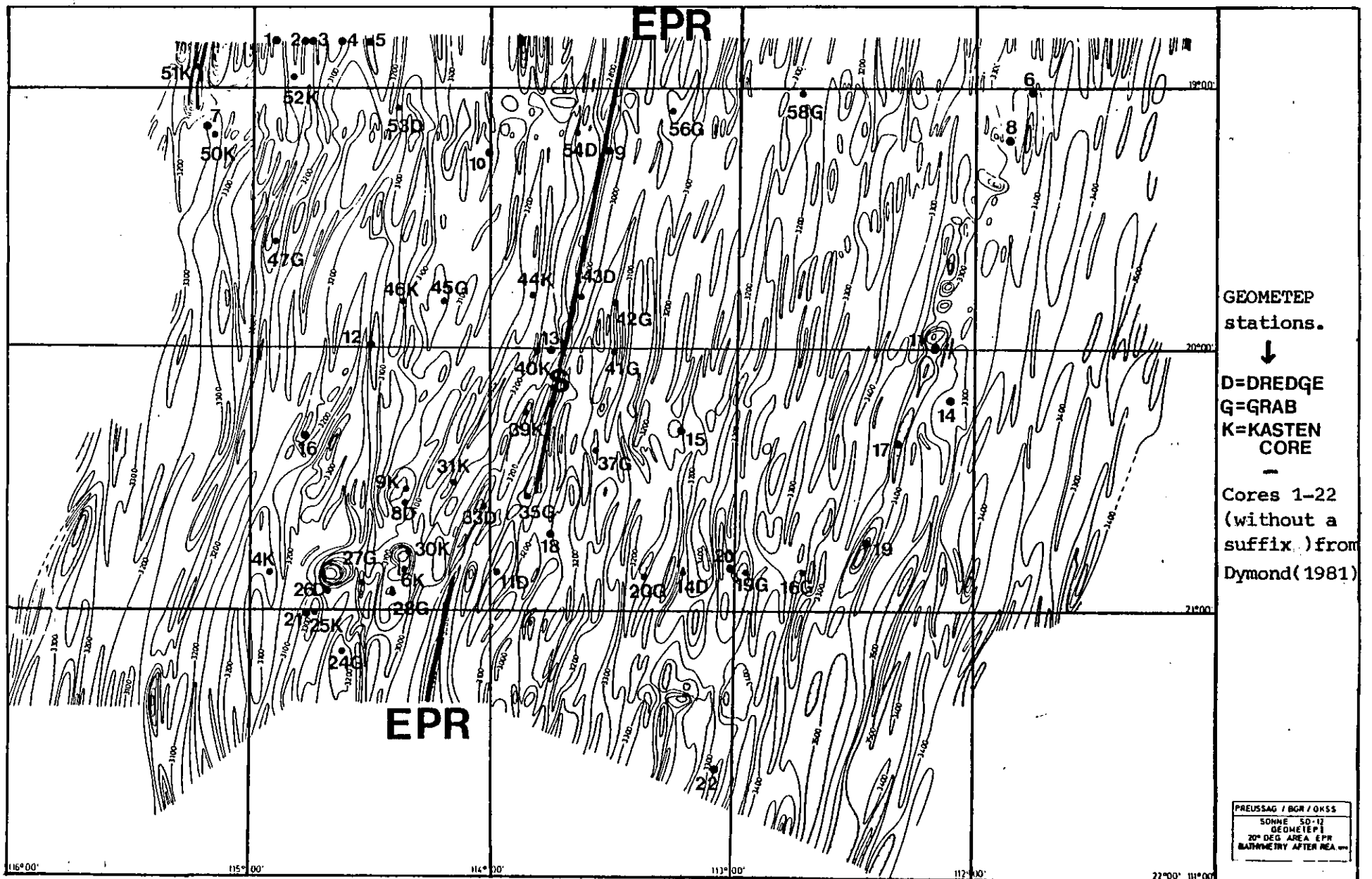


PLATE 10.3.1. The underside of the black Mn crust from station 14D. Note the mud-cracks and the bulbous fissure infilling (in light grey). x1/2

PLATE 10.3.2.



FIG.10.4.1. Surface sediment locations in the 19-21°S area of the East Pacific Rise.



### 10.3.2. Ferromanganese oxide crusts.

Ferromanganese oxide crusts were recovered from dredge stations 14D and 26D (see Plates 10.3.1 and 10.3.2). Four sub-samples were taken from the station 14D crust shown in Plate 10.3.1. Three of the sub-samples are as follows:

(i) a sample of surface crust.
(ii) a composite of surface and sub-surface crusts.
(iii) a secondary infilling of a fissure in the main crust.

The secondary infilling is shown in Plate 10.3.1, along with a fourth sub-sample which consists of orange mud exhibiting well developed mud-cracks. Compositional differences between samples are described later.

An orange coloured ferromanganese crust from station 26D displays an unusual fine-scale mamillar structure. Plate 10.3.2 shows the surface of this sample which is coated with a light dusting of carbonate-rich sediment.

## 10.4 SURFACE SEDIMENT GEOCHEMISTRY

Surface sediment data from 35 GEOMETEP stations have been augmented by data from 22 other stations (Dymond, 1981), to produce the most comprehensive coverage currently available of the axial region of the E.P.R. in the 20°S area. The locations of these surface sediments are shown in Figure 10.4.1. Previously, it has been stated that where $CaCO_3$ values are high, results reported on a carbonate-free basis and on a carbonate and salt-free basis, are not comparable. To circumvent this problem, the data of Dymond (1981) have been recalculated on just a carbonate-free basis, as GEOMETEP data are (see Appendix C).

The following sections describe the distribution of $CaCO_3$, $SiO_2$ and the following elements and element ratios in the 19 - 21°S area:-
Fe, Mn, Cu, Zn, Ni, Mo, As, Sb, Bi, Cu/Zn, P/La.

FIG.10.4.2. Fe in surface sediments from the 19-21°S area of the E.P.R.

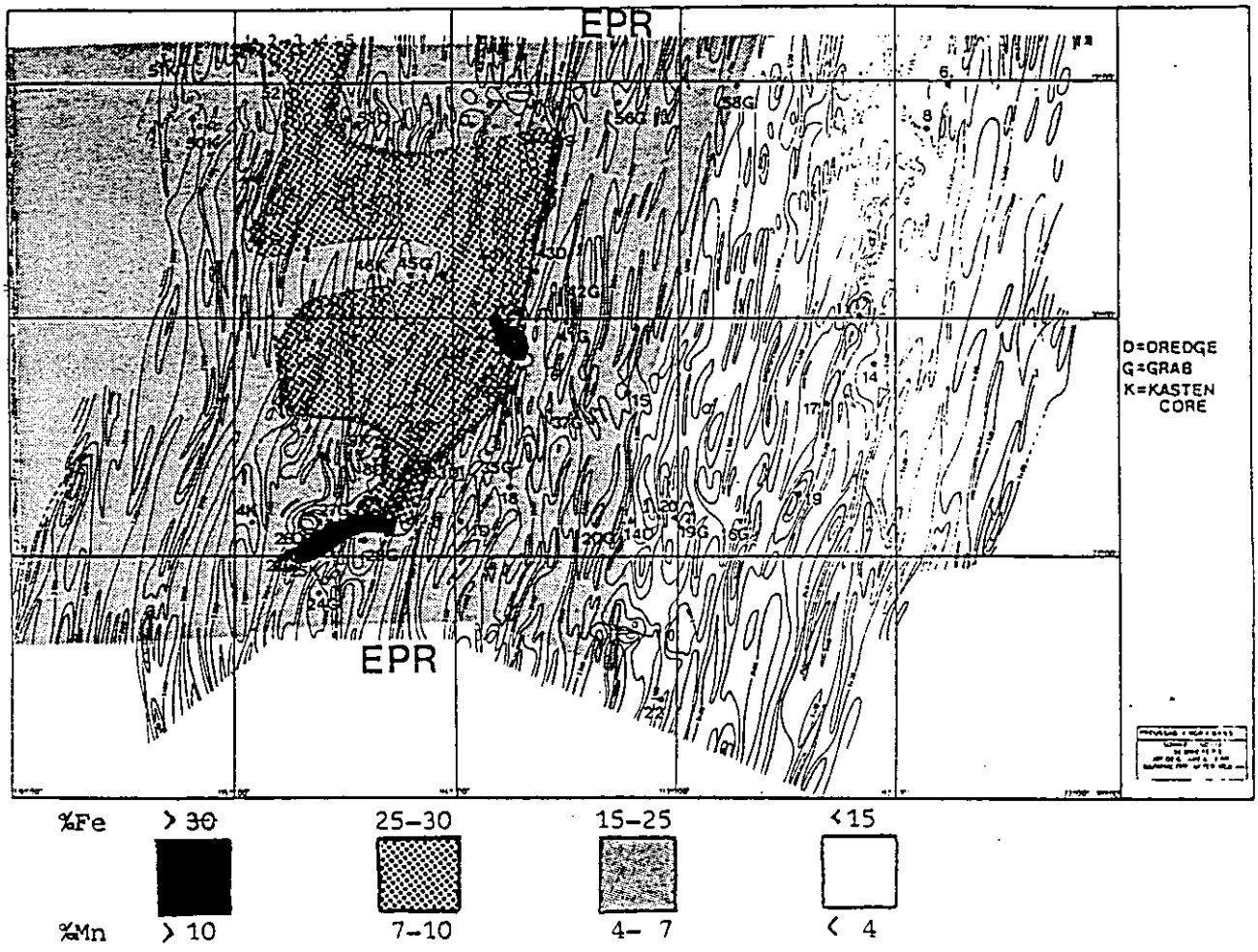
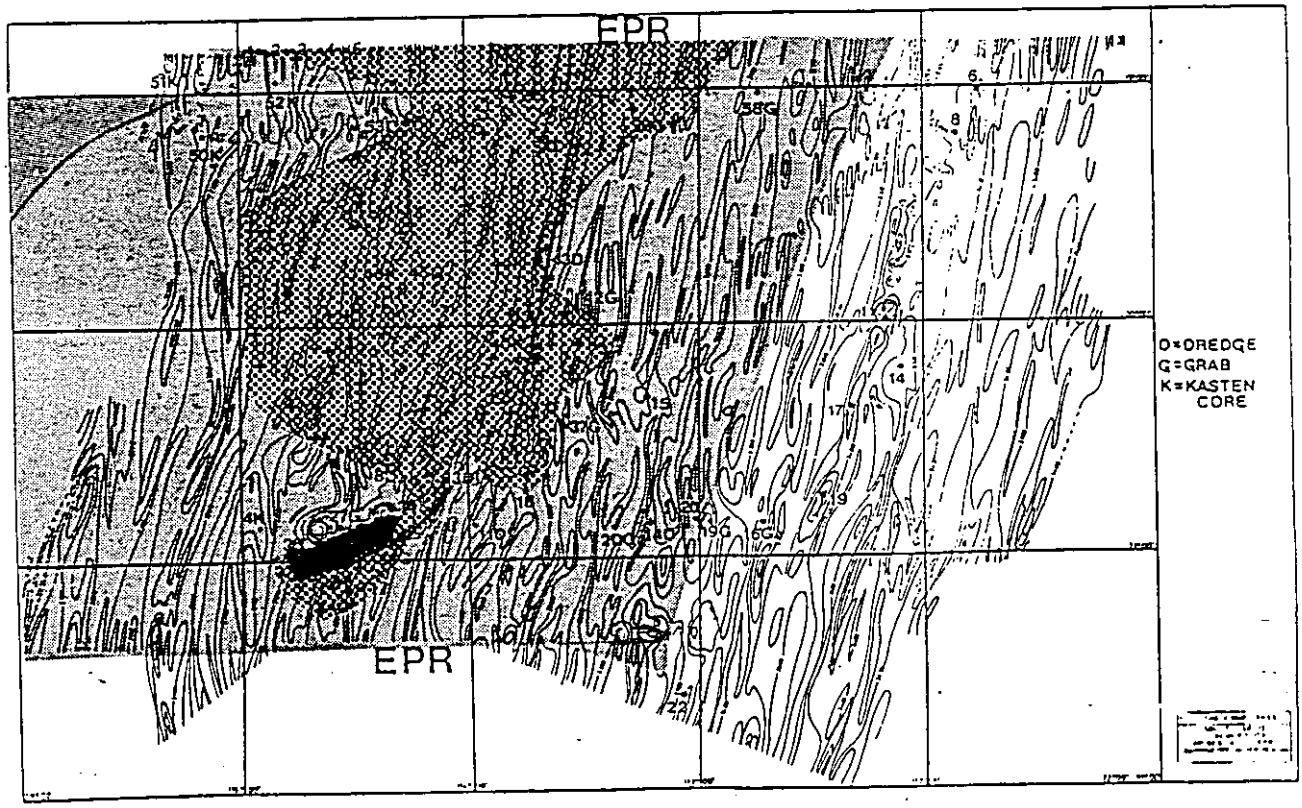



FIG.10.4.3. Mn in surface sediments from the 19-21°S area of the E.P.R.



*Fe*

The distribution of Fe in surface sediments has been sub-divided into the four ranges shown in Figure 10.4.2. Two areas display high Fe values of greater than 30%; one area just south of 20°S surrounds the sulphide locality mentioned earlier, while the second area is located west of the E.P.R. axis, south of the offset, at about 20°50'S. This second area encloses stations 6K, 25K and 27G, the former with the maximum Fe value (30.8%) in this area.

Fe values exceeding 25% are restricted to the west flank of the E.P.R., as shown in Figure 10.4.2 and similar west flank high values have been previously described in the 13 - 15°S area (see Chapter 9). Fe values less than 15%, with a minimum of 4% for station 16G surface sediment, predominate on the east flank of the E.P.R., further than about 80 Kms from the spreading centre. The stations sampled from the west flank are more enriched in Fe and all values are higher than 16%, thus producing the observed asymmetry in Fe values about the E.P.R. axis.

*Mn*

The Mn distribution in 19 - 21°S area surface sediments is broadly similar to that of Fe, in that higher values occur on the west flank than on the east flank of the E.P.R. (see Figure 10.4.3). However, important differences between these elements do occur. Only one area with Mn values higher than 10% can be found, with a maximum of 12% for station 27G surface sediment, and this area coincides with the second area of high Fe values described above. The area enclosing the sulphide locality, on the E.P.R. axis, does not contain Mn values exceeding 10%, although station 40K surface sediment contains 9.3% Mn.

Surface sediment Mn contents ranging from 4 - 7% cover a wider area than the corresponding sub-division of the Fe data (see Figures 10.4.2 and 10.4.3) but similar depletions in both of these elements occur in east flank sediments located further than 80 - 100 Kms from the E.P.R. axis.

FIG.10.4.4. Cu in surface sediments from the 19-21°S area of the E.P.R.

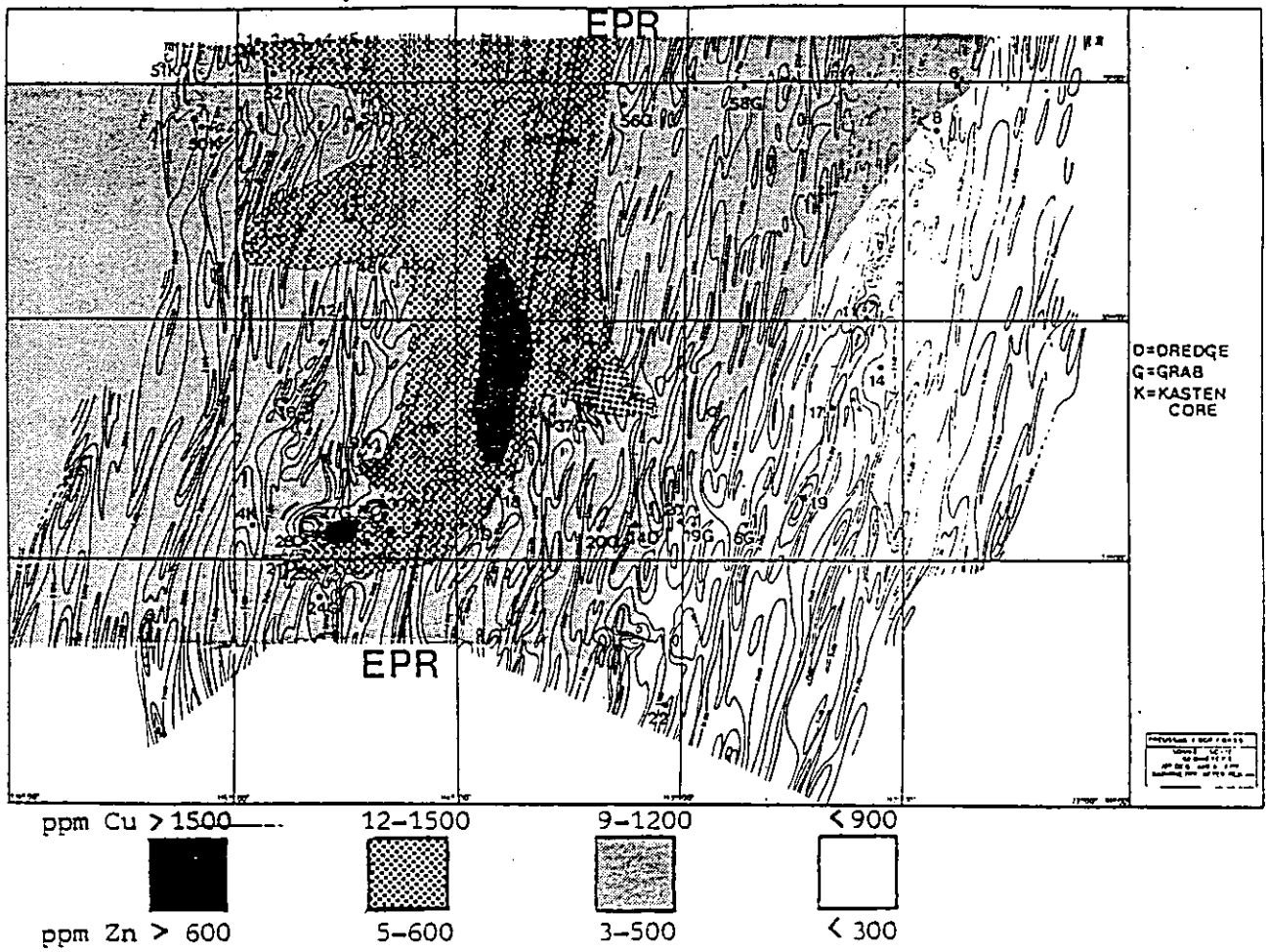
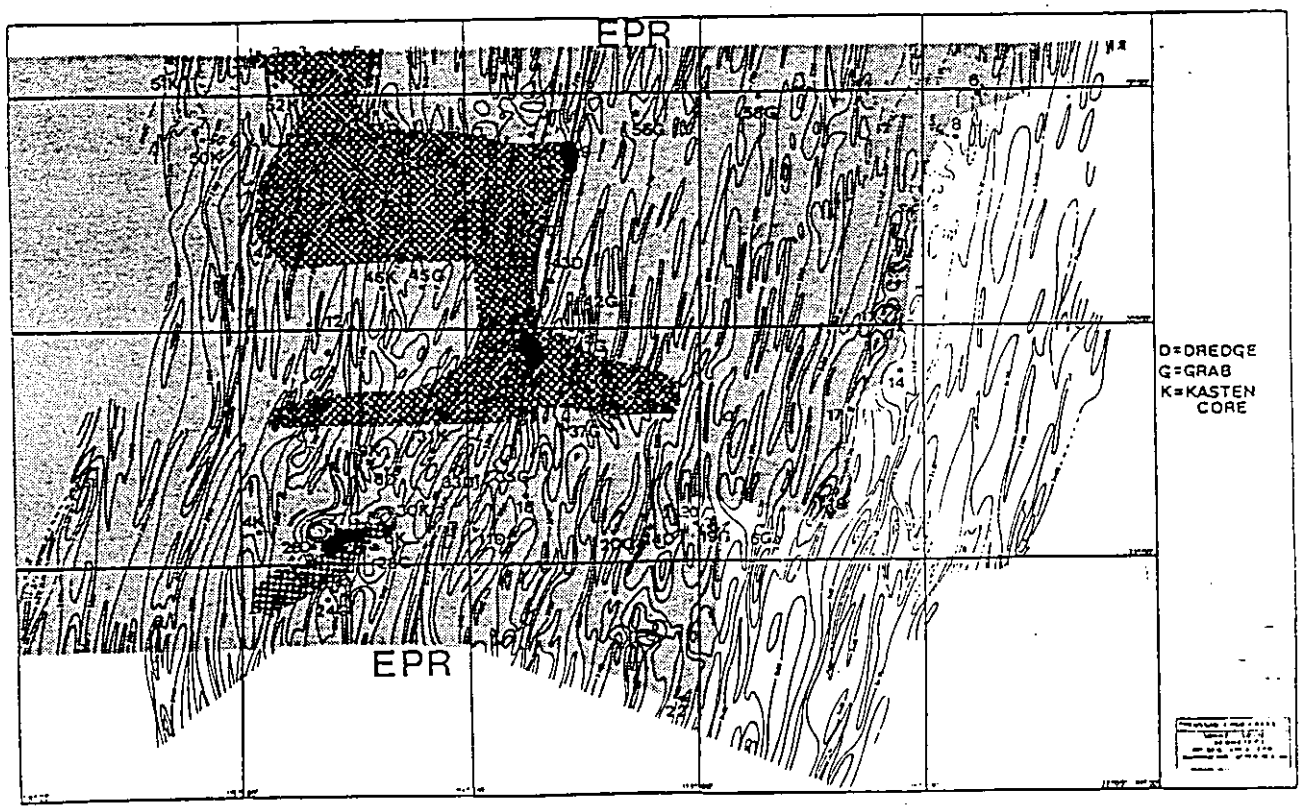



FIG.10.4.5. Zn in surface sediments from the 19-21°S area of the E.P.R.



*Cu*

The distribution of Cu in 19 - 21°S area surface sediments (see Figure 10.4.4) exhibits two areas of very high enrichment, with values exceeding 1500 ppm. The larger area is centred on the axial sulphide locality, where surface sediment from station 40K contains 1780 ppm Cu, while core 13 contains 1890 ppm (Dymond, 1981). This area of Cu enrichment in surface sediments is very large, trending along the axial region for about 85 Kms, and is not just restricted to the immediate vicinity of the sulphide discovery.

The second area of highly Cu-enriched surface sediments is located to the east of the seamount, in the vicinity of station 27G, where 1510 ppm Cu is found. Both of the two areas described coincide with areas of high Fe contents. The axial region of the E.P.R. is characterised by surface sediments with Cu contents ranging from 1200 to 1500 ppm, while those located further than about 100 Kms east of the E.P.R. axis contain less than 900 ppm.

*Zn*

Surface sediment Zn contents exceed 600 ppm in 3 separate areas (Figure 10.4.5). Two of these areas coincide with the areas of high Fe and Cu values (see above), but the area of Zn enrichment containing up to 650 ppm Zn which surrounds the sulphide locality, is much smaller than that observed for Cu. The third area of high Zn values is located on the E.P.R. axis at about 19°10'S (see core 9 in Figure 10.4.1).

The distribution of Zn values between 500 and 600 ppm is unusual. These values are largely restricted to the west side of the axial region but two lobes extend east and west of the E.P.R. axis at 20°20'S, north of the axial offset. Low Zn values of less than 300 ppm, with a minimum of 120 ppm in surface sediment from station 16G, characterise east flank sediments located further than about 150 Kms from the E.P.R. axis.

*Cu/Zn*

Cu/Zn ratios greater than 3.0 occur in axial region surface sediments and in two small areas on the east flank of the E.P.R. (Figure 10.4.6).

FIG.10.4.6. Cu/Zn in surface sediments from the 19-21°S area of the E.P.R.

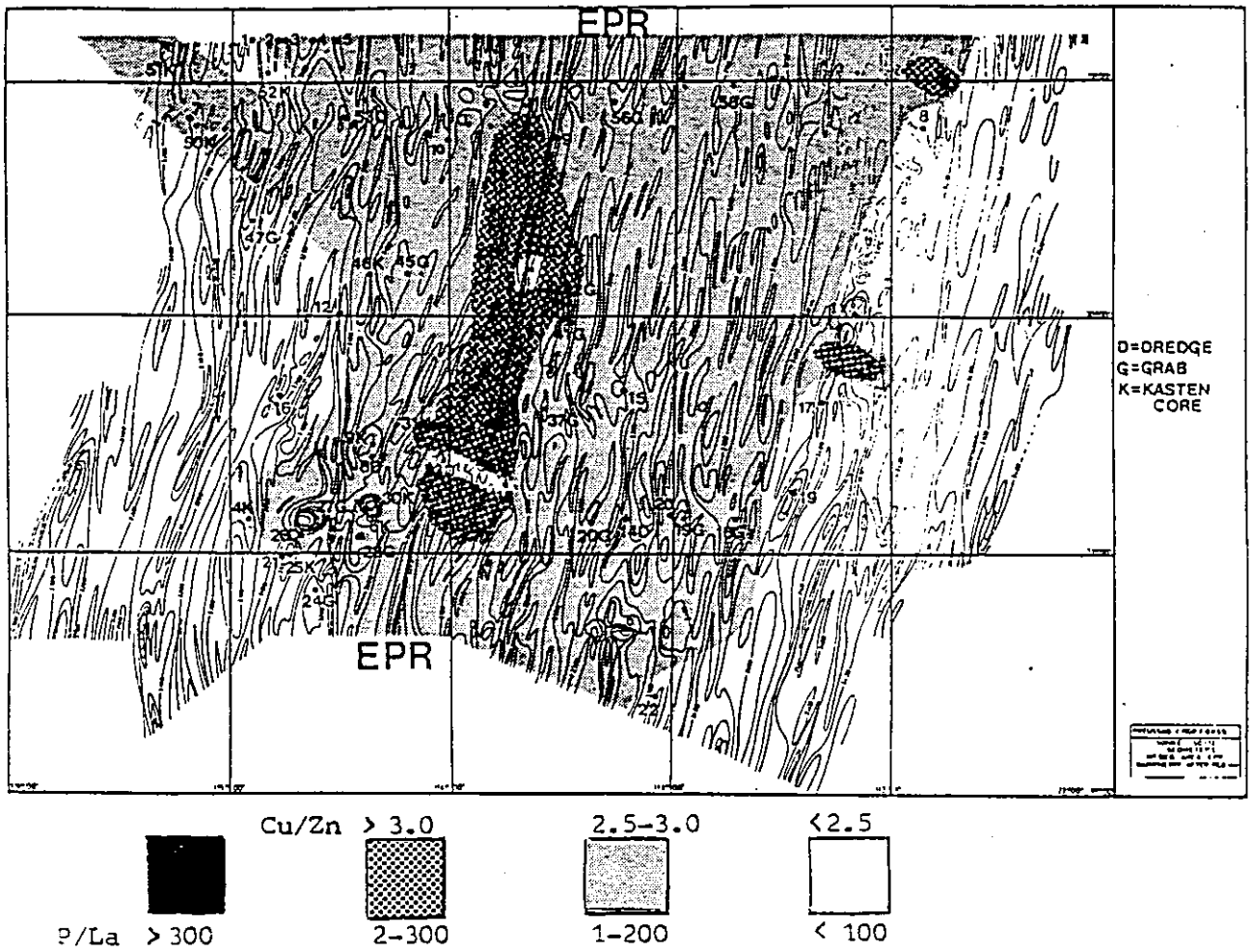



FIG.10.4.7 P/La in surface sediments from the 19-21°S area of the E.P.R.

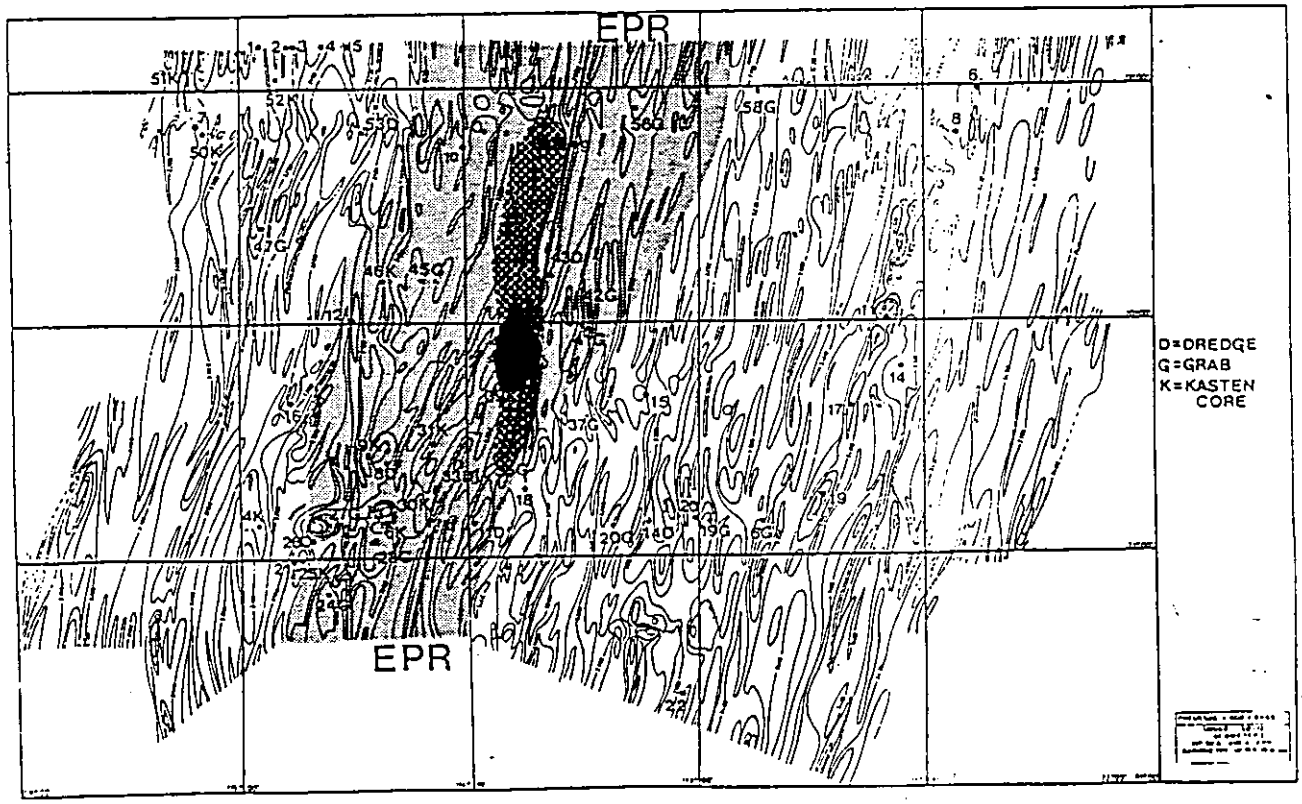


FIG.10.4.8 . Mo in surface sediments from the 19-21°S area of the E.P.R.

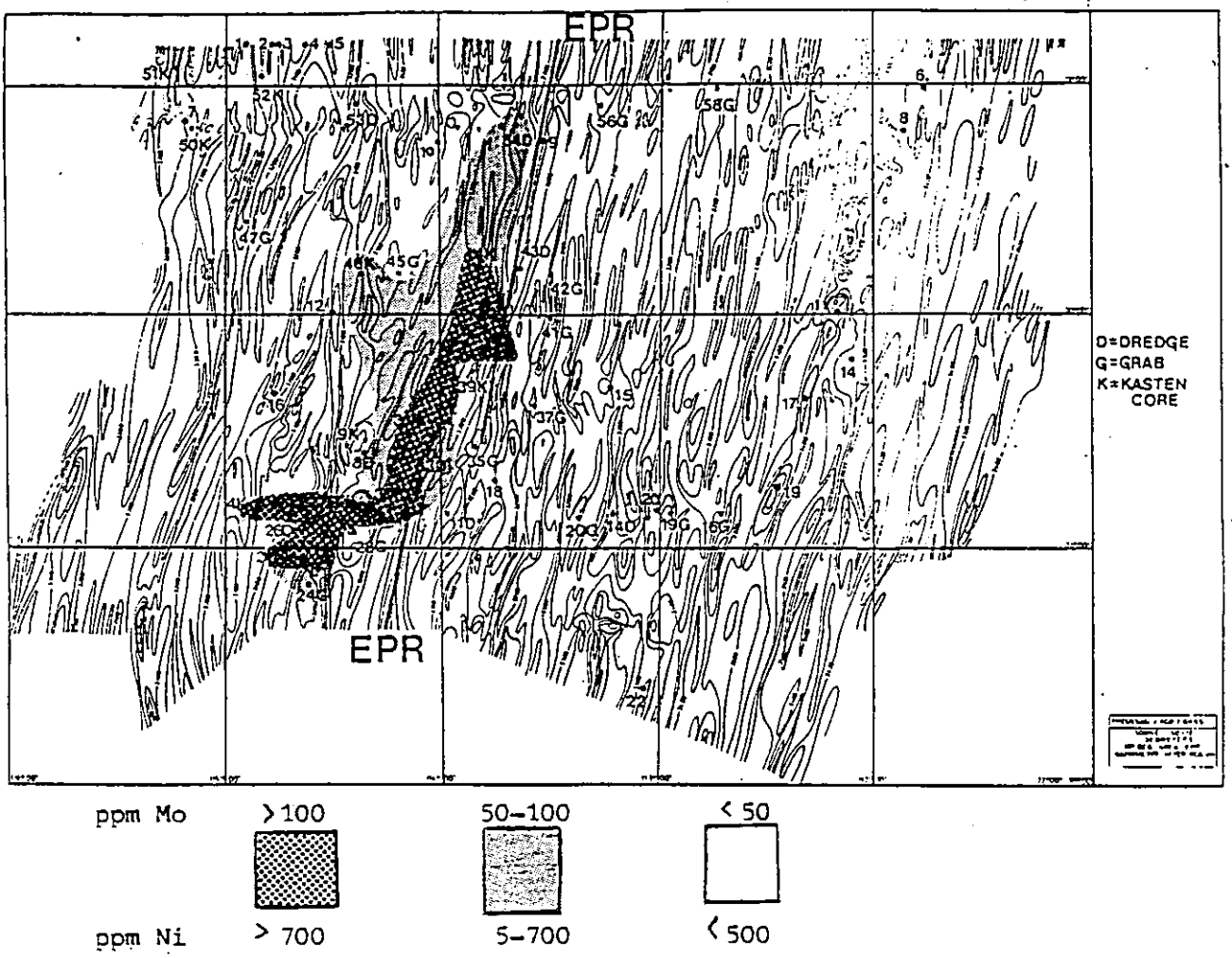
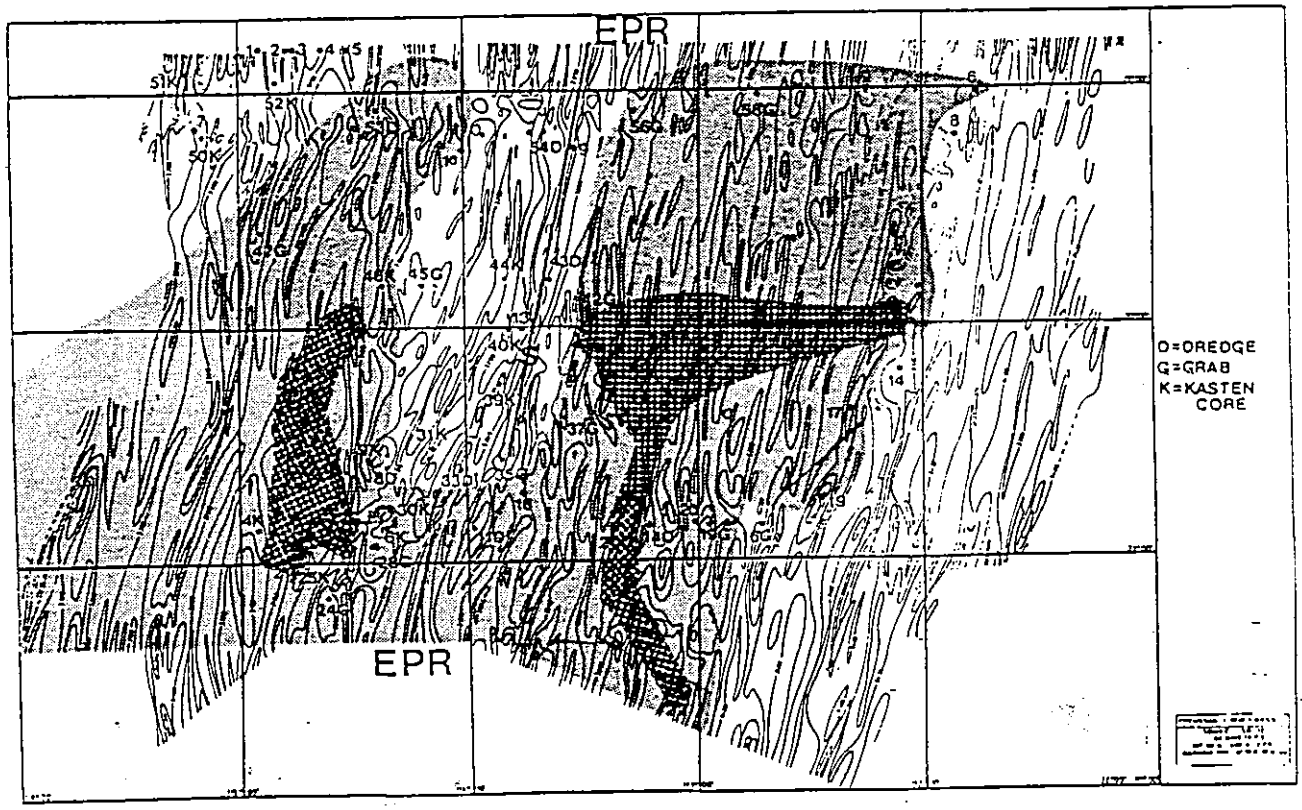



FIG.10.4.9 . Ni in surface sediments from the 19-21°S area of the E.P.R.



Apart from the generally higher values along the E.P.R. axis, isolated low Cu/Zn ratios occur in two areas where sediments contain increased amounts of Al and Ti which were found to be caused by abundant volcanic glass shards. The distribution of Cu/Zn ratios shows a general decrease with distance from the E.P.R. axis in the 19 - 21°S area and as shown previously, is indicative of axial hydrothermal activity.

*P/La*

The P/La ratio reaches a maximum of 405 in station 39K surface sediment and is also high (302) in surface sediment from station 40K (see Figure 10.4.7). Both of these stations are located in the vicinity of the recently discovered sulphide deposit, which further supports the use of the P/La ratio in sediments as an indicator of hydrothermal activity. High values for the P/La ratio, between 200 and 300, are found to the west of the E.P.R. axis and these values trend parallel to that feature. The P/La ratio fails to identify a possible hydrothermal centre (with high Fe, Mn, Cu and Zn content) to the east of the seamount at 20°50'S, 114°40'W, indicating that its value in detecting hydrothermal centres cannot always be relied upon.

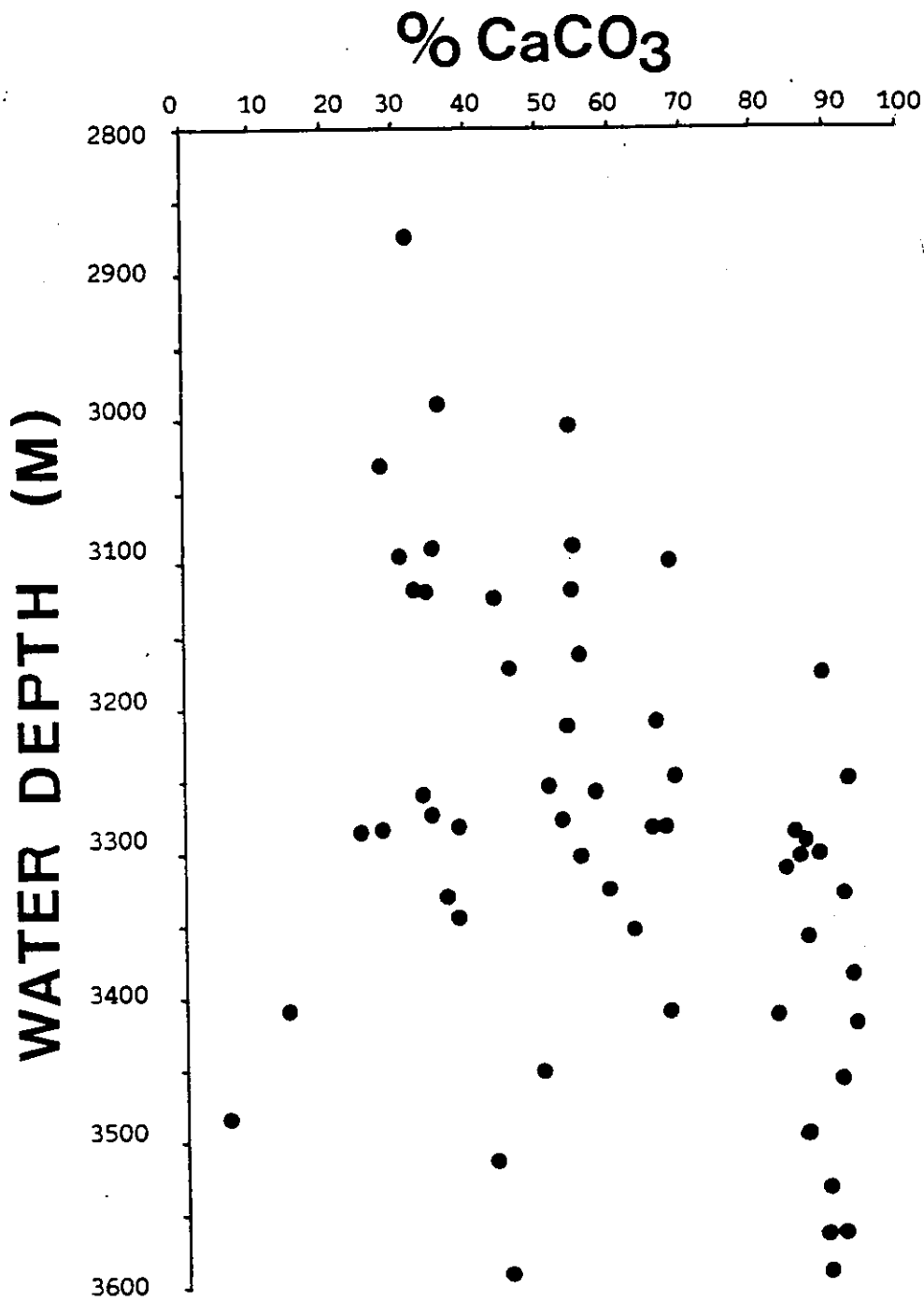
*Mo*

Molybdenum was only reported in the GEOMETEP data set (this work), as this element was not analysed by Dymond (1981). Bostrom and Peterson (1969) and Horowitz (1970) have shown that Mo enrichment of up to 127 ppm (on a carbonate free basis) occurs in near-surface sediments from the 14°S area of the crestal region of the E.P.R. The Mo content of surface sediments from the 19 - 21°S area (Figure 10.4.8) exceeds 100 ppm in an area located close to, but west of the E.P.R. axis. The maximum enrichment of 172 ppm Mo is found for surface sediment from core 25K. Mo values greater than 50 ppm are restricted to the west flank of the E.P.R.

*Ni*

The distribution of Ni in 19 - 21°S area surface sediments is strikingly different to the distribution of any of the elements/element ratios

FIG.10.4.10. Plot of $CaCO_3$ versus Water Depth in 19–21°S area surface sediments.



previously studied (Figure 10.4.9). The axial region of the E.P.R. contains sediments with less than 500 ppm Ni. Ni values greater than 700 ppm, with a maximum of 1020 ppm in core 15 surface sediment (see Figure 10.4.1 for the location of core 15), are confined to surface sediments in off-axial locations. The different distribution of Ni and its low abundance in sediments close to known or suspected hydrothermal sources suggest a hydrogenous source for this element in 19 - 21°S area sediments.

*$CaCO_3$*

The data shown in Figure 10.4.10 indicate no visible trend for the relationship between $CaCO_3$ and water depth. In view of the widescale slumping, winnowing and dilution of $CaCO_3$ by ferromanganese oxides occurring on the mid-ocean ridge (Chapter 9; Cronan and Varnavas, 1981), this is not surprising. Berger et al. (1976) stated that the C.C.D. is located at about 4000 m water depth in this area while high $CaCO_3$ values decrease to low ones in a transition zone of 500 m thickness above the C.C.D. Some samples contain low $CaCO_3$ contents which may reflect this dissolution process in the transition zone, e.g. 6% $CaCO_3$ (Dymond, 1981) in surface sediment from station 22, located at a water depth of 3480 m.

*$SiO_2$*

Clay minerals were found to be depleted in GEOMETEP 19 - 21°S area surface sediments, deduced from the failure to isolate significant amounts of the $< 2\mu$ fraction of sediments for oxygen isotope analysis. As a consequence of this, only ten surface sediments were analysed for $SiO_2$, by the method described in Appendix B. $SiO_2$ values are low and vary between 5.2% and 9.4%, on a carbonate free basis (Appendix C). Marchig and Gundlach (1982) showed that 19 - 21°S area sediments contain an average of 7.5% $SiO_2$.

*As*

The elements As, Sb and Bi were analysed after the generation of volatile hydrides, using the inductively coupled plasma spectrometer (see Appendix B). Cronan (1972) found that As is enriched in sediments from the Mid-Atlantic Ridge at 5°N, where a maximum of 360 ppm occurs

TABLE 10.4.1 As, Sb, Bi Data for Surface Sediments from the 20°S Area

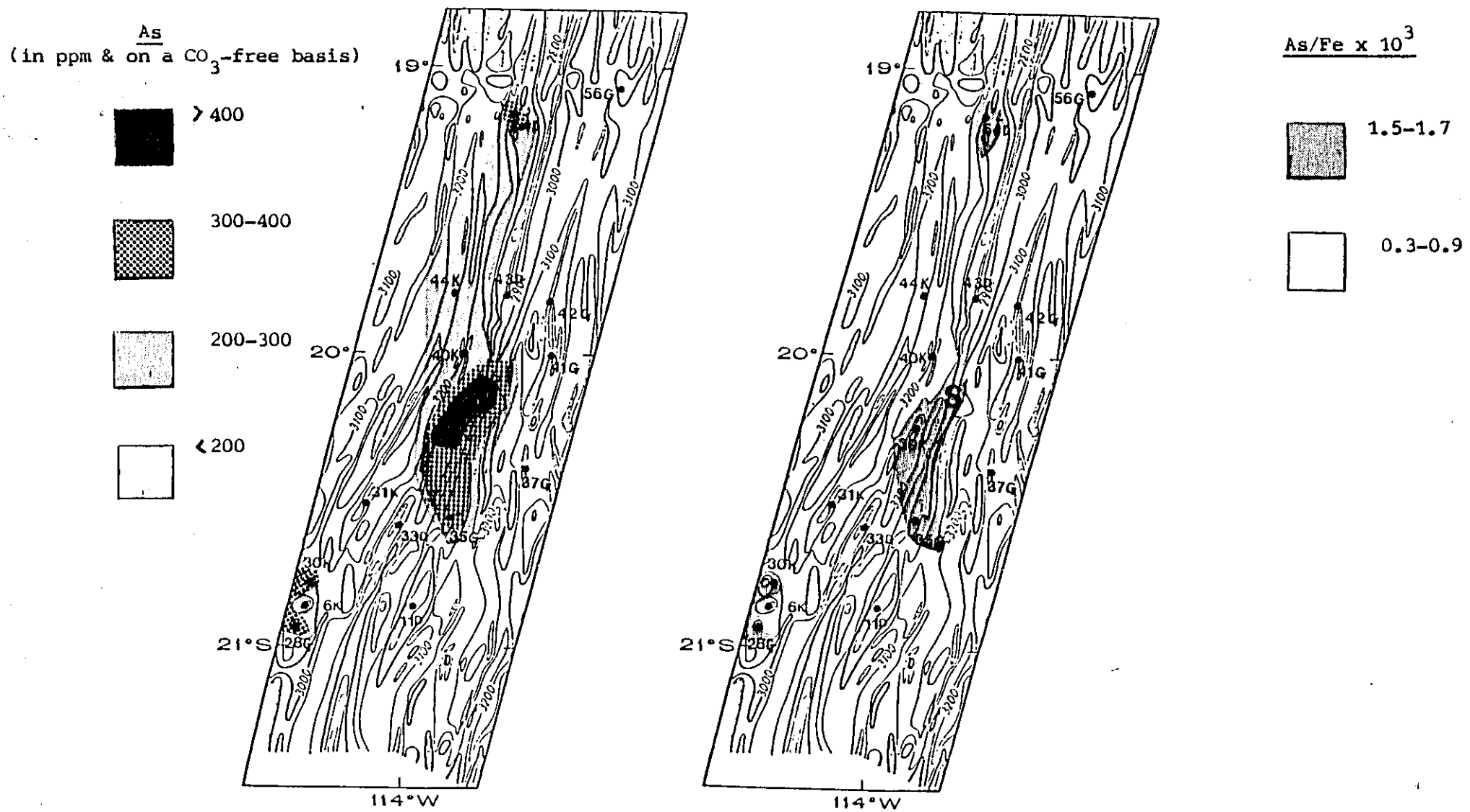
(in ppm and on a Carbonate Free Basis)

| CORE NUMBER | SAMPLE DEPTH (cms) | AS | SB | BI |
|---|---|---|---|---|
| 04K | 0 - 25 | 180 | 2.9 | 1.0 |
| 06K | 10 - 25 | 230 | 6.5 | 0.6 |
| 09K | 0 - 25 | 210 | 5.3 | 0.4 |
| 11D | DREDGE | 190 | 5.4 | 0.7 |
| 27G | GRAB | 220 | 5.2 | 0.5 |
| 28G | GRAB | 350 | 1.4 | 0.3 |
| 30K | 0 - 25 | 380 | 1.3 | 0.3 |
| 31K | 0 - 25 | 200 | 4.1 | 0.4 |
| 33D | DREDGE | 30 | 0.8 | 0.1 |
| 35G | GRAB | 330 | 0.8 | 0.2 |
| 37G | GRAB | 140 | 1.9 | 0.4 |
| 39K | 0 - 25 | 460 | 1.4 | 0.4 |
| 40K | 0 - 25 | 200 | 1.1 | 0.5 |
| 41G | GRAB | 160 | 2.1 | 0.5 |
| 42G | GRAB | 150 | 1.3 | 0.3 |
| 43D | DREDGE | 80 | 0.3 | 0.1 |
| 44K | 0 - 25 | 210 | 4.0 | 0.4 |
| 54D | DREDGE | 350 | 0.9 | 0.2 |
| 56G | GRAB | 170 | 1.9 | 0.4 |
| 59K | 0 - 25 | 290 | 2.1 | 0.7 |
| | DETECTION LIMITS | 0.02 | 0.04 | 0.02 |

Data reported to nearest 10 ppm for As or to 1 decimal place for Sb and Bi.

Core Locations are reported in Appendix C.

FIG.10.4.11. The distribution of As and the As/Fe ratio in crestal surface sediments from 19-21°S on the E.P.R.



(on a carbonate free basis). Arsenic has been studied in more detail in E.P.R. sediments (Bostrom and Peterson, 1969; Bostrom and Valdes, 1969; Bostrom et al., 1974; Rydell et al., 1974). The second named authors reported a maximum As anomaly in near-surface sediment of 450 ppm (C.F.B.) from the 14°S area of the E.P.R., compared to an average of about 40 ppm (C.F.B.) in pelagic sediments. Arsenic is known to be a valuable pathfinder element in the search for land-based hydrothermal ore-bodies, and As haloes can delineate certain areas of mineralisation (C.J. Moon, 1983).

To investigate the distribution of As in surface sediments from the crestal region of the E.P.R. in the 20°S area, a total of 20 samples were analysed. The distribution of As is shown in Figure 10.4.11 and the map includes 16 of the 20 samples studied. A maximum As anomaly of 460 ppm (see Table 10.4.1) is found for station 39K surface sediment, in the vicinity of the hydrothermal sulphide deposit. Arsenic haloes surround the deposit and values decrease with distance from the ridge crest. A constant enrichment of 200 ppm to 300 ppm As is found over much of the axial region.

Two further areas of high As values in surface sediments are indicated, with As between 300 ppm and 400 ppm. On the basis of the samples studied, these areas appear to be more localised than the As haloes surrounding the sulphide deposit. These two areas coincide with previously defined areas of high Fe, Cu and Zn concentrations, thus supporting the postulated existence of hydrothermal vents at these localities.

Surface sediments located off the E.P.R. axis contain less than 200 ppm As. Samples from stations 33D and 43D contain low values of 30 ppm and 80 ppm As, which may be attributed to the dilution of hydrothermal ferromanganese oxides by abundant basaltic debris.

Cronan (1972) showed that As is closely associated with Fe, with a value of 0.75 for the correlation coefficient, r, for a batch of 16

samples. This is statistically significant at the 99.9% level of confidence. However, the batch of 20 GEOMETEP samples shows that $r = 0.52$ for As and Fe, which is only significant at the 95% level of confidence.

An examination of the As/Fe ratio in sediments from the 20°S area of the E.P.R. shows that values of 1.5 to 1.7 x $10^{-3}$ characterise surface sediments from areas of intense hydrothermal activity. Stations located at distance from these centres contain sediments with low As/Fe ratios, ranging from 0.3 to 0.9 x $10^{-3}$. The increased concentrations of As relative to Fe in the three areas described above would support a hydrothermal supply of this element prior to its adsorption from seawater on colloidal Fe-oxyhydroxides.

Marchig et al. (1982) suggested the possibility that As contents in the sediments may simply reflect their Fe contents, as a result of adsorption. However, this possibility can be discounted in the 20°S area, on the basis of higher As/Fe ratios observed in the hydrothermally active areas of the E.P.R. crest than elsewhere.

*Sb and Bi*

Data for Sb and especially Bi have seldom been published for rise crest metalliferous sediments. Turekian and Bertine (1971) have suggested that Sb may be fixed in marine sediments under anaerobic conditions, after derivation from seawater. This process is unlikely to occur at 20°S on the E.P.R. due to the highly oxidising conditions in the sediment column. Bostrom and Valdes (1969) suggested that, due to the similar geochemical behaviour of As and Sb, Sb should be enriched in hydrothermal metalliferous sediments on active mid-ocean ridges. However, Marchig et al. (1982) reported similar values of 2.5 ppm and 2.8 ppm for hydrothermal metalliferous sediments from the E.P.R. and calcareous-siliceous oozes from the Peru Basin, respectively.

Gurvich et al. (1976) noted that As/Sb ratios in metalliferous sediments are about 8 and this value is close to the ratios of As/Sb in solution in

TABLE 10.4.2 Element concentrations and element ratios for station 14D and 26D ferromanganese crusts

| Station No | Sample Type | % Fe | % Mn | Co ppm | Ni ppm | Cu ppm | Zn ppm | Mn/Fe | Mn/Co | Mn/Ni | Mn/Cu | Mn/Zn | Fe/Cu |
|---|---|---|---|---|---|---|---|---|---|---|---|---|---|
| 14D | Surface Crust | 2.50 | 47.0 | 30 | 1,300 | 154 | 116 | 19 | 15,670 | 362 | 3,050 | 4,050 | 162 |
| 14D | Bulk Crust | 2.15 | 47.0 | 29 | 979 | 166 | 126 | 22 | 16,210 | 480 | 2,830 | 3,730 | 130 |
| 14D | Fissure Crust | 0.08 | 49.6 | 20 | 545 | 180 | 96 | 620 | 24,800 | 910 | 2,760 | 5,170 | 4 |
| 26D | Bulk Crust | 27.4 | 12.0 | 1,230 | 2,580 | 1,660 | 650 | 0.44 | 98 | 47 | 72 | 185 | 165 |
| LINE ISLAND CRUSTS (n = 59) (taken from Aplin, 1983) | | 17.0 | 20.4 | 5,450 | 3,860 | 1,540 | 590 | 1.2 | 37 | 53 | 132 | 346 | 110 |

seawater. The authors considered that Sb, a highly mobile element in seawater, is enriched in metalliferous sediments due to adsorption and co-precipitation with the hydroxides of hydrothermally-supplied Fe and Mn. They also concluded that the original source of the Sb must remain an open question.

The distribution of Sb in GEOMETEP surface sediments from the 20°S area shows no particular trends. A maximum of 6.5 ppm Sb (see Table 10.4.1) is contained in station 6K surface sediment, while the average content of Sb is 2.5 ppm for the 20 sediments analysed. This average value agrees exactly with the average reported by Marchig et al. (1982), for E.P.R. metalliferous sediments. As/Sb ratios vary between 35 and 411, with an average of 147 for the 20 GEOMETEP sediments. These highly variable ratios indicate the lack of any close association between As and Sb and also the increased amounts of As found in sediments compared to As/Sb ratios in seawater.

Bi values average 0.4 ppm, with a maximum of 1.0 ppm in surface sediment from station 4K. These values are relatively uniform and do not display any similarity in their distribution to the values of As. Sb and Bi are correlated with each other ($r = 0.51$) at the 95% confidence level. Similarly, Mn correlates with Sb ($r = 0.53$) and with Bi ($r = 0.46$). Neither Sb or Bi correlate with Fe at the 95% confidence level.

The data described above suggest that As is closely associated with Fe and that both of these metals are supplied by hydrothermal solutions. On the other hand, although Sb and Bi are associated with Mn, this does not support a hydrothermal origin for these elements. It is thought that the distributions and concentrations of Sb and Bi are compatible with a hydrogenous origin for these elements which are adsorbed by Mn oxides and then incorporated in sediments.

*Ferromanganese Crusts*

In an attempt to determine whether an excess supply of metals has been added to crusts 14D and 26D, compared to that supplied from a hydrogenous source, various element ratios were studied (see Table 10.4.2). An excess

supply of metals in these crusts could indicate hydrothermal activity in the immediate vicinity. The method used has been discussed in Chapter 9.

Station 14D crusts are extremely manganiferous in nature, with a maximum Mn/Fe of 620 present in the fissure infilling Mn crust. Mn contents vary between 47.0% and 49.6%, while Fe varies between 0.08% and 2.50%. The most Mn-rich, Fe-poor crust is the sub-sample taken from the infilled fissure. Apart from relatively high Ni contents in these crusts, ranging from 545 ppm to 1300 ppm, trace metal contents are low, as is found in hydrothermal Mn oxide-rich crusts from the Galapagos Rift (Moore and Vogt, 1976).

On the basis of the major/trace element ratios (Table 10.4.2) calculated for station 14D crusts, no metals other than Mn have been supplied in excess of the hydrogenous supply to ferromanganese crusts, even though Ni contents are high. The presence of an Fe oxide-rich mud on the underside of the station 14D crust (see Plate 10.3.1), with 22.8% Fe (Appendix C) and a Mn/Fe of 0.65, indicates the rapid fractionation of Fe from Mn in this deposit, as found in the GRAFZI area (see Chapter 2). The Fe oxide-rich mud also contains higher Co, Cu, Zn and Pb contents than the Mn oxide-rich crusts.

The ferromanganese oxide crust from station 26D has a Mn/Fe of 0.44. A crust of similar chemical composition was described in Chapter 9 and located in the vicinity of the E.P.R. axis at $13^{\circ}20'S$. The 26D ferromanganese crust is therefore much more ferruginous and less manganiferous than the 14D crust.

On the basis of element concentrations and element ratios described above for 19 - $21^{\circ}S$ area surface sediments, the area from which the station 26D crust was recovered has been identified as hydrothermally active. The excess supply of Ni, Cu and Zn, normalised to Mn, in the station 26D crust (see Table 10.4.2) further supports a hydrothermal supply

# TABLE 10.5.1.

SURFACE SEDIMENT CORRELATION MATRIX.

| | NA | K | MG | AL | MN | FE | CA | SIO2 |
|---|---|---|---|---|---|---|---|---|
| K | .869 | | | | | | | |
| MG | .677 | .777 | | | | | | |
| AL | | | .898 | | | | | |
| MN | .813 | .681 | | | | | | |
| FE | .892 | .789 | | | .970 | | | |
| CA | -.896 | -.929 | -.753 | | -.800 | -.878 | | |
| SIO2 | .898 | .811 | .926 | | .819 | .913 | -.843 | |
| LI | | | .690 | .812 | | | | .531 |
| SR | -.576 | -.747 | -.925 | -.860 | | | .739 | |
| LA | .630 | | | | .880 | .819 | -.593 | |
| TI | | | .900 | .998 | | | | |
| V | .927 | .822 | .535 | | .953 | .983 | -.915 | .882 |
| MO | .547 | | | | .723 | .763 | | .743 |
| CO | .908 | .878 | .699 | | .870 | .923 | -.951 | .872 |
| NI | .579 | .573 | | | .886 | .826 | -.686 | |
| CU | .821 | .684 | | | .939 | .946 | -.777 | .929 |
| ZN | .871 | .769 | | | .966 | .984 | -.873 | .902 |
| PB | .739 | .531 | | | .921 | .902 | -.687 | .857 |
| P | .879 | .679 | | | .903 | .930 | -.754 | .859 |

| | LI | SR | LA | TI | V | MO | CO | NI |
|---|---|---|---|---|---|---|---|---|
| SR | -.783 | | | | | | | |
| LA | | | | | | | | |
| TI | .838 | -.873 | | | | | | |
| V | | | .785 | | | | | |
| MO | | | .784 | | .701 | | | |
| CO | | -.608 | .736 | | .954 | .598 | | |
| NI | | | .822 | | .785 | | .725 | |
| CU | | | .725 | | .932 | .673 | .831 | .769 |
| ZN | | | .793 | | .977 | .750 | .926 | .806 |
| PB | | | .831 | | .881 | .734 | .806 | .719 |
| P | | | .717 | | .924 | .594 | .823 | .634 |

| | CU | ZN | PB |
|---|---|---|---|
| ZN | .967 | | |
| PB | .896 | .918 | |
| P | .948 | .931 | .889 |

Correlation coefficient (r) = 0.52 at 99.9% confidence.

(n = 86)

DOWNCORE SEDIMENT CORRELATION MATRIX.

| | NA | K | MG | AL | MN | FE | CA | SIO2 |
|---|---|---|---|---|---|---|---|---|
| K | .719 | | | | | | | |
| MG | .753 | .652 | | | | | | |
| AL | .383 | .501 | .844 | | | | | |
| MN | .618 | .304 | .408 | | | | | |
| FE | .756 | .480 | .562 | | .939 | | | |
| CA | -.837 | -.661 | -.777 | -.373 | -.794 | -.896 | | |
| SIO2 | .898 | .811 | .926 | | .819 | .913 | -.843 | |
| LI | | .298 | .662 | .807 | | | -.307 | .531 |
| SR | -.653 | -.663 | -.826 | -.727 | | -.400 | .716 | -.300 |
| LA | .398 | | | | .844 | .783 | -.561 | .341 |
| TI | .416 | .599 | .839 | .986 | | | -.398 | .481 |
| V | .725 | .434 | .582 | | .955 | .979 | -.897 | .882 |
| MO | | | | | .353 | .325 | | .743 |
| CO | .725 | .457 | .684 | | .906 | .921 | -.881 | .872 |
| NI | .451 | | .338 | | .902 | .858 | -.702 | |
| CU | .663 | .306 | .410 | | .927 | .923 | -.789 | .929 |
| ZN | .722 | .383 | .534 | | .953 | .954 | -.853 | .902 |
| PB | .634 | .327 | .377 | | .785 | .809 | -.673 | .857 |
| P | .824 | .522 | .482 | | .794 | .855 | -.789 | .859 |

| | LI | SR | LA | TI | V | MO | CO | NI |
|---|---|---|---|---|---|---|---|---|
| SR | -.622 | | | | | | | |
| LA | | | | | | | | |
| TI | .800 | -.739 | | | | | | |
| V | | -.407 | .776 | | | | | |
| MO | | | .605 | | .332 | | | |
| CO | | -.449 | .773 | | .941 | .322 | | |
| NI | | | .845 | | .857 | .520 | .810 | |
| CU | | | .712 | | .930 | | .873 | .802 |
| ZN | | -.353 | .763 | | .963 | .302 | .935 | .841 |
| PB | | | .736 | | .788 | .429 | .785 | .711 |
| P | | -.360 | .585 | | .836 | | .770 | .573 |

| | CU | ZN | PB |
|---|---|---|---|
| ZN | .966 | | |
| PB | .767 | .841 | |
| P | .835 | .850 | .745 |

Correlation coefficient (r) = 0.29 at 99.9% confidence.

(n = 137)

of metals at this locality. The 26D ferromanganese oxide crust, with associated hydrothermally derived Cu, Zn and to a lesser extent, Ni, may be related to a formation from hydrothermal solutions convected by a seamount heat source, while the trace element poor (apart from Ni) 14D crusts may be products of off-axial hydrothermal venting. The greater supply of trace metals to the former than to the latter deposit could be due to higher temperatures in the hydrothermal solutions.

## 10.5 GEOCHEMISTRY OF SURFACE AND BURIED SEDIMENTS FROM THE 19 - 21°S AREA

The following study, as in Chapter 9, is devoted to an investigation of the downcore variations in hydrothermal activity, as deduced from downcore geochemical variations in the sediments. Element associations significant at the 99.9% level of confidence for both surface and downcore sediments are reported in Table 10.5.1. Both batches of data produce similar correlations, as was found for 13 - 15°S area sediments. However, the following correlations are found only in downcore sediments:- Ti with Na, Ti with K; Mg with Fe, Mn, Ni, Cu, Zn, Pb, P; $SiO_2$ with La, $SiO_2$ with Ti. In surface sediments, Mo correlates positively with Cu and P, but not with Ni, while the reverse is true in downcore sediments. The similar distributions of Mo, Cu and P in surface sediments have been described in Section 10.4, while the distribution of Ni differs significantly.

The correlations of Ti with Na, Ti with K, $SiO_2$ with La, $SiO_2$ with Ti, observed in downcore sediments suggest contributions to the sediment from clay minerals and basaltic debris. However, both of these phases are generally of minor abundance in 19 - 21°S area sediments. Marchig and Gundlach (1982) have shown that volcanic glass constitutes $<0.1\%$ of the bulk sediment in cores 4K, 9K, 25K, 46K and 59K.

The depletion of Mg in hydrothermal solutions and its fixing in the Mg hydroxysulphate hydrate phase has been predicted on the basis of experimental work (Bischoff and Seyfried, 1978). This has also been found in natural systems, where the Mg-bearing mineral phase was named

FIG.10.5.1.

Fe vs Mg in 19–21S Area sediments

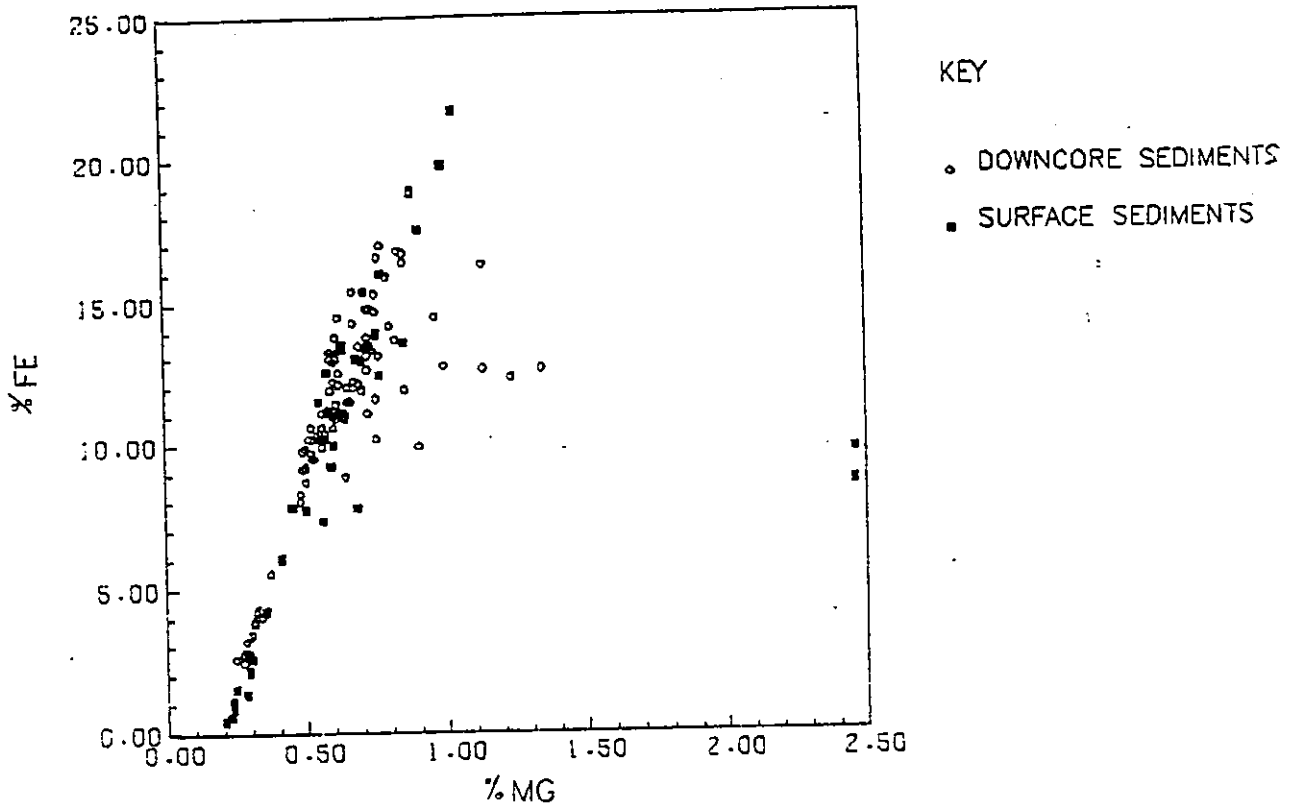



FIG.10.5.2.

Mn vs Mg in 19–21S Area sediments

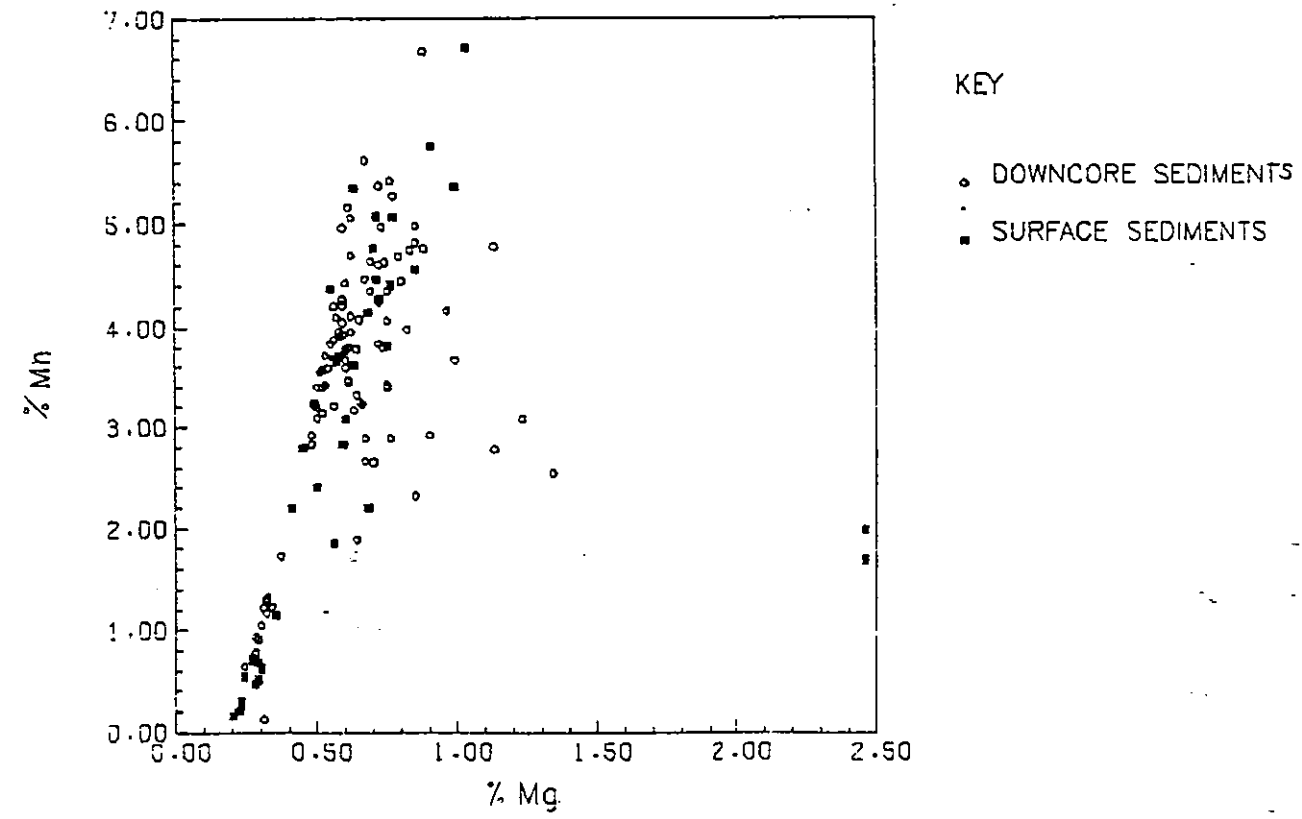


FIG.10.5.3

Fe vs Mn in 19–21°S Area sediments

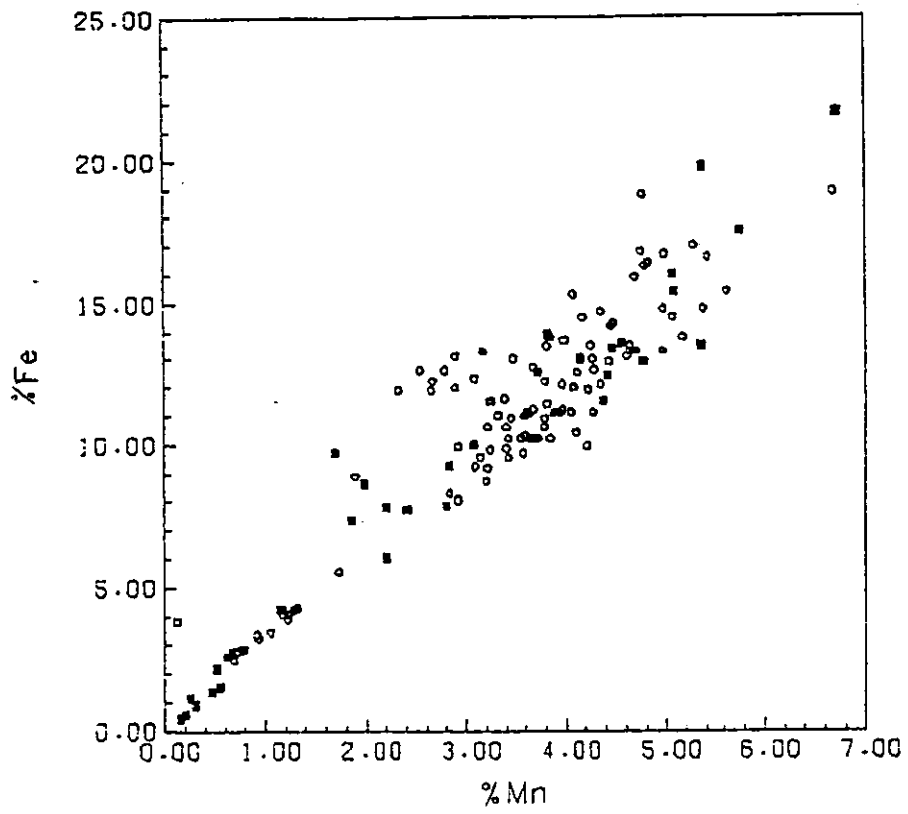



FIG.10.5.4.

Cu vs Fe in 19–21°S Area sediments

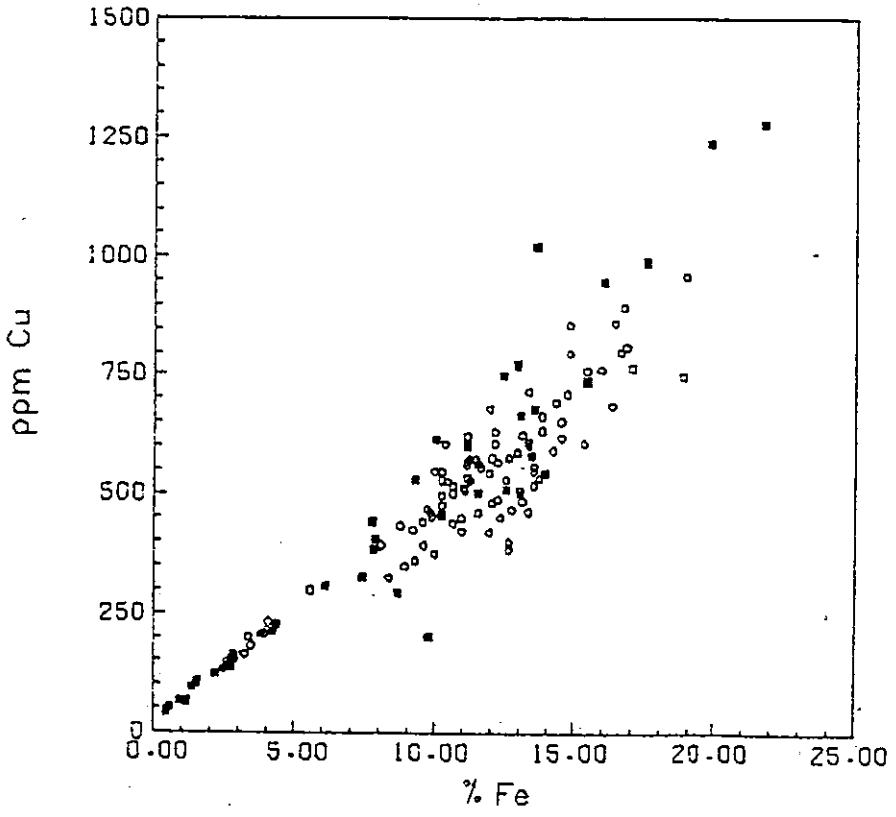


FIG.10.5.5.

Zn vs Mn in 19–21°S Area sediments

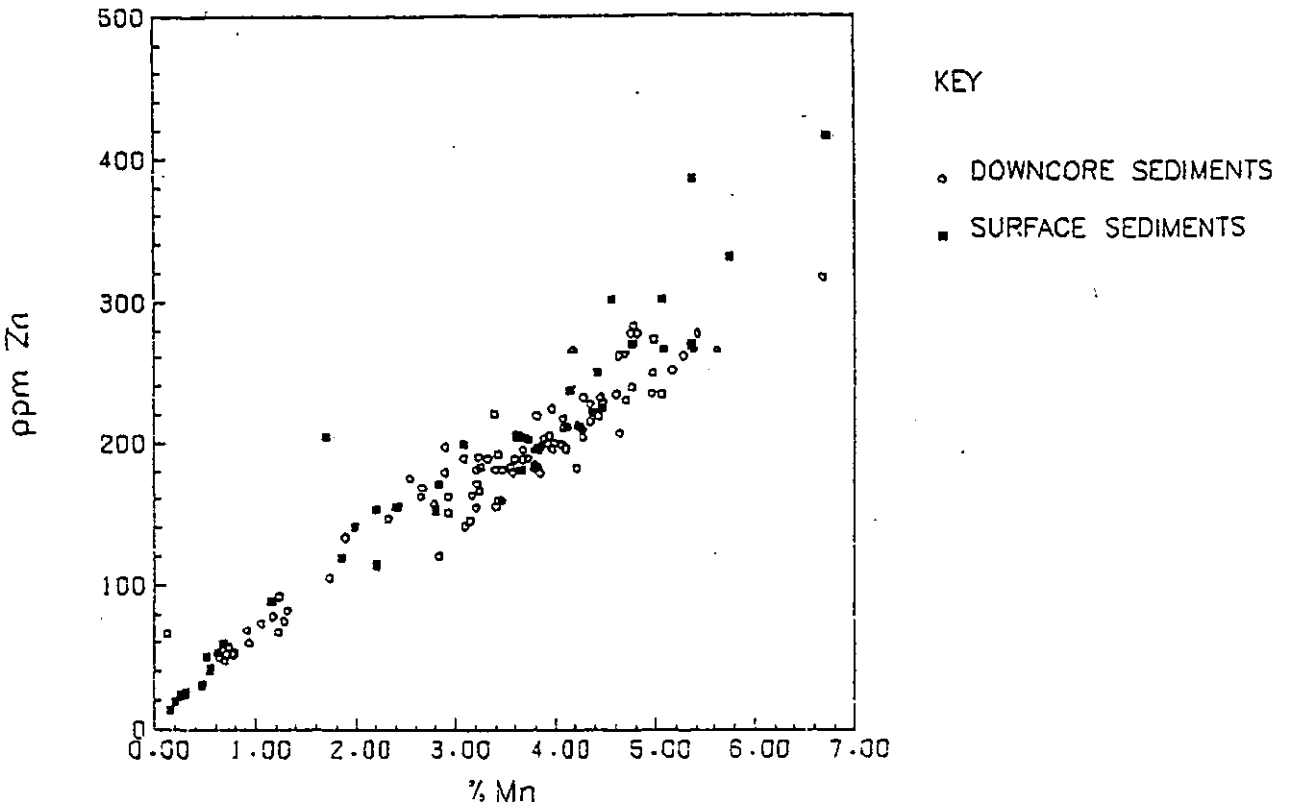
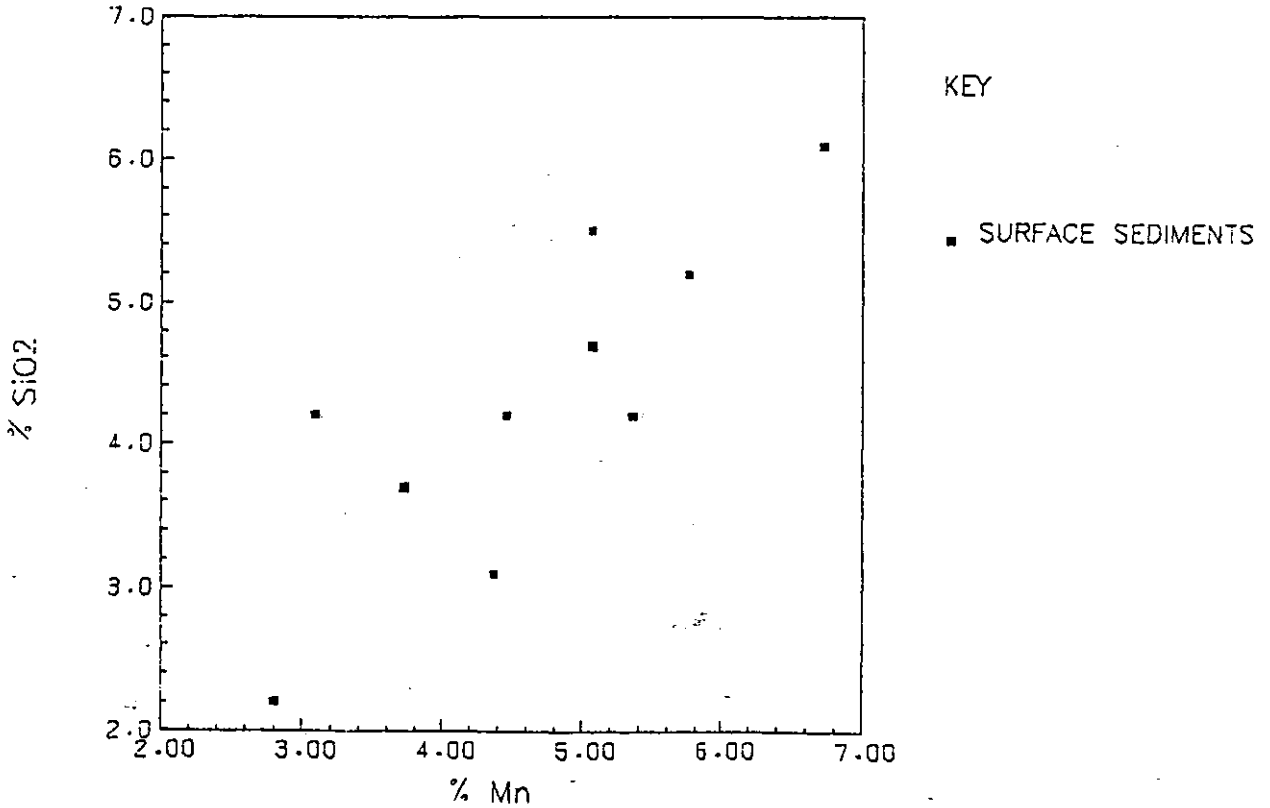



FIG.10.5.6.

SiO2 vs Mn in 19–21°S Area sediments



"caminite", after its discovery by Haymon and Kastner (1981), in the E.P.R. 21°N sulphide deposit. Therefore, it is unusual that Mg shows strong correlations with Fe, Mn (see Figures 10.5.1 and 10.5.2), Ni, Cu, Zn, Pb and P. Marchig and Gundlach (1982) also found similar correlations with Mg, though this was based on far fewer samples than this study. It has been suggested that the correlations of Mg with Fe, Mn, Ni, Cu, Zn, Pb and P are not observed in surface sediments. However, a closer inspection of the raw data in Figures 10.5.1 and 10.5.2 reveals that 2 statistical outliers exist in the surface sediment data which mask significant correlations between Mg with Fe and Mg with Mn. If these two samples are ignored then strong significant correlations do exist between Mg with Fe and Mn. These two samples, with about 2.5% Mg, represent sediments from stations 33D and 43D which are rich in volcanogenic debris. In summary therefore, 19 - 21°S sediments show that Mg is closely associated with the ferromanganese oxides (with the above 2 exceptions) and may have a similar hydrothermal derivation, but a hydrogenous source of Mg cannot be ruled out.

The correlations of Fe with Mn, Cu with Fe and Zn with Mn (Figures 10.5.3 to 10.5.5) exemplify the similarity in composition of surface and downcore sediments from the 19 - 21°S area. While the highest metal values are observed in surface sediments, the two sets of data span a similar range in concentration. Sediments from the 13 - 15°S area of the E.P.R. (see Chapter 9) also show this similarity of composition between surface and downcore sediments.

The correlation coefficient, r = 0.92, is significant at the 99.9% confidence level for the scatterplot of $SiO_2$ with Mn (Figure 10.5.6). $SiO_2$ also shows a similar correlation with Fe. Although $SiO_2$ can be associated with significant quantities of Fe in certain clay minerals (McMurtry and Yeh, 1981), Mn is not present in them in abundance. For this reason and the observation that clay minerals could not be isolated from 19 - 21°S area surface sediments, it is thought that $SiO_2$ is not

present in clays in these sediments. It may be present as amorphous or biogenic $SiO_2$ mixed with ferromanganese oxides and its correlation with Fe and Mn possibly being due to dilution by a third phase (Chayes, 1960). Amorphous silica of a hydrothermal origin has been described in the GRAFZI deposit (see Chapter 3) and a similar origin may apply here. In support of this possibility, $SiO_2$ correlates with Fe, Mn, Cu and Zn (of a hydrothermal origin) but does not correlate with Ni (see Table 10.5.1) which has been shown to have a non-hydrothermal origin (see Figure 10.4.9).

Dymond et al. (1973) observed that metalliferous sediments display little tendancy to recrystallise with time. On the basis of this observation, the above data and the findings of Marchig and Gundlach (1982) that diagenesis has not altered the bulk geochemistry of GEOMETEP sediments, metal variations in the present sediment cores from the 19 - 21°S area of the E.P.R. are thought to reflect primary temporal variations in hydrothermal activity.

## 10.6 DISCUSSION OF 19 - 21°S AREA HYDROTHERMAL ACTIVITY

Previous investigators (Dymond, 1981; Marchig and Gundlach, 1982) have noted a uniform chemical composition of hydrothermal precipitates on the E.P.R. Dymond (1981) suggested that E.P.R. hydrothermal processes may be unique in that they produce vast areas of Fe-Mn oxide-rich sediments without extensive fractionation of Fe from Mn. However, the author perceived that constraints on sampling, due to the necessity of coring in off-axial basins to ensure full-core recovery, may have biased the sampling. Dymond (1981) suggested that physical homogenisation of originally fractionated hydrothermal precipitates may have produced the observed uniform chemical composition, as has been noted in the 13 - 15°S area (Chapter 9).

The present work utilises sediments recovered both near to and distant from the E.P.R. axis and there are distinct variations in sediment composition, in contrast to the uniformity of sediment composition described in the previous paragraph.

The discovery of the axial sulphide deposit (Francheteau and Ballard, in press) and the decrease in metal values with distance from the hydrothermal source, indicate that the E.P.R. is not unique as a hydrothermal centre. The metalliferous sediments do not just represent an undifferentiated prototype, but these deposits are part of the continuum of sulphides - silicates - Fe oxides - Mn oxides observed elsewhere on the World Mid-Ocean Ridge System.

In addition to the polymetallic sulphide locality recently discovered on the E.P.R. axis near 20°S, the surface sediment geochemistry indicates a second sulphide deposit in the vicinity of the west flank seamount at 20°50'S. Collectively, these areas contain surface sediments with anomalous concentrations of Fe, Mn, Cu, Zn, Mo, As, As/Fe, Cu/Zn and P/La.

A third area exists at 19°10'S on the E.P.R. axis which, on the basis of anomalously high As and Zn contents in surface sediments, may also contain sulphides. However, while this third area can be tentatively identified as a future exploration target, the greater Cu contents of sediments from the other two areas indicates their greater potential for containing polymetallic sulphides.

Apart from these three areas of high metal contents, there is a general high level of enrichment in E.P.R. crestal sediments of Fe, Mn, Cu, Mo and As, while the Zn pattern of enrichment in the sediments is irregular. The distributions of Fe, Mn, Zn, Mo and to a lesser extent Cu, are asymmetrical about the E.P.R. axis, being higher on the west flank than the east. This phenomenon of asymmetrical metal distribution over the E.P.R. crestal region has been described by Dymond (1981) and also in Chapter 9 of this thesis. The asymmetry is not as marked as in the 13 - 15°S area of the E.P.R., where hydrothermal debris is swept westwards from an axial source by mid-depth ocean circulation (Lupton and Craig, 1981; Reid, 1981). This may suggest a weaker influence by these currents in the 19 - 21°S area. However, an alternative explanation for the asymmetry in metal distribution, involves the injection of hydrothermal

solutions from sources on the west flank of the E.P.R. axis. This possibility is supported by the geophysical data of Rea (1978) which shows that there is asymmetry in bathymetry, spreading rates and heat flow, on the west and east flanks of the E.P.R. (Section 10.2). The author suggested the presence of a heat source under the west flank in order to explain this. The model could also explain the metallogenesis associated with the seamount area at 20°50'S, 114°40'W, where an off-axial heat source may have convectively circulated seawater to produce highly metalliferous sediments on the E.P.R. west flank.

The distribution of Ni in the sediments is unlike that of any of the other elements studied (see Section 10.4). A hydrogenous source of Ni seems the best way of explaining the highest concentrations of this element observed in off-axial locations, i.e. at distance from known hydrothermal vents. Dymond (1981) calculated that only 39% of the total Ni in E.P.R. rise-crest sediments is supplied hydrothermally.

## 10.7 CONCLUSIONS

Data from this thesis has been combined with data from other sources to produce the most detailed sample coverage of the 19 - 21°S area of the E.P.R. available to date. A synthesis of this data has led to the following conclusions:-

1. The carbonate free fraction of surface sediments from the 19 - 21°S area does not display a uniform chemical composition. This observation is in contrast to that of Marchig and Gundlach (1982) who based their assumption that the sediments were chemically of relatively uniform composition, on fewer samples than studied here and which were cored in off-axial basins. Variations in metal contents of sediments and the discovery of sulphide deposits on the E.P.R. between 20°05'S and 20°10'S, attest to the fact that hydrothermal deposits on this part of the E.P.R. should be regarded as a continuum, which can be related to the Red Sea Model.

2. On the basis of the collective distributions of Fe, Mn, Cu, Zn, As and the P/La ratio, three areas show the greatest potential for containing polymetallic sulphides, with one of these areas (Area 1) already shown to contain them. The areas are:-

   (i) Area 1 - on the E.P.R. axis, between $20^{\circ}05'S$ and $20^{\circ}10'S$.
   (ii) Area 2 - to the east of the seamount located at about $20^{\circ}50'S$, $114^{\circ}40'W$.
   (iii) Area 3 - on the E.P.R. axis, at about $19^{\circ}10'S$.

3. The general metal enrichment that is observed in surface sediments over the axial region of the E.P.R. is asymmetrical, and displaced towards the west flank.

4. The westward flow of mid-depth currents has been invoked as the cause of this asymmetry in the 13 - $15^{\circ}S$ area (see Chapter 9), where the asymmetry is more marked than in the 19 - $21^{\circ}S$ area. However, in the 19 - $21^{\circ}S$ area of the E.P.R., a west flank heat source (Rea, 1978) may be responsible for the observed asymmetry in metal distribution, by causing off-axial hydrothermal venting.

5. In contrast to the other metals studied, Ni appears to be supplied hydrogenously to 19 - $21^{\circ}S$ area sediments, most probably by adsorption from seawater onto ferromanganese oxides. Although an ultimate hydrothermal source cannot be ruled out for Ni, if this element has such a source its distribution suggests a longer residence time in seawater than the other metals.

# PART 3

## Chapter 11 Summary and Conclusions.

# CHAPTER 11

# SUMMARY AND CONCLUSIONS

## 11.1 THE GALAPAGOS RIFT

Three study areas have been investigated on the Galapagos Rift and these are located in:-

1. The GRAFZI (Galapagos Rift and Fracture Zone Intersection) Area at 86°W.
2. The De Steiguer Deep Area at 95°W.
3. The Hess Deep Area at 101°W.

Although each area has been studied in isolation, the relationship of the hydrothermal processes that have collectively formed sulphides, silicates, iron and manganese oxides in these areas can be related to the Red Sea model.

The GRAFZI deposits comprise the full suite of hydrothermal precipitates observed in and around the Atlantis II Deep, but the spatial relationship between them is not so clear as in that area. The sulphide deposit represents the locus of hydrothermal activity at the rift valley faulted-margin. A model has been devised to account for the formation of poly-metallic sulphides. Precipitation from the hydrothermal solutions has produced a late-stage chalcopyrite/pyrite dominated assemblage with a temperature of formation of about 390°C, calculated by sulphur isotope geothermometry. It has been suggested that sub-surface sulphide precipitation in the stockwork may have sealed the outlets of the mineralising fluids , which were then forced to follow another path to the seabed. Sulphur isotope data indicate a seawater source for the sulphide sulphur and derivation from a heavily-seawater dominated system in either a well-fractured oceanic crust or with rapid hydrothermal solution flow rates (or both).

Chemical and mineralogical studies of the sulphides indicate a distinct difference between the GRAFZI deposit and the E.P.R., 21°N deposit (Hékinian et al., 1980). The latter sulphide deposit is depleted in Cu but highly enriched in Zn, while the former deposit displays an opposite trend. Temperature is the dominating factor in determining whether a Cu-rich (high temperature) or a Zn-rich (lower temperature) sulphide may form. The identification of "Caries Textures", where previously deposited sphalerite has undergone dissolution and replacement by pyrite in a later fluid of different chemistry and higher temperature, allows an explanation of high Zn and Mn contents observed in sediments surrounding the polymetallic sulphide deposit. The Zn is lost from the mounds and scavenged by Mn oxides. The Cu/Zn ratio in sediments increases towards the polymetallic sulphide deposit and is a useful exploration tool.

No indications were found that may identify the De Steiguer Deep Area of the Galapagos Rift, at 95°W, as a possible site for polymetallic sulphides. However, Fe oxide-stained basalts and a Mn oxide crust described by Moore and Vogt (1976), attest to the fact that the "oxide facies" of hydrothermally derived precipitates is represented.

Hess Deep cores, from water depths of up to 5440 m, revealed abundant chrysotile serpentine minerals. These minerals have probably been incorporated in unconsolidated sediments by gravity slides from shallower, exposed peridotites, as described by Bonatti et al. (1973), in the Romanche Fracture Zone of the Mid-Atlantic Ridge. Direct evidence of serpentine formation from an ultramafic precursor mineral has been found by scanning electron microscopy. There is no support for the model of direct precipitation of chrysotile from hydrothermal solutions percolating through Hess Deep sediments, as proposed by Schmitz et al. (1982).

## 11.2 THE EAST PACIFIC RISE

Approximately 300 samples have been analysed from four study areas on the E.P.R., situated in the following locations:-

1. The Quebrada Fracture Zone at 4°S.
2. The 10°S Area of the E.P.R.
3. The 13 - 15°S Area of the E.P.R., including the Garret Fracture Zone.
4. The 19 - 21°S Area of the E.P.R.

The samples studied comprise variably metal-enriched foraminiferal marls and oozes, and ferromanganese crusts with highly contrasting Fe/Mn ratios. Data accumulated in this thesis has been combined with previously published data in order to obtain the most extensive sample coverage of the areas studied.

The 10°S area of the E.P.R. contains two different sources of hydrothermal activity which have produced anomalously high metal concentrations in sediments. The most regionally extensive hydrothermal activity is associated with the E.P.R. axis and has affected the whole axial region at 10°S. Uniform Fe/Mn and Cu/Zn ratios characterise crestal zone surface sediments. Heath and Dymond (1981) proposed that the westward transport of hydrothermal debris has produced metal-enriched west flank sediments. The dating of a metalliferous sediment horizon in east flank cores has shown that from about 194,000 years ago until recently, sediments from the east flank have been depleted in Fe, Mn, Cu and Zn. Two factors can account for this observation. Firstly, the inception of westward flowing bottom currents at about 194,000 years ago and secondly, the decreased supply of hydrothermally-derived metals due to seafloor spreading which has transported the core locations away from the axial source region. A recent phase of increased hydrothermal activity has produced increased enrichments in Fe, Mn, Cu and Zn (Heath and Dymond, 1981) in near-surface sediments from the 10°S area.

The second type of hydrothermal activity is more localised and is found in the vicinity of the AMPH D2 Fe oxide deposit of Bonatti and Joensuu (1966). The high degree of fractionation, with regard to Fe/Mn and Cu/Zn

ratios, of the sediments in this area was not found in sediments enriched in hydrothermally-derived metals from an axial source. On the basis of geochemical analyses of surface sediments from the vicinity of the AMPH D2 seamount structure, a direct comparison can be made with "Larson's Seamounts" on the E.P.R. at 21°N (Lonsdale et al., 1982). The latter area contains polymetallic sulphide deposits and it has been suggested that the westerly-located AMPH D2 seamount summit has potential for their future discovery.

A similar asymmetrical metal distribution to that observed at 10°S on the E.P.R. has been observed in the 13 - 15°S area where it is more marked. Surface sediments display a considerable uniformity in their Fe/Mn and Cu/Zn ratios which can be accounted for by the physical homogenisation of hydrothermal precipitates by westward flowing bottom currents.

There is ongoing metallogenesis in the 13 - 15°S area associated with both the E.P.R. crest and the Garret Fracture Zone deduced from;

1. The recovery of hydrothermal ferromanganese crusts with an excess supply of Zn to that supplied hydrogenously (as in the GRAFZI area).
2. The recovery of Fe-oxide stained basalts.
3. Anomalously high metal concentrations in surface sediments.

Surface and buried sediments display a similar geochemistry and therefore, diagenesis does not modify the bulk composition of buried sediments which thus, reflect temporal hydrothermal variations. Although sedimentation rate data may be variable, a value has been assumed and a layer of highly metalliferous sediment has been dated at between 169,000 and 304,000 years of age. The cessation of this pulse of intense hydrothermal activity was followed by a period when east flank sediments were starved of hydrothermal material, while west flank sediments were supplied by westward flowing bottom currents.

Surface sediments from the 19 - 21°S area of the E.P.R. do not display a uniform chemical composition. Due to the acquisition of more samples, from axial and off-axial locations, than have hitherto been recovered

from the 19 - 21°S area, it has been possible to locate 3 areas with sediments which collectively contain high values of Fe, Mn, Cu, Zn, Mo, As, Cu/Zn and P/La. One of these areas (Area 1) has recently been found to contain polymetallic sulphides (Francheteau and Ballard, in press). The three areas are:-

1. Area 1 - on the E.P.R. axis between 20°05'S and 20°10'S.
2. Area 2 - to the east of the seamount located at 20°50'S, 114°40'W.
3. Area 3 - on the E.P.R. axis, at about 19°10'S.

Asymmetry in metal distributions observed over the E.P.R. axial region can be ascribed to the westward flowing bottom currents mentioned previously and also west flank off-axial hydrothermal venting. The latter process is supported by the suggestion of Rea (1978) that a heat source exists under the west flank of the E.P.R.

As in the 13 - 15°S area, diagenesis has not significantly modified the bulk composition of 19 - 21°S area sediments. A study of metal variations with depth in the cores has revealed that hydrothermal processes were operative throughout the history of sediment formation, with periods of intensified activity.

Ni has shown a different distribution pattern to the other elements/element ratios studied and is thought to have been supplied to sediments from a hydrogenous source, by adsorption onto ferromanganese oxides.

The 19 - 21°S area shows the greatest potential of all the areas studied on the E.P.R. for further discoveries of hydrothermal loci, with high temperature polymetallic sulphide assemblages. These are concentrated principally on the E.P.R. axis, but are also associated with off-axial seamounts.

# APPENDICES

# APPENDIX A

## SAMPLE COLLECTION

The samples used in this investigation were collected during the cruises of the R/V's 'CONRAD/ALVIN', 'DISCOVERY' and 'SONNE' in 1980. The former cruise was responsible for the recovery of 69 samples from short cores, dredges and submersible operations in the 86°W area of the Galapagos Rift and these were donated by the National Ocean Survey, of the National Oceanic and Atmospheric Administration, The 'DISCOVERY' cruise to the Hess Deep recovered sediments and a ferromanganese oxide-encrusted pebble which were donated by the Institute of Oceanographic Sciences. From this material, 21 samples were taken. The 'SONNE' cruise (Legs 1, 2 and 3) visited 233 Kasten core, dredge, grab and water sampling stations in seven study areas on the Galapagos Rift and E.P.R. Approximately 300 samples were collected by the writer at sea, on Legs 1 and 2, which were later supplemented by 150 samples from Leg 3, collected from the Preussag Laboratories at Berkhopen. All of the 450 samples from the 'SONNE' cruise were donated by Preussag A.G.

Sediments collected at sea on 'SONNE' Legs 1 and 2 were sampled at 25 cm depth intervals along the core lengths or at different depth intervals according to variations in lithology. The sediments were subsequently sieved and the amount of the $< 63\mu$ fraction determined.

The remaining sediment cores, after refrigeration, were sampled at Imperial College. It was necessary to refrigerate the cores in order to minimise pore-water migration. After allowing a period of time for the cores to thaw, they were then split in two halves (one half for storage, one half for sampling) using a hacksaw blade to penetrate the outer plastic liner and a cheese-wire and palette knife to divide the sediment. Sampling proceeded according to the visual identification of different lithological units and the sediments were described using standard colour coding systems (see Appendix D).

Sediments were freeze-dried and then ground to a fine powder using an agate mortar and pestle, after which they were stored in plastic vials prior to analysis.

Ferromanganese oxide crusts were also ground to a fine-grained powder, but these samples were stored in a dessicator to prevent water absorption before they were analysed.

# APPENDIX B

## ANALYTICAL TECHNIQUES

### B.1 GENERAL ELEMENT DETERMINATIONS (USING GEN HF ATTACK)

Chemical analysis of GRAFZI sulphides, silicates, Fe oxides, Mn oxide crusts and sediments was carried out by a Perkin Elmer 5000 Atomic Absorption Spectrophotometer (A.A.S.), for Ca, Mn, Fe, Al, Ti, Co, Ni, Cu, Zn, Ag and Pb. The remaining GEOMETEP and DISCOVERY samples were analysed by an A.R.L. 34,000C I.C.P. Atomic Emission Spectrometer (I.C.P.A.E.S.) which added the following elements to those shown above; Na, K, Mg, Li, Sr, La, V, Mo and P.

The chemical digestion that is used in the Applied Geochemistry Research Group for general element attacks is described below. After weighing out 0.25 g of dry, finely-ground samples; 8 $cm^3$ of HF, 3 $cm^3$ of $HClO_4$ and 3 $cm^3$ of $HNO_3$ were added to them in P.T.F.E. beakers. The solutions were then heated on a hot-plate at about 100°C for 2 hours, after which a further 2 $cm^3$ of HF was added. The acid digestion was allowed to proceed overnight. In the next morning, 2 $cm^3$ of $HClO_4$ was added to the nearly-dried samples and the solutions were then heated to dryness at 180 - 200°C. Five $cm^3$ of 6M HCl was added to the remaining bead of samples (along with 1 or 2 drops of $H_2O_2$ if Mn was abundant in the samples). After dilution to a constant volume, the solutions were submitted to the A.A.S. or I.C.P.A.E.S. in a 1M HCl matrix.

When P.T.F.E. test-tubes became available, it was possible to reduce the amounts of sample and reagent used in the general element attack. The 0.10 g of sample and proportionately lesser amounts of reagents which were used for the test-tube attack made this adaption considerably more cost-effective than the beaker attack.

A modification to the concentration of the final matrix of the solution was needed when Ag was analysed. Solutions were submitted for analysis

in 2M $HNO_3$ and 2M HCl, in order to prevent possible AgCl precipitation which may have occurred in a 1M HCl matrix. Both 2M $HNO_3$ and 2M HCl matrices produced similar Ag analyses.

Molybdenum analyses are susceptible to interference effects (Thompson et al., 1982) and a manual correction was applied to Mo values to counter Mn interference. For this reason, and also the poor precision of Mo values at concentrations around the detection limit, an artificial raised "detection limit" of 30 ppm (see Appendix C) was taken and only values above 30 ppm have been reported. This raised "detection limit" does not affect the interpretation of the results as highly anomalous samples with more than 100 ppm Mo exist.

B.2 THE DETERMINATION OF $SiO_2$ (USING THE ROCK ATTACK)

The procedure of Watkins (1980) was followed for the analysis of $SiO_2$ by I.C.P.A.E.S. In brief, this analytical technique involves the fusion of the samples (0.10 g) with a mixed flux of 1 part $LiBO_2$ and 2 parts $Li_2B_4O_7$ (0.30 g). The flux/sample ratio is normally 3/1 and fusion is carried out at 1000°C in an electric muffle furnace. After 30 minutes the molten sample bead is tipped into a mixture of 10 $cm^3$ 2M $HNO_3$ and 60 $cm^3$ $H_2O$. The shattered bead is dissolved in the solution by using a magnetic stirrer for about 30 minutes and this is then made up to a final volume of 100 $cm^3$ (a final dilution factor of 1000). The solution is then ready for analysis.

In samples with exceptionally high Fe contents, the flux/sample ratio was increased to 10/1, as suggested by Watkins (1980).

B.3 THE DETERMINATION OF As, Sb AND Bi (BY VOLATILE HYDRIDE GENERATION)

This method is described fully in Pahlavanpour et al. (1980) and consists of a magnesium nitrate attack on the samples. The samples are submitted to the I.C.P. Spectrometer in a matrix of 5M HCl, and As, Sb and Bi are analysed in a stream of argon gas, after the generation of their volatile hydrides.

## B.4 CLAY MINERAL ISOLATION

The isolation of the clay/smectite fraction of E.P.R. sediments was attempted by the writer at the Hawaii Institute of Geophysics (H.I.G.) in 1980, to fulfil two aims. First, in order to establish the chemical composition of the smectite-rich fraction of E.P.R. sediments. Second, to subject E.P.R. smectites to oxygen isotope analysis to find their temperatures of formation. Both aims failed due to the lack of smectite in E.P.R. sediments from the 20°S area. However, it was possible to isolate Galapagos Rift smectites during later work carried out at Imperial College and these were analysed by I.C.P. Spectrometry. The clay mineral isolation technique was developed at H.I.G., and is an adaption of the method of Jackson (1958) which was devised for soils. The method used is outlined below.

### Salt Removal

The samples were thoroughly washed in tap water and suspended by means of a rubber-tipped stirring rod. To aid flocculation, the samples were then centrifuged and the water decanted. This procedure was followed for at least 4 washings - the latter 2 being carried out with de-ionised water. After decanting the excess water and transferring the sediment to a glass beaker in a relatively dry state, the sample was ready for:-

### Ferric Oxide Removal

Theoretically, the % of iron should be estimated by chemical analysis, and the appropriate amounts of citrate and bicarbonate solutions added to the sample, in the proportions of 8/9 0.3M sodium citrate and 1/9 1M sodium bicarbonate. However, for the approximate 10 g samples that were used, 80 $cm^3$ citrate and 10 $cm^3$ bicarbonate was found to provide a workable amount of reagent.

The glass beakers with suspended samples were mixed and heated in the water-bath for at least 30 minutes, at a temperature between 75°C and 80°C but NEVER exceeding 80°C, as this would have resulted in iron sulphide precipitation. Periodically, 0.5 g of sodium dithionite was added until the brown colouration of the samples became a blue/green colour and the sediments remained spongey and suspended. It was found

that a stirring rod pushed against the side of the vessel could not smear the sample on the glass, if reaction had ceased, and all the ferric oxide had been reduced, with $Fe^{2+}$ chelated by the citrate solution.

After reaction, 20 $cm^3$ of each of acetone and saturated sodium chloride solutions were added to aid flocculation. The vessel was then heated for about 5 minutes. Subsequently, the samples were centrifuged for 15 minutes and the supernatant liquid decanted. This procedure was repeated at least 4 times and if a brown/red colour still persisted in the sediment, then the attack was repeated.

Calcium Carbonate Removal

The E.P.R. samples were sieved (38 micron mesh size) prior to reaction, in order to remove excess foraminifera. Approximately 50 $cm^3$ of pH 5 sodium acetate buffer solution was added for each 5 g of sample. The samples were then suspended and reacted, in the water bath, at boiling point for at least 30 minutes, while the solutions were continually stirred. In each case, after centrifuging and decanting the supernatant solutions, E.P.R. samples were re-reacted due to the great abundance of $CaCO_3$. Finally, the $CaCO_3$-free samples were centrifuged and washed, at least 4 times, prior to preliminary X-ray diffraction to examine their smectite purity.

Manganese Oxide Removal

Relatively dry samples were reacted with 30% $H_2O_2$ solution. Caution is needed when $H_2O_2$ is added as the reaction is violently exothermic and the analyst should be armed with a water-bottle in order to cool down the beaker and slow down the reaction. When reaction had ceased, the supernatant liquid was decanted, after centrifugation, and this was repeated at least 4 times. By now, the sediment should have a greenish hue and resemble a clay mineral assemblage. If this was not the case, then the sediment was dried and powdered with a pestle and mortar, and re-reacted with $H_2O_2$ .

Size Separation (of the <0.5/^Fraction)

Size separation of the <0.5/^ fraction of the sediment residue, after the above chemical attacks, was achieved by centrifugal acceleration of particle settling times. For example, at a centrifuging speed of 1500 R.P.M., then the <0.5/^ fraction remains suspended while larger particles are sedimented after a period of 9 minutes (see Jackson, 1958). Similarly, at a centrifuging speed of 2000 R.P.M., the <0.5/^ fraction can be decanted after a period of 5 minutes. The supernatant solutions were then evaporated to dryness and the <0.5/^ fraction of the sediment was scraped into a plastic vial, before final X.R.D. analysis to check the smectite purity.

## B.5 MINERALOGICAL DETERMINATIONS

Standard determinative mineralogical techniques were carried out by a Phillips X-Ray Diffractometer and a Cambridge Microscan 5 Electron Microprobe. X-ray imaging by the latter instrument produced element maps and the technique is described in 'Physical Methods in Determinative Mineralogy' (Zussman, 1977). The detection limits for electron microprobe chemical analyses were calculated from the counting statistics, where the detection limit was taken as being equal to 2 standard deviations of the data.

## B.6 STABLE ISOTOPE DETERMINATIONS

Isotopic analysis of S (converted to $SO_2$) and O (converted to $CO_2$) was carried out in late 1981, in the Isotope Geology Unit of the Institute of Geological Sciences. Sulphur dioxide was produced by the method of Robinson and Kusakabe (1975), by heating sulphide in vacuo with cuprous oxide. The gas evolved was collected and analysed using a V.G. Micromass 602-C double collector mass spectrometer. Raw data were corrected for change-over valve leakage (crosstalk) and isobaric interference (Coleman, 1980). Oxygen was liberated by fluorination (Clayton and Mayeda, 1963), and after conversion to $CO_2$, was analysed on a V.G. Micromass 903 triple collector mass spectrometer.

## APPENDIX C

### BULK GEOCHEMICAL DATA

The geochemical data for the seven study areas described in this thesis are reported on a carbonate-free basis and are stored on microfiche inside the back cover. The core location, sample depth interval, station type (i.e. core, dredge or grab) and water depth are also included with the geochemical data.

## APPENDIX D

### COLOUR CODING SYSTEMS

In order to standardise visual observations of sediment colours, the U.S.G.S. and Munsell Colour Coding Systems were used and the range of hues found are shown below.

Munsell System

| | |
|---|---|
| 2.5 YR 4/4 - Reddish brown | 10 YR 6/4 - Light yellowish brown |
| 7.5 YR 4/4 - Brown/dark brown | 10 YR 6/6 - Brownish yellow |
| 10 YR 4/4 - Dark yellowish brown | 5 YR 5/2 - Olive grey |

U.S.G.S. System

| | |
|---|---|
| 10 YR 4/2 - Dark yellowish brown | 10 YR 4/2 - Greyish olive |
| 10 YR 5/4 - Moderate yellowish brown | 10 Y 6/2 - Pale olive |
| | 10 Y 8/2 - Pale greenish yellow |
| 10 YR 7/4 - Greyish orange | 5 GY 7/2 - Greyish yellow green |
| 5 Y 4/4 - Moderate olive brown | 10 GY 7/2 - Pale yellowish green |
| 5 Y 5/6 - Light olive brown | 10 G 4/2 - Greyish green |
| 5 Y 6/4 - Dusky yellow | 10 G 6/2 - Pale Green |
| 5 Y 8/4 - Greyish yellow | |

# APPENDIX E

## DATA HANDLING

The geochemical data in Appendix C have been reported on a carbonate-free basis for two main reasons. First, for comparison with previously published data. Second, in order to examine the geochemical variations in the non-carbonate fraction of the sediments. However, due to the close association of Sr with $CaCO_3$ (Emiliani, 1955), this element has not been treated on a carbonate-free basis and is reported in raw data form.

The $CaCO_3$ contents of the sediment samples were calculated from analytically determined Ca values using the method of Dymond et al. (1976), as shown below:-

$$\text{Wt \% } CaCO_3 = \frac{Ca_T - 0.41S - Ca_{NC}}{Ca_C - Ca_{NC}}$$

In this equation:
- $Ca_T$ = Wt % of analytically determined Ca.
- $Ca_{NC}$ = Wt % of Ca in the non-carbonate fraction.
- $Ca_C$ = Wt % of Ca in $CaCO_3$ = 40.04%.
- S = Wt. fraction of salt in the sample.
- 0.41 = A constant to allow for the Wt % of Ca in the salt fraction of the sample, which Dymond et al. (1976) report as 1.14% for sea salts

Due to the different nature of Galapagos Rift and East Pacific Rise sediments, values of $Ca_{NC}$ and S were determined for a representative group of samples from each area. $Ca_{NC}$ was determined after the chemical removal of $CaCO_3$ from the sample (see Appendix B). S was determined by a weight loss calculation, after thoroughly washing the sediments with de-ionised water. The results are shown below:-

| | $Ca_{NC}$ | S |
|---|---|---|
| Galapagos Rift (n = 7) | 2.34% | 0.065 |
| East Pacific Rise (n = 8) | 0.99% | 0.043 |

It should be noted that at high $CaCO_3$ contents, a small error in the determination of $CaCO_3$ values may cause a large variation in the correction factor used on data for that particular sample. However, Varnavas (1979) has shown that the method of Dymond et al. (1976) produces $CaCO_3$ values which agree well with a volumetric method of analysis, using the Collins Calcimeter.

TABLE F1.

INTRA-BATCH: TOTAL ELEMENT PRECISION (Atomic Absorption Spectrophotometry)

* Each sample was duplicated in one run.

| PRECISION | FE | MN | CA | ZN | CU | NI | PB | CO | AL | TI |
|---|---|---|---|---|---|---|---|---|---|---|
| Average % (N = 45) precision over whole batch | $\pm$2.07 | $\pm$3.10 | $\pm$0.80 | $\pm$4.48 | $\pm$7.75 | $\pm$11.81 | $\pm$7.80 | $\pm$17.50 | $\pm$4.12 | $\pm$4.33 |
| % Maximum precision (worst agreement) | $\pm$11.0 | $\pm$27.7 | $\pm$4.5 | $\pm$14.9 | $\pm$33.9 | $\pm$53.0 | $\pm$7.8 | $\pm$33.3 | $\pm$33.3 | $\pm$14.3 |

Precision good throughout but noticeably worse at lower (trace-metal) concentrations, which are sometimes near detection limit.

INTER-BATCH: TOTAL ELEMENT PRECISION (Atomic Absorption Spectrophotometry)

* Precision between different runs, for internal standard.

| % PRECISION | FE | MN | CA | ZN | CU | NI | PB | CO | AL | TI |
|---|---|---|---|---|---|---|---|---|---|---|
| VAS-01 | $\pm$6.1 | $\pm$33.3 | $\pm$2.1 | $\pm$3.7 | GOOD | GOOD | GOOD | $\pm$33.3 | $\pm$3.8 | GOOD |
| S.P. VARN. | $\pm$8.1 | $\pm$14.9 | GOOD | $\pm$10.6 | $\pm$8.4 | $\pm$11.1 | GOOD | $\pm$13.0 | $\pm$3.0 | $\pm$<20.0 |

ACCURACY: TOTAL ELEMENT ACCURACY related to external standards (Atomic Absorption Spectrophotometry)

| SAMPLE | FE(%) | MN(%) | CA(%) | ZN | CU | NI | PB | CO | AL(%) | TI | AG |
|---|---|---|---|---|---|---|---|---|---|---|---|
| SU1 (found) | 23.91 | 0.094 | 2.68 | 260 | 9000 | 14900 | 228 | 683 | 5.08 | 5270 | 7.5$\pm$1.0 |
| SU1 (std) | 22.87 | 0.085 | 2.86 | 294 | 8700 | 15100 | 249 | 630 | 4.92 | 6070 | 4.0 |
| % ACCURACY | +4.5 | +10.6 | -6.3 | -11.6 | +3.4 | -1.3 | -8.4 | +8.4 | +3.3 | -13.2 | ? |
| RED CLAY (found) | 5.61 | 0.427 | 1.49 | 140 | 110 | 120 | 41 | 69 | 9.88 | 4930 | |
| RED CLAY (std) | 5.60 | 0.450 | 1.47 | 130 | 100 | 120 | 33 not reported | | 9.48 | 4900 | |
| % ACCURACY | +0.1 | -5.1 | +1.4 | +7.7 | +10.0 | GOOD | +24.2 | — | +4.2 | | |
| Argillaceous Lst (found) | | | 37.5 | | | | | | | | |
| Arg.Lst (std) | | | 36.4 | | | | | | | | |
| % ACCURACY | | | +3.0 | | | | | | | | |

TABLE F2. QUALITY CONTROL: Precision and Accuracy

Internal standard 09K 0-25 cms, average and standard deviation of 25 analyses

(I.C.P. Spectrometry.)

| | Li | % Na | % K | % Mg | % Ca | Sr | % Al | La | Ti | V | Mo | % Mn | % Fe | Co | Ni | Cu | Zn | Pb | P | % $SiO_2$ |
|---|---|---|---|---|---|---|---|---|---|---|---|---|---|---|---|---|---|---|---|---|
| Av. | 1.07 | 2.03 | 0.148 | 0.706 | 16.0 | 1080 | 0.130 | 34.2 | 149 | 410 | <30 | 4.46 | 13.4 | 30.9 | 264 | 579 | 225 | 46.8 | 5950 | 4.18 |
| σn-1 | 0.46 | 0.12 | 0.02 | 0.05 | 1.20 | 70 | 0.02 | 5.8 | 16 | 18 | | 0.25 | 0.83 | 1.5 | 13.5 | 27 | 16 | 12.4 | 590 | |

External standards

| Sample Description | | Fe | Mn | Cu | Zn | No.of analyses |
|---|---|---|---|---|---|---|
| RED CLAY (I.O.S ) | Found | 5.41 | 0.436 | 110 | 145 | 8 |
| | Reported | 5.60 | 0.450 | 100 | 130 | |
| | % Accuracy | -3 | -3 | +10 | +12 | |
| MAG#1 (U.S.G.S.) | Found | 4.53 | 0.069 | 30.7 | 145 | 4 |
| | Reported | 4.76 | 0.078 | 33.0 | 140 | |
| | % Accuracy | -5 | -12 | -7 | +4 | |
| PCC-1 (U.S.G.S.) | Found | 5.24 | 0.081 | 9.1 | 38.0 | 3 |
| | Reported | 5.80 | 0.090 | 8.0 | 41.0 | |
| | % Accuracy | -10 | -10 | +14 | -7 | |
| IRON ORE (Brit.Chem.Std) | Found | 22.8 | 0.90 | 17.8 | 252 | 2 |
| | Reported | 24.7 | 1.01 | NR | NR | |
| | % Accuracy | -8 | -11 | | | |
| MANGANKNOLLENPROBE II (Preussag) | Found | 11.7 | 23.2 | 4990 | 830 | 1 |
| | Reported | 13.2 | 22.3 | 5100 | 820 | |
| | % Accuracy | -11 | +4 | -2 | +1 | |

# APPENDIX F

## QUALITY CONTROL

The geochemical data presented in this thesis have been subjected to rigorous quality control. Every sample has been analysed in duplicate and the average value is given in Appendix C. In each run, a number of reagent blanks, duplicates and reference materials were randomly inserted to ensure that the data produced was of high quality. Reagent blanks constituted about 5% of the sample batch and allowed some measure of the level of contamination, while duplicated samples (about 10% of the sample batch) allowed a measure of machine drift with time. Reference materials normally accounted for > 5% of the sample batch and consisted of external standards and an 'in-house' standard. In addition, machine calibrator solutions were run at regular intervals to monitor machine drift and to restrict this occurrence to acceptable levels.

Quality control data for Atomic Absorption Spectrophotometer (A.A.S.) analyses, generated after the GEN HF attack (see Appendix B), are reported in Table F1. In one sample batch, each sample was duplicated in order to test the intra-batch precision, reported as a % variation from the mean value. The average intra-batch precision for the whole data-set is better than $\pm$ 18% and is worst (e.g. $\pm$ 53% for Ni) at low concentrations, as was also shown by Thompson and Howarth (1976).

Between-batch or inter-batch precision estimates were carried out by running internal standards (i.e. VAS-O1, see Horder, 1979; S.P.VARN, see Varnavas, 1979) with each sample batch and these are shown in Table F1. A comparison of A.A.S. analyses with reported data for external standards showed that all A.A.S-analysed elements were accurate within a range from +24% to -13%, relative to the external standards.

Quality control data for I.C.P. Spectrometry analyses, generated after the GEN HF attack, are shown in Table F2. Within each sample batch, an internal standard (O9K 0-25 cms) was analysed and the standard deviation

TABLE F3.

RECISION AND ACCURACY DATA FOR (INDUCTIVELY COUPLED PLASMA) SILICA ANALYSIS

| PRECISION | $SiO_2$ |
|---|---|
| Average % (N=3) | ±1.8 |
| % Maximum | ±4.4 |

| SAMPLE | $SiO_2$ |
|---|---|
| NIM-G (found)<br>NIM-G (std) | 7.53<br>7.57 |
| % ACCURACY | -0.5 |
| SGD-1A (found)<br>SGD-1A (std) | 18.26<br>18.56 |
| % ACCURACY | -1.6 |
| SY-3 (found)<br>SY-3 (std) | 29.05<br>29.84 |
| % ACCURACY | -2.6 |

ource of Standard Data:

rgillaceous Limestone ..... United States National Bureau of Standards (1b)
IM-G ..... Geological Survey of Canada, Paper 80-14, Part 6 (1979 Edition)
ed Clay ..... Institute of Oceanographic Sciences (RED CLAY)
GD-1A ..... Geological Survey of Canada, Paper 80-14, Part 6 (1979 Edition)
.P.Varn ..... S.P. Varnavas, unpubl. thesis (1979)
U1 ..... Spectroscopic Society of Canada, Falconbridge Nickel Mines Std; Revised values, G.H.Fayne & R.Sutarno (1976)
Y-3 ..... Geological Survey of Canada, Paper 80-14, Part 6 (1979 Edition)
AS-O1 ..... M.F. Horder, unpubl. thesis (1979)

for each element was determined over 25 runs. As with A.A.S. analyses, the analytical accuracy was found by the use of external standards and the errors vary from -12% to +14% for Fe, Mn, Cu and Zn, relative to the standards.

The determination of silica by I.C.P. spectrometry has been described in Appendix B (see the ROCK attack) and the precision and accuracy for the data is shown in Table F3. It can readily be seen that this method of analysis is both very precise and very accurate.

## REFERENCES


ADAMIDES, N.G. (1979). The Form and Environment of Formation of the Kalawasos Ore Deposits, Cyprus. In: Proc. Int. Ophiolite Symp., Geol. Survey, Cyprus, p.117-127.

ANDERSON, R.N. and SCLATER, J.G. (1972). Topography and Evolution of the East Pacific Rise between 5° and 20°S. Earth Planet. Sci. Lett., 14, p.433-441.

ANDERSON, R.N., FORSYTH, D.W., MOLNAR, P. and MAMMERICKX, J. (1974). Fault Plane Solutions of Earthquakes on the Nazca Plate Boundaries and the Easter Plate. Earth Planet. Sci. Lett., 24, p.188-202.

ANDERSON, R.N., HOBART, M.A., VON HERZEN, R.P. and FORNARI, D.J. (1978). Geophysical Surveys on the East Pacific Rise-Galapagos Rise System. Geophys. J.R. Astron. Soc., 54, p.141-166.

APLIN, A.C. (1983). Geochemistry and Environment of Deposition of some Ferromanganese Oxide Deposits from the South Equatorial Pacific. Unpubl. Ph.D. Thesis, Univ. London.

ARNOLD, M. and SHEPPARD, S.M.F. (1981). The East Pacific Rise at Latitude 21°N: Isotopic Composition and Origin of Hydrothermal Sulphur. Earth Planet. Sci. Lett., 56, p.148-156.

ARRHENIUS, G., BRAMLETTE, M.N. and PICCIOTTO, E. (1957). Localisation of Radioactive and Stable Heavy Nuclides in Ocean Sediments. Nature, 180, p.85-86.

BACKER, H. (1976). Fazies und Chemische Zusammensetzung Rezenter Ausfallungen aus Mineralquellen im Roten Meer. Geol. Jahrb., Reihe D, 17 p.151-172.

BACKER, H. and RICHTER, H. (1973). Die Rezente Hydrothermal-Sedimentare Lagerstte Atlantis II Tief im Roten Meer. Geol. Rundsch, 62, p.697-741.

BALLARD, R.D., HOLCOMB, R.T. and VAN ANDEL, T.H. (1979). The Galapagos Rift at 86°W: 3, Sheet Flows, Collapse Pits and Lava Lakes of the Rift Valley. J. Geophys. Res., 84, p.5407-5422.

BERGER, W.H., ADELSECK, C.G. and MAYER, L.A. (1976). Distribution of Carbonate in Surface Sediments of the Pacific Ocean. J. Geophys. Res., 81, p.2617-2627.

BERNER, R.A. (1973). Phosphate Removal from Seawater by Adsorption on Volcanogenic Ferric Oxides. Earth Planet. Sci. Lett., 18, p.77-86

BIDEAU, D., HEBERT, R. and HEKINIAN, R.(1982). Metagabbro and Metaperidotite from the Garret Transform Fault (East Pacific Rise, near 13°S). Contribution du Océanologique de Bretagne.

BIGNELL, R.D. (1975). The Geochemistry of Metalliferous Brine Precipitates and Other Sediments from The Red Sea. Unpubl. Ph.D. Thesis, Univ. London.

BIGNELL, R.D., CRONAN, D.S. and TOOMS, J.S. (1976). Metal Dispersion in The Red Sea as an aid to Marine Geochemical Exploration. Trans. Inst. Min. Metall.(B), 85, p.B274-278.

BISCHOFF, J.L. (1969). Red Sea Geothermal Brine Deposits; their Mineralogy, Chemistry and Genesis. In E.T. Degens and D.A. Ross (Editors), 'Hot Brines and Recent Heavy Metal Deposits in the Red Sea.' Springer, New York, p.368-401.

BISCHOFF, J.L. (1972). A Ferroan Nontronite from The Red Sea Geothermal Area. Clays Clay Miner., 20, p.217-223.

BISCHOFF, J.L. (1980). Geothermal System at 21°N, East Pacific Rise: Physical Limits on Geothermal Fluid and Role of Adiabatic Expansion. Science, 207, p.1465-1469.

BISCHOFF, J.L. and MANNHEIM, F.T. (1969). Economic Potential of Red Sea Heavy Metal Deposits. In: E.T. Degens and D.A. Ross (Editors), 'Hot Brines and Recent Heavy Metal Deposits in the Red Sea.' Springer, New York, p.535-541.

BISCHOFF, J.L. and SEYFRIED, W.E. (1978). Hydrothermal Chemistry of Seawater from 25° to 350°C. Amer. Journ. Sci., 278, p.838-860.

BLOCH, S. (1978). Phosphorus Distribution in Smectite-Bearing Basal Metalliferous Sediments. Chem. Geol., 22, p.353-359.

BOILLOT, G., GRIMAUD, S., MAUFFRET, A., MOUGENOT, D., KORNPROBST, J., MERGOIL-DANIEL, J. and TORRENT, G. (1980). Ocean-Continent Boundary off the Ibernian Margin: A Serpentinite Diapir West of the Galicia Bank. Earth Planet. Sci. Lett., 48, p.23-24.

BONATTI, E. and JOENSUU, O. (1966). Deep-Sea Iron Deposit from the South Pacific. Science, 154, p.643-645.

BONATTI, E., FISHER, D.E., JOENSUU, O. and RYDELL, H.S. (1971). Postdepositional Mobility of some Transition Elements, Phosphorous, Uranium and Thorium in Deep-Sea Sediments. Geochim. Cosmochim. Acta. 35, p.189-201.

BONATTI, E., HONNOREZ, J. and GARTNER, S. (1973). Sedimentary Serpentinites from the Mid-Atlantic Ridge. J. Sediment. Petrol., 43, p.728-735.

BONATTI, E., HONNOREZ, B.M.G., and HONNOREZ, J. (1976). Copper-Iron Sulphide Mineralisation from the Equatorial Mid-Atlantic Ridge. Econ. Geol., 71, p.1515-1525.

BOSTROM, K. (1973). The Origin and Fate of Ferromanganoan Active Ridge Sediments. Stockholm Contrib. Geol., 27., p.149-243.

BOSTROM, K. (1976). Particulate and Dissolved Matter as Sources for Pelagic Sediments. Stockholm Contrib. Geol., 30, p.15-79.

BOSTROM, K. and PETERSON, M.N.A. (1966). Precipitates from Hydrothermal Exhalations on the East Pacific Rise. Econ. Geol., 61, p.1258-1265.

BOSTROM, K. and PETERSON, M.N.A. (1969). The Origin of Aluminium-Poor Ferromanganoan Sediments in Areas of High Heat Flow on the East Pacific Rise. Mar. Geol., 7, p.427-447.

BOSTROM, K. and VALDES, S. (1969). Arsenic on Ocean Floors. Lithos, 2, p.357-360.

BOSTROM, K. JOENSUU, O., KRAEMER, T., RYDELL, H., VALDES, S., GARTNER, S. and TAYLOR, G. (1974). New Finds of Exhalative Deposits on the East Pacific Rise. Geol. Foren. Stockholm Forh., 96, p.53-60.

BOTTINGA, J. and JAVOY, M. (1973). Comments on Oxygen Isotope Geothermometry. Earth Planet. Sci. Lett., 20., p.250-265.

BRINDLEY, G.W. and BROWN, G. (1980). Crystal Structures of Clay Minerals and their X-Ray Identification. Eds., Monograph No. 5, Min. Soc., London.

BRULAND, K.W. (1980) Oceanographic Distributions of Cadmium, Zinc, Nickel and Copper in the North Pacific. Earth Planet. Sci. Lett., 47, p.176-198.

BRULAND, K.W., KNAUER, G.A. and MARTIN, J.H. (1978). Zinc in the North East Pacific Waters. Nature, 271, p.741-743.

BRUNEAU, L., JERLOV, N.G., and KOCZY, F. (1953). Reports of the Swedish Deep Sea Expedition, Vol. 3, "Physics and Chemistry".

BURNETT, W.C. and PIPER, D.Z. (1977). Rapidly-formed Ferromanganese Deposit From the Eastern Pacific Hess Deep. Nature, 265, p.596-600.

BURNS, R.G. and BURNS, V.M. (1977). Mineralogy of Ferromanganese Nodules. In: "Marine Manganese Deposits", (Ed., G.P. Glasby), Ch.7. Elsevier, Amsterdam.

BURTON, J.D. (1966). Some Problems Concerning the Marine Geochemistry of Vanadium. Nature, 212, p.976-978.

CANN, J.R. and STRENS, M.R. (1982). Black Smokers Fuelled by Freezing Magma. Nature, 298, p.147-149.

CANN, J.R., WINTER, C.K. and PRITCHARD, R.G. (1977). A Hydrothermal Deposit From the Floor of the Gulf of Aden. Mineral Mag., 41, p.193-199.

CASEY, W.H. and TAYLOR, B.E. (1982). Oxygen, Hydrogen and Sulphur Isotope Geochemistry of a Portion of the West Shasta Cu-Zn District, California. Econ. Geol., 77, p.38-49.

CHAYES, F. (1960). On Correlation between Variables of Constant Sum. J. Geophys. Res., 65, p.4185-4193.

CHERNOSKY, J.V. (1973). The Stability of Chrysotile, $Mg_3Si_2O_5(OH)_4$, and the Free Energy of Formation of Talc, $Mg_3Si_4O_{10}(OH)_2$. Geol. Soc. Am. Abstr. 1973 Meet.

CHESTER, R. and ASTON, S.R. (1976). The Geochemistry of Deep-Sea Sediments. In: J.P. Riley and R. Chester (Eds.), Chapter 34, Chemical Oceanography 6. Academic Press, London, 2nd Ed., p.281-390.

CHESTER, R. and MESSIHA-HANNA, R. (1970). Trace Element Partition Patterns in North Atlantic Deep-Sea Sediments. Geochim. Cosmochim. Acta, 34, p.1121-1128.

CHRISTENSEN, N.I. (1972). The abundance of Serpentinites in the Oceanic Crust. J. Geol., 80, p.709-719.

CLAYTON, R.N. and MAYEDA, T.K. (1963). The Use of Bromine Penafluoride in Extraction of Oxygen from Oxides and Silicates for Isotopic Analysis. Geochim. Cosmochim. Acta., 27, p.43-52.

COLEMAN, R.G. (1971). Petrologic and Geophysical Nature of Serpentinites. Bull. Geol. Soc. Am., 82, p.897-918.

COLEMAN, M.L. (1980). Corrections for Mass Spectrometer Analysis of Sulphur Dioxide. Inst. Geol. Sci., Stable Isotope Report No. 45.

CORLISS, J.B. and BALLARD, R.D. (1977). Oases of Life in the Cold Abyss. Natl. Geogr., 152, p.440-453.

CORLISS, J.B., LYLE, M., DYMOND, J. and CRANE, K. (1978). The Chemistry of Hydrothermal Mounds near the Galapagos Rift. Earth Planet. Sci. Lett., 40, p.12-24.

CORLISS, J.B., DYMOND, J., GORDON, L.I., EDMOND, J.M., VON HERZEN, R.P., BALLARD, R.D., GREEN, K., WILLIAMS, D., BAINBRIDGE, A., CRANE, K. and VAN ANDEL, T.H. (1979). Submarine Thermal Springs on the Galapagos Rift. Science, 203, p.1073-1088.

CRAIG, H., WELHAN, J.A., KIM, K., POREDA, R. and LUPTON, J.E. (1980). Geochemical Studies of the 21°N East Pacific Rise Hydrothermal Fluids. EOS, 61, p.992.

CRONAN, D.S. (1972). The Mid-Atlantic Ridge near 45°N., XVII - Al, As, Hg and Mn in Ferruginous Sediments from the Median Valley. Can. J. Earth Sci., 9, p.319-323.

CRONAN, D.S. (1975). Geological and Geochemical Factors Determining the Variability of Marine Manganese Nodules. 3rd Oceanology International, Brighton, p.118-120.

CRONAN, D.S. (1980). 'Underwater Minerals' Academic Press, London, 362p.

CRONAN, D.S. and VARNAVAS, S.P. (1981). Hydrothermal and Dissolution Related Geochemical Variations in Sediments from an E.P.R. Fracture Zone, 9°S. Oceanol. Acta, No. SP, p.47-58.

CRONAN, D.S., GLASBY, G.P., MOORBY, S.A., THOMSON, J., KNEDLER, K.E. and McDOUGALL, J.C. (1982). A Submarine Hydrothermal Manganese Deposit from the South West Pacific Island Arc. Nature, 298, p.456-458.

CYAMEX SCIENTIFIC TEAM. (1981). First Manned Submersible Dives on the East Pacific Rise, 21°N (Project RITA): General Results. Marine Geophys. Res., 4, p.345-379.

DASCH, E.J. (1981). Lead Isotopic Composition of Metalliferous Sediments from the Nazca Plate. Geol. Soc. Amer. Memoir 154, p.199-209.

DASCH, E.J., DYMOND, J. and HEATH, G.R. (1981). Isotopic Analysis of Metalliferous Sediments from the East Pacific Rise. Earth Planet. Sci. Lett., 13, p.175-180.

DEGENS, E.T. and ROSS, D.A. (1969). Eds: Hot Brines and Recent Heavy Metal Deposits in the Red Sea. New York, Springer-Verlag, 600p.

DELANEY, J.R., KOSKI, R.A., CLAGUE, D.A., BISCHOFF, J.L., and NORMARK, W.R. (1982). Massive Zinc-Iron Rich Sulphide Deposits Associated with Hot Springs on the Juan de Fuca Ridge. Abstr., S.E.P.M. Conf., Calgary.

DYMOND, J. (1981). Geochemistry of Nazca Plate Surface Sediments: an Evaluation of Hydrothermal, Biogenic, Detrital and Hydrogenous Sources. Geol. Soc. Am., Memoir 154.. p.133-173.

DYMOND, J. and VEEH, H.H. (1975). Metal Accumulation Rates in the South East Pacific and the Origin of Metalliferous Sediments. Earth Planet. Sci. Letts., 28, p.13-22.

DYMOND, J., CORLISS, J.B., HEATH, G.R., FIELD, C.W., DASCH, E.J. and VEEH, H.H. (1973). Origin of Metalliferous Sediments from the Pacific Ocean. Bull. Geol. Soc. Am., 84. p.3355-3372.

DYMOND, J., CORLISS, J.B. and STILLINGER, R. (1976). Chemical Composition and Metal Accumulation Rates of Metalliferous Sediments from Sites 319, 320 and 321. In: Initial Reports of the D.S.D.P., 34, p.575-588. Yeats R.S., Hart, S.R. et al. (Eds.), U.S. Govt. Print Office, Wash., D.C.

DYMOND, J., CORLISS, J.B. and HEATH, G.R. (1977). History of Metalliferous Sedimentation at D.S.D.P. Site 319, in the South Eastern Pacific. Geochim. Cosmochim. Acta, 41,p.741-753.

EDMOND, J.M., MEASURES, C., MACDUFF, R.E., CHAN, L.H., COLLIER, R., GRANT, B., GORDON, L.I. and CORLISS, J.B. (1979). Ridge Crest Hydrothermal Activity and the Balances of the Major and Minor Elements in the Ocean: the Galapagos Data. Earth Planet. Sci. Lett ., 46, p.1-19.

ELDERFIELD, H. and GREAVES, M.J. (1982). The Rare Earth Elements in Seawater. Nature, 296, p.214-219.

EL WAKEEL, S.K. and RILEY, J.P. (1961). Chemical and Mineralogical Studies of Deep-Sea Sediments. Geochim. Cosmochim. Acta, 25, p.110-146.

EMILIANI, C. (1955). Mineralogical and Chemical Composition of the Tests of Certain Pelagic Foraminifera. Micropalaeont., 1, p.377-380.

FAYNE, G.H. and SUTARNO, R. (1976). Certified Compositional Reference Materials for the Earth Sciences. Canad. Mineral., 14, p.164-171.

FEVRIER, M. (1981). Hydrothermalisme et Mineralisations sur la Dorsale Est Pacifique à 21°N. Ph.D. Thesis, Univeristy of Bretagne Occidentale.

FLEISCHER, M. (1955). Minor Elements in some Sulphide Minerals. Econ. Geol., 50th Anniv. Vol., p.970-1024.

FRANCHETEAU, J. and BALLARD, R.D. (1983). The East Pacific Rise at 21°N, 13°N and 20°S: Inferences for Along-Strike Variability of Axial Processes of the Mid-Ocean Ridge. Earth Planet. Sci. Lett., (in the press).

FROELICH, P.N., BENDER, M.L. and HEATH, G.R. (1977). Phosphorous Accumulation Rates in Metalliferous Sediments on the East Pacific Rise. Earth Planet. Sci. Lett., 34, p.351-359.

GLACCUM, R. and BOSTROM, K (1976). (Sodium, Potassium)-Phillipsite: Its Stability Conditions and Geochemical Role in the Deep Sea. Mar. Geol. 21, p.47-58.

GOLDBERG, E.D. (1954). Marine Chemistry I: Chemical Scavengers of the Sea. J. Geol., 62, p.249-265.

GOLDBERG, E.D. and ARRHENIUS, G. (1958). Chemistry of Pelagic Pacific Sediments. Geochim. Cosmochim. Acta. 13. p.153-212.

GOLDBERG, E.D., BROECKER, W.S., GROSS, M.G. and TUREKIAN, K.K. (1971). Marine Chemistry. In: 'Radioactivity in the Marine Environment', Nat. Acad. Sci., Wash. D.C., p.137-146.

GOLDSCHMIDT, V.M. (1937). The Principles of Distribution of Chemical Elements in Minerals and Rocks. J. Chem. Soc., p.655-672.

GORDEEV, V.V. and DEMIMA, L.L. (1979). Direct Observations of Hydrothermal Waters on the Bottom of the Pacific Ocean (Galapagos Active Zone and Hess Depression). Geochem. Int'l., 16, p.132-146

GOULART, E.P. (1976). Different Smectite Types in Sediments of the Red Sea. Geol. Jahrb., D17, p.135-149.

GRILL, E.V., CHASE, R.L., MACDONALD, R.D. and MURRAY, J.W. (1981). A Hydrothermal Deposit from Explorer Ridge in the North East Pacific Ocean. Earth Planet. Sci. Lett., 52, p.142-150.

GURVICH, Y.G., BOGDANOV, Y.A., KURINOV, A.D. and KATARGIN, N.V. (1976). Antimony in the Metalliferous Sediments of the Pacific Ocean. Oceanol., 16, p.279-283.

HAJASH, A. (1975). Hydrothermal Processes along Mid-Ocean Ridges: An Experimental Investigation. Contrib. Mineral. Petrol., 53, p.205-226.

HANDSCHUMACHER, D.W. (1976). Post-Eocene Plate Tectonics of the Eastern Pacific. In: G.H. Sutton et al. (Eds.), 'The Geophysics of the Pacific Ocean Basin and its Margin (Woollard Volume).' Amer. Geophys. Union. Geophys. Monogr., 19, p.177-202.

HARDER, H. (1976). Nontronite Synthesis at Low Temperatures. Chem. Geol., 18, p.169-180.

HAYMON, R.M. and KASTNER, M. (1981). Hot Spring Deposits on the East Pacific Rise at 21°N: Preliminary Description of Mineralogy and Genesis. Earth Planet. Sci. Lett., 53, p.363-381.

HEATH, G.R. and DYMOND, J. (1977). Genesis and Transformation of Metalliferous Sediments from the East Pacific Rise, Bauer Deep and Central Basin, North West Nazca Plate. Bull. Geol. Soc. Am., 88, p.723-733.

HEATH, G.R. and DYMOND, J. (1981). Metalliferous Sediment Deposition in Time and Space: East Pacific Rise and Bauer Basin, Northern Nazca Plate. Geol. Soc. Am., Memoir 154, p.175-197

HEATON, T.H.E. and SHEPPARD, S.M.F. (1976). Hydrogen and Oxygen Isotope Evidence for Seawater Hydrothermal Alteration and Ore Deposition, Troodos Complex, Cyprus. In: 'Volcanic Processes in Ore Genesis.' Proc. Inst. Min. Met. and Geol. Soc., London, p.42-57.

HEIN, J.R., YEH, H.W. and ALEXANDER, E. (1979). Origin of Iron-Rich Montmorillonite from the Manganese Nodule Belt of the North Equatorial Pacific. Clays Clay Miner., 27, p.185-194.

HEKINIAN, R., ROSENDAHL, B.R., CRONAN, D.S., DMITRIEV, Y., FODOR, R.V., GOLL, R.M., HOFFERT, M., HUMPHRIS, S.E., MATTEY, D.P., NATLAND, J., PETERSEN, N., ROGGENTHEN, W., SCHRADER, E.L., SRIVASTAVA, R.K. and WARREN, N. (1978). Hydrothermal Deposits and Associated Basement Rocks from the Galapagos Spreading Centre. Oceanol. Acta., 1, p.473-482.

HEKINIAN, R., FEVRIER, M., BISCHOFF, J.L., PICOT, P. and SHANKS, W.C. (1980). Sulphide Deposits from the East Pacific Rise near 21°N. Science, 207, p.1433-1444.

HEM, J.D. (1977). Reactions of Metal Ions at Surfaces of Hydrous Iron Oxide. Geochim. Cosmochim. Acta., 41, p.527-538.

HERRON, E.M. (1972). Seafloor Spreading and the Cainozoic History of the East-Central Pacific. Geol. Soc. Am. Bull., 83, p.1671-1692.

HEY, R.N. (1977). Tectonic Evolution of the Cocos-Nazca Spreading Centre. Geol. Soc. Am. Bull., 88, p.1404-1420.

HEY, R.N., DEFFEYES, K.S., JOHNSON, G.L. and LOWRIE, A. (1972). The Galapagos Triple Junction and Plate Motions in the East Pacific. Nature, 237, p.20-22.

HEY, R.N., JOHNSON, G.L. and LOWRIE, A. (1977). Recent Plate Motions in the Galapagos Area. Geol. Soc. Am. Bull., 88, p.1385-1403.

HOFFERT, M., PERSEIL, A., HEKINIAN, R., CHOUKROUNE, P., NEEDHAM, H.D., FRANCHETEAU, J., and LE PICHON, X. (1978). Hydrothermal Deposits Sampled by Diving Saucer in Transform Fault 'A' near 37°N on the Mid-Atlantic Ridge, FAMOUS Area. Oceanol. Acta, 1, p.73-86.

HORDER, M.F. (1979). Geochemical Investigations of Deep Sea Sediments from the Indian Ocean. Unpubl. Ph.D. Thesis, Univ. London.

HOROWITZ, A. (1970). The Distribution of Pb, Ag, Sn, Ti, Zn in Sediments on Active Ocean Ridges. Mar. Geol., 9, p.241-259.

HUMPHRIS, S.E. and THOMPSON, G. (1978). Hydrothermal Alteration of Oceanic Basalts by Seawater. Geochim. Cosmochim. Acta, 42, p.107-126.

JACKSON, M.L. (1958). 'Soil Chemical Analysis.' Constable, London.

KAJIWARA, Y. and KROUSE, H.R. (1971). Sulphur Isotope Partitioning in Metallic Sulphide Systems. Can. J. Earth Sci., 8, p.1397-1408.

KAPLAN, J.R., SWEENEY, R.E. and NISSENBAUM, A. (1969). Sulphur Isotope Studies on Red Sea Geothermal Brines and Sediments. In: E.T. Degens and D.A. Ross (Eds.) 'Hot Brines and Recent Heavy Metal Deposits in the Red Sea.' Springer, New York, p.474-498.

KINNIBURGH, D.G. (1973). Cation Sorption by Hydrous Metal Oxides. Ph.D. Thesis, Univ. Wisconsin, Madison, Wisconsin.

KLINKHAMMER, G., BENDER, M. and WEISS, R.F. (1977). Hydrothermal Manganese in the Galapagos Rift. Nature, 269, p.319-320.

KLITGORD, K.D. and MUDIE, J.D. (1974). The Galapagos Spreading Centre: a Near Bottom Geophysical Survey. Geophys. J.R. Astron. Soc., 38, p.563-586.

KRAUSKOPF, K.B. (1956). Factors Controlling the Concentrations of Thirteen Rare Metals in Sea-Water. Geochim. Cosmochim. Acta, 9, p.1-32

KRAUSKOPF, K.B. (1957). Separation of Manganese from Iron in Sedimentary Processes. Geochim. Cosmochim. Acta, 12, p.61-84.

LANGSETH, M.G. and VON HERZEN, R.P. (1971). Heat Flow through the Floor of the World's Oceans. In: A.E. Maxwell (Ed.) 'The Sea', Volume 4, Part 1. San Fransisco, Wiley-Interscience, p.299-353.

LE BEL, L. and OUDIN, E. (1982). Fluid Inclusion Studies of Deep-Sea Hydrothermal Sulphide Deposits on the East Pacific Rise near 21°N. Chem. Geol., 37, p.129-136.

LONSDALE, P.F. (1977). Deep-tow Observations at the Mounds Abyssal Hydrothermal Field, Galapagos Rift. Earth Planet. Sci. Lett., 36, p.92-110.

LONSDALE, P.F. (1977a). Regional Shape and Tectonics of the Equatorial East Pacific Rise. Mar. Geophys. Res., 3, p.295-315.

LONSDALE, P.F. (1977b). Structural Geomorphology of a Fast-Spreading Rise Crest: The East Pacific Rise near 3°25'S. Mar. Geophys. Res., 3, p.251-295.

LONSDALE, P.F., BISCHOFF, J.L., BURNS, V.M., KASTNER, M. and SWEENEY, R.E. (1980). A High Temperature Hydrothermal Deposit on the Sea-Bed at a Gulf of California Spreading Centre. Earth Planet. Sci. Lett., 49, p.8-20.

LONSDALE, P.F., BATIZA, R. and SIMKIN, T. (1982). Metallogenesis at Seamounts on the East Pacific Rise. Mar. Tech. Soc. J., 16, No.3, p.54-61.

LUPTON, J.E. and CRAIG, H. (1981). A Major $^{3}He$ Source at 15°S on the East Pacific Rise. Science, 214, p.13-18.

LUPTON, J.E., WEISS, R.F. and CRAIG, H. (1977). Mantle Helium in Hydrothermal Plumes in the Galapagos Rift. Nature, 267, p.603-604.

LYNN, D.C. and BONATTI, E. (1965). Mobility of Manganese in Diagenesis of Deep-Sea Sediments. Mar. Geol., 3, p.457-474.

MALAHOFF, A. (1982). Ecuador's Offshore 25-Million Ton Sulphide Deposit. Ocean Industry, Jan., p.90.

MALAHOFF, A., McMURTRY, G.M., WILTSHIRE, J.C. and YEH, H.W. (1982). Geology and Chemistry of Hydrothermal Deposits from Active Submarine Volcano Loihi, Hawaii. Nature, 298, p.234-239.

MALAHOFF, A., EMBLEY, R.W., CRONAN, D.S. and SKIRROW, R. (1983). The Geological Setting and Chemistry of Hydrothermal Sulphides and Associated Deposits from the Galapagos Rift at 86°W. Mar. Mining, 4, p.123-137.

MAMMERICKX, J., ANDERSON, R.N., MENARD, H.W. and SMITH, S.M. (1975). Morphology and Tectonic Evolution of the East Central Pacific. Geol. Soc. Am. Bull., 86, p.111-118.

MARCHIG, V. and GUNDLACH, H. (1982). Iron-Rich Metalliferous Sediments on the East Pacific Rise: Prototype of Undifferentiated Metalliferous Sediments on Divergent Plate Boundaries. Earth Planet. Sci. Lett., 58, p.361-382.

MARCHIG, V., GUNDLACH, H., MOLLER, P. and SCHLEY, F. (1982). Some Geochemical Indicators for Discrimination between Diagenetic and Hydrothermal Metalliferous Sediments. Mar. Geol., 50, p.241-256.

MARTIN, J.H. (1970). The Possible Transport of Trace-Metals via Moulted Copepod Exoskeletons. Limnol. Oceanog., 15, p.756-761.

MATSUHISA, Y., GOLDSMITH, J.R. and CLAYTON, R.N. (1979). Oxygen Isotope Fractionation in the System Quartz-Albite-Anorthite-Water. Geochim. Cosmochim. Acta, 43, p.1131-1140.

McARTHUR, J.M. and ELDERFIELD, H. (1977). Metal Accumulation Rates in Sediments from Mid-Indian Ocean Ridge and Marie Celeste Fracture Zone. Nature, 266, p.437-439.

McMURTRY, G.M. and YEH, H.W. (1981). Hydrothermal Clay Mineral Formation of East Pacific Rise and Bauer Basin Sediments. Chem. Geol., 32, p.189-205.

McMURTRY, G.M., VEEH, H.H. and MOSER, C. (1981). Sediment Accumulation Rate Patterns on the North West Nazca Plate. Geol. Soc. Am., Memoir 154, p.211-249.

MOODY, J.B. (1976). Serpentinisation: a review. Lithos, 9, p.125-138.

MOON, C.J. (1983). Factors Controlling the Surficial Dispersion of As, Sb, Bi and Se from Mineral Deposits in the British Isles. Unpubl. Ph.D. Thesis, Univ. London.

MOORBY, S.A. and CRONAN, D.S. (1983). Chemical Composition of Sediments from Sites 506, 507, 508 and 509, Leg 70, D.S.D.P. In: J. Honnorez, R.P. Von Herzen, et al., Init. Rep. D.S.D.P., Leg 70, (in the press).

MOORBY, S.A. and CRONAN, D.S. (1983a). The Geochemistry of Hydrothermal and Pelagic Sediments from the Galapagos Hydrothermal Mounds Field, D.S.D.P., Leg 70. Mineral. Mag. (in the press)

MOORE, W.S. and VOGT, P.R. (1976). Hydrothermal Manganese Crusts from Two Sites near the Galapagos Spreading Axis. Earth Planet. Sci. Lett., 29, p.349-356.

MOORES, E.M. (1973). Geotectonic Significance of Ultramafic Rocks. Earth Sci. Rev., 9, p.241-258.

MORGAN, W.J. (1972). Deep Mantle Convection Plumes and Plate Motions. Bull. Am. Assoc. Pet. Geol., 56, p.203-213.

MOTTL, M.J. and HOLLAND, H.D. (1978). Chemical Exchange during Hydrothermal Alteration of Basalt by Seawater. I. Experimental Results for Major and Minor Components of Seawater. Geochim. Cosmochim. Acta, 42, p.1103-1115.

MOTTL, M.J. and SEYFRIED, W.E. (1980). Subseafloor Hydrothermal Systems: Rock vs. Seawater Dominated. In: 'Benchmark Papers in Geology', (Ed. P.A. Rona), 56, p.66-82.

MOTTL, M.J., HOLLAND, H.D. and CORR, R.F. (1979). Chemical Exchange During Hydrothermal Alteration of Basalt by Seawater. II. Experimental Results for Fe, Mn and Sulphur Species. Geochim. Cosmochim. Acta, 45, p.868-884.

MURDMAA, I.O. and ROZANOVA, T.V. (1976). Hess Deep Bottom Sediments. In: 'Geological-Geophysical Researches in the South East Part of the Pacific Ocean'. Nauka, Moscow, p.252-260.

MUEHLENBACHS, K. and CLAYTON, R.N. (1972). Oxygen Isotope Geochemistry of Submarine Greenstones. Can. J. Earth Sci., 9, p.1104-1105.

MURRAY, J.W. and BREWER, P.G. (1977). Mechanisms of Removal of Manganese, Iron and Other Trace Metals from Seawater. In: 'Marine Manganese Deposits'. (Ed. G.P. Glasby), Elsevier, Amsterdam. Chap. 10, p.291-326.

NEAVE, H.R. 'Elementary Statistical Table'. Alden Press, Oxford, 48p.

OHMOTO, H. and RYE, R.O. (1979). Isotopes of Sulphur and Carbon. In: 'Geochemistry of Hydrothermal Ore Deposits,' (Ed. H.L. Barnes), 2nd Edn., Wiley, New York, p.509-567.

OHMOTO, H., COLE, D.R. and MOTTL, M.J. (1976). Experimental Basalt Seawater Interaction: Sulphur and Oxygen Isotope Studies. EOS, 57, p.342.

OLAUSSON, E. (1960). Descriptions of Sediment Cores from the Central and Western Pacific with Adjacent Indonesian Region. Rep. Swed. Deep-Sea Exped., 1947-1948, 6, p.161-214.

OUDIN, E. (1981). Etude Minéralogique et géochimique des dépôts sulfurés sous-marins actuels de la Ride Est Pacifique (21°N). Documents du B.R.G.M., 25, 241p.

OUDIN, E. (1983). Hydrothermal Sulphide Deposits of the East Pacific Rise (21°N). Part 1: Descriptive Mineralogy. Mar. Mining, 4, p.39-72.

OZCELIK, M.(1982). The Petrology and Geochemistry of Volcanic Rocks and Associated Sulphide Deposits of the South East Anatolian Ophiolite Belt, Near Malatya, Turkey. Unpubl. Ph.D. Thesis, Univ. Durham.

PAHLAVANOUR, B., THOMPSON, M. and THORNE, L.T. (1980). Simultaneous Determination of Trace Concentrations of As, Sb and Bi in Soils and Sediments by Volatile Hydride Generation and Inductively Coupled Plasma Emission Spectrometry. Analyst, 105, p.756-761 .

PEARCE, J.A., ALABASTER, T., MALLICK, D. and ELBOUSHI, I. (1979). Characteristics and Geological Setting of the Lasail Massive Sulphide Deposit, Oman. J. Geol. Soc., 136, p.625.

PLAYFAIR, J. (1802). 'Illustrations of the Huttonian Theory of the Earth.' Edinburgh.

RAMDOHR, P. (1981). 'The Ore Minerals and Their Intergrowths'. Pergamon Press, 4th Edn.

REA, D.K. (1975). Tectonics of the East Pacific Rise, 5° to 12°S. Ph.D. Thesis, Oregon State Univ., 139p.

REA, D.K. (1976). Analysis of a Fast-Spreading Rise Crest: The East Pacific Rise, 9° to 12°S. Mar. Geophys. Res., 2, p.291-313.

REA, D.K. (1978). Asymmetric Sea-Floor Spreading and a Non-Transform Axis Offset: The East Pacific Rise, 20°S Survey Area. Geol. Soc. Am. Bull., 89, p.836-844.

REA, D.K. and BLAKELY, R.J. (1975). Short Wavelength Magnetic Anomalies in a Region of Rapid Seafloor Spreading. Nature, 255, p.126-128.

REA, D.K., DYMOND, J., HEATH, G.R., HEINRICHS, D.F. and JOHNSON, S.H. (1973). New Estimates of Rapid Seafloor Spreading Rates and the Identification of Young Magnetic Anomalies on the East Pacific Rise, 6° and 11°S. Earth Planet. Sci. Lett., 19, p.225-229.

REID, J.L. (1981). Mid-depth Circulation. In: C. Wunsch and B. Warren (Eds. 'Evolution of Physical Oceanography', MIT Press, Cambridge, 70.

REVELLE, R.R. (1944). Scientific Results of Cruise VII of the CARNEGIE during 1928-1929 under Command of Captain J.P. Ault. Oceanography - II. 1. Marine Bottom Samples Collected in the Pacific Ocean by the Carnegie on its seventh cruise. Carnegie Inst. Wash. Publ., 556, p.1-180.

RILEY, J.P. and CHESTER, R. (1971). 'Introduction to Marine Chemistry'. Academic Press, London, 465p.

RILEY, J.P. and SINHASENI, P. (1958). Chemical Composition of Three Manganese Nodules from the Pacific Ocean. J. Mar. Res., 17, p.466-482.

ROBINSON, B.W. and KUSAKABE, M. (1975). Quantitative Preparation of Sulphur Dioxide, for $^{34}S/^{32}S$ Analyses, from Sulphides by Combustion with Cuprous Oxide. Analyt. Chem., 47, p.1179-1181.

ROZANOVA, T.V. (1976). Cerolite, Pyrrhotite and Troilite in Sediments of the Hess Depression. Litol. Polezn. Iskop., 2, p.22-34. (English Abstr. in Chem. Abstr., 85, p.140).

RYDELL, H., KRAMER, T., BOSTROM, K. and JOENSUU, O.(1974). Postdepositional Injection of Uranium-Rich Solutions into East Pacific Rise Sediments. Mar. Geol., 17, p.151-164.

RYE, R.O. and OHMOTO, H. (1974). Sulphur and Carbon Isotopes and Ore Genesis: A Review. Econ. Geol., 69, p.826-842.

SAKAI, H., VEDA, A. and FIELD, C.W. (1978). $\delta^{34}S$ and Concentration of Sulphide and Sulphate Sulphurs in some Ocean-Floor Basalts and Serpentinites. In: 'Short Papers of the Fourth International Conf., Geochronology, Cosmochronology, Isotope Geology.' R.E. Zartman (Ed.), U.S.G.S. Open-File Rep. 78-101, p.372.

SCHEIBNER, E. and PEARCE, J.A. (1978). Eruptive Environments and Inferred Exploration Potential of Metabasalts from New South Wales. J. Geochem. Expl., 10, p.63-74.

SCHMITZ, W., SINGER, A., BACKER, H. and STOFFERS, P. (1982). Hydrothermal Serpentine in a Hess Deep Core. Mar. Geol., 46, p.M17-M26.

SCHNEIDER, W. and SCHUMANN, D. (1979). Tonminerale in Normalsedimenten, Hydrothermal Beeinflussten Sedimenten und Erzchlammen des Roten Meeres. Geol. Rundsch., 68, p.631-648.

SCLATER, J.G. and KLITGORD, K.D. (1973). A Detailed Heat Flow, Topographic and Magnetic Survey across the Galapagos Spreading Centre at 86°W. J. Geophys. Res., 78, p. 6951-6975.

SCLATER, J.G., ANDERSON, R.N. and BELL, M.L. (1971). The Elevation of Ridges and the Evolution of the Central Eastern Pacific. J. Geophys. Res., 76, p.7888-7915.

SCLATER, J.G., CROWE, J. and ANDERSON, R.N. (1976). On the reliability of oceanic Heat Flow Averages. J. Geophys. Res., 81, p.2997-3006.

SCOTT, M.R., SCOTT, R.B., RONA, P.A., BUTLER, L.W. and NALWALK, A.J. (1974). Rapidly Accumulating Manganese Deposit from the Median Valley of the Mid-Atlantic Ridge. Geophys. Res. Lett., 1, p.355-358.

SEYFRIED, W.E. and BISCHOFF, J.L. (1981). Experimental Seawater-Basalt Interaction at 300°C, 500 bars, Chemical Exchange, Secondary Mineral Formation and Implications for the Transport of Heavy Metals. Geochim. Cosmochim. Acta., 45, p.135-147.

SEYFRIED, W.E. and DIBBLE, W.E. (1978). Chemical Exchange and Secondary Mineral Formation during Seawater-Peridotite Interaction: an Experimental Study. Geol. Soc. Am., Abstr. with Programs, 10, p.490.

SEYFRIED, W.E. and MOTTL, M.J. (1977). Origin of Submarine metal-rich Hydrothermal Solutions: Experimental Basalt-Seawater Interaction in a Seawater-dominated System at 300°C, 500 bars. Proc. of the Second Intl. Symp. on Water-Rock Interaction, I.A.G.C., Strasbourg, France, p.IV173-IV180.

SHANKS, W.C. and BISCHOFF, J.L. (1975). Sulphur Isotopes and Sulphide Deposition in the Red Sea Geothermal System. Abstr. with Programs, 7, Geol. Soc. Am., p.1330.

SKIRROW, R and COLEMAN, M.L. (1982). Origin of Sulphur and Geothermometry of Hydrothermal Sulphides from the Galapagos Rift, 86°W. Nature, 299, p.142-144.

SKIRROW, R. and COLEMAN, M.L. (1982a). Stable Isotope Evidence for the Evolution of Galapagos Rift Inactive Hydrothermal Sulphide Mounds, at 86°W. Inst. Geol. Sci., Isotope Geol. Unit, Stable Isotope Rep. No. 76.

SLEEP, N.H. (1969). Sensitivity of Heat Flow and Gravity to the Mechanism of Sea-Floor Spreading. J. Geophys. Res., 74, p.542-549.

SLEEP, N.H. and WOLERY, T.J. (1978). Egress of Hot Water from Mid-Ocean Ridge Hydrothermal Systems: Some Thermal Constraints. J. Geophys. Res., 83, p.5913-5922.

SMITH, P.A. and CRONAN, D.S. (1975). The dispersion of Metals Associated with an Active Submarine Exhalative Deposit. Proc. 3rd Oceanology Intl., p.111-114.

SOUTHWOOD, M. (1982). Exhalative Cu-Pb-Zn Sulphide Mineralisation at Morfa Du, Parys Mt., Anglesey. Inst. Min. Met., Trans. Sect. B., 91, p.B101.

SPIESS, F.N. et al. (the RISE Project Group), (1980). East Pacific Rise: Hot Springs and Geophysical Experiments. Science, 207, p.1421-1432.

SPOONER, E.T.C. (1976). Hydrodynamic Model for Origin of Ophiolitic Cupriferous Pyrite Ore Deposits of Cyprus. In: 'Volcanic Processes in Ore Genesis.' Proc. Inst. Min. Met. and Geol. Soc. London, p.58-71.

SPRINGER, R.K. (1974). Compositional and Structural Variations in Garnierites. Can. Mineral., 12, p.381-388.

STAKES, D.M. (1978). Submarine Hydrothermal Systems: Variations in Mineralogy, Chemistry, Temperature and Alteration of Oceanic Layer II. Ph.D. Thesis, Oregon State Univ.

STANTON, R.L. (1972). 'Ore Petrology' McGraw-Hill, New York.

STYRT, M.M., BRACKMANN, A.J., HOLLAND, H.D., CLARK, B.C., PISUTHA-ARNOLD, V. ELDRIDGE, C.S. and OHMOTO , H. (1981). The Mineralogy and the Isotopic Composition of Sulphur in Hydrothermal Sulphide/Sulphate Deposits on the East Pacific Rise, 21°N Latitude. Earth Planet. Sci. Lett., 53, p.382-390.

TATLOCK, D.B. (1966). Rapid Modal Analysis of Some Felsic Rocks from Calibrated X-Ray Diffraction Patterns. U.S.G.S. Bull. 1209, Govt. Print. Off., Wash., D.C.

TAYLOR, S.R. (1964). Abundance of Chemical Elements in Continental Crust. Geochim. Cosmochim. Acta, 28, p.1280-1281.

THOMPSON, M. and HOWARTH, R.J. (1976). Duplicate Analysis in Geochemical Practice (2 Parts). Analyst, 101, p.690-709.

THOMPSON, M., RAMSEY, M.H. and COLES, B.J. (1982). Interactive Matrix Matching: a New Method of Correcting Interference Effects in Inductively Coupled Plasma Spectrometry. Communication in Analyst, October, p. 1286-1288.

TOTH, J.R. (1980). Deposition of Submarine Crusts Rich in Manganese and Iron. Geol. Soc. Am. Bull., 91, p.44-54.

TUREKAIN, K.K. and BERTINE, K.K. (1971). Deposition of Molybdenum and Uranium along the Major Ocean Ridge Systems. Nature, 229, p.250-251.

UYTENBOGAARDT, W. and BURKE, E.A.J. (1971). 'Tables for Microscopic Identification of Ore Minerals.' 2nd Rev. Edn., Elsevier, Amsterdam.

VAN ANDEL, T.H., HEATH, G.R. and MOORE, T.C. (1976). Cainozoic History of the Central Equatorial Pacific: A Synthesis based on D.S.D.P. Data. In: G.H. Sutton et al. (Eds.) 'The Geophysics of the Pacific Ocean Basin and its Margin' (Wollard Volume). Amer. Geophys. Union, Geophys. Monogr., 19, p.281-297.

VARNAVAS, S.P. (1979). Geochemical Investigations on Sediments from the Eastern Pacific. Unpubl. Ph.D. Thesis, Univ. London.

VARNAVAS, S.P. and CRONAN, D.S. (1981). Partition Geochemistry of Sediments from D.S.D.P. 424 in the Galapagos Hydrothermal Mounds Field. Mineral. Mag., 44, p.325-331.

VEEH, H.H. (1981). Uranium and Thorium Isotopic Investigations in Metalliferous Sediments of the North West Nazca Plate. Geol. Soc. Am. Memoir 154, p.251-267.

VEEH, H.H. and BOSTROM, K. (1971). Anomalous $^{234}U/^{238}U$ on the East Pacific Rise. Earth Planet. Sci. Lett., 10, p.372-374.

VOGT, P. and JOHNSON, G.L. (1973). Magnetic Telechemistry of the Oceanic Crust. Nature, 245, p.373-375.

WATKINS, P.J. (1980). Analysis of Silicates using a Single Solution Procedure. Tech. Rep. 8, Min./Pet. Section, Dept. Geol., Imperial College.

WELBY, C.W. (1958). Occurrence of Alkali Metals in Some Gulf of Mexico Sediments. J. Sediment. Petrol., 28, p.431-452.

WICKS, F.J. (1969). X-Ray Optical Studies of Serpentine Minerals. D.Phil. Diss., Oxford Univ.

WILLIAMS, D.L., VON HERZEN, R.P., SCLATER, J.G., and ANDERSON, R.N. (1974). The Galapagos Spreading Centre: Lithospheric Cooling and Hydrothermal Circulation. Geophys. J.R. Astron. Soc., 38, p.507-608.

WYLLIE, P.J. (1967). 'Ultramafic and Related Rocks.' John Wiley & Sons, New York.

YEATS, R.S. and HART, S.R. et al. (1976). Initial Reports of the Deep Sea Drilling Project, 34. U.S. Govt. Print. Off., Wash., D.C., 1757p.

ZONENSHAIN, L.P., KOGAN, L.I., SAVOSTIN, L.A., GOLMSTOCK, A.J. and GORODNITSKII, A.M. (1980). Tectonics, Crustal Structure and Evolution of the Galapagos Triple Junction. Mar. Geol., 37, p.209-230.

ZUSSMAN, J. (1977). 'Physical Methods in Determinative Mineralogy.' Academic Press, 2nd Edn., 720p.